



2011

annual progress report

Propulsion Materials

**U.S. Department of Energy
Office of Vehicle Technologies
1000 Independence Avenue S.W.
Washington, DC 20585-0121**

FY 2011

Progress Report for Propulsion Materials

Energy Efficiency and Renewable Energy
Office of Vehicle Technologies
Advanced Materials Technologies

Patrick B. Davis	Program Manager, OVT
Carol L. Schutte	Team Leader, Advanced Materials Technologies
Jerry L. Gibbs	Technology Manager

January 2012

CONTENTS

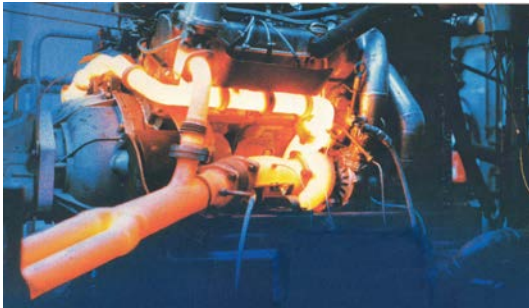
INTRODUCTION.....	1
PROJECT 18516 - MATERIALS FOR HYBRID AND ELETRIC DRIVE SYSTEMS.....	11
Agreement 19201 - Non-rare Earth Magnetic Materials.....	11
Agreement 23278 - Low-Cost Direct Bonded Aluminum (DBA) Substrates.....	17
Agreement 23279 - Improved Organics for Power Electronics and Electric Motors.....	25
Agreement 23726 - Novel Manufacturing Technologies for High Power Induction and Permanent Magnet Electric Motors (GM CRADA).....	31
Agreement 13257 - High Performance Embedded Capacitors.....	37
Agreement 13295 - Permanent Magnet Development for Automotive Traction Motors.....	47
PROJECT 18518 - MATERIALS FOR HIGH EFFICIENCY ENGINES.....	63
Agreement 8697 - NO _x Sensor Development	63
Agreement 9440 - Fabrication of Micro-orifices for Diesel Fuel Injectors.....	73
Agreement 11752 - Materials for HCCI Engines.....	81
Agreement 11754 - Hydrogen Materials Compatibility.....	87
Agreement 13329 - Design Optimization of Piezoceramic Multilayer Actuators for Heavy Duty Diesel Engine Components.....	95
Agreement 15050 - Materials Testing with ACERT Engine (Caterpillar CRADA).....	105
Agreement 15054 - Fatigue Enhancements by Shock Peening.....	109
Agreement 15055 - Tailored Materials for High Efficiency CIDI Engines (Caterpillar CRADA).....	117
Agreement 16303 - Materials for High Pressure Fuel Injection Systems.....	129
Agreement 16304 - High Performance Valve Materials (HVPM).....	133
Agreement 17058 - Compact NO _x Sensor with Built-in Reference.....	139
Agreement 17257 - Materials for Advanced Turbocharger Designs.....	147
Agreement 17894 - NDE Development for ACERT Engine Components.....	151
Agreement 18571 - Materials Issues Associated with Exhaust Gas Recirculation Systems....	161
Agreement 19192 - Titanium for Vehicle Propulsion Applications.....	169
Agreement 19202 - Titanium Friction and Wear: Surface Engineering of Connecting Rods and Other Bearing Components.....	175
Agreement 19217 - Ultra-fast Chemical Conversion Surfaces.....	181
Agreement 23284 - Friction Reduction Through Surface Modification: Integrated Surface Texturing and Coating	189
Agreement 23725 - Tailored Materials for Improved Internal Combustion Engine Efficiency (GM CRADA).....	193
PROJECT 18519 – MATERIALS FOR CONTROL OF EXHAUST GASES AND ENERGY RECOVERY SYSTEMS.....	201
Agreement 9130 - Development of Materials Analysis Tools for Studying NO _x Adsorber Catalysts (CRADA with Cummins, Inc.).....	201
Agreement 10461 - Durability of Diesel Particulate Filters (CRADA with Cummins, Inc.)	213
Agreement 10635 - Catalysis by First Principles.....	225
Agreement 19214 - Effects of Biodiesel Fuel on Diesel Particulate Filter Materials.....	243
Agreement 20091 – Electrically Assisted Diesel Particulate Filter Regeneration.....	253

PROJECT 18865 – APPLICATION SPECIFIC MATERIALS SIMULATION, CHARACTERIZATION, AND SYNTHESIS.....	273
Agreement 9105 - Ultra-High Resolution Electron Microscopy for Characterization of Catalyst Microstructures and Deactivation Mechanisms	273
Agreement 13721 – Low-friction Hard Coatings.....	287
Agreement 13723 - Residual Stresses in Thin Films.....	293
Agreement 14957 - Modeling of Thermoelectrics.....	301
Agreement 15529 – Utilization of Nanofluid Coolants.....	309
Agreement 16308 - Thermoelectrics Theory and Structure	315
Agreement 18340 - Thermoelectric Materials for Advanced Vehicle Energy Recovery.....	321
Agreement 20370 - Life Cycle Modeling of Propulsion Materials.....	343
Agreement 22495 - Nanofluids for HEV Cooling.....	345

INTRODUCTION

Propulsion Materials R&D: Enabling Technologies to Meet Vehicle Technologies Program Goals

The Department of Energy's (DOE's) Office of Vehicle Technologies (OVT) is pleased to introduce the *FY 2011 Annual Progress Report for the Propulsion Materials Research and Development Program*. Together with DOE national laboratories and in partnership with private industry and universities across the United States, the program continues to engage in research and development (R&D) that provides enabling materials technology for fuel-efficient and environmentally friendly commercial and passenger vehicles.



This introduction summarizes the objectives, progress, and highlights of the program in FY 2011. The Propulsion Materials Technology actively supports the energy security and reduction of greenhouse emissions goals of the OVT Program by developing advanced materials that enable development of higher efficiency powertrains for ground transportation. Propulsion Materials works closely with the other disciplines within the OVT Program to identify the materials properties essential for the development of

cost-effective, highly efficient, and environmentally friendly next-generation heavy and light duty powertrains. The technical approaches available to enhance propulsion systems focus on improvements in both vehicle efficiency and fuel substitution, both of which must overcome performance limitations of materials currently in use. The Propulsion Materials Technology activity works with National Laboratories, industry experts, and OVT Program teams on strategies to overcome materials limitations in powertrain performance. The technical maturity of projects funded range from basic science to subsystem prototype validation.

The Propulsion Materials activity is a partner and supporter of the OVT Program Hybrid and Vehicle Systems, Energy Storage, Power Electronics and Electrical Machines, Advanced Combustion Engines, and Fuels and Lubricants research and development (R&D) activities. Projects within the Propulsion Materials activity address materials concerns that directly impact the critical technical barriers in each of these programs -- barriers such as fuel efficiency, thermal management, emissions reduction, waste-heat recovery and reduced manufacturing costs. The program engages only the barriers that involve fundamental, high-risk materials issues.

Enabling Technologies

The Propulsion Materials Technology activity focuses on key technical deficiencies in materials performance that limit expanded capabilities of advanced combustion engines, electric-drive systems, and fuels and lubricants. It provides materials R&D expertise and enabling advanced materials that support the goals of combustion, hybrid, and power electronics development. The program provides enabling materials support for combustion, hybrid, and power electronics development, including the following:

- Materials for high-efficiency combustion technologies, for example, homogenous-charge compression-ignition
- Materials for 55% thermal efficiency heavy-duty diesel engines
- Materials for waste-heat recovery via thermoelectric modules, with potential 10% increase in fuel efficiency

- Materials technologies for effective reduction of tailpipe emissions, including diesel particulate filters, catalyst characterization and testing, and exhaust-gas recirculation (EGR) coolers
- Materials technologies for electric and hybrid-electric vehicles, including advanced power electronics materials and electric motors
- Materials for alternate-fuels vehicles, including materials compatibility and corrosion
- Alternatives to rare and costly materials, for example, rare-earth elements, and technologies to improve overall materials availability, for example, recycling.

The program supports these core technology areas by providing materials expertise, testing capabilities, and technical solutions for materials problems. The component development, materials processing, and characterization that the program provides are enablers of the successful development of efficient and emissions-compliant engines.

Program Organization

The Propulsion Materials Program consists of four R&D projects that support the OVT Program propulsion technologies. Each project consists of several related R&D agreements.

- Materials for Electric and Hybrid Drive Systems
 - Develop materials appropriate for automotive power electronics, electric motors, and other electric and hybrid system applications
- Materials for High Efficiency Engines
 - Develop materials for efficient engine components, such as valve train components, fuel injectors, and turbochargers
- Materials for Control of Exhaust Gases and Energy Recovery Systems
 - Develop materials for exhaust aftertreatment and waste heat recovery applications
- Materials by Design (Application Specific Materials Simulation, Characterization and Synthesis)
 - Adopt computational materials – atomic-scale characterization protocol to develop advanced materials for NO_x catalysts, lithium-ion batteries, thermoelectric generators, and electric motors

Research and development projects and agreements are evaluated annually using strategic objectives. Agreements are evaluated on relevance to OVT Program objectives and supported team's priorities, strength of industrial support for the activity, and perceived value of the R&D activity to the OVT Program. In order to keep the program fresh and up-to-date, more than 10% of the agreements are retired annually. New projects are selected by competitive solicitation in accordance with identified OVT needs.

Selected Highlights:

Materials for Electric and Hybrid Drive Systems

The goal of the Automotive Power Electronic and Electric Machines (APEEM) Program is to reduce the size, weight, and volume of the power electronics without increasing the cost or reducing the reliability. Many, if not most, technical barriers are directly linked to the contemporary material limitations of subcomponents found within devices that comprise inverters, converters, and motors. The material limitations include:

- Insufficient temperature capability
- Excessive thermal insulations
- Excessive electrical insulation

- Insufficient power density in permanent magnets
- Insufficient bandgap

The role of Propulsion Materials is to provide materials support for the components and systems under development by the APEEM sub-program. Research activities will develop improved materials and processes for development of improved thermal management systems, capacitors, motors, and power electronics.

In one project, researchers at Oak Ridge National Laboratory (ORNL) are developing higher-temperature-capable thermally conductive epoxy molding compounds (EMCs) to combat higher junction and service temperatures of power electronic and electric motor components. This entails the combined use of high-temperature-capable thermosets (epoxies) and controlled volume fraction (Vf) and particle size distribution (PSD) of electrically insulative (ceramic) filler. To examine the effect of Vf and PSD on thermal conduction, software was developed that uses those parameters as input and that outputs an input file for use in commercial finite element analysis (FEA) software. An illustration of the thermal transfer through a modeled EMC is shown in Fig. 1.

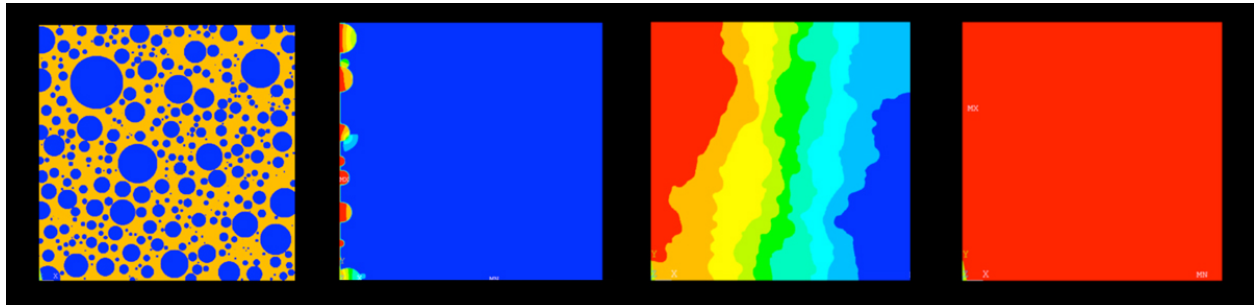


Figure 1. A schematic of a particle-filled EMC is shown to the left. It is thermally "flashed" at the left-hand-side of the second image, and then time-dependent temperature transfer is modeled until it reaches a uniform temperature (far right). The time-temperature profile is then used to estimate thermal diffusivity and thermal conductivity.

Results such as these are guiding the optimization of Vf and PSD and the choice of the thermoset matrix and filler materials. This is important because higher-temperature-capable and thermally conductive EMCs would enable new and improved means to reduce the junction and service temperatures of power electronic modules and electric motor components. For example, if the thermal conductivity of an EMC of a hypothetical film capacitor is 0.5 W/mK – the maximum temperature of the outer annulus is predicted to be 116°C. If the thermal conductivity of the EMC could be increased from 0.5 to 5.0, the temperature of the outer annulus of the capacitor would decrease by more than 50°C. This could lead to more efficient, and smaller and lighter cooling hardware, and consequential longer service lifetimes too of those automotive components.

Materials for High Efficiency Engines

In support of the OVT Program goal of developing a heavy-duty engine with 55% thermal efficiency by 2013, the materials for high efficiency engines project develops materials, material treatments, coatings, and surface treatments necessary to overcome the technical hurdles to these objectives. This project focuses on key material related technical issues identified by the Advanced Combustion Engine (ACE) group and industrial partners.

R&D agreements for high-efficiency engines are either driven by industry needs for specific classes of components, or by the invention of new methods of processing materials or new alloys, which can be exploited to respond to the needs of industry for new materials for high-efficiency engines. The R&D efforts in this Project involve materials development for valvetrain materials, turbochargers, exhaust-gas recirculation (EGR) systems and fuel systems. In addition, processing-driven efforts include those that exploit new technologies in joining, shock peening, friction-stir processing, and processing specifically of titanium alloys. An engine test cell and dedicated diesel engine have been made available for testing advanced materials and components. Highlights from those efforts are described below.

Propulsion Materials Program researchers have been working with Honeywell to develop more robust materials for advanced turbocharger designs. Turbochargers, such as that shown in Fig. 2, are used to increase the mass of air to the cylinders, thereby increasing the efficiency and power output of the engine without increasing the regulated emissions. The dramatic improvements are enabling automotive manufacturers to utilize more efficient six cylinder engines in vans, SUVs and light trucks in place of eight cylinder engines and four cylinder engines for many passenger cars instead of less efficient 6-cylinder engines.



Figure 2. Honeywell turbocharger wheel/shaft assembly consisting of a Ni-based superalloy turbine wheel welded to a steel shaft.

Honeywell is a major internationally competitive turbocharger supplier with their equipment recently being showcased in the high-profile Chevy Cruze Eco* engines in small cars and Ford EcoBoost engines in light trucks and SUVs. Oak Ridge National Laboratory has been working with Honeywell in this project to develop improved materials for the next generation of turbochargers that will be operating at significantly higher temperatures and pressures for further efficiency improvements. Turbocharger housings for diesel and gasoline engines are typically made of cast irons, which have limitations in terms of temperature capability. To overcome this limitation, ORNL has developed a special cast austenitic stainless steel, CF8C-Plus, with higher temperature capability and greater durability for exhaust component applications. Alloying additions of manganese and nitrogen give this alloy excellent castability as well as improved high-temperature strength based on nanoscale dispersions of carbide and nitride precipitates. The CF8C-Plus steel also has good fatigue resistance and aging resistance. Comparisons of CF8C-Plus steel to various cast irons established its superiority. The alloy demonstrated much better creep rupture resistance compared to other more expensive commercial stainless alloys such as HK30Nb (Fig. 3). CF8C-Plus has been commercialized since 2006, with over 450 tons being used for commercial use in diesel engine applications. CF8C-Plus has not yet been commercialized for Honeywell turbochargers, but the material is showing promise for use in next-generation turbochargers that will operate at higher temperatures.

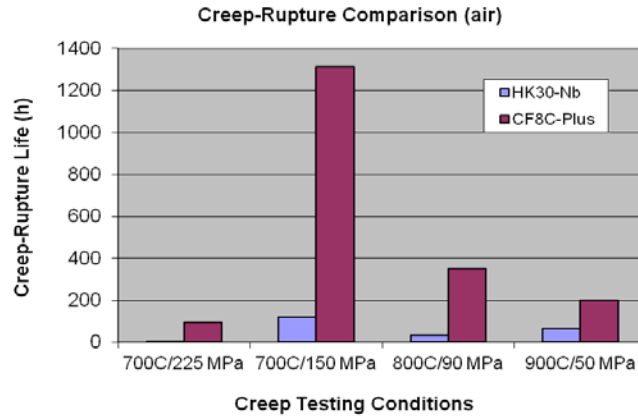


Figure 3. Creep rupture data comparison of CF8C-Plus and HK30Nb cast austenitic stainless steels.

The improved properties and low cost of CF8C-Plus are enabling Honeywell to take the next steps to implement it as an upgrade material to cast irons for turbocharger housings in 4-cylinder and 6-cylinder engines. The initial steps to utilize CF8C-Plus steel as an upgrade material for the turbocharged 3.5L V-6 Ecoboost gasoline engine used to power the Ford light truck series were initiated by Honeywell in FY 2011.

Materials for Control of Exhaust Gases and Energy Recovery Systems

Roughly 30% of the chemical energy stored in the fuel consumed by an internal combustion engine is contained within the flow of engine exhaust gases. This project focuses on development of materials necessary to efficiently control the flow of these exhaust gases while extracting the maximum amount of usable energy from them with minimal negative impact on overall efficiency. The evolving combustion regimes and fuels that high efficiency engines will need to utilize in the future complicate the objectives of this project. Materials developed under this project will be used for high performance components including: thermo-electrics, high temperature exhaust manifolds, exhaust gas recirculation (EGR) coolers, advanced turbochargers, direct energy conversion devices, exhaust gas sensors, and exhaust aftertreatment devices and catalysts.

The advantages of diesel engines over other internal combustion engines are well known: greater fuel efficiency, longer engine life, less waste heat, and minimal carbon monoxide (CO) emissions. Nevertheless, they also exhibit comparably greater emission levels of nitrogen oxide (NO_x) and particulate matter (PM), both of which are regulated by the Environmental Protection Agency. Prominent among the exhaust aftertreatment devices for PM control are diesel particulate filters (DPFs). More stringent regulation of PM went into effect in 2007, and efficient DPFs are essential to meeting these requirements.

Critical to vehicle emissions control, the filter removes soot and particulates from diesel exhaust. Most DPFs are ceramic (cordierite, silicon carbide or aluminum titanate) with hundreds of channels that are plugged in a way that forces the exhaust gas to flow through the ceramic wall thereby leaving the PM behind. Increasing the porosity of the filter materials reduces the back pressure which improves the overall efficiency. As the filter becomes loaded with PM or 'soot cake' the back pressure increases which necessitates a regeneration of the filter which is done by injecting fuel into the emissions system thereby burning the soot. Because ceramics are highly heat resistant, they can typically withstand the high temperatures of the regeneration cycle; however under excessive stress, the DPF can crack and fail.

Diesel particulate filter service life predictions are based on a combination of experimentally determined strength data, stress analyses of the component using a finite-element analysis, and selection of

This issue of a lower elastic modulus is positive news because it indicates that, while the filter is under thermally-induced strain, such as during regeneration, the actual internal stresses are much lower and mechanical reliability is much higher than manufacturer models have predicted in the past. Oak Ridge National Laboratory's modeling techniques have proven successful in developing a better understanding of the relationship between microstructural properties of ceramic materials and their performance in DPFs. Additional advances in the research and modeling of diesel engine component performance can promote greater acceptance of diesel engines by the public, resulting in better fuel efficiency and reduced petroleum usage while still meeting EPA regulations.

Materials by Design (Application Specific Materials Simulation, Characterization and Synthesis)

Application specific materials simulation, characterization, and synthesis is a materials discovery and development approach consisting of computational modeling and materials characterization, often at the nanoscale (i.e., at length scales down to and including atomic and sub-atomic) to elucidate and enable the prediction of structure-function relationships of materials to be developed for specific applications. Propulsion materials research uses "materials by design" to ensure the success of emerging technologies such as new power electronics, advanced internal combustion engines, hybrid systems, and emission reduction technologies. This approach, along with advanced materials characterization instrumentation and synthesis techniques, will be used to postulate new materials, compositions, and structures to greatly enhance the materials properties necessary for advanced high performance propulsion systems.

Ultra-high-resolution aberration-corrected electron microscopy is making important contributions to understanding atomic-level mechanisms that control the behavior and performance of catalytic materials. Fundamental imaging studies of the distribution of catalytic species down to the single-atom level on both real and experimental catalysts have shown the ability of single atoms to catalyze reactions. These techniques are being extended via advanced capabilities for *in situ* studies of catalytic reaction processes. Oak Ridge National Laboratory is partnering with another national laboratory (e.g., Pacific Northwest National Laboratory), universities (e.g., University of Michigan, University of Missouri-St. Louis), and industry partners (e.g., Ford) to use these capabilities for studies of catalytic materials and reactions leading to improved automotive catalysts.

Oak Ridge National Laboratory contributions to this project are furthering catalyst studies with our partners through the development of innovative new capabilities for treating catalytic materials *in situ* at elevated temperatures and under reactive gas conditions. This allows atomic-level imaging in the aberration-corrected electron microscope that elucidates mechanisms of catalyst behavior in environments similar to real-world exhaust conditions.

We have been working for several years with industry partner Protochips Co. (Raleigh, NC) who provide unique heater devices (Aduro™) based on microelectromechanical systems fabrication processes that are adaptable to electron microscope holders. We are currently using a third-generation design (Gen 3) environmental cell, or "E-cell," holder for reaction studies that incorporates Aduro™ heaters. This new holder is part of a suite of other heating holders that have been developed at ORNL, that provide the ORNL research staff with unsurpassed capability for *in situ* experimentation.

Working with partners at the University of St. Louis and the Chinese Academy of Sciences, we have also shown via sub-Ångström resolution imaging coupled with surface analytical techniques that single atoms can catalyze reactions, and be stable for long times.

New NO_x-reduction materials called "intelligent catalysts," are currently being studied in conjunction with Ford and the University of Michigan. They are composed of precious metal species such as Pt and Rh in perovskite (i.e., CaTiO₃ or 'CTO') supports. *In situ* oxidation and reduction cycling experiments are being conducted to obtain a fundamental understanding of the mechanisms and kinetics of the cyclic

dissolution and subsequent reformation of catalytic nanoparticles on support surfaces during the redox cycles. Remarkably, studies of a Rh-CTO catalyst in the Gen 3 E-cell showed that atomic structure at the Angstrom level can be imaged at elevated temperatures in gas pressures up to a full atmosphere in the cell, with essentially no loss of signal. This capability is demonstrated in Fig. 6.

Figure 7 shows results of a reduction experiment on a Pt-CTO material. An as-oxidized aggregate of CTO (left) shows nascent Pt nanoparticles present, imaged at 250°C with vacuum in the cell (HAADF image). Because the Aduro™ heaters allow heating and cooling at a rate of 1 million degrees centigrade per second, a reduction treatment in a hydrogen/argon gas mixture at 50 Torr pressure was then conducted for precisely 60 sec at 800°C, and a similar HAADF image was then made (right). Results show many additional Pt nanoparticles decorating the CTO aggregate, and particularly in profile on the surface of the aggregate. ORNL's *in situ* heating technology is the only method in the field that presently allows such precision control of a reaction process, in time, temperature and pressure.

Platinum (Pt) atoms (single-atom catalyst) on an iron oxide support, at a loading of 0.17% Pt, showed more stability and better activity than a commercial gold/iron-oxide catalyst with 4.4% loading of Au, for catalyzing the oxidation of CO (see Fig. 8). Our results were published in *Nature Chemistry*, **V.3**, pp. 634-41, August 2011.

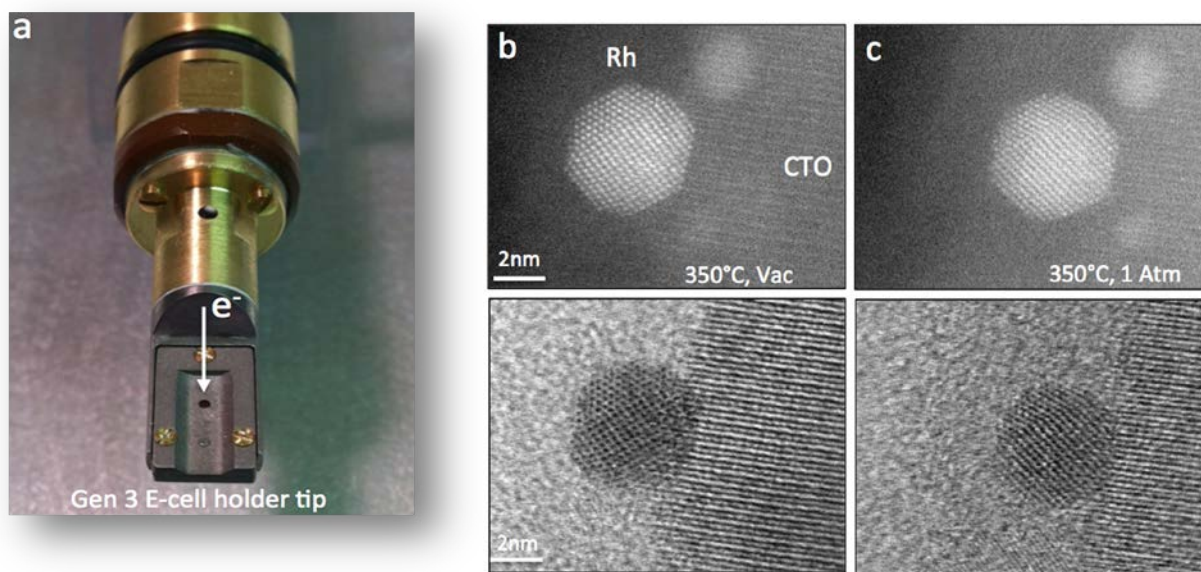


Figure 6. A view of the E-cell in panel (a), and a well-oriented Rh nanoparticle on a CTO support particle, with vacuum in the cell, and with air at atmospheric pressure in the cell, in panels (b) and (c) respectively. Top images are high-angle annular dark-field (HAADF) mode, and bottom images are bright-field mode. Dark field shows higher atomic numbers in brighter contrast.

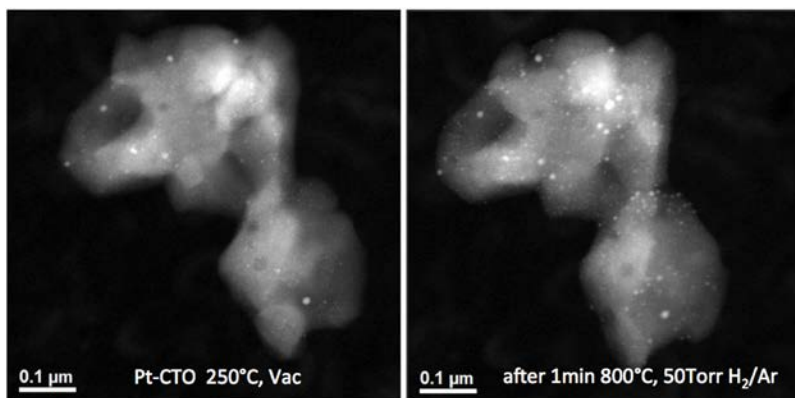


Figure 7. Results of a reduction experiment on a Pt-CTO material using ORNL’s specialized *in situ* heating technology.

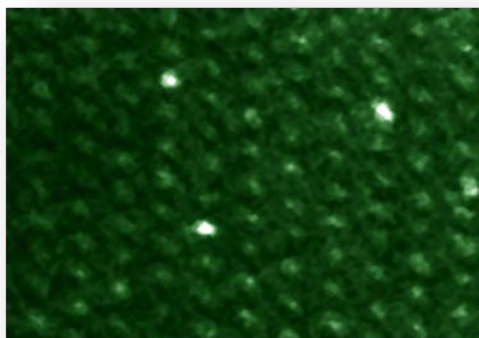


Figure 8. HAADF image (colorized) showing 3 Pt atoms on the surface of an iron oxide (Fe_2O_3) support particle. First example of a “single-atom” catalyst.

Research utilizing the novel E-cell is advancing the understanding of catalytic processes and mechanisms – and we hope will eventually lead to the development of aftertreatment systems that lower vehicle emissions at reduced cost (due to lower catalyst loadings) and better performance.

Carol L. Schutte
Team Leader, Advanced Materials Technologies
Office of Vehicle Technologies
Energy Efficiency and Renewable Energy

Jerry L. Gibbs
Technology Manager
Office of Vehicle Technologies
Energy Efficiency and Renewable Energy

Project 18516 – Materials for Hybrid and Electric Drive Systems

Agreement 19201 – Non-Rare Earth Magnetic Materials

M. A. McGuire, N. J. Ghimire, D. J. Singh*

Materials Science and Technology Division

Oak Ridge National Laboratory

P.O. Box 2008, MS 6056, Bldg. 3150

Oak Ridge, TN 37831-6056

(865) 574-5496; fax: (865) 574-4814; e-mail: m McGuire@ornl.gov

** University of Tennessee, Knoxville, TN*

DOE Technology Manager: Jerry L. Gibbs

(202) 586-1182; fax: (202) 586-1600; e-mail: jerry.gibbs@ee.doe.gov

ORNL Technical Advisor: David P. Stinton

(865) 574-4556; fax: (865) 241-1034; e-mail: stintondp@ornl.gov

Contractor: Oak Ridge National Laboratory, Oak Ridge, Tennessee

Prime Contract No.: DE-AC05-00OR22725

Objectives

- Discover new, strong, permanent magnet materials which do not contain rare earth elements.
- Develop an understanding of the magnetic properties of discovered materials using properties measurements and first-principles calculations to direct work towards improved permanent magnet properties.

Approach

- Investigate understudied known materials and search for new materials in rare earth-free chemical systems which hold promise for the discovery of new high-temperature ferromagnets with the large magnetic moments and strong anisotropies required for technologically useful permanent magnet materials.
- Target materials which contain a high concentration of magnetic *3d* elements (e.g. Cr, Mn, Fe, Co) along with heavier *4d* or *5d* transition metals (e.g. Zr, Hf, Nb, Ta, Mo, W) which have strong spin-orbit coupling.
- Focus on anisotropic crystal structures to allow strong magnetocrystalline anisotropy.

Accomplishments

- Demonstrated increased energy product of Hf₂Co₁₁-based melt-spun alloys by varying composition and synthesis conditions. Imaged microstructure showing complex, multi-phase composition.
- Discovered ferromagnetism with Curie temperatures up to 270 K, and evidence for competing magnetic behaviors in ZrFe_{12-x}Al_x and HfFe_{12-x}Al_x. Determined crystal structure and T-dependence of physical properties.
- Identified metal-flux crystal growth technique as a promising route to new ternary materials containing the chemical elements relevant for this project and demonstrated proof-of-principle.

Future Direction

- Focus on discovery of new ternary and quaternary materials in candidate chemical systems combining Cr/Mn/Fe with heavy transition metals and light p-block elements using metal-flux crystal growth technique identified in FY2011.
 - Pursue magnetic field processing of ferromagnetic materials in collaboration with the Materials Processing Group at ORNL to examine potential benefits of synthesizing, annealing, and consolidating materials at high temperatures and magnetic fields.
 - Examine the feasibility and effects on magnetic properties of the addition of small amounts of nitrogen to intermetallic ferromagnets through reaction with ammonia vapor.
-

Introduction

The strategic importance of rare earth elements (REEs) and the associated potential problems are receiving increased attention due to their use in permanent magnets (PMs) for electric motors. There are currently no alternative PM materials competitive with $\text{Nd}_2\text{Fe}_{14}\text{B}$ which do not contain REEs. The development of such materials would allow progress toward lowering the cost of electrical propulsion systems toward the performance goals of \$12 /kW by 2015 and \$8 /kW by 2020 for the Hybrid and Electric Propulsion subprogram set forth by the FreedomCAR and Vehicles Technologies Program. The Propulsion Materials Technology activity has identified limited domestic supply of materials required for advanced vehicle technology, among them REEs, as a key barrier to enabling expanded capabilities of electric drive systems.

The technical barrier that must be overcome in this research area is related to the role that the REE plays in current state-of-the-art PMs. Realizing good PM behavior (large remanent magnetization and high coercivity) requires strong magnetic anisotropy. This anisotropy gives preference to a particular orientation of the magnetic moment, and presents an energetic barrier to the reorientation of the net moment required to demagnetize the material. There are two sources of magnetic anisotropy: shape anisotropy (an extrinsic property) and magnetocrystalline anisotropy (an intrinsic property). Shape anisotropy results from the difference in demagnetization factors along different directions in non-spherical magnetic particles. Magnetocrystalline anisotropy arises from the interactions between the magnetic moments and the crystal lattice, giving a preferred direction for the magnetization. Spin-orbit interactions couple the magnetic moment (spin) to the atomic orbitals of the magnetic atoms. Strong covalent bonding can fix the orientation of these atomic orbitals with respect to the crystal structure. The combination of these two phenomena, covalent bonding and spin-orbit coupling, results in a preferred direction for the alignment of the magnetic moments, which is manifested as magnetocrystalline anisotropy. This is expected to be strongest in materials with anisotropic crystallographic structures (non-cubic).

In REE magnets, the strong spin-orbit coupling and large magnetic moment of the REE is crucial to providing strong magnetic anisotropy. The primary

technical barrier to the development of better non-RE PMs is achieving strong magnetocrystalline anisotropy in the absence of REEs. Strong spin-orbit coupling is not unique to REEs. Its strength is proportional to the atomic number, and is thus high in all heavy elements. PtCo has strong magnetocrystalline anisotropy due to the large spin-orbit coupling of Pt and its interaction with the 3d Co moments. Despite the high cost of Pt, this material has seen commercial use in magnetic recording applications. This example demonstrates the potential of using heavy *d*-block transition metals to play the role of REEs.

We believe that the most promising chemical systems for discovery and development of new PM materials are those that include the 3d transition metals Cr, Mn, Fe, and Co with heavy 4d or 5d metals like Zr, Hf, Nb, Ta, Mo, W. Early in this work we investigated binary W_6Fe_7 -type materials and effects of replacing W and Fe with other heavy and light transition metals, respectively. Compounds we studied in this structure type proved to be antiferromagnetic or non-magnetic. In FY2011, first principles calculations were performed on the ferromagnetic binary Laves phase HfFe_2 to access its PM potential. The results indicated little intrinsic anisotropy is expected. Identifying and analyzing candidates such as these among known compounds is one path toward new hard ferromagnets. However, the discovery of entirely new materials is likely to have the largest long term impact on technology. This requires examining ternary (or higher) systems, as binary compositional phase diagrams are generally well characterized. We note that moving beyond binary compounds was important in the development of RE magnets as well. Better PM properties are realized in ternary $\text{Nd}_2\text{Fe}_{14}\text{B}$ -based materials than the in the best binary compounds based on SmCo_5 .

This project's objective is to use the ideas outlined above to target new and known materials with the aim of identifying rare earth-free chemical systems which contain permanent magnets with potential for use in electric motors. Replacing $\text{Nd}_2\text{Fe}_{14}\text{B}$ is a serious and important materials challenge which likely will require long term research efforts, and which must begin with advancements in performance and understanding of non-RE magnets, and perhaps most importantly, the discovery and development of new materials.

Results

We discuss here several accomplishments from our research in FY2011. These include results from our continued study of melt-spun alloys based on Hf_2Co_{11} . We have demonstrated effects of melt-spinning conditions and boron concentrations on the energy product, a figure of merit for hard ferromagnets. We have also used microstructure imaging and high temperature magnetization measurements to deduce the presence of more than one magnetic phase in these alloys. We also report here our discovery of ferromagnetism in Zr/Hf-Fe-Al compounds with the $ThMn_{12}$ structure-type, and evidence for complex magnetic behavior in some compositions. Finally, we comment on the identification of metal-flux crystal growth as a route to new materials in the chemical systems of interest in this research area.

Hf₂Co₁₁-based alloys

These materials were identified as promising candidates for non-rare earth permanent magnets based on the following criteria: (1) they contain a high concentration of Co, (2) they contain the heavy transition metal Hf, (3) they adopt an anisotropic crystal structure, and (4) the Zr analogue has been reported to be a high temperature ferromagnet. Our study of these materials is ongoing. Here we report the most interesting findings for these alloys from FY2011.

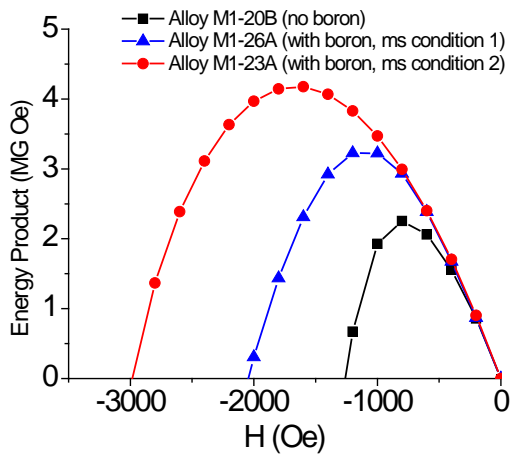


Figure 1. Demonstration of the effects of boron addition and melt-spinning (ms) conditions on the magnetic energy product for $Hf_2Co_{11}B_x$.

The materials are synthesized by arc melting followed by melt-spinning. The melt-spun ribbons

show hard magnetic behavior at room temperature. The magnetic energy product for three samples is shown in Figure 1. The energy product (BH) is defined as the product of the magnetic induction of the sample (B) and the applied magnetic field (H) obtained in the second quadrant of the magnetic hysteresis loop, or the demagnetization curve. Here $B = 4\pi M + H$ where M is the measured magnetic moment of the sample. The maximum in the energy product is used as a figure of merit for PM materials. The data in Figure 1 show that the PM properties are improved by the addition of boron to the melt, as well as by tuning the melt-spinning conditions. We find that all of these Hf_2Co_{11} based materials have similar remanent magnetizations (~4500 G), and that improvements in BH arise primarily from increases in coercive field from about 1200 to about 3000 Oe.

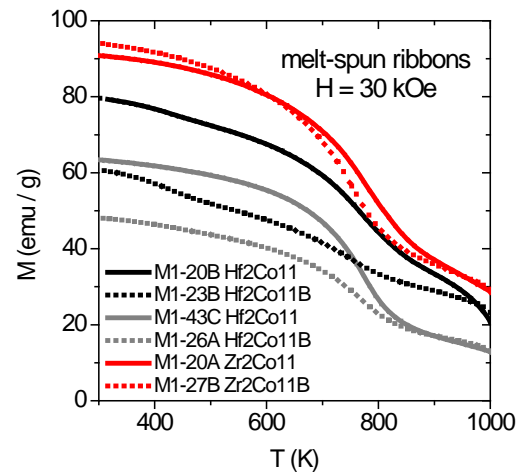


Figure 2. Magnetization vs. temperature measured on cooling from 1000 K in an applied field of 30 kOe. The black and gray data for the Hf containing materials represent two different melt-spinning conditions.

Through collaboration with researchers at the University of Tennessee, we have measured the magnetization up to 1000 K of melt-spun materials containing either Hf or Zr, as well as with and without the addition of boron. The results are summarized in Figure 2. All of the materials show Curie temperatures near 750 K which we associate with the primary phase of the material. However, evidence for ferromagnetism at even higher temperatures is also observed. The measured moment is large up to the highest temperatures, and shows a

curvature suggesting a second Curie temperature above 1000 K. This is a strong indication that the melt-spun materials are multiphase.

In an effort to understand the multiphase nature, as well as the magnetic anisotropy and resulting coercivity in these materials, we have used scanning electron microscopy to image the microstructure of an as-made ribbon of composition $\text{Hf}_2\text{Co}_{11}$. This work was performed through collaboration with Orlando Rios in the Materials Processing Group at ORNL. One of the images collected from a cross section of the ribbon is shown in Figure 2. The results show an evolution of the microstructure from fine-grained at the surface which contacted the Cu wheel, to a dendritic-like interior, to a coarser-grained free side. The relative brightness of a region in Figure 2 is related to its chemical composition; brighter regions have higher average atomic number. The material clearly contains at least two phases, with a Co-rich “dark” phase at the interfaces between grains of the primary “light” phase.

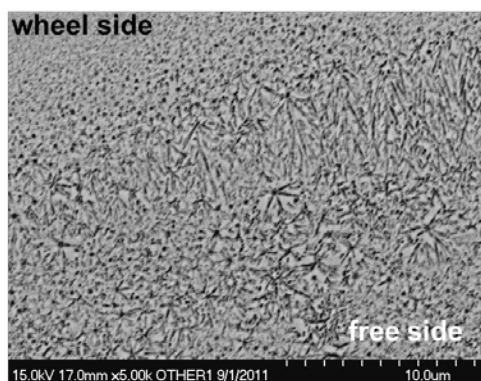


Figure 3. Scanning electron microscopy image of a cross section of a melt-spun $\text{Hf}_2\text{Co}_{11}$ ribbon. The backscattered electron image is brightest in regions with largest average atomic number (highest Hf content).

In addition to the intrinsic magnetocrystalline anisotropy, the microstructure shown in Figure 3 suggests that shape and grain boundary effects are likely also important. We have observed that annealing the melt-spun ribbons in an inert atmosphere for at 600 °C strongly softens the magnetic properties, decreasing the coercive field by more than a factor of two. Figure 4 shows the microstructure of the annealed material. In comparison with the as-spun material shown in Figure 3, the annealed sample

shows significantly less contrast between phases, and most importantly, the phase fraction of the “dark” phase is strongly reduced. These observations indicate the Co-rich “dark” phase makes an important contribution to the hard magnetic properties of these materials.

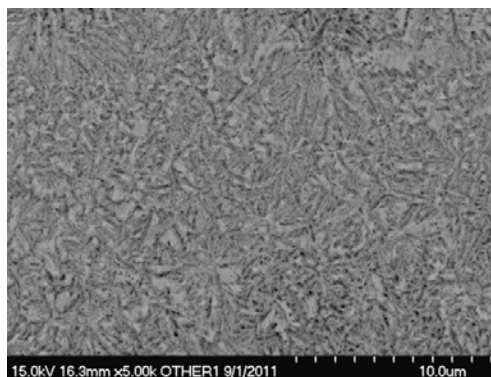


Figure 4. Scanning electron microscopy image of a cross section of a melt-spun $\text{Hf}_2\text{Co}_{11}$ ribbon after annealing at 600 °C for 2 days, for comparison with the as-spun ribbon shown in Figure 2.

We expect that the features in the microstructure to be dependent upon synthesis procedures. Microstructure studies on samples synthesized with varying boron content and melt-spinning conditions are still underway. The results will provide valuable information when coupled with the observed dependence of the magnetic behavior upon these variables.

$\text{ZrFe}_{12-x}\text{Al}_x$ and $\text{HfFe}_{12-x}\text{Al}_x$

Our investigation of new materials with the aim of discovering hard ferromagnets has focused on ternary phase diagrams containing Fe/Mn/Cr with heavy transition metals Hf/Ta/W and the third period p-block elements Al/Si/P. The ThMn_{12} structure type attracted our attention, as it is uniaxial (tetragonal) and is known to combine some of these target elements. This structure-type is often adopted by rare earth – transition metal intermetallics, but also forms with some heavy transition metals in place of the REE.

Study of these materials led to our discovery of ferromagnetism in $\text{ZrFe}_{12-x}\text{Al}_x$ and $\text{HfFe}_{12-x}\text{Al}_x$. Powder x-ray diffraction was used to determine the crystal structure and atomic site occupancies for materials with $x = 6.0, 6.5,$ and 7.0 . The crystal structure is

shown in Figure 5. We find the variation in Fe content ($12-x$) to affect primarily the occupation of a single, mixed Fe/Al site, while other site occupancies remain unchanged.

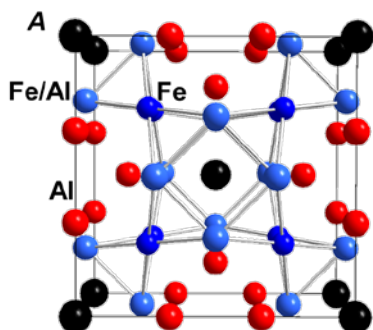


Figure 5. A view of the ThMn_{12} crystal structure type adopted by $\text{AFe}_{12-x}\text{Al}_x$. The relative amounts of Fe and Al occupying the site labeled Fe/Al is controlled by “ x ” in the chemical composition.

Magnetization measurements (Figure 6) revealed ferromagnetic transitions occurring just below room temperature (near 270 K) in ZrFe_5Al_7 and HfFe_5Al_7 . Increasing the iron content to obtain ZrFe_6Al_6 and HfFe_6Al_6 surprisingly resulted in a decrease in the Curie temperature to approximately 200 K. In addition, increased iron content results in a non-monotonic temperature dependence of the magnetic susceptibility below the Curie temperature as shown in Figure 6. This suggests that the iron on the mixed Fe/Al site may couple antiferromagnetically to the primary ferromagnetic iron sublattice. Better PM properties may be achieved by replacing some of the Fe with other transition metals so that increased 3d metal concentrations can be achieved without inducing antiferromagnetic-like behavior. This could result in higher Curie temperatures and larger saturation moments. Such experiments are currently underway.

Flux growth of metal rich ternary compounds

The high melting temperatures of many of the metals of interest for PM applications complicates the inclusion of more volatile elements as constituents in the ferromagnetic phases. Exploration of compounds which contain these volatile components often cannot proceed by traditional melting proce-

dures. We have begun examining ternary phosphide phase diagrams, and have identified the molten-metal-flux growth technique as a promising route to new phases in these systems. In this technique, a low melting point metal like tin or aluminum is used as a solvent (flux) to dissolve other elements at elevated temperatures. Crystal growth ensues upon cooling the mixture. Available binary phase diagrams help to determine which fluxes should work best for which target elements.

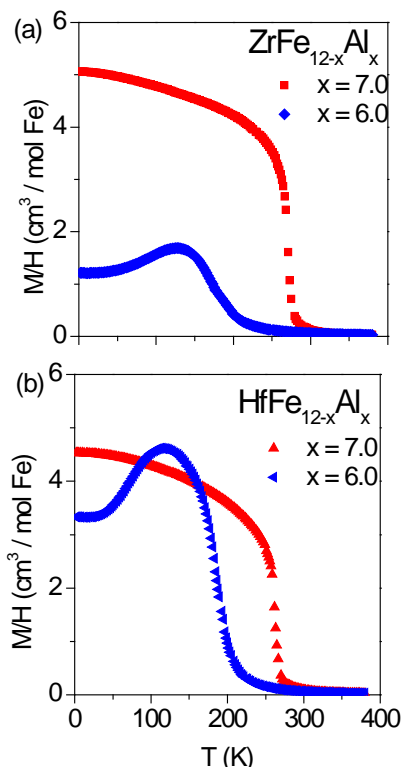


Figure 6. Low field magnetic susceptibility of $\text{ZrFe}_{12-x}\text{Al}_x$ and $\text{HfFe}_{12-x}\text{Al}_x$ measured upon cooling from 380 K showing Curie temperatures approaching room temperature and evidence of competing magnetic interactions as the iron content is increased.

Examination of published literature shows that this procedure has been used successfully to produce many phosphorus rich binary and ternary compounds with a tin flux. We have begun expanding this to metal rich compounds which contain a low concentration of phosphorus. We have already had success in growing crystals in the following chemical systems: Hf-Fe-P, Hf-Mn-P, Zr-Fe-P, and Ta-Fe-

P. The addition of a second component to the flux has been found to aid in the crystallization of some of these materials, likely due to increased solubility for one or more constituent. Crystals of ternary materials containing about 70 atomic percent iron have been synthesized. These are encouraging results and will be pursued further as the project continues.

Conclusions

In FY2011 we continued our investigation of rare earth-free, transition metal rich systems begun in the previous year. We have demonstrated improvements in both performance and understanding of our $\text{Hf}_2\text{Co}_{11}$ -based alloys. We expect further improvements to come as we learn more about the composition and microstructure of these interesting materials. Our search for new materials led to the discovery of ferromagnetism in $\text{HfFe}_{12-x}\text{Al}_x$ and $\text{ZrFe}_{12-x}\text{Al}_x$. Curie temperatures in these materials are just below room temperature, but may be improved with other transition metals. In addition, we have identified the metal-flux growth technique as a promising route to new metal rich phosphides, and demonstrated its usefulness for compounds relevant for new PM materials research.

We are continuing to make progress by following our strategy of combining strongly magnetic 3d transition metals with heavy transition metals and other light elements in new ways to produce interesting new magnetic materials. We will build on the results from FY2011 as the project continues to identify and characterize new, rare earth-free compounds with potential for PM applications.

Agreement 23278 – Low-Cost Direct Bonded Aluminum (DBA) Substrates

H.-T. Lin, A. A. Wereszczak, and S. B. Waters

Ceramic Science and Technology Group

Oak Ridge National Laboratory

P.O. Box 2008, MS 6068, Bldg. 4515

Oak Ridge, TN 37831-6068

(865) 576-8857; fax: (865) 574-6098; e-mail: linh@ornl.gov

DOE Technology Manager: Jerry L. Gibbs

(202) 586-1182; fax: (202) 586-1600; e-mail: jerry.gibbs@ee.doe.gov

ORNL Technical Advisor: David Stinton

(865) 574-4556; fax: (865) 241-1034; e-mail: stintondp@ornl.gov

Contractor: Oak Ridge National Laboratory, Oak Ridge, Tennessee

Prime Contract No.: DE-AC05-00OR22725

Objectives

- Develop low-cost, high quality, and thermomechanically robust direct-bonded aluminum (DBA) substrates
- Develop low-cost, direct-bonded alumina substrates that are at least 25% lighter than conventional direct-bonded copper substrates.

Approach

- Develop innovative ways to fabricate their ceramic constituent (e.g., low-cast AlN substrate)
- Benchmark existing commercial available DBA and direct-bonded copper (DBC) substrates
- Develop test method to measure interfacial shear strengths of Al-ceramic interface.

Accomplishments

- Completed literature survey of Al-Si phase diagrams and Al-ceramic bonding patents and references.
- Completed microstructure and chemical composition analysis of commercial DBA and DBC substrates.
- Completed initial screening and trial of Al-ceramic bonding routes.

Future Direction

- Benchmark commercial DBA and DBC substrates via measurements of physical and mechanical properties.
- Develop innovative interfacial bonding materials such as Al-Si brazing paste or tape-casted Al-Si thin film.
- Develop innovative routes to their manufacture via brazing, bridging metallurgical coating, induction heating or field-assisted bonding process.

Introduction

Application of low-cost direct-bonded aluminum (DBA) substrates will enable to lessen the cost of the inverter insulated gate bipolar transistor (IGBT) power modules while concomitantly sustaining or improving thermal management and improving thermomechanical

reliability performance. Compared to copper and direct-bonded copper (DBC) substrates, aluminum has a lower elastic modulus so it imparts a lower stress on the ceramic substrate it sandwiches, and this contributes to improved mechanical reliability of the entire substrate. Also, wire and ribbon used for bonding in power electronic modules tends to be aluminum, so the apparent coefficient of thermal

expansion of DBAs is compatible with them unlike DBCs. And new sintering technologies would be more compatible with DBAs than DBCs too. The use of a DBA substrate will also lessen the weight up to 50% compared to presently used DBC substrates, and this would contribute to the substantial weight reduction goals of the inverter and converter in the Advanced Power Electronics and Electric Motors (APEEM) program as well.

On the other hand, reducing cost, improving volumetric power, extending reliability, and improving thermal management are all barriers to the goals for the Vehicle Technology's APEEM program. If DBAs could be fabricated cheaply, then their use would inherently address those other barriers. DBA substrates are presently difficult to fabricate due to the inherent bonding issue between aluminum and alumina. These DBAs are now only available from a limited numbers of suppliers, and therefore are expensive. Despite Toyota presently using DBA substrates in their 2010 Prius, domestic automotive OEMs would more seriously consider using DBA substrates in their own inverters if they were cheaper and more readily available.

The objective of this subtask is to develop low-cost, high quality, and thermomechanically robust DBA substrates, which are comparable to those commercially available ones. The ultimately goal is to facilitate the achievement of 2015 APEEM goal of \$12/kW for electric traction system.

Results

Literature survey

A literature search including phase diagram, patents, and published references was conducted in the beginning of this fiscal year on conventional and alternative processing methods to directly bond aluminum (Al) to alumina (Al_2O_3) or alumina nitride (AlN). In general, Al could be bonded to Al_2O_3 (and AlN) substrates by placing and then melting a piece of brazing film (e.g., Al-Si alloys) between the two materials, as depicted in Fig. 1 [1-4]. The diffusion of brazing element (like Si) into Al would result in a good bonding. The other approach involved in the direct melting or casting of Al on Al_2O_3 (and AlN) substrate without the use of brazing film [5]. On the other hand, the transient-liquid-phase (TLP) approach has been widely

applied to manufacture direct bonded aluminum (DBA) substrates [6-9]. Aluminum is known to form transient eutectic liquid phase products with elements of Si (577°C), Ge (420°C), Ag (567°C), and Cu (548°C), as depicted in Fig. 2. These elements could be deposited on the Al surface via the vapor deposition or slurry screen-printing process prior to the final bonding step carried out above the eutectic liquid temperatures. Results showed that the use of Si and Cu exhibited relatively better reliability and lifetime performance after thermal cycle testing [7].

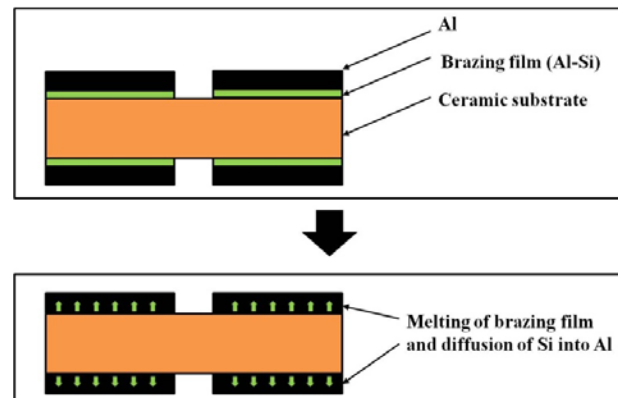


Figure 1. Schematic depicts the bonding process of DBA via the use of Al-Si brazing film.

Benchmarking of commercial DBA and DBA

Microstructure - Microstructure characterizations of commercially available DBA and DBC substrates were performed to provide a reference database. Figure 3 and 4 show the typical microstructure of DBA substrates acquired from two commercial companies (designated as DBA-A and DBA-B) in Japan. Both substrates have the aluminum sheets that are cladded on both sides of the aluminum nitride (AlN) substrate, and the interface is very intact and coherent without any type of defects. At a higher magnification the commercial DBA-A substrate shows the presence of an interfacial layer ($\sim 20 \mu\text{m}$) with random distribution of Al-Si particles between the Al and AlN (Fig. 3b), suggesting the use of Al-Si alloy for the bonding manufacturing process. On the other hand, the presence of Al-Si layer is not very apparent in the commercial DBA-B substrate (Fig. 4b). Note that the light secondary phase in the AlN ceramic substrate is identified to be with the

chemical elements of Y, Al, and O, consistent with the Y_2O_3 and Al_2O_3 additives typically used in the sintering of AlN ceramics. Figure 5 and 6 show the microstructure of a commercial DBC-A and DBC-B substrate. There is a distinctive interfacial layer (~50 μm) between Cu and AlN ceramic with chemical composition of Ag, Cu, Al, and Mg, which suggests the use of Ag-containing material for the bonding of this DBC-A. However, there is a clean interface observed in DBC-B substrate, suggestive the use of O-Cu eutectic liquid phase approach to form this DBA.

physical properties would be used for modeling the temperature profile and thermomechanical stress under simulated application condition and thus probabilistic reliability prediction. The measured CTE of commercial Al_2O_3 and AlN substrate is $7.5 \times 10^{-6} / ^\circ C$ and $4.5 \times 10^{-6} / ^\circ C$, respectively, which are consistent to the reported values of $8.2 \times 10^{-6} / ^\circ C$ and $4.5 \times 10^{-6} / ^\circ C$. In addition, results showed that the CTE values of Al_2O_3 were insensitive to the substrate thickness (between 0.64 mm and 53 mm) investigated in this study, suggesting the reproducibility of the data and consistency of the quality of Al_2O_3 material substrates. In addition, properties of Young's modulus and Poisson ratio of Al_2O_3 and AlN are measured using the resonance ultrasonic spectroscopy (RUS), and results are listed in Table 1. The obtained properties are also consistent with the reported values provided by material suppliers as well as literatures.

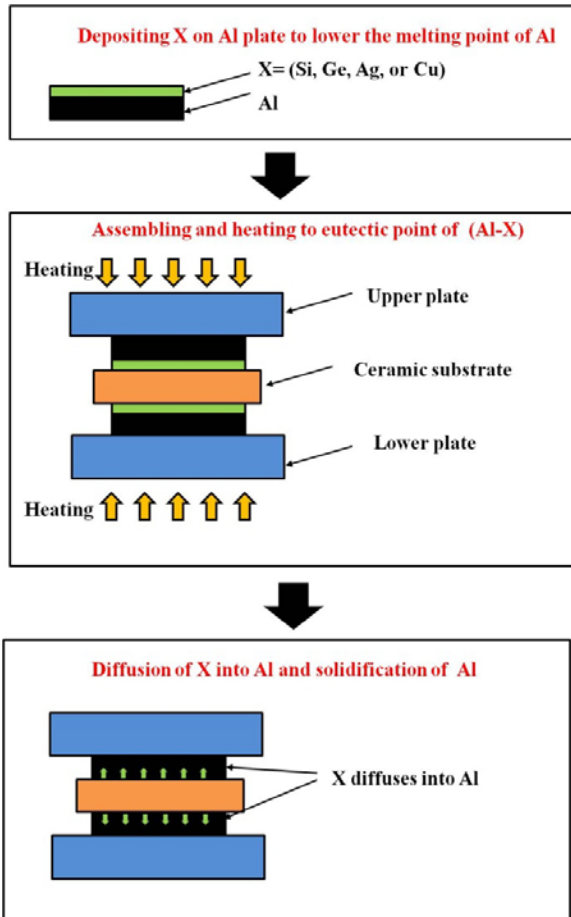


Figure 2. Schematic depicts the fabrication process of DBA substrates via transient liquid phase (TLP) process.

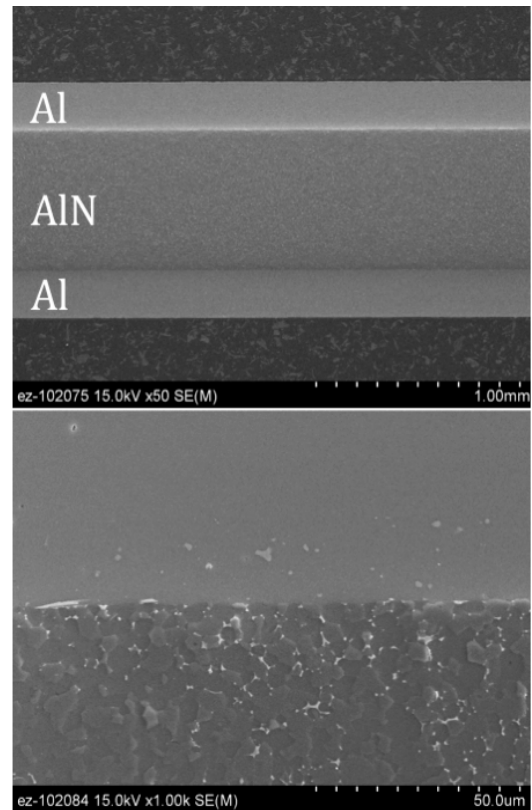


Figure 3. SEM micrograph of commercial DBA-A.

Physical properties - The coefficient of thermal expansion (CTE) of commercial Al_2O_3 and AlN substrate was measured and analyzed. These

Development of DBA substrates

The particle morphology and chemical composition of a commercial Al-12Si brazing paste (designated as DayBraze 729) inquired from Johnson Manufacturing Company, Princeton, Iowa were well characterized prior to the bonding study. Figure 7 shows the typical microstructure of the Al-Si paste with average particle size of 1-2 micron and the particle size distribution is somewhat uniform. The EDAX analysis shows the paste containing chemical elements of Al, Si, K, and F. Note that the addition of F is typically used as a flux agent. A preliminary experimental run to bond the aluminum to both Al₂O₃ and AlN substrates was performed to study the feasibility of this commercial Al-Si paste.

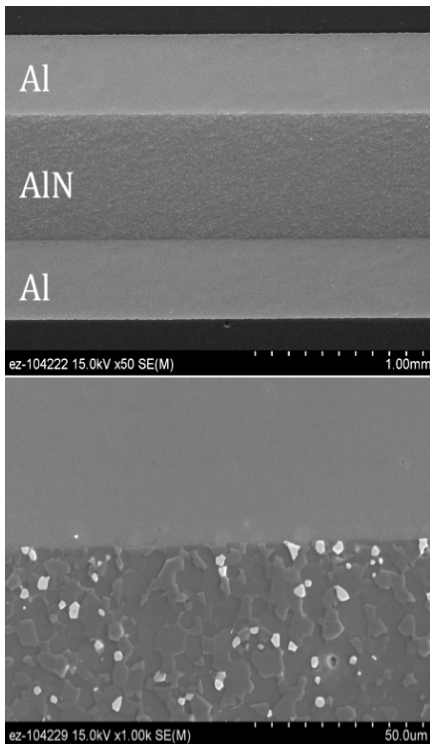


Figure 4. SEM micrograph of commercial DBA-B.

The Al₂O₃/Al and AlN/Al specimens with Al-12Si brazing paste were hot pressed at 640°C and 15 MPa for 30 minutes in flowing argon environment. Figure 8 shows the photo of the two samples after bonding process. The visual observations of these two experimental DBA substrates looked intact. The joined substrates were sliced and polished for

subsequent detailed SEM analysis to assess the bonding integrity.

SEM observations show there is a crack formed after metallographic polishing. This is the typical microstructure observed for both bonded Al-AlN and Al-Al₂O₃ substrate (Figure 9). The crack formation could be possibly caused by weak interfacial bonding strength between two constituents. However, further detailed and systematic bonding studies would need to be performed to learn the cause of origin. On the other hand, the SEM analysis at higher magnification shows there are discrete, but uniform reaction layer formed on Al and Al₂O₃ and AlN substrate side.

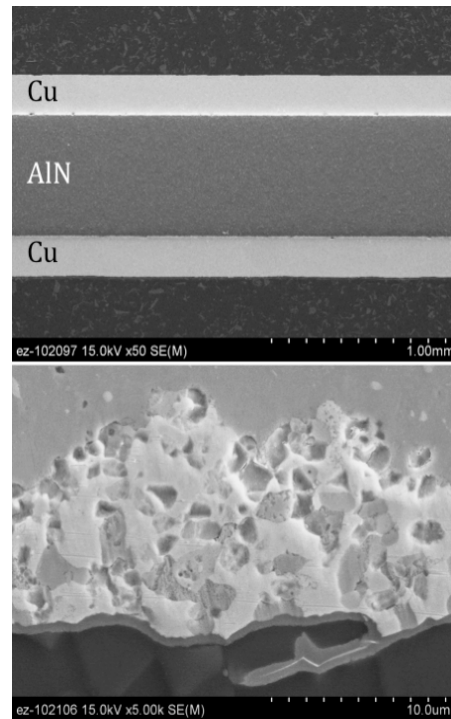


Figure 5. SEM micrograph of commercial DBC-A.

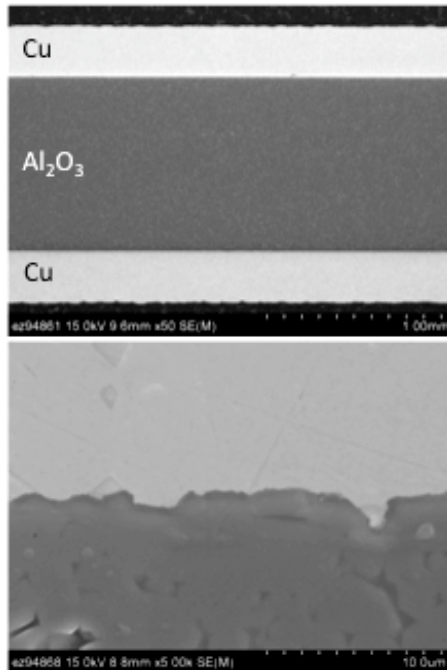


Figure 6. SEM micrograph of commercial DBC-B.

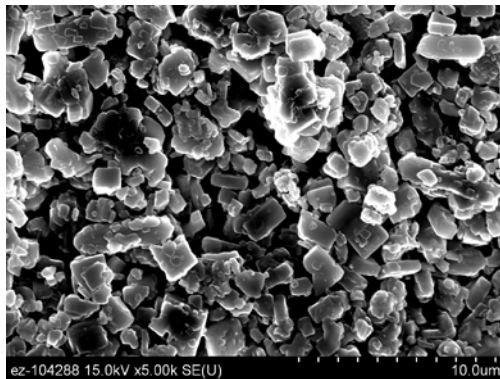


Figure 7. SEM micrograph of commercial Al-Si brazing paste.

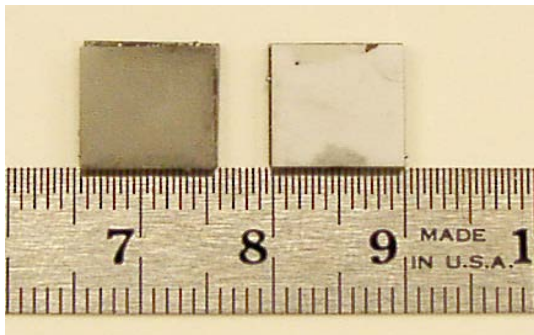


Figure 8. Photo of experimental DBA substrates after bonding process.

The elements mapping on the AlN substrate side was performed to understand the element distribution after bonding process. Result shows that the Si distribution is not continuous and uniform along the reaction interface, as shown in Fig. 10, which might play a part in the weak interface bonding strength of the system studied. An engineered approach will be devised in FY2012 to ensure an initial uniform thickness of Al-Si paste. Note there is also a presence of Al₂O₃ thin film layer due to the oxidation of Al plates that could inhibit the effectiveness of Al-Si brazing paste. Thus, the Al plates would be cleaned via the use of HNO₃ to remove the Al₂O₃ thin film layer prior to the bonding process.

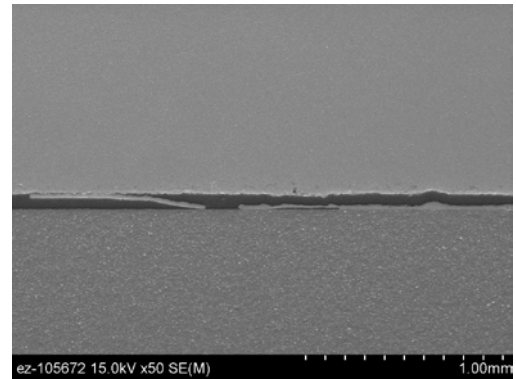


Figure 9. SEM of polished cross-section of Al-AlN substrate.

Summary

The literature survey on phase diagram, existing patent, and bonding approaches for Al-AlN and Al-Al₂O₃ was completed. Also, characterizations of microstructure and initial physical properties of commercial DBA and DBC substrates were also achieved. Results will serve as a reference for the DBA substrates developed under this subtask. The preliminary Al-AlN and Al-Al₂O₃ via the employment of commercial Al-Si paste reveals defect and crack formation at bonding interface. SEM analysis at interface shows non-uniform distribution of Si, which may play a part in the observed crack formation possibly due to weak interface strength. Identification of alternative processing methods (e.g., brazing, bridging metallurgical coatings, induction heating, and field-assisted bonding) to fabricate DBA substrates that has potential for low-cost manufacture will be

continued in FY2012. This is the first primary step in accelerating availability of low-cost DBA substrates. Also, method would be developed to fabricate Al-Si thin film via sol-gel and tape cast process for bonding media.

References

1. H. Yoshida, Y. Kuromitsu, M. Toriumi, M. Yuzawa, Ceramic substrate used for fabricating electric or electronic circuit, US Patent No. 5130498, 1992.
2. Y. Nagatomo, R. Muranaka, H. Hayashi, Y. Kuromitsu, N. Kuwano, Fracture Process of Aluminum/Aluminum Nitride Interfaces during Thermal Cycling, *Materials Science Forum*, 638-642, 3895, 2010.
3. S. Gerhard, Method for manufacturing a power semiconductor device and direct bonded substrate thereof, US Patent No. 6670216, 2003.
4. J.Y. Kim, J.S. Hardy, and K.S. Weil, Aluminum Air Brazing for Joining Ceramics, in *Advances in Ceramic Coatings and Ceramic-Metal Systems: Ceramic Engineering and Science Proceedings*, 26, 3, 2008.
5. X.S. Ning, C. Nagata, M. Sakuraba, T. Tanaka: Process for preparing a ceramic electronic circuit board and process for preparing aluminum or aluminum alloy bonded ceramic material, US patent No. 5965193, 1999.
6. M. Nobuyuki, K. Hajime, S. Yasuyuki, Method for directly bonding ceramic and metal members and laminated body of the same, US Patent No. 4849292, 1989.
7. Y. Kuromitsu, Y. Nagatomo, H. Tonomura, K. Akiyama, C.M. Montesa, N. Shibata, T. Tohei, and Y. Ikuhara, Direct Bonded Aluminum (DBA) on Aluminum Nitride (AlN) substrates through Transient Liquid Phase and its Application, *6th International Conference on Integrated Power Electronic Systems (CIPS) Proceedings*, 2010.
8. H. Knoll, W. Weidenauer, P. Ingram, S. Bennemann, S. Brand, M. Petzold, , Ceramic substrates with aluminum metallization for power application, *Electronic System-Integration Technology Conference (ESTC), 2010 3rd*, 1-5, 13-16, 2010.
9. A. Lindemann, Properties of Direct Aluminum Bonded Substrates for Power Semiconductor Components, *IEEE Transactions on Power Electronics*, 22 (2), 2007.

Publications/Presentations

1. Poster on this project was presented at DOE Annual Merit Review, Arlington, VA, May 11, 2011
2. Presentation on “Low-cost DBA substrates” was made to the Electric and Electronic Tech Team on August 25, 2011.

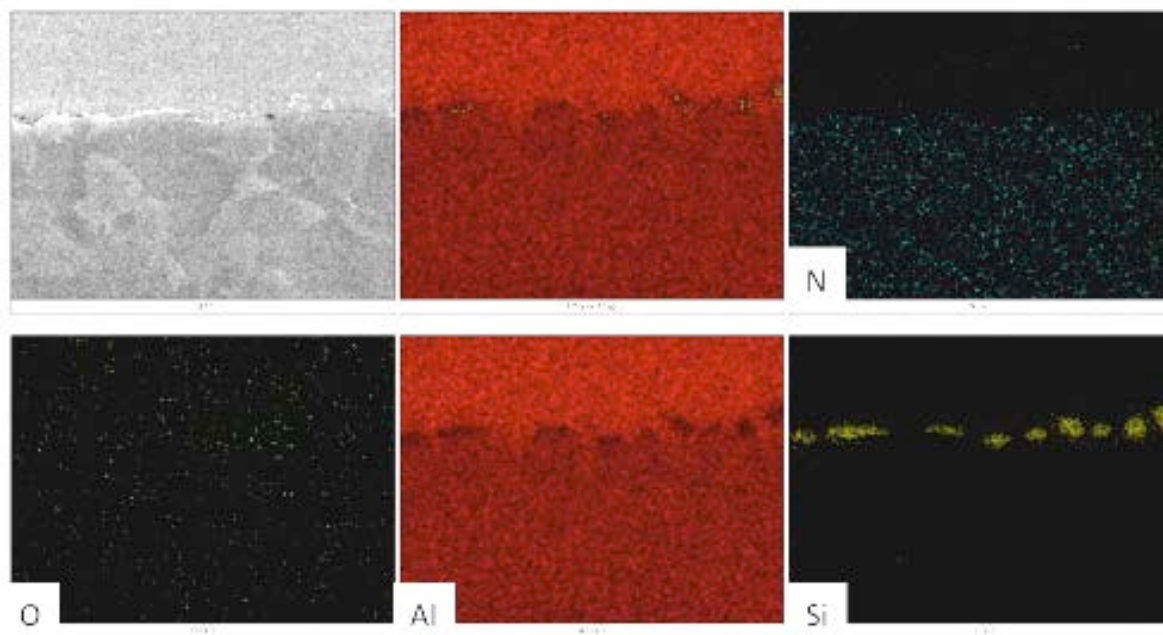


Figure 10. SEM and EDAX element map of AlN-Al interface.

Table 1.

	Length (mm)	Width (mm)	Thickness (mm)	Mass (g)	Density (g/cm ³)	Young's modulus (GPa)	Possion's ratio
Al ₂ O ₃ CoorsTek	10.066	9.995	0.776	0.2902	3.7170	328.3083	0.2424
Valley Design AlN	10.076	9.999	0.890	0.2930	3.2676	314.4820	0.2441

Agreement 23279 - Improved Organics for Power Electronics and Electric Motors

A. A. Wereszczak, R. H. Wiles, M. K. Ferber, T. G. Morrissey, H. Wang, and C. W. Ayers

Oak Ridge National Laboratory

P.O. Box 2008, MS 6068, Bldg. 4515

Oak Ridge, TN 37831-6068

(865) 576-1169; fax: (865) 574-6098; e-mail: wereszczakaa@ornl.gov

DOE Technology Manager: Jerry L. Gibbs

(202) 586-1182; fax: (202) 586-1600; e-mail: jerry.gibbs@ee.doe.gov

ORNL Technical Advisor: David P. Stinton

(865) 574-4556; fax: (865) 574-6098; e-mail: stintondp@ornl.gov

Contractor: Oak Ridge National Laboratory, Oak Ridge, Tennessee

Prime Contract No.: DE-AC05-00OR22725

Objectives

- Develop thermally conductive and low-cost epoxy molding compounds (EMCs) with sustained electrical insulation for dielectric and thermal management applications in power electronics and electric motors.
- Enable new or improved thermal management strategies in power electronics and electric motors that decrease the maximum temperature of their operation.

Approach

- Pursue the use of alternative or previously unconsidered fillers that are characteristically low-cost, electrically insulative, and thermally conductive.
- Collaborate with EMC manufacturer(s) to optimize particle size distribution so to fully exploit filler properties.
- Collaborate with power module and electric motor designers, manufacturers, and end-users to integrate and exploit thermally conductive EMCs.

Accomplishments

- Developed software that inputs any measured filler particle size distribution and volume fraction and enables modeling of the thermal conductivity of an EMC containing that filler.
- Modeled the effects of using a thermally conductive filler in several electric and motor components and identified a produced EMC thermal conductivity of only 5 W/mK can significantly lessen the maximum operation temperature.

Future Direction

- Choose two filler candidates and pursue processing of EMCs containing them.
 - Refine thermal conductivity modeling of EMCs to optimize filler size distribution and volume fraction.
 - Collaborate with EMC manufacturers and power module and electric motor designers, manufacturers, and end-users to integrate them into developed thermally conductive EMCs.
-

Introduction

The Vehicle Technology Program's Advanced Power Electronics and Electric Motors (APEEM) program has expressed emphasis on cost-reducing research targets, challenges, and areas. These include high-temperature components, packaging, and reliability for long-term transformation technologies, and thermal management technologies to reduce volume and enhance thermal reliability. The technical goals of this project directly strike at that emphasis.

The goals of this project are to develop, characterize, and test candidate organic or epoxy molding compounds (EMCs) that are thermally conductive and that have the potential to be low-cost, volume-reducing, and better-performing alternatives to presently used compounds for at least the following applications:

- dielectrics in power electronic devices,
- potting compounds used with capacitors, and
- potting compounds used in motors.

In the first case involving dielectrics, "better performing" represents a higher-temperature capability and the sustainment of dielectric and gel-like mechanical damping properties under thermal cycling and vibratory conditions. For better-performing potting compounds for both capacitors and motors, interest exists to identify alternatives that have higher thermal conductivity (or that enhance the thermal conductivity of existing compounds) or that benefit structural or damping performance without compromising thermal performance or both.

An example of an EMC is shown in Fig. 1. In this example, a wide particle size distribution of silicon-dioxide-filler is used. But silicon dioxide has a low thermal conductivity (see Table I) and the continuous epoxy phase does too, so this EMC will consequently have an overall low thermal conductivity too.

Our approach is to use different fillers that are thermally conductive with optimized particle size distribution and volume fraction to produce a thermally conductive EMC.

Unfortunately, the more thermally conductive fillers listed in Table I have other limitations that lessen their attractiveness for use. Boron nitride, silicon carbide, aluminum nitride, and beryllium

oxide all have high thermal conductivities, but either are expensive or have issues of toxicity, and are not under serious consideration. Aluminum oxide and magnesium oxide are under consideration and another filler material (that has not been a candidate before, and is not listed in Table I due to intellectual property development associated with it).

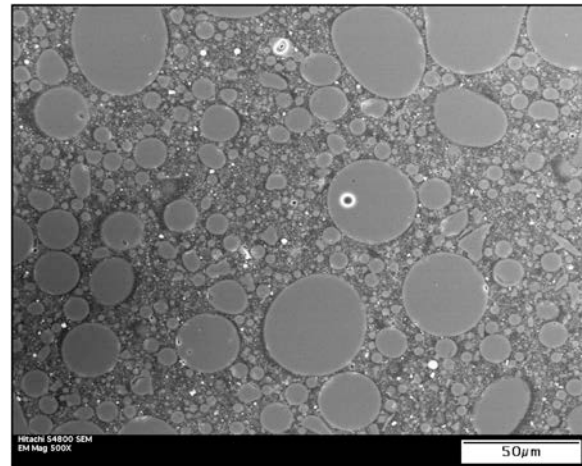


Figure 1. Example of a SiO₂-based filled EMC from a power module from a hybrid vehicle's inverter. Photo used with permission of ORNL's Z. Liang.

Table I. Examples of candidate fillers for EMCs.

Material	Electrical Resistivity at 25°C (Ω•cm)	Thermal Conductivity	Heat Capacity	Density (kg/m ³)	Coefficient of Thermal Expansion
		at 25°C - κ - (W/m•K)	- Cp - (J/kg•K)		- ρ - (x 10 ⁻⁶ /°C)
Silica (SiO ₂) silicon dioxide	> 10 ¹⁴	2	700	2600	0.5
Alumina (Al ₂ O ₃) aluminum oxide	> 10 ¹⁴	30	900	3900	8
Boron nitride (BN) * Has anisotropy	> 10 ¹⁴	275*	1600	1900	1*
Magnesia (MgO) magnesium oxide	> 10 ¹⁴	40	900	3600	10
Silicon carbide (SiC)	> 10 ¹⁴	120	800	3100	4
Aluminum nitride (AlN)	> 10 ¹⁴	250	700	3200	5
Beryllia (BeO) beryllium oxide	> 10 ¹⁴	280	600	2900	9
Epoxy	> 10 ¹²	0.05 - 0.4	1500	1200	30-60

Results

The description of this year’s progress is divided into two sections. The first describes the development of modeling to predict thermal conductivity of an EMC structure; this will enable us to eventually optimize the choice of the filler particle size distribution and volume fraction. The second section overviews thermal modeling of electronic and motor components whose results show that increasing the thermal conductivity of EMCs can have a significant effect on lessening the maximum temperature of the constituents they are encapsulating.

EMC Thermal Modeling

Achieving an EMC with high thermal conductivity will be predicated on both the use of thermally conductive filler and a filler that has an optimized particle size distribution and volume fraction.

The method to optimize filler particle size distribution and volume fraction is shown in Fig. 2. The goal is to maximize thermal conductivity of the EMC without compromising rheological control during injection molding or potting.

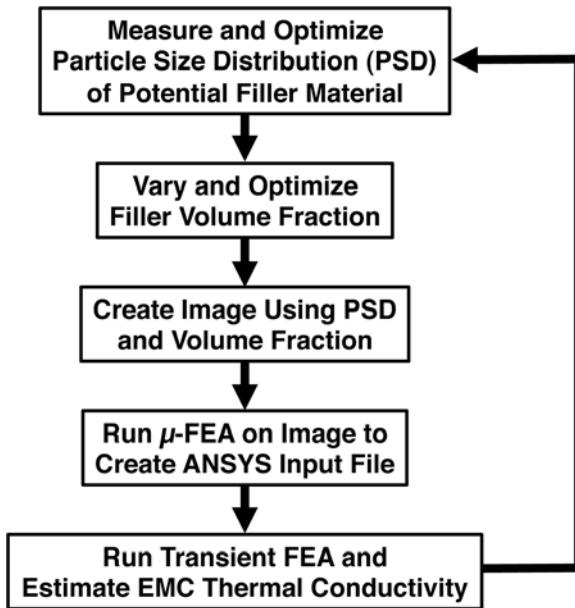


Figure 2. Flowchart describing the method to produce a high-thermal-conductivity EMC.

A software program was developed in-house that uses a measured particle size distribution (e.g., that shown in Fig. 3) and a user-specified volume fraction. The software (see panels of it in Fig. 4) then uses their combination to create a picture whose thermal diffusivity and conductivity can be modeled. An example of that transient thermal analysis is shown in Fig. 5.

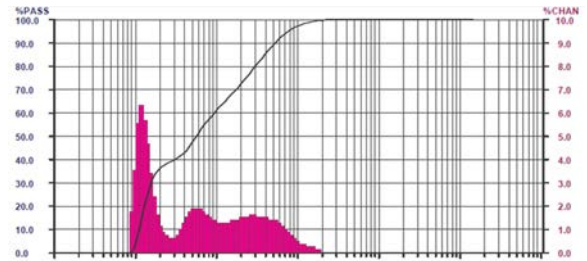


Figure 3. Arbitrary particle size distribution of a powder filler.

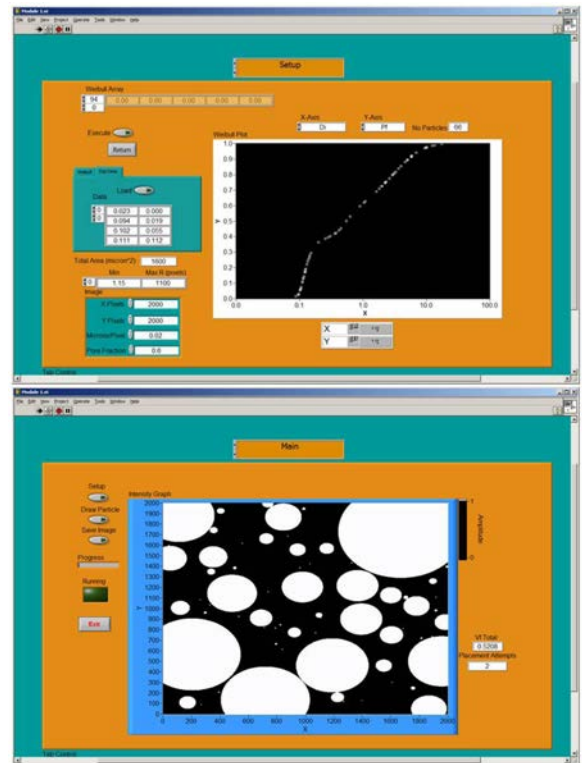


Figure 4. Software was developed that takes inputted particle size distribution and then creates a 2-D portrayal of it along with volume fraction.

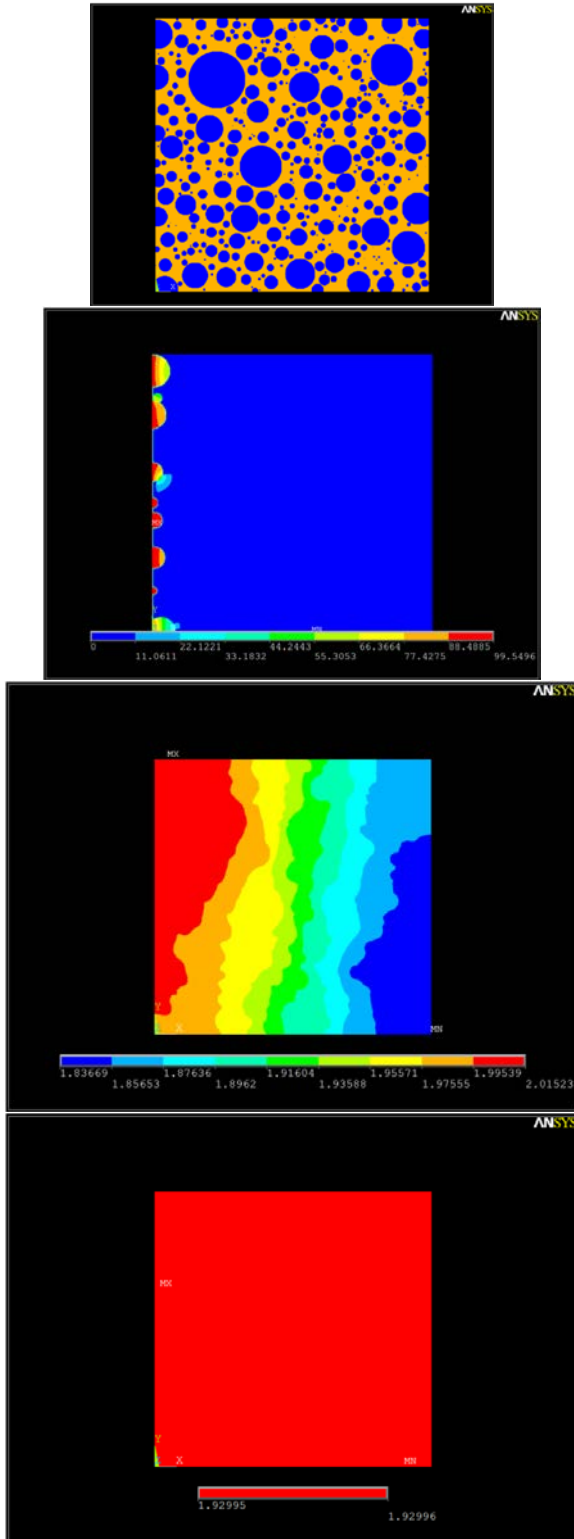


Figure 5. Example of a PSD (top) and increasing times of temperature transfer after "flash" heating on the left side.

The temperature-time response shown in Fig. 5 is analyzed by examining how long it takes to reach an asymptotic temperature using the classical Parker thermal diffusivity analysis. An example of one of those trials is shown in Fig. 6. From the produced curve shown in Fig. 6, we estimate the thermal conductivity, and using the approach shown in Fig. 2, we vary the filler size distribution and volume fraction with the intent of increasing the EMC thermal conductivity. This is allowing us to identify what a desired particle size distribution and volume fraction need to be.

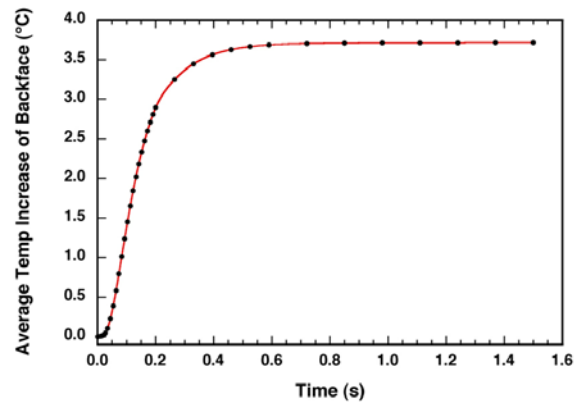


Figure 6. Example of a temperature-time profile of the side opposite the flashed side in Fig. 5.

Electronic and Motor Component Thermal Modeling

Thermal modeling of hypothetical components that use EMCs or epoxy was conducted to start to judge how much thermal conductivity increase was realistically needed in a new or developed EMC. A film capacitor (Fig. 7), a motor component (Fig. 8), a power module (Fig. 9), and a printed circuit board (Fig. 10) were modeled.

In each case, a one order-of-magnitude increase in thermal conductivity, from 0.5 to 5.0 W/mK significantly reduces the maximum temperature of the component. Additional thermal conductivities were considered in all their analyses; however, these shown results guide our future milestones to try to develop and achieve new EMCs whose thermal conductivity is at least 5 W/mK.

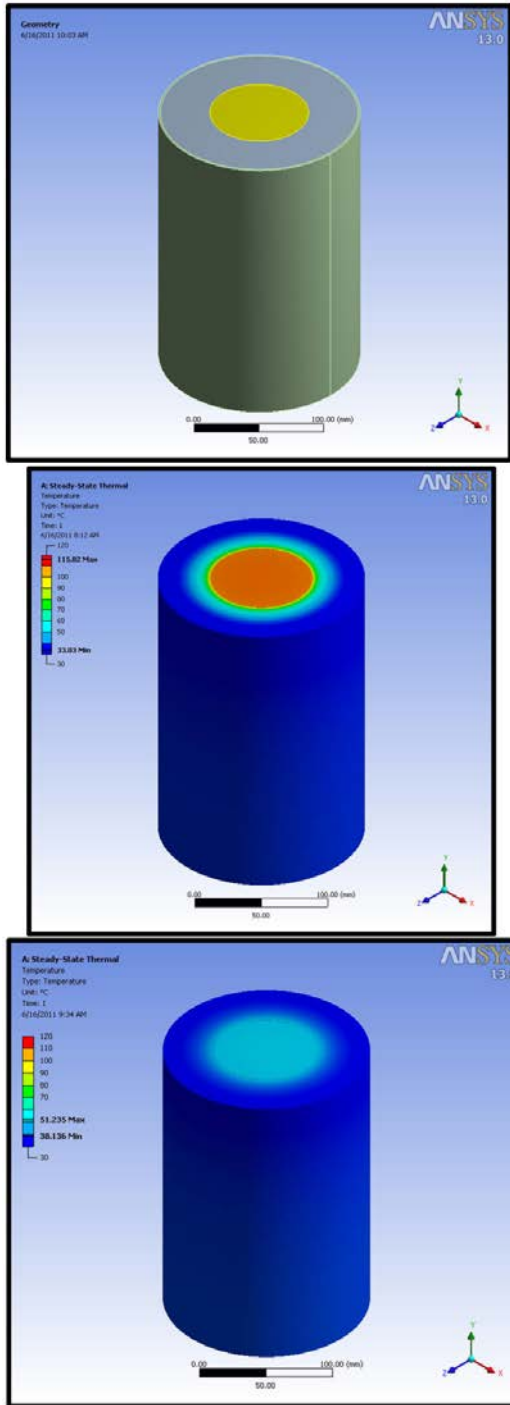


Figure 7. The thermal response of a hypothetical film capacitor (top) was modeled. If the epoxy (outer annulus) has a thermal conductivity of 0.5 W/mK, then the maximum temperature was 116°C. Using a EMC with a thermal conductivity of 5 W/mK instead lowers that maximum temperature to 51°C.

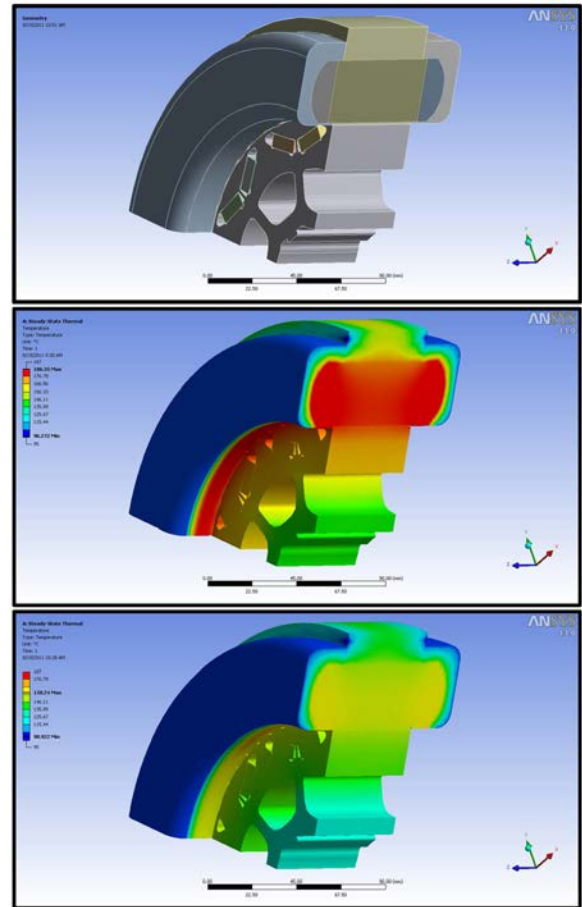


Figure 8. The thermal response of a hypothetical motor component (top) was modeled. If the potting compound has a thermal conductivity of 0.5 W/mK, then the maximum temperature was 186°C. Using a EMC with a thermal conductivity of 5 W/mK instead lowers that maximum temperature to 158°C.

Conclusions

Software was developed to enable the optimization of particle size distribution and volume fraction of filler used in EMCs.

Thermal modeling of hypothetical electronic and motor components show an EMC with a thermal conductivity of only 5 W/mK can significantly lower the maximum temperature in them.

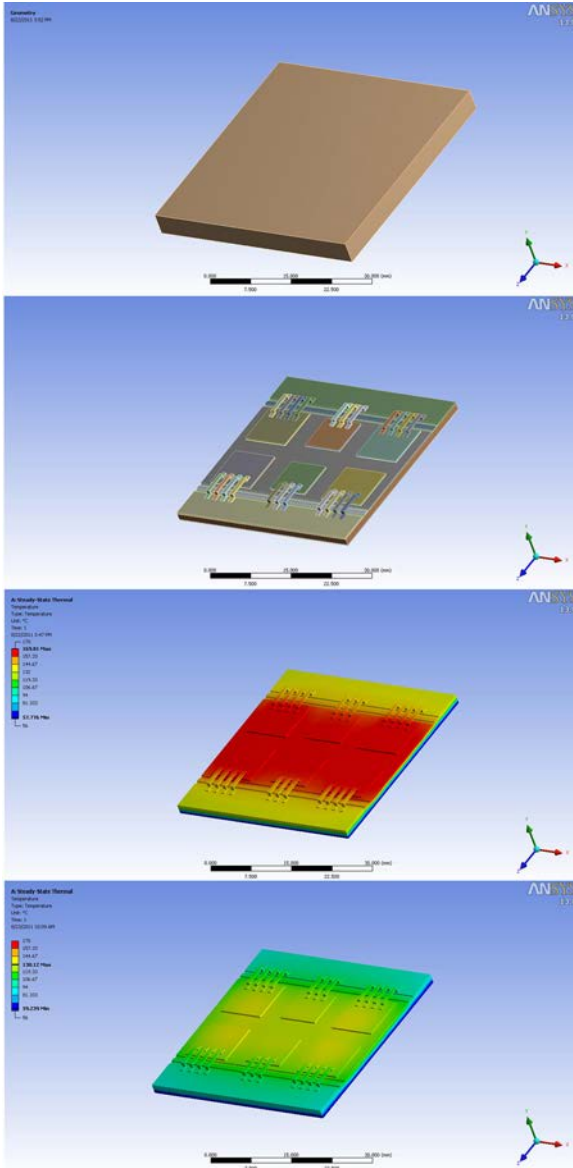


Figure 9. The thermal response of a hypothetical power module (top) was modeled. The EMC encapsulates this, so it is hidden in the other three images so to show the internal temperature field. If the potting compound has a thermal conductivity of 0.5 W/mK, then the maximum temperature was 170°C. Using a EMC with a thermal conductivity of 5 W/mK instead lowers that maximum temperature to 130°C.

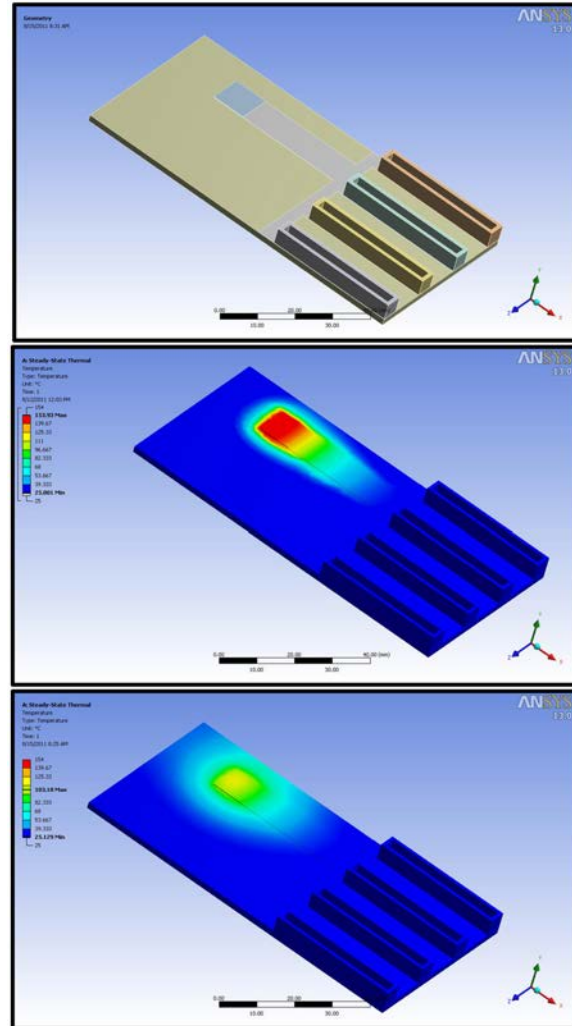


Figure 10. The thermal response of a hypothetical circuit board (top) was modeled. If the potting compound has a thermal conductivity of 0.5 W/mK, then the maximum temperature was 154°C. Using a EMC with a thermal conductivity of 5 W/mK instead lowers that maximum temperature to 103°C.

Agreement 23726 - Novel Manufacturing Technologies for High Power Induction and Permanent Magnet Electric Motors – (GM CRADA)

Principal Investigator: Glenn J. Grant

Energy Materials

Pacific Northwest National Laboratory

902 Battelle Blvd., K2-03

Richland, Washington 99356

(509) 375-6890; fax: (509) 375-4448; e-mail: glenn.grant@pnnl.gov

Blair E. Carlson

Manager, Lightweight Materials Processing

General Motors R&D

30500 Mound Rd.

Warren, Michigan 48090

E-mail: blair.carlson@gm.com

DOE Technology Manager: Jerry L. Gibbs

(202) 586-1182; fax: (202) 586-1600; e-mail: jerry.gibbs@ee.doe.gov

Field Technical Manager: Dean Paxton

(509) 375-2620; fax (509) 375-2186; e-mail: dean.paxton@pnnl.gov

Contractor: Pacific Northwest National Laboratory

Contract No.: DE-AC05-76RL01830

Objective

- To develop and deploy high power induction and permanent magnet rotors and stators that are lighter weight, have better cooling, and are a lower cost to manufacture through the application of novel solid-state joining and fabrication technologies.
- The project will apply solid-state processing techniques to improve performance of a low-cost soft magnetic material used in the rotors of high power induction motors.

Approach including partner/collaborator and path to technology transfer and commercialization

- This project will develop solid-state joining techniques and manufacturing processes that will increase the efficiency of electric motors through lightweighting; through improvements in electric and magnetic properties; and through improvements in assembly space efficiency, packaging, and cost.
- The project will develop the friction-stir welding (FSW) process parameters, as well as evaluate proper tool materials and techniques to produce defect-free FSWs in copper alloys specified by project partners.
- The project will develop a fundamental understanding of solid-state joints between copper materials and between dissimilar copper-aluminum materials. This fundamental knowledge is expected to lead to strategies and techniques that will be used to produce a joining process with low thermal input, low distortion of adjacent parts, and produce joints with a high degree of structural integrity and with high thermal and electrical continuity.
- The fundamental information gained will be used to develop techniques to manufacture copper and aluminum rotor and stator assemblies for high power induction and permanent magnet motor systems.

Joined or processed components will be evaluated and tested by industry collaborators to demonstrate efficiency benefits and commercial applications.

- Performance data and manufacturing technology will be transferred to industry through the mechanism of a Cooperative Research and Development Agreement (CRADA) with General Motors (GM), ensuring a clear path to commercialization.

Milestones, Metrics and Accomplishments

- **Milestone:** Identify key component requirements necessary for improved motor performance and develop a work plan to address those requirements. 9/15/2011 (Completed)
- **Future Milestone:** Characterize the microstructure and mechanical properties of Cu/Cu joints. Joints will be evaluated based on metrics established by the team including strength, toughness, and fatigue performance. Gate is established on minimum mechanical performance threshold established by the project team. (On track)

Introduction

The purpose of this project is to develop and deploy high power induction and permanent magnet rotors and stators that are lighter weight, have better cooling, and are a lower cost to manufacture through the application of novel solid-state joining and fabrication technologies. Barriers to achieving these objectives have been identified that focus on the manufacturability of novel rotor designs. The project team will apply FSW to join copper subassemblies and copper (Cu)/ aluminum (Al) joints to eventually produce prototype lightweight, high-efficiency rotor assemblies. Fundamental work tasks will first focus on Cu/Cu FSW and dissimilar Cu/Al FSW joints. Later tasks will involve full rotor assembly and testing by GM. In addition, the project will apply solid-state processing techniques to improve the performance of a low-cost soft magnetic material used in the rotors of high power induction motors. While GM provides the motor design, Pacific Northwest National Laboratory (PNNL) will employ a novel method to fabricate the ferrous-based laminates specific to the GM motor. The PNNL-developed method is based on nanoscale powder synthesis and friction extrusion/consolidation. This new fabrication process may allow for fewer energy-intensive processing steps to reach the microstructure and laminate thicknesses required for a high performance soft magnetic material at a lower manufacturing cost. The project is a cost-shared CRADA between PNNL and GM.

Background

Previous work by PNNL and others has shown that FSWs can be made in copper alloys that have excellent mechanical, electrical and thermo-mechanical performance. FSW has a particular advantage in welding copper due to the wide range of weld-specific energy levels that can be applied by the process. Conventional fusion welding must deliver a high level of energy to melt the copper on each side of the joint line. In many applications, the high part temperatures during fusion welding can lead to distortion or overheated adjacent parts. Often, copper joining is required in assemblies where heat sensitive electronics, wiring, or coated laminates or substrates are located nearby. FSW may provide a lower heat input joining technique in these special applications where adjacent parts in the assembly can be damaged.

In addition, the next generation of rotor designs may be copper/aluminum hybrids or have aluminum components to reduce the rotating mass. It is anticipated joints will be needed between copper and aluminum. Solid-state joining techniques like FSW are logical to develop for specialized dissimilar joints like these that cannot be fusion welded due to the radically different melt temperatures of the components.

Approach

The project will develop the FSW process parameters, as well as evaluate proper tool materials and techniques to produce defect-free FSWs in copper alloys specified by project partners. In addition, the project team will

develop statistical confidence around the manufacturing process used to fabricate high power induction motor rotor assemblies by applying a set of mechanical test methods and procedures to evaluate process robustness. The project team will also investigate the application of FSW to other joining issues around electric drive systems, including dissimilar joining between aluminum and copper and potentially Al – Al joints in specific configurations.

Finally, to address the overarching goal of improved energy efficiency of the induction motor design, the project team will apply solid-state processing techniques to fabricate a low-cost soft magnetic material with unique properties that has the potential to display high magnetic flux density (B) and low iron loss (W) at around the fundamental frequency. Amorphous iron-based metal and alloys offer excellent soft magnetic properties. Literature reports the material may reduce the core losses of motors by more than 70%, and the efficiency of an induction motor with amorphous iron core can easily reach 80%. However, the production cost of an amorphous iron core is high. Specifically, the thickness of amorphous iron sheet cannot exceed 25 μ m because of the requirement of ultra-fast quenching. In this task, we will focus on developing a cost-effective method to produce soft iron alloy sheet with magnetic properties comparable to that of the amorphous iron alloy and with thickness greater than 100 μ m. This method is based on modified friction consolidation and extrusion method, where the material is subjected to high strain under a hydrostatic state of stress. This solid-state process has shown the ability to produce ultra-fine grain size in bulk solids.

This project will be divided into three primary task areas: Task 1 will focus on solid-state joining of copper materials used in the rotor assemblies of high power induction motors. Task 2 will focus on dissimilar material joining primarily copper to aluminum with an emphasis on components and assembly performance improvement. Task 3 will develop a unique solid-state process to create appropriate microstructures and magnetic performance in bulk soft magnetic materials that may be able to improve on the efficiency of stack laminates in the rotor assembly.

Results

The project began in late fiscal year (FY) 2011 and has focused primarily on defining the specific tooling and process methods to join copper materials in the geometries appropriate for the application. An early challenge that emerged during the tooling and process scoping stage involves the robustness of the friction stir tool itself. Conventional tool materials used to FSW aluminum do not have the high temperature strength to survive some welding conditions while welding copper. Figure 1 shows a typical FSW tool composed of H13 steel. While this tool will survive some limited weld conditions, there are other process conditions that will overheat the tool and cause the probe to twist off due to lower material strength at high temperature. Tool failures were observed for several tool materials, including tungsten-based materials. Solving this challenge will be one of the early focus areas of this project.



Figure 1. Many process conditions tested led to tool probe failure due to the drop in yield strength of the tool material at high temperatures

Figure 2 shows the result of a broken probe. At the end of the weld, there is typically a deep open feature after a FSW tool is withdrawn from the substrate. In Figure 2, the exit hole is flat

indicating the probe no longer is penetrating the base material. This is a significant problem obviously because the weld is no longer achieved but also because it is not clear where the probe broke off. Repair of this part is not an option because it is not possible to re-stir through a broken probe fragment. In manufacturing, the anticipated rotor welds will be late in the assembly process, leading to loss of an expensive assembly. Clearly, probe tool robustness must be a key feature of the process.

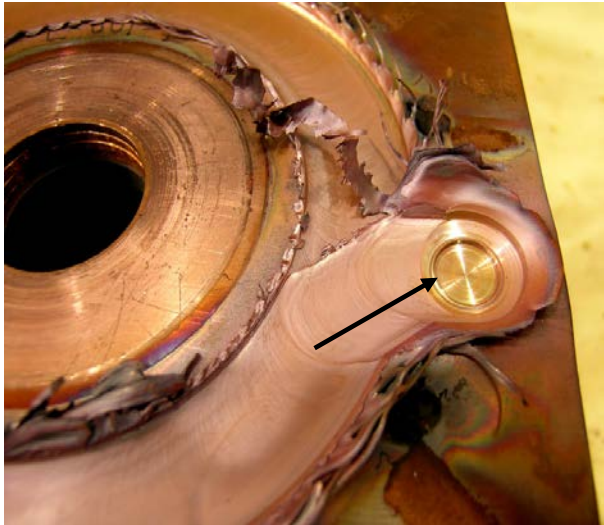


Figure 2. The shallow exit hole (arrow) is evidence at the end of the weld that the probe tip of the FSW tool has failed during the weld

During early FY2012, the project team will investigate a wide range of tool materials, tool designs and process parameters so that a robust process can be established. Figure 3 shows a process window established for C101 copper using a FerroTic® tool with a 0.25-in. deep penetration. The circular dots indicate conditions in which either the tool failed or the weld had significant defects. Square symbols are successful welds (based on surface condition only). Welds, with optimum mechanical properties, will exist within the region of the square symbols. The process of parameter development narrows the weld conditions to those with the appropriate defect-free quality and appropriate mechanical performance.

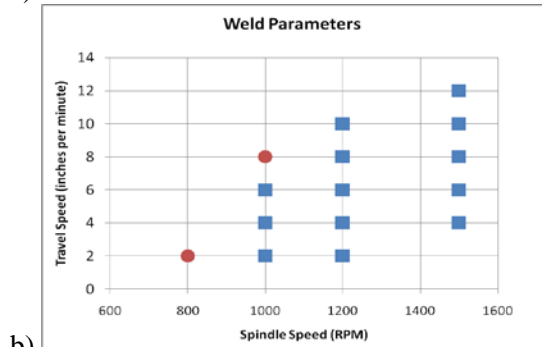


Figure 3. a) Typical FSW weld in C101 copper, b) copper FSW weld parameter map using a FerroTic stepped spiral tool. Circle symbols indicate failed welds, and square symbols indicate conditions where the visual observation of the weld surface passed a set of criteria

The weld process parameter development will also focus on several tool designs. Figure 4 shows two of the primary tool concepts that will be tested—the Stepped Spiral tool and the Triflat tool. These designs and variations of these tools are well known in commercial applications of FSW, especially in aluminum welding, but their performance in copper welds is yet to be determined.

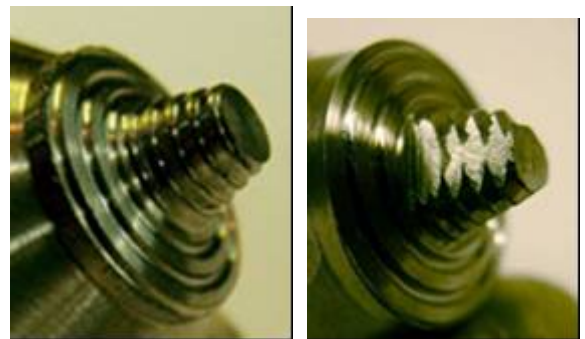


Figure 4. Two tool designs that will be investigated in this project include the stepped spiral tool (on the left) and the three flat tool (on the right). (Pictures are for illustration only; actual designs will vary.)

Conclusions

Motor designs, like all complex assemblies, are a compromise between performance and cost (both cost of materials and cost of manufacturing). New manufacturing processes can be critical in this balance because they can both be enabling of lower cost materials and can introduce a lower cost manufacturing process. In many cases, the new manufacturing process may even directly increase the efficiency of the part by producing an assembly that displays better thermal, mechanical or electric/magnetic properties. This project will use new solid-state joining and processing technologies to achieve both increased performance and a lower manufacturing cost.

Specifically, the project will develop the fundamental understanding of solid-state joints between copper materials and between copper aluminum dissimilar joints so that they can be accomplished with low thermal input, low distortion of adjacent parts, with a high degree of structural integrity, and with a high degree of thermal and electrical continuity. The fundamental information gained will be used to develop techniques to manufacture copper and aluminum rotor and stator assemblies for high power induction and permanent magnet motor systems. Joined or processed components will be evaluated and tested by the industry collaborators to demonstrate efficiency benefits and commercial applications.

Acronyms

CRADA: Cooperative Research and Development Agreement

FSW: friction-stir welding

FY: fiscal year

GM: General Motors

PNNL: Pacific Northwest National Laboratory

Agreement 13257 - High Performance Embedded Capacitors

(co-funded by Project 19025 – Advanced Power Electronics)

U. (Balu) Balachandran, B. Ma, S. Chao, S. Liu, M. Narayanan, S. Tong, and S. E. Dorris

Argonne National Laboratory

9700 S. Cass Avenue

Argonne, IL 60439-4838

(630) 252-4250; fax: (630) 252-3604; e-mail: balu@anl.gov

DOE Technology Manager: Jerry L. Gibbs

(202) 586-1182; fax: (202) 586-1600; e-mail: jerry.gibbs@ee.doe.gov

ANL Technical Advisor: U. (Balu) Balachandran

(630) 252-4250; fax: (630) 252-3604; e-mail: balu@anl.gov

Contractor: Argonne National Laboratory, Argonne, Illinois

Contract No.: DE-AC02-06CH11357

Objective

- The purpose of this effort is to develop ceramic capacitors that have excellent high temperature performance and meet the Vehicle Technologies Program specifications for power electronic systems in electric drive vehicles. **This project is jointly funded by the Propulsion Materials and Advanced Power Electronics programs.**

Approach

- Fabricate a high permittivity ferroelectric material, $(\text{Pb,L a})(\text{Zr,Ti})\text{O}_3$ (abbreviated as PLZT), on base-metal foils and metallized Si substrates.

Accomplishments

- Developed a method for the fabrication of high-quality PLZT film-on-foil capacitors using a polyvinylpyrrolidone (PVP)-modified sol-gel solutions.
- Grown dense crack-free PLZT films with per-coating thickness that is three times thicker than that was reported in FY10.
- Fabricated film-on-foil capacitors exhibiting high dielectric constant and self-clearing properties.
- Measured temperature dependent dielectric properties and breakdown strength of PLZT film-on-foil fabricated by PVP-modified method.

Future Direction

- Continue to fabricate high quality PLZT on larger area substrates. Using small area top electrodes, the R&D effort has demonstrated that the properties of PLZT film-on-foils are suitable for power electronics operating at under-the-hood temperatures. The next step is to optimize the processing and fabrication conditions to make large area capacitors with the desired dielectric properties. Important processing issues such as substrate polishing, defects in the films, humidity level, clean room processing, pyrolysis and crystallization temperatures have been identified.
 - Our preliminary results showed that PVP-modified method is promising. We will optimize synthesis conditions and fabricate and characterize the dielectric properties of PLZT film-on-foils with larger area top electrodes.
 - Develop fabrication technique for adaptation by capacitor industry.
-

Introduction

Power inverter modules are a critical subsystem within electric drive vehicles (EDVs) and their performance directly affects fuel efficiency and battery life. Capacitors occupy $\approx 35\%$ of the inverter volume and account for $\approx 25\%$ of the weight in current designs. Thus, even if all other components in the inverter are reduced significantly, the capacitor requirement is a serious impediment to achieving the required volume and weight reduction. In addition, the use of high-temperature coolants further exacerbates the situation because existing film capacitors lose their capability to absorb ripple currents at elevated temperature, necessitating the addition of extra capacitors. Increasing the volumetric performance (capacitance per unit volume) of DC bus capacitors is required, and their maximum operating temperature also must be increased to assure reliability requirements. Theoretically, ceramic capacitors have the greatest potential for volume reduction; they could be as small as 20% of the volume of an aluminum electrolytic capacitor. Ceramics offer high dielectric constants and breakdown fields and, therefore, high energy densities. They also can tolerate high temperatures with a low equivalent series resistance (ESR), enabling them to carry high ripple currents even at elevated temperatures, although the capacitance may vary strongly with temperature.

Driven by the increasing demand for passive power electronics with improved performance, high reliability, and reduced size and weight, much attention has been paid to the so-called “film-on-foil” technology, in which ceramic films deposited on metal foils are embedded into a printed circuit board (PCB). Our previous research [1-3] had shown that the lead lanthanum zirconate titanate ($\text{Pb}_{0.92}\text{La}_{0.08}\text{Zr}_{0.52}\text{Ti}_{0.48}\text{O}_3$, PLZT) films deposited on nickel or copper foils possess excellent dielectric properties, which are promising for high power applications such as plug-in hybrid electric vehicles. In power electronics, capacitors with high capacitance are required to work under high voltages. This requirement imposes the additional challenge of fabricating thicker ($>1\ \mu\text{m}$) films. However, due to the well-known critical thickness effect, per-layer thickness that can be achieved by conventional sol-gel method is generally limited to $\approx 0.1\ \mu\text{m}$, thus making the conventional method less

attractive to industry when thicker films are needed to meet the operation voltage requirement.

The objective of this R&D program is to utilize ceramic dielectric films with high capacitance density in developing capacitors that meet, if not surpass, DOE’s Vehicle Technology (VT) program goals for higher operating temperatures, improved packaging and reliability, and reduced size, weight, and cost. Our approach uses ferroelectric thin films (PLZT) on base-metal foils (film-on-foils) that are either stacked on or embedded into PCBs. Embedded film-on-foil capacitors reduce the component footprint area, shorten interconnect lengths, and reduce parasitic inductive losses and electromagnetic interference. Reliability is improved because the number and size of interconnects are reduced. Solder joints that are most susceptible to failure are no longer needed.

Our R&D efforts focus on examining the underpinning issues of film-on-foil capacitor performance and reliability, developing low cost capacitor designs, making multilayer film-on-foil capacitors, fabricating high-voltage-capable film-on-foil capacitors defined by the inverter application requirements, establishing robust fabrication protocols that are commercially and economically viable, and transferring the technology to industry for manufacturing. This R&D effort is funded jointly by the Advanced Power Electronics and Propulsion Materials Technology programs. The goal of the activity funded by the Propulsion Materials Technology program is to explore fabrication processes to make thicker per-coating thickness of dense ceramic films to meet the desired operation voltage requirement. We investigated introduction of polyvinylpyrrolidone (PVP) into the sol-gel solution. The method can substantially increase the critical per-coating thickness due to the structural relaxation effect as PVP suppressed the condensation reaction because of the strong hydrogen bonds between the amide groups of PVP and the hydroxyl groups of the metalloxane polymers. It has greater potential for production of large area film-on-foil sheets for stacking and/or embedding to produce large capacitors for the power electronic applications. As a first step, we fabricated film-on-foil capacitors with up to 5-mm-diameter top electrodes. Next, we will fabricate larger area capacitors.

Approach

PLZT precursor solutions of 0.6M concentration were prepared by a modified 2-methoxyethanol (2MOE) synthesis route by using the following raw materials: 99% lead acetate tri-hydrate, 97% titanium isopropoxide, 70% zirconium n-propoxide in 1-propanol, and 99.9% lanthanum acetate hydrate (all from Sigma-Aldrich Co.). Detailed experimental conditions for the modified 2MOE method can be found in earlier reports [3-4]. To form the chemical solution for deposition, PVP (PVP10, Sigma-Aldrich Co., with an average molecular weight of 10,000 g/mol) was added to PLZT stock solution in a PLZT:PVP = 1:2 or 1:3 molar ratio (PVP is defined by its monomer). The PVP-added PLZT solution was aged for approximately 12 h before coating. The aged solution, after passing through a 0.2- μm syringe filter, was deposited on a substrate by means of a spin coater (Laurell Technologies, North Wales, PA) at 2000 rpm for 30 sec. The substrate was a platinized silicon wafer with $\approx 100\text{-nm}$ thick Pt layer (Nova Electronic Materials, Flower Mound, TX). After deposition the films were first dried at 150°C for 3 min in furnace. Then, the films were subjected to two different pyrolysis processes: rapid thermal annealing (RTA) or a step-wise preheat treatment (SPT). In the RTA process, films placed on an alumina boat were directly inserted into a tube furnace preheated at 450°C for 10 min. In the SPT process, films were preheated at 300°C for 5 min, then 400°C for another 5 min, and finally at 450°C for 10 min (by pushing the film into separate hot zones with designated temperatures in an electric furnace). After pyrolysis, all films were crystallized at 650°C for 10 min. The deposition, pyrolysis, and crystallization steps were repeated to build up thickness to about 1.6 μm for all samples; in order to avoid the possible thickness effect on dielectric properties. Final crystallization and densification were conducted at 650°C for 30 min. All heat treatments were performed in ambient atmosphere.

Platinum (100-nm thickness) was deposited on samples through a shadow mask by electron-beam evaporation as top electrodes. Samples with Pt top electrodes were annealed at 450°C in air for 5 min for electrode conditioning. A Signatone QuieTemp® probe system with heatable vacuum chuck (Lucas Signatone Corp., Gilroy, CA) was used for dielectric property characterization. Phase identification was

conducted on a Bruker D8 AXS diffractometer with General Area Detector Diffraction System (GADDS). Microstructure observation was performed with a Hitachi S4700 field-emission scanning electron microscope (SEM). An Agilent E4980A Precision LCR Meter was used to measure the capacitance and dissipation factor under an applied bias field. Then, the dielectric constant was calculated from the diameter of the electrode (250- μm diameter electrode was used for all electrical tests) and the thickness of the film. Hysteresis loops were measured on a Radiant Technologies Precision Premier II tester using a field sweeping frequency of 1 kHz. Breakdown strength and current-voltage characteristics were measured on a Keithley 237 high-voltage source meter. Leakage current density was determined by fitting the current density relaxation data to the Curie-von Schweidler [5] equation.

Results

Figure 1 shows the XRD patterns of PLZT films prepared by SPT- or RTA-process with PLZT:PVP ratios of 1:2 and 1:3. For comparison, the XRD pattern of a PLZT sample prepared with the same PLZT stock solution but without PVP addition is also presented. A (111) preferential orientation was observed for this sample; however, all the other samples with PVP addition showed a random orientation, with (110) as the most intense peak. The (111) preferential orientation was attributed to the lattice matching between the (111)-oriented Pt substrate and the PLZT film [6], while the absence of this orientation is likely related to the PVP decomposition. Yamano and Kozuka [7] believed that orientation became difficult in PZT films derived from the solution containing PVP due to the large number of nucleation sites provided by the porosity. Except for this difference, all samples are phase-pure perovskite without any detectable secondary phases, such as pyrochlore. Film thickness was determined from the SEM cross-sectional images (Fig. 2). The thicknesses of the PLZT films after 5 or 6 deposition cycles were in the range of 1.5-1.7 μm , corresponding to per-layer thickness of ≈ 266 nm and ≈ 340 nm for solutions with PLZT:PVP = 1:2 and 1:3 ratio, respectively. The film thickness was not influenced by the different pyrolysis conditions. The relatively low per-layer thickness is due to the low molecular

weight PVP used in present study, as layer thickness is mainly determined by the viscosity of the solution. We did not observe the so-called “rosette” structure, which is common in Pb-containing ferroelectric films derived from a polymer [PVP or poly(ethylene glycol)]-modified sol-gel solution [8]. Two trends were identified by observing the surface morphology of the films. First, the number of the pores and their size increased with increasing PVP addition. Second, for samples prepared from the same solution (same PVP content), pore sizes were smaller in the SPT-treated samples. The more PVP added, the more polymer was burned out eventually; therefore, it is reasonable to expect more residual pores left in the films prepared from the solution with high PVP content. It is interesting that, although the final pyrolysis temperature was the same (450°C), films treated with additional thermal heating steps at lower temperatures demonstrated a higher degree of integrity. Previous research showed that PVP starts to decompose to carbonaceous species in the temperature range of 250-320°C, and the carbonaceous species are oxidized at \approx 360-460°C [9]. Therefore, our assumption was that additional heating stages at 300°C and 400°C would assist the decomposition and removal of PVP in a gradual and smooth manner, preventing it from directly decomposing into gaseous species in a sudden and violent manner, which is likely to result the formation of large size pores and/or even micro-cracks.

Figure 3 plots dielectric constant and dissipation factor as a function of applied bias field for the SPT- or RTA-treated samples with PLZT:PVP = 1:2 and 1:3; The properties were measured at 20°C and 150°C. The SPT-treated samples have much higher dielectric constant than the RTA-treated samples. The dielectric constant for the SPT-treated vs. the RTA-treated samples increases by \approx 38% and \approx 50% at 20°C and 150°C, respectively, for the PLZT:PVP=1:2 solution, and it increases by \approx 44% and \approx 56% at 20°C and 150°C, respectively, for the PLZT:PVP=1:3 solution. For samples derived from the solutions with a given PLZT to PVP ratio, since XRD analysis did not reveal any preferred crystallographic orientation and secondary phase, the difference in dielectric constant is ascribed to the difference in microstructures as a result of the different pyrolysis conditions. Furthermore, dielectric constant for both the SPT- and the RTA-

treated samples drops rapidly with the increase of the PVP content in the precursor solution. As shown in Fig. 2, samples with various PVP contents and pyrolyzed in different ways exhibited different microstructures. In general, SPT-treated samples with less PVP content exhibited a denser microstructure, and these samples thus showed higher dielectric constant. The dielectric constant values of the RTA-treated samples with PLZT:PVP = 1:2 are close to those of PLZT films deposited by an acetic-acid-based sol-gel process without PVP addition [10]. Dissipation factor of these samples is about 0.05 to 0.06 at room temperature, and it decreased slightly to 0.04 to 0.05 at 150°C, which is also at the same level as our previous results.

Figure 4 shows polarization-electric field (P-E) hysteresis loops of the PLZT films measured at room temperature. A high electric field up to 1000 kV/cm was applied. In general, all films show a relatively slim hysteresis loop, which is desirable for energy storage applications, as the area enclosed by the charge and discharge curves represents energy loss. Note that with increasing of PVP content, the shape of the loop starts to become “fatty,” it means that a larger portion of the electric energy stored would not be retrievable upon discharge. In addition, we found an increase in average remnant polarization [$P_r = (+P_r - (-P_r))/2$] and a decrease in average coercive field [$E_c = (+E_c - (-E_c))/2$] when the pyrolysis process was changed from RTA to SPT for the films derived from the solution with same PLZT:PVP ratio. For the PLZT:PVP = 1:2 solution, P_r increased from 13.3 to 13.9 $\mu\text{C}/\text{cm}^2$, while for the PLZT:PVP = 1:3 solution, P_r increased from 12.4 to 14.5 $\mu\text{C}/\text{cm}^2$. In terms of coercive field, E_c decreased from 83 to 59 kV/cm for the PLZT:PVP = 1:2 and from 112 to 91 kV/cm for the PLZT:PVP = 1:3 solution. Again, these differences can be explained by the microstructural features.

Time-relaxation data of leakage current density measured with 100 kV/cm field are given in Fig. 5. The decay in dielectric relaxation current obeys Curie-von Schweidler equation [5],

$$J = J_s + J_0 \cdot t^{-n} \quad (1)$$

where J_s is the steady-state current density, J_0 is a fitting constant, t is the relaxation time in seconds, and n is the slope of the log-log plot. The calculated steady-state current densities are listed in table 1. We can see that it follows a logical trend that films

with high PVP content and pyrolyzed with the RTA process show higher leakage current. In addition to the microstructural defects that can be used to interoperate this difference, more residual carbon left inside the films with high PVP content and pyrolyzed in a rapid way may also contribute to high leakage current. The leakage current value measured for the SPT-treated sample with PLTZ:PVP = 1:2 is close to that of the films deposited on nickel substrates using the same chemical solution but without PVP [3].

Table 1. Steady-state leakage current densities of the PLZT films.

Samples	Leakage current density (A/cm ²)
1:2 RTA	1.38×10^{-8}
1:2 SPT	5.43×10^{-9}
1:3 RTA	7.20×10^{-8}
1:3 SPT	4.12×10^{-8}

Dielectric breakdown strength (BDS) was measured on 25 samples tested in a top-to-bottom electrode configuration. Failure of the sample was defined by a 1- μ A criterion. The BDS data for the films derived from the PLZT:PVP = 1:2 solution presented as Weibull plots [3] (Fig. 6) due to the inherently statistical nature of failure. The samples treated by the SPT process show slightly higher mean BDS (BDS \approx 2.1 MV/cm) than the samples treated by the RTA process (BDS \approx 1.9 MV/cm). Furthermore, their Weibull moduli (β) exhibit a larger difference ($\beta=9.5$ for the RTA sample and $\beta=27.3$ for the SPT sample). Weibull modulus is a measure of distribution of the data: the higher the value of β , the smaller the variation of the data. Thus, a higher modulus indicates a better representation of the sample-to-sample performance as measured by mean breakdown strength. Here, the higher modulus found in the SPT-treated samples is attributed to their denser microstructure (Fig. 2), as residual porosity (especially so-called “critical flaws” that initiate the breakdown process) is always detrimental to the breakdown strength [11]. High breakdown strength, together with small data scattering, is of great importance for ceramic capacitors, as reliability is still one of the biggest concerns for this type of capacitor. Here, we demonstrated that with appropriate control of the

pyrolysis conditions, PLZT films with high reliability can be fabricated by a PVP modified sol-gel process.

Summary

In summary, we have grown high-quality ferroelectric PLZT films by a PVP modified sol-gel process. This process enables a per-layer coating thickness 3 times higher than the process without PVP addition. We developed a step-wise preheat treatment (SPT) procedure that is effective for preparation of high quality PLZT films, as it reduced the number and the size of the defects left by the decomposition of PVP. The PLZT films prepared by the SPT process exhibited good dielectric properties: dielectric constant \approx 860, dissipation factor \approx 0.06, leakage current \approx 5.4×10^{-9} A/cm², and breakdown strength \approx 2.1 MV/cm. These values are comparable to those of the films grown by the sol-gel method without PVP addition. This process should be potentially applicable for fabrication of film-on-foil capacitors with thickness >1 μ m for power electronics.

References

- [1] B. Ma, D.-K. Kwon, M. Narayanan, and U. Balachandran, *J. Electroceram.* 22, 383-389 (2009).
- [2] D.Y. Kaufman, S. Saha, and K. Uprety, *Proc. 12th US-Japan Seminar on Dielectric and Piezoelectric Ceramics*, Annapolis, MD, 305-308 (2005).
- [3] B. Ma, D.-K. Kwon, M. Narayanan, and U. Balachandran, *Mater. Lett.* 62, 3573-3575 (2008).
- [4] Q. Zou, H. E. Ruda, and B. G. Yacobi, *Appl. Phys. Lett.* 78, 1282 (2001).
- [5] K. Jonscher, *Dielectric Relaxation in Solids*, Chelsea Dielectrics Press, London (1983).
- [6] Y. Liu and P.P. Phule, *J. Am. Ceram. Soc.* 79, 495-498 (1996).
- [7] A. Yamano and H. Kozuka, *J. Am. Ceram. Soc.* 90, 3882-3889 (2007).
- [8] Z. H. Du and T. S. Zhang, and J. Ma, *J. Mater. Res.* 22, 2195-2203 (2007).

[9] H. Kozuka and S. Takenaka, *J. Am. Ceram. Soc.* 85, 2696-2702 (2002).

[10] B. Ma, S. Tong, M. Narayanan, S. Liu, S. Chao and U. Balachandran, *Mater. Res. Bull.* 46, 1124-1129 (2011).

[11] S. Chao, V. Petrovsky, and F. Dogan, *J. Mater. Sci.* 45, 6685-6693 (2010).

Publications and Presentations

[1] *Effect of dead layer and strain on the diffuse phase transition of PLZT relaxor thin films*, S. Tong, M. Narayanan, B. Ma, R. E. Koritala, S. Liu, U. Balachandran, D. Shi, *Acta Mater.*, 59, 1309, 2011.

[2] *Fabrication and dielectric property of ferroelectric PLZT films grown on metal foils*, B. Ma, S. Tong, M. Narayanan, S. Liu, S. Chao, U. Balachandran, *Mater. Res. Bull.*, 46, 1124, 2011.

[3] *Sol-Gel Synthesis of High-Quality SrRuO₃ Thin-Film Electrodes Suppressing the Formation of Detrimental RuO₂ and the Dielectric Properties of Integrated Lead Lanthanum Zirconate Titanate Films*, M. Narayanan, S. Tong, R. E. Koritala, B. Ma, V. Pol, U. Balachandran, *Chem. Mater.*, 23, 106, 2011.

[4] *Fabrication and Characterization of Ferroelectric PLZT Film Capacitors on Metallic Substrates*, B. Ma, M. Narayanan, S. Tong, U. Balachandran, *J. Mater. Sci.*, 45, 152, 2010.

[5] *Development of PLZT Dielectrics on Base-Metal Foils for Embedded Capacitors*, U. Balachandran, D. K. Kwon, M. Narayanan, B. Ma, *J. European Cer. Soc.*, 30, 365, 2010.

[6] *Improved Dielectric Properties of Lead Lanthanum Zirconate Titanate Thin Films on Copper Substrates*, M. Narayanan, B. Ma, and U. Balachandran, *Mater. Lett.*, 64, 22, 2010.

[7] *Dielectric Spectroscopy of Pb_{0.92}La_{0.08}Zr_{0.52}Ti_{0.48}O₃ Films on Hastelloy Substrates with and without LaNiO₃ Buffer Layers*, M. Narayanan, B. Ma, U. Balachandran, and W. Li, *J. Appl. Phys. Lett.*, 107, 024103, 2010.

[8] *Dielectric Properties and Energy Storage Capability of Antiferroelectric Pb_{0.92}La_{0.08}Zr_{0.95}Ti_{0.05}O₃ Film-on-Foil Capacitors*, B. Ma, D. K. Kwon, M. Narayanan, U. Balachandran, *J. Mater. Res.*, 24, 2993, 2009.

[9] *Chemical Solution Deposition of Ferroelectric Lead Lanthanum Zirconate Titanate Films on Base-*

Metal Foils, B. Ma, D. K. Kwon, M. Narayanan, and U. Balachandran, *J. Electroceram.*, 22, 383, 2009.

[10] *Fabrication of Antiferroelectric PLZT Films on Metal Foils*, B. Ma, D. K. Kwon, M. Narayanan, U. Balachandran, *Mater. Res. Bull.*, 44, 11, 2009.

[11] *Dielectric Strength and Reliability of Ferroelectric PLZT Films Deposited on Nickel Substrates*, B. Ma, M. Narayanan, U. Balachandran, *Mater. Lett.*, 63, 1353, 2009.

[12] *Method for Fabrication of Ceramic Dielectric Films on Copper Foils*, B. Ma, M. Narayanan, S. E. Dorris, and U. Balachandran, Patent Application US 2010/0302706A1, published Dec. 2, 2010.

Acronyms

2MOE	2-methoxyethanol
AXS	Analytical X-ray system
BDS	Dielectric breakdown strength
DF	Dissipation factor
GADDS	General area detector diffraction system
EDV	Electric drive vehicle
ESR	Equivalent series resistance
LNO	Lanthanum nickel oxide
PLZT	Lead lanthanum zirconium titanate
PVP	polyvinylpyrrolidone
PCB	Printed circuit board
RTP	Rapid thermal annealing
SPT	Step-wise preheat treatment
VT	Vehicle Technology
XRD	X-ray diffraction

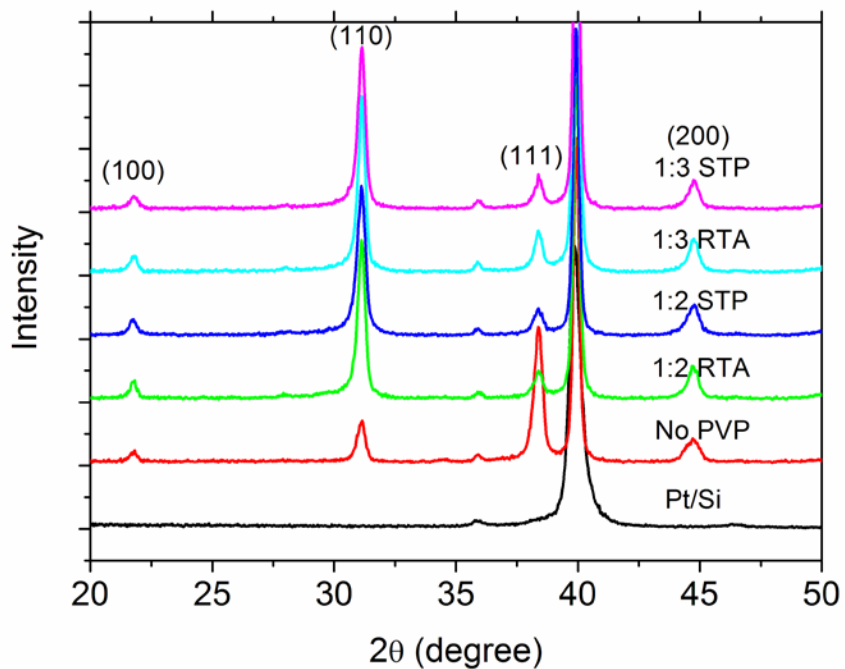


Figure 1. X-ray diffraction patterns of the PLZT films prepared by the SPT and RTA with different PLZT:PVP ratios.

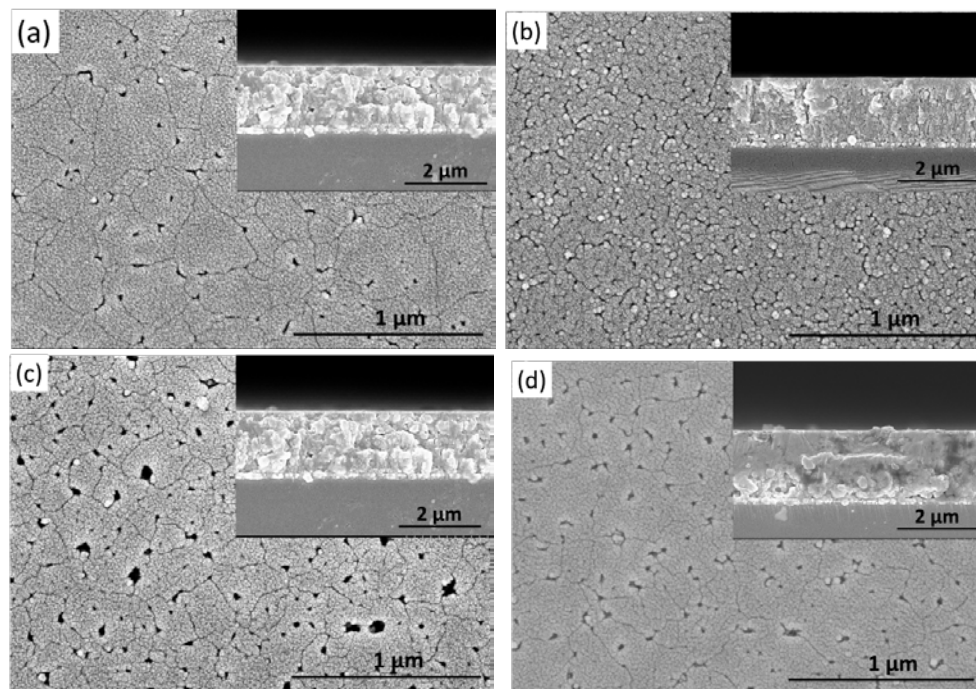


Figure 2. SEM images showing the surface and cross-sectional (insets) morphology of the PLZT films: (a) RTA, PLZT:PVP = 1:2; (b) SPT, PLZT:PVP = 1:2; (c) RTA, PLZT:PVP = 1:3; and (d) SPT, PLZT:PVP = 1:3.

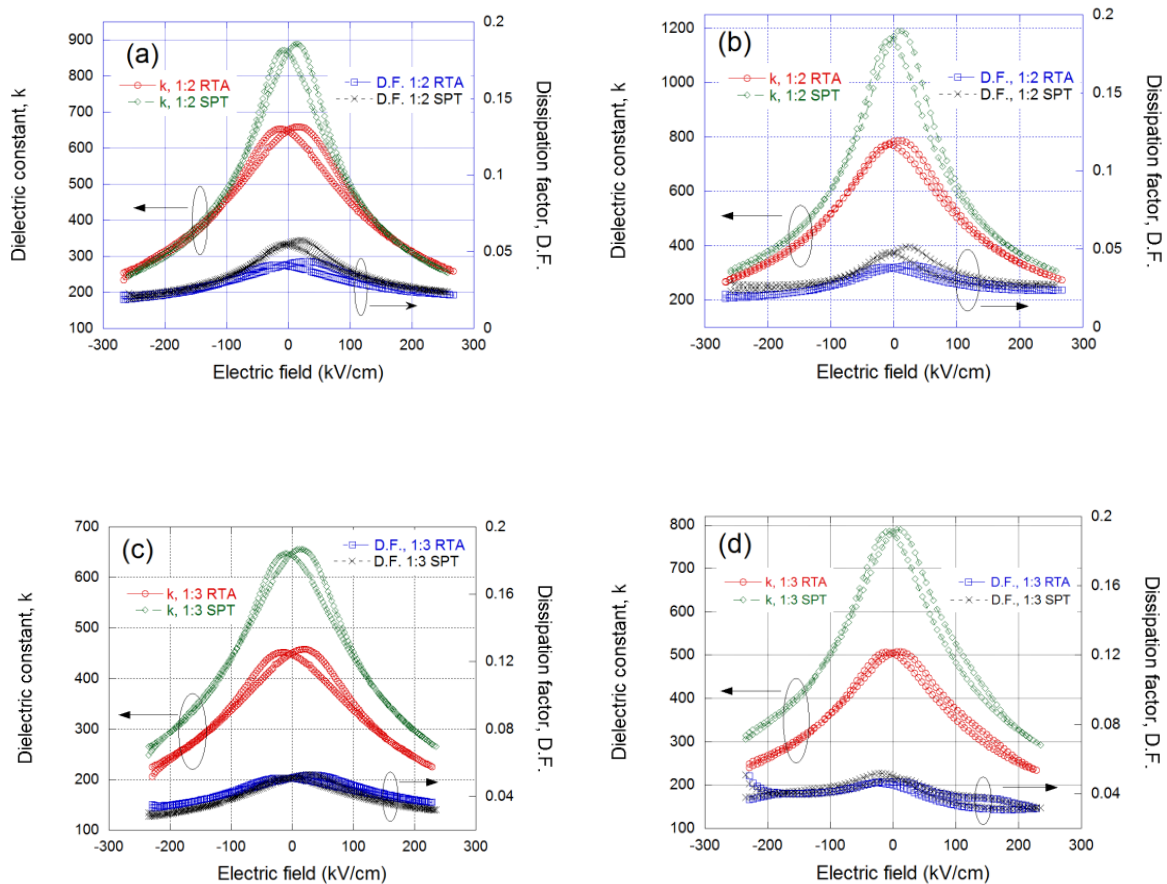


Figure 3. Dielectric constant (k) and dissipation factor (D.F.) of the PLZT films as a function of bias field: (a) PLZT:PVP=1:2, 20°C; (b) PLZT:PVP=1:2, 150°C; (c) PLZT:PVP=1:3, 20°C; and (d) PLZT:PVP=1:3, 150°C.

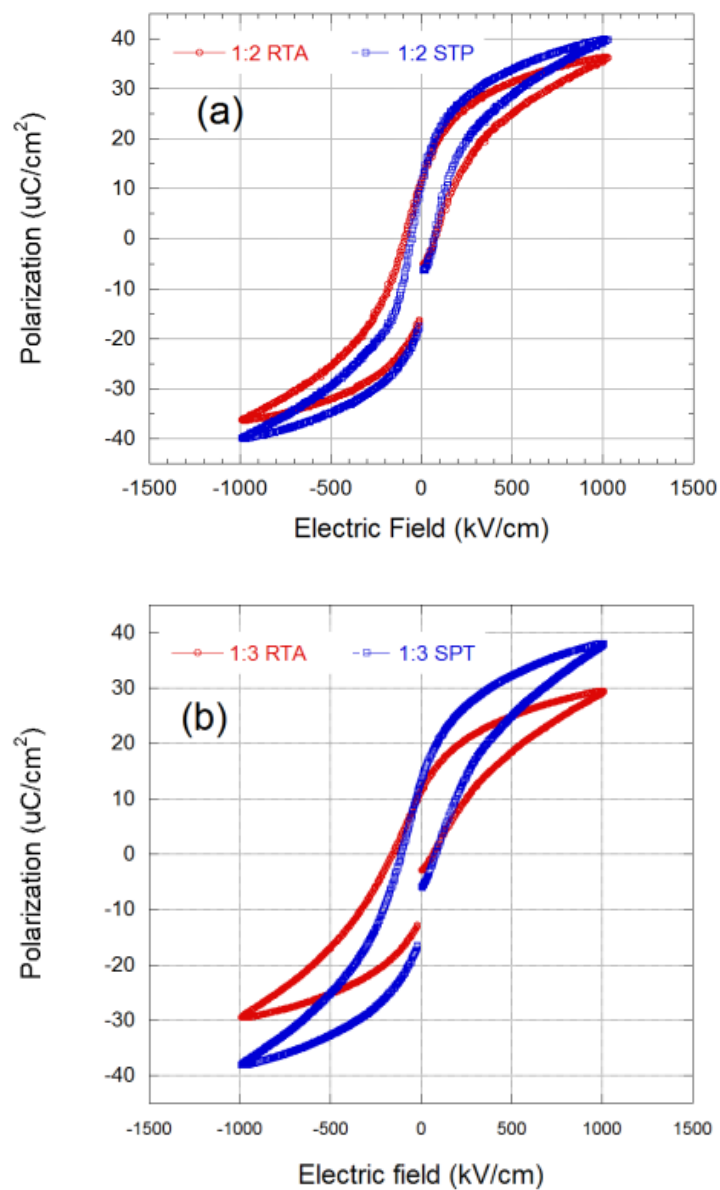


Figure 4. Hysteresis loops of the PLZT films at room temperature: (a) PLZT:PVP=1:2 and (b) PLZT:PVP=1:3.

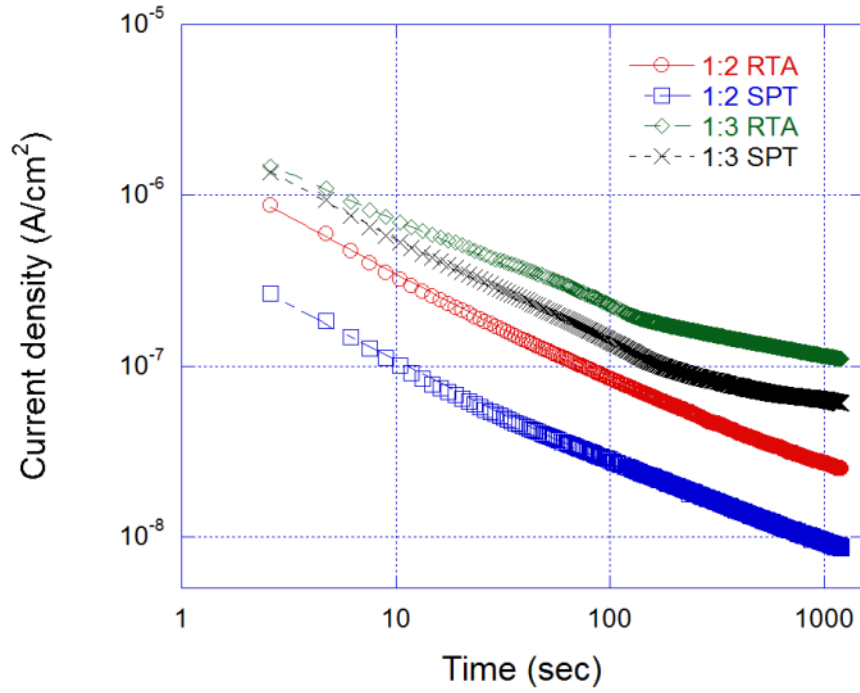


Figure 5. Current density relaxation of the PLZT films measured at 100 kV/cm at room temperature. Symbols are experimental data and solid lines are the fitting curves.

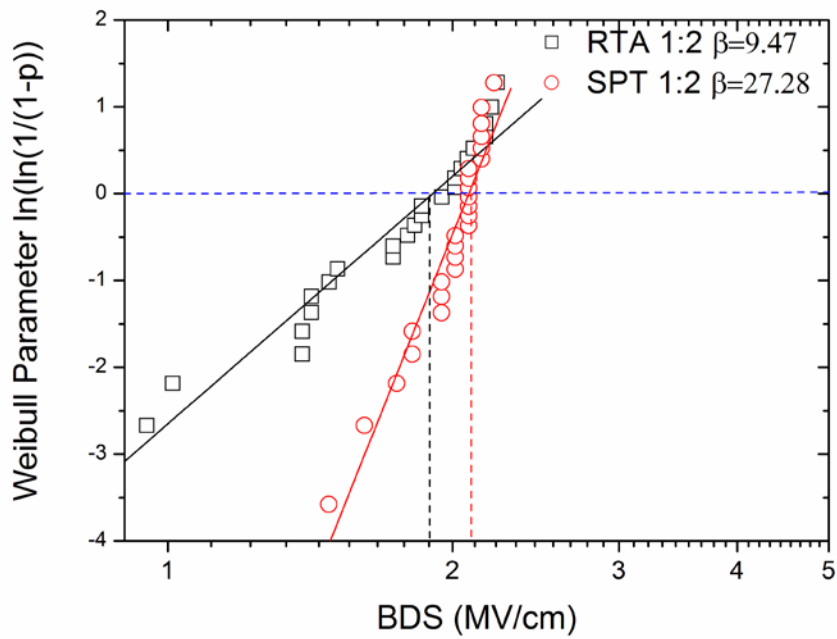


Figure 6. Weibull plots and corresponding parameters for dielectric breakdown strength of the films derived from the PLZT:PVP=1:2 solution and pyrolyzed by RTA and SPT.

Agreement 13295 - Permanent Magnet Development for Automotive Traction Motors (co-funded by Project 19026 – Electric Motors)

Principal Investigator: Iver E. Anderson

Division of Materials Sciences and Engineering

Ames Laboratory, Iowa State University

Ames, IA 50011

Voice: 515- 294-9791; Fax: (515) 294-8727; E-mail: andersoni@ameslab.gov

DOE Technology Development Manager: Susan A. Rogers

Voice: 202-586-8997; Fax: 202-586-1600; E-mail: Susan.Rogers@ee.doe.gov

DOE Technology Manager (Propulsion Materials): Jerry L. Gibbs

(202) 586-1182; fax: (202) 586-1600; e-mail: jerry.gibbs@ee.doe.gov

Objectives

- Develop the materials and processes needed to fabricate high performance permanent magnets (PM) that can be used for advanced traction drive motors with an internal PM rotor design to meet APEEM goals for enhanced performance at elevated temperature (180-200°C) and reduced cost.
- Anisotropic magnets should be developed to satisfy the need for magnets with maximum magnetic energy density and minimum content of valuable materials. If possible, improved magnet forming processes and mechanical properties also should be developed to further reduce manufacturing costs and extend lifetime in service.
- While magnet materials meeting the technical specifications are most readily achieved using rare earth (RE) permanent magnets, the market factors of rising RE demand/cost and near total foreign control of RE supplies dictate that in the long term, alternative non-RE magnets must be developed.

Approach

This program consists of two major thrust areas.

- Continue investigation of ***RE anisotropic*** permanent magnets, as recommended in an industry expert study, placing effort on generating anisotropic particulate for bonded magnets and on novel processing of sintered RE permanent magnets, exploiting the improved high temperature tolerance of the Ames mixed rare earth (MRE)-Fe-B alloys.
- Develop aligned microstructures in MRE-Fe-B magnet alloy particulate with little or no Dy content, preferably by controlled rapid solidification as a low cost route to make large gains in bonded magnet strength and reduced magnet cost for simplified motor manufacturing.
- Further develop anisotropic sintered permanent magnets from micron-sized single crystal particles of MRE-Fe-B alloys using pressure-driven liquid phase sintering with intrinsic or extrinsic sintering additives for fully dense magnets of the highest magnetic strength, aiming for greatly reduced Dy content.
 - It should be noted that techniques being developed to produce anisotropic RE magnets probably can be used in the second thrust area, as well.
- New high strength ***non-RE anisotropic*** permanent magnets will be developed that meet the requirements for advanced interior PM electric traction motors. The investigation will involve theory and modeling efforts, as well as experimental synthesis of magnet compounds and prototype magnet fabrication and characterization.

- Development of non-RE anisotropic permanent magnets will include attempts to improve on known systems, e.g., Alnico, by gaining enhanced knowledge of coercivity mechanisms with more sensitive characterization techniques and by innovative processing to improve coercivity using greater control of microstructure.
- Non-RE anisotropic permanent magnets also will be pursued with help from theory and modeling, seeking to discover new phases based on Fe-Co with beneficial intrinsic properties, i.e., high Curie temperature, magnetization and magnetic anisotropy.
- If the new non-RE permanent magnet phases have insufficient magnetic properties as single-phase magnets, increased properties will be sought with further extrinsic manipulation, including use a soft magnetic second phase to produce enhanced exchange coupling.
 - It should be noted that this task area is extremely high risk, but if successful it will revolutionize the cost structure of permanent magnet motors and reduce the reliance on foreign controlled commodities for hybrid and electric vehicle production.

Major Accomplishments

- For RE magnets, a large Dy reduction was enabled by targeted diffusion (at 900°C) of DyF₃ “paint” to the interior microstructure in anisotropic sintered MRE_{2.5}(Fe, Co)₁₄B magnets, where MRE = [Nd_{0.45}(Y₃Dy₁)_{0.55}], which achieved an energy product, (BH)_{max}, of 31.4MGOe and a coercivity, H_{ci}, of 15 kOe, both at ambient temperature, and a temperature coefficient of H_{ci}, β, of -0.5%/°C, all equivalent to commercial Nd-based Nd₂Fe₁₄B magnets that are used in drive motors for 200°C operation (EH grade, containing 8-10% Dy), but by using only 5.3wt.% Dy or about 45% less Dy for large magnet cost decrease.
- In development of particulate for anisotropic bonded MRE_{2.2}Fe₁₄B_{1.1} magnets without Dy, where MRE = [Y_{0.55}Nd_{0.45}], highly aligned columnar solidification patterns resulted from a novel Ag micro-alloying (<1at.% Ag) effect that achieved strong and unique texture control in ribbon samples that were melt spun at low speed (5m/s), producing an anisotropic particulate that was crushed for epoxy bonding and testing, but further microstructure scale refinement and texture design is needed before this concept is tailored for bonded magnets that can achieve suitable coercivity levels.
- In our search for non-RE permanent magnets, a genetic algorithm (GA) method was adapted to enable computational phase diagram exploration for alloys based on Fe-Co, speeding up by at least 1000 times the search for candidate chemical compositions with desirable structures and properties. Using only a shared computer cluster at Ames, an initial structure search of Fe-Co alloys successfully predicted structures at a specific range of compositions that have energies lower (more favorable) than those proposed in the literature, but further GA searching of Fe-Co-X systems for enhanced crystalline anisotropy will require the increased capabilities of a dedicated cluster and DOE supercomputer facilities, e.g., at ORNL.
- As a tool for rapid structural analysis in our “beyond RE magnets” (BREM) thrust, a multiple sample staging system was developed at the DOE synchrotron X-ray source at Stanford Synchrotron Research Laboratory and demonstrated by characterization of thin film samples from a Fe-Co-W combinatorial “library” of compositions, determining that an upper W content of about 15 at.% is set in this system by the onset of dominant amorphous phase formation.
- In the portion of the BREM thrust devoted to improvement of existing Alnico magnets, a series of density functional theory (DFT) calculations predicted that the magnetic anisotropy of Fe-Co layers at the interface of Fe-Co precipitates and the NiAl matrix phase is increased by two orders of magnitude, indicating that a significant coercivity benefit could result from reducing the spinodal spacing to far less than the typical 50 nm. TEM studies of commercial Alnico 5-7 magnets indicated that the chemical partitioning of Fe and Co in the NiAl matrix phase is far from complete, with about 30-40 at.% Fe-Co measured in this region, suggesting a further direction for microstructure improvement that can benefit the magnetic properties.

Future Directions

- Continue focused work on improved processing of ***RE anisotropic*** permanent magnets, stepping up studies on innovative processing of sintered RE permanent magnets and on direct solidification processing of anisotropic particulate for bonded magnets, exploiting the improved high temperature tolerance of the Ames mixed rare earth (MRE)-Fe-B alloys with little or no Dy content.
 - Focus on development of anisotropic sintered MRE magnets using pressure assisted sintering with extrinsic additives to permit greatly reduced temperatures for full consolidation, exploring additive alloy design to diminish or eliminate Dy use.
 - Enhance development of micro-alloying for direct solidification of MRE magnet alloy without Dy to refine spacing of aligned columnar microstructure in resulting ribbons and accentuate magneto-crystalline anisotropy in precursor particulate for bonded microcrystalline magnets.
 - Enhance the theory side of the effort to develop new high strength ***non-RE anisotropic*** permanent magnets that meet the requirements for advanced interior PM electric traction motors based on the critical need for compositional clarification of experimental directions. This will follow a compressed down-selection of promising magnet alloy compositions that is planned for early in FY2012. In general, it is critical that the investigation maintains close collaboration of theory and modeling efforts, of experimental magnet material synthesis work, and of detailed characterization studies on the new materials.
 - Refine and implement genetic algorithm calculations for rapid theoretical investigation of potential new phases in Fe-Co and Fe-Co-X alloys, starting with (by priority) W, Hf and Zr on a new dedicated cluster and on external supercomputer resources.
 - Focus density functional theory calculations on for Fe_mT_n , Co_mT_n , and $(\text{Fe-Co})_m\text{T}_n$, starting with (by priority) T=W, Hf, Zr, Mo, Ta, and Nb, to look for the most promising ternary compositions and use theory to investigate anti-phase boundaries and twinning effects on coercivity with small dedicated cluster computer.
 - Employ combinatorial synthesis experiments to explore limited composition ranges of $(\text{Fe-Co})_m\text{T}_n$, where T = Hf, Zr, Ta, and Nb, as well as any follow-up work needed on W and Mo, to look for the most promising ternary compositions, with detailed feedback from characterization efforts to enable effective screening of these systems.
 - Extend cluster deposition experiments to explore specific compositions of $(\text{Fe-Co})_m\text{T}_n$, starting with T=W and Hf to try promising new ternary compositions in highly metastable nano-particle configurations, where detailed characterization by TEM, XRD, and magnetometers will assist in search for promising M_s , K_1 and H_a values.
 - Develop chemical synthesis and self-assembly methodologies for limited composition ranges of Fe_mT_n , Co_mT_n , and $(\text{Fe-Co})_m\text{T}_n$, starting with W, Hf, and Zr, to gain understanding of the processing parameters for promising binary and ternary compositions in these nano-particle configurations. Desirable layered structures also will be developed as a step toward preparation of enhanced exchange coupled magnets.
 - Begin development of bulk magnet fabrication approaches to support the eventual need for full magnet sample testing of $(\text{Fe-Co})_m\text{T}_n$ alloys.
 - Utilize detailed characterization results for commercial Alnico as starting point for theoretical analysis of degree of improvement possible in this magnet family.
 - Implement initial theoretical analysis of a possible coercivity enhancement method in Alnico by microstructure control experiments, intending to refine precipitation size and spacing and to enhance solute segregation. Also, begin theoretical and experimental studies of Vicalloy system to determine potential for increased coercivity.
 - Conduct Annual Workshop (Nov. 2011---completed) and Spring Workshop (May 2012).
-

Technical Discussion

Accomplishments in Rare Earth Anisotropic ($R_2Fe_{14}B$ -type) Magnet Research

Dy Reduction in Anisotropic Sintered RE Magnets: Especially for temperatures above 120°C, the magnetic properties of isotropic MRE-based magnets are superior to those of current commercially available isotropic Nd-based magnets. Recently, grain-aligned sintered MRE-based magnets were developed with a maximum energy product $(BH)_{\max}$ above 25 MGOe, compared to the 12 MGOe of the MRE isotropic magnets. However, the sintered anisotropic MRE magnets exhibited a far stronger (undesirable) temperature dependence for the coercivity (i.e. higher β absolute value), similar to Nd-based magnets. An improved β value may be obtained by adding heavy rare earth elements such as Dy to the bulk magnet alloy to achieve higher magnetic anisotropy of the 2:14:1 phase to increase coercivity, but in the current commercial environment, this would add unacceptable high cost. It is known that the interface between the matrix phase and grain boundaries of the 2:14:1 grains in sintered magnets provides the nucleation sites for magnetization reversal, resulting in a low coercivity. Thus, we decided to attempt the targeted introduction of Dy at the grain boundary regions to strengthen magnetic anisotropy of the localized interfacial 2:14:1 phase regions and to more effectively improve coercivity of our MRE-based magnets with a significantly reduced Dy addition.

Based on this concept, Dy was introduced as a segregant into $MRE_2(Fe, Co)_{14}B$ magnets by using DyF_3 powder in two different methods, since this type of Dy addition can be less costly and much less susceptible to oxidation during processing. One method is referred to as a grain boundary diffusion treatment, where finished

sintered magnets with a thickness of 1.5mm were coated with DyF_3 powder (from an ethyl alcohol-based paint) and heated to 900°C to promote Dy diffusion along grain boundaries and into grain exteriors, producing “diffusion” magnets. Another method is that the magnet alloy powder is blended with DyF_3 powder and then made into sintered magnets by conventional methods, producing “blended” magnets. In this conventional method, ingots with an initial composition of $[Nd_{0.45}(Y_3Dy_1)_{1/(r+1)*0.55}]_{2.6}Fe_{bal}Co_{0.7}B$ were prepared by arc melting in an Ar atmosphere. The alloy ingots were then free-jet melt spun on a Cu wheel at a low wheel speed of about 2 m/s to obtain strip cast flakes. The strip cast flakes were subjected to hydrogen decrepitation (HD) treatment and milled into powders using conventional ball milling. The powders were aligned with a magnetic field of 1.8T, pressed and finally sintered in vacuum at 1050-1080°C for 2-4h to obtain a “baseline” magnet. In addition, the magnet alloy powder for making baseline magnets was blended with 5wt.% DyF_3 powder before ball milling and sintered/aligned to make blended magnets.

Magnetic properties were measured using a Quantum Design MPMS SQUID magnetometer with a maximum field of 5.0 T. As illustrated in the second quadrant of the hysteresis loop that is shown in Fig. 1, processing improvements raised $(BH)_{\max}$ @ RT of anisotropic sintered $MRE_{2.5}(Fe, Co)_{14}B$ “baseline” magnets from 25.6 to 32.7 MGOe, very similar to the ambient temperature energy product of industrial sintered magnets that are currently used for hybrid electric vehicles. The Dy addition to diffusion enhanced magnets raised H_{ci} to 15 kOe with $(BH)_{\max}$ maintained at 31.4 MGOe. The blended Dy addition to MRE magnets (5wt% DyF_3) also raised H_{ci} to 17.8 kOe, but the $(BH)_{\max}$ was reduced to 25.4MGOe, due to a considerable reduction of remanence.

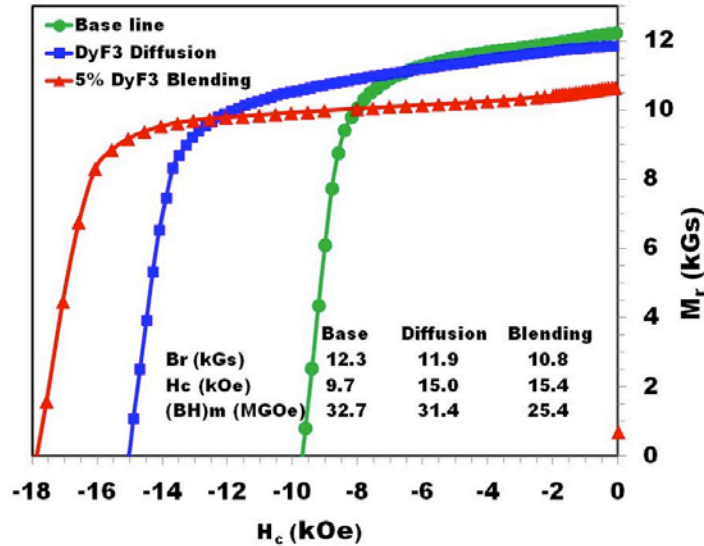


Figure 1. Summary of data from the second quadrant of the hysteresis loop for baseline, diffusion, and blended samples of MRE-(Fe-Co)-B, showing the effect of DyF₃ additions.

High temperature magnetic properties were measured by a vibrating sample magnetometer (VSM) with a field of 9.0T. The effect of coercivity on the temperature coefficients of coercivity in the temperature range of 27 to 127°C is shown in Fig. 2. For comparison, the magnetic properties of commercial Neomax magnets (from their data sheets) are also included in the figure. It is seen that the temperature coefficient of coercivity decreases with increasing coercivity. However, these magnets need quite different coercivities in

order to achieve the same acceptable β value, for example 0.5%/°C. The commercial Neomax magnets require a coercivity above 30 kOe, while the MRE magnets modified by DyF₃ blending and diffusion needed only 16 and 15 kOe, respectively. This means that the blending and diffusion modified MRE magnets need a lower amount of Dy to achieve the same thermal stability as Nd-based Neomax magnets, and that initial magnetization of Neomax magnets that are mounted in a soft magnetic (Fe-Si) rotor is more difficult.

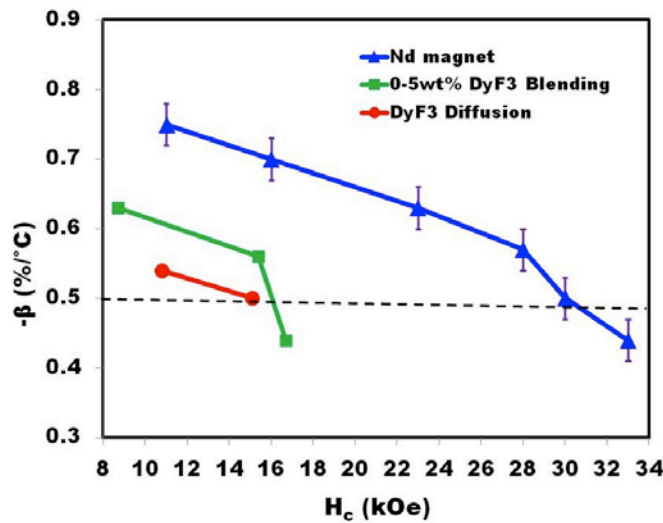


Figure 2. Summary of the effect of coercivity on the temperature coefficients of coercivity in the DyF₃ modified MRE magnet alloys for temperature range of 27 to 127°C, compared to data for commercial Neomax magnets.

Actually, Dy content vs. β value (seen in Fig. 3) clearly shows this fact. The Dy contents of the diffusion magnets were calculated according to the weight gain before and after diffusion treatment. The Dy contents of Nd-based magnets were estimated according to the data from published references, including product information on Neomax magnets. It is seen from Fig.3 that the diffusion or blending modified

MRE magnets with the same β value always require a lower amount of Dy than the Nd-based magnets. For example, the total Dy concentration in the MRE-based diffusion magnets with a β value of $-0.5\%/^{\circ}\text{C}$ was 5.3 wt%, while typical commercial Nd-based magnets that achieved such a useful β value needed about 10 wt% Dy.

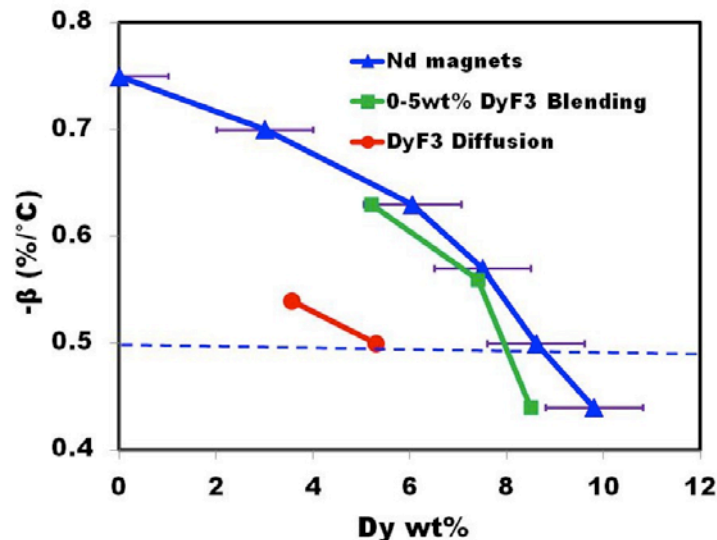


Figure 3. Summary of Dy content vs. β value, as further analysis of the data in Fig. 2.

These results indicate that the intrinsic temperature compensation effect contributed by the $\text{MRE}_2\text{Fe}_{14}\text{B}$ magnet alloy (containing Y and Dy, along with Nd) offers a significant advantage for high temperature operation, especially with DyF_3 diffusion modification of the sintered $\text{MRE}_2\text{Fe}_{14}\text{B}$ magnets. Thus, anisotropic sintered $\text{MRE}_{2.5}(\text{Fe}, \text{Co})_{14}\text{B}$ magnets achieved an energy product, $(\text{BH})_{\text{max}}$, of 31.4MGOe and a coercivity, H_{ci} , of 15 kOe, both at ambient temperature, and a temperature coefficient of H_{ci} , β , of $-0.5\%/^{\circ}\text{C}$. These characteristics are competitive with commercial Nd-based $\text{Nd}_2\text{Fe}_{14}\text{B}$ magnets that are used in drive motors for 200°C operation (EH grade, containing 8-10% Dy), but by using only 5.3wt.% Dy or about 45% less Dy for a large magnet cost decrease. For further advantage, new work will be started on DyF_3 diffusion magnets in a lower Dy version of MRE magnet alloy with a 6:1 ratio of Y:Dy, based on our earlier observations with isotropic magnets.

Aligned Particulate for Anisotropic Bonded RE Magnets: Control of microstructure and texture is of critical importance in forming rare earth (RE)-iron-boron particulate suitable for anisotropic bonded permanent magnets in order to obtain the highest performance from these alloys. Particulate for these applications must be able to maintain coercivity as well as having a large enough particle size to avoid excessive oxidation. Especially in the case of polymer-bonded magnets, anisotropic magnets would have a great advantage over current isotropic bonded magnets, up to 4X the maximum energy product. In this study, the selected approach to controlling grain size, while maintaining texture, is through stabilization and refinement of directional growth in melt-spun ribbons. To obtain suitable anisotropic particulate from these melt-spun ribbons, a mild crushing would be needed, followed by bonding with a polymer (or an alternative extrinsic binder phase) under an imposed magnetic field.

One avenue to obtain suitable directional growth in melt-spun ribbons was studied previously by Kramer et al.^{2,3} who determined the mechanism by which Nd-Fe-B ribbons that were melt-spun at low wheel speed (e.g. ~5-10 m/s) developed a $\langle 00l \rangle$ texture¹ on the free surface. This observation could not be directly exploited for the current study because there was often a final zone of coarse dendrites on the free surface and there was no obvious means to refine significantly the spacing of the columnar dendrites, which would be needed for anisotropic bonded magnets. However, we hypothesized that this refinement might be achieved by using a segregating (highly insoluble) additive, e.g., Ag, at the proper concentration to introduce instability in the Fe-rich liquid interface, promoting growth of a finer, textured structure. Moreover, the Nd-based 2-14-1 magnetic phase ($\text{Nd}_2\text{Fe}_{14}\text{B}$) is known to have poor high temperature magnetic properties. Fortunately, suitable MRE alloy particulate for isotropic polymer-bonded magnets for use at high temperatures (up to 200° C) previously was developed (in this project) through the addition of yttrium and a heavy rare earth element, i.e. Dy^2 , but concerns over price and availability of heavy rare earths have led us to experiment on Dy-free MRE alloys to see if a simple MRE of Y-Nd would provide sufficient high temperature magnetic properties. Thus, varying concentrations of Ag (0.3-1.7 at.% Ag) were added to melt-spun ribbons (produced with a 5 m/s wheel speed) of a base composition of $(\text{Y}_{0.55}\text{Nd}_{0.45})_{2.2}\text{Fe}_{14}\text{B}_{1.1}$.

In samples containing no Ag, significant variation in microstructure exists with some

regions displaying a columnar microstructure, but Fig. 4a shows a more typical microstructure. Along the wheel surface of these ribbons, a fine, equiaxed region exists (labeled “1” in Fig. 4a), but as growth proceeds a columnar region forms that is quickly interrupted by either large equiaxed grains (labeled “4” in Fig. 1a), or fine dendritic regions characterized by a large degree of secondary arm branching (labeled “5” in Fig. 4a). The bright phase in this micrograph corresponds to the RE-rich intergranular phase observed in typical sintered magnets. In all ribbons containing Ag, a layer of fine equiaxed grains, approximately 20 μm thick, was present near the wheel surface (identified in Fig.4b of the ribbon with 0.6 at. % Ag by the arrow labeled “1”). Projecting out of this region, columnar dendrites of $\text{MRE}_2\text{Fe}_{14}\text{B}$, extend through the thickness of the ribbon (denoted by the arrow labeled “2” in Fig. 4b). Alloys where $x \geq 0.1$ (0.6 at. % Ag) displayed a fine secondary phase, enriched in Ag and Nd (the bright spots labeled “3” in Figs. 4b), dispersed along the boundaries of the columns. Energy dispersive spectroscopy (EDS) of a TEM sample (not shown) indicated that this phase is likely a 2:1 (Ag:RE) intermetallic compound, with approximately 80% of the RE as Nd, with the remainder Y. This composition is consistent with a study of Nd-Fe-Ag equilibrium by Takeda et al. The morphology and distribution of the Ag_2RE phase indicated that the phase likely coarsened during cooling. In the sample with 0.3 at. % Ag (not shown), a more continuous RE-rich film coated the columnar dendrites, similar to the intergranular phase observed in sintered Nd-Fe-B magnets.

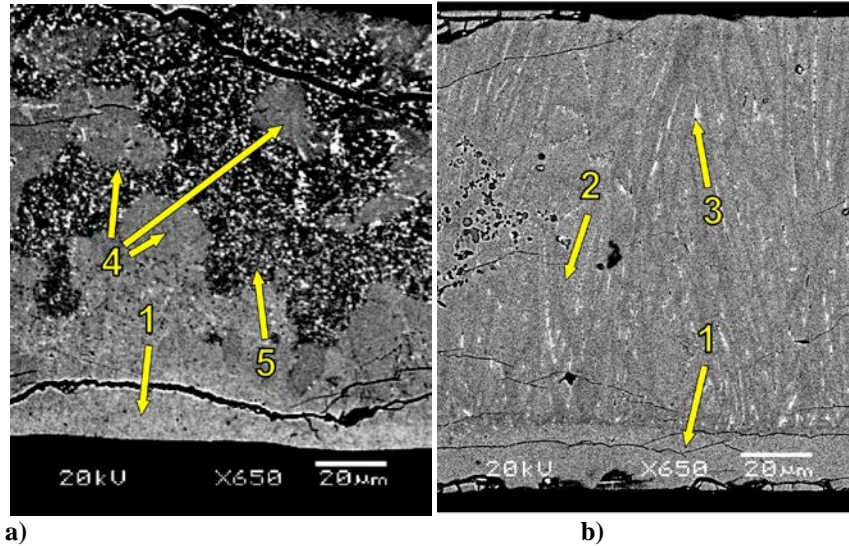


Figure 4 - Cross section BSE micrographs of $(Y_{0.55}Nd_{0.45})_{2.2}Fe_{14}B_{1.1}Ag_x$ ribbon melt-spun at 5 m/s, where x is a) 0.0, and b) 0.1 in at.%. Arrows point to features described in the text.

Average center-to-center column spacing was determined using a line-intercept method. This was plotted as a function of distance from the equiaxed/columnar grain interface (where columnar growth initiates) to determine the degree to which columnar growth is stabilized and refined (Fig. 5). All cases show a fine grain spacing ($\sim 2 \mu\text{m}$) near the interface between the equiaxed zone and the start of directional growth. The spacing slowly increases through the thickness of the ribbon. In the Ag-containing

alloys, the concentration of Ag seems to have some effect on the stability of spacing of the columns, with 0.10 wt.% Ag (0.6 at.%) as the most stable. However, an average error of $\pm 1.2 \mu\text{m}$ adds uncertainty to this finding. In the case without silver, the columnar structure breaks down and grain spacing increases drastically as the columnar grains give way to larger, equiaxed ones.

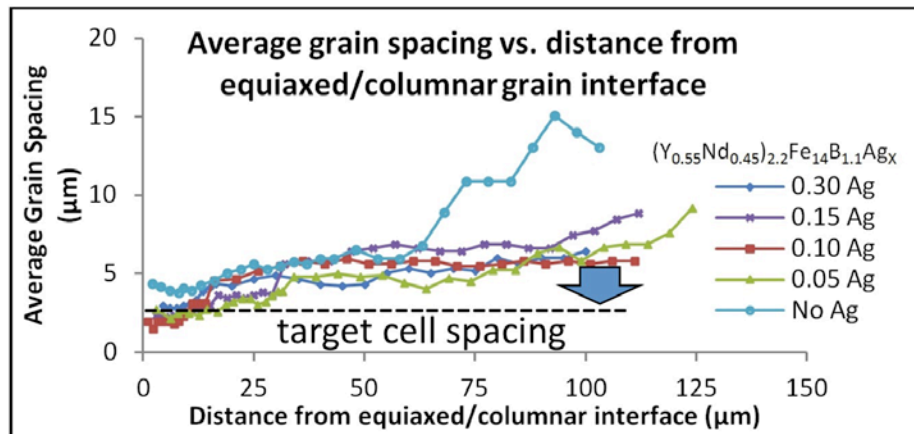


Figure 5. Summary of average center-to-center column spacing from line-intercept method in all ribbon alloys studied vs. distance from the equiaxed/columnar grain interface, where the labeled Ag contents are in wt.%.

It was determined that Ag stabilized through-thickness columnar growth in the ribbons with additions as small as 0.3 at. %, but the Ag also

produced a unique texture in the ribbons, compared to alloys with no Ag added. In MRE-Fe-B ribbons without Ag (see Fig. 6a), a strong

$\langle 00l \rangle$ texture was observed in the X-ray diffraction (XRD) patterns at the free surface, consistent with the Kramer^{2,3} mechanism. In all Ag-containing ribbons (0.6 at.% Ag shown in Fig

6b), the observed texture is canted to both the c- and a-axes, but the mechanism for this change is unclear.

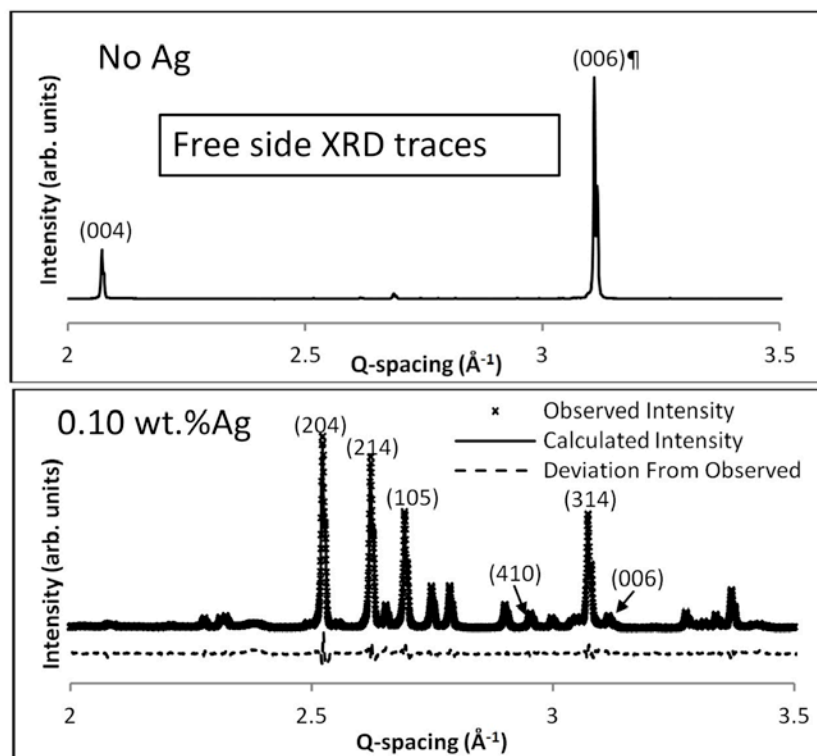


Figure 6. Comparison of the XRD patterns for a) a ribbon without Ag (top), and b) a ribbon with 0.6 at.% Ag (bottom).

The addition of Ag to RE-Fe-B alloys provided significant modification to the microstructure and growth observed and a columnar structure was stabilized through nearly the entire thickness of the ribbon. The spacing of these columns increased gradually as growth proceeded and this trend seemed to vary slightly with Ag concentration. The Ag also altered the texture in the ribbons, indicating a disruption in the normal $\text{RE}_2\text{Fe}_{14}\text{B}/\alpha\text{-Fe}$ templating mechanism⁴ for Ag-free magnet alloy ribbons melt-spun at low wheel speeds. While the novel texture obtained is not a single crystalline orientation (as desired for ease in optimum alignment), improved understanding of the new solidification sequence could lead to additional refinement (to the level indicated in Fig 5) and texture design, producing suitable coercivity levels in ribbons that could be crushed to form fragmented particulate for anisotropic bonded magnets fabrication.

Accomplishments in Beyond Rare Earth Magnets (BREM) Research

Genetic Algorithm for Rapid Computational Prediction of Magnet Materials:

Computational materials discovery now is being applied to the pursuit of superior permanent magnetic (PM) materials that do not contain rare earth (RE) elements, which are quickly rising in global strategic importance. Ames has developed computational algorithms and codes to perform supercomputer assisted phase diagram exploration and materials structure prediction and discovery, especially for iron-based alloys. This breakthrough speeds up the search process by at least 1000 times, making it possible to perform accelerated computational studies to identify candidate chemical compositions and structures that have desirable properties.

Ames' algorithm development represents a new paradigm to accelerate the discovery process. This computational approach is effectively coupled with a strong experimental synthesis effort in the Beyond Rare Earth Magnets (BREM) partnership, supplying mutual feedback to greatly speed up the materials discovery process far beyond trial and error methods. The algorithms, code, and experience gained in this effort will be directly applicable to other accelerated materials discovery efforts as well.

Using the shared cluster computer available at Ames Laboratory, an initial structure search for

Fe-Co binary alloys has successfully predicted structures at a range of compositions that have energies lower than those structures proposed in the literature (see Fig. 7). With the help of peta-scale computing power from Oak Ridge National Laboratory, for example, that should become available with further code development and demonstration, we hope to be able to explore much larger structural space, including Fe-Co-X alloys for enhanced crystalline anisotropy. We are confident that many new promising structures of Fe-based compounds can be discovered from these calculations to guide experimental design and synthesis of new non-RE permanent magnets.

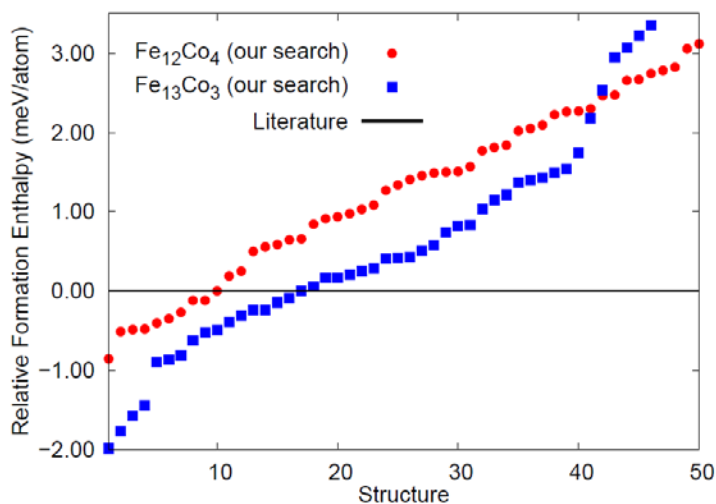


Figure 7. Structures of Fe₁₂Co₄ and Fe₁₃Co₃ obtained from our genetic algorithm search with energies lower than that of the best structures proposed in the literature.

Rapid Crystal Structure and Phase Composition Mapping: The BREM Characterization group (I. Takeuchi and M. Kramer) was successful in getting a Program User Proposal awarded at Stanford Synchrotron Research Laboratory (SSRL), a DOE User Facility, to develop a versatile instrument for systematically carrying out micro-diffraction for high-throughput studies. The instrument will allow us to perform rapid scanning of composition using energy dispersive spectroscopy (EDS) and crystal structure using micron resolution X-ray diffraction (XRD), thus providing rapid elemental and phase mapping on a variety of thin film and bulk samples. The instrument will be able to perform moderately high temperature (up to 1200°C) annealing in a

controlled environment (inert, oxidizing and vacuum) with programmable heating rates to obtain complete composition and phase analysis of a multiple sample array in a single experiment. The sample holder will be flexible so as to hold combinatorial thin film libraries and diffusion multi-couples that cover multi-component phase diagram regions. Combined with other rapid characterization methods, this instrument will allow quick navigation of phase space to search for novel compounds with enhanced magnetic properties. The next critical step will be the development of software to analyze the large amount of data obtained, enabling easy visualization and searching of the database that is generated.

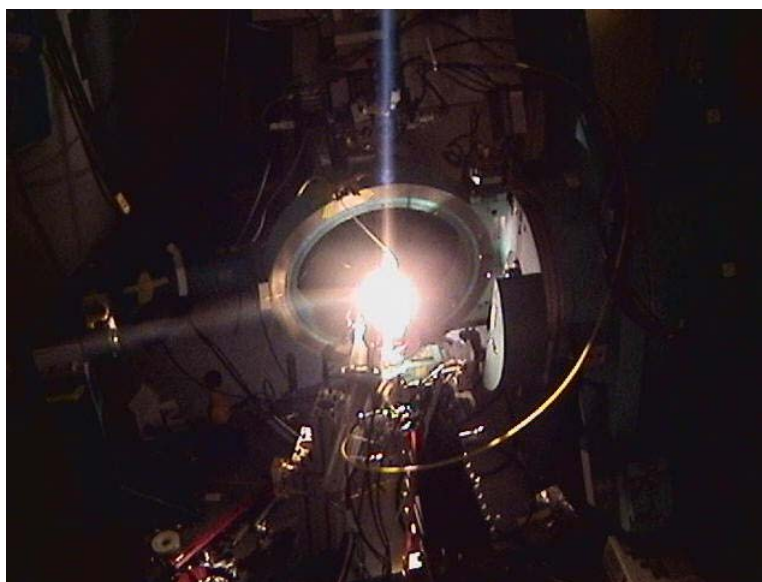


Figure 8. Photograph of prototype system in-use for high through-put chemical and structural phase mapping at SSRL.

In February of 2011, we carried out preliminary experiments at SSRL using a vacuum lamp heating set up, and it was verified that in situ annealing and phase mapping experiments could be performed (Fig. 8). The system studied was a ternary Fe-Co-W thin film combinatorial “library.” The library, composed of an array of discrete “tiles”, was formed by co-sputtering from separate Fe, Co, Fe-50W, and Co-50W (in at.%) sources onto a 10 cm Si/SiO₂ wafer. Most of the tile regions in the as-deposited films were amorphous material so the sample was externally annealed at 600°C. The XRD mapping showed that there were clear structural changes between samples with less than about 15%W. The low W regions were crystalline bcc-Fe (Fig. 9) and had higher magnetization

and coercivity (from separate mapping experiments) than the mostly amorphous regions that were richer in W (Fig. 10). In the future, we plan to heat these samples in situ.

Improvements to Alnico Magnets: Of the commercially viable non-RE magnets, ALNICO has the highest remanent magnetization however it is severely limited by its low coercivity. This is due to the fact that the anisotropy in ALNICO is a result of shape anisotropy of the magnetic phase, Fe-Co, and an essentially nonmagnetic phase, NiAl (Figure 11). Commercial ALNICO magnets have coercivities approaching the limit of shape anisotropy so that improvements will be dependent on our ability to add other forms of anisotropy such as surface anisotropy.

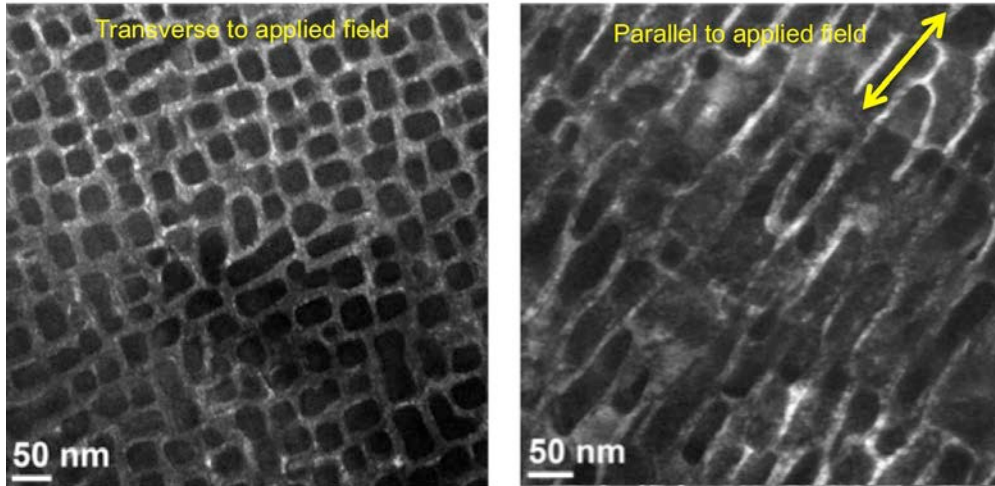


Figure 11. TEM dark field images of Arnold Alnico 5-7 magnet microstructure with Fe-Co precipitates (dark) in a NiAl matrix (light).

Using density functional theory (DFT) we have predicted that the magnetic anisotropy of Fe-Co layers at the interface of Fe-Co precipitates and the NiAl matrix phase is increased by two orders of magnitude over that of the bulk (Figure 12). This suggests that both improving the sharpness of the interface and increasing the interfacial area should lead to increasing the coercivity of the magnets. Current studies have focused on characterizing the interface structure and chemistry.

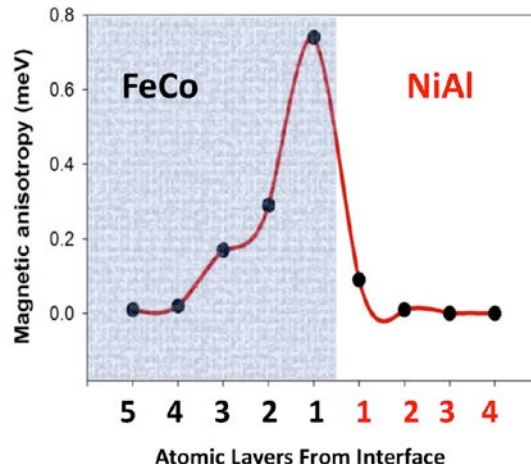


Figure 12. Density functional theory (DFT) calculations predict that anisotropy of Fe-Co layers at the Fe-Co/NiAl interface is increased by two orders of magnitude.

TEM studies of commercial ALNICO 5-7 magnets (Fig. 13) indicated that the chemical partitioning of Fe and Co in the NiAl matrix phase is far from complete, with about 30-40 at.% Fe-Co measured in this region compared to an equilibrium value of less than 10% according to the published phase diagrams. This suggests

improving the sharpness of the chemical partitioning of the spinodal can greatly improve the magnetic properties. In order to refine our knowledge of the spinodal kinetics, further characterization of ALNICO alloys with various heat treatments are planned using atom probe tomography (APT).

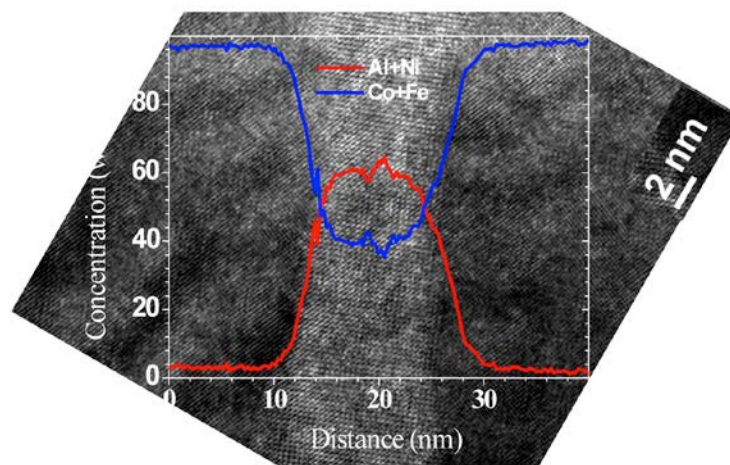


Figure 13. Representative EDS line scan (in the TEM) across the cubic NiAl interface between two bcc Fe-Co precipitates, showing concentration in at. %.

In order to increase the interfacial area, the spinodal spacing must be reduced to far less than the typical 50 nm. Theoretically, it should be possible to adjust the spinodal spacing by adjusting the heat treatment schedule for the decomposition and experimental studies are expected to verify this. Changes in the heat treatment are also expected to alter the concentration profiles of Fe and Co in the ALNICO.

Conclusions

For RE magnets, a large Dy reduction was enabled by targeted diffusion (at 900°C) of DyF₃ “paint” to the interior microstructure in anisotropic sintered MRE_{2.5}(Fe, Co)₁₄B magnets. This work achieved an energy product, (BH)_{max}, of 31.4MGOe and a coercivity, H_{ci}, of 15 kOe, both at ambient temperature, and a temperature coefficient of H_{ci}, β, of -0.5%/°C. These magnetic properties are all equivalent to commercial Nd-based Nd₂Fe₁₄B magnets that are used in drive motors for 200°C operation, containing 8-10% Dy. Our diffusion method for targeted enhancement of Dy additions used only 5.3wt.% Dy or about 45% less Dy, which could enable a large magnet cost decrease. In development of particulate for anisotropic bonded MRE_{2.2}Fe₁₄B_{1.1} magnets without Dy, highly aligned columnar solidification patterns resulted from a novel Ag micro-alloying (<1at.% Ag) effect. A strong and unique texture was achieved in these ribbon samples. In a

demonstration of the concept, mild crushing produced an anisotropic particulate that was bonded with epoxy and tested, but further microstructure scale refinement and texture design is needed before such magnets that can achieve suitable coercivity levels.

In our search for non-RE permanent magnets, a genetic algorithm (GA) method was adapted to enable computational phase diagram exploration for alloys based on Fe-Co, speeding up by at least 1000 times the search for candidate chemical compositions with desirable structures and properties. Using only a shared computer cluster at Ames, an initial structure search of Fe-Co alloys successfully predicted structures at a specific range of compositions that have energies lower (more favorable) than those proposed in the literature, but further GA searching of Fe-Co-X systems for enhanced crystalline anisotropy will require the increased capabilities of a dedicated cluster and DOE supercomputer facilities, e.g., at ORNL. As an experimental tool for rapid structural analysis in our “beyond RE magnets” (BREM) thrust, a multiple sample staging system was developed at the DOE synchrotron X-ray source at Stanford Synchrotron Research Laboratory and demonstrated by characterization of thin film samples from a Fe-Co-W combinatorial “library” of compositions. It was determined that an upper W content of about 15 at.% exists

in this system for the onset of dominant amorphous phase formation. For improvement of existing Alnico magnets, a series of density functional theory (DFT) calculations predicted that the magnetic anisotropy of Fe-Co layers at the interface of Fe-Co precipitates and the NiAl matrix phase is increased by two orders of magnitude. These results indicated that a significant coercivity benefit could result from reducing the spinodal spacing to far less than the typical 50 nm. TEM studies of commercial Alnico 5-7 magnets indicated that the chemical partitioning of Fe and Co in the NiAl matrix phase is far from complete, with about 30-40 at.% Fe-Co measured in this region, suggesting a further direction for microstructure improvement that can benefit the magnetic properties.

Publications

W. Tang, Y. Q. Wu, N. T. Oster, K. W. Dennis, M. J. Kramer, I. E. Anderson, and R. W. McCallum, *Improved energy product in grained aligned and sintered MRE₂Fe₁₄B magnets MRE=Y+Dy+Nd*, *J. Appl. Phys.*, 107, 09A728 (2010).

R. Skomski, V. Sharma, B. Balamurugan, J. E. Shield, A. Kashyap, and D. J. Sellmyer, *Anisotropy of Doped Transition-Metal Magnets*, Proc. REPM'10, Eds.: S. Kobe and P. McGuinness, Jozef Stefan Institute, Ljubljana, pp. 55-60, 2010.

P. Manchanda, P. Kumar, V. Sharma, A. Kashyap, R. Skomski, and D. J. Sellmyer, *Proximity Moment and Anisotropy in Fe-Rich Thin Films*, Proc. REPM'10, Eds.: S. Kobe and P. McGuinness, Jozef Stefan Institute, Ljubljana, pp. 157-160, 2010.

V. Sharma, P. Manchanda, R. Skomski, D.J. Sellmyer, and A. Kashyap, *Anisotropy of Heavy Transition Metal Dopants in Co*, *J. Appl. Phys.* **109**, 07A727 (1-3) (2011).

A. Kashyap, R. Skomski, P. Manchanda, J.E. Shield, and D.J. Sellmyer, *Layered Transition-Metal Permanent-Magnet Structures*, *J. Appl. Phys.* **109**, 07A714 (1-3) (2011).

R. Skomski, A. Kashyap, A. Enders, *Is the Magnetic Anisotropy Proportional to the Orbital Moment?*, *J. Appl. Phys.* **109**, 07E143 (2011).

References

1. D. Dadon, Y. Gefen, and M. Dariel, "The texture of melt spun Fe₇₆Nd₁₆B₈ ribbons," *Magnetics, IEEE Transactions on*, vol. 23, pp. 3605-3606, 1987.
2. M. J. Kramer, N. Yang, R. W. McCallum, K. W. Dennis, and L. H. Lewis, "In situ determination of Nd-Fe-B crystallization pathways," *J. Appl. Physics*, vol. 91, pp. 8156-8158, 2002.
3. M. J. Kramer, L. H. Lewis, L. M. Fabietti et al., "Solidification, microstructural refinement and magnetism in Nd₂Fe₁₄B," *Journal of Magnetism and Magnetic Materials* **241** (1), 144-155 (2002).

Patents

1. R. W. McCallum, Y-W. Xu, I. E. Anderson, K. W. Dennis, and M. J. Kramer, U.S. Patent Application (PCT) filed November 18, 2002, "Permanent Magnet Alloy with Improved High Temperature Performance," under examination.

Project 18518 – Materials for High Efficiency Engines

Agreement 8697 - NO_x Sensor Development

Leta Y. Woo and Robert S. Glass

Lawrence Livermore National Laboratory

P.O. Box 808, L-103

Livermore, CA 94551-9900

(925) 423-7140; fax: (925) (422-5844); e-mail: glass3@llnl.gov

DOE Technology Manager: Jerry L. Gibbs

(202) 586-1182; fax: (202) 586-1600; e-mail: jerry.gibbs@ee.doe.gov

Contractor: Lawrence Livermore National Laboratory, Livermore, California

Prime Contract No.: W-7405-Eng-48; LLNL-TR-510234

Objectives

- Develop an inexpensive, rapid-response, high-sensitivity and selective electrochemical sensor for oxides of nitrogen (NO_x) for compression-ignition, direct-injection (CIDI) OBD II systems
- Explore and characterize novel, effective sensing methodologies based on impedance measurements and designs and manufacturing methods that are compatible with mass fabrication
- Collaborate with industry in order to (ultimately) transfer the technology to a supplier for commercialization

Approach

- Use an ionic (O²⁻) conducting ceramic as a solid electrolyte and metal or metal-oxide electrodes
- Correlate NO_x concentration with changes in cell impedance
- Evaluate sensing mechanisms and aging effects on long-term performance using electrochemical techniques
- Collaborate with Ford Research Center to optimize sensor performance and perform dynamometer and on-vehicle testing

Accomplishments

- Completed licensing of the LLNL NO_x technology to a company, EmiSense Technologies, LLC, which is located in Salt Lake City and has extensive resources for the development of advanced emission technology
- Used dynamometer testing to demonstrate application of cross-sensitivity mitigation strategies and to confirm robust performance of LSM sensor prototype while also using additional advanced emission test protocols requested by commercialization entities
- Publications/Presentations:
 - L.Y. Woo, R.S. Glass, R.F. Novak, and J.H. Visser, "Diesel engine dynamometer testing of impedancemetric NO_x sensors." *Sensor Actuat. B-Chem.*, 157:115-121, 2011.
 - L.Y. Woo, R.S. Glass, R.F. Novak, and J.H. Visser, "Impedance Analysis of High-Temperature Electrochemical NO_x Sensor Based on Porous Yttria-Stabilized Zirconia (YSZ)," 2011 Spring Meeting of the Materials Research Society, San Francisco, California, April 25-29, 2011.
 - L.Y. Woo and R. S. Glass, "NO_x Sensor Development," project ID #PM005, Annual Merit Review and Peer Evaluation. Washington, D.C., June 10, 2010

Future Directions

- Continue developing more advanced prototypes suitable for cost-effective, mass manufacturing and for optimizing performance, including long-term stability and cross-sensitivity, in laboratory, dynamometer, and on-vehicle tests
- Develop CRADA with EmiSense Technologies, LLC and initiate collaborative program along with Ford Motor Company to bring the NO_x sensor technology to commercialization and mass production (project on-vehicles by 2016)

Introduction

NO_x compounds, specifically NO and NO₂, are pollutants and potent greenhouse gases. Compact and inexpensive NO_x sensors are necessary in the next generation of diesel (CIDI) automobiles to meet government emission requirements and enable the more rapid introduction of more efficient, higher fuel economy CIDI vehicles.¹⁻³

Because the need for a NO_x sensor is recent and the performance requirements are extremely challenging, most are still in the development phase.⁴⁻⁶ Currently, there is only one type of NO_x sensor that is sold commercially, and it seems unlikely to be able to meet more stringent future emission requirements.

Automotive exhaust sensor development has focused on solid-state electrochemical technology, which has proven to be robust for in-situ operation in harsh, high-temperature environments (e.g., the oxygen stoichiometric sensor). Solid-state sensors typically rely on yttria-stabilized zirconia (YSZ) as the oxygen-ion conducting electrolyte, which has been extensively explored, and then target different types of metal or metal-oxide electrodes to optimize the response.²⁻⁶

Electrochemical sensors can be operated in different modes, including amperometric (current based) and potentiometric (potential based), both of which are direct current (dc) measurements. Amperometric operation is costly due to the electronics necessary to measure the small sensor signal (nano-ampere current at ppm NO_x levels), and cannot be easily improved to meet the future technical performance requirements. Potentiometric operation has not demonstrated enough promise in meeting long-term stability requirements, where the voltage signal drift is thought to be due to aging effects associated with electrically driven changes, both morphological and compositional, in the sensor.⁷

Our approach involves impedancemetric operation, which uses alternating current (ac) measure-

ments at a specified frequency. The approach is described in detail in previous reports and several publications.⁸⁻¹² Impedancemetric operation has shown the potential to overcome the drawbacks of other approaches, including higher sensitivity towards NO_x, better long-term stability, potential for subtracting out background interferences, total NO_x measurement, and lower cost materials and operation.⁸⁻¹¹

Past LLNL research and development efforts have focused on characterizing different sensor materials and understanding complex sensing mechanisms.⁸⁻¹² Continued effort has led to improved prototypes with better performance, including increased sensitivity (to less than 5 ppm) and long-term stability, with more appropriate designs for mass fabrication, including incorporation of an alumina substrate with an imbedded heater and a protective sensor housing (see Fig. 1). Using multiple frequency measurements, an algorithm has been developed to subtract out that portion of the response due to interfering species.

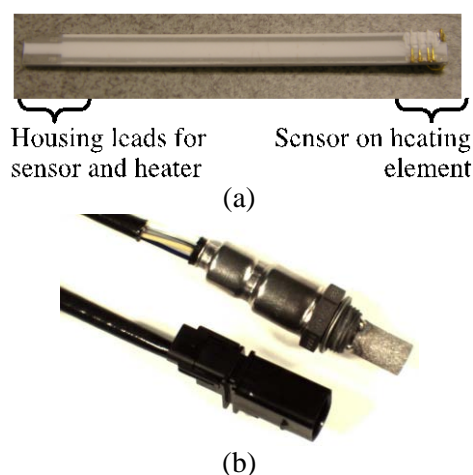


Figure 1. Picture of (a) alumina substrate with imbedded heater, provided by Ford Motor Company, suitable for packaging into (b) protective sensor housing.

Efforts in FY2011 have focused on using the previously developed algorithm to demonstrate how data from controlled laboratory evaluation could be applied to data from real-world engine testing. Other progress this year included dynamometer vehicle testing using advanced emission test protocols to confirm robustness and durability and also evaluating advanced material processing methods for mass manufacturing. As noted above, the LLNL NO_x sensor technology has been licensed to EmiSense Technologies, located in Salt Lake City. This will greatly accelerate the commercialization for this technology.

Background

For a two-electrode electrochemical cell, impedancemetric sensing requires that at least one of the electrodes act as the “sensing” electrode with selective response to NO_x over other gas phase components. This contrasts to the case in potentiometric sensing, which relies on differential measurements between the two electrodes. The impedancemetric sensor design is quite flexible and can either contain one sensing electrode and one counter (i.e., non-sensing) electrode, or two sensing electrodes. It opens up the opportunity to use a wide variety of materials, both metal and metal oxides.

Both electrode composition and microstructure influence sensitivity, which relies on limiting the oxygen reaction on the electrode so that the NO_x reaction can be resolved.⁹⁻¹¹ In general, for the “sensing” electrode a dense microstructure is required with appropriate composition to limit the catalytic activity towards oxygen.¹⁰⁻¹¹

Measured sensor impedance is a complex quantity with both magnitude and phase angle information. The phase angle has been found to provide a more stable response at higher operating frequencies and we prefer it for the sensor signal.⁸⁻¹²

In previous work, impedancemetric sensing using either gold or strontium-doped lanthanum manganite (LSM) electrodes, the latter being an electronically conducting metal oxide, was investigated in laboratory and engine testing. Preliminary results indicated that gold electrodes have good stability and the potential for low water cross-sensitivity, but also have a higher thermal expansion coefficient and lower melting temperature than the YSZ electrolyte, which limit processing flexibility. LSM electrodes have high melting temperatures and better thermal expansion match with YSZ, but have shown higher water cross-sensitivity than gold.

Experimental

The prototype incorporated a Au wire sensing electrode and a Pt counter electrode.¹² The prototype used a dense alumina substrate (99.6% Al₂O₃, 10 mm x 10 mm x 0.5 mm, Valley Design Corp.). The counter electrode was formed using platinum ink (Engelhard 6082) that was applied to the substrate and fired for two hours at 1200°C. A slurry of yttria-stabilized zirconia (YSZ) powder (Tosoh Corp., 8 mol % Y₂O₃-doped ZrO₂) mixed with ethanol, binder (polyvinyl butyral, Butvar), dispersant (phosphate ester), and plasticizer (dipropylene glycol dibenzoate) was then applied on top of the fired Pt counter electrode. Au wire (0.25 mm diameter, Alfa Aesar) electrodes were wrapped around the entire substrate with additional YSZ slurry applied on top of the wires. The assembled prototype was fired for two hours at 1000°C. Figure 2 shows a schematic of the Au wire NO_x sensor prototype, which consists of porous Pt, porous YSZ, and dense Au wire. Additional ceramic adhesive (Ultra-Temp 516, Aremco Products, Inc.) was applied along the edges to secure the Au wire electrodes to the alumina substrate.

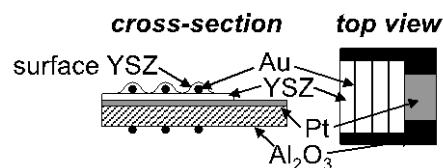


Figure 2. Schematic of Au wire NO_x sensor prototype.

Laboratory experiments were performed in a quartz tube (21.4 mm I.D.) placed inside a tube furnace with both electrodes exposed to the same environment. The gas composition was controlled by mixing air, N₂, and a 1000 ppm NO/NO₂ feed using a standard gas handling system equipped with thermal mass flow controllers. The total gas flow rate was fixed at 500 ml/min. The water concentration was controlled to approximately 2% by flowing mixtures of air and N₂ through a water bubbler and combining with dry mixtures of N₂, NO, and NO₂, which prevented NO_x from dissolving in the water. Measurements were made at 650°C.

Impedance measurements were performed using a Solartron 1260 Impedance Analyzer in combination with a Solartron 1287 Electrochemical Interface, while engine testing at Ford used a stand-alone Solartron 1260 Impedance Analyzer. Computer-

controlled data acquisition used the commercially available ZPlot software (Scribner Associates, Inc.).

Dynamometer testing of diesel engine exhaust was performed at Ford Research Center using an engine test cell with engine gas recirculation (EGR) and a urea-based selective catalytic reduction (SCR) system for reducing NO_x emissions. A portion of the tailpipe exhaust was extracted from the main exhaust and fed into a furnace containing the Au wire NO_x prototype sensor. Due to variations in the exhaust gas flow rate for different engine conditions, temperature fluctuations in the furnace were monitored using a thermocouple placed in close proximity to the sensor prototype. Measured temperatures ranged from approximately 650 to 670°C. A commercial NO_x sensor was located downstream of the prototype.

Data in tailpipe exhaust were obtained using a constant engine speed of 2750 rpm, and the exhaust gas composition was altered as described by the following. The exhaust gas composition, consisting of CH₄, NO, NO₂, NH₃, CO, CO₂, and H₂O, was determined using Fourier transform infrared (FTIR) spectroscopy, and O₂ concentration was determined using a paramagnetic oxygen analyzer.

A flow diagram of the dynamometer test setup is shown in Fig. 3. Two different protocols were used for the engine test. The first protocol involved constant throttle operation while stepping through different rates of urea injection, while the second protocol involved a fixed amount of urea injection while stepping through different percents of engine throttle.

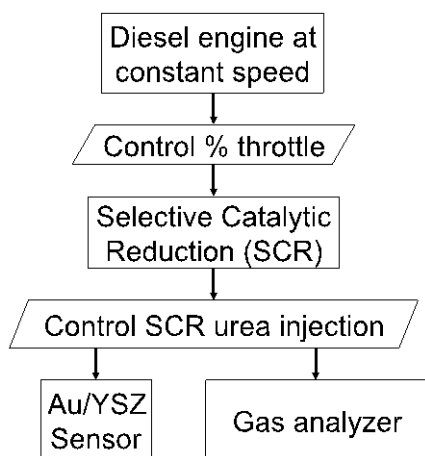


Figure 3. Simplified flow diagram of dynamometer test.

Results and Discussion

Laboratory testing of Au wire prototypes

Before testing in diesel engine dynamometer exhaust, laboratory testing of the Au wire NO_x prototype was conducted with controlled gas compositions. Figure 4a shows sensing behavior of the prototype using the phase angle as the measured response parameter, in degrees, at 10 Hz and 25 mV excitation as the input signal. Data were taken at 650°C in 10.5% O₂ and ~2% H₂O. The NO concentration was then adjusted in two-minute steps starting at a 0 ppm NO baseline. The NO concentration was then stepped to 100, 50, and 20 ppm, and at this point stepped in 5 ppm increments to 0 ppm and then back to 20 ppm, and then stepped to 50 and 100 ppm before returning to baseline. All changes, including the 5 ppm increments, are clearly resolved.

Figure 4b shows the phase angle response vs. NO concentration corresponding to the data shown in Fig. 4a. In Fig. 4b, the phase angle behavior was approximated using two separate linear regimes, one at low NO concentrations (0 to 20 ppm), and another at high NO concentrations (50 to 100 ppm). The sensitivity at low NO concentrations, as indicated by the slope (m_{low}), is ~0.05 deg/ppm NO, while the sensitivity decreased at high NO concentrations (m_{high}) to ~0.03 deg/ppm NO.

To investigate the effect of O₂ interference, laboratory testing also included measuring the phase angle response of the sensor over a range of O₂ concentrations: 4, 7, 10.5, and 12.6%. The phase angle vs. O₂ concentration is similar to the behavior in Fig. 4b, and could also be approximated using two separate linear regimes, one at low O₂ concentrations (4 to 7%, m_{low} of ~2 deg/% O₂), and another at high O₂ concentrations (10.5 to 12.6%, m_{high} of ~0.7 deg/% O₂). While it is possible to correct for the O₂ interference using a dual-frequency approach (as discussed in Ref. 8), in this study we used the measured O₂ concentration, which is described by the following.

Engine testing of Au wire prototype: Isolating influence of NO_x

After laboratory testing, the same Au wire prototype sensor was then evaluated in an engine dynamometer test cell. Two different protocols, as described in the experimental section, were used which either allowed for the isolation of the effect of NO_x or for the effect of O₂ interference.

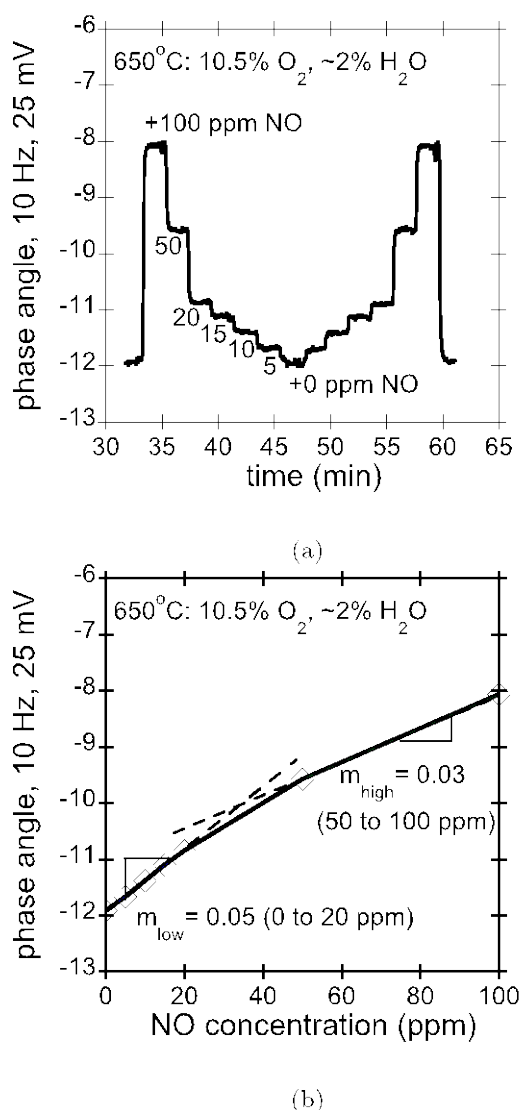


Figure 4. (a) Phase angle response of Au wire NO_x sensor prototype stepping in two min. increments through 0-100-50-20-15-10-5-0 ppm NO, and then reversing this sequence. (b) Corresponding plot of phase angle signal (deg) vs. NO concentration (ppm) with linear curve fits and calculated slopes (m_{low} and m_{high}).

To isolate the effect of NO_x, the engine was first operated under constant percent throttle and rate of urea injection until reaching minimal levels of NO_x. Then, the rate of urea injection was lowered in steps about every ten minutes, before finally being turned off. The results are shown in Fig. 5a, which includes a comparison of the prototype sensor response, results from gas analysis using Fourier transform infrared (FTIR) spectroscopy, and a commercial sensor signal (located downstream of the prototype).

In Fig. 5b, it is observed that the predominant NO_x species during engine testing was NO, with low levels of NO₂ and NH₃. The decreasing frequency of the urea injection levels led to smaller amounts of urea in the SCR to react with the NO_x, and therefore higher concentrations of NO in the exhaust. Measurements of O₂, CO₂, H₂O, CO, and CH₄ in the exhaust taken concurrently with the data shown in Fig. 5 show minimal changes and therefore cannot be used to explain changes seen in the measured sensor response. In addition, only small temperature changes were measured during this test, in the range of ~664 to ~670°C (see Fig. 5c), and showed no correlation with the measured response from the NO_x prototype, indicating that the measured response is fairly tolerant to changes in temperature over at least this range.

Specific requirements for the NO_x sensor will ultimately depend on the design of the entire exhaust after-treatment system, which is currently in development. However, the most promising technologies being investigated suggest that the sensor will need to detect levels typically less than ~20 ppm NO_x. As shown in Fig. 4b, laboratory testing has demonstrated that the NO_x prototype had better sensitivity at lower concentrations (less than 20 ppm) than at higher concentrations.

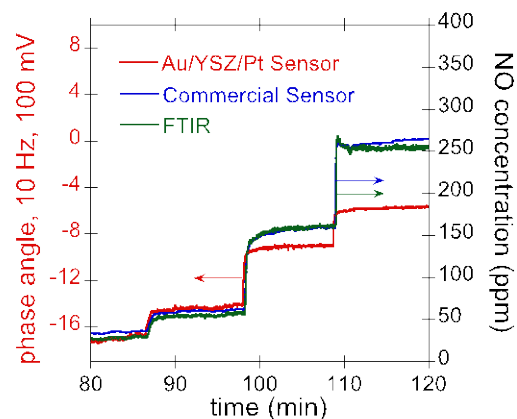
Figure 5a shows that both the commercial sensor and FTIR match over this concentration range. The prototype response qualitatively tracks the commercial sensor and FTIR measurements; however, the sensitivity differs, with more pronounced differences at NO concentrations higher than ~100 ppm. The behavior of the prototype sensor in engine testing appears to show higher sensitivity to NO at lower concentrations, which is in agreement with results from laboratory evaluation (Fig. 4b).

To account for the different sensitivities at high and low NO concentrations, an adjustment was applied to the measured phase angle (θ_{meas}) in engine dynamometer testing using the laboratory data. The adjusted values for the phase angle signal (θ_{adj}) were calculated using the two different sensitivity values shown in Fig. 4b. The adjusted values are given by the following equations:

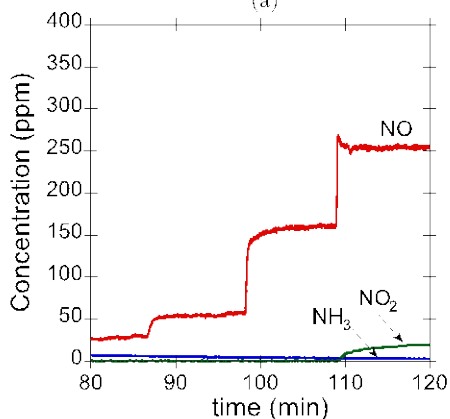
$$\theta_{adj} = \theta_{baseline} + \Delta\theta_{adj} \quad (1)$$

$$\Delta\theta_{adj} = \frac{\theta_{meas} - \theta_{baseline}}{m_{high}} m_{low} \quad (2)$$

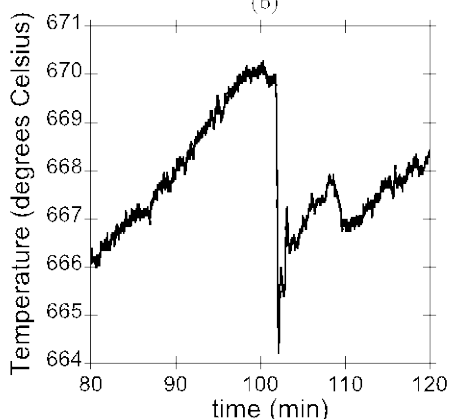
The measured phase angle at the initial prevalent NO_x concentration of ~30 ppm was used as the baseline (θ_{baseline}), which was measured from about 80 to 86 min in Fig. 5 with a value of about -14 deg.



(a)



(b)



(c)

Figure 5. Dynamometer test: (a) Phase angle response of Au wire prototype sensor (red, left y-axis) compared with a commercial sensor (blue, right y-axis) and FTIR gas analysis (green, right y-axis); (b) FTIR results for NO, NO₂, and NH₃; and (c) variation in temperature.

Figure 6 shows the adjusted phase angle signal after accounting for the sensitivities at different NO concentrations, which has better agreement with both the commercial sensor and FTIR compared to the raw data shown in Fig. 5a.

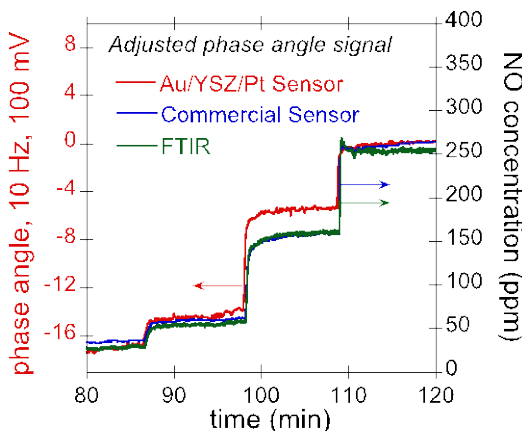


Figure 6. Adjusted phase angle response of Au wire prototype sensor (red, left y-axis) shows better agreement with a commercial sensor (blue, right y-axis) and FTIR (green, right y-axis) compared to raw data in Fig. 5a.

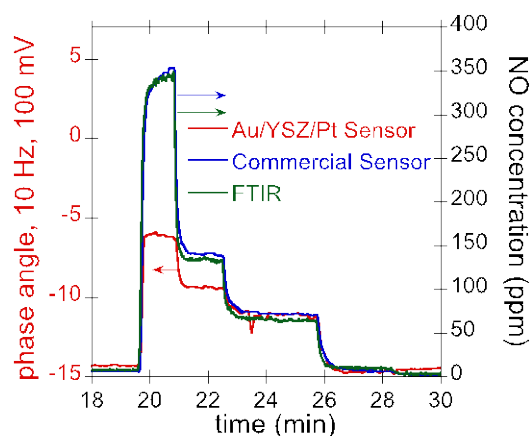
In Fig. 6, the adjusted sensor signal for ~150 ppm, measured from 100 to 110 min, shows less correlation between the prototype and the commercial sensor and FTIR measurements, indicating that the linear approximation extracted from laboratory evaluation does not completely account for the nonlinear sensitivity over the entire range of concentrations of NO.

Engine testing of Au wire prototype: O₂ interference

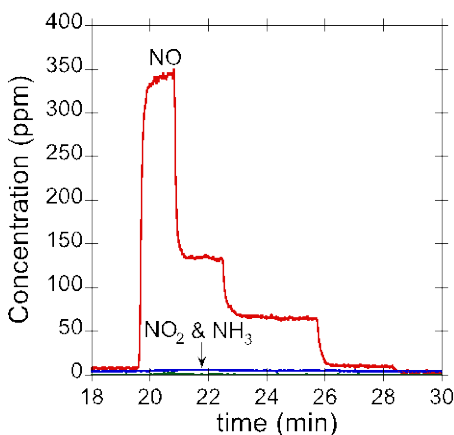
The second protocol used investigated the effect of O₂ cross-sensitivity where the engine was again first operated under constant percent throttle and rate of urea injection with low levels of NO_x. The level of urea injection was then kept constant while the percent throttle was first increased and then stepped to lower levels. The results are shown in Fig. 7a, including a comparison of the prototype sensor with FTIR results and the commercial sensor signal. As shown in Fig. 7b, the predominant NO_x species measured by FTIR was NO, with very low levels of NO₂ and NH₃. The initial increase in percent throttle at 19 min corresponded to an abrupt increase in the level of NO, with progressively decreasing amounts of NO at lower percent throttle.

Figure 8 shows measurements for O₂, CO₂, H₂O, CO, and CH₄ taken during the same engine testing

cycle shown in Fig. 7. The initial percent throttle increase corresponded to an increase in CO₂ and H₂O, and a decrease in O₂. Subsequent changes to lower percent throttle levels corresponded to decreasing amounts of CO₂ and H₂O, and increasing amount of O₂. The CO and CH₄ concentrations were in all cases low and constant during engine testing. Temperature variations did not show a correlation with sensor response, indicating that the measured signal is fairly tolerant to temperature changes over the measured range of ~654 to ~660°C.



(a)



(b)

Figure 7. Dynamometer test with O₂ interference: (a) Phase angle response of Au wire prototype sensor (red, left y-axis) compared with a commercial sensor (blue, right y-axis) and FTIR gas analysis (green, right y-axis); (b) FTIR results for NO, NO₂, and NH₃.

In Fig. 8, both CO₂ and H₂O changed over a range of ~2%, while O₂ concentration changed over a range twice as large, from about 5 to 9%. Laboratory evaluation indicated that changes in O₂ from 4 to 7% corresponded to a phase angle sensitivity of about 2 deg/% O₂ (see discussion above). Therefore, changes in both O₂ and NO_x concentration influenced the measured phase angle signal.

To compensate for the O₂ interference in the measured phase angle (θ_{meas}), an adjustment was applied using the measured O₂ concentration, $[O_2]_{meas}$, and the sensitivity values for low O₂ concentrations (4 to 7%, $m_{low} = 2 \text{ deg}/\% \text{ O}_2$). A baseline value for the measured O₂, $[O_2]_{baseline}$, was chosen at the initial concentration of ~9%, shown in Fig. 8. The adjusted values were calculated using the following equations:

$$\theta_{O_2,adj} = \theta_{meas} - \Delta\theta_{O_2} \quad (3)$$

$$\Delta\theta_{O_2} = ([O_2]_{meas} - [O_2]_{baseline})m_{low} \quad (4)$$

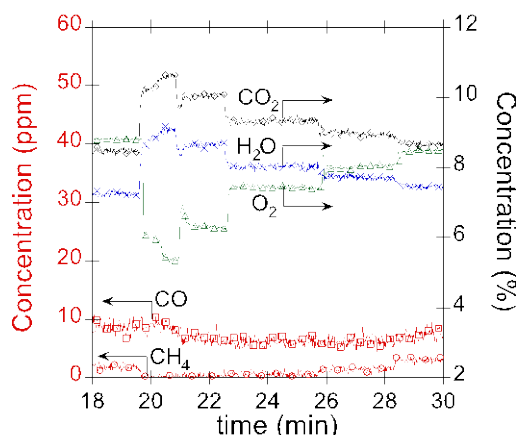


Figure 8. Dynamometer test with O₂ interference showing steady-state values for CO and CH₄ and changes in CO₂, H₂O, and O₂.

In addition to the O₂ interference adjustment (Eqs. 3 and 4), the different NO sensitivity at low and high concentrations also needed to be accounted for (Eqs. 1 and 2 as discussed above). Therefore, the phase angle adjusted for O₂ interference ($\theta_{O_2,adj}$) was then used in Eqs. 1 and 2, where $\theta_{meas} = \theta_{O_2,adj}$. The same sensitivity values were used as before, given by the two slopes in Fig. 4b, and an appropriate baseline value ($\theta_{baseline}$) was chosen.

Figure 9 shows the adjusted phase angle signal after accounting for both the O₂ interference and the different sensitivities at low and high NO concentrations.

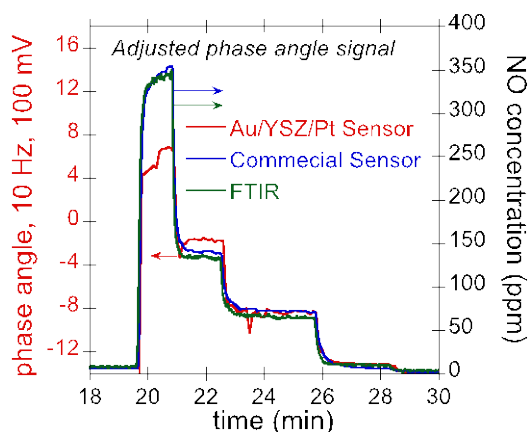


Figure 9. Adjusted phase angle response of Au wire prototype sensor (red, left y-axis), and commercial (blue, right y-axis) and FTIR (green, right y-axis).

The adjusted phase angle signal has better agreement with both the commercial sensor and FTIR. However, data at higher NO concentrations greater than ~100 ppm show less agreement, again indicating that the linear approximation from laboratory testing does not completely account for the non-linear sensitivity over the entire range of concentrations. Furthermore, although changes in both CO₂ and H₂O occurred over a small 2% range, they could also be contributing to the measured phase angle signal.

Conclusions

Work in FY2011 focused on using an algorithm developed in FY2010 in a simplified strategy to demonstrate how data from controlled laboratory evaluation could be applied to data from real-world engine testing. The performance of a Au wire prototype sensor was evaluated in the laboratory with controlled gas compositions and in dynamometer testing with diesel exhaust. The laboratory evaluation indicated a nonlinear dependence of the NO_x and O₂ sensitivity with concentration. For both NO_x and O₂, the prototype sensor had higher sensitivity at concentrations less than ~20 ppm and ~7%, respectively, compared to lower NO_x and O₂ sensitivity at concentrations greater than ~50 ppm and ~10.5%, respectively. Results in dynamometer diesel exhaust generally agreed with the laboratory results. Diesel exhaust after-treatment systems will likely require

detection levels less than ~20 ppm in order to meet emission regulations.

The relevant mathematical expressions for sensitivity in different concentration regimes obtained from bench-level laboratory evaluation were used to adjust the sensor signal in dynamometer testing. Both NO_x and O₂ exhibited non-linear responses over the concentration regimes examined (0-100 ppm for NO_x and 4-7% for O₂). Adjusted sensor signals had better agreement with both a commercial NO_x sensor and FTIR measurements. However, the lack of complete agreement indicated that it was not possible to completely account for the nonlinear sensor behavior in certain concentration regimes. The agreement at lower NO_x levels (less than 20 ppm) was better than at higher levels (50-100 ppm).

Other progress in FY2011 included dynamometer testing of sensors with imbedded heaters and protective housings that were mounted directly into the exhaust manifold. Advanced testing protocols were used to evaluate the sensors. These experiments confirmed the potential for sensor robustness and durability. Advanced material processing methods appropriate for mass manufacturing, such as sputtering, are also being evaluated. A major milestone for this past year was the licensing of the LLNL NO_x sensor technology to EmiSense Technologies, LLC. EmiSense has extensive experience and resources for the development of emission control sensors. A CRADA is in development that will allow LLNL to work in partnership with EmiSense to bring the LLNL NO_x sensor technology to commercialization. Ford Motor Company is also a partner in this effort.

References

1. N. Yamazoe, *Sens. Actuators, B*, **108**, 2 (2005).
2. R. Moos, *Int. J. Appl. Ceram. Technol.*, **2**, 401 (2005).
3. S. Akbar, P. Dutta, and C. Lee, *Int. J. Appl. Ceram. Technol.*, **3**, 302 (2006).
4. F. Menil, V. Coillard, and C. Lucat, *Sensors and Actuators B*, **67**, 1 (2000).
5. S. Zhuiykov and N. Miura, *Sens. Actuators, B*, **121**, 639 (2007).
6. J. W. Fergus, *Sens. Actuators, B*, **121**, 652 (2007).
7. S. -W. Song, L. P. Martin, R. S. Glass, E. P. Murray, J. H. Visser, R. E. Soltis, R. F. Novak, and D. J. Kubinski, *J. Electrochem. Soc.*, **153**, H171 (2006).

8. L. P. Martin, L. Y. Woo, and R. S. Glass, *J. Electrochem. Soc.*, **154**, J97 (2007).
9. L. Y. Woo, L. P. Martin, R. S. Glass, and R. J. Gorte *J. Electrochem. Soc.*, **154**, J129 (2007).
10. L. Y. Woo, L. P. Martin, R. S. Glass, W. Wang, S. Jung, R. J. Gorte, E. P. Murray, R. F. Novak, and J. H. Visser. *J. Electrochem. Soc.*, **155**, J32 (2008).
11. L.Y. Woo, R.S. Glass, R.F. Novak, and J.H. Visser. *J. Electrochem. Soc.*, **157**, J81 (2010).
12. L.Y. Woo, R.S. Glass, R.F. Novak, and J.H. Visser. *Sensor Actuat. B-Chem.*, **157**, 115 (2011).

Publications/Presentations

L.Y. Woo, R.S. Glass, R.F. Novak, and J.H. Visser. "Diesel engine dynamometer testing of impedancemetric NO_x sensors." *Sensor Actuat. B-Chem.*, 157:115-121, 2011.

L.Y. Woo, R.S. Glass, R.F. Novak, and J.H. Visser, "Impedance Analysis of High-Temperature Electrochemical NO_x Sensor Based on Porous Yttria-Stabilized Zirconia (YSZ)," 2011 Spring Meeting of the Materials Research Society, San Francisco, California, April 25-29, 2011.

L.Y.Woo and R. S. Glass, "NO_x Sensor Development," project ID #PM005, Annual Merit Review and Peer Evaluation. Washington, D.C., June 10, 2010.

Agreement 9440 - Fabrication of Micro-orifices for Diesel Fuel Injectors

George R. Fenske and Nicholas Demas

Argonne National Laboratory

9700 South Cass Avenue

Argonne, IL 60439

(630)252-5190; fax (630)252-4798; e-mail: gfenske@anl.gov

DOE Technology Manager: Jerry Gibbs

(202) 586-1182; fax: (202) 586-1600; e-mail: jerry.gibbs@ee.doe.gov

Contractor: Argonne National Laboratory, Argonne, Illinois
Prime Contract No.: DE-AC02-06CH11357

Objectives

- Develop a methodology for reducing the diameters of fuel injector orifices to 50 μm by applying material to the internal diameter (ID) of the orifice. Micro-orifices should improve fuel distribution, increase efficiency, and reduce emissions in compression-ignition, direct-injection (CIDI) engines.
- Characterize the spray and combustion properties of the fuel injector system coated with electroless nickel (EN) and other advanced ID coating processes.
- Transfer the developed technology to DOE industrial partners.

Approach

- Reduce the orifice diameter by coating its interior with EN plating for improving the surface finish and reducing deposit formation on injector nozzles.

Accomplishments

- In collaboration with the U.S. Environmental Protection Agency (EPA), characterized the spray characteristics of EN-coated commercial nozzles.
- In concert with Imagineering, Inc. (a commercial plating company), developed a method for improving the surface finish of commercial-scale plated nozzles.
- Used x-ray phase imaging for nondestructive examination of thin EN coatings applied onto the nozzles.
- Examined the microstructure and micro-hardness of commercial nozzles.
- Evaluated coating integrity using micro-indentation and examined the variation of coating thickness as a function of depth using non-destructive x-ray imaging analysis.
- Established collaboration with injector manufacturer (Robert Bosch GmbH) to perform engine testing of plated nozzles for deposit mitigation.
- Simulated cavitation erosion and evaluated the impact of EN plating on erosion.

Future Direction

- Characterize spray properties of EN-coated multi-sized orifice nozzles in collaboration with the U.S. EPA.
 - Explore establishing a consortium with industrial partners to integrate EN process into a production setting.
 - Evaluate EN-plated nozzles under actual engine testing conditions.
-

Introduction

In 2007, EPA regulations mandated reduction in diesel engine emissions to 0.01 grams of particulate matter (PM) per engine horsepower per hour and 0.2 grams of nitrogen oxide (NO_x) per engine horsepower per hour. Further reductions are expected for 2012. To achieve these levels, CIDI engines are being redesigned to reduce in-cylinder soot production. One design change under consideration is the reduction of the diameter for the fuel injector orifice.

Pickett and coworkers^{1,2} demonstrated significant reductions of soot in a test cylinder using experimental injectors with orifice diameters of 50 μm, even with high levels of exhaust gas recirculation and concomitant reduction in NO_x emissions. National Vehicle and Fuel Emissions Laboratory (NVFEL) researchers observed reduced PM emissions from a light-duty diesel engine equipped with 75-μm-diam injector orifices. These reductions arise from increases in fuel atomization efficiency, leading to more complete combustion.³ Although 100-μm-diam orifices can now be economically mass produced by electrical discharge machining (EDM), further reductions in hole size are accompanied by unacceptable fabrication error rates.

Reducing the orifice diameter (e.g., from 150 to 50 μm) carries with it a number of other penalties. It will reduce the amount of fuel that can be delivered to the combustion chamber without increasing the number of spray holes, the injection pressure, and/or the discharge coefficient. The potential impact of coking on smaller orifices is also much greater, as smaller holes will be more readily blocked by coking deposits on the injector tip and in the spray holes themselves. Coking deposits are a particular problem with tapered-orifice nozzles, another technique for increasing fuel atomization and thus reducing PM emissions.

Another issue is alternative fuels. One method to minimize dependence on foreign oil is the increased use of bioderived fuels, such as vegetable oil esters. Because of the

presence of carbon-carbon double bonds in the carboxylic acid chain precursors, these fuels readily form coking deposits in the combustion chamber—a major problem in concert with smaller spray holes. Other alternative fuels include alcohols such as methanol or ethanol. These are not typically used neat but are blended with conventional diesel fuel. One emissions reduction strategy is to inject an ethanol/water mixture along with conventional fuel, reducing the combustion temperature and NO_x emissions. However, alcohol partial oxidation products can include corrosive carboxylic acids, which will damage the steel nozzles over time.

In concert with more commonly used fabrication techniques, EN plating has been used to prepare fuel injector nozzles with orifice diameters as small as 50 μm.^{4,5} EN plating promises to mitigate or solve all of the difficulties described above. The plated surface is corrosion-resistant and smoother, and the discharge coefficient of the plated orifices is higher. This method can be used to deposit a wide variety of alloys, offering the possibility of tailoring surface chemistry to reduce or eliminate deposit formation.

Approach

As described in previous progress reports, the diameter of an orifice can be reduced by coating its interior with EN plating. This technique has been used to deposit nickel/phosphorus or nickel/boron alloys onto metallic surfaces from aqueous solutions. It has been successfully used in previous years to reduce the orifice diameter from 200 to 50 μm on a bench scale, and from 180 to 75–80 μm on a commercial scale. Other metal alloys have been deposited by the same technique.

Having demonstrated that EN plating reduces the orifice diameter to the desired size, we next sought to demonstrate the usefulness of EN-plated nozzles for solving the challenges described in the Introduction: improving spray properties and discharge coefficients, reducing deposit formation, and resisting corrosion. To this end, phase-

contrast x-ray imaging at Argonne's Advanced Photon Source (APS) was explored for nondestructive examination of plated nozzles.⁶ This technique is capable of measuring coating thicknesses on internal passages and was applied as a quality check on nozzles that were sent to the EPA for engine tests.⁷

In collaborative studies with the EPA, fuel sprays produced with EN-coated commercial nozzles yielded encouraging results, and during FY10, we explored the application of EN plating to produce multi-sized orifices (e.g., 50 μm and 125 μm) on a given nozzle. Research also continued to evaluate the use of EN coatings as an approach to mitigate erosive wear.

Results

In FY11, activities were continued to develop/demonstrate the ability to fabricate multi-sized orifices that improve the ability to direct fuel to a broader area in the combustion chamber, as well as to evaluate the potential of EN platings for mitigating orifice erosion. The microstructure and composition of the nozzles were characterized using secondary electron microscopy (SEM) and energy dispersive x-ray (EDX) analysis, respectively. EDX analysis near the orifices revealed the presence of tungsten, which originated from the wire used to EDM the holes. This impurity compromised coating integrity in some samples and was responsible for cosmetic surface blemishes on the nozzles. Mechanical polishing removed the blemishes and resulted in a greatly improved surface around the holes.

Our latest work has involved a coordinated effort between various industrial partners to fabricate multi-sized orifice nozzles. During FY11, coated nozzles consisting of 12 orifices (six 50- μm holes and six 120- μm holes) were sent for regrinding. During the regrind, the interior surface of the nozzle-body collar was out-of-round, which made it difficult to be matched to the needle guide. To overcome these

unforeseen issues and prepare the matched assembly for testing, all the nozzles were ground to a larger ID bore size, and new needles were manufactured to fit the nozzle. After significant delay, the nozzles were received and prepared for spray visualization studies. To address the issues encountered during the regrinding, a masking process during EN plating is being pursued, in which the interior surface of the nozzle-body collar is protected by Teflon[®] tubing. Positive results have been obtained when using the mask. However, additional work is required to determine the optimum length to be masked and to address adhesion issues that have arisen when trying to mask the interior surface of the nozzle body.



Figure 1. Photograph of the spray of a nozzle with two sets of holes mounted into a pop-tester used for spray tests

Also, in FY11, high-speed photography of the spray patterns produced by nozzles with multi-sized orifices was performed using a pop-tester setup specifically developed for this purpose. The spray of one of the nozzles obtained with the pop-tester is shown in Figure 1. The injection pressure for all nozzles was 200-400 bar (the spray was injected into lab air at 1 bar). This rig is used to confirm that the orifices are not blocked. As seen in this figure, all 12 orifices are open, and one can discern a difference between the small and large orifices.

A set of commercial-size nozzles containing eight 119- μm orifices was sent to an outside company that specializes in EDM processing of nozzles. This company completed EDM processing of 178- μm orifices equally spaced between the 119- μm orifices. Upon close examination of the inside of the nozzle using a boroscope, we noted that the orifices were not placed precisely. Figure 2 illustrates the problem.

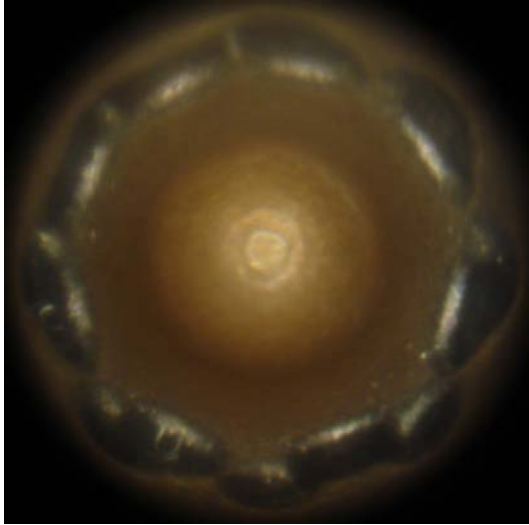


Figure 2. Boroscope image of the nozzle interior after EDM

Examination of the pre-existing orifices on a number of nozzles indicated that the orifices were not at the locations specified in the schematics that were provided by the manufacturer. Using one of the orifices as a reference point, we located the remaining orifices and found that the remaining 7 orifices were out of position up to 6°. This discrepancy would account for the overlap of the holes on the inside of the nozzle bore observed in Figure 2.

Figure 3 shows a micrograph of the top-view of a nozzle. The red lines denote the proper orifice locations. At 0° there is the first 178- μm orifice placed by our EDM industrial partner. Every 45°, the rest of the 178- μm orifices can be seen, and it is obvious that they have been placed correctly. However, the 119 μm orifices, which would be expected at 22.5° and every 45° after that, have not been placed

correctly. The blue and green lines show actual locations. The 119- μm orifices are out of position by up to 5.5°.

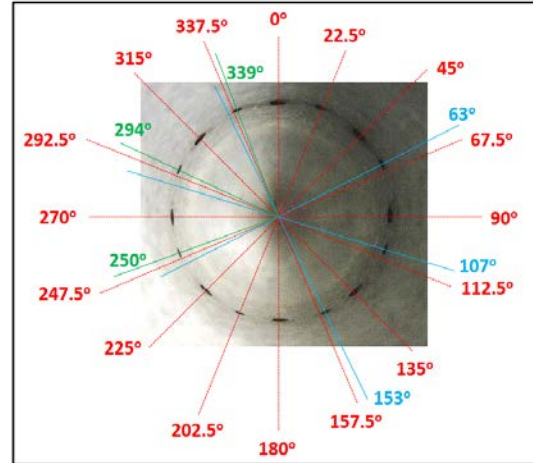


Figure 3. Micrograph of nozzle showing orifice locations and deviations of the pre-existing orifices from schematics provided by the manufacturer

We are in communication with the nozzle manufacturer to circumvent this issue by either starting with blank nozzles or determining whether there was an error in the batch of nozzles we received.

During FY11 we examined a limited number of nozzles using a 3-D X-ray imaging system. We are using this non-destructive analysis supplemented by microscopy measurements to look for surface defects and coating uniformity, and to measure the sizes of the holes. As previously mentioned, the technique allows for 3-D rendering so that areas of interest may be targeted, as well as selective 2-D imaging. Figure 4 shows a top-down “slice” of one of the latest eight-orifice nozzles after EN plating using this technique.

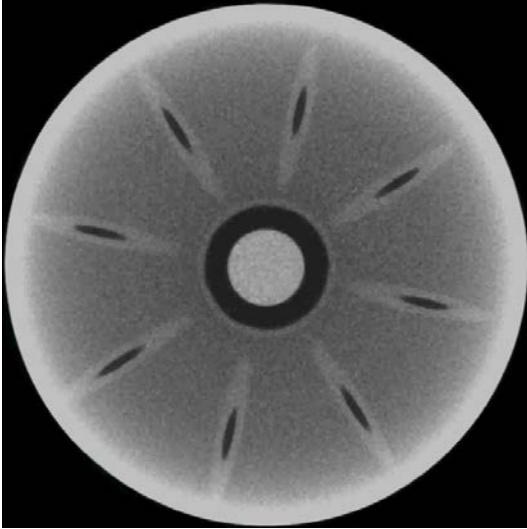


Figure 4. X-ray top-down slice of a multi-orifice nozzle

Plating can be seen around the holes as a lighter shade of gray. A single frame of a 3-D rendered video is shown in Figure 5. Using this technique, we can examine interior passages during the 3-D rendering “mode,” as seen in this figure.

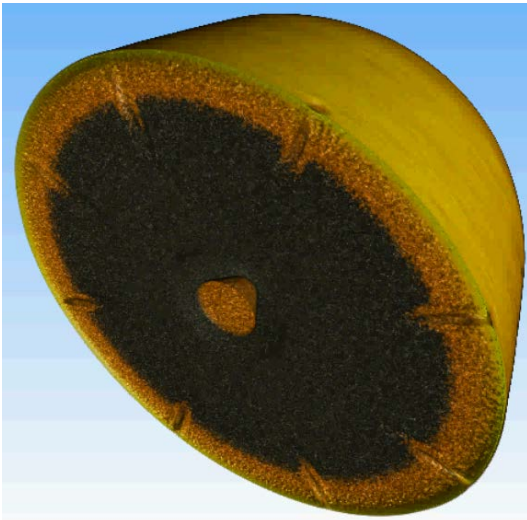


Figure 5. Snapshot of a 3-D rendering showing the tip of a nozzle

Using a micro-indentation technique at the coating/substrate interface, we demonstrated that the adhesion of the EN coatings to the orifices is very good. A benchtop ultrasonic apparatus was developed to simulate cavitation erosion and evaluate the impact of different alloy compositions and treatments on erosion. Specimens were machined out

of a very similar material in composition to that of a nozzle and tested according to the ASTM G32-09 standard (“Standard Test Method for Cavitation Erosion Using Vibratory Apparatus”). A test coupon is shown in Figure 6.

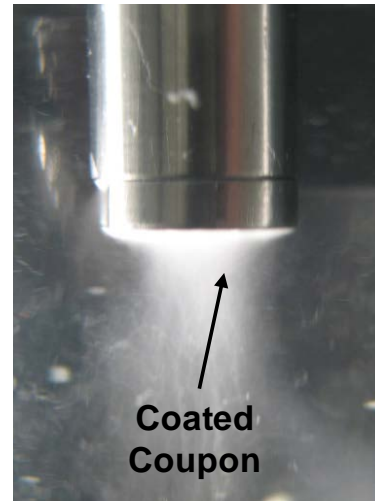


Figure 6. Photograph of an H13 coupon during cavitation erosion test

This method produces cavitation damage on the face of the specimens vibrated at high frequency while immersed in liquid (distilled water). The vibration induces the formation and collapse of cavities in the liquid, and the collapsing cavities produce erosion of the specimen. A specimen is attached by threading into the tip of a horn, which is then attached to the ultrasonic transducer. The specimen is immersed into a container with distilled water, which must remain at a specified temperature during operation while the specimen is vibrated at specified amplitude. The test specimen is weighed before and during testing to quantify mass loss as a function of time. Figure 7 shows cumulative mass loss versus time vibrated at 50% amplitude. From this figure we can see that the plated samples lose mass significantly faster than their bare metal counterparts. Tests were repeated for the first 4 hours, showing similar results. These are also included in Figure 7.

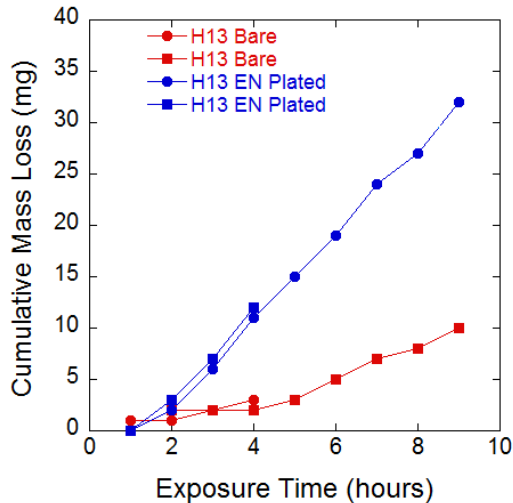


Figure 7. Cumulative mass loss versus time for bare and coated H13 coupons

Photographs of the H13 bare and plated samples are shown in Figure 8 before and after 9 hours of exposure.

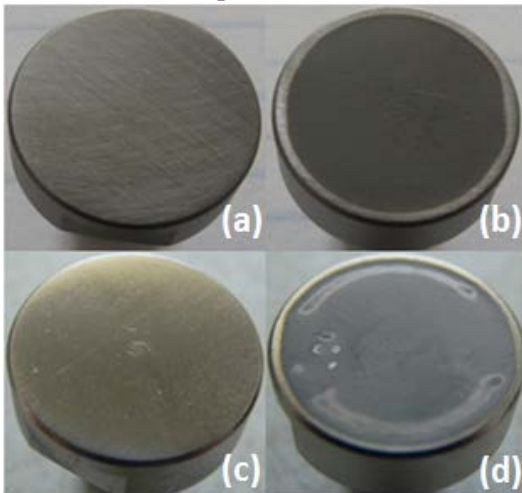


Figure 8. Photographs of bare H13 specimens before (a) and after (b) 9 hours of exposure, and EN-plated H13 samples before (c) and after (d) 9 hours exposure

It is evident that the tests caused some surface damage in both cases. After testing, the bare specimen exhibited a discolored concentric circle, and the EN-plated coupon had surface blemishes in addition to discoloration.

Conclusions

Through a collaborative effort, multi-sized orifices have been fabricated starting

with blank nozzles or nozzles with a set of holes, adding holes by an EDM process, honing, grinding and EN plating. Development of the EN aqueous-based plating process has advanced to the stage where commercial nozzles can be treated. Furthermore, an advanced phase-contrast x-ray imaging technique can be used for the non-destructive evaluation of finished nozzles and examination of EN plating.

During FY11, unforeseen manufacturing issues delayed x-ray imaging and spray visualization. A pop tester setup was used to test the nozzles for blockage using high-speed spray photography and ensure spray pressures between 200-400 psi. Cavitation erosion tests were also performed.

Efforts will continue, based on funding availability during FY12, to fabricate large batches of multi-sized orifices in preparation for flow-spray studies.

References

1. L.M. Pickett and D.L. Siebers, Paper No. 2001-ICE-399, ICE Vol. 37-1, 2001 Fall Technical Conference, American Society of Mechanical Engineers, 2001.
2. L.M. Pickett, D.L. Siebers, A.F. Morales, J. Hachman, and A.K. Sinensky, "An Investigation of Diesel Soot Formation Processes Using High Aspect Ratio Micro-Orifices," presented at HARMST 2003 High-Aspect Ratio Micro-Structure Technology Workshop, Monterey, CA, 2003.
3. J.B. Heywood, *Internal Combustion Engine Fundamentals*, McGraw-Hill, New York, 1988.
4. G.R. Fenske and N.G. Demas, "Fabrication of Micro-orifices for Diesel Fuel Injectors," 2009 Annual Progress Report, *Automotive Propulsion Materials*, U.S. Department of Energy, Washington, D.C., 2007.
5. G.R. Fenske, J. Woodford, J. Wang, and R. Schaefer, "Fabrication and Characterization of Micro-orifices for Diesel Fuel Injectors," SAE 2008-01-1595, Society of Automotive Engineers, 2008.

6. K. Fezzaa, W-K. Lee, S-K. Cheong, C. F. Powell, J. Wang, and M-C. Lai, "Ultrafast X-ray Phase-Enhanced Microimaging for Visualizing Fuel Injection Process," SAE 2005-24-093, Society of Automotive Engineers, 2005.
7. R. Schaefer, US EPA-NVFEL, private communication, July 2007.

Publications and Presentations

J.B. Woodford and G.R. Fenske, "Fabrication of Small Orifice Fuel Injectors," DEER (Diesel Engine Emissions Reduction) Conference, August 2005.

J.B. Woodford and G. R. Fenske, *Fabrication of Small-Orifice Fuel Injectors for Diesel Engines*, Argonne National Laboratory Report, ANL-05/06, March 2005.

G.R. Fenske, J. B. Woodford, J. Wang, and R Schaefer, "Fabrication and Characterization of Micro-orifices for Diesel Fuel Injectors," presented at the 2008 SAE International Powertrains, Fuels and Lubricants Congress, June 23-25, 2008, Shanghai, China, SAE paper 2008-01-1595.

G.R. Fenske, J. Wang, E. El-Hannouny, R Schaefer, and F. Hamady, "Fabrication of Micro-orifices for Diesel Fuel Injectors," DEER (Diesel Engine Emissions Reduction) Conference, August 2008.

J.B. Woodford, G. R. Fenske, and J. M. Perez, "Deposit Formation on Electroless Nickel," submitted to *Energy & Fuels*.

G.R. Fenske, N.G. Demas, R.A. Erck, "Fabrication of Micro-orifices for Diesel Fuel Injectors," 2010 *Annual Progress Report, Automotive Propulsion Materials*, U.S. Department of Energy, Washington, D.C., 2010.

Agreement 11752 – Materials for HCCI Engines

G. (Murali) Muralidharan, and Rick Battiste

(865)574-4281; fax: (865) 574-4357; e-mail: muralidhargn@ornl.gov

Bruce G. Bunting

Engineering Science and Technology Division

(865) 946-1512; fax: (865) 946-354; e-mail: buntingbg@ornl.gov

DOE Technology Manager: Jerry L. Gibbs

(202) 586-1182; fax: (202) 586-1600; e-mail: jerry.gibbs@ee.doe.gov

ORNL Technical Advisor: Dave Stinton

(865) 574-4556; fax: (865) 241-0411; e-mail: johnsondr@ornl.gov

Contractor: Oak Ridge National Laboratory, Oak Ridge, Tennessee

Prime Contract No.: DE-AC05-00OR22725

Objectives

- Identify and catalog the materials operating conditions in homogeneous charge compression-ignition (HCCI) engines and use computational design concepts to develop advanced materials for such applications.
- Interact with designers of HCCI engines and manufacturers of components in order to identify the components that will be affected by the harsh operating conditions resulting from the HCCI design.

Approach

- Identify engine components, currently used materials, and current operating conditions and compare them with the expected component operating conditions for HCCI engines.
- Demonstrate the feasibility of the “materials-by-design” approach for the highest-priority item. Improve material performance for HCCI applications through computational modeling and experimental validation.

Accomplishments

- Several larger batches of new ORNL-developed alloys have been prepared based upon high temperature tensile properties
- Fatigue properties of new ORNL alloys have been evaluated using rotating beam tests at 870°C
- Results show that one of the alloys has exceeded a lifetime of 100 million cycles at a stress of 25ksi at 870°C

Future Direction

- Additional alloys will be developed to achieve lifetime of 100 million cycles at a stress of 30-35ksi at 870°C
- Continue to communicate with automotive companies, valve manufacturers, and other teams on the progress made through computational design.

Introduction

There has been an increasing interest in HCCI combustion in recent years because of its potential to increase engine combustion efficiency and reduce emissions. However, the use of HCCI combustion will subject the engine components to significantly higher temperatures and pressures. The temperatures for diesel engines will reach over 1600°F, and pressure may reach > 2000 psi, which is approximately

four times that of the normal combustion engine. Such severe engine operating conditions will require a significant improvement in materials performance in order to take advantage of the HCCI engine concept. This project deals with identifying materials requirements for HCCI engines for automotive and truck applications and the development of advanced, yet cost-effective, materials through computational design.

“Materials-by-design” is an Oak Ridge National Laboratory (ORNL) concept that encompasses a collection of materials-related techniques including modeling, correlation, and materials modification. The premise behind materials-by-design is that mechanical properties are correlated to microstructure and phase chemistry. The phase composition and microstructure can be achieved through thermodynamic equilibrium or through non-equilibrium techniques such as quenching, rapid casting solidification, or mechanical working. These characteristics can then be correlated to desired mechanical properties through equilibrium thermodynamics or through a variety of correlation techniques. The correlations allow untested compositions or treatments to be modeled so that desired trends can be rapidly established. Small heats of targeted materials can then be processed to confirm the modeled properties and to broaden the correlation data base.

Finally, there are several techniques, such as magnetic processing or low-temperature carburizing, that can be applied to allow further modification and optimization of desired properties. Materials-by-design is ideally suited to cast materials and heavily thermally processed materials (e.g., stainless steels, Ni alloys, cast irons, alloy steels, and brazed wrought aluminum alloys), and the concept has been successfully applied in such diverse areas as high-temperature furnace components, exhaust valves, exhaust manifolds, and tube fittings. Figure 1 and Table 1 provide an outline of the materials-by-design approach and a summary of the techniques that can be applied.

In our approach, we examined critical heavy-duty diesel engine materials and identified means to reduce their cost for acceptance in HCCI applications. This was accomplished through the following tasks:

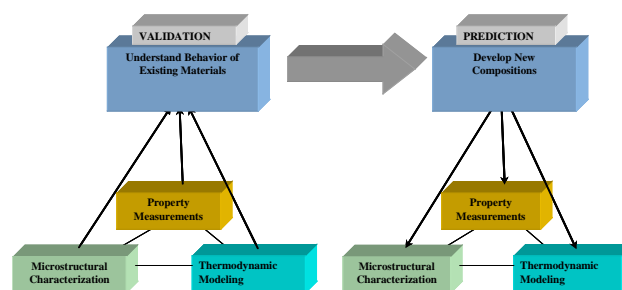


Figure 1. Overall approach for materials-by-design.

Task 1. Identify critical material requirements for HCCI engines based on their operating conditions. This task will be accomplished through interactions with advanced engine and component designers. The interactions will include personal visits to six companies: Caterpillar, Cummins Engine, Deer, International Truck, Eaton Corp., and General Motors. Visits will be supplemented by a literature search, a review of advanced engine design studies, and follow-up discussions afterward. The key outcomes from this task will include (1) identifying operating conditions for advanced engine concepts, with a focus on the HCCI concept; (2) identifying components most affected by these operating conditions; (3) identifying currently used materials, new requirements, and performance targets; and (4) ranking the highest-priority items for study by the materials by design approach.

Task 2. Demonstrate the feasibility of materials-by-design approach for the highest-priority item. In this task, we will identify the details of the currently used material for the highest-priority item. Specifically, we will examine material compositions, processing methods, mechanical properties, corrosion properties, and cost. Based on the available mechanical properties data, microstructural analysis, and thermodynamic phase stability calculations, we will identify the underlying mechanism that delivers the current properties.

Table 1. ORNL materials-by-design toolbox

Modeling	Experimentation	Characterization
Thermodynamic modeling of material properties vs alloy composition	Ultra-high-gauss magnetic stabilization of alloy steels	Advanced microscopy techniques
Neural-network modeling of diverse, nonlinear materials properties and process variations	Low-temperature gas carburization of finished components	X- ray and neutron scattering
Detailed microstructure based empirical modeling	Ability to produce small quantities of materials and fabricate them into test bars for property measurements and production of prototype components by a variety of methods, including sand and die casting, extrusion, forging and rolling	Surface and bulk property measuring techniques
Non-equilibrium modeling of solidified structures		
Extrapolation of properties from simple alloy systems to complex systems using interaction parameters		

Task 3. Improve materials performance for HCCI application through computational modeling and experimental validation.

In this task, we will use computational modeling (key basis for the material-by-design concept) to identify compositions that will deliver the desired phases for two purposes: (1) improving property performance and (2) finding alternatives to reduce cost for both current and improved performance. The outcome of the analysis will be validated through experimentation. The validation will be carried out in the following steps:

1. Prepare compositions identified based on computational design in 1-lb heats for microstructural analysis and very limited property determination; compare the results with output based on computational analysis for validation.
2. Scale up the validated composition into 20-lb to 100-lb heats and cast them into ingots for processing trials. In most cases, the material is expected to be used in the wrought condition. However, if it is to be used in the cast condition, we will save part of the ingots for analysis of as-cast properties.
3. Subject cast ingots to processing steps that are currently used by industry. Develop optimum processing and heat-treatment conditions to obtain the desired microstructure.

4. Carry out microstructural analysis and mechanical properties analysis on the material processed and heat-treated with optimum conditions.
5. Prepare prototype components for HCCI engine tests.

Extensive interaction with industrial partners will occur during all three tasks. This collaboration is expected to result in the rapid transfer of materials improvement from this project to industry for use in HCCI and other advanced engine concepts.

Results

Materials Development through Computational Design

Ni-based alloys have been identified as potential candidates for improved valve materials. There is particular interest in increasing the operating temperature of exhaust valves to about 1600°F (870°C). High temperature fatigue strength has been identified as a critical factor in determining the performance of these alloys in the valve application. An evaluation of the microstructure of various Ni-based alloys and correlation with limited information on the fatigue properties that are available show that the volume fraction of the γ' phase is likely to be a dominant factor in determining the performance of these alloys at high temperatures.

Since the size of the strengthening precipitates is also critical, it is anticipated that the kinetics of coarsening this phase would also be influential in the long-term performance of the alloys in this application. Based upon discussions with various users and suppliers, a range of Ni-based alloys with potentially varying weight fractions (or volume fractions) of γ' have been identified in efforts to correlate the fatigue properties with the microstructure of the alloys. To obtain initial information on the microstructures of these alloys at equilibrium, thermodynamic calculations have been carried out using JMatPro V4.1. Comparison of the results of the calculations showed that all alloys have a matrix of γ with the major strengthening phase as γ' . One or more carbide phases such as $M_{23}C_6$, MC, and M_7C_3 may also be present in different alloys. The primary difference between the microstructures of the various alloys is in the weight percent of the γ' phase at a given temperature and the highest temperature at which the γ' phase is stable in the different alloys.

Development of Improved Alloys through Computational Modeling

Using the microstructures of these alloys as a guide, computational thermodynamics was used to identify additional alloys with microstructure similar to the commercial alloys with desirable properties. In contrast to the commercially available alloys with Ni-contents in the range of 50 wt. % to 60 wt. %, the Ni-content in these alloys ranges from about 30 wt. % to 45 wt. % with the potential to achieve comparable properties. This implies that the alloys will be of lower cost with the potential to achieve targeted fatigue life.

Based upon the results of alloy design, small batches of alloys were cast. The alloys were then homoge-

nized, and rolled at high temperatures. Small tensile specimens were machined from these alloys and tensile tests were conducted *in-situ* at 870°C. Based upon the results of the tensile tests, several of the alloys from the newly developed alloys were down-selected for the preparation of larger sized heats. These were cast under inert gas cover and then mechanically processed into plates for further machining. Figure 2 shows an optical image of the processed plates.

Fatigue Property Measurement

Rotating beam fatigue tests were conducted on the new alloys *in-situ* at a temperature of 870°C and stresses of 25 Ksi(172.4 MPa), 35 Ksi (241.3MPa) and 45 Ksi(310.2MPa). Results on cycles to failure are shown in Figure 3. Results show that one of the alloys exceeded the lifetime of 100 million cycles at 25 Ksi. Further improvement in properties is needed to achieve better life at higher stresses and will be the focus of future alloy development work.



Figure 2. Larger sized heats prepared from down-selected alloys to enable high temperature fatigue testing.

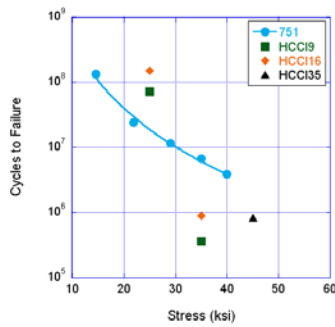


Figure 3. Rotating beam fatigue tests at 870°C show that one of the new alloys exceeds a lifetime of 100 million cycles at a stress of 25Ksi.

Conclusions

- Computational thermodynamics models have been used to identify several promising alloy compositions with the potential to have desirable fatigue performance at higher temperatures and small heats have been cast and tensile properties were measured at 870°C.
- Larger batch of several alloy were prepared based upon the measured tensile properties of new alloys at 870°C
- Rotating beam fatigue tests performed on the new alloys showed a life of over 100 million cycles at 25 Ksi, 870°C.
- Further work is required to improve lifetime at higher stresses

Agreement 11754 - Hydrogen Materials Compatibility

Principal Investigator: Kyle J. Alvine

S. Pitman, V. Shutthanandan, M. Vijayakumar, W. Bennett, D. Skorski

Pacific Northwest National Laboratory

P.O. Box 999

Richland, Washington 99354

(509) 376-0356; fax: (509) 376-0418; e-mail: kyle.alvine@pnnl.gov

Alan Welch

Westport Innovations; e-mail: awelch@westport.co

Brad Boyer

Ford Motor Company; e-mail: bboyer1@ford.co

DOE Technology Manager: Jerry L. Gibbs

(202) 586-1182; fax: (202) 586-1600; e-mail: jerry.gibbs@ee.doe.gov

Field Technical Manager: Dean Paxton

(509) 375-2620; fax: (509) 375-2186; e-mail: dean.paxton@pnnl.gov

Contractor: Pacific Northwest National Laboratory

Contract No.: DE- AC05- 76RL01830

Objectives (FY 2006 –FY 2011)

- Develop an understanding of the levels of hydrogen absorption, diffusion, and damage in piezoelectric materials for the ultimate goal of mitigating absorption or removal of hydrogen.
- Measure the friction and wear characteristics of injector materials in hydrogen environments, including *in situ* and *ex situ* materials characterization.
- Qualify nanolaminate coatings and identify impactful deposition factors for optimization.
- Develop a design approach to hydrogen injectors based on material behavior and performance in hydrogen based on experimental data.

Approach, Including Partner/Collaborator and Path to Technology Transfer and Commercialization (FY 2006–FY 2011)

- Working with industrial partners, the overall approach is to improve the performance and endurance of piezoelectric actuators. These actuators are used in hydrogen internal combustion test engine to improve output, efficiency, and endurance. A major milestone was achieved in engine efficiency (45% brake thermal efficiency) by the Ford Motor Company team in fiscal year (FY) 2009, using actuators designed by Westport Innovations. These efficiencies are comparable to those that may ultimately be achieved by fuel cell technologies, at significantly lower cost.
- Further advances in efficiency and reliability require prolonged actuator lifetime. This requires the development of piezoelectric actuators that are robust in the required service conditions and meet the stringent requirements for actuator speed and accuracy.
- Hydrogen diffusion and absorption in the piezoelectric materials and associated hydrogen damage are the limiting factors for actuator life. These issues are being addressed using experimental methods.

- Using advanced ion scattering techniques at Pacific Northwest National Laboratory (PNNL), researchers are able to measure the hydrogen uptake and damage in piezoelectric and electrode systems.
- Using advanced neutron scattering techniques at the National Institute of Standards and Technology Center for Neutron Research and nuclear magnetic resonance (NMR) at PNNL, researchers were able to measure the hydrogen diffusion over a range of temperatures in both lead zirconium titanate (PZT) and barium titanate (BTO).

Milestones, Metrics and Accomplishments for FY 2011

FY 2011 focused on completing hydrogen/piezoelectric measurements

- Milestones:
 - Complete quantification of hydrogen diffusion in piezoelectrics
 - Complete quantification of hydrogen absorption and damage in PZT/electrode systems as a function of electrode material.
- Metrics:
 - Measure and analyze neutron and NMR hydrogen diffusion data from PZT and barium titanate
 - Measure and analyze ion scattering data on hydrogen absorption and Pb migration in PZT with five different electrode materials and bare PZT
 - Present results at the Annual Merit Review in Washington, D.C. in 2011
 - Disseminate results by submitting articles to peer-reviewed scientific journals.
- Accomplishments:
 - Completed quantification of hydrogen diffusion in piezoelectrics with NMR and neutron scattering
 - Completed quantification of hydrogen absorption and damage in PZT/electrode systems
 - Results presented at 2011 Annual Merit Review in Washington D.C.
 - Published results in peer-reviewed journal, *Applied Physics Letters*
 - Submitted additional articles containing results to peer-reviewed journals
 - Three articles have been submitted to peer-reviewed journals in FY 2011 and are currently under review
 - One additional article is nearly complete and will be submitted in the first quarter of FY 2012.

Future Directions

- Quantify high-pressure hydrogen effects as a function of temperature
- Quantify potential hydrogen barriers such as paralyne and aluminum oxide
- Quantify new ultra-low hydrogen compatible friction coatings.

Introduction

In the transportation sector, hydrogen internal combustion engines (HICE) using direct injection are viewed as a high-efficiency/low-emission technology for bridging the transition process to the hydrogen economy based upon fuel cell technology. Researchers estimate that a direct injection HICE can be integrated into a hybrid vehicle system that would demonstrate fuel consumption (fuel energy used per unit distance) only about 15% to

20% greater than a hybridized fuel cell vehicle of similar mass [1, 2]. Significantly lower hardware cost (compared to present fuel cell systems) and use of existing manufacturing facilities for conventional reciprocating engines makes this an attractive consideration. Some engine manufacturers have identified robust fuel injection technology as one of the key enablers for commercialization of advanced hydrogen direct injection engines.

Originally, the basic piezoelectric-driven hydrogen actuator-injector architecture was designed and developed for earlier natural gas direct injection engine programs. Fundamental issues limiting injector durability were expected due to previously identified problems with hydrogen materials compatibility. Potential engineering solutions were evaluated by PNNL researchers and their partners, Westport Innovations and Ford Motor Company [3]. Overall, the injectors used in the research have been useful tools for developing engine combustion strategies and assessing fuel system technology. If there were a significant level of interest in this type of engine technology, the long-range intention is to advance the injector technology to the point at which it could enter limited commercial production in vehicles or stationary power.

Compared to liquid hydrocarbon fuels, hydrogen is a challenging fluid to use in precision injectors because it has very low viscosity and low density, and it can alter material properties through atomic diffusion or chemical reduction. The goal of this multi-year effort was to understand the basic hydrogen interaction mechanisms that limit injector lifetime and identify promising strategies to significantly improve the technology for the next phase of research and development.

Technical Challenges

The following two issues are critical to the success of the hydrogen direct injection technology (Figure 1):

1. High-pressure hydrogen damage of the piezoelectric/electrode stack in the actuator caused by hydrogen absorption, diffusion, and subsequent effects.
2. Impact and sliding wear between the needle and the jacket enhanced under high-pressure hydrogen.

In previous years, PNNL has taken a parallel approach and studied both piezoelectric damage and wear issues. In FY 2011, PNNL instead focused on completion of the hydrogen-piezoelectric damage issues [3].

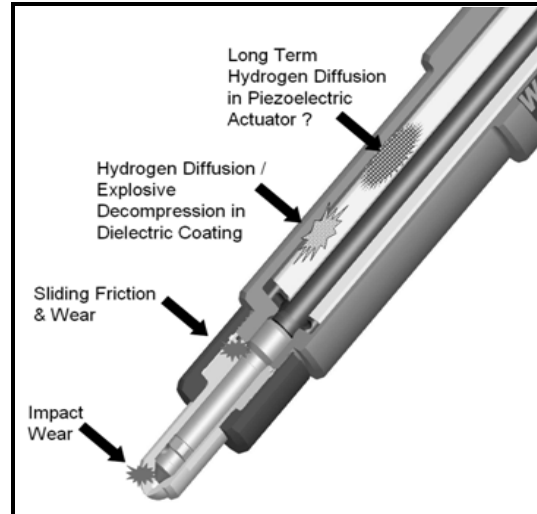


Figure 1. Hydrogen materials compatibility challenges for the HICE injector

Hydrogen Diffusion and Damage in Piezoelectrics Background: Previous experiments in this project and OEM (Ford, Westport) studies have shown that piezoelectric actuators that inject hydrogen tend to fail prematurely in a high-pressure hydrogen environment. This severely limits the reliability and lifetime of the direct injection HICE and makes the option less attractive to industry. By developing an understanding of the failure mechanisms of the piezoelectric in hydrogen, researchers can then develop the tools to address technical issues and bring the direct injection HICE closer to the marketplace.

It is known from the literature that even low-pressure hydrogen can damage piezoelectric materials from studies of ferroelectric random access memory (FeRAM) [4-6]. However, studies on the effects of high-pressure hydrogen on piezoelectric materials are lacking. The PNNL studies in this area are designed to fill this knowledge gap by addressing the following three main areas: hydrogen diffusion within piezoelectrics; hydrogen absorption in piezoelectrics; and

hydrogen-induced damage in piezoelectrics. PNNL has designed a series of experiments over the past few years to increase the knowledge base in this area to understand the problems and provide industry with the tools to mitigate them. Experiments have utilized a combination of microscopy, NMR, as well as ion and neutron scattering techniques that are uniquely suited to studying hydrogen and its effects.

Technical Approach:

Hydrogen Absorption and Damage of Piezoelectrics: To quantify the damage that high-pressure hydrogen can do to actuators, PNNL designed a simple piezoelectric-electrode thin film stack geometry as shown in Figure 2. This allows us to isolate the effects of the high-pressure hydrogen on those components uncomplicated by epoxy and adhesives as well as potential sectioning issues.

This approach has many benefits. The first is that results are then more easily comparable to the low-pressure hydrogen results in the references, which used sputtered piezoelectric films. The second is the films are of very high quality and low roughness, thus ensuring that surface damage is more easily observed and that roughness does not affect the surface scattering results. PNNL has quantified hydrogen effects in both a bare piezoelectric system as well as piezoelectric films coated with metal as in the actuator. The metal coating strongly influences the catalytic properties of the system for disassociating and absorbing hydrogen as well as damage.

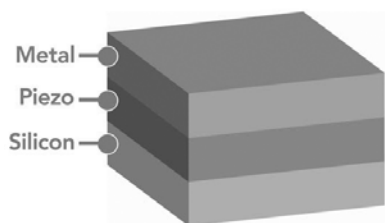


Figure 2. Schematic of thin film samples

To quantify the response to high pressure hydrogen environments that an actuator

would be exposed to in service, the piezoelectric samples were exposed to high pressure hydrogen (2500 psi) and 100°C in a high pressure autoclave at PNNL for 24 hrs to 1 week (see Figure 3). Both lead PZT and BTO piezoelectrics have been quantified.



Figure 3. High-pressure hydrogen autoclaves used to charge piezoelectric samples

Ion Scattering: Ion scattering techniques, including Rutherford back-scattering spectrometry (RBS) and elastic recoil detection analysis (ERDA) were used to quantify both hydrogen absorption (ERDA) and heavy ion migration (RBS). In both ERDA and RBS, the thin film stack is hit with high energy He ions that can penetrate up to ½ micron into the sample, necessitating the thin films. In ERDA, the He ions at near grazing incidence will eject absorbed H⁺ ions, which collected at the detector, where a thin Al foil blocks the forward scattered He ions. In RBS (see Figure 4), the He ions back-scatter off of heavier elements within the films, such as Pb, Zr, Ti, O, and are collected with a detector. A typical RBS spectrum is shown in Figure 5. The RBS and ERDA spectrum are readily analyzed with the SIMNRA program to evaluate atomic composition.

ERDA is an especially valuable tool for this project for measuring small amounts of absorbed hydrogen. There are very few techniques that are capable of measuring absorbed hydrogen due to the very small atomic number. Neutrons and ion scattering are the primary techniques for such

absorption studies. ERDA is able to detect absorbed hydrogen at levels of a tenth of an atomic percent. This is especially useful for our systems where the absorption is on such a small scale and where even these low amounts can lead to significant damage.

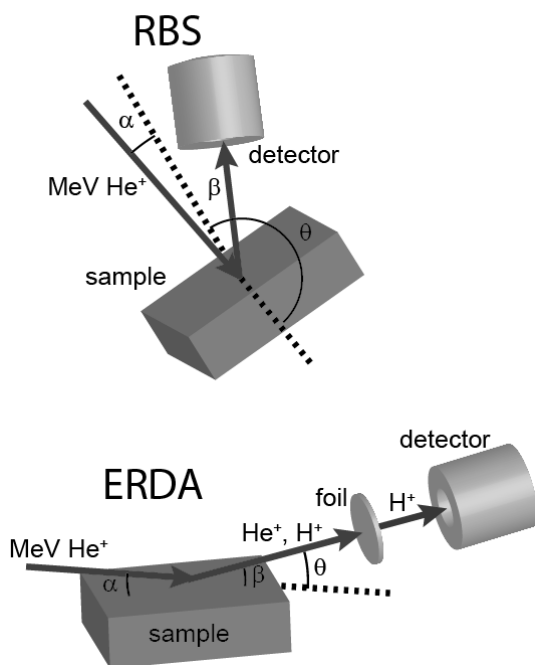


Figure 4. Ion scattering geometry; top: RBS geometry; bottom: ERDA geometry

In addition to hydrogen absorption and diffusion, high-pressure hydrogen can lead to chemical reduction of heavy elements within the piezoelectric such as Pb in the PZT material allowing for migration into the electrode region. This is detrimental as it degrades the PZT and can damage the electrode material as well.

In FY 2010, PNNL quantified the hydrogen absorption in bare PZT and BTO and films Pd with both ERDA and RBS [7]. PNNL found with ERDA that the bare PZT and BTO films absorbed on the order of 5-10 atomic % of hydrogen after exposure to high-pressure hydrogen. Films with Pd absorbed significantly higher amounts of hydrogen (20-25 atomic %) due to the catalytic nature of the Pd layer. In addition, RBS demonstrated significant migration of

Pb into the Pd layer. It should be noted that Pd is not a typical electrode material for actuators and was used as a “worst-case” test due to its high catalytic activity for hydrogen. In FY 2011, PNNL expanded these studies to include multiple metal electrodes, including Al, Cu, Ti, and W on PZT films. These metals were chosen to have a wide range in catalytic activity for hydrogen and varied barrier properties as well. The rationale is that with the results from these select metals, researchers and industry could then predict the effects of other metals with similar catalytic or barrier properties.

ERDA results showed the hydrogen absorption was highest in Al and Pd and lowest in W. Since Al forms an oxide that has low hydrogen permeability, the high degree of hydrogen absorption in the PZT/Al is surprising. The explanation is that Al films are typically full of pin-hole type defects that can allow easy passage of the hydrogen gas, regardless of the aluminum oxide barrier properties. It is not surprising that W yields low absorption as it has very low catalytic properties for hydrogen absorption and disassociation compared to other metals.

RBS demonstrated significant Pb diffusion into the upper electrode layer in the case of Pd, Cu, and W on PZT. A representative RBS spectra showing mixing in Pd/PZT is shown in Figure 5. Pb migration was not observed with RBS in Ti and Al films, although microscopy did indicate significant Pb migration through the Al film. Interestingly, Ti films fared the best in several respects. Namely, Ti had the smallest difference in hydrogen content between the hydrogen exposed and control and the least Pb migration. However, both the control and hydrogen exposed Ti samples did show relatively high levels of hydrogen (8 atomic %). This is reasonable since Ti is known to readily form hydrides. The decent performance of Ti is likely due to the formation of a Ti oxide that acts as a hydrogen permeability barrier layer. These

ion scattering results have been compiled into two manuscripts for publication. Measurements were also done on BTO samples that were not yet analyzed at the time of writing this report.

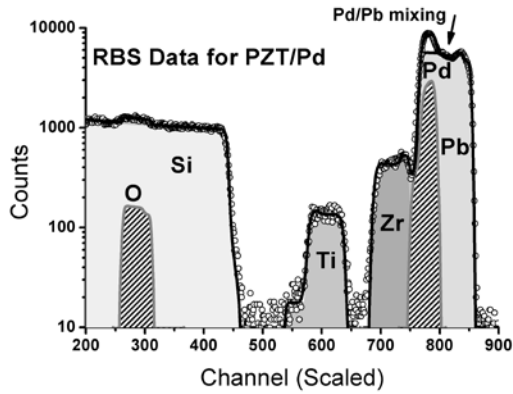


Figure 5. RBS data showing the different elemental spectra Pd, Pb, Zr, Ti, and O. Overlapping Pb and Pd spectra indicate elemental mixing at the piezo/electrode interface.

Surface Degradation – Blistering: In addition to Pb migration and mixing at the electrode, PNNL has also seen evidence of surface blistering on the piezoelectric materials. Blistering is common in some metals that have been exposed to large amounts of hydrogen. Atomic hydrogen within the system can recombine into hydrogen at cracks or voids within the system. When the external hydrogen pressure is removed rapidly, the hydrogen within the system can rapidly expand, causing a void to form. If this occurs on the surface, it is called a blister. Blistering is shown for a PZT film, along with a schematic of blistering in Figure 6. Blistering was observed in several PZT and BTO metal systems and remains a serious issue for piezoelectric use in high-pressure hydrogen.

Hydrogen Diffusion in Piezoelectrics:

Hydrogen diffusion is an important parameter that is critical to understanding the kinetics of degradation of the piezoelectric materials. There have been relatively few studies to date on this topic. One study [4] measures hydrogen diffusion

of PZT films charged electrochemically via the mapping of a color change propagation along the cross-section of the PZT.

After gaseous charging of the piezoelectrics at 100 °C, a color change was not observed as it was in the electrochemical experiments. This indicated that the electrochemical hydrogen charging is a substantially different mechanism than the gaseous charging that an actuator would experience. The color change is likely due to significant reduction of the PZT and removal of the oxygen from the lattice. Thus, instead of electrochemical charging, PNNL used gaseous charging via the high-pressure hydrogen autoclaves described previously. NMR and quasi-elastic neutron scattering (QENS) methods were then employed to probe the local hydrogen motion in BTO and PZT powder samples charged via a simple gaseous exposure route identical to what an actuator in a HICE would experience.

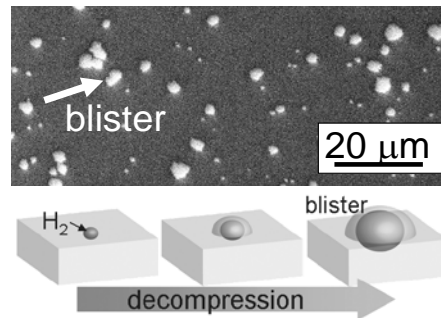


Figure 6. Hydrogen blistering in PZT and a schematic of the blistering process

With NMR, slow dynamics of hydrogen motion within the piezoelectrics on the order of $1 \times 10^{-17} \text{ m}^2/\text{s}$ were observed for both PZT and BTO. With QENS, a faster dynamic diffusion process in PZT on the order of $3 \times 10^{-10} \text{ m}^2/\text{s}$ was observed. It is likely the fast process dominates hydrogen absorption within these materials. Oddly, while BTO also shows rapid diffusion processes, this diffusion appears to be more of a local diffusion and differs from the PZT motion.

Further Piezoelectric/Hydrogen Studies:

While this project was completed at the end of FY 2011, PNNL has identified several further areas of study that would be beneficial to the HICE and possibly natural gas ICE also.

- Temperature studies on hydrogen uptake.
- Evaluation of barrier materials such as paralyene to block hydrogen uptake.
- Further studies on new nano-laminate films for reduced friction.

Conclusions

The adsorption and diffusion of hydrogen was studied in a variety of piezoelectric and metal systems deemed appropriate to actuator/ direct injection HICE systems. The following conclusions were reached:

- Hydrogen absorption is strongly dependent on the metal electrode catalytic and barrier properties.
- Pb diffusion into the electrode metal appears to occur in nearly all cases, regardless of the electrode used, and is a serious issue to be addressed.
- Hydrogen diffusion is likely dominated by a fast process with a diffusion constant on the order of 3×10^{-10} m²/s for PZT.

Presentations/Publications

- Alvine KJ, V Shutthanandan, WD Bennett, CC Bonham, D Skorski, SG Pitman, ME Dahl, and CH Henager, Jr. 2010. "High Pressure Hydrogen Materials Compatibility of Piezoelectric Films." *Applied Physics Letters* 97, 221911.
- Alvine KJ, V Shutthanandan, BW Arey, C Wang, WD Bennett, SG Pitman. "High-Pressure Hydrogen Induced Growth of Pb Nanowires." Submitted 2011. (Unpublished.)
- Alvine KJ. "Electrode Effect on High-Pressure Hydrogen Degradation of Lead Zirconate Titanate Films." Submitted 2011 (Unpublished.)
- Alvine KJ. "Hydrogen Diffusion in Lead Zirconate Titanate and Barium Titanate." Submitted 2011. (Unpublished.)

- Alvine KJ. "Hydrogen Species Motion in Piezoelectrics." Submitted 2011. (Unpublished.)
- Alvine et al. 2011. "Hydrogen Materials Compatibility." *DOE Annual Merit Review*, Washington, D.C.

References

- [1] White CM, RR Steeper, and AE Lutz. 2006. "The Hydrogen-Fueled Internal Combustion Engine: A Technical Review." *International Journal of Hydrogen Energy* 31(10): 1292-1305.
- [2] Verhelst S and T Wallner. 2009. "Hydrogen-Fueled Internal Combustion Engines." *Progress in Energy and Combustion Science* 35(6): 490-527.
- [3] Welch A, D Mumford, S Munshi, J Holbery, B Boyer, M Younkins, and H Jung. 2008. "Challenges in Developing Hydrogen Direct Injection Technology for Internal Combustion Engines." 2008-01-2379, SAE 2008.
- [4] Huang HY, WY Chu, YJ Su, KW Gao, JX Li, and LJ Qiao. 2007. "Hydrogen-Induced Semiconductor Transformation of Lead Zirconate Titanate Ferroelectric Ceramics." *Journal of the American Ceramic Society* 90(7): 2062-2066.
- [5] Kushida-Abdelghafar, K, H Miki, K Torii, and Y Fujisaki. 1996. "Electrode-Induced Degradation of Pb(ZrxTi1-x)O-3 (PZT) Polarization Hysteresis Characteristics in Pt/PZT/Pt Ferroelectric Thin-Film Capacitors." *Applied Physics Letters* 69(21): 3188-3190.
- [6] Aggarwal S, SR Perusse, CW Tipton, R Ramesh, HD Drew, T Venkatesan, DB Romero, VB Podobedov, A Weber. 1998. "Effect of Hydrogen on Pb(Zr, Ti)O-3-based Ferroelectric Capacitors." *Applied Physics Letters* 73(14): 1973-1975.
- [7] Alvine, KJ, V Shutthanandan, WD Bennett, CC Bonham, D Skorski, SG

Pitman, ME Dahl, and CH Henager, Jr.
2010. "High-Pressure Hydrogen Materials
Compatibility of Piezoelectric Films."
Applied Physics Letters 97(22).

Acronyms

BTO: barium titanate
DOE: U.S. Department of Energy
ERDA: elastic recoil detection analysis
FeRAM: ferroelectric random access
memory
HICE: hydrogen internal combustion
engines
NMR: nuclear magnetic resonance
PNNL: Pacific Northwest National
Laboratory
PZT: lead zirconium titanate
QENS: quasi-elastic neutron scattering
RBS: Rutherford back-scattering
spectrometry

Agreement 13329 - Design Optimization of Piezoceramic Multilayer Actuators for Heavy Duty Diesel Engine Fuel Injectors

Hua-Tay Lin, Hong Wang, Kewei Zhang, and Andrew A. Wereszczak
Ceramic Science and Technology Group
Oak Ridge National Laboratory
P.O. Box 2008, MS 6068
Oak Ridge, TN 37831-6068
(865) 576-1169; fax: (865) 574-6098; e-mail: linh@ornl.gov

DOE Technology Manager: Jerry L. Gibbs
(202) 586-1182; fax: (202) 586-1600; e-mail: Jerry.gibbs@ee.doe.gov
ORNL Technical Advisor: David P. Stinton
(865) 574-4556; fax: (865) 241-1034; e-mail: stintondp@ornl.gov

Contractor: Oak Ridge National Laboratory, Oak Ridge, Tennessee
Contract No.: DE-AC05-00OR22725

Objectives

- Adapt established structural ceramic probabilistic design and reliability analysis to improve the reliability of piezoelectric multilayer actuators (PMLAs) that are being considered for use in diesel engine fuel injectors.
- Generate required micromechanical property data on lead zirconate titanate (PZT) piezoceramics and macromechanical property data on PMLAs for input into the design and reliability analysis of the latter.
- Identify minimum mechanical performance requirements for fuel injector PMLAs.
- Adapt these strategies to improve reliability of PMLAs under candidacy for use in diesel engine fuel injectors.

Approach

- Evaluate PMLA reliability under representative service conditions.
- Link constituent piezoceramic micro-mechanical and PMLA macro-mechanical responses.

Accomplishments

- Upgraded electric loading capacity and measurement capability of BOR (ball-on-ring) setup, including electric liquid tank and Sawyer-Tower (ST) circuit.
- Study showed aging effect was significant in the case open circuit, near 0.0 kV/mm, but de-aging of up to 54-months aged samples occurred when the electric field was substantially high ($> \pm 2.4$ kV/mm).
- Application of on-line measurement to piezo-stack under test proves to be an effective approach to testing and characterizing the electrical fatigue response because it approaches the working condition of the stack deployed in fuel injection system.

Future Direction

- Develop database for screened piezoceramics and PMLAs of Cummins with the suggested environmental factors included.
 - Measure and compare piezoelectric and mechanical reliabilities of screened PZT piezoceramics.
 - Fabricate additional PMLA fatigue test frames.
-

Introduction

The use of piezoelectric multilayer actuators (PMLAs) as diesel fuel injectors has the potential to reduce injector response time, provide greater precision and control of the fuel injection event, and increase fuel efficiency. Compared to conventional solenoid operation of an injector, the alternative use of a PMLA can enable precise rate shaping of the entire injection cycle that accurately controls injection timing and fuel quantity. Piezoelectric multilayer actuators (or piezo-stacks) fuel injectors contain a solid-state ceramic actuator that converts electric energy into linear motion precisely controlling the needle's opening and closing. This capability results in an engine with outstanding performance, improved fuel economy, low noise, and low emissions. Though their use is very attractive for the reasons mentioned above, uncertainty continues to exist over how reliable piezo-actuated fuel injectors will be in the challenging environment of a heavy vehicle diesel engine. Though piezoelectric function is the obvious primary function of lead zirconate titanate (PZT) ceramic PMLAs for fuel injectors, their reliability can be a performance and life limiter because the PZT ceramic within them is brittle, lacks high strength, and may exhibit fatigue susceptibility. That brittleness and relatively low strength can be overcome with proper probabilistic component design methodology.

This project undertakes the reliability characterization of candidate PMLAs used in these

fuel injectors and the piezoceramics used in the PMLAs. Test and characterization on the piezoceramics and piezo stacks have continued based on recommendations from Cummins, Inc. At the same time, the testing facilities have been modified accordingly at ORNL to accommodate the requirements for testing related materials and devices. The PZT products from three suppliers such as Kinetic Ceramics, Inc. (KCI, Hayward, CA), Piezo System, Inc. (PSI, Woburn, MA), and EPCOS AG (Munich, Germany) have been evaluated and characterized.

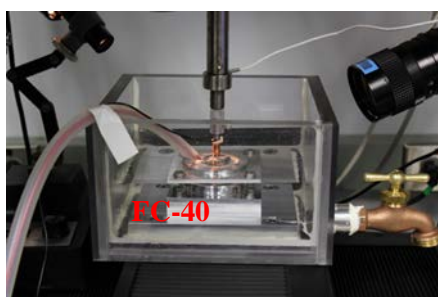
Approaches

1. Piezoceramic Characterization

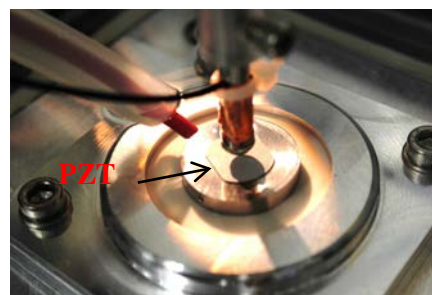
Mechanical reliability of comprising PZT layers remains as a critical issue in developing and deploying PZT stacks in fuel injection system in heavy-duty diesel engine. This includes the mechanical responses of PZT under various loading environments. To meet these requirements, efforts have been made to extend the current BOR testing into high electric fields and high humidity levels.

An electric liquid container was designed and incorporated into the BOR setup as shown in Fig. 1. The electric liquid of FC-40 allows the electric field more than 4 times the coercive of PZT-5A to be applied without any interrupt of dielectric breakdown.

Two PZT materials were tested using the upgraded BOR system.



(a)



(b)

Fig. 1 Ball-on-ring setup (a) general view with FC-40 container attached on the test stage, and (b) enlarged area showing PZT specimen, loading ball and supporting ring that sits on an alumina disk.

- The first PZT examined was as-received KCI PZWT, supplied by Cummins, Inc. Each PZT specimen was a circular plate with two opposite segments cut off. The nominal diameter was 15.00 mm, distance between two cuts 12.26 mm, and thickness 0.500 mm. Mechanical and electrical loading controls were described previously.¹
- The second PZT was PSI-5A4E, obtained from Piezo System, Inc. The experimental study included two specimen states: aged and as-received. Each PZT specimen was a plate of 10mm × 10mm and 0.276 mm thick. Mechanical and electrical loading controls were described previously.^{2,3,4}
- The effect of electric loading-path and loading levels on mechanical responses of the PZT was emphasized. This is important because the PZT is required to subject to as high as 4 times the coercive field level. Polarization state of the poled PZT can be changed substantially under such extreme condition, and currently there is no data available. Monitoring the polarization of stressed PZT has been enabled by using a modified Sawyer-Tower circuit.

allows the treatment of PZT specimen in a specified period.

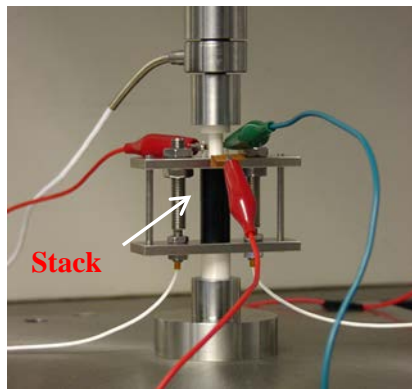
2. PMLA Characterization

Degradation of candidate PZT stack was observed to be significant, and effects included cracking, dielectric breakdown, and stroke loss. Testing and characterization of piezo-stacks continued.

Test facility has been updated with high-frequency displacement amplifiers (410-XS-6WB, 6 kHz, Capacitac) as shown in Fig. 2. The introduction of the amplifiers allows the displacement channels to be monitored and data acquired on-line.

An aged EPCOS stack was used in this stage. The tested piezo-stack, ANOX-8500b, had an overall size of 6.5mm×6.5mm×30mm, capacitance of 2.9 μF, and rated voltage of 160V. The cycling was carried out under an electric loading condition of 50 Hz, 0/160V sine wave with a mechanical preload of 766 N. Data processing and evaluation were conducted by following the procedures given in reference.^{5,6}

In the earlier stages of this project, three stacks of same model but from different sources were tested (two purchased from EPCOS, and one



(a)



(b)

Fig. 2 (a) Piezo-stack section showing a stack in center, load cell on top, displacement gages (Capacitac gages) on both sides, and (b) high frequency amplifiers for Capacitac displacement sensors.

Humidity chamber was obtained. The potassium bromide solution under controlled room temperature can maintain the relative humidity around 81%. This

supplied by Cummins, Inc.). However, the measurements in those tests were done when the cycling was paused in a lower frequency loading of

2 Hz with two mechanical preloads: 16 and 766N. These previous data will be used as a baseline of our analysis.

Results

1. Piezoceramics Characterization

1.1 KCI PZT Results

Data on the flexure strength of poled KCI were collected in three different electric conditions: open circuit (OC), +2Ec, and -2Ec. The data denoted as Y10 are shown in Fig. 3 as confidence ratio rings along with those obtained with those acquired in FY2009 (denoted as Y09). The specimen conditions of Y09 and Y10 were pretty similar, even though they came in different times. It can be observed that:

- 1) Two groups of specimens (Y09 and Y10) seemingly delivered different mechanical strengths, but the difference can be seen not significant. Two confidence ratio rings (in the case of OC, 0.00 kV/mm) barely separated.
- 2) The effect of electronic fluid (FC-40) on the KCI flexure strength is insignificant in most of the electric conditions examined as validated from the overlaying confidence ration rings.
- 3) Exception existed for the data set with -Ec, in which the mechanical strength decreased to a certain degree.

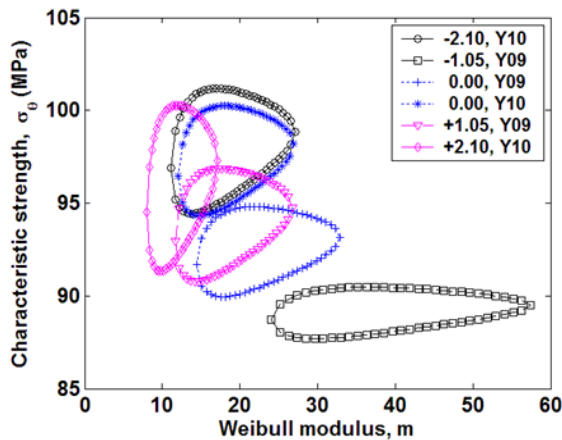


Fig. 3 Confidence ratio rings of flexural strength for KCI PZT under various electric conditions at 95% confidence level; data for Y10 specimens were obtained with FC-40, and data for Y09 obtained in open air.

The insensitivity of flexure strength for Y10 KCI on the electric field within the tested field range again demonstrated that the role of polarization as affected by the electric field did not influence the mechanical property in the case of KCI PZT samples.

1.2 PSI PZT Results

Characteristic strength and Weibull modulus of aged PSI-5A4E are presented in Fig. 4. Data generated in previous studies are also included for comparison. It shall be notified that each data set consists of at least 12 test points. Apparently, no trend exists on the Weibull modulus with the change of electric field level. However, the effect of electric field on the characteristic strength is obvious. The following observations can be made:

- 1) Aging effect was significant in the case OC, near 0.0 kV/mm.
- 2) De-aging occurred when the electric field was substantially high. Mechanical strength of the aged PZT in negative field from 0 to -3.6 kV/mm follows that of the as-received PZT.
- 3) Overshoots of Sawyer-Tower circuit were observed in the loading of aged 54 months to -3.6 kV/mm. The reason was not clear.
- 4) Continued electric field loading from -3.6 to +3.6 kV/mm resulted in a V-shaped curve.
- 5) Mechanical strength stayed quite higher when electric field crossed the negative coercive field, -Ec, and returned to the levels of the as-received in OC and +1.2 kV/mm.
- 6) It seems that the original polarization was maintained just as anew, even though the PZT had experienced a cycle of high negative loading field. The further increase in electric field resulted in higher levels of mechanical strength relatively to the as-received PZT.

Characteristic strength and Weibull modulus of as-received PSI-5A4E are presented in Fig. 5. Data generated in the aged specimens are also included for comparison. The electric field as high as 4 times the coercive field of PZT-5A, 4.8 kV/mm, was examined in this study. This was made possible because of the introduction of FC-40 as a surrounding medium. It shall be noted also that each

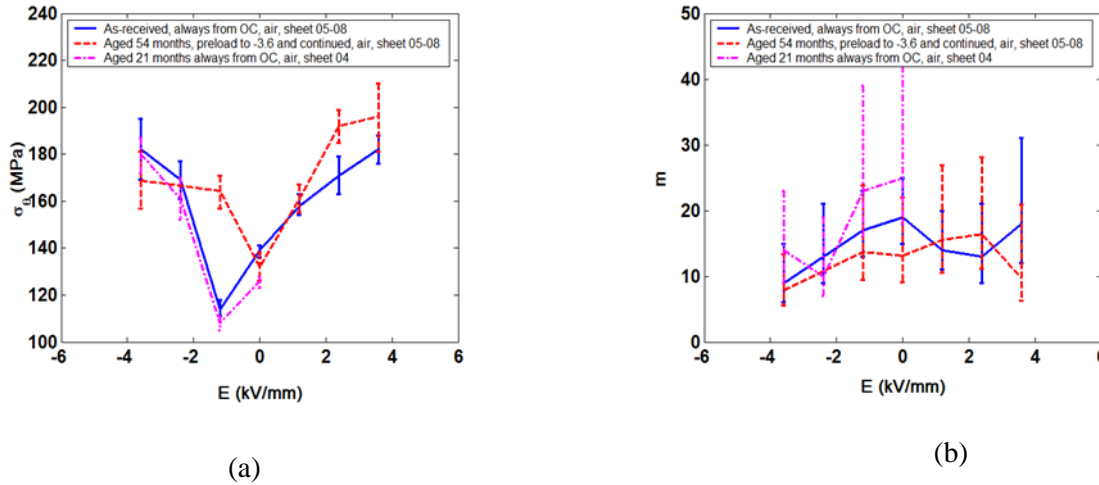


Fig. 4 (a) Variation of characteristic strength of aged PSI-4A5E with electric field, and (b) variation of Weibull modulus. Data of Aged 54 months were obtained in the open air at each stop of the electric loading path starting from $-3E_c$: $0 \rightarrow -3E_c \rightarrow -E_c \rightarrow 0 \rightarrow E_c \rightarrow 2E_c \rightarrow 3E_c$; rate was 0.36 kV/mm/s . Those of as-received and 21 month aged were from previous studies.^{2,3}

data-set consists of at least 12 test points. Again, no trend exists on the Weibull modulus with the change of electric field level. However, the effect of electric field on the mechanical strength is markedly visible. The following observations can be made:

- 1) Effect of loading-path existed on the mechanical strength of the PZT.
- 2) Depolarization and its effect on the mechanical strength were significant around $-E_c$ or -1.2 kV/mm .
- 3) Same level of mechanical strengths was found for those of the PZT being poled or repoled, disregarding the aging state of PZT specimens and initial electric loading direction.
- 4) The ST circuit curve is stable under high field loading. But the circuit box was found to have been broken in the later stage of study. A replaced one was used.
- 5) High field loading in FC-40 obviously resulted in higher levels of mechanical strength relative to that tested in the air.

SEM studies for aged PSI-5A4E showed that fracture surfaces were dominated by transgranular fracture. Figure 6 is an SEM image for a fracture surface in which the porous region can be seen as a

failure origin near the tensile face of the flexure specimen.

1.3 PSI test with humidity factor

The tests will be started when the PZT specimens are received.

2. PMLA Characterization

An EPCOS stack aged 2 years was tested more than 8×10^7 cycles. The stack was found to be short-circuited after an unexpected power outage when cycled to 10^8 cycles. The responses of the stack were measured during the cycling (50 Hz, 0/160 V, 766 N). The variations of mechanical strain and charge density are given in Fig. 7 along with those of the two as-received stacks studied previously. It is worthwhile noting that, although the cycling condition was same among these data group, the stack state and measurement condition were different, in terms of aging, measurement frequency and mechanical load. Nevertheless, an increase in strain in the earlier stage of cycling, around 10^5 cycles, was observed perhaps because of the poling from unipolar cycling. This was followed by a decrease in the late stage of cycling. Overall, the strain level of aged stack was lower than that of as-received ones under same mechanical preload, 766

N. At same time, the charge density was found to be fluctuated without any defined trend during the entire cycling period.

The variations of piezoelectric hysteresis and dielectric hysteresis are given in Fig. 8 also along with those of the two as-received stacks studied previously. It is interesting to see that the hysteresis obtained from on-line measurement with 50Hz,

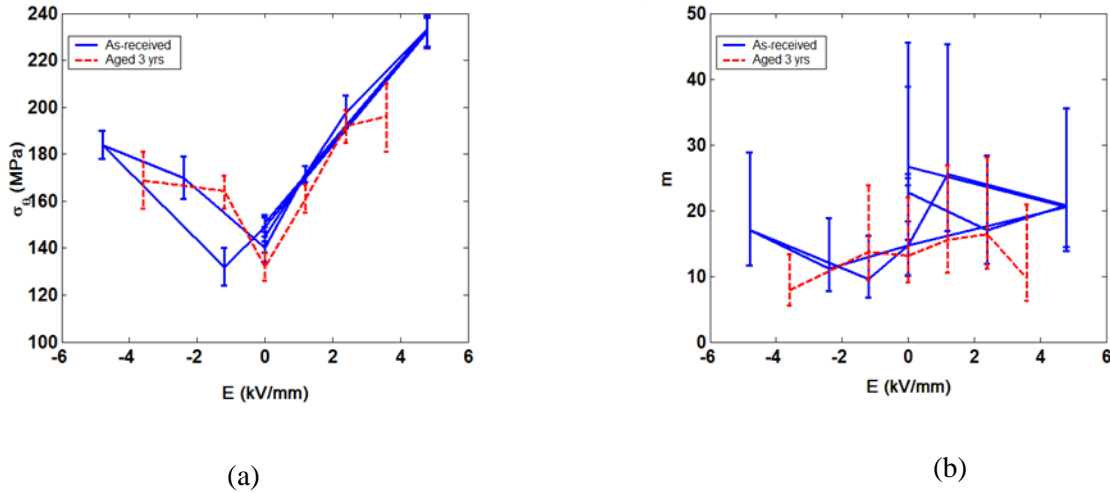


Fig. 5 (a) Variation of characteristic strength of as-received and aged PSI-4A5E with electric field, and (b) variation of Weibull modulus. Data of the as-received PSI-5A4E were obtained in FC-40 at each stop of the electric loading path: $0 \rightarrow 4E_c \rightarrow 0 \rightarrow -E_c \rightarrow -4E_c \rightarrow -2E_c \rightarrow 0 \rightarrow E_c \rightarrow 4E_c \rightarrow 2E_c \rightarrow 0$; rate was 0.48kV/mm/s. Those of more than 3 year aged or 54 months are same as those in Fig. 4.

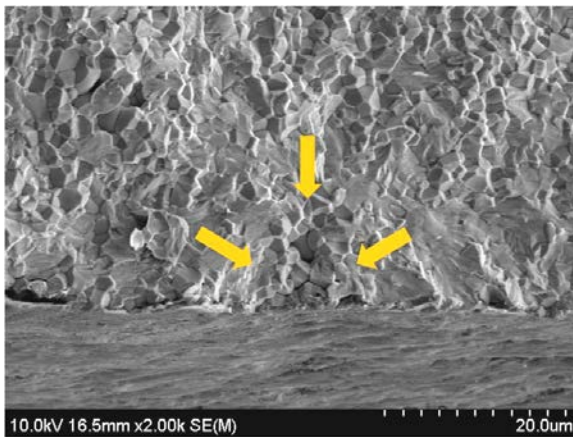


Fig. 6 SEM image of a fracture surface showing the failure origin of a PZT plate (aged 54 months) tested under $3E_c$ with a preload electric field from 0 to $-3E_c$ (as indicated in Fig. 4). The failure stress is 204 MPa.

766N showed a pretty close response to that of 2Hz, 16N. The mechanisms involved with these observations remain to be investigated.

Conclusions and Future Work

1. Conclusions

Testing and characterization were focused on the candidate piezoceramics and piezo stacks that are currently considered in the use of heavy diesel engine fuel system. Main conclusions can be drawn as follows.

- 1) The high electric field test container functioned very well as designed with FC-40. The dielectric breakdown in the BOR testing with electric field coupled has been suppressed effectively.
- 2) Effect of electronic liquid on the mechanical strength was not substantially significant as validated from OC results in air.
- 3) Sawyer-Tower circuit captured the charge response of PZT under test, and that enabled the

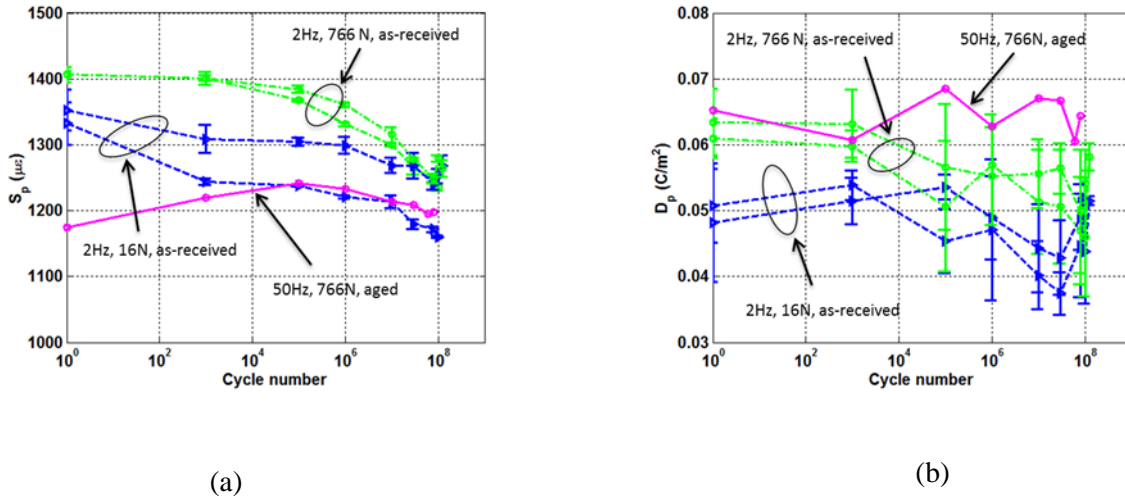


Fig. 7 (a) Variation of mechanical strain with cycle number, and (b) variation of charge density with cycle number for EPCOS stack ANOX-8500b. The fatigue data for the aged stack were generated in this study.

monitoring of polarization status of PZT in electro-mechanical testing.

- 4) De-aging of an aged PZT as measured by mechanical strength can be obtained by using high electric field under a control loading condition.
- 5) Electric loading-path had a substantial effect on the mechanical response of poled PZT when the driving electric field went as high as 2 times the coercive field.
- 6) Depolarization near negative coercive field of a poled PZT had a significant negative impact on the mechanical strength of the PZT.
- 7) On-line measurement of piezo-stack under test can be an effective approach to testing and characterizing the fatigue response because it approaches the working condition of the stack deployed in fuel injection system.
- 8) The understanding of on-line measurements and responses of piezo-stack under test remains to be developed, including measurement frequency.

2. Future Work

2.1.1 Piezoceramics Characterization

- 1) As-received PZT-5A, PSI-5A4E (10mm×10mm×0.267mm, 6 nF), will be treated under a controlled humidity near 81% R.H. in a specified period.
- 2) The sensitivity of treatment time on the moisture content and the effect on the mechanical strength will be investigated using BOR.
- 3) Electric field effect on mechanical strength of the PZT will be studied in more detail using BOR, especially the influence of depolarization.
- 4) Immersion heating will be introduced into the FC-40 container to study the effect of temperature on the mechanical and piezoelectric responses using BOR and piezodilatometer.

2.2 PMLA Characterization

- 1) 10-layer PZT plates, NOLIAC CMAP07 (5mm×5mm×2mm, 10 nF, rated voltage 200 V), will be tested under a controlled electric loading by using piezodilatometer. The piezodilatometer is currently equipped with

a Trek PZD 2000A that has a current capacity of ± 400 mA at ± 2 kV enabling accelerating fatigue test. Fatigue mechanisms at various temperatures will be investigated.

- 2) Piezo-stack fatigue test facility will be modified to accommodate the target EPCOS stack (12mm \times 12mm \times 54mm, 16.15 μ F, rated voltage 160 V). Uncapsulated stacks will be wired and tested under a controlled electric waveform. The on-line displacement measurement and temperature monitoring will be conducted.
- 3) A new PZT stack test facility that has a loading frame of high stiffness or required rigidness will be developed and fabricated. Currently, Cummins, Inc. is considering lending ORNL a piezo drive and a test rig for such testing. The factors to be investigated by using the planned facility include the driving mode, temperature, and mechanical preload.
- 4) The work will be initiated on the finite element analysis to include the above generated data into the probabilistic design for the recommended stack configurations.

References

- [1] Wang, H., Matsunaga, T., and Lin, H.-T., Characterization of poled single-layer PZT for piezo stack in fuel injection system, *Ceram. Eng. Sci. Proc.*, 31 (2), 2010, 127-136.
- [2] Wang, H. and Wereszczak, A. A., Effects of electric field and biaxial flexure on the failure of poled lead zirconate titanate, *IEEE Trans. Ultrasonic, Ferroelectrics, and Frequency Control*, 55 (12), 2008, 2559-2570.
- [3] Wang, H., Lin, H.-T., and Wereszczak, A. A., Strength properties of poled lead zirconate titanate subjected to biaxial flexural loading in high electric field, *J. Am. Ceram. Soc.*, 93 (9), 2010, 2843-2849.
- [4] Zhang, K., Wang, H., and Lin, H.-T., Strength properties of aged poled lead zirconate titanate subjected to electromechanical loadings, in review, 2011.
- [5] Wang, H., Wereszczak, A. A., and Lin, H.-T., Fatigue response of a PZT multilayer actuator under high-field electric cycling with mechanical preload, *J. Appl. Phys.*, 105 (1), 2009, 014112.

- [6] Wang, H., Cooper, T. A., Lin, H.-T., and Wereszczak, A. A., Fatigue responses of lead zirconate titanate stacks under semi-bipolar electric cycling with mechanical preload, *J. Appl. Phys.*, 108 (8), 2010, 084107.

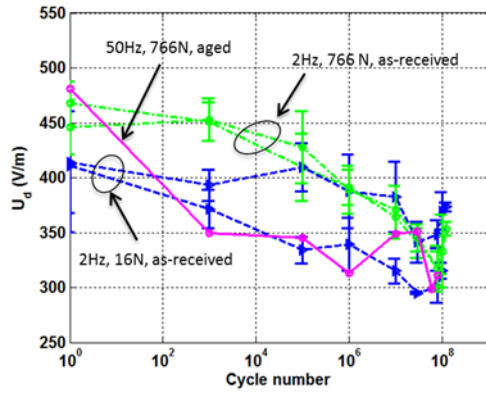
Presentations and Publications

Presentations

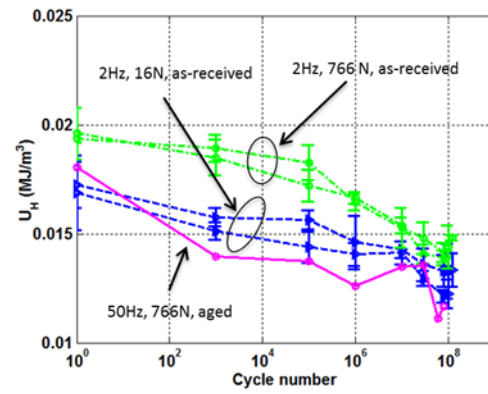
1. Lin, H.-T., Wang, H., and Wereszczak, A. A., "Design Optimization of Piezoceramic Multilayer Actuators for Heavy Duty Diesel Engine Fuel Injectors" at the 2011 DOE Annual Merit Review, May 9-12, Arlington, VA.

Publications

1. Zhang, K., Wang, H., and Lin, H.-T., Strength properties of aged poled lead zirconate titanate subjected to electromechanical loadings, in review, 2011.
2. Wang, H., Matsunaga, T., and Lin, H.-T., Effects of temperature on mechanical strength of pressed PZT, in preparation, 2011.
3. Wang, H., Matsunaga, T., Lin, H.-T., and Mottern, A. M., Piezoelectric and dielectric performance of poled lead zirconate titanate subjected to electric cyclic fatigue, submitted, 2011.



(a)



(b)

Fig. 8 (a) Variation of piezoelectric hysteresis with cycle number, and (b) variation of dielectric hysteresis with cycle number for EPCOS stack ANOX-8500b. The fatigue data for the aged stack were generated in this study.

Agreement 15050 – Materials Testing with ACERT Engine (CRADA with Caterpillar)

M. D. Kass, T. J. Theiss, R. Wagner, and N. Domingo

Fuels, Engines and Emissions Group

Oak Ridge National Laboratory

NTRC Building

2360 Cherahala Blvd.

Knoxville, TN 37932

(865) 946-1241; fax: (865) 946-1354; e-mail: kassmd@ornl.gov

H. T. Lin

Ceramic Science and Technology Group

Oak Ridge National Laboratory

P.O. Box 2008, MS 6068, Bldg. 4515

Oak Ridge, TN 37831-6068

DOE Technology Manager: Jerry L. Gibbs

(202) 586-1182; fax: (202) 586-1600; e-mail: Jerry.gibbs@ee.doe.gov

ORNL Technical Advisor: David Stinton

(865) 574-4556; fax: (865) 574-6098; e-mail: stintondp@ornl.gov

Contractor: Oak Ridge National Laboratory, Oak Ridge, Tennessee
Prime Contract No.: DE-AC05-00OR22725

Objectives

- Improved diesel engine performance, efficiency, and emissions through the applications of materials enabled technologies.
- Evaluate material/component performance on a heavy-duty diesel engine platform.

Approach

- Evaluate components and materials for improved efficiency in a 2004 Caterpillar C-15 ACERT instrumented for thermal and combustion analysis.

Accomplishments

- Installed and commissioned transient capability
- Evaluated novel valve materials improved high temperature performance and durability

Future Direction

- Install and evaluate new exhaust manifold alloy for improved thermal performance
 - Install Tier IV engine for aftertreatment studies
-

Introduction

The purpose of this Cooperative Research and Development Agreement between UT-Battelle Inc. and Caterpillar, Inc. is to improve diesel engine performance, efficiency, and emissions through the application of materials-enabled technologies. The demands of meeting new emissions and fuel economy goals are continuing to push heavy-duty diesel engine components to higher temperatures and pressures and improved durability. Engine manufacturers have recognized several key needs that need to be addressed in order for heavy duty diesel engines to achieve a national efficiency goal of 55% by the year 2012. These include 1) improved structural materials to accommodate higher cylinder pressures and temperatures (associated with advanced combustion methodologies), 2) improved thermal management and waste heat recovery technologies, 3) improved durability, 4) improved transient performance, and 5) better aftertreatment performance. These needs address barriers associated with high parasitic losses, high-efficiency clean combustion and thermal management of the cylinder and exhaust.

This CRADA brings together expertise and facilities from the ORNL Materials Science & Technology and Engineering & Transportation Science Divisions. Similarly, materials and engine research staff at Caterpillar are also working together. In anticipation of this CRADA, Caterpillar provided ORNL with two 600 hp motoring dynamometers and C15 ACERT engine. Caterpillar (working with ORNL) will develop and provide components to be evaluated on the engine platform. ORNL engine research staff will evaluate the engine performance with emphasis on combustion diagnostics, optimization and modeling. Materials scientists at ORNL will examine material performance and provide guidance to materials development.

Results

During the 2011 yearly period, the dynamometer controller was programmed for transient operation and infrared thermocouples were utilized to assess exhaust surface temperatures without physical modification to the components, which could affect performance. A photograph showing the engine and dynamometer is shown in Figure 1.



Figure 1. Photograph showing mounted engine and dynamometer. Engine has been instrumented for 2nd Law Analysis.

The industry partner provided ORNL with a series of baseline and prototype exhaust valves. The prototype valves were composed of a high temperature nickel-alloy to evaluate high temperature durability and performance. The Caterpillar C15 ACERT™ engine at ORNL was outfitted with a combination of standard steel valves in cylinders 2, 4, and 6 and experimental nickel-alloy valves in cylinders 1, 3, and 5, as illustrated in Figure 2.

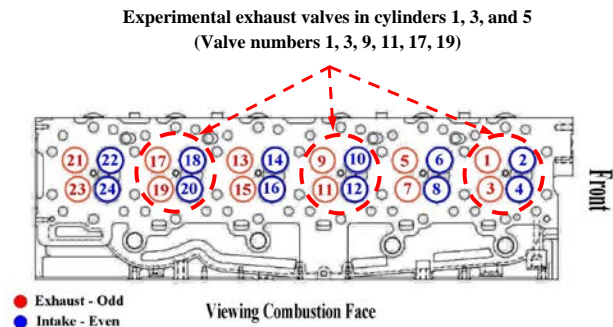


Figure 2. Schematic diagram showing location of baseline and experimental valves.

Caterpillar also provided an aggressive transient test cycle (see Figure 3) and the engine was operated according to this protocol for 200 hours. The valve lash was measured for the initial untested condition and periodically during the course of the 200 hour test period. These results are shown in Table 1 and do not indicate a significant difference in the valve recession for those composed of the nickel-based alloy compared to the standard valves. The valves were removed from the engine for further evaluation by personnel at Caterpillar, Inc. Throughout the

experimental run, the engine performance and efficiency was noted. The results showed no decrease in performance with the new alloys. At the conclusion of the experiments, the valves were removed from the engine and return to the industry partner for metallographic analysis.

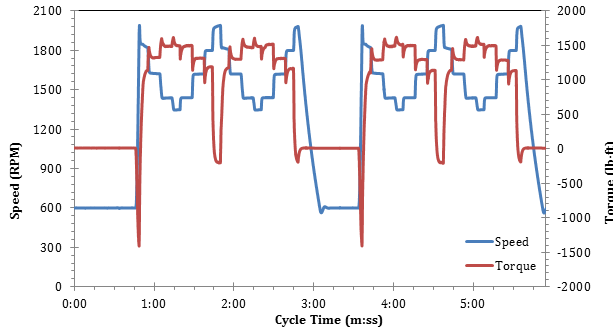


Figure 3. Transient test protocol.

Table 1. Valve lash measurements taken at intervals during the transient test cycle.

Cylinder #	Exhaust Valve Material	Valve #	0 hours	30 hours	50 hours	77 hours	200 hours
1	Ni Alloy	1	0.030	0.028	0.028	0.028	0.028
		3	0.030	0.028	0.028	0.028	0.028
2	Standard	5	0.030	0.028	0.028	0.028	0.028
		7	0.030	0.028	0.028	0.028	0.028
3	Ni Alloy	9	0.030	0.028	0.028	0.028	0.028
		11	0.030	0.028	0.028	0.028	0.028
4	Standard	13	0.030	0.028	0.027	0.027	0.027
		15	0.030	0.028	0.027	0.027	0.027
5	Ni Alloy	17	0.030	0.029	0.028	0.028	0.028
		19	0.030	0.028	0.028	0.028	0.028
6	Standard	21	0.030	0.028	0.027	0.027	0.027
		23	0.030	0.028	0.027	0.027	0.027

Conclusions

The dynamometer controller was successfully modified to enable transient operation and a novel valve alloy material was evaluated under an aggressive test protocol. The experimental valves exhibited excellent performance and are being evaluated for metallography. Future efforts will revolve around testing novel exhaust manifold materials to assess thermal shock resistance.

Agreement 15054 - Fatigue Enhancements by Shock Peening

Principal Investigators: Mark T. Smith and Elizabeth V. Stephens

Energy Materials Group

Pacific Northwest National Laboratory

P.O. Box 999, MS K2-03

Richland, WA 99352

(509) 375-4478; fax: (509) 375-4448; e-mail: mark.smith@pnnl.gov

(509) 375-6836; fax: (509) 375-4448; e-mail: elizabeth.stephens@pnnl.gov

Yong-Ching Chen

Cummins, Inc.

(812) 377-8349; e-mail: yong-ching.c.chen@cummins.com

DOE Technology Manager: Jerry L. Gibbs

(202) 586-1182; fax: (202) 586-1600; e-mail: jerry.gibbs@ee.doe.gov

Field Technical Manager: Dean Paxton

(509) 375-2620; fax: (509) 375-2186; e-mail: dean.paxton@pnnl.gov

Contractor: Pacific Northwest National Laboratory

Contract Number: DE-AC05-76RL01830

Objectives

- Evaluate the capability for surface modification techniques such as laser shock peening (LSP), water jet peening (WJP), and friction stir processing (FSP) to improve the fatigue performance of steel, aluminum, and cast iron engine components.
- Evaluate the fatigue performance impact offered by these surface treatments to induce compressive residual stresses and to modify microstructure in the surface of aluminum, steel, and cast iron engine components.
- Compare fatigue performance and thermal stability of these novel surface treatment approaches to traditional shot peening methods.

Accomplishments

- Completed waterjet peening evaluations of A354-T6 aluminum specimens. Specimens showed a significant improvement in fatigue life in comparison to the control.
- Identified and processed components via WJP for full-scale test evaluations.
- Achieved thermally stable, consolidated 7.5- in. friction stir welds (with the use of cover plates and no preheating) for cast iron.

Future Directions

- Complete development of surface treatment techniques of cast iron material via FSP.
 - Complete LSP and WJP processed components full-scale test evaluations.
 - Complete final Cooperative Research and Development Agreement (CRADA) project reporting.
-
-

Introduction

The primary objective of this project is to evaluate the impact of LSP, WJP, and FSP on the fatigue performance of aluminum, cast iron, and steels. Fatigue performance is an important factor in propulsion materials, especially for fuel system components, cylinder heads and blocks, etc. With the advent of faster injector response and higher pressures for better control of combustion events, cam stresses are significantly increased leading to reduced contact and flexural fatigue life. Cyclic fatigue improvements of forming dies made from tool steels have been achieved by selectively applying compressive residual stresses at the surface. Methods to apply these stresses vary, but among them, LSP has been used successfully. LSP not only induces compressive residual stresses at the surface, improving cyclic fatigue life more than five times, but it also decreases the susceptibility of steels to stress corrosion cracking. However, there are some uncertainties with the application of the LSP process for engine components: 1) knowing exactly where to optimally apply the process based on part starting condition and ultimate performance requirements; 2) the parameters required to effectively improve performance based on failure modes encountered; and 3) the effect of surface finish on the fatigue performance.

For softer metals like aluminum, a lower-energy option that operates similarly to LSP is high-pressure WJP. This process is still in its infancy, but it has shown promise for improving fatigue performance in aluminum castings and wrought products with better control of residual stress distribution. Like that of LSP of high-strength steels, the fatigue life enhancement mechanisms of WJP and optimum processing parameters are not yet well defined. Further understanding of the effects of LSP on aluminum alloys is also needed.

A cost and energy-efficient way of localized processing of metals to improve their fatigue

life and wear resistance is by using FSP. This process is known to increase fatigue life by refining the grain structure and homogenizing the microstructure of the metal, thereby eliminating defects, if any, within the processed area. Porosity is inherent to a cast metal, and its strength is always lower than that of a forged metal. By friction stir processing the area of interest, forged properties can be attained in a cast component and low cost, high-strength castings still can be produced. This is ideal for applications like cylinder heads and engine blocks, where high strength and wear properties are desired in localized areas such as the combustion chamber, bolt hole bosses, etc. This process can deliver high strength in aluminum, cast iron, and steel. Significant challenges exist in understanding the effect of FSP process parameters on mechanical properties of high-temperature materials like steel and cast iron.

This project is a 3-year development and demonstration effort and includes active participation by Cummins, Inc. In October 2007 (fiscal year [FY] 2008), a formal CRADA was established with Cummins, Inc. In FY2011, this project is scheduled to be completed; however, final project reporting and completion will carry over into early FY2012.

Technical Approach

In this research, two approaches are being implemented to meet the objectives and deliverables of the project: Technology Development and Technology Transfer and Commercialization. Technology development includes 1) demonstrating that surface treatments can induce deep subsurface compressive residual stresses in test specimens; 2) characterizing the stress distributions in test specimens, as well as the surface roughness after treatments and comparing results to control specimens; 3) evaluating the mechanical properties of surface-treated bar specimens using rolling contact fatigue and rotating beam fatigue tests methods; 4) performing thermal

stability tests of surface-modified specimens; 5) demonstrating FSP technique for processing of cast iron; and 6) developing a cost model for process deployment. Technology transfer and commercialization includes Cummins demonstrating LSP and WJP surface modification approaches on a full-scale steel and/or aluminum component using engine systems qualification tests; Cummins and Pacific Northwest National Laboratory (PNNL) developing and demonstrating a cost-effective process sequence for LSP/WJP of a relative high-volume production; and Cummins disseminating technology benefits to product design and development groups.

Results and Discussion

Experimental Characterization of A354-T6 Cast Aluminum

In FY2011, characterization continued on the WJP evaluations where waterjet technology was used for peening the A354 cast alloy to enhance its fatigue life. Task 3 consisted of fabricating and processing rotating beam fatigue specimens with parameters determined from Task 2 and completing fatigue tests.

As previously reported in FY2010, the methodologies evaluated consisted of regular round waterjet, fan waterjet (where

air is spread into a flat sheet of high-speed water), and “fuzzy” waterjet (where air is entrained into the waterjet stream). In Task 2, a quadratic model design of experiments (DOE) was applied where the supply pressures, air pressure, stand-off distance, and traverse rate was varied to determine the optimum processing parameters from the promising WJP methodologies described. It was found that waterjet peening can produce surface compressive residual stresses in A354 while maintaining the surface finish. A Pareto analysis of the DOE results showed that the supply pressure and traverse rate were key contributors on the resulting max residual stress and surface roughness observed on the specimens. From these results, two of the waterjet methodologies were pursued for further evaluations.

From the Task 2 results (focusing on the residual stress and surface roughness relationship), three processing conditions were selected for Task 3: WJP methods A, B, and C. Methods A and B consisted of the same peening method with different processing parameters. Table 1 compares the residual stress measurements, along with the surface roughness measurements for each waterjet peening method. Figure 1 provides representative surface images of specimens processed by each peening method.

Table 1. Residual stress measurement and surface roughness measurement results.

WJP Method	Residual Stress at Surface <i>ksi</i>		Max Residual Stress <i>ksi</i>		Depth at Max Stress <i>in. x 10⁻³</i>	Max Depth of Stress Field <i>in. x 10⁻³</i>	Areal Ra <i>microinch</i>
Set A	-32.7	± 0.8	-32.7	± 0.8	0	2.5	34.6
Set B	-36.4	± 0.9	-38.2	± 0.9	0.4	5	69.8
Set C	-34.1	± 0.9	-34.1	± 0.9	0	1	43.2

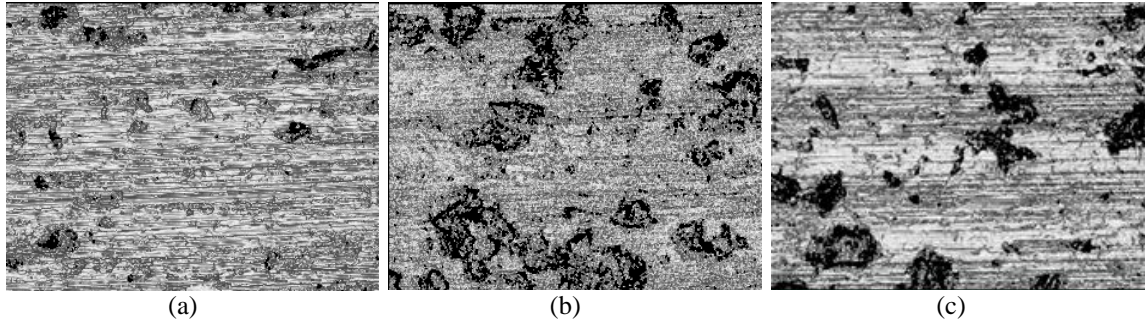


Figure 1. Representative surface image of specimens processed via waterjet peening method Set A (a), Set B (b), and Set C (c).

In Task 3, three sets/populations of rotating beam fatigue specimens were fabricated and processed with the WJP parameters determined from Task 2, Set A, B, and C. No secondary machining was performed. Fatigue tests were completed in FY2011 and the results are plotted in Figure 2. The WJP A354 specimens show significant improvement in fatigue life in comparison to the control even with the variations in resulting surface topography and different depths of residual stress. All three waterjet

peening conditions resulted in a 40–50% increase in the stress amplitude 10^7 cycles in comparison to the control. Figure 3 is a representative fracture image of specimens that endured 10^7 cycles or more. Although the fatigue initiation site for several specimens, regardless of peening method, occurred beneath the surface, many fatigue initiation sites could not be identified due to excessive oxide formation on the surface.

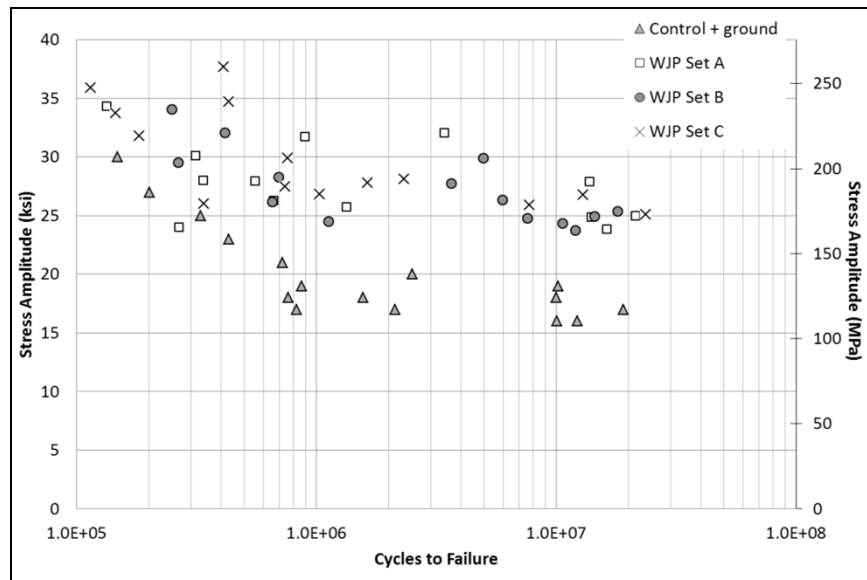


Figure 2. Comparison of the rotating beam fatigue tests results of the WJP specimens and control.

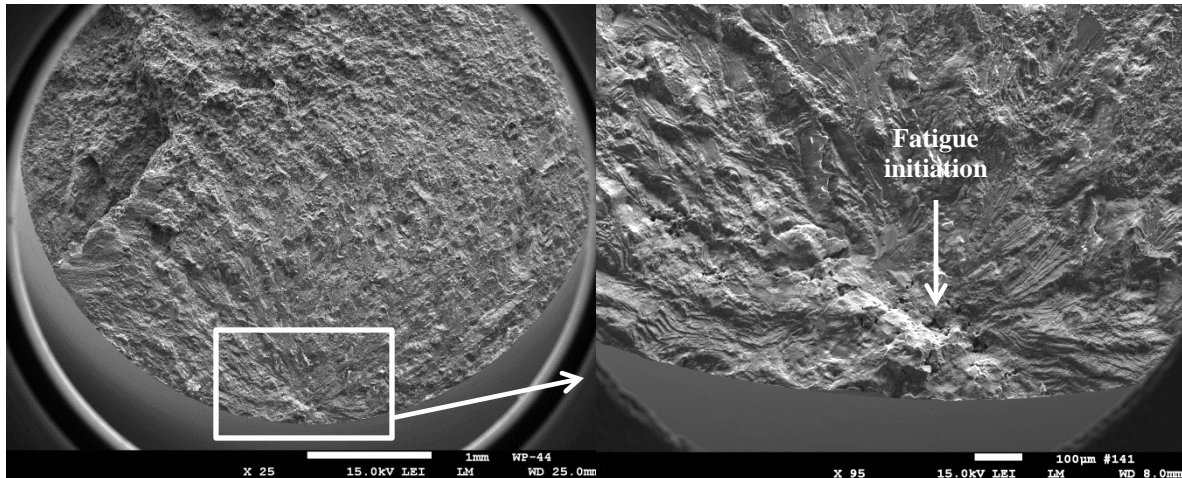


Figure 3. Fracture surface image of a fatigue specimen processed via WJP Set C where the fatigue initiation site occurred beneath the surface.

Promising fatigue results prompted Cummins, Inc. to process components via WJP for further evaluations. Component testing in a test cell to evaluate fatigue life of components are currently being pursued with Cummins Turbo Technology.

Friction Stir Processing Development of Cast Iron

The overall goal of the development is to demonstrate enhancements achieved by FSP for Grade 40 cast iron. This is a collaborative effort between Cummins Inc., South Dakota School of Mines and Technology (SDSMT), and PNNL. Previously, work focused on evaluating challenges of FSP/welding cast iron and investigating potential solutions to overcome these challenges (i.e., preheating, use of cover plates, cover plate thickness, etc.). Last year, we were able to achieve plasticization of the material with the use of cover plates (304L stainless steel, 1018 steel, and copper) to aid in the development of FSP for cast iron without preheating the material and to either prevent the extrusion of cast iron material or nugget pull-out during friction stir welding. Figure 4 shows a cross-section of a consolidated joint between the cast iron and the 304L shim/copper cover plate. No

gross defects were observed, but realignment of the graphite flakes was observed between the copper and cast iron on both the advancing side and retreating side of the weld nugget. In addition, the weld was only a 1-in. translation.

In FY 2011, emphasis was placed on translation of the tool and processing parameter development. Evaluations were performed where processing parameters varied from 0.5 to 1 inch per minute and 1000 to 1200 rotations per minute at force control loads of 3300 and 5000 lbs. Applying the same processing parameters to longer weld translations did not achieve the same results as observed in shorter, 1-in. weld translations. Thermally stable welds were still achieved with different processing parameters. Figure 5 is an image of a 7.5-in. weld translation.

Tensile specimens were prepared from the welds that yielded longitudinal tensile strengths of ~33 ksi with 1.3% elongation. However, the welds had no strength in the transverse direction. In addition, graphite alignment was still observed in the cross-sections, and may have attributed to the low strengths observed.

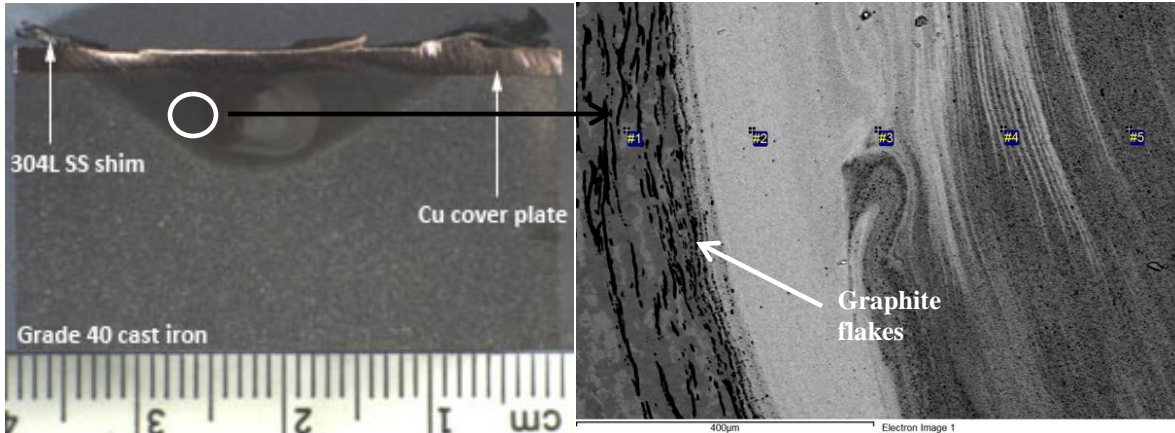


Figure 4. Cross-section of the copper cover plate on cast iron showing a consolidated joint. The micrograph illustrates alignment of graphite flakes at the weld nugget interface.

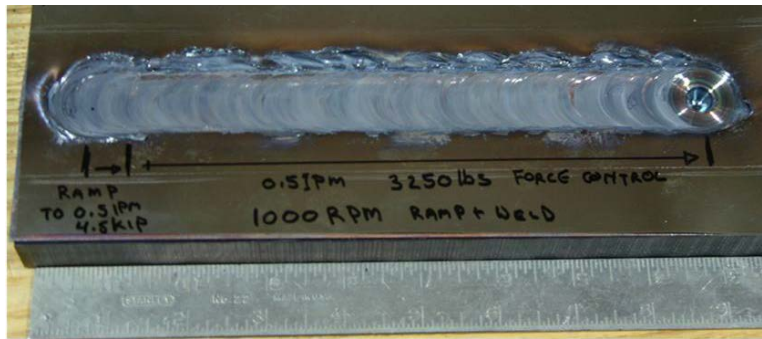


Figure 5. Image of a 7.5-in. weld translation of cast iron.

The presence of graphite is inherent to the cast iron parent material, so research progressed to determine means to minimize graphite alignment to increase weld strengths. SDSMT began evaluating changes in pin-tool material from a polycrystalline cubic boron nitride to W-Re tool and tool design. Promising results were observed where the graphite alignment was minimized, strengths increased, and welds were repeatable. Further valuations are currently ongoing.

Conclusions

During this reporting period, the following conclusions were reached:

- WJP cast aluminum alloy A354 specimens showed a significant improvement in fatigue life in comparison to the control.

- Cummins, Inc. identified and processed components via WJP for full-scale test evaluations.
- Thermally stable, consolidated friction stir welds (with the use of cover plates and no preheating) can be achieved for cast iron.

Presentations/Publications/Patents

Cummins Internal Project Review, December 2010.

DOE Hydrogen Program and Vehicle Technologies Program Annual Merit Review, May 2011.

Waterjet Technology Association Conference and Expo, September 2011.

Acronyms

CRADA: Cooperative Research and
Development Agreement
DOE: Design of Experiments
FSP: friction stir processing
Ksi: kilo-pound-force per square inch
LSP: laser shock peening
MPa: megapascal
PNNL: Pacific Northwest National
Laboratory
WJP: water jet peening

Agreement 15055 – Tailored Materials for High Efficiency CIDI Engines (Caterpillar CRADA)

Principal Investigator: Glenn J. Grant

Energy Materials

Pacific Northwest National Laboratory

902 Battelle Blvd., K2-03

Richland, Washington 99356

(509) 375-6890; fax: (509) 375-4448; e-mail: glenn.grant@pnl.gov

Nate Phillips

T&SD AMT–High Temp Materials

M. Brad Beardsley

Technology Leader-Surface Engineering

Caterpillar, Inc.

Technical Center Bldg. C-13, PO Box 1875

Peoria, Illinois 61656-1875

(309) 578-5788; cell: (309) 361-8309; e-mail: Phillips_Nate@cat.com

DOE Technology Manager: Jerry L. Gibbs

(202) 586-1182; fax: (202) 586-1600; e-mail: Jerry.gibbs@ee.doe.gov

Field Technical Manager: Dean Paxton

(509) 375-2620; fax (509) 375-2186; e-mail: dean.paxton@pnl.gov

Contractor: Pacific Northwest National Laboratory

Contract No.: DE-AC05-76RL01830

Objective

- To develop friction stir processing (FSP) to tailor the properties of conventional, low-cost engine materials (cast iron, alloy steels, and aluminum alloys) with the goal of increasing their high-temperature performance, durability, and thermal properties.
- To deploy FSP components that can enable energy-efficient combustion strategies, especially those that will require higher peak combustion pressure or higher temperature operation.

Approach Including Partner/Collaborator and Path to Technology Transfer and Commercialization

- The overall approach is to develop surface modification techniques, modified materials, and components. The project is a Cooperative Research and Development Agreement (CRADA) with Caterpillar, Inc., but also involves input from piston suppliers for diesel engines.
- The project is primarily investigating FSP, a new technology that can produce functionally graded surfaces with unique and tailored properties that will allow propulsion materials to withstand higher temperatures and pressures without appreciably losing strength, hot hardness, or wear resistance, and exhibit improved resistance to thermal fatigue.
- FSP-treated components will be evaluated and tested by the industry collaborators to demonstrate efficiency benefits and potential commercial applications.

Milestones, Metrics and Accomplishments

- **Milestone:** Demonstrate property improvements from FSP that can reach the following metrics established by the project team: minimum twofold improvement in fatigue life, significant reduction in thermal fatigue crack initiation and growth rate, and 20% improvement in average failure stress level at N cycles. (Completed)
 - FSP was found to produce significant improvement in fatigue performance when compared to as-cast aluminum alloy 356. Depending on the stress ratio and the stress level, the FSP-processed materials showed from 5–15 times improvement in fatigue life over as-cast material. In addition, FSP-processed materials showed up to 80% improvement in fatigue strength across a wide range of maximum stress levels.
- FSP also was used to modify the surface of an aluminum alloy analog to a production piston alloy. Tooling was developed, and process parameters were explored that allow for processed regions showing very fine-grained, homogeneous microstructure.
- FSP was used to physically “stir-in” multi-wall carbon nanotubes and several different carbon nanofiber compositions into aluminum surfaces to a depth of 5.8 mm.
- **Milestone:** Demonstrate consolidated FSP regions in a ferrous piston alloy, and establish process window to successfully stir particulate into the surface of steel.
- The tooling and process parameter space for accomplishing thick section (up to 13-mm thick) FSP of steel materials was investigated. Fully consolidated process zones were demonstrated, but tool survivability must be improved.
- **Milestone:** Demonstrate a FSP zone in a circular configuration appropriate to a piston bowl rim modification in an aluminum piston alloy. (Completed)
- **Milestone (September 2011):** Complete final report and transfer data on process and properties of FSP materials to industrial partners. (Completed)

Introduction

The overall goal of the project is to enable the implementation of new combustion strategies, such as homogeneous charge compression ignition (HCCI), that have the opportunity to significantly increase the energy efficiency of current diesel engines and decrease fuel consumption and environmental emissions. These strategies, however, are increasing demands on conventional engine materials, either from increases in peak cylinder pressure (PCP) or from increases in the temperature of operation. The specific objective of this project is to investigate the application of a new material processing technology, FSP, to improve the thermal and mechanical properties of engine components. The concept is to modify the surface of conventional, low-cost engine materials. The approach is to produce components with functionally graded surfaces that are optimized for thermal properties and better in-service performance without suffering the cost penalty of using exotic or expensive materials. Low-cost, higher-performance materials will allow new combustion strategies to be implemented that can improve energy efficiency. This project is a CRADA in partnership with Caterpillar, Inc.

Background

Almost since the inception of internal combustion engines, there has been a steady rise in specific power (SP) output, or the power per liter of engine displacement. Specific power is correlated with efficiency and is the combined effect of better optimization of combustion, fuels, engine materials and design, reduction in parasitic losses, and improved heat management. Figure 1 shows that from 1970 to 2001, there has been a steady increase in SP. After 2001, the SP levels dropped due to emission and after-treatment devices and controls mandated by federal legislation (primarily increased exhaust gas recirculation rates and particulate filters). The drop in SP from 2001 to about 2003 would have been even greater were it not for significant advances in engine management, computer control, higher injection pressures, etc., made during this period to compensate for the power losses. However, around 2003, a different restriction on the optimization of the combustion process was beginning to force diminishing returns. The restriction is illustrated in Figure 1 as the plot of the PCP. As the peak pressure increases, more work can be done by the piston as it is forced downward in the bore, resulting in a higher SP.

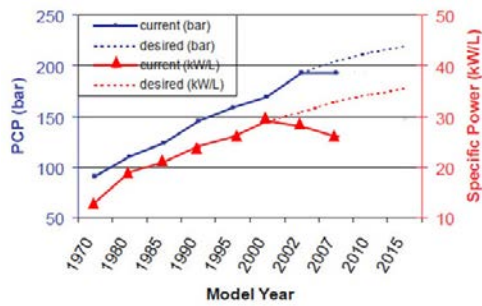


Figure 1. Plot showing the increase in SP and PCP for typical heavy-duty diesel engines over the last 38 years. (Figure modified from the Southwest Research Institute website at <http://www.swri.org/>.)

Since 2003, PCP has leveled at around 190 bar to 200 bar because above this level, conventional engine materials in pistons, cylinder liners, and cylinder heads will be beyond strength and fatigue limits.¹ To further increase efficiency, either unconventional, expensive materials (i.e., nickel alloys, titanium, compacted graphite iron, nodular iron, or micro-alloyed steels) must be used or conventional materials must be modified in a way that increases their durability. New energy-efficient combustion strategies, especially HCCI, will increase PCP potentially above 220 bar. Accordingly, materials must be improved to enable this process.

One of the major challenges for conventional materials under increasing peak pressure environments is resistance to thermal fatigue failure. Pistons and cylinder heads are particularly vulnerable to this failure mode because of the cyclic nature of the loading and temperature changes in the combustion chamber.

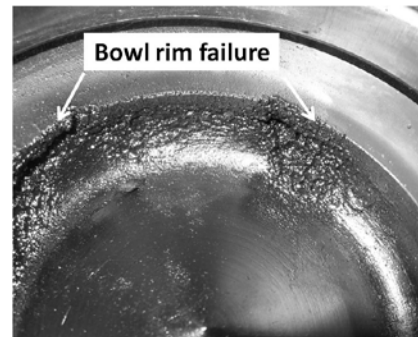
Figure 2 shows failures of pistons in the bowl rim area when subjected to high PCP over time.



a)



b)



c)

Figure 2. a) Piston in bore; b) cracks on inside edges of bowl rim; and c) bowl rim failure

Rather than substitute a potentially high-cost, high-temperature, monolithic material, one low-cost strategy to enable higher PCP involves using techniques to improve the thermal fatigue performance of current materials. In the case of thermal fatigue in the bowl rim area, the technique need only be applied to the narrow area around the bowl rim itself because failures of this area drive the overall material selection.

FSP is a new technology that can be used to create engineered regions on selective areas of a part. In

¹ Figure 1 represents data primarily from medium-duty to heavy-duty diesel engines. Production automotive diesel engines (light duty, high speed) now achieve SP levels up to 75kW/L in turbocharged and intercooled configurations.

recent years, Pacific Northwest National Laboratory has developed techniques and tools that allow FSP to be accomplished in steel, cast iron, and aluminum.

FSP is an outgrowth of friction stir welding (FSW), which was invented 18 years ago by TWI, Ltd. (Figure 3). The same techniques and processes used to make a friction stir weld could be used to process a material for enhanced properties. The process can be selectively applied to the surface of a material, and it alters the microstructure by the severe plastic deformation that occurs in the processed zone. FSP can create a robust and graded structure with fundamentally different properties than the underlying surface, and it has been shown to produce surface regions with improved fatigue life, ductility, and strength.

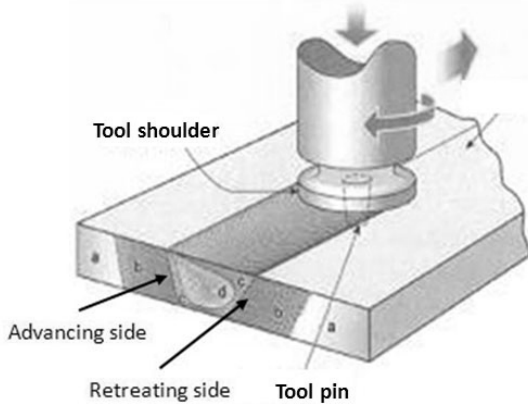


Figure 3. FSP illustration (top) and typical friction stir tools

FSP produces a surface modified region that is different from a coating. Commonly, surface treatments designed to enhance wear or thermal performance include various coating methods or

fusion-welded hard facings. Most of these processes are liquid state and often involve detrimental temperature effects on the base material. Heat-affected zones in the base metal and various deleterious high-temperature reactions can create a coated part with less-than-desirable properties.

In addition, traditional thin coatings can suffer from issues involving the nature of the interface between the coating and the base material (spalling, debonding, and cracking on the interface), especially under high-stress, gouging wear conditions or under cyclic-thermal conditions where coefficient of thermal expansion (CTE) mismatch is an issue. Also, failure of a coating under high-loading conditions can occur when the substrate below a thin, hard coating fails by plastic deformation. Regions treated with FSP can be significantly more robust than traditional coatings for two reasons: 1) FSP produces a modified region that transitions to the base material without a sharp interface (Figure 4), and 2) the modified region is generally thicker and the transition region wider than traditional coating because the plasticized region depth is related to the tool geometry—specifically the depth and size of the pin.

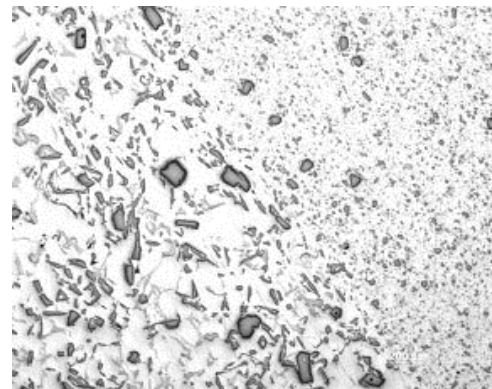


Figure 4. Micrograph of the edge of a stirred zone showing particle refinement in the processed region. (FSP can close porosity in castings and decrease both size and aspect ratio of particles, thus producing better fatigue performance.)

It also is possible to use FSP to “stir” insoluble particles from the surface into the substrate to depths limited only by the FSP tool geometry (Figure 5). This engineered metal matrix

composite layer can create unique surface properties, including increased hardness, wear resistance, and thermal characteristics. To date, the addition of up to 20% ceramic to aluminum has been demonstrated and approximately 10% addition to steel has been achieved.

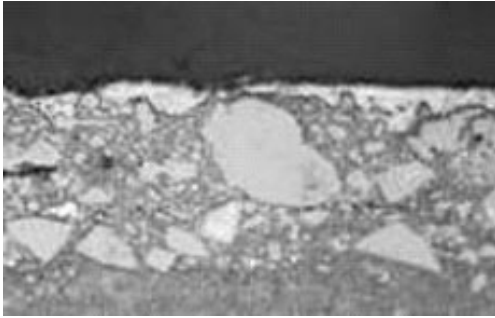


Figure 5. Ceramic particulate also can be stirred into the surface to produce functionally graded surfaces and near-surface metal matrix composites.

FSP can be used to alter the original microstructure, create surface composites and new alloys, and has the potential to produce selective areas of improved material performance. This project will investigate several opportunities for FSP to improve engine materials to enable increases in engine efficiency.

Approach

This objective of this project is to experimentally develop the FSP processes and technologies required to engineer the surface of propulsion materials for improved properties. The application focus is to tailor the mechanical properties and thermal conductivity of engine materials, both ferrous and nonferrous materials, by using FSP techniques. This microstructural modification is expected to lead to a set of materials with enhanced surface properties that can handle increased combustion pressure and exhaust temperatures, resulting in improved engine efficiency.

The project scope will involve developing the FSP manufacturing parameters, and selecting and evaluating proper tool materials and techniques to produce defect-free FSP regions. Coupon-level testing and evaluation of the thermal and mechanical properties will be conducted. These

efforts will focus on specific performance targets identified by project partners. If performance metrics are met for sample materials enhanced by FSP, additional research will include developing and demonstrating the appropriate method to apply this process to two-dimensional and three-dimensional geometry. If successfully developed, this class of engineered materials can significantly impact the efficiency and durability of compression ignition direct injection (CIDI) and potentially address some of the technical barriers to implementing HCCI engines.

In 2010, the primary focus of project work was on FSP of aluminum piston materials used for light-duty and medium-duty CIDI engines. The work is intended to improve the thermal fatigue performance of typical piston alloys to allow them to be used in higher peak-stress environments without suffering premature bowl rim failure. This concept is illustrated in Figure 6. If FSP were applied to the area of a piston blank (prior to final machining) that will be the bowl rim area, then, after final machining, the bowl rim will be composed entirely of fine-grained FSP “nugget” material that will possess improved fatigue performance. Adjacent areas of the piston will remain unmodified.

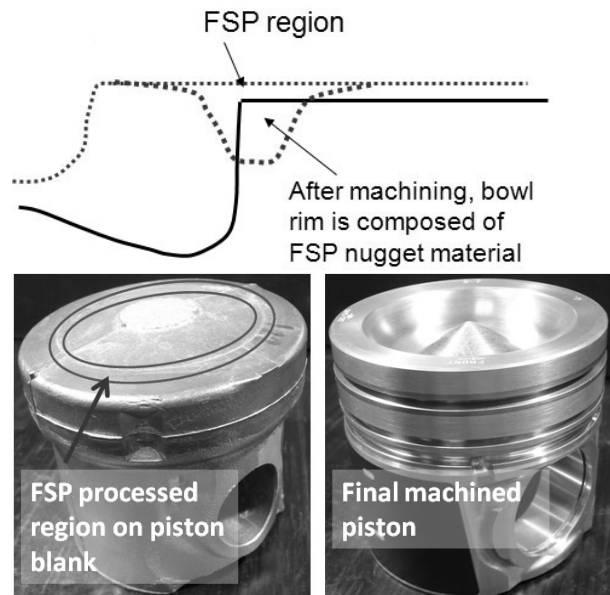


Figure 6. Cast piston blank. (The area in the bowl rim after machining will be FSP for improved microstructure.)

The project approach is to first develop the techniques (i.e., process parameters, friction stir tools, and methods) needed to create robust process zones, then physically perform the FSP process on full-sized piston blanks, machine them to shape, and test them in actual operating conditions on test cell engine dynamometers or single-cylinder test engines.

Results

During fiscal year (FY) 2010 and FY2011, the project focused primarily on FSP in aluminum materials that are compositional analogs to the typical piston and head alloys seen in small- to mid-sized CIDI engines. Investigations focused primarily on the following two areas: 1) FSP of cast hypo-eutectic aluminum (Alloy 356/357) with no introduction of any new component materials (with a demonstration of a circular processed zone for a prototype piston top) and 2) FSP of aluminum alloys involving physically “stirring-in” various quantities of carbon nanotubes, nanofibers, and large-scale carbon fiber ribbons. Summary discussions of the two investigations follow.

FSP of Alloy 357:

FSP significantly refines microstructure, closes casting porosity, and reduces the aspect ratio of the Si particles in cast Al-Si alloys. These three features produce a dramatic improvement in fatigue life. Figure 7 shows the S/N curves for both tensile and bending fatigue performance comparing the as-cast to the FSP-processed material. A 90% improvement in maximum tensile stress at the fatigue limit and improvements in bending fatigue lifetime up to an order of magnitude can be shown for this alloy.

In current applications of these alloys, especially for pistons and cylinder heads, fatigue (particularly thermal fatigue) is the primary limiting condition on part life. As CIDI engines evolve to lean-burn technologies and potentially more HCCI-like conditions (i.e., maximum stress in bowl rim edges, ring landings, bridge areas between valves, etc.), much higher stress levels than current designs will exist. The improvements offered by selective FSP of these regions may enable these energy-efficient combustion strategies.

Work during FY 2010/2011 demonstrated the techniques necessary for the practical application of FSP by demonstrating a circular “two-dimensional” processed region on a simulated piston top. Figure 8a shows the circular weld region and Figure 8b shows the machined final piston top with the processed region on the bowl rim.

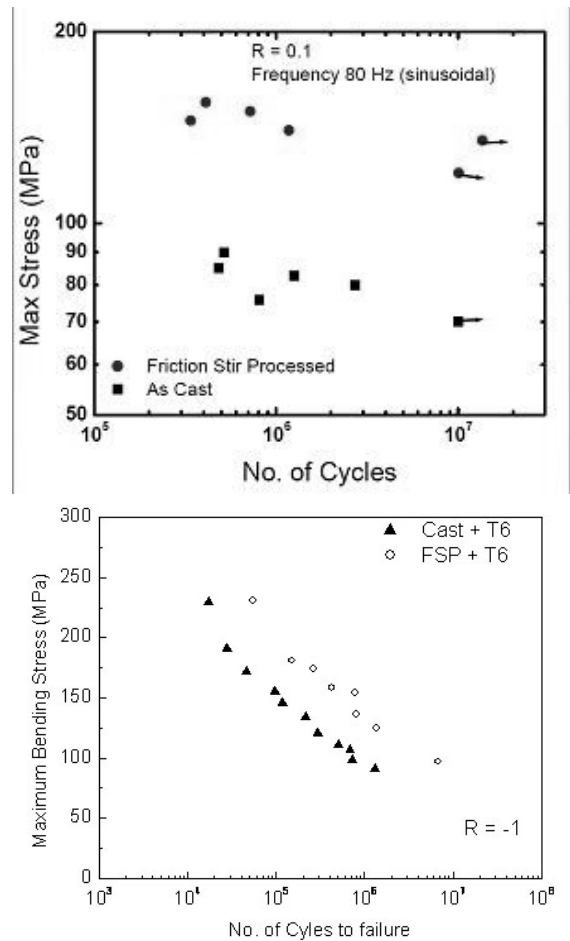


Figure 7. S-N curve for tensile loading (top) at R=0.1 (showing as-cast 356 versus FSP-processed 356) and S-N curve for bending (bottom) at R=-1 (showing as-cast 357 versus FSP-processed 357 [1, 2, 3]).

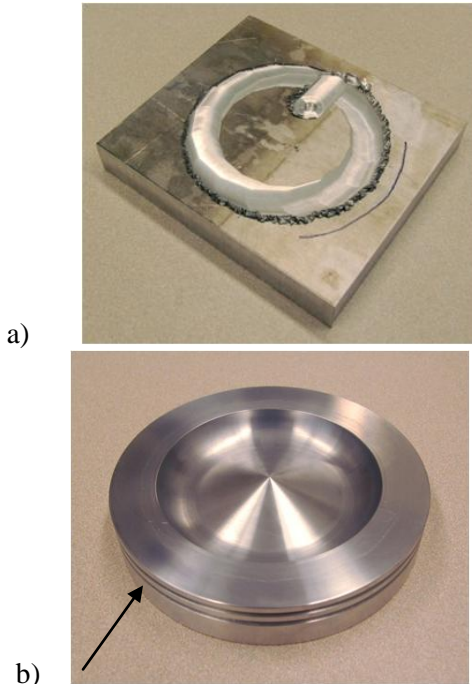


Figure 8. a) Circular process region created by “welding” in a counterclockwise direction then turning to center and exiting where the piston bowl will be located. b) The arrow points toward a faint line demarking the edge of the FSP processed zone on the bowl rim after machining. The processed region is fully consolidated and composed of material with a highly refined microstructure to resist thermal fatigue cracking.

FSP—“Stirring-in” Carbon Nanotubes and Nanofibers:

The primary failure at high PCP in service is fatigue and thermal fatigue at several locations on the piston and head. The goal is to use FSP to improve the microstructural and mechanical properties that most influence thermal fatigue (i.e., CTE, conductivity, and to a lesser extent, high temperature strength). Primarily, the goal is to reduce CTE and increase conductivity. Table 1 shows candidate materials that could be stirred into the base metal to selectively modify mechanical properties.

Table 1. Potential additions to the base material

Material	Modulus	CTE	Conductivity
Aluminum	80 GPa	25 $\mu\text{m}/\text{m}^\circ\text{C}$	180 W/m-K
SiC	410 GPa	4.4 $\mu\text{m}/\text{m}^\circ\text{C}$	150 W/m-K
Al ₂ O ₃	370 GPa	8.5 $\mu\text{m}/\text{m}^\circ\text{C}$	13 W/m-K
Carbon Nanotubes	>600 GPa	Low or Can be negative !	> 1000 W/m-K

Of these, carbon nanotubes and fibers offer the best potential to improve thermal fatigue because of their very low CTE and high conductivity. The bulk of the experimental effort in FY2010 and FY2011 was devoted to developing the methods, procedures, FSP tools, and process parameters needed to create processed regions with even distributions of particulate. This work continues efforts undertaken in FY 2009 to find the best methods of stirring in particulate into the aluminum substrate while producing the most homogeneous and highest particulate loading possible.

During FY 2010/FY 2011, two different carbon fibers, polyacrylonitrile (PAN) and graphite (GRPH), were used as reinforcements added into 6061 aluminum plates by FSP. Two different carbon fibers were chosen to study their effect on the thermal conductivity and the mechanical properties of the processed region. In general, graphite fibers show significantly higher conductivity values compared to PAN fibers. However, PAN fibers are known for their better mechanical properties. The carbon fibers were added into the 6061 aluminum matrix by first cutting a number of grooves (1.0-in. long, 0.25-in. wide, and 0.20-in. deep) along the length of the aluminum plate, with a 0.10-in. spacing between adjacent grooves. This is shown schematically in Figure 9. After filling the grooves with continuous 1-in.-long carbon fiber woven strips, metal plugs made of 6061 aluminum were press fitted into these grooves. Finally, the aluminum plate was subjected to FSP along the length of the grooves. Because the grooves were wider than the friction stir tool pin diameter; multiple passes were employed to create the processed zone. The aluminum plate was finally cross-sectioned perpendicular to the FSP run direction to study the

distribution of the carbon fibers inside the process zone.

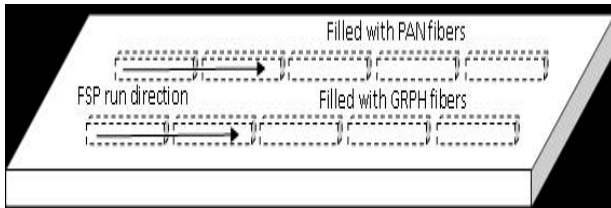


Figure 9. Schematic drawing of the technique used for reinforcing aluminum plate with carbon fiber

Cross-section images of both the PAN-filled and GRPH-filled grooves indicated the presence of large cavities inside the processed region. Figures 10a and 10b show typical examples of PAN and GRPH fiber-filled processed regions, respectively. Cavities marked by arrows are visible on both the images.

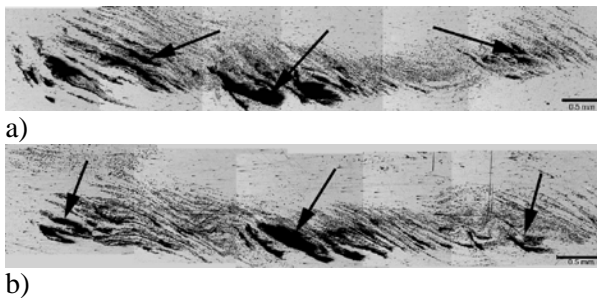


Figure 10. Cross-section images of the process region: a) PAN-filled and b) GRPH-filled.

Because the initial trials left large cavities, some regions were reprocessed to fill those cavities. This was done by positioning the friction stir tool pin in the center of those cavities and then running it along the entire length of the aluminum plate. Figures 11a and 11b show cross-section images obtained from two separate locations along the PAN-filled reprocessed region. It is evident from both images that the reprocessing technique led to a significant reduction of cavities inside the processed zone. However, as shown by the arrow in Figure 11b, some porosity still remained even after the reprocessing runs. Moreover, after comparing Figures 11a and 11b, it is noted that there is variability in carbon fiber distribution inside the process region along the length of the aluminum plate.

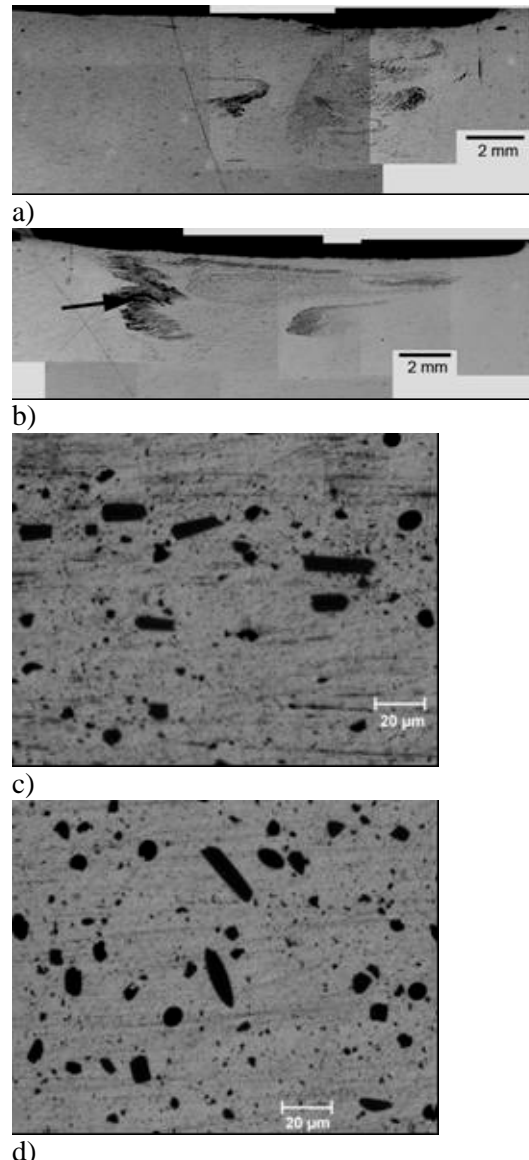


Figure 11. Cross-section images from the PAN-filled process zone. a, b) Low-magnification overview of the process zone at two locations. c, d) Morphology of the individual carbon fibers after FSP.

Higher magnification images from the reprocessed region showed that, in fine detail, the carbon fibers were broken and distributed in the aluminum matrix (Figures 11c and 11d). The FSP process was able to chop the continuous carbon fibers into smaller sections. FSP resulted in random orientation of the carbon fibers inside the process zone. The size of most of the carbon fibers was found to be ~10 μm, although a small fraction of carbon fiber fragments were noted to have significantly smaller or larger sizes than average.

Chopping of carbon fibers inside the process zone was confirmed by scanning electron microscope (SEM) images as well.

To determine the effects of carbon-fiber reinforcements on the mechanical properties of the 6061 aluminum plate, hardness profile maps were generated. A hardness profile map of a PAN-filled reprocessed section showed considerable softening of the aluminum matrix. The 6061 aluminum is a heat-treatable alloy; therefore, significant softening of the matrix occurred during FSP because of the associated multiple heating events. To eliminate the softening effects from repeated heating and cooling during FSP on the 6061 aluminum matrix, sections from both the PAN-filled and the GRPH-filled reprocessed material were given a T6 heat treatment. Hardness profile maps were then determined on the T6 temper sections. Figures 12a and 12b show a hardness profile map and a macrograph of the profiled area from a PAN-filled cross section after T6 treatment, respectively. The hardness profile map has been superimposed on the macrograph for a better understanding of the effects of carbon fiber on hardness. Significant strengthening of the aluminum matrix after the T6 treatment is evident from the hardness profile plot. However, areas of the cross-section that were carbon-fiber rich showed a lower hardness compared to the rest of the aluminum matrix. Because the average size of the chopped carbon fibers was $\sim 10\ \mu\text{m}$, significant strengthening of the aluminum matrix is not expected from their presence. We speculate that the lower hardness in the carbon-fiber-rich areas may be the result of the presence of subsurface porosity in and around the carbon-fiber-rich areas. Similar results were obtained for GRPH-filled sections as well.

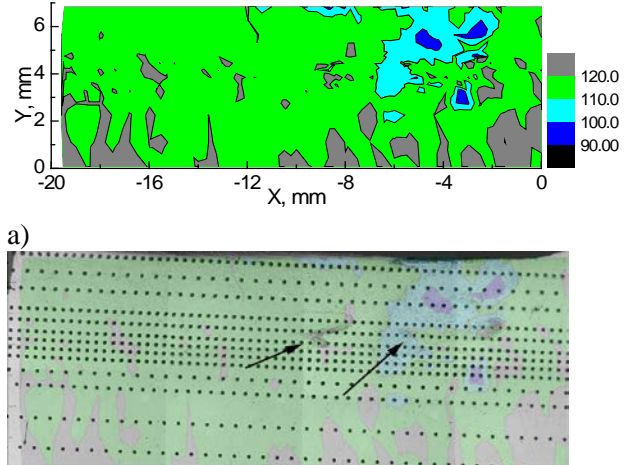


Figure 12. a) Hardness profile plot for T6-treated PAN-filled section. b) Macrograph of the profiled section. Hardness map has been superimposed. Arrows indicate carbon-fiber-rich locations. Incorporation of PAN carbon fiber did not result in any appreciable matrix strengthening.

Samples from the process zone also were tested for thermal conductivity. For the thermal conductivity test, three aluminum samples from parent metal, seven PAN-filled samples, and seven GRPH-filled samples were tested. Thermal diffusivity was determined first from room temperature to 400°C using a laser flash technique specified in ASTM E1461, "Standard Test Method for Thermal Diffusivity by the Flash Method." Bulk density of the samples was then determined from the sample's geometry and mass. Finally, specific heat, C_p , was measured using differential scanning calorimetry. Thermal conductivity values were calculated as a product of these quantities (i.e., conductivity = diffusivity \times C_p \times density). The average bulk density of the various samples used in this study is summarized in Table 2. Bulk density of both the PAN and GRPH samples are less than the parent. Moreover, scatter in the density data is also high. Since, bulk density of the carbon fiber (2.25 g/cc) is less than that of Al (2.69 g/cc); both the PAN and GRPH filled samples should be lighter. A simple rule of mixture calculation indicates around 20% volume fraction incorporation in the carbon fiber reinforced samples. However, the microstructural analysis did not show any signs of such a high volume fraction of carbon fibers in the Al matrix. Presence of micro-porosity around carbon-fiber-

rich areas inside the process zone might be the other significant reason for the lower density of PAN or GRPH samples. Figure 13a shows the average measured thermal diffusivity data as a function of temperature. Thermal diffusivities for both the PAN and the GRPH samples are found to be considerably lower than the parent. Moreover, the scatter in the data for PAN or GRPH samples is quite high. Calculated thermal conductivity values as a function of temperature are shown in Figure 13b.

Table 2. Bulk density (g/cc) of samples in this study

Parent Aluminum	PAN-Filled Samples	GRPH-Filled Samples
2.69 ± 0.003	2.60 ± 0.008	2.61 ± 0.026

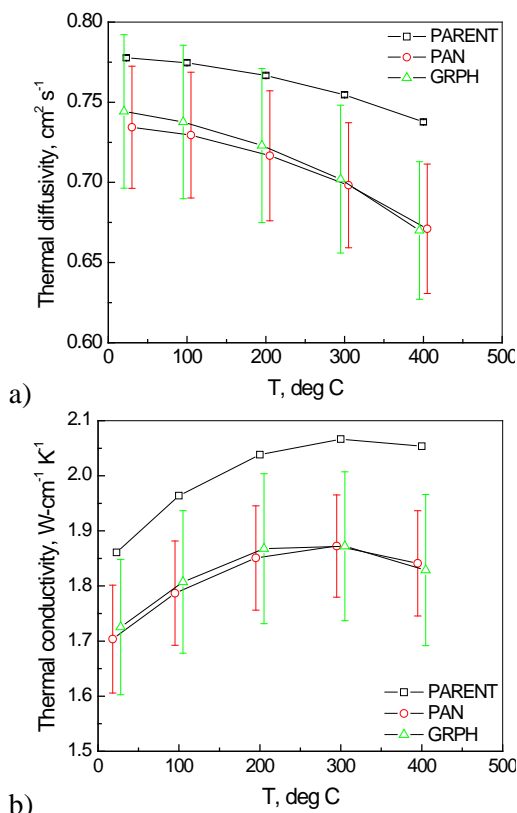


Figure 13. a) Thermal diffusivity vs. temperature, and b) thermal conductivity vs. temperature

Since, thermal conductivity is a product of thermal diffusivity, specific heat, and density, the lower density of C-fiber added samples show comparatively lower thermal conductivity than the parent samples. The presence of micro-porosity or gap at the C-fiber/Al matrix interface might have

played a critical role in keeping the thermal diffusivity value low.

The drop in thermal conductivity may have a beneficial aspect too because a lower thermal conductivity means a reduced thermal loss through piston tops and more retained heat in the combustion chamber to do work. However, the effect of increased temperature as a result of lower thermal conductivity on the mechanical performance of piston material is not understood at this moment, especially in the presence of C-fibers. Further work is necessary to understand this effect.

Summary of Carbon Fiber Work:

- Carbon-fiber reinforcement of the aluminum matrix is possible by the current FSP technique. However, two major problems associated with the current technique are porosity around the carbon fibers and non-uniform distribution of chopped carbon fibers inside the process zone. It is possible that the size of the grooves used in this study may be too large to be closed effectively. Use of smaller grooves or a different/larger friction stir tool may lead to better carbon-fiber distribution.
- Use of carbon fiber as a reinforcement did not result in hardness enhancement of the matrix. This is an expected result, given the size of the chopped carbon fibers. However, lower hardness in carbon-fiber-rich areas may indicate the presence of porosity. It is highly possible that the “true” effect of carbon fibers on hardness might have been masked by porosity.
- Finally, incorporation of carbon fibers led to an overall decrease in density and thermal conductivity. The second feature, the decrease in thermal conductivity, is a surprising result due to the very high thermal conductivities of the graphitic materials. This may be attributed to the potential lack of good bonded interfaces between the aluminum and the carbon fiber, and the presence of microporosity near the fiber particles.

Conclusions

The goal of this project is to develop FSP components that can enable energy-efficient combustion strategies, especially strategies that will require higher PCP or higher temperature operation. FSP produces selected, graded structures that have shown increased strength and durability in fatigue. Surface modification through FSP may address some emerging material problems seen in very high combustion pressure systems such as HCCI engines. In addition, the process enables the incorporation of particulate into the surface, potentially selectively modifying the properties of materials to alter the thermal environment for increased thermal efficiency.

Experimental work to date on aluminum systems has shown significant increases in fatigue lifetime and stress-level performance in aluminum-silicon alloys using friction processing alone, but work to demonstrate the addition of carbon nanotubes and fibers into aluminum substrates has shown mixed results due primarily to the difficulty in achieving porosity-free, homogeneous distributions of the particulate.

The project overall has demonstrated property improvements that are available from this unique and new surface modification technology, Friction Stir Processing. Functionally graded materials can be anticipated through this solid-state process that cannot be fabricated any other way. This project developed a set of tools and techniques that can be passed to designers who require materials that will operate at every increasing stresses and temperatures where part durability is the primary barrier to increased engine efficiency.

Presentations/Publications/Patents

- 1) Jana S, RS Mishra, JB Baumann, and G Grant. 2009. "Effect of Stress Ratio on the Fatigue Behavior of a Friction Stir Processed Cast Al-Si-Mg Alloy." *Scripta Materialia* 61(10):992-995.
- 2) Jana S, RS Mishra, JB Baumann, and G Grant. 2009. "Effect of Friction Stir Processing on Fatigue Behavior of an Investment Cast Al-7Si-0.6 Mg Alloy." *Acta Materialia* 58(3):989-1003.
- 3) Jana S, RS Mishra, JB Baumann, and GJ Grant. 2010. "Effect of Friction Stir Processing on Microstructure and Tensile Properties of an Investment Cast Al-7Si-0.6Mg Alloy." *Metallurgical and Materials Transactions. A, Physical Metallurgy and Materials Science* 41A (10):2507-2521.

Acronyms

CIDI: compression ignition direct injection
 CRADA: Cooperative Research and Development Agreement
 CTE: coefficient of thermal expansion
 FSP: friction stir processing
 FSW: friction stir welding
 FY: fiscal year
 GRPH: graphite
 HCCI: homogeneous charge compression ignition
 PAN: polyacrylonitrile
 PCP: peak cylinder pressure

Agreement 16303 – Materials for High Pressure Fuel Injection Systems

Peter J. Blau*, Amit Shyam*, and Nan Yang[#]

*Oak Ridge National Laboratory, P. O. Box 2008, Mail Stop 606, Oak Ridge, TN 37831-6063
(865) 574-5377; fax: (865) 574-4913; e-mail: blaupj@ornl.gov

[#] Caterpillar Inc., Technical Center Bldg. E-854, P.O. Box 1875, Peoria, IL 61656-1875

DOE Technology Manager: Jerry L. Gibbs

(202) 586-1182; fax: (202) 586-1600; e-mail: Jerry.gibbs@ee.doe.gov

ORNL Technical Advisor: David P. Stinton

(865) 865-574-4556; fax: (865) 241-0112; e-mail: stintondp@ornl.gov

Contractor: Oak Ridge National Laboratory, Oak Ridge, TN
Prime DOE Contract Number DE-AC05-00OR22725

Objectives

- To determine, through residual stress measurements and notched fatigue crack growth studies, whether current heat-treated alloy steels will function well in high pressure fuel injector nozzles in the next-generation of energy-efficient, low-emissions diesel engines.
- To investigate the feasibility of using state-of-the-art x-ray and neutron methods to resolve residual stress gradients in the tips of production fuel injector nozzles.

Approach

- Using unique facilities at ORNL and other national laboratories, evaluate the potential for using x-ray and neutron methods to measure residual stress at tips of fuel injector nozzles.
- Determine the fatigue life and crack nucleation sites near notches in fuel injector alloys.

Accomplishments

- Due to limitations in the resolution, no x-ray or neutron beam method was able to precisely measure residual stress at nozzle tips. Slight compressive stress was indicated.
- Axial fatigue tests were completed using heat-treated fuel injector alloys. Two stress-dependent regimes of fatigue crack initiation and propagation were discovered.
- First the first time, transmission electron microscopy was used to reveal the nanostructure of EDM spray holes in fuel injector nozzles, showing potential fatigue nucleation sites.

Future Directions

- Working with Caterpillar, develop plans to use emerging, new residual stress methods may be used to accurately resolve strain gradients in the sack area of fuel injector nozzles.
 - As field experience with high-pressure injectors emerges, the tools and insights gained during the current project can be applied to alternative, even higher-performance alloys.
-

Introduction

Over the years, in order to improve fuel efficiency and control emissions, diesel engine designers have raised the pressures imposed on the fuel injectors. Repetitive pressurization exceeding 30,000 psi could stress the walls of the tips of the fuel injector nozzles above their endurance limit, leading to fatigue cracking and fracture. Therefore, the ability of injector nozzle materials to resist fatigue at high stress levels is important to understand.

As a diesel engine operates, physical processes begin to affect the ability of spray holes to deliver a precise quantity of fuel and desired fuel spray pattern. These processes include hole erosion and the formation of carbonaceous deposits. If one or more spray holes become clogged, fuel delivery characteristics change.

Figure 1 shows a new fuel injector nozzle after heat treatment. Later, six tiny spray holes are produced by electro-discharge machining with fine wires ('wire-EDM'). The tip is referred to as the 'sack.' Its microstructure, its residual stress state, and the effects of the spray holes on fatigue life were of interest in this project.



Figure 1. A new fuel injector nozzle prior to the wire-EDM production of spray holes in the sack. The base is approximately 25 mm in diameter.

Pressure spikes are created by rapid pulsation of a plunger within the nozzle to compress a metered volume of fuel-air mixture. Since the pressure distribution can be affected by hole diameter, cleanliness, and blockage, stresses on the material could exceed those calculated assuming clean and open spray holes.

The objective of this Cooperative Research and Development Agreement (CRADA) between ORNL and Caterpillar Inc was to investigate the ability of current and selected alternative steel alloys to withstand cyclic high pressures in diesel engine fuel injector sacks, and to characterize the microstructures near spray holes as potential locations for fatigue crack initiation. This project concluded in 2011.

Approach

A three-pronged approach was used: (1) microstructural characterization and hole metrology, (2) characterization of residual stress, and (3) fatigue testing of smooth and notched specimens. There was no work on residual stress measurement during FY 2011, so progress reported here focuses on items (1) and (3). Residual stress results may be found in prior reports and in reference (5) of this report.

Progress

Microstructural Characterization and Hole Metrology. Metallurgical characterization began in FY 2009 with cross-sectioning of sacks to reveal the microstructures of the nozzles and the walls of the spray holes. Vertical scanning interferometry, coupled with precision sectioning, enabled the roughness of the hole walls to be measured.

The wire-EDM hole making process results in the formation of recast layers on hole walls (see Figures 3 and 4 in the FY2010 annual report). In FY 2010, a focused ion beam (FIB) system was used to prepare a thin cross-section of the hole wall for high magnification examination in a transmission electron microscope (TEM). *To the best of our knowledge this was the first such application of TEM and FIB to fuel injectors.*

Additional characterization included the use of specialized acid etchants (see Figure 2), and

both micro- and nano-indentation hardness tests to probe mechanical properties near spray hole walls. Detailed results of that work may be found in publications (3) and (5).

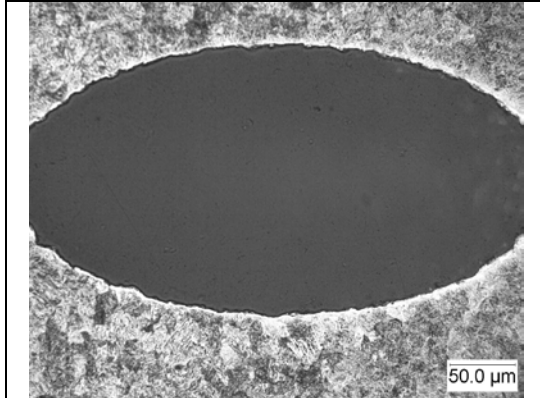


Figure 2. Etched microstructure near a hole wall with a thin recast layer (white). The oval shape is from the angle of cross-sectioning.

Fatigue testing. Fatigue tests were performed both at the Caterpillar Technical Center and at ORNL. Caterpillar used rotating bend tests to compare candidate alloys with the current fuel injector steel. The current steel was slightly worse in fatigue life than some candidate alloys when tested in a high-stress (low-cycle fatigue) range, but had longer lifetimes at a lower applied stress.

Axial fatigue tests were run on smooth bars, with and without controlled flaws. Figure 3 shows a polished, notched specimen with an EDM notch of similar size to a spray hole.

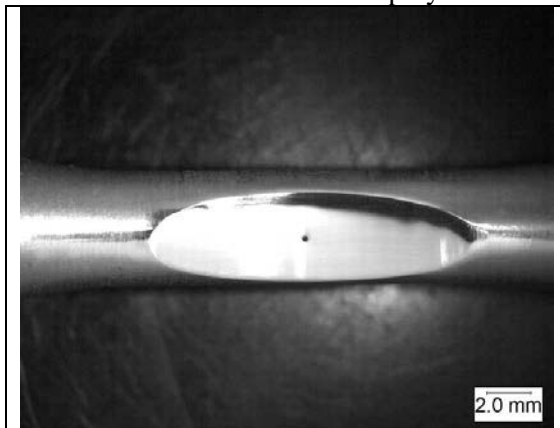


Figure 3. Polished gauge section of a fatigue specimen showing an EDM notch to simulate the presence of a spray hole. The axial loading direction in this view is horizontal.

Axial (tension/compression) fatigue tests were performed under load control at ORNL using a frequency of 20 Hz. The load ratio (R), defined as minimum load/maximum load, was kept constant ($R = -1$). The maximum stress per cycle was varied to obtain stress-life ($S-N$) characteristics. From earlier work in the project, it was known that a transition in fatigue behavior occurred at an applied stress of about 800 MPa; therefore, crack propagation rates were measured at or near this stress level. Cracks growing from a simulated spray hole are shown in Fig. 4.

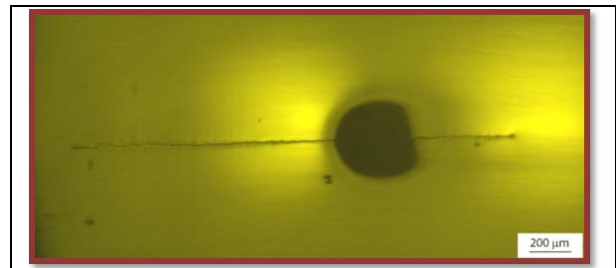


Figure 4. Crack growing from an EDM notch. The cyclic load was applied in the vertical direction. (Questar™ tele-microscope image)

Current work on the growth rate of fatigue cracks indicated that the crack initiation time represented a significant fraction of the total fatigue life. *In fact, the presence of a notch the size of a spray hole in the current steel could reduce its fatigue life by as much as four orders of magnitude.*

Since fatigue resistance concerns both crack initiation and growth, the results of this study have significant implications for the future selection and use of alloy steels for high-pressure fuel injector nozzles.

Current alloys may perform adequately in high-cycle fatigue, as long as the local pressure on the fatigue-critical regions of the component (sacks or nozzle walls) does not exceed a critical level. If the stress rises higher than that, initiation may occur earlier at machining flaws or EDM holes, leading to substantial reductions in life. Treating alloys to impart beneficial residual compressive stresses could help, but more research remains to be done in that area.

Summary and Conclusions

- Characterization of the microstructures of diesel engine fuel injector nozzle hole walls identified the potential for fatigue crack initiation in certain areas, like hole wall artifacts caused by EDM.
- Rotating bend-type fatigue tests at Caterpillar Technical Center investigated the high and low-cycle smooth fatigue of current and several candidate alloys steels. Current steels may be adequate in the near term, but as stress levels rise, alternative alloys begin to look more attractive.
- Fatigue tests at ORNL studied the transitions in initiation and propagation rates of fatigue cracks as a function of applied stress on both smooth and notched specimens. Notches can reduce the fatigue life of the current alloy by as much as four orders of magnitude.
- Without field failure data collected from next-generation diesel engines or test cells that operate fuel injectors at very high pressures, the extent to which fatigue failure at nozzle walls or sacks presents a serious engine reliability problem cannot be confidently determined. However, as additional field data become available, the characterization methods and analyses developed during this study can readily be applied to select better performing alloys.

Publications/Presentations

- 1) A. Shyam, P. J. Blau, and M. J. Pollard “The very high cycle fatigue behavior of tool steel materials for diesel fuel injectors,” presented at the 5th International Conference on Very High Cycle Fatigue, Berlin, Germany, June 28-July 1, 2011.
- 2) A. Shyam, P. J. Blau, T. Jordan, N. Yang and M. J. Pollard, “The Very High Cycle Fatigue behavior of Tool Steel Materials” in the Proceedings of the Fifth International

Conference on High Cycle Fatigue, Eds. C. Berger and H.-J. Christ, DVM, 2011, pp. 525-530.

3) P. J. Blau, J. Y. Howe, D. Coffey, R. M. Trejo, L. R. Walker, B. C. Jolly, and N. Wang, “Microstructure, Morphology, and Nanomechanical Properties Near Fine Holes Produced by Electro-Discharge Machining,” accepted for publication in *Materials Engineering and Performance* (2011).

4) A. Shyam, P. Blau, T. Jordon and N. Yang, “The fatigue behavior of alloy steels,” accepted for presentation at the ASM Materials Science and Technology Conference and Expo, Columbus, OH (October 16-20, 2011).

5) P. Blau, A. Shyam, C. Hubbard, J. Howe, R. Trejo, N. Yang, and M. Pollard, *Materials for High-Pressure Fuel Injection Systems*, Final Report ORNL, NFE-08-01498, 21 pp., in press October 2011.

Project 18518 – Materials for High Efficiency Engines

Agreement 16304 – High Performance Valve Materials (HPVM)

P. J. Maziasz and N. D. Evans

Materials Science and Technology Division

Oak Ridge National Laboratory

P.O. Box 2008, MS-6115

Oak Ridge, TN 37831-6115

(865) 574-5082; fax: (865) 576-6298; e-mail: maziaszpj@ornl.gov

M.D. Veliz

Advanced Materials Technology

Caterpillar Technical Center

14009 Old Galena Rd.

Mossville, IL 61552

(309) 578-2700; fax: (309) 578-2953; e-mail: veliz_mark_d@cat.com

DOE Technology Manager: Jerry L. Gibbs

(202) 586-1182; fax: (202) 586-1600; e-mail: jerry.gibbs@ee.doe.gov

ORNL Technical Advisor: David P. Stinton

(865) 574-4556; fax: (865) 241-0112; e-mail: stintondp@ornl.gov

Contractor: Oak Ridge National Laboratory, Oak Ridge, Tennessee

Contract No.: DE-AC05-00OR22725

Objectives

- Characterize current engine exhaust seats and valves to define and understand temperature, performance and durability limitations
- Use understanding of the behavior of current valves and seats to enable advanced designs and/or selection of advanced materials and processing to upgrade temperature capability and performance/durability limitations.

Approach

- Team with Caterpillar (CAT) diesel engine valve and seat suppliers to define temperature/performance limitations of current technology, and provide upgraded seat and valve options that are commercially viable, so that prototype modified components can be supplied for testing and evaluation.
- Microanalysis at ORNL of the various seat and valve components from simulation-rig or engine testing to define the nature and causes of wear/degradation of exhaust valve/seat pairs relative to fresh components.
- ORNL perform critical mechanical properties testing to define the benefits of Ni-based superalloys for exhaust valves with more temperature capability and performance than standard Pyromet 31V.
- Use detailed data and analyses to guide component manufacturers in producing prototype valves and seats with upgraded performance and capability.

Accomplishments

- ORNL and Caterpillar identified commercial Ni-based superalloys with upgraded capabilities, based both on mechanical properties specimens for testing at ORNL and prototype valves for wear-rig testing at Caterpillar.

- ORNL completed tensile testing and creep-testing at 816-871°C that defined the benefits of Ni-based alloy 1 relative to 31V.
- Caterpillar completed the initial wear-rig testing at 850°C that defined significant benefits of Ni-based alloy 1 relative to 31V alloy.

Future Direction

- Perform longer-term rig-testing of upgraded exhaust valves and oxidation testing to define durability limits of Ni-based superalloys with upgraded capabilities (CAT).
-

Introduction

This is a continuing ORNL CRADA project with Caterpillar, NFE-07-00995 and DOE, OVT Agreement 16304, which began in 2007, and was scheduled to last for about 2.5 years. This CRADA was extended for 12 more months previously, and last year, due to technical success with identifying and testing new upgraded valve alloys, was extended for an additional 24 months, with extended and expanded workscope. This CRADA project has addressed the wear and failure modes of current on-highway heavy-duty diesel exhaust valves and seats, and then changed seat-insert processing and selected advanced exhaust-valve Ni-based superalloys with higher temperature capability. The need for such upgraded valve-seat alloys is driven by the demands to meet new emissions and fuel economy requirements, which then continue to push diesel exhaust component temperature higher. Requests for more detailed information on this project should be directed to Caterpillar, Inc.

Approach

Caterpillar provides and analyzes the baseline wear and mechanical behavior characteristics of engine-exposed valves and seats, and similar exposure of those components to laboratory simulation-rig testing at Caterpillar. ORNL completes more in-depth characterization and

microanalysis of those valves and seats. These data established the root-cause analyses which then provided the basis for modifying seat processing, and for selecting Ni-based superalloys with upgraded performance relative to standard Pyromet 31V last year. Last year, Caterpillar and ORNL teamed with Caterpillar's component suppliers to implement these solutions and obtain prototype components for wear-rig testing at Caterpillar, and specimens for testing and characterization at ORNL. This year, test results were completed, and microstructure analysis to understand the improved behavior of the valves was performed.

Upgrading the temperature capability of the various critical exhaust components will enable the increased engine temperatures needed to allow a 3% decrease in fuel consumption for on-highway trucks.

Technical Progress

Caterpillar

Last year, a valve supplier provided prototype valves of two Ni-based superalloys that Caterpillar and ORNL identified previously as having more performance and temperature capability than the standard 31V alloy. Caterpillar began testing the new prototype valves (Ni-based 1 and 2 alloys) in the wear-rig facility. Results for 480 h testing of

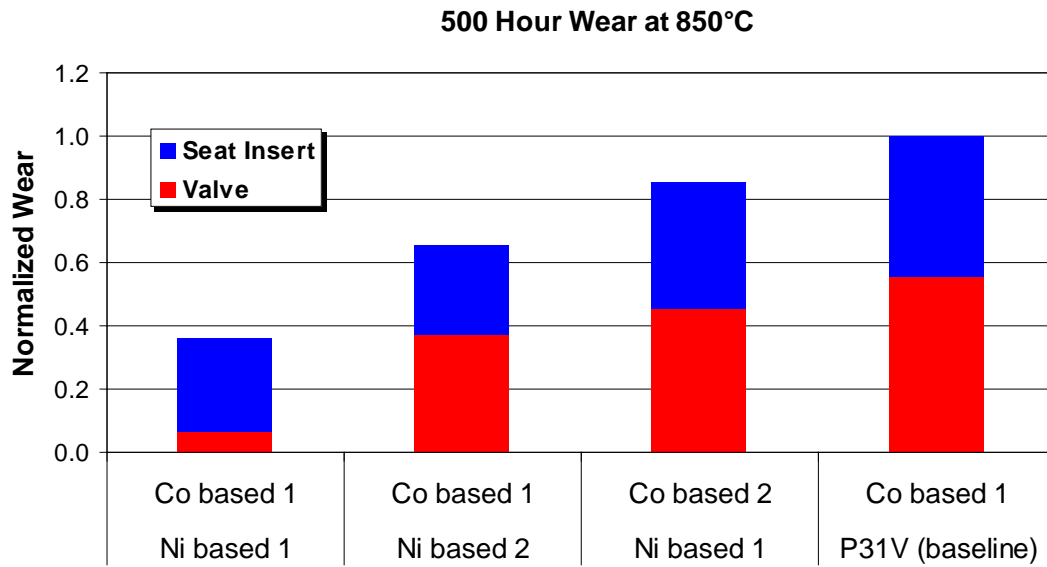


Figure 1 – Summary of Caterpillar wear-rig testing data, showing the separate wear of seat and valve components, and the cumulative wear (valve and seat-insert), for standard 31V alloy exhaust valves and new Ni-based 1 and 2 superalloy prototype valves at 850°C in air. The Ni-based 1 alloy shows showed a 2.7x improvement in total wear life with the standard Co-based seat alloy (1) relative to the standard 31V valve alloy.

Ni-based alloys 1 and 2 and standard 31V valves tested against the standard seat-inserts at 850°C in air are shown in Figure 1. After 500 h of testing, the upgraded Ni-based 1 alloy valves show a 200% reduction in cumulative wear (valve + seat) relative to the standard 31V alloy. Valves from these rig tests were sent to ORNL for characterization.

ORNL

ORNL completed thorough microstructural and microcompositional characterization studies of the standard valve and seat components last year, which defined the detailed changes occurring at the oxidation-surfaces. Analysis included surface oxides as well as the underlying metal interface and bulk regions (including fresh and aged, non-wear control specimens). Root-cause analysis of the 31V alloy at 760-850°C showed that there was dissolution of gamma-prime and the formation of internal oxidation (of Al and Ti), which weaken the subsurface region relative to the underlying base metal. This information indicated Ni-based alloys with more temperature capability (better oxidation resistance and more gamma-prime) than 31V were needed, and ORNL and Caterpillar identified several commercial Ni-based superalloys as upgrade materials. Caterpillar’s valve supplier provided prototype valves to Caterpillar, and mechanical properties specimens (tensile and creep) from the rod-stock used to forge valves to ORNL for mechanical properties testing. This year, ORNL also did scanning electron microscope (SEM) analysis and nano-hardness profiling of some of Caterpillar rig-tested valves.

ORNL also conducted creep-rupture testing at 816 and 871°C of these 3 alloys at stress of 15-30 ksi. Despite Ni-based 2 alloy having slightly higher YS at 816°C, the Ni-based 1 alloy clearly has much better creep-rupture resistance, as shown for creep in air at 871°C and 15 ksi in Figure 2, and at 816°C and 30 ksi in Figure 3.

ORNL performed SEM analysis and nano-hardness mapping of the cross-section at the valve seat wear scar for Ni-based alloy 1 rig-tested at 850°C, and that is shown in Figure 4. The hardness increased in the deformed region just

below the wear scar relative to the base metal, indicating that work-hardening is part of the reason that this alloy exhibits better wear-resistance during rig-testing.

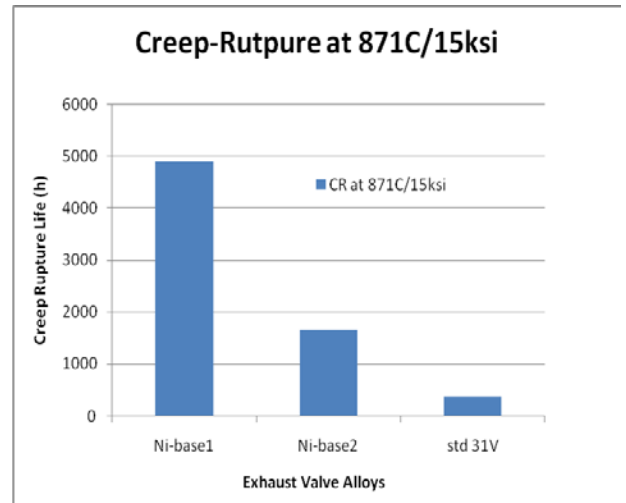


Figure 2 – Creep-rupture life of the standard 31V exhaust valve alloy and two alternate upgrade Ni-based superalloys, for creep tests run in air at 871°C and 15 ksi.

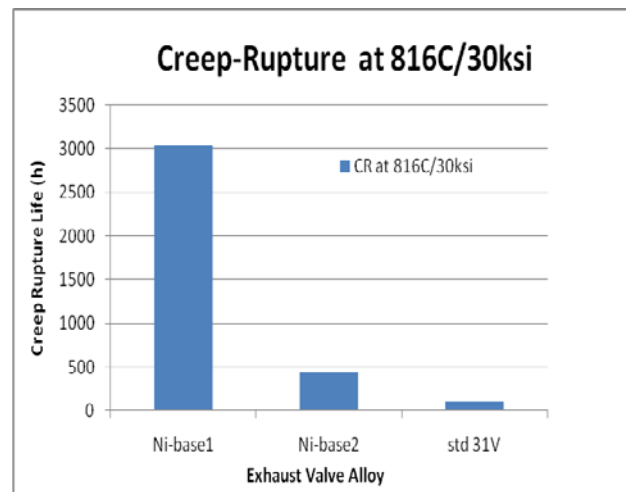


Figure 3 – Creep-rupture life of exhaust valve alloys, as determined for creep-testing in air at 816°C and 30 ksi. The Ni-based 1 alloy clearly has more creep-rupture resistance than the other two alloys.

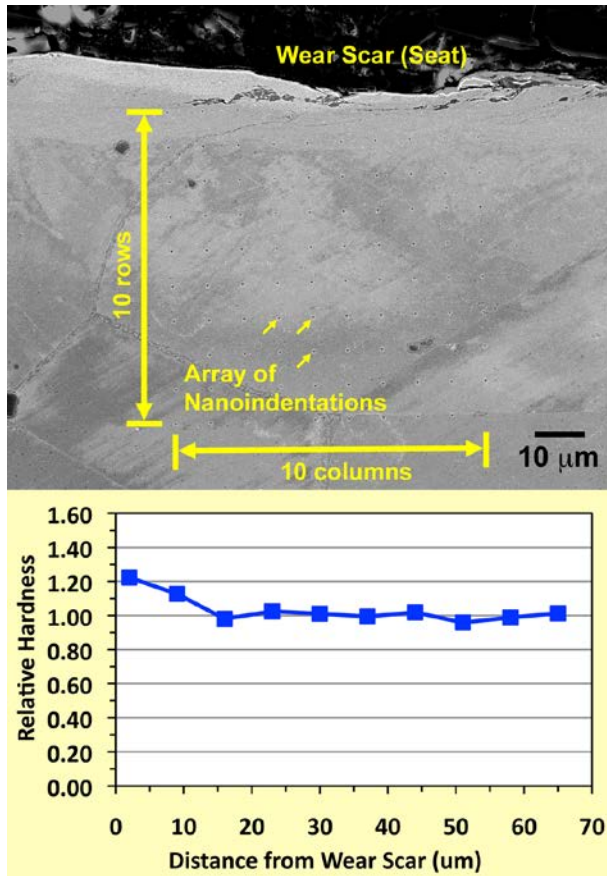


Figure 4 – SEM imaging of the valve seat wear surface cross-section, after rig testing of Ni-based alloy 1 at Caterpillar at 850°C. Nano-hardness mapping at ORNL, shows clear evidence of work-hardening beneath the seat surface consistent with the wear-resistance observed in rig-testing.

Conclusions

Caterpillar received prototype valves of 2 commercial Ni-based alloys with more performance and temperature capability than the standard 31V alloy. Wear-rig testing to about 500h at 850°C shows considerably less cumulative wear for the Ni-based 1 alloy relative to Ni-based 2 alloy and the standard 31V alloy.

ORNL received tensile and creep specimens made from the rod-stock used to forge valves of Ni-based 1 and 2 alloys and the standard 31V alloy. Creep-rupture testing at 816 and 871°C at stresses on 15-30 ksi shows that the Ni-based 1 alloy has much more creep-rupture resistant than 31V or Ni-based alloy 2. SEM and nano-hardness

analyses show that there is considerable work-hardening below the wear-scar surface of the valve seat, for Ni-based 1 alloy rig-tested at 850°C. This behavior is likely a factor in the wear-resistance of this alloy exhibited during rig-testing.

Publications/Presentations

None

Special Recognitions and Awards/Patents Issued

None

Agreement 17058 – Compact NO_x Sensor with Built in Reference

Principal Investigators: J. L. Routbort, D. Singh (co-workers: Elena Timofeeva and Kristen Pappacena)

Argonne National Laboratory

9700 S. Cass Avenue

Argonne, IL 60439-4838

(630) 252-5065; fax: (630) 252-5568; e-mail: routbort@anl.gov

DOE Technology Manager: Jerry L. Gibbs

(202) 586-1182; fax: (202) 586-1600; e-mail: jerry.gibbs@ee.doe.gov

Contractor: UChicago Argonne LLC

Contract No.: DE AC03 06CH11357

Objective

- Use joining technique to produce compact oxygen and NO_x sensors with internal reference
- Develop electronic conducting ceramic to replace the Pt electrodes in the sensor
- Develop technique to directly join the conducting ceramic to the YTZP body of the sensor

Approach

- Vary the composition of LaSrAlMnO (LSAM) such that the electrical conductivity is maximum at the operating temperature of the sensor
- Modify the composition such that the LSAM can be plastically deformed at the same temperature and strain rates as the YTZP

Accomplishments

- Strong, pore-free joints have been made with various ceramics, cermets, intermetallics, composites, and biomaterials, with and without various interlayers, fracture occurs away from interface at the region of maximum residual stress
- Demonstrated that grains in SrTiO₃ rotate during deformation
- R&D 100 Award for oxygen sensor
- Developed initial NO_x sensor
- Published 27 journal papers, 3 patents issued for plastic joining process, one patent for the NO_x sensor and 2 patent applications filed for the oxygen sensor and the LSAM interconnect have been filed, negotiations for licensing of oxygen sensor started

Future Direction

- Project finished FY11
-

Introduction

Monitoring oxygen and NO_x concentrations in combustion gases is crucial to optimizing combustion efficiency in power plant and engine applications, and thus improving energy efficiency and minimizing environmental pollution. Recently, based on Nernst principle, high temperature compact gas sensors have been developed that have a built-in reference gas source created by a metal-metal oxide (such as Pd/PdO) mixture placed in a sealed chamber [1]. Typically, yttria-stabilized tetragonal zirconia (Y-TZP) discs joined by a plastic deformation process are used to create a hermetically sealed chamber. The voltage difference generated between a Pt electrode placed in the chamber and one placed on the outside of the sensor housing is used to sense the gas concentrations. The opening in the reference gas chamber where the Pt electrode exits from the sensor housing is plugged with a glass seal to maintain hermicity of the reference gas chamber. The glass seal, however, limits the operational temperature, as it melts around 900°C . For this reason, a preliminary investigation of replacing the Pt electrode with an aluminum-doped lanthanum strontium manganese oxide (LSAM) electronic ceramic was performed [2]. Figure 1 is a schematic diagram of the sensor, and the location of the glass seal that needs to be replaced is highlighted.

Lanthanum-strontium-manganese oxide (LSM) materials have been studied in the fuel cell literature as electronic conductors, but they react with the YSZ electrolytes, causing a low conductivity phase [3-6]. For this reason, aluminum doping has been investigated to limit the reaction while maintaining electrical conductivity [5-6]. Holc demonstrated the relationship between Al content and electrical conductivity, as well as the extent of the reaction with YSZ [5]. Fu examined the effect of Al doping on the conductivity

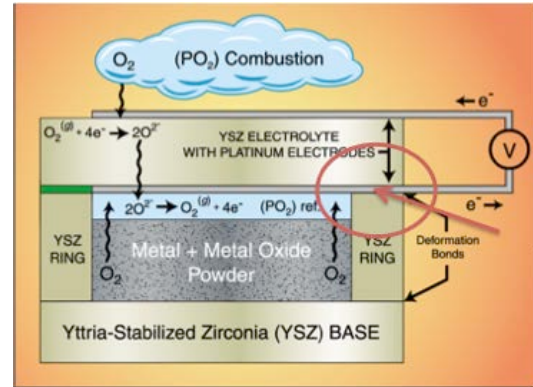


Figure 1. Schematic of the internal reference oxygen sensor. The arrow points to the circled glass seal.

in different atmospheres [6]. Spirig took this idea to the level of joint formation, and demonstrated that with very high Al doping levels, successful joints were created between LSAM and YSZ with no interfacial reaction. However, with high Al doping the electrical conductivity of LSAM degrades significantly [2,7].

FY10 was spent optimizing the Al-doping levels such that LSAM has sufficient electrical conductivity. Further, using a high temperature deformation process, an optimized LSAM formulation was demonstrated to join to YTZP to produce seamless joints. Characterization of the joint interface was conducted using a variety of analytical techniques. The results presented here demonstrate the potential of LSAM as an electrode material for sensing the internal reference cell voltage and precludes the use of Pt electrode and its associated glass seal requirements.

Experimental Details and Results

(a) Processing of LSAM materials

Lanthanum strontium aluminum manganese oxide ($\text{La}_y\text{Sr}_{1-y}\text{Al}_x\text{Mn}_{1-x}\text{O}_3$) materials of four compositions, $\text{La}_{0.73}\text{Sr}_{0.27}\text{Al}_{0.03}\text{Mn}_{0.97}\text{O}_{3.64}$, $\text{La}_{0.65}\text{Sr}_{0.35}\text{Al}_{0.18}\text{Mn}_{0.82}\text{O}_{3.64}$, $\text{La}_{0.6}\text{Sr}_{0.4}\text{Al}_{0.48}\text{Mn}_{0.52}\text{O}_{3.63}$, and $\text{La}_{0.8}\text{Sr}_{0.2}\text{Al}_{0.5}\text{Mn}_{0.5}\text{O}_3$, were fabricated using traditional ceramic processing techniques. First, appropriate amounts of the precursors,

lanthanum nitrate, strontium nitrate, aluminum nitrate and manganese chloride (Alfa Aesar), were milled together in acetone using an alumina milling media. The resulting mixed suspension was dried to remove the acetone before calcining at 1000°C for 4 hours and again at 1200°C for 50 hours to ensure complete reaction. The calcined powders, suspended in iso-propyl alcohol (IPA), were milled in a particle size-reducing grinder, dried using a centrifuge, and pressed into pellets of either discs or rectangular bars prior to sintering at 1450°C for 50 hours. The resulting sintered ceramics were then fully characterized. Induction Coupled Plasma – Optical Emission Spectroscopy (ICP-OES) was used to determine the actual concentrations of each element in the resulting materials to establish the stoichiometry of the final sintered products.

(b) SEM, XRD, density characterization

The microstructures of the LSAM sintered ceramics were investigated using scanning electron microscopy (SEM) (Hitachi 4700) with energy dispersive x-ray spectroscopy (EDS). X-ray diffraction was performed on crushed sintered pellets with silicon powder added as a standard to normalize the 2- θ axis. Density and open porosity were measured using Archimedes' method in water.

(c) Electrical conductivity

D-C electrical conductivity was performed using a computer controlled four-point probe test set-up. Details of the test set-up are described elsewhere [8]. Samples were heated to the test temperature and held for 2 hours. At each test temperature, at 60 s intervals, a 10 mA current were applied through the sample using two outer probes. The voltage generated across a specific sample length was recorded using the two inner probes. Using the applied current, sample cross-section area and distance between the probes over which the voltage was measured, the sample conductivity was calculated. Over a two-hour hold period at a particular temperature, approximately 120

conductivity measurements were made. An average value was reported. This process was conducted at test temperatures ranging from room temperature up to 800°C at intervals of 100°C.

(d) Joining

LSAM samples were joined to commercially obtained YTZP (Custom Technical Ceramics, Inc., Arvada, CO). Joining was carried out using an Instron Universal Testing Machine (Instron, Model 1125). Individual bars of LSAM and YTZP were cut and roughly polished to produce parallel sides prior to testing. The samples were attached with superglue to each other and to Pt foil coated alumina platens to form a sandwich structure prior to being placed into the Instron furnace. Pt foil was used to prevent reaction between LSAM and alumina platens. The samples were joined at two strain rates ($5 \times 10^{-6}/s$ and $1 \times 10^{-5}/s$) at 1250°C. As the furnace heated up, a load of 5 N was maintained on the sample. The sample was equilibrated at the joining temperature before the load was applied at a fixed crosshead speed resulting in a nearly constant strain rate. The samples were allowed to deform until a steady-state flow stress was reached. The total strain on the samples was on the order of few percent.

(e) Joint characterization

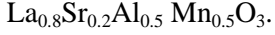
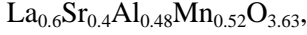
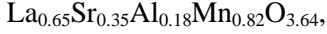
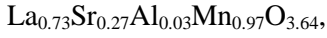
Following joining, SEM, X-ray diffraction and Raman spectroscopy were used to characterize the joint. The joined material cross-section was polished before SEM examination. EDS mappings were used to identify the location of each element and determine if any inter-diffusion had occurred. Following SEM analysis, X-ray diffraction and Raman spectroscopy were performed on the interface to identify any reaction phases that may be present. X-ray diffraction patterns were acquired using (Philips X'pert MPD) in the range $2\theta=20-100^\circ$ with a step size of 0.5° and a dwell time of 1s. Raman spectroscopy (Raman Microscope (Renishaw, UK) with 633 nm laser excitation) was also used, at room temperature, to investigate the presence of

any new phases resulting during the joining process.

Results and Discussion

a. Material synthesis

LSAM materials were successfully fabricated using traditional powder processing techniques. ICP-OES was used to determine the compositions, which were



These materials had open porosities of 1.48%, 0.97%, 1.3%, and 4.91%, respectively. Corresponding sample densities were 5.39 g/cm³, 5.95 g/cm³, 5.67 g/cm³ and 5.96 g/cm³, respectively. The low open porosity observed in the fabricated samples is desirable for forming a gas-tight joint.

b. Electrical conductivity

The electrical conductivity as a function of temperature is shown in Fig. 2 for each composition of LSAM. Literature values for similar compositions are also shown [5]. For each composition, the electrical conductivity increases with increasing temperature. For x=0.03 sample there is a small dip around 100°C, which is a known discontinuity for LSM near its magnetic transition temperature. [9] As the Al concentration increases, the electrical conductivity decreases. Each of the LSAM materials tested had much higher electrical conductivities than that of zirconia, which is ≈ 0.005 S/cm at 700°C. [10].

(b) Joining

Joining was successfully performed with $La_{0.8}Sr_{0.2}Al_{0.5}Mn_{0.5}O_3$ samples and YTZP at a temperature of 1250°C and strain rates of 1×10^{-5} /s and 5×10^{-6} /s. Fig. 3 shows an example of a stress vs. strain curve for LSAM and YTZP. There are a few important features to note. The initial section shows an elastic behavior. At about 90 MPa plastic deformation begins. The sample reached a strain of ≈3.5% before the test was stopped.

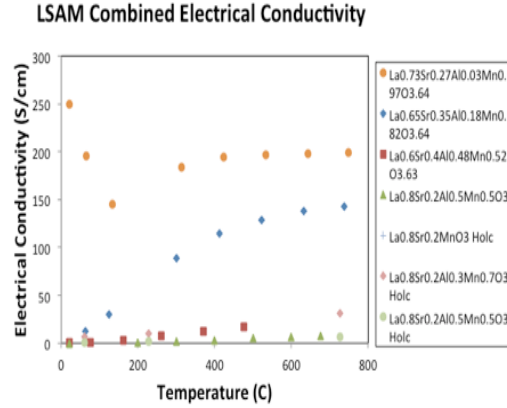


Figure 2. Electrical conductivity of different compositions of LSAM along with literature values [5]. Error bars shown are within the symbol size.

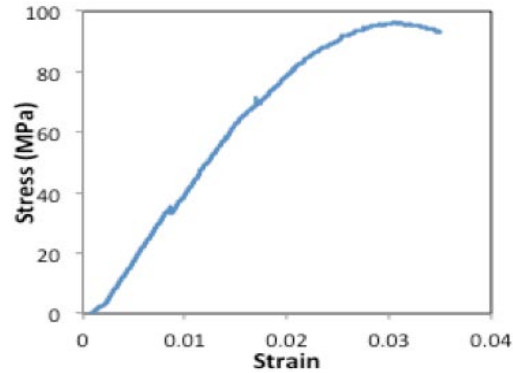


Figure 3. An example of stress vs. time curve from a joining experiment of LSAM with YTZP at 1250°C and a strain rate of 5×10^{-6} /s.

(c) Joint Characterizations

An SEM image of the joining plane is shown in Fig. 4. Arrows indicate the joining plane, where the LSAM and YTZP formed a pore-free bond, with the LSAM region labeled on the left and the YTZP region labeled on the right. A series of EDS mappings of each element present in the LSAM and YTZP materials is shown in Fig. 5. The Mn and Al each remain strictly on the LSAM side. At the interface, a band of La, Sr, Y and Zr are present, indicating inter-diffusion of these species. The Y and Zr concentrations do not change significantly across the interface, whereas the

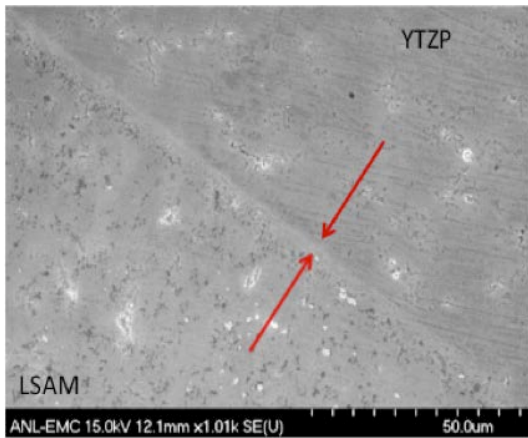


Figure 4. Arrows indicate the joining plane between the LSAM (0.5 Al) and the YTZP

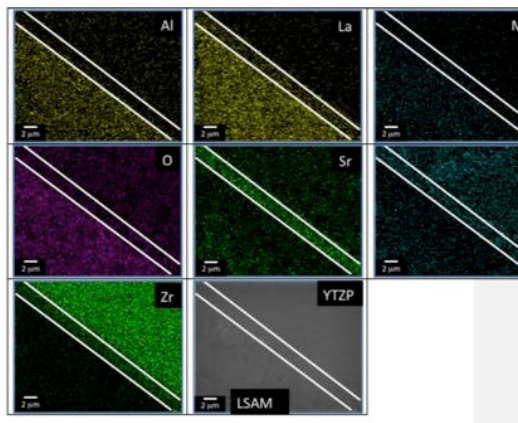


Figure 5. Energy Dispersive Spectrum mapping of the various elements at the YTZP /LSAM interface.

La and Sr show different concentrations in the interface than in the LSAM bulk. This suggests that the La and Sr species diffused into the zirconia side to form the interfacial region. The La presence in the interface is very faint, indicating only a small amount of migration. The Sr concentration, however, is quite high at the interface, but appears to be depleted on the LSAM side of the interface, indicating the migration of Sr out of the LSAM and into the interface.

In order to determine what phases are present as a result of the La and Sr migration into the zirconia at the interface between the two materials, x-ray diffraction was performed on the surface of the joined

sample. Fig. 6 shows the x-ray pattern of the interface, and the phases present are indicated. LSAM and YTZP phases are present, as expected. The extra peaks, representing the interfacial region, were identified as SrO and SrZrO₃, confirming the migration of Sr from the LSAM, as well as some reaction with the zirconia. Sr is known to diffuse out of the LSAM at the surface [4], correlating well to the positioning of the Sr depleted region just outside of the interface, as well as the freedom of the Sr species to react with the zirconia.

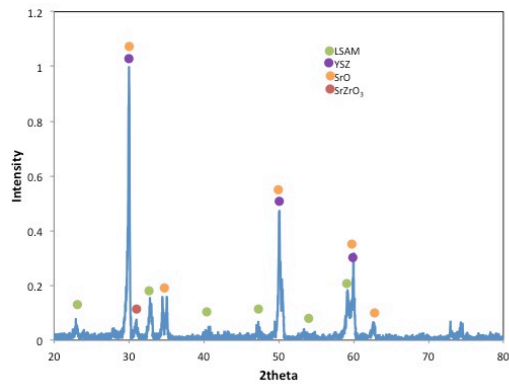


Figure 6. X-ray diffraction pattern of the interfacial cross section. Phases present are labeled.

This Sr migration phenomenon is likely due to Zener relaxation of lattice distortions that arise upon Sr substitution on the La sites [11]. Zener relaxation is a stress induced reorientation of elastic dipoles by atomic jumps between equivalent crystallographic sites in distorted perovskite structures with low concentrations of A-type cation substitutions in ABO₃ type manganites [11]. Previous theoretical work on LSM materials indicated that the lattice distortion required for Zener relaxation effect disappears as the Sr concentration approaches 0.25 [12]. For the La_{0.8}Sr_{0.2}Al_{0.5}Mn_{0.5}O₃ system in particular, Zener relaxation can occur at the high temperatures and pressures of the joining procedure, thus causing the Sr migration, and second phase formation at the LSAM/zirconia interface,

assisting in the chemical bonding between the two phases. Any La containing second phases that may be present at the interface are probably masked by the background noise in the x-ray pattern.

Raman spectroscopy was also performed on the interface to further investigate the reaction phases. The spectra were taken 1 μm apart along a line across the interface. Fig. 7 shows representative

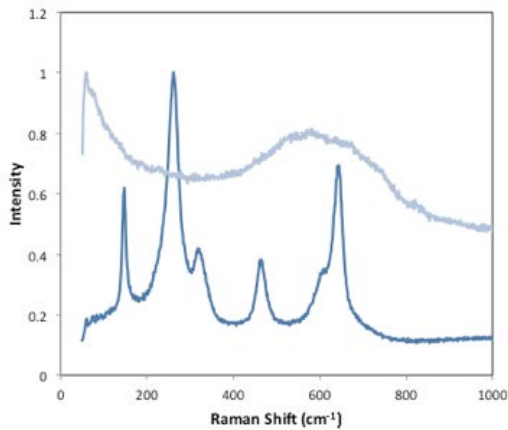


Figure 7: Representative Raman spectra from YTZP and LSAM materials.

spectra from the LSAM side and the YTZP side, away from the joint. The two spectra are easily distinguishable, making identification simple. YTZP shows a number of sharp peaks that were previously identified for this material [2]. The Raman spectrum of LSAM shows only extremely broad features between 400 and 800 nm that are similar to those reported for LSMO films [13]. The broadened Raman peaks (Raman bands) in this region are recognized as a feature of the mixed valence manganites.

Spectra from a 5 μm linear region across the interface taken with a 1 μm step size are shown in Fig. 8. The first and last spectra are clearly from the YTZP and LSAM sides, respectively. As the Raman step moves across the interface, the gradual change in position and intensity of the peaks reveal the change in the composition of the joint. The most pronounced changes occur in the spectral region of 400-1000 cm^{-1} . The deconvolution of peaks in this region

(Gaussian distribution is used) allowed identification of the individual contributions from different Raman components and their evolution across the interface.

The spectrum closest to the YTZP side of the interface (spectrum 22) closely resembles that of bulk YTZP, but with a few shoulders on the major peaks seen in Fig. 7. Five individual peaks can describe this region on spectra 22 with maxima indicated on Fig. 8. Spectrum 21 is 1 μm closer to the interface, and shows only four

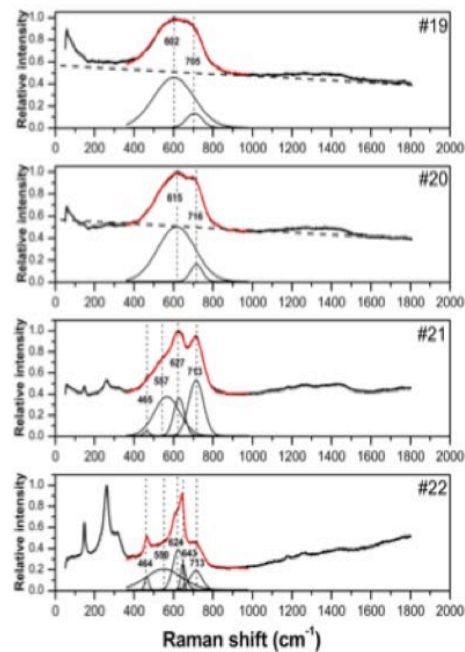


Figure 8: Raman spectra for one micron steps across the interface.

peaks. The peak at 643 cm^{-1} (a primary YTZP peak) is not observed here. A slight shift towards higher wavenumbers for the remaining four peaks indicates a change in the bonding structure. Further along (spectrum 20) peaks 464 cm^{-1} and 557 cm^{-1} also disappear, as does the shoulder they created in spectra 21-22 on the left, leaving only peaks at 624 cm^{-1} and 715 cm^{-1} behind. Spectrum 19 is very close to the LSAM spectrum seen in Fig. 7, and appears to be the end of the interfacial region. The gradual progression of the Raman shifts and

the presence of characteristics of both the LSAM and the YTZP phases in the interfacial region correlate well with the migration of Sr and La containing species across the interface. This further confirms the reaction phase present within 3-5 micron thick interface that assists with the joining of the two materials.

To further characterize the joint, Vickers indentations were made (at 200 to 300 g) to generate cracks near the interface. The crack behavior can give an indication of the strength of the bond; specifically whether or not the crack travels through the interface or separates the two materials. Fig. 9 illustrates the indentation induced crack traversing the interface, and not being

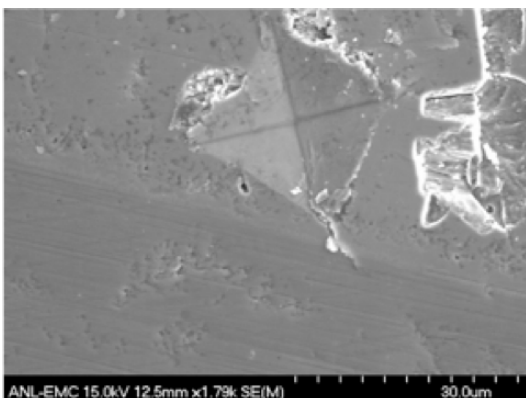


Figure 9: Vicker's indentation cracks traverse the LSAM/YTZP interface.

diverted in between the samples. This result suggests a strong bond exists between these two materials such that a crack is unable to separate them.

A strong joint was created between the LSAM and the YTZP phases using the high-temperature deformation process. The presence of the reaction layer suggests that the Sr was a migratory species and assisted in forming an intermediate phase that resulted in joining the two materials together. The success of the joint, along with the sufficient electrical conductivity, indicates that the LSAM material has potential for use in high-temperature applications as an electrode material. Further, it is a viable option for replacing the current Pt-electrode from the current gas

sensors that have a built-in reference gas chamber.

Conclusion

Al-doped lanthanum strontium manganese oxide ceramic has demonstrated electrical conductivity for a variety of doping levels and stoichiometries. A successful joint was formed between the LSAM material with a composition of $\text{La}_{0.8}\text{Sr}_{0.2}\text{Al}_{0.5}\text{Mn}_{0.5}\text{O}_3$ and YTZP. At the interface between the two materials, the strontium migrates from the LSAM to the YTZP phase, where it forms a reaction layer composed of SrO and SrZrO_3 . This intermediate interfacial phase forms a strong pore-free bond that does not separate as a result of Vickers's indentation induced cracking. These results indicate that the LSAM material has potential for use in a high temperature electro-chemical device.

Project Summary

We believe that this project has been both scientifically rewarding and cost effective. In addition to the 27 published papers in peer-reviewed journals, many invited presentations at universities, national and international conferences, 4 patents and 2 patent applications pending, we have received several inquiries from various industries. Additionally, the project has provided projects for 2 Ph.D. students (both completed their degrees from Ohio State University) and 3 postdocs

References

- [1] J.V. Spirig, R. Ramamoorthy, A.A. Sheikh, J.L. Routbort, D. Singh, P.K. Dutta "High temperature zirconia oxygen sensor with sealed metal/metal oxide internal reference" *Sensors and Actuators B* 124(2007) 192-201.
- [2] J.V. Spirig, J.L. Routbort, D. Singh, G. King, P.M. Woodward, P.K. Dutta, "Joining of highly aluminum-doped lanthanum strontium manganese oxide with tetragonal zirconia by plastic deformation" *Solid State Ionics* 179 (2008) 550-557.

- [3] A. Mitterdorfer, L.J. Gaukler “La₂Zr₂O₇ formation and oxygen reduction kinetics of the La_{0.85}Sr_{0.15}Mn_yO₃, O₂(g)|YSZ system” *Solid State Ionics* 11 (1998) 185-218.
- [4] S.P. Jiang, J.-P. Zhang, K. Foger, “Chemical interactions between 3 mol % yttria zirconia and Sr-doped lanthanum manganite” *Journal of the European Ceramic Society* 23 (2003) 1865-1873.
- [5] J. Holc, D. Kuscer, M. Hrovat, S. Bernik, D. Kolar, “Electrical and microstructural characterization of (La_{0.8}Sr_{0.2})(Fe_{1-x}Al_x)O₃ and (La_{0.8}Sr_{0.2})(Mn_{1-x}Al_x)O₃ as possible SOFC cathode materials” *Solid State Ionics* 95 (1997) 259-268.
- [6] Q.X. Fu, F. Tietz, P. Lersch, D. Stover, “Evaluation of Sr- and Mn-substituted LaAlO₃ as potential SOFC anode materials” *Solid State Ionics* 177 (2006) 1059-1069.
- [7] J.V. Spirig, “A New Generation of High Temperature Oxygen Sensors.” Thesis Dissertation, The Ohio State University, Columbus, OH (2007).
- [8] D.M. Gruen, P. Bruno, R. Arenal, J. L. Routbort, D. Singh, and M. Xie, “Thermoelectric Power Factors of Nanocarbon Ensembles as a Function of Temperature,” *J. Appl. Physics*, **105**, 073710 (2009).
- [9] H. Kamata, Y. Yonemura, J. Mizusaki, H. Tagawa, K. Naraya, T. Sasamoto “High temperature electrical properties of the perovskite-type oxide La_{1-x}Sr_xMnO_{3-δ}”, *J. Phys. Chem. Solids* 56(7), (1995).943-950
- [10] A Ghosh, G.K. Dey, A. K. Suri, “Correlation of Electrical Conductivity with Microstructure in 3Y-TZP System: From Nano to Submicrometer Grain Size Range,” *Journal of the American Ceramic Society* 91 (11) (2008) 3768-3770
- [11] H.R. Salva, S.S. Seiro, A. A. Ghilarducci. “Relaxation of substitutive atoms in manganites La_{2/3}A_{1/3}MnO₃, with A=Ca, Sr and Ba.” *Physica B* 398 (2007) 259-261.
- [12] F.L. Tang, X. Zhang, Y. Shao. “Sr ion distribution and local structure in La_{1-x}Sr_xMnO₃. *J. Phys.: Condens. Matter* 18 (2006) 5579-5586.
- [13] C.Z. Chen, C.B. Cai, Z.Y. Liu, L. Peng, B. Gao, F. Fan, Y.M. Lu, R. Zeng, Z.P. Guo, W.X. Li, S.X. Dou, “Stress evolution and lattice distortion induced by thickness variation and lattice misfit in La_{0.67}Sr_{0.33}MnO_{3-δ} films”, *Solid State Communications* 150 (2010) 66-69

Agreement 17257 – Materials for Advanced Turbocharger Designs

P. J. Maziasz and A. Shyam

Materials Science and Technology Division

Oak Ridge National Laboratory

P.O. Box 2008, MS-6115

Oak Ridge, TN 37831-6115

(865) 574-5082; fax: (865) 576-6298; e-mail: maziaszpj@ornl.gov

K. Pattabiraman

Global Materials Engineering Manager

Honeywell – Turbo Technologies

3201 W. Lomita Blvd.

Torrance, CA 90505

(310) 571-1616; fax: (310) 539-7061; e-mail: kalathur.pattabiraman@honeywell.com

DOE Technology Manager: Jerry L. Gibbs

(202) 586-1182; fax: (202) 586-1600; e-mail: jerry.gibbs@ee.doe.gov

ORNL Technical Advisor: David P. Stinton

(865) 574-4556; fax: (865) 241-0112; e-mail: stintondp@ornl.gov

Contractor: Oak Ridge National Laboratory, Oak Ridge, Tennessee

Contract No.: DE-AC05-00OR22725

Objectives

- CRADA NFE-08-01671 – Provide the critical test data for new, improved materials, which in turn will enable the design of advanced turbocharger systems with upgraded performance, durability and reliability relative to conventional systems.

Approach

- CRADA NFE-08-01671 – This is a 3 year project designed to consider both materials for the turbine and compression sections, and to consider turbochargers for both passenger/gasoline and commercial/diesel engines. Honeywell assesses and prioritizes the components that benefit most from materials upgrades or alloy development. ORNL works with Honeywell materials/component suppliers to obtain new materials for testing and evaluation.

Accomplishments

- CRADA NFE-08-0171 started at the beginning of FY2010. ORNL and Honeywell defined neutron-scattering residual stress measurements, first for turbine wheel/shaft components, and then for turbine housings. Long-term creep and oxidation evaluation of CF8C-Plus cast stainless steel continued for diesel and automotive turbine housings.
- Honeywell is taking the first steps to introduce CF8C-Plus as the turbo-housing material for the Ford V-6 3.5L twin-turbocharged EcoBoost gasoline engine used in light trucks.

Future Direction

- CRADA – Upgrade materials for wheel, shaft and housing of the turbine portion of the turbocharger will continue to be assessed. Supporting the Honeywell commercialization of CF8C-Plus for the Ford light duty truck application will be a priority.
-

Introduction

This ORNL CRADA project with Honeywell, NFE-08-01671 (DOE/EERE/OVT Agreement 17257) began in September, 2009, and will last for 3 years. This CRADA project addresses the limitations of lifetime or use-temperature for the various components (casing, wheel, shaft, bearings) of both the turbine and compressor parts of the turbocharger system. This year it also involved neutron scattering experiments at ORNL/HTML Neutron Residual Stress Facility 2 (NRSF2) at HFIR. Requests for more detailed information on this CRADA project should be directed to Honeywell, Inc.

Approach

The CRADA project, which began in September, 2009, will extend for 3 years, and covers several different tasks. The first task assesses and prioritizes the various components that need or would most benefit from materials upgrades to increase temperature capability and performance, as well as durability and reliability. The next tasks examine current performance and degradation modes of wheel/shaft assemblies for turbines and compressors, and turbine housings, particularly for automotive applications. New materials will then be obtained and tested to verify upgraded performance and benefits.

Technical Progress

This CRADA project began in September, 2009, and is comprised of six tasks, which will span the 3y duration of this project. ORNL and Honeywell discussed the priority of the various tasks and turbocharger components for materials upgrades at a kick-off meeting held in Torrance, CA in October, 2009.



Figure 1 – Honeywell turbocharger wheel/shaft assembly used for neutron-scattering experiments, consisting of a Ni-based superalloy turbine wheel welded to a steel shaft.

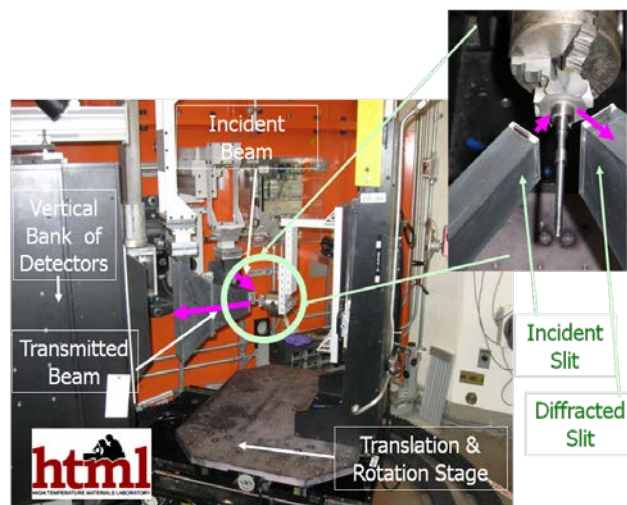


Figure 2 – The Neutron Residual-Stress Facility 2 (NRSF2) at the HFIR beam port, with the specific neutron scattering geometry used for the Honeywell turbocharger wheel/shaft assembly shown in the magnified inset. The NRSF2 is part of the High Temperature Materials Laboratory (HTML) at ORNL, and these experiments were run by Tom Watkins and Cam Hubbard of the Residual Stress User Center.

The turbine wheel-shaft assembly was chosen as the first component for analysis of residual stresses near the weld-joint of the Ni-based superalloy wheel to the steel shaft, using neutron-scattering at the HFIR reactor at ORNL. These wheel/shaft assemblies can develop

vibrations if there is any asymmetry in the weld-joint. A typical wheel/shaft assembly used for the ORNL residual stress measurements is shown in Figure 1. The Neutron Residual Stress Facility 2 (NRSF2) at the HFIR is shown in Figure 2, with a wheel/shaft assembly in place for neutron scattering measurements. Several sets of experiments were completed this year, and show that there is an asymmetry in the residual stress circumferentially in the as-welded condition. Some additional experiments varying post-weld processing conditions were also examined.

Additional testing was done to extend previous work by ORNL and Honeywell comparing the new CF8C-Plus steel to HK30-Nb, a standard commercially available upgrade material for turbochargers for heavy-duty truck diesel engines when temperatures exceed the limitations of SiMo cast iron. Previous work clearly showed that CF8C-Plus had better yield strength at 800 and 900°C than HK30Nb. Previous creep-testing at several different conditions at 700-900°C also clearly showed that CF8C-Plus steel had better creep-resistance than the HK30-Nb alloy.

Additional creep-testing was done on the CF8C-Plus steel at 600 and 700°C this year. At 600°C, one creep test at a lower stress failed after 7300 h, while another one at a lower stress has exceeded 10,000 h without rupture. Materials comparisons and additional testing will be included to enable CF8C-Plus steel to be evaluated for turbine housings for passenger vehicle gasoline engines.

Finally, Honeywell has taken the initial steps to commercialize CF8C-Plus steel for a Ford gasoline engine light-truck application. CF8C-Plus steel is planned as the turbo-housing material for the 3.5L V-6 twin-turbo EcoBoost engines for the Ford light-truck series. This effort will continue next year.

Conclusions

CRADA – The benefits of CF8C-Plus steel relative to HK-30Nb steel at 700-900°C were defined for diesel turbocharger housing

applications, and additional long-term creep-testing of CF8C-Plus at 600-700°C continued. Neutron-scattering residual stress experiments were completed for the welded region of turbine wheel/shaft assemblies for passenger vehicle turbochargers, and these showed stress asymmetries in the as-welded condition. The effects of processing on the residual stresses are in-progress.

Publications/Presentations

None

Special Recognitions and Awards/Patents Issued

None

Agreement 17894 - NDE Development for ACERT Engine Components

Jiangang Sun

Argonne National Laboratory

9700 South Cass Avenue

Argonne, IL 60439

630-252-5169; fax: 630-252-2785; e-mail: sun@anl.gov

DOE Technology Manager: Jerry L. Gibbs

(202) 586-1182; fax: (202) 586-1600; e-mail: Jerry.gibbs@ee.doe.gov

ORNL Technical Advisor: Dave Stinton

(865) 576-6832; fax: (865) 574-4556; e-mail: stintondp@ornl.gov

Contractor: Oak Ridge National Laboratory, Oak Ridge, Tennessee

Contract No.: DE-AC05-00OR22725

Subcontractor: Argonne National Laboratory, Argonne, Illinois

Objectives

- Develop rapid, reliable, and repeatable nondestructive evaluation (NDE) methods for inspection of advanced materials and processing technologies to support the material-enabled high-efficiency diesels program.
- Establish NDE methods and test procedures for characterization of advanced materials and components being tested in an ACERT experimental engine at ORNL.

Approach

- Investigate synchrotron x-ray CT for NDE characterization of material flaws and welding quality of light-weight metallic components for diesel engines.
- Develop phased-array ultrasonic methods to inspect welding flaws in turbocharger components.
- Develop infrared thermal imaging methods for quantitative measurement of thermal barrier coating (TBC) properties and 3D imaging of TBC structures to determine TBC degradation and detect delamination.

Accomplishments

- Demonstrated high accuracy and sensitivity of synchrotron x-ray CT for detection and characterization of 3D casting flaws within TiAl turbine-wheel casts and welding flaws between TiAl turbine wheel and Ti-alloy shaft.
- Investigated synchrotron x-ray CT inspection for power module and TBCs.
- Developed preliminary data-processing algorithm to remove artifact and enhance CT images.
- Developed phased-array ultrasonic methods to inspect welding flaws in turbocharger components.

Future Direction

- Develop/evaluate x-ray, optical, infrared thermal, and ultrasonic imaging NDE technologies for inspection of diesel engine components.
-

Introduction

Application of advanced materials in diesel engines may enhance combustion and reduce parasitic and thermal losses, thereby improving fuel efficiency while meeting the emission standard. Engine components developed from advanced materials and processing technologies, however, require rigorous assessment to assure their reliability and durability in higher temperature and pressure operating conditions associated with advanced engine systems. To address these materials challenges, selected materials/components are being prepared and tested in a Caterpillar heavy-duty C15 ACERT experimental diesel engine located at ORNL. The engine tests will provide crucial information on material performance/durability and effect to engine efficiency and parasitic losses in combustion and thermal management systems¹. In collaboration with materials scientists and engine engineers from Caterpillar and ORNL, these engine materials and components are being characterized by nondestructive evaluation (NDE) technologies at ANL to determine their reliability and durability for engine applications. The objective of this work is to develop and assess various NDE methods for characterization of advanced materials and components for ACERT engine systems. NDE technologies established at ANL, including optical scanning, infrared thermal imaging, vibrothermography, ultrasonic imaging, and x-ray computed tomography (CT), are being further developed for detection of volumetric, planar, and other types of flaws that may limit the performance of these components. The goal is to achieve higher spatial resolution and detection sensitivity.

The primary effort in FY 2011 was focused on developing and evaluating high-energy synchrotron x-ray CT for NDE characterization of various diesel engine materials and components, including turbocharger components made from light-weight materials, power modules, and thermal barrier coatings (TBCs). Another effort was directed on developing phased-array ultrasonic method for joint inspection. This research is collaborated with Caterpillar Inc. and ORNL.

Approach

Titanium aluminide (TiAl) has been identified as a promising material for rotating and oscillating components in gasoline and diesel engines². One of

the most promising TiAl engine components is the turbocharger wheel, which is joined with a Ti-alloy shaft by friction welding. Various processing flaws may present in the wheel casting and the joint. Of particular interest for this investigation is the detection of defects (e.g., cracks) within the friction-welded joints, as well as voids/cracks inside TiAl casts. These flaws limit the strength and reliability of the component, and have been a major concern for the utilization of TiAl materials for engine applications. Traditionally, these flaws are detected by ultrasonic and radiographic NDE techniques. These have lower sensitivity and cannot provide detailed flaw information which is critical for processing development and optimization. In this investigation, a high-energy synchrotron x-ray CT system, located at the advanced photon source (APS) at ANL, was developed to detect and characterize detailed 3D flaw distribution within metallic diesel-engine components. The synchrotron x-ray source has a high peak energy (selectable between 60 keV and 225 keV) necessary to penetrate thick metallic materials and the detector (imager) has a high spatial resolution (from 5 to 50 μm proportional to the object size) to resolve small flaws. Figure 1 shows a photograph of the experimental setup for imaging a turbocharger rotor.

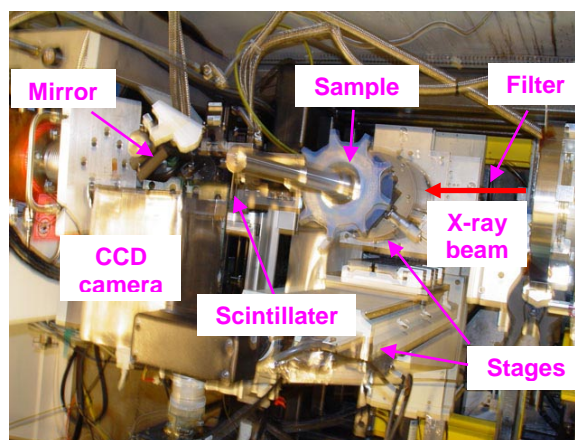


Figure 1. Top view of synchrotron x-ray CT facility at ANL's Advanced Photon Source (APS).

Although synchrotron X-ray CT may detect all significant flaws, this technology cannot be used in industrial facilities to inspect manufactured components. Industrial inspections rely on low-cost and fast inspection technologies. For weld inspection, ultrasonic technology is widely used³.

Because flaw detection by x-ray CT is based on transmission contrast while by ultrasonic is based on reflection, detection sensitivity for these two technologies can be different. It is therefore necessary to establish a detection-sensitivity correlation between them for various flaw types and sizes. In addition, because x-ray CT data can provide accurate information on the flaw size, geometry, orientation, and location within a component, the correlation may also aid for quantitative interpretation of ultrasonic data especially for complex flaw configurations. For this investigation, an ultrasonic phased-array system at ANL was utilized. Figure 2 is a photograph of this system.

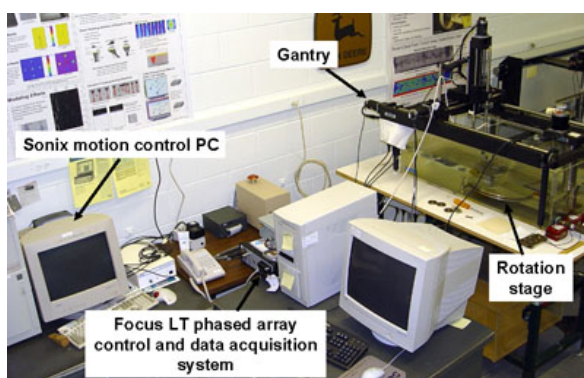


Figure 2. Ultrasonic phased-array system at ANL.

Results

Traditional X-Ray Radiography and CT Inspection of Joints

A traditional x-ray CT system located at ANL's NDE group was evaluated for NDE inspection of flaws within TiAl turbocharger joints. The system consists of a 450kV x-ray source and a line detector with 80 μ m pixel-size sensors and a large-panel area detector with 200 μ m pixel size. Three friction-welded joints were evaluated. Figure 3 shows enhanced digital radiographs of two samples (in Figs. 5a and 8a). The weld cracks in both samples are detected, although the detected crack lengths appear shorter than observed because of the low spatial resolution of the area x-ray detector (200 μ m). Figure 4 shows a CT slice obtained using the line detector (80 μ m) for the sample shown in Fig. 10a; it is apparent that this image is of low resolution and high noise to be useful for detailed material analysis.

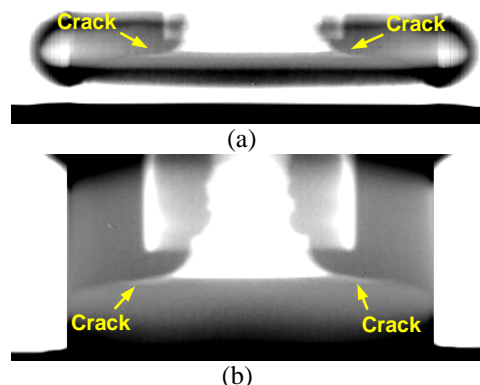


Figure 3. Digital radiographs of a (a) cut and (b) complete friction-welded joint samples.

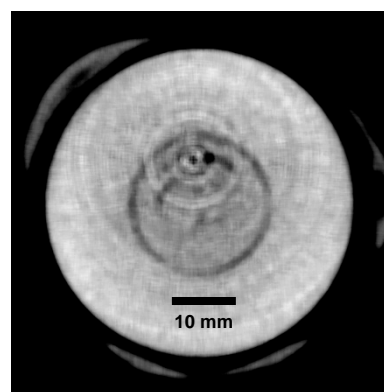


Figure 4. X-ray CT slice of a joint sample.

Synchrotron X-Ray CT Analyses of Joints

Three friction-welded turbocharger rotors were tested using the x-ray CT setup shown in Fig. 1. Two rotors were poorly welded, with large cracks at the welding interface. One of these rotors was cut along the central axis to display the welding cracks; it is identified as a calibration sample and used to establish a crack-detection correlation between CT and visual data. The third rotor contains internal cracks at the joint region. Experimental results for these samples are presented and discussed below.

CT Results for Calibration Weld Sample #1

Figure 5a shows the cut turbocharger-rotor sample used as a calibration standard to validate the crack detection sensitivity and resolution of the synchrotron x-ray CT technique. From the photograph, the welding interface between the TiAl cast and the Ti-alloy shaft is clearly visible; it has a slight angle along the radius. The x-ray scans were performed over an axial length of 6.12mm as

illustrated in Fig. 5a, which covered the entire region of the weld interface. The flashing material from the friction welding process, the curved structure outside the shaft, was not removed from the sample.

Figure 5b shows 5 typical CT slices within the scanned region. In these CT slices, the internal area belongs to the TiAl cast wheel (or air) and the external region to the Ti-alloy shaft. The TiAl material has a slightly lower x-ray attenuation parameter, resulting from a different composition and lower density, than that of the Ti-alloy. The welding crack is the darker semicircle of irregular shape between the two materials, with some small voids within the TiAl material.

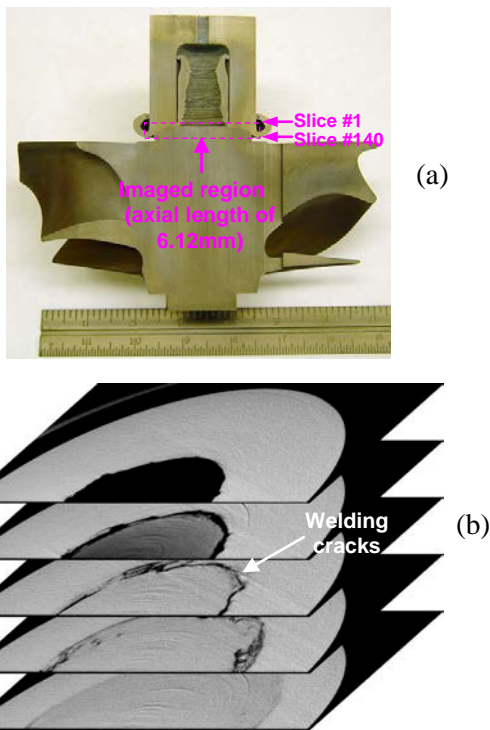


Figure 5. (a) A cut turbocharger rotor sample and (b) typical x-ray CT slices around weld interface.

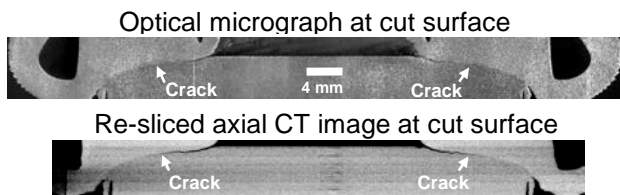


Figure 6. Comparison of optical and CT images at the same cut edge of the calibration sample.

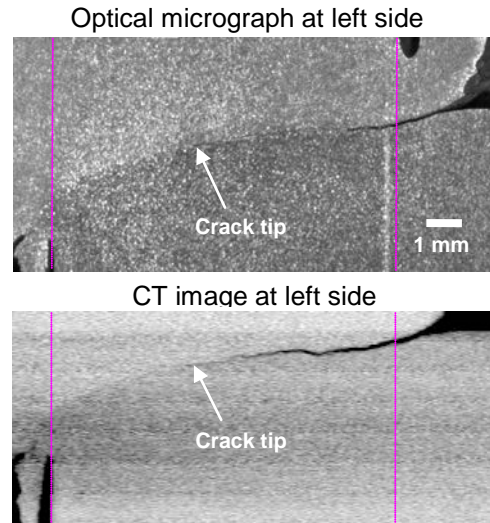


Figure 7. Detailed comparison of optical and CT images at left-side cut edge of the calibration sample.

All cross-section slices acquired for this calibration sample, total of 140 slices, were then composed together and re-sliced in the axial direction for a better visualization of the cracks. Figure 6 shows the comparison of an optical image and a re-sliced axial CT image at the same cut surface. The axial CT image displays 7 segments along the axial direction because 7 scans were performed to cover the axial length of ~6 mm. The cracks are extended more than one-half of the width of the shaft wall. From a detailed comparison (Fig. 7) it is apparent that the CT image shows a better contrast of the welding crack. Although the crack gap is very narrow, especially near the tips, the crack length can easily be determined. The crack dimensions determined from the CT image are similar to those observed in the optical micrographs, indicating that the spatial resolution of the x-ray CT experiments is adequate to resolve such welding cracks.

CT Results for Weld Sample #2

Figure 8 shows the welding sample #2 (Fig. 8a) and typical reconstructed CT slices (Fig. 8b). For this sample, the plane CT slices display a complex structure of the welding cracks. The radial geometry and length of the welding cracks can be easily determined from the re-sliced axial CT image, as shown in Fig. 9.

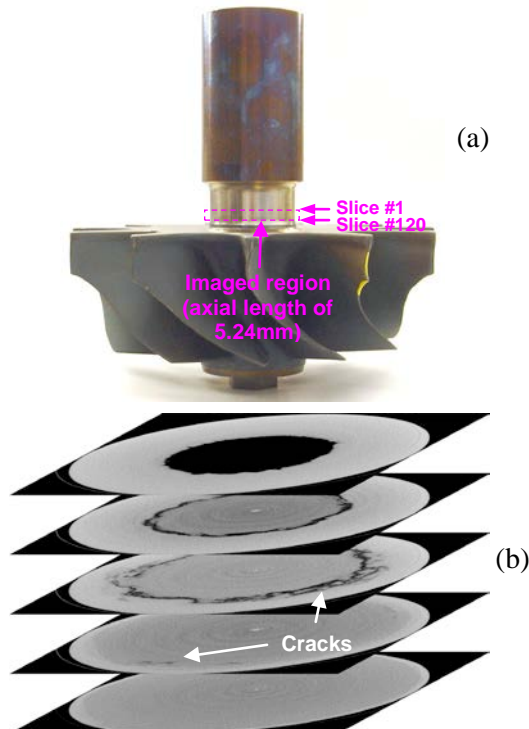


Figure 8. (a) Welding sample #2 and (b) typical x-ray CT slices around weld interface.

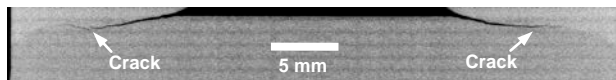


Figure 9. A re-sliced axial CT image of the weld sample #2 shown in Fig. 6a.

CT Results for Weld Sample #3

Figure 10a shows a photograph of the joint region of the weld sample #3. The flash material generated during the welding process was not removed from this joint. The synchrotron x-ray inspection scanned a region of 21.9mm axial length around the joint. Figure 10b shows 5 CT slices. The axial location of the slices is labeled from 0 to 4 mm to facilitate the discussion, where 0 mm is at the welding interface. At 0-mm plane, the welding crack extending in the radial direction is observed. The exact crack configuration of this welding crack has to be determined from multiple CT slices because it is not confined in this plane. Within the TiAl material just beneath the welding interface, a “circular” crack and a radial crack are visible, and they extend along the axial direction up to ~4.3 mm into the TiAl cast material. Figure 11 is a re-sliced axial CT image; it shows clearly the radial dimension of the welding crack at the weld interface

and the axial length of the circular/axial cracks extending inside the TiAl casting material.

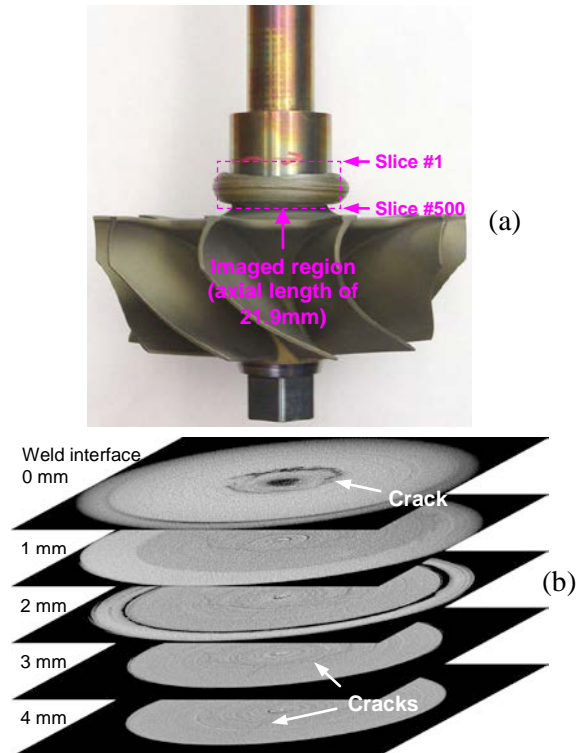


Figure 10. (a) Welding sample #3 and (b) typical x-ray CT slices around the welding interface.

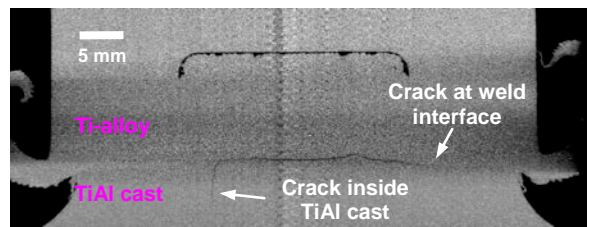


Figure 11. A re-sliced axial CT image for welding sample #3 shown in Fig. 8a.

Synchrotron X-Ray CT Characterization of TiAl Turbine-Wheel Casts

TiAl wheels are made by casting followed by hot-isostatic pressing (HIPing) to close the internal porosity. Cast TiAl wheels may contain various types of defects², including micro and macro porosities in the core region and near surface. These casting defects are investigated using the synchrotron x-ray CT method. Figure 12 shows a typical TiAl turbine-wheel cast. Figure 13 shows two cross-sectional CT slices: Slice #1 is at the elevation with a thicker core diameter and Slice

#380 at a thinner core diameter. It is seen that the reconstruction introduced extra black lines near the center, because the blades were outside the field of view. These artifacts are more intense in thicker sections of the wheel (Slice #1), and they may affect the identification of small voids near the cast center.

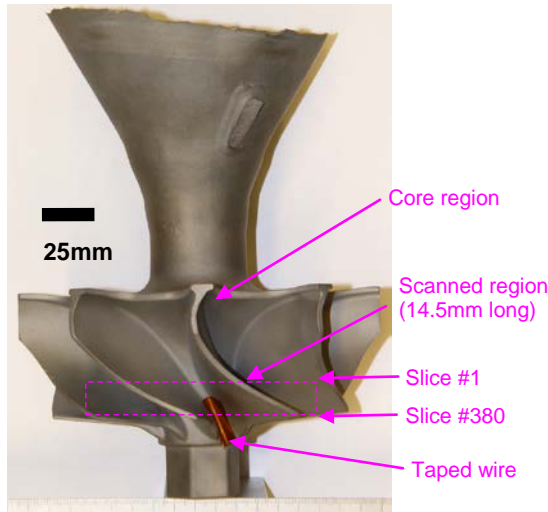


Figure 12. A TiAl turbine-wheel cast.

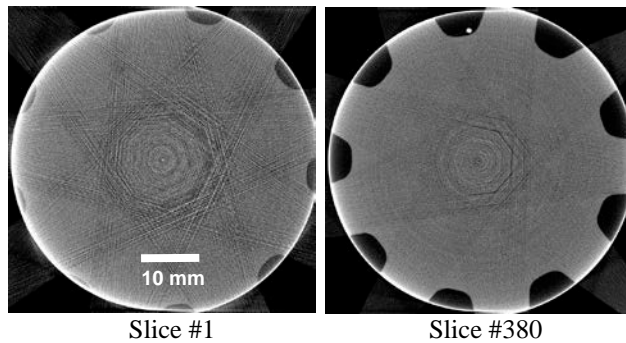


Figure 13. Typical X-ray CT slices at locations shown in Fig. 10.

To increase x-ray CT scan speed and improve data quality, two cast wheels, one as-cast and one after HIPing, were machined into 2"-diameter cylindrical core samples as shown in Fig. 14. Each sample contains both the core and the blade-root regions that are of interest for the NDE examination. Because of the smaller sample diameter, x-ray scan time was significantly reduced and the signal-to-noise ratio in the acquired data was consequently improved.

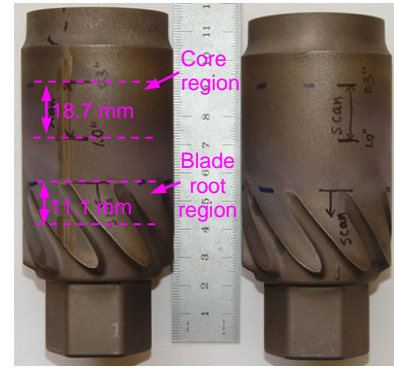


Figure 14. Two machined cylindrical core samples of TiAl turbine wheels.

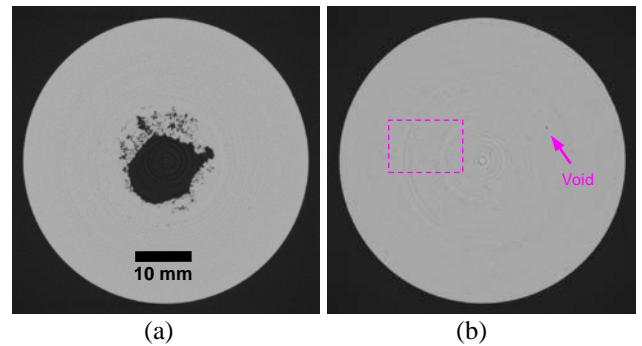


Figure 15. Typical x-ray CT slices for the as-cast cylindrical core sample: (a) within the core region and (b) within the blade-root region.

Figure 15 shows two CT slices of the as-cast sample: one located within the core region and the other within the blade-root region (see locations as illustrated in Fig. 14). A large void of ~12mm in diameter was detected at the center of the core region (Fig. 15a). Adjacent to this large void, the material is porous with distributed voids of various sizes. The cast material is generally dense outside this porous central region, although small voids may still be found. Small voids may also be found within the blade-root region, as seen in Fig. 15b. Many of these voids are partially filled with material (not completely empty), as seen from the enlarged image in Fig. 16 (from the region marked in Fig. 15b). Figure 16 also shows the ring artifacts. If these ring artifacts are removed, flaws can be identified more easily.

All cross-section slices acquired for the as-cast cylindrical core sample were composed together into a 3D volume data and sliced in the axial direction. Figure 17 is an axial CT slice. In this image, the

axial size and geometry of the voids are clearly visualized.

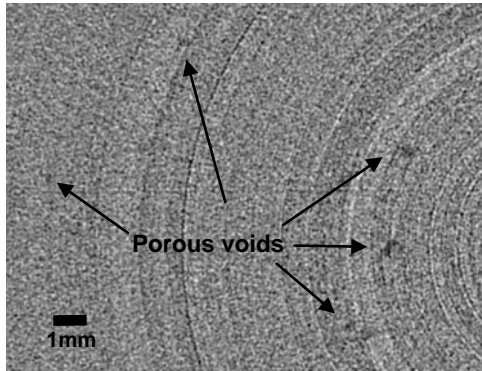


Figure 16. An enlarge and re-scaled image of the CT slice shown in Fig. 2b.

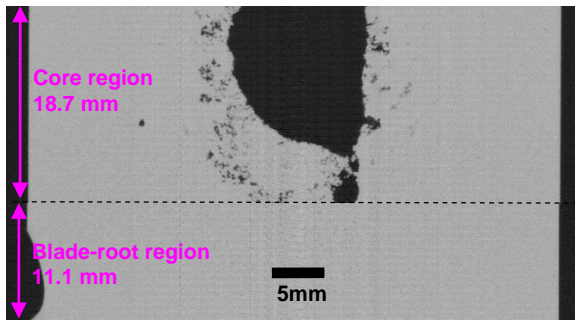


Figure 17. Reconstructed axial CT slice image for the as-cast cylindrical core sample.

Synchrotron X-Ray CT Characterization of a Power Module and TBCs

A new generation of power control unit (PCU) was developed for compact-size hybrid vehicles⁴. The PCU features size reduction, light weight, and high efficiency. Among the improvements includes a direct cooling structure with greatly improved cooling efficiency. The structure consists of a punched-hole plate between the insulating substrate and the cold plate to reduce the thermal stress. Therefore, the bonding of the punched plate is important to the power module performance. One power module (Fig. 18a) was examined by synchrotron x-ray CT. Typical plane and cross-sectional CT slices for the punched plate are shown in Fig. 18b. It is apparent that the CT data can be used to determine detailed hole geometry as well as its bonding quality with adjacent plates.

Thermal barrier coatings (TBCs) have been investigated extensively using optical and thermal

imaging NDE techniques⁵. These TBCs were also examined by synchrotron x-ray CT. Figure 19 shows a typical CT slice of two TBCs, one at as-received condition and the other after thermal cycling. The CT data show clearly the presence of a relatively uniform coating on the as-received sample, while the coating on the thermal-cycled sample had mostly gone. More detailed coating microstructure can be obtained by high-resolution imaging (e.g., using imaging pixel size of 5 μm).

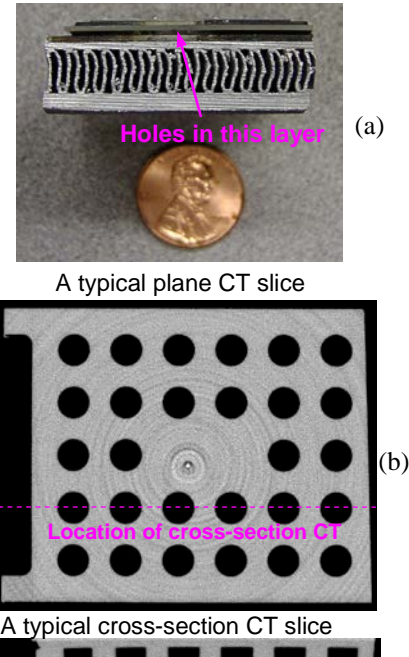


Figure 18. (a) A power module sample and (b) typical plane and cross-section CT slices of punched layer.

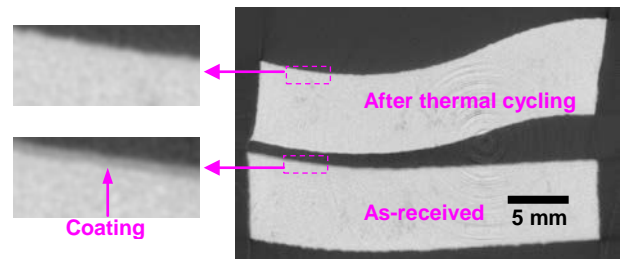


Figure 19. Typical x-ray CT slice of TBCs.

Correction of Ring Artifact in X-Ray CT Data

Ring artifacts in synchrotron CT data are observed as the darker/brighter semicircles that are more prominent near centers (see Fig. 16). This artifact is caused by the sensitivity variation of the

individual x-ray sensors during the x-ray scan period. Because it has well-defined characteristics, it may be removed through advanced image processing. One algorithm is being developed; a preliminary result is shown in Fig. 20. It is seen that most of the artifacts are removed. Such improvement may help for better identification of small and weak defects within material.

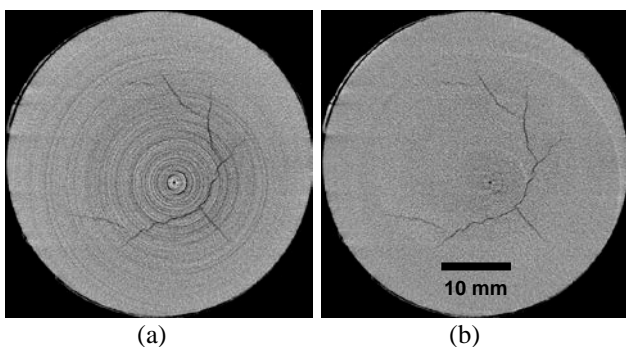


Figure 20. (a) Original and (b) ring-artifact removed x-ray images.

Ultrasonic inspection of Friction-Welded Joints

A phased-array ultrasonic system shown in Fig. 2 was utilized to inspect friction-welded joints between TiAl turbine wheel and Ti-alloy shaft. Because ultrasonic detection is based on reflection, it is important to align the ultrasonic probe in a direction so a reflection from a flaw may return to the probe. In this investigation, the welding crack oriented along the weld plane is examined using a 128-element phased-array probe. A schematic system setup is shown in Fig. 21a and a photograph of the experimental setup is in Fig. 21b. The phased-array probe scans the welding plane in both radial and circumferential directions, resulting in 2D scan images of the weld plane. This system, although in principle may not detect cracks perfectly aligned along the weld plane, should be able to detect real cracks that normally have imperfect crack planes.

Figure 22 is a C-scan image of the region ± 3 mm from the nominal weld interface of a defective weld sample, plotted as a function of radial distance from the outer edge on the vertical axis and angular position on the horizontal. This image shows a weld defect at $\sim 180^\circ$ and nominally 7-9 mm from the outer edge of the shaft. The defect appears to be composed of two separate features. This defect has been confirmed from x-ray CT data.

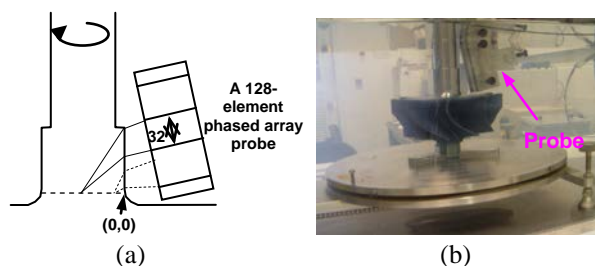


Figure 21. (a) Schematic and (b) photograph of an ultrasonic system to detect welding cracks.

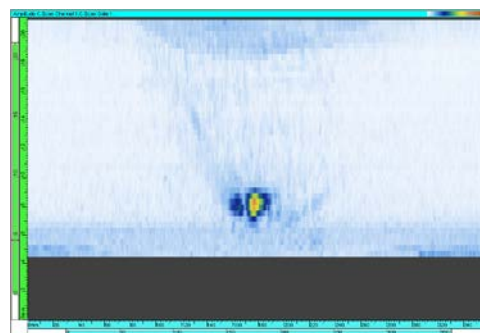


Figure 22. C-scan image of a weld interface, showing a weld defect at $\sim 180^\circ$ and nominally 7-9 mm from the outer edge of the shaft.

Conclusions

The primary effort in FY 2011 was focused on developing and evaluating a synchrotron x-ray CT system at ANL's APS for NDE characterization of various diesel engine materials and components, including turbocharger components made from light-weight materials, power modules, and TBCs. The system consists of an x-ray source with high peak energies (up to 225 keV) to penetrate thick metallic materials, and a detector (imager) with high spatial resolutions (5-50 μ m) to resolve small flaws. For NDE characterization of friction-welded joint between TiAl turbine wheel and Ti-alloy shaft, a calibration test demonstrated that the CT system has high spatial resolutions to detect welding cracks including the locations of crack tips. The experimental results from several weld samples showed that x-ray CT can be used to determine quantitatively the 3D configuration and dimensions of complex 3D cracks in the welding plane. For inspection of TiAl turbine-wheel cast, CT data revealed casting voids of various sizes and fill conditions throughout the cast volume. In addition, synchrotron x-ray CT was successfully used to

inspected power module and TBC samples. With the development of advanced data-processing algorithms to removing CT artifacts, it was demonstrated that significant improvement in image quality can be achieved, which will help for identification and quantitative analysis of detailed flaw structures within materials/components.

Phased-array ultrasonic method was investigated for NDE inspection of friction-welded joint between TiAl turbine wheel and Ti-alloy shaft. The developed system was demonstrated to be highly sensitive to detect welding flaws. Because ultrasonic method is of low-cost and fast, it can and has been used in industrial NDE inspections. By correlating ultrasonic data with x-ray CT data which contain detailed 3D information of flaw size, geometry, orientation, and location, accurate, reliable, and quantitative ultrasonic inspection can be achieved. This correlation is especially useful and necessary for inspection of complex material structures.

References

1. M.D. Kass, et al., "Materials Testing with ACERT Engine," *Annual Report for FY2008, Heavy Vehicle Propulsion Materials Program*.
2. H. Baur, et al., "Titanium Aluminides for Automotive Applications," *Gamma Titanium Aluminides 2003*, pp. 23-31, The Minerals, Metals & Materials Society, 2003.
3. Nan Yang, et al., "Development of Titanium Alloys for Heavy-Duty Diesel Engines," *Quarterly Progress Report for April through June 2005, Heavy Vehicle Propulsion Materials Program*.
4. N. Nozawa, et al., "Development of Power Control Unit for Compact-Class Vehicle" *SAE International Journal of Passenger Cars - Electronic and Electrical Systems*, v 2, n 1, p 376-382, 2009.
5. J.G. Sun, "NDE Development for ACERT Engine Components," *Annual Report for FY2010, Heavy Vehicle Propulsion Materials Program*.

Presentations and Publications

J.G. Sun, "Nondestructive Evaluation of Ceramic Materials by Thermal Tomography," presented at the 35th International Conference and Exposition on Advanced Ceramics and Composites, Daytona Beach, FL, January 23-28, 2011.

Z.P. Liu, J.G. Sun, and Z.J. Pei, "Cross-Polarization Confocal Imaging of Subsurface Flaws

in Silicon Nitride," *Int. J. Appl. Ceram. Technol.*, Vol. 8, No. 2, pp. 411-422, 2011.

J.G. Sun, "Quantitative Thermal Tomography Imaging of Complex Material Structures," paper presented at the 38th Annual Review of Progress in Quantitative Nondestructive Evaluation, Burlington, VT, July 17-22, 2011.

J.G. Sun, J.A. Kropf, D.R. Vissers, W.M. Sun, J. Katsoudas, N. Yang, and D. Fei, "Synchrotron X-Ray CT Characterization of Friction-Welded Joints in TiAl Turbocharger Components," paper presented at the 38th Annual Review of Progress in Quantitative Nondestructive Evaluation, Burlington, VT, July 17-22, 2011.

J.G. Sun, "Thermal Imaging Measurement Accuracy for Thermal Properties of Thermal Barrier Coatings," in *Ceramic Eng. Sci. Proc.*, eds. S. Widjaja and D. Singh, Vol. 32, no. 3, pp. 15-22, 2011.

Agreement 18571 – Materials Issues Associated with Exhaust Gas Recirculation Systems

M. J. Lance, C. S. Sluder, H.Z. Bilheux#, J. Gregor[‡], and M.K. Ferber*

Ceramic Science and Technology Group

Oak Ridge National Laboratory

P.O. Box 2008, MS 6068, Bldg. 4515

Oak Ridge, TN 37831-6068

(865) 241-4536; fax: (865) 574-6098; e-mail: lancem@ornl.gov

** Fuels, Engines and Emissions Research Center, ORNL*

Neutron Scattering Science Division, ORNL

‡ Dept. of Elec Engr and Computer Science, University of Tennessee

DOE Technology Manager: Jerry L. Gibbs

(202) 586-1182; fax: (202) 586-1600; e-mail: Jerry.gibbs@ee.doe.gov

ORNL Technical Advisor: David P. Stinton

(865) 574-4556; fax: (865) 241-1034; e-mail: stintondp@ornl.gov

Contractor: Oak Ridge National Laboratory, Oak Ridge, Tennessee

Prime Contract No.: DE-AC05-00OR22725

Objectives

- Provide information to industry specialists about fouling deposit properties so as to enable improved models and potential design improvements to reduce fouling and its impact on the performance of EGR (exhaust gas recirculation) coolers.

Approach

- Assemble EGR engineers from member companies of the Diesel Crosscut Team to serve as an advisory board for this project.
- Develop a bench-top flow reactor for aging EGR deposits in a controlled environment.
- Obtain and evaluate EGR coolers from industry members that exemplify plugging failure.

Accomplishments

- Characterized industry-provided deposits using neutron tomography.
- A bench-flow tube reactor was designed and set-up which will allow for aging of deposits under controlled conditions.
- Four of the EGR team members have provided seven real-world coolers for a second round of analysis that will focus on EGR cooler plugging.

Future Direction

- The 2nd round of industry-provided coolers will be characterized.
 - Use exhaust sampler system to generate PM deposits that will be aged in controlled conditions using a bench-flow reactor so as to evaluate the effect of water, hydrocarbon and cycling on deposit properties.
 - Thermo-mechanical properties of lacquer-like deposits will be compared to dry PM deposits.
-

Introduction

High-pressure exhaust gas recirculation (HP-EGR) is the dominant NO_x -reduction technology used by the diesel engine community today. With EGR, some fraction of the exhaust gas is recirculated back into the combustion chamber where it has the effect of reducing the amount of oxygen available for combustion, thereby limiting the formation of oxides of nitrogen. In addition, the exhaust gas is usually cooled by a heat exchanger (or cooler) so as to increase the density of the intake charge. However, there is also particulate matter (PM) in the exhaust gas and this PM is light enough that when it passes through the EGR cooler, it will migrate to the cooler wall through thermophoresis. The resulting deposit that forms has a very low density owing to the string-of-pearls nanostructure of diesel PM. Indeed, the cooler deposit is an ideal thermal insulator with a thermal conductivity comparable to Styrofoam [1]. As the thickness of the deposit increases, the effectiveness of the EGR system goes down due to the inability to cool the exhaust gas. This is known as cooler fouling.

In February of 2009, a team consisting of engineers responsible for EGR systems was assembled from nine diesel engine manufacturers: Caterpillar, Cummins, Detroit Diesel, Ford, GM, John Deere, Navistar, PACCAR (now DAF Trucks) Volvo/Mack and one heat exchanger supplier, Modine. They were surveyed to identify the biggest problem facing EGR systems. The clear winner was EGR cooler fouling. The EGR Team then recommended the purchasing of a traditional engine-on-dynamometer to generate fouling deposits on model tubes. They also agreed to send a real-world cooler from an actual engine that had seen enough operation to categorize it as 'half-useful-life'. Of the 10 team members, the 8 companies that currently use HP-EGR all sent at least one cooler for analysis with the data obtained to be shared with the entire team. A second round of seven coolers that

have more details concerning operating conditions have recently been obtained from 4 EGR team members and are in the process of being analyzed.

Experimental Approach

A GM 1.9 L engine on a Drivven controller is currently operational in standard and PCCI modes and is being used as a pollution generator in order to foul model $\frac{1}{4}$ -inch square tubes. The EGR team recommended this set-up as opposed to the proposed genset as an exhaust generator. Fig. 1 shows the model tube assembly is attached to the exhaust of the engine to generate deposits. This system is based on a previous sampling system designed at ORNL that directs exhaust gas through square tubes that are externally-cooled to temperatures similar to those existing in actual EGR coolers.



Figure 1: Two views of the heat exchanger used to generate deposit samples.

Following deposit formation using the engine and tube sampler, a bench flow reactor is used for accelerated aging of deposits at controlled temperatures and gas composition. This allows for the characterization of microstructural changes that occur in the deposits due to engine transients, and water/HC condensation. Fig. 2 shows the tube reactor system that consists of a gas manifold supplied by two digital mass flow controllers flowing air or bottled gases, a water vapor introduction system, a gas heater and a water jacket to cool or heat the sample tube. The same kind of heat exchanger shown in Fig. 1 and used to form deposits with the engine is used to age deposits with the tube reactor. The system is equipped with multiple thermocouples to monitor gas temperature before and after the sample and the cooling water entry and exit temperatures as well as the furnace temperature.

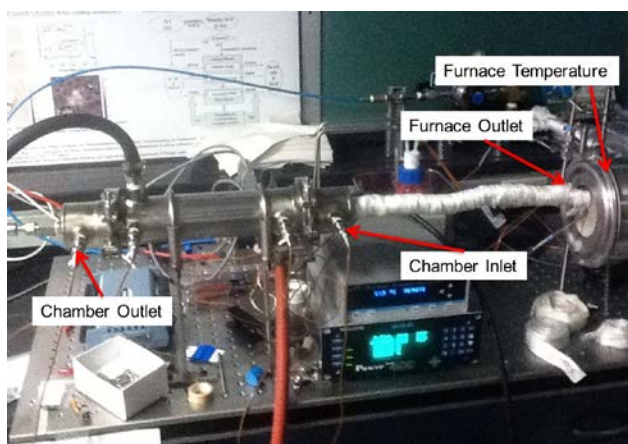


Figure 2. The tube reactor system.

The effectiveness (ε) of a heat exchanger is defined as the actual heat transfer divided by the maximum possible heat transfer. This can be further defined in terms of temperatures according to Equation (1):

$$\varepsilon = (T_{Gas\ In} - T_{Gas\ Out}) / (T_{Gas\ In} - T_{Coolant\ In}) \quad (1)$$

The effectiveness, then, is the ratio of the actual change in temperature of the EGR gas stream divided by the maximum change in temperature that

the EGR gas stream could have experienced by being cooled to the temperature of the coolant. Since actual heat transfer rate for a given heat exchanger depends upon the flow rates and properties of the gases and coolants, effectiveness also varies with these characteristics independent of fouling. Nevertheless, it is a useful measure of performance as it is easily calculated from measurable quantities.

Table 1 shows the effectiveness of the tube reactor under varying gas flow, inlet and coolant temperature conditions. The effectiveness of the heat exchanger improves with lower flow rates due to the fact that the gas has more time to be cooled. Increasing the coolant temperature also improves the effectiveness since the gas doesn't have to be cooled as much. The last condition in Table 1 is a fouled tube which causes the effectiveness to drop 3% which shows the effect of the deposit on the heat transfer.

Table 1: Effectiveness of bench-flow reactor under various conditions.

Condition	Air Flow (SLPM)	Coolant Temperature (°C)	Furnace Temperature (°C)	Inlet Gas Temperature (°C)	Outlet Gas Temperature (°C)	Effectiveness (%)
Empty	20.0	45.0	606.3	383.2	74.8	91.2
Empty	15.0	44.9	600.7	369.4	69.0	92.6
Empty	10.0	45.5	606.8	320.5	61.0	94.3
Empty	15.0	65.1	599.5	383.3	87.2	93.0
Empty	15.0	91.1	600.7	389.6	106.1	95.0
Fouled	15.0	43.8	595.9	360.6	76.9	89.6

Results

Laboratory-Generated Samples

Two baseline conditions were formed using the tube sampler and the 1.9 L engine that broadly represent light-duty and heavy-duty operating conditions. The light-duty condition was 2.6 Bar BMEP, ~225°C inlet temperature, 144 ppm HC, 95 ppm NO_x, and 1.36 FSN. The heavy-duty condition was 7-8 Bar BMEP, ~325°C inlet, 28 ppm HC, 310 ppm NO_x, 0.97 FSN. Both deposits were generated at 1500 rpm and a EGR flow rate of ~30 SLPM for 4 hours. Coolant temperature was 90°C. Fig. 3 shows fracture surfaces for both deposits. The light-duty condition was thinner (123

$\pm 28 \mu\text{m}$) compared to the heavy-duty condition ($135 \pm 24 \mu\text{m}$) and was also denser, 0.023 g/cm^3 compared to 0.0133 g/cm^3 . This higher density will increase the thermal conductivity of the deposit which likely produced the measured lower effectiveness loss of the light-duty deposit; 11.4% compared to 13.7% for the heavy-duty. The light-duty deposit also had a clumpier surface whereas the heavy-duty sample appears more dendritic. These longer dendrites of the heavy-duty sample apparently allow more large-scale pores to form during deposition. Fig. 4 shows one of the pores from the heavy-duty deposit. Large-scale pores that are >1000 times larger than the primary PM size produce a deposit with a very high porosity and correspondingly a low thermal conductivity. This project will proceed by addressing both the light-duty and heavy-duty diesel communities using these two baseline conditions as representative starting conditions. Using the tube reactor, these two deposits will be exposed to different exhaust conditions in order to understand the change in deposit properties resulting from engine transients, hydrocarbon and water condensation.

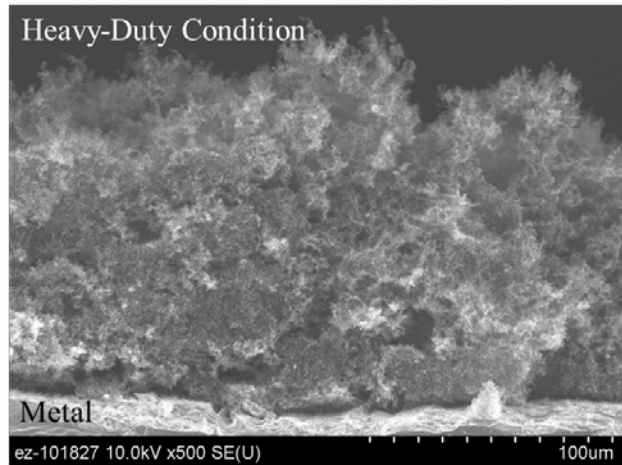
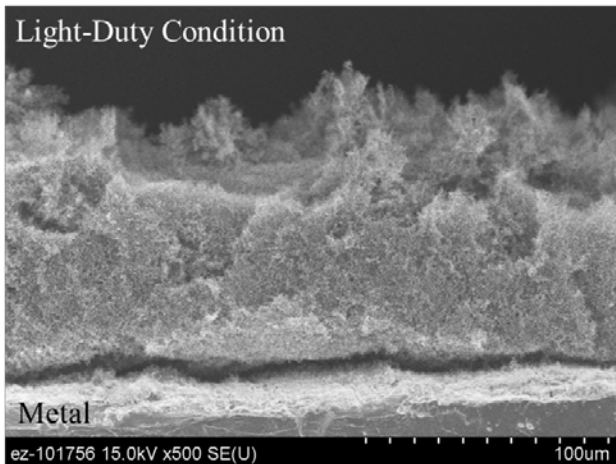


Figure 3. Baseline deposits formed using tube sampler

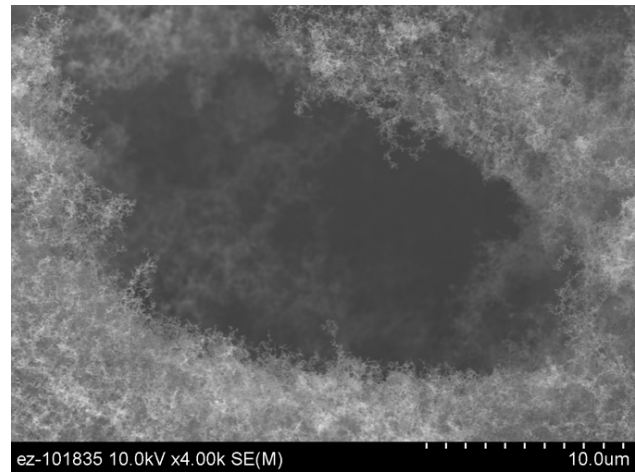


Figure 4. Large-scale pore from the heavy-duty deposit.

Industry-Provided Samples

Eight companies provided twelve coolers for forensic analysis of the cooler deposits, the results of which are shown in Table 2. Every cooler showed a gradient in the deposit microstructure from coarse to fine moving away from the metal. This effect may be caused by the collapsing of the PM nanostructure due to hydrocarbon and/or water condensation during operation. Also, most coolers showed similar deposit removal mechanisms; mud-cracking, spallation and grooves along the gas flow direction. The results of this survey were published[2] however, a major criticism of this work was that little information was provided about the operating conditions of the engines that produced these EGR coolers. Therefore, a second

round of coolers was requested except this time with more information about the origins of the coolers. Specific operating conditions were requested that would represent common fouling conditions of coolers. Seven more coolers are now being analyzed in this 2nd round of testing. Most of the coolers represent low temperature idling conditions (typical of a school bus, for instance) which will provide insight into a different failure mode than what has been studied to date.

Table 2. Summary of observations on industry-provided coolers.

Observation	1	2	3	4	5	6	7	8	9	10a	10b
Plugging			X	X							
Corrosion	X								X		
Density Gradient	X	X	X	X		X	X	X	X	X	X
Mudcracking	X	X	X			X	X	X			
Spallation	X	X						X			
Grooving		X					X	X	X		
Silicates							X				

Neutron tomography is being investigated as a way of non-destructively imaging the deposit on the inside of heat exchangers. Since neutrons transmit through metal and are attenuated by hydrogen, hydrocarbon in the deposit will preferentially block neutrons from transmitting to the detector. Samples are rotated and 720 images are collected and reconstructed to provide a 3-D tomograph of the sample. Fig. 5 shows a slice taken from a tomographic set of a cylindrical tube geometry cooler that has a single spiral running down the length of the tube. For this slice, it was determined that the deposit was thinner on top of the turbulator (the flat region of the tube) but thicker on either side. Fig. 6 shows a 2 dimensional map of the same sample. Here delaminations between the deposit and the metal wall can be observed. These results show that neutron tomography can be used to observe the location of the deposit with respect to the cooler geometry and to identify potential deposit removal mechanisms.

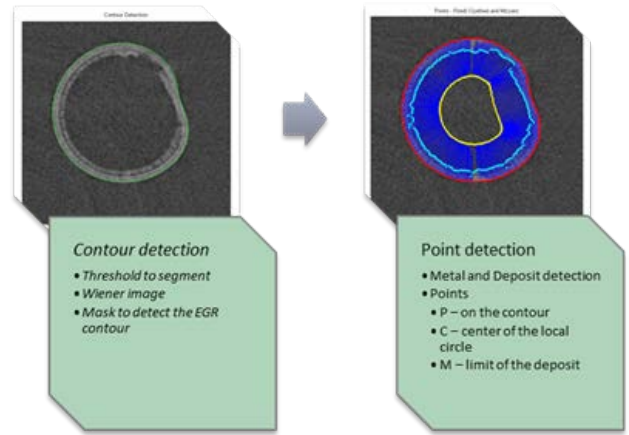


Figure 5. One neutron image generated from a 3-D tomographic set of a tube from cooler #1. The image is processed in order to measure the thickness of the deposit as a function of the radius around the tube.

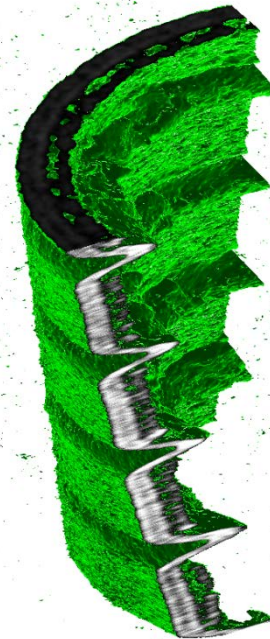


Figure 6. One-quarter isosurface of cooler #1.

All remaining samples provided by the EGR team (1st round of samples) were imaged using neutron tomography at HFIR (High-Flux Isotope Reactor). Dr. Jens Gregor at the University of Tennessee was contracted to develop a new code to reconstruct the 3-D tomographic

sets from the raw images that helps to reduce the number of artifacts. Fig. 7 shows one slice taken through two EGR sections using the previous commercially-available reconstruction code that produces lines emanating from the corners of the samples. Using a new PSIRT reconstruction code, Dr. Gregor has successfully eliminated these artifacts as shown in Fig. 8.

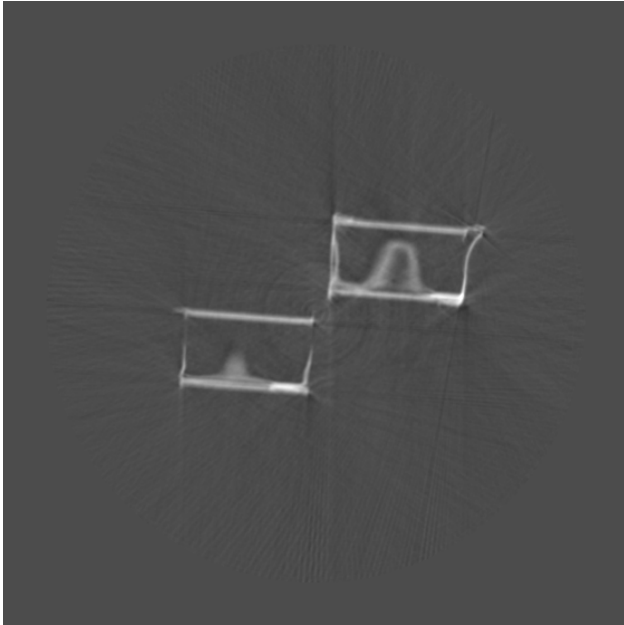


Figure 7. Two EGR sections imaged using neutron tomography. These slices were reconstructed using a Feldkamp algorithm which results in streaks in the image.



Figure 8. The same slices in Fig. 7 except reconstructed using the PSIRT reconstruction algorithm.

Conclusions

A team of industry advisors has been assembled that will help guide future research directions of this pre-competitive research.

Laboratory-generated deposits were successfully formed on model cooler tubes using two standard operating conditions.

A bench-top tube reactor is now completed and being tested.

Forensic analysis of cooler deposits may allow one to infer deposit formation and removal mechanisms.

Neutron tomography was shown to be a valuable tool for imaging EGR cooler fouling and will have broad application to many other emission control technologies.

References

1. Michael J. Lance, C. Scott Sluder, Hsin Wang, John M.E. Storey, "Direct Measurement of EGR Cooler Deposit Thermal

- Properties for Improved Understanding of Cooler Fouling,” SAE 2009-01-1461 April 2009.
2. Michael Lance, Charles Scott Sluder, John M.E. Storey, and Samuel A. Lewis “Characterization of Field-Aged EGR Cooler Deposits,” SAE 2010-01-2091.

Publications and Presentations

- Michael J. Lance, C. Scott Sluder, Hassina Bilheux, Keely Willis, Andrea Strzelec, John M.E. Storey, and Samuel A. Lewis Jr., “Characterization of Field-Aged Exhaust Gas Recirculation Cooler Deposits” presented at 2010 DEER conference.
- Michael J. Lance, Hassina Bilheux, Keely Willis, Andrea Strzelec, C. Scott Sluder, “Characterization of Field-Aged Exhaust Gas Recirculation Cooler Deposits using Neutron Tomography,” presented at the Global Powertrain Conference, Troy, MI, 2010.
- Diesel Crosscut Team Meetings: January 13th, 2011; March 17th, 2011; July 20th, 2011.

Agreement 19192 - Titanium for Vehicle Propulsion Applications

Principal Investigators: Curt A. Lavender and Vineet Joshi

Energy Materials Group

Pacific Northwest National Laboratory

PO Box 999, MS K2-44

Richland, WA 99352

(509) 372-6770; fax: (509) 375-2186; e-mail: curt.lavender@pnl.gov

(509) 372-6211; fax (509) 375-2186; e-mail: vineet.joshi@pnl.gov

Yong-Ching Chen

Cummins Inc.

(812) 377-8349; e-mail: yong-ching.c.chen@cummins.com

Vladimir Moxson

ADMA Products Inc.

(330)650-4000; e-mail: moxson@admaproducts.com

DOE Technology Manager: Jerry L. Gibbs

(202) 586-1182; fax: (202) 586-1600; e-mail: jerry.gibbs@ee.doe.gov

Field Technical Manager: Dean Paxton

(509) 375-2620; fax: (509) 375-2186; e-mail: dean.paxton@pnl.gov

Contractor: Pacific Northwest National Laboratory

Contract No.: DE-AC05-76RL01830

Objective

- Increase the efficiency of vehicle engines by reducing the mass of rotating and reciprocating components through the use of titanium and titanium alloys.
- Increase the efficiency of vehicle engines by increasing the operating temperature of selected components through the use of titanium and titanium alloys.
- Predict the engine efficiency improvements made possible through the use of titanium.

Approach, including industrial partner/collaborator and path to technology transfer and commercialization

- Develop, prototype, and evaluate the performance of components at Cummins Inc. to ensure that components developed produce the predicted performance improvements in actual engine systems.
- Use suppliers to fabricate most titanium components to ensure that processing used is prototypic of a full-scale production process.

Milestone, Metrics and Accomplishments

- The Ti6Al4V alloy produced from TiH₂ powder was hot-worked in the alpha plus beta phase field and heat treated to produce a highly refined duplex structure. The fatigue life from the Ti6Al4V was measured and matched the wrought processed handbook values for the alloy.
- The low-cost beta titanium alloy Ti1Al8V5Fe processing schedule was enhanced and exhibited fatigue properties equal to the reported values from wrought processing.
- Two engine components have been identified for further development and ultimately systems testing at Cummins Inc.

Future Direction

- Complete fabrication of forge blanks of low-cost Ti6Al4V from titanium hydride for rotating component applications.
- Complete fabrication of bar stock of low-cost Ti1Al8V5Fe from titanium hydride for reciprocating component applications.
- Perform a modeling study on the effect of titanium on the fuel economy of a vehicle through substitution of materials used in propulsion applications.
- Complete cost analysis of the ADMA Products, Inc. process for Ti6Al4V and Ti1Al8V5Fe production.

Introduction

This project is a collaborative effort between Cummins Inc., ADMA Products, Inc., and Pacific Northwest National Laboratory (PNNL) focused on the development and evaluation of low-cost titanium components produced by emerging production technologies.

Over the past 30 years, many original equipment manufacturers, researchers, and titanium companies have demonstrated the ability of titanium to increase internal combustion engine efficiency. However, titanium has only been used in a limited number of production applications and sometimes only over limited production periods. Even though performance benefits resulting in engine efficiency improvements of as much as 20% have been demonstrated, the high cost of producing titanium components using current technologies has been a limiting factor.

In recent years, the U.S. Department of Defense (DOD) and the commercial aerospace industry (the largest consumers of titanium) have become increasingly reliant on titanium to meet performance needs. A study commissioned by the Defense Logistics Agency revealed that not only was titanium raw material costly, but the manufacturing processes used to produce titanium components often had production yields of 5%, meaning the DOD was buying as much as 20 times the titanium as was used in the final application. To address this cost, the Defense Advanced Projects Agency (DARPA) began an activity to reduce titanium component cost. The DARPA project started many activities, new low-cost-titanium development projects, and stimulated titanium production activity

throughout the world—with as many as 20 methods under development.

In prior reporting periods, this project was focused on assessing “emerging” low-cost development activities by using technical evaluation and cost modeling to analyze the products for suitability in vehicle and engine applications. It was determined that two of the processes, developed by International Titanium Powder and ADMA Products, Inc., could produce titanium raw materials at costs that approach those needed to achieve widespread titanium usage and have an impact on the overall fuel economy in the United States.

The next step for these emerging processes is to identify applications and create a demand for the titanium to move these applications from development to full-scale production, thus meeting the cost projections associated with high-volume production.

The purpose of this project is to identify and demonstrate applications within the vehicle propulsion system which, when titanium is used, would produce an increase in engine and vehicle efficiency. The project will be performed in three topical areas: the first is focused on vehicle propulsion system modeling, the second is focused on technical development of the titanium semi-finished products, and the third is focused on technical demonstration of the components in systems level tests.

The goal of the project is to use titanium, where appropriate, to increase the efficiency of vehicle propulsion systems. This report summarizes progress toward that goal.

Approach

This project will increase vehicle efficiency through use of titanium by 1) identifying—through vehicle system models—critical components to be made from titanium that will impact efficiency; 2) demonstrating that those titanium components can be made from emerging low-cost processing; and 3) demonstrating efficiency improvements through systems level tests at Cummins Inc.

Vehicle system modeling will be performed at the University of Michigan at Dearborn (UMD) by disassembling two engines—one fueled by diesel and the second by gasoline. Each component will be weighed and measured, then analyzed and redesigned for titanium to determine the impact of the component on efficiency. A component by component analysis will then be conducted to determine the overall vehicle efficiency impact. Components will be manufactured by a combination of suppliers and PNNL to ensure the components developed can be produced in commercial settings. Systems level component testing will be carried out by Cummins Inc. using the appropriate engine test system.

Results and Discussion

Vehicle System Modeling: In the previous year, UMD analyzed the mass of the Toyota Echo engine (Figure 1) a modern, multi-valve 80 kW engine with variable valve timing and multipoint electronic fuel injection. The engine is representative of a high-efficiency modern internal combustion engine. The next step in vehicle system modeling will be to analyze an engine provided by Cummins Inc. Cummins will provide an engine during fiscal year (FY) 2012 for disassembly and analysis.



a)



b)

Figure 1. Toyota 1.5 liter VVT-I engine a) shown in the vehicle and b) outside the vehicle, before dismantling into components

Component Fabrication: During this reporting period, component fabrication focused on two semifinished products that would be used for titanium part fabrication. The first was a large, blocky, pressed and sintered part from the Ti6Al4V alloy and the second was a bar stock from a beta alloy.

The Ti6Al4V was pressed and sintered into a right cylinder that could be used for components that require forging and machining to produce the final shape. The challenge with producing a forged part from a pressed and sintered block is achieving adequate fatigue strength. During the previous reporting period, it was determined that the interstitial level for the Ti6Al4V would be established by the tensile strength levels and rotating beam fatigue (RBF) life.

The fatigue testing of the as-sintered and HIPed Ti6Al4V from TiH₂ was determined to be nearly

identical to a wrought processed Ti6Al4V alloy, indicating that fundamentally the alloy processed from the TiH₂ can be made to be identical to the wrought material. However, the as-sintered microstructure shown here in Figure 2 does not produce the high cycle fatigue typically desired in propulsion applications.

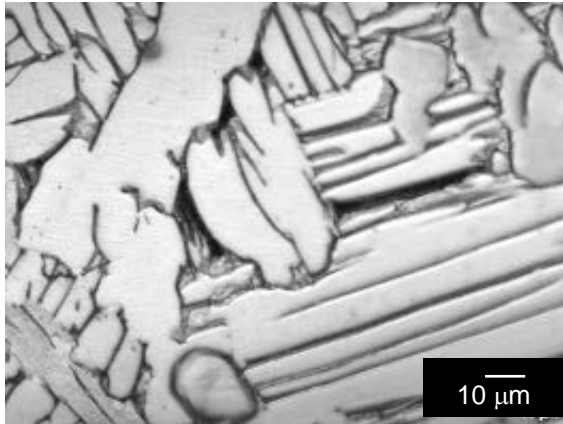


Figure 2. Typical basket-weave microstructure observed in optical microscopy for the low-cost TiH₂ powder produced Ti6Al4V alloy

To develop the correct microstructure for propulsion applications, the Ti6Al4V was subjected to hot-working and heat treatment to refine and develop a duplex microstructure. Hot forming in the alpha plus beta phase field resulted in transformation of the structure to the fine lamellar structure shown in Figure 3.

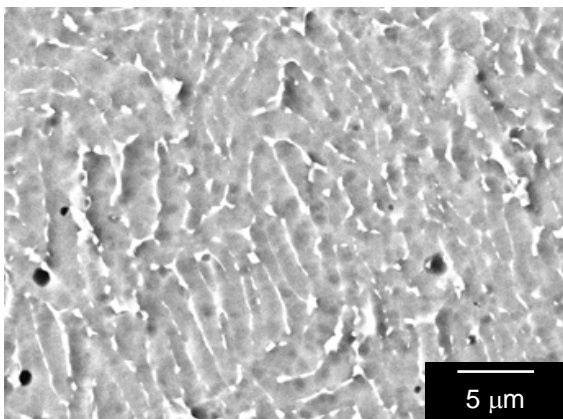


Figure 3. Highly refined lamella microstructure observed in the low-cost TiH₂ powder produced Ti6Al4V alloy after hot-working in the alpha plus beta phase field

The hot working reduced the lamella size from 10 to 2 micrometers (μm). In addition to lamella size reduction, the grain size was reduced from approximately 100 μm to approximately 35 μm . The hot-worked material was then subjected to a solution heat treatment and age heat treatment to develop the fine duplex structure shown in Figure 4.

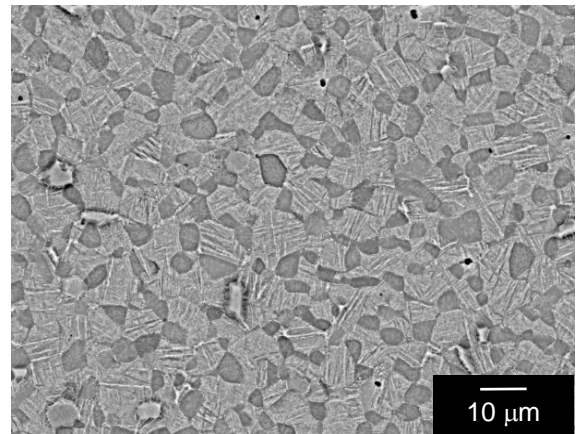


Figure 4. Duplex microstructure in the low-cost TiH₂ powder produced Ti6Al4V alloy after hot-working in the alpha plus beta phase field and solution heat treatment and aging

The duplex structure shown in Figure 4 exhibits the equi-axed alpha of approximately 5 μm and a very fine submicron lamella. The two new microstructures are known to produce increased high-cycle fatigue life in Ti6Al4V.

RBF testing was performed on the hot-worked and hot-worked plus heat treated Ti6Al4V and is summarized in Figure 5.

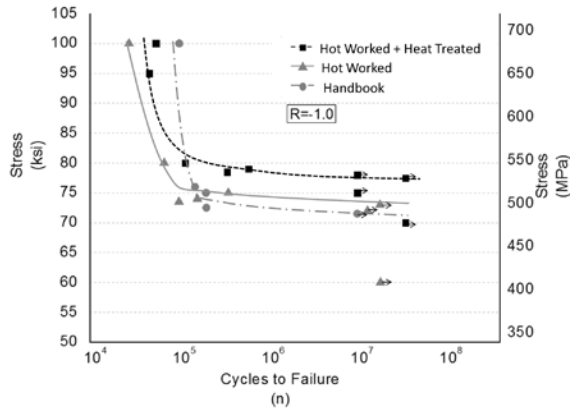


Figure 5. Rotating beam fatigue stress versus cycles to failure curve for the low-cost TiH₂ powder produced Ti6Al4V alloy in the hot worked and hot worked plus solution and aging heat treatment. Arrows indicate that the sample did not fail and that the test was stopped.

The RBF testing showed the hot-worked and hot worked plus heat treated Ti6Al4V produced from the TiH₂ had performance equal to or greater than that for wrought-processed Ti6Al4V with equivalent microstructure. This important result shows that, when processed appropriately, the low-cost Ti6Al4V produced TiH₂, which can meet the high-cycle fatigue life desired for propulsion applications. The next step of the Ti6Al4V development is to produce Ti6Al4V hot worked blanks of sufficient size for Cummins Inc. to fabricate components for testing.

The second phase of the component development was focused on production of a low-cost beta alloy bar stock using the TiH₂ powder. The alloy chose was the Ti1Al8V5Fe alloy due to low cost alloying addition of Fe at a level not possible with the ingot processing due to Fe segregation. In the previous reporting period, the alloy was processed using a process previously developed by Mallory Sharon in the 1950s to demonstrate that the high strength properties could be reproduced using low cost TiH₂.

The initial phase of the Ti1Al8V5Fe work was successful and the properties from TiH₂ were identical to those developed by Mallory Sharon. However, the microstructure contained an excessive amount of grain boundary alpha and

as expected, the fatigue life was poor. A second batch of billets were prepared and rolled using a schedule to prevent excessive grain boundary alpha. This second “phase” produced very little grain boundary alpha as shown in Figure 6, and second phase materials were subjected to RBF testing using heat treatments similar to those previously reported.

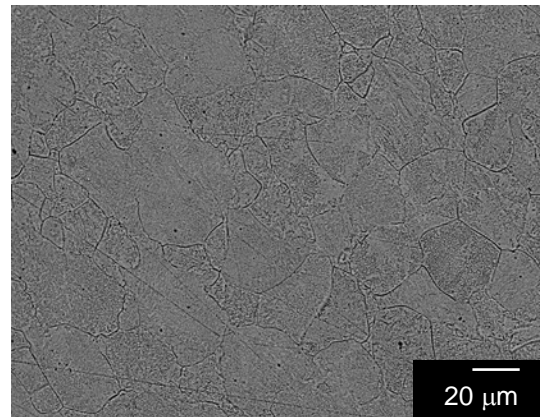


Figure 6. Optical micrograph of the as-hot-rolled microstructure for the Ti1Al8V5Fe low-cost beta alloy produced from the TiH₂ powder

The RBF results, summarized in Figure 7, were higher than those reported in the literature for the alloy (perhaps due to the elimination of Fe segregation?), and the Ti1Al8V5Fe alloy produced from TiH₂ solution heat treated at 787°C and aged at 482°C exhibited at threshold stress of greater than 600 MPa.

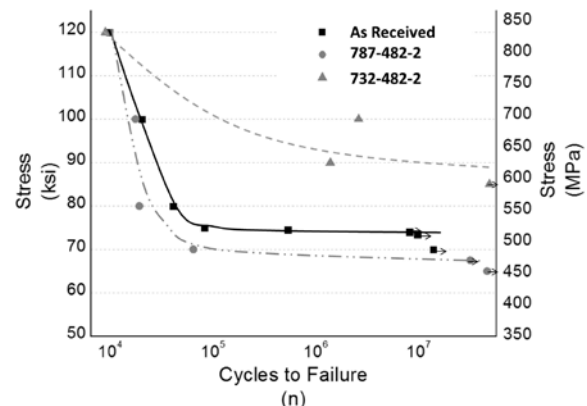


Figure 7. Rotating beam fatigue stress versus cycles to failure curve for the Ti1Al8V5Fe low-cost beta alloy produced from the TiH₂ powder. Arrows indicate that the sample did not fail and the test was stopped.

Cummins Inc. has identified a potential application within a propulsion system and full-scale component fabrication has been initiated.

Cost Analysis of ADMA Processing: In previous reporting periods, technical challenges had made cost analysis difficult because it was not clear what additional processing steps, such as hot isostatic pressing, would be required to make the ADMA Products, Inc. material perform in propulsion applications. The success this year with refining the processes and producing the desired microstructures now make a cost model feasible. Preliminary cost modeling indicate that the ADMA Products, Inc. process for the Ti6Al4V alloy may produce propulsion grade blanks for less than 40% of the current cost with a cycle time reduction from more than 55 weeks to less than 3 weeks. In addition, process analysis will be performed next year and will be finalized as the performance is better understood.

Component Testing: Cummins Inc. has identified components of interest and property targets for both the Ti6Al4V and Ti1Al8V5Fe alloys. Future work will be focused on producing the semifinished products required for the Cummins Inc. components.

Conclusions

During this reporting period, the following conclusions were reached:

- The challenges at developing high fatigue performance from alloys produced from the TiH₂ powders have been addressed by process refinements. The fatigue life for both the Ti6Al4V and Ti1Al8V5Fe produced from the TiH₂ now meet the thresholds normally observed in wrought processing.
- Cost analysis has been initiated and indicates the ADMA Products, Inc. processed TiH₂ may reduce component cost by 60% and reduce cycle times by more than a factor of 30.

Also during this period, development activities were initiated at UMD to determine the maximum impact that titanium can have for vehicle efficiency. Cummins Inc. also identified components for vehicle system testing during the next fiscal year.

Presentations/Publications/Patents

- Lavender CA, YC Chen, and VS Moxson. 2011. "Low Cost Titanium – Propulsion Applications." Presented by Curt Lavender (Invited Speaker) at DOE-VTP Merit Review, June 10, 2010, Washington D.C.
- Lavender CA (Invited Speaker), E Stephens, E Nyberg, V Moxson, and V Duz. 2011. "Development of High Strength Titanium Alloy Bar Stock from TiH₂ Powder." Presented by Curt Lavender (Invited Speaker) at TMS Annual Meeting, February 2011, Seattle, WA.
- Joshi V, CA Lavender, V Moxson, V Duz and E Nyberg. "Development of β and $\alpha+\beta$ Titanium Alloys Using a Low Cost TiH₂ Powder Feedstock." MS&T 2011 Conference & Exhibition, October 16-20, 2011, Columbus, Ohio.

Keywords

Titanium, titanium alloys, solid state consolidation, rod-rolling, beta titanium alloys, cold isostatic press and sinter, titanium alloy, and heat treatment.

Acronyms

FY: fiscal year

RBF: rotating beam fatigue

UMD: University of Michigan at Dearborn

Agreement 19202 – Titanium Friction and Wear: Surface Engineering of Connecting Rods and Other Bearing Components

Peter J. Blau and Dinesh Bansal*

Oak Ridge National Laboratory, P. O. Box 2008, Mail Stop 606, Oak Ridge, TN 37831-6063

**(865) 574-5377; fax: (865) 574-4913; e-mail: blaupj@ornl.gov*

DOE Technology Manager: Jerry L. Gibbs

(202) 586-1182; fax: (202) 586-1600; e-mail: Jerry.gibbs@ee.doe.gov

ORNL Technical Advisor: David P. Stinton

(865) 865-574-4556; fax: (865) 241-0112; e-mail: stintondp@ornl.gov

*Contractor: Oak Ridge National Laboratory, Oak Ridge, TN
Prime DOE Contract Number DE-AC05-00OR22725*

Objectives

- To increase the vehicle freight efficiency by substituting lightweight titanium (Ti) alloy moving parts and bearing surfaces into diesel engine and drivetrain components like connecting rods.
- To identify novel surface engineering approaches, including combinations of mechanical and diffusion treatments, that can reduce both friction and wear of commercial Ti alloys.

Approach

- Using an ASTM standard tribology test method, developed at ORNL under a previous DOE sponsored program, prescreen candidate surface treatments for a Ti-6Al-4V alloy and down-select the most promising of them for further investigation under simulative engine conditions.
- Design and build a computerized, variable load, sleeve bearing tester to evaluate the tribological performance of down-selected surface treatments for Ti alloys.

Accomplishments

- From over 20 candidate surface engineering treatments (including commercial and experimental surface treatments) down-selected five promising ones for further study. These included nitriding, oxygen diffusion treatment, and a commercial chromium nitride treatment.
- Completed mechanical design and construction of a variable-load bearing test (VLBT) apparatus.

Future Directions

- Using the VLBT complete engine oil-lubricated friction and wear tests on the most promising surface treatment options for Ti alloys.
 - Based on VLBT data, ASTM coupon test results, and detailed metallurgical studies of wear surfaces, prepare guidelines for the use of surface engineering treatments on Ti alloys for lightweight connecting rod bearings and related, friction and wear-critical engine components.
-

Introduction

The Department of Energy's heavy vehicle research and development plan has targeted a 50% increase in freight efficiency (measured in ton miles per gallon). A combination of approaches is being used to achieve this goal. This includes a reduction in parasitic losses (e.g., friction, aerodynamic drag, etc.), more efficient designs, and the use of lightweight structural materials in vehicles.

Properly processed and treated, titanium (Ti) based alloys are strong, corrosion-resistant, and lighter in weight than similarly-sized steel or cast iron parts. Once used mainly in aerospace components, Ti's use has expanded into areas as diverse as human joint replacements, dental implants, and sports equipment. Recent developments in processing raw materials promise to make Ti alloys more affordable, and thus expand their use into fuel-efficient heavy vehicles.

Despite their advantages, Ti alloys used on load bearing surfaces have a propensity for scuffing, galling, and adhesive wear. Lubricant formulations that were designed for ferrous alloys do not work on bare Ti surfaces. If, however, the friction and wear of Ti could be improved by surface engineering, there would be new opportunities to use these alloys in pistons, cam shafts, valves, valve guides, crank shafts, tappet shims, and connecting rod bearing surfaces.

Approach

A three-phased project plan is being conducted:

Phase I: Selection and bench-testing of candidate surface engineering treatments and coatings (completed in FY 2010).

Phase II: Design, construction, and use of a bearing simulator to impart variable loads, as would be seen by a large-end connecting rod bearing (FY2011-12).

Phase III: Preparation of engineering guidelines for use of surface engineered Ti in connecting rod bearings and related engine components subjected to rubbing contact.

Progress in FY 11

Down-selection of candidate surface treatments and coatings. Following a comprehensive literature review and discussions with suppliers, more than two dozen candidate surface treatment and coating approaches for Ti were initially considered. The FY 2010 annual report, and the first publication cited at the end of this report describe the sources of the materials and the test results in greater detail. In summary, materials, coatings, or treatments whose average three-test friction coefficients (lubricated) were less than 0.15, and which also survived 400 m sliding distance of an ASTM G133 test procedure were designated as having 'passed.'

Six materials passed:

- 1) CDA 932 bearing bronze (baseline)
- 2) DLC coating (from ANL)
- 3) TiN hard coating
- 4) CrN hard coating
- 5) Oxygen-diffusion treated Ti-6Al-4V
- 6) Nitrided Ti-6Al-4V

Evaluation of these six materials, coatings, and surface treatments has begun and will continue during FY 2011-12 using a specialized apparatus, described below.

Design and construction of variable load bearing tester (VLBT). The design and construction of the VLBT was completed and initial baseline experiments were performed. The test fixtures are shown in Figure 1. A robust, three-phase variable speed motor, controlled by a computer, rotates a 25.4 mm diameter steel rod that simulates an engine crankshaft. The flat test bearing surface is loaded against the shaft from underneath to permit lubricating it with oil in a cylinder-on-flat contact. A servo-actuator (at the upper right) applies the load through a lever and pivot bearing arrangement. A load cell mounted at one end of the load lever measures the normal force while another near the bearing specimen (center of the image) measures the friction force. Initial designs for the apparatus were modified to reduce the rotating inertial mass, to

improve alignment between the test specimens, and to simplify specimen mounting and removal.

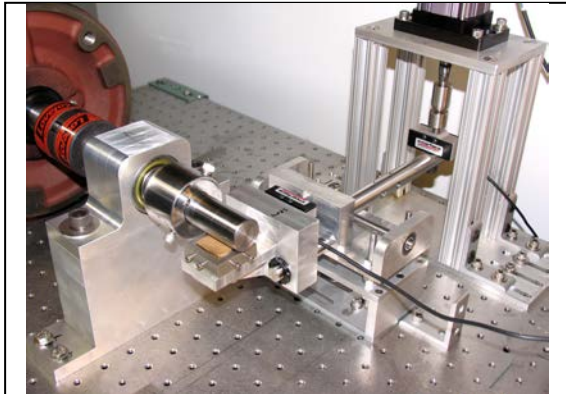


Figure 1. VLBT test apparatus. A bronze specimen is shown mounted below the steel shaft.

Initial VLBT experiments on CDA 932 bronze, Ti-6Al-4V (Ti64), and diamond-like-carbon (DLC) coated Ti64 were performed under a normal load of 115 N, sliding speed of 1 m/s (752 rpm) in the presence of 3-4 drops of fresh SAE 15W40 diesel engine oil, and for a sliding distance of 1000 meters. Non-treated Ti-6Al-4V and the DLC-coated Ti64 failed within first few minutes of sliding, but, as shown in Figure 2, the bronze specimen had much less wear even after 1 km of sliding.

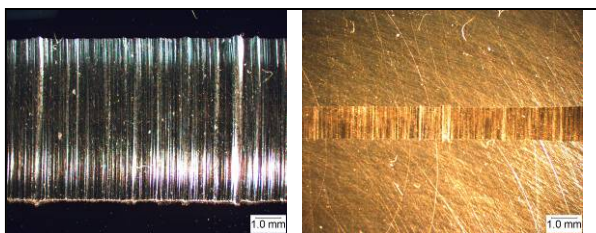


Figure 2. Wear scars on: (a) DLC coated Ti64, and (b) bearing bronze specimens.

The DLC coating performed well enough to pass the screening tests (reported in FY 2010), but it did not do as well in the more aggressive test conditions imposed by the VLBT. Observation of a worn DLC coating in a scanning electron microscope indicated different

forms of material damage at the leading and the trailing edges of the contact. For example, the appearance of the leading edge of the wear scar suggests brittle coating fracture (Fig. 3a) while the trailing edge (Fig. 3b) shows smeared substrate material and agglomerated debris.

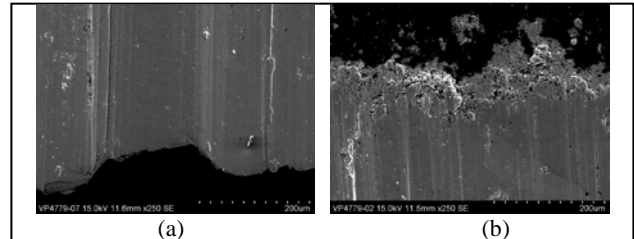


Figure 3. (a) Leading edge, and (b) trailing edge of contact on DLC coated Ti64 specimen.

In FY 2012, diesel engine operating information from Cummins will be used in conjunction with the techniques of design of experiments, to select appropriate loads, sliding speeds, and test duration for a fair evaluation of the down-selected surface treatments on the VLBT.

Optimization of oxygen diffusion treatment.

One of the surface treatments that passed acceptance criteria in Phase 1 was oxygen diffusion (OD). To further explore its potential benefits, three variants of OD were studied. After specimens were polished, they were heated in a furnace at 800 °C for 2 hours. Two specimens (OD-1, OD-2) were cooled in the furnace while a third (OD-3) was air cooled. The surfaces of OD-2 and OD-3 were further polished with 600-grit SiC to remove oxide scales. Figure 4 shows the variation in nano-hardness with depth on cross-sectioned OD specimens. Air cooling produced a much harder surface layer than the furnace cooled specimens.

Reciprocating sliding wear tests were run using a counterface of AISI 52100 steel ball under non-lubricated conditions. The load was 25 N, the stroke length was 10 mm, the frequency of oscillation was 10 Hz, and the sliding distance was 100 m. Figure 5 illustrates the variation in the coefficient of friction for each of the three variants of OD treatment. Table 1 lists the corresponding wear volumes.

Specimen OD-3, having the highest nanohardness number near the surface, yielded the smallest wear volume.

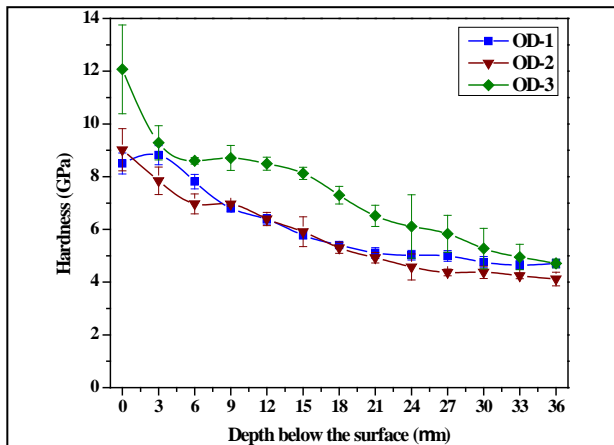


Figure 4. Variation in hardness along the depth for different variants of OD treated specimens.

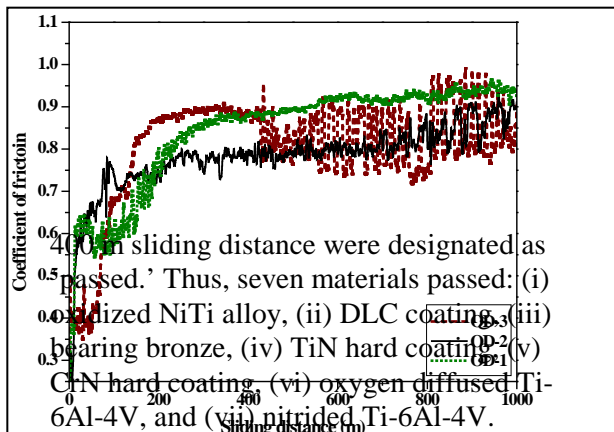


Figure 5. Variation in coefficient of friction during sliding for different OD treatments.

Table 1. Wear Volumes of OD-treated Ti64 Test Specimens (against 52100 steel)

OD Treatment	Wear volume (mm ³)
OD-1	2.64 ± 3.3
OD-2	0.042 ± 0.018
OD-3	0.008 ± 0.006

Figure 6 shows wear track cross-sections for the Ti64 specimens treated with different OD treatments. For OD-1 treated specimen gross

plastic deformation is observed while for the other two cases, mild wear is observed.

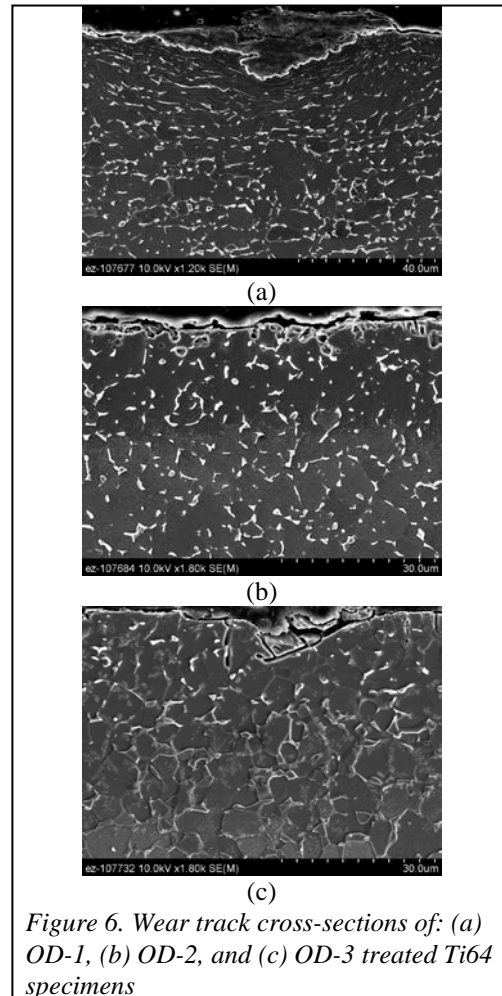


Figure 6. Wear track cross-sections of: (a) OD-1, (b) OD-2, and (c) OD-3 treated Ti64 specimens

Results obtained in FY 2011 illustrate an important principle for surface treatment selection; namely, that it is unwise to conclude that one or another type of treatment or coating will or will work in an application based on limited testing of only one variant of that treatment. In fact, the relative friction or wear rankings of a set of candidate surface engineering approaches could change after each has been optimized for that application.

Future Work

- Determination of appropriate parameters for testing different Ti surface treatments on the

variable load bearing tester (VLBT) to simulate typical engine conditions.

- Conduct VLBT tests on leading candidates for Ti surface enhancement under variable loads and speeds.
- Conduct an optimization study on one or more down-selected surface treatments.
- Prepare guidelines for the use of Ti surface treatments on large-end bearings and other tribosurfaces of engine parts.

International, Materials Science and Technology 2011 Conference, Oct. 17-21, Columbus, OH.

Summary and Conclusions

- Over 20 candidate materials were selected, obtained, and evaluated using the ASTM G133 friction and wear test method. A diesel engine drain oil was used as the lubricant. Five of these were down-selected for studies during FY 2012.
- A variable-load, friction and wear tester to simulate the interfacial conditions in bearings for connecting rods has been completed and will be used during FY 2012.
- Based on bench tests, the most promising treatments for Ti-6Al-4V were a nitriding treatment, an oxygen-diffusion treatment, a chromium nitride coating, and a low-friction diamond film. Initial VLBT tests performed in FY 2011, however, indicated less favorable behavior for the DLC-coated Ti alloy than that observed during the earlier tests.

Publications/Presentations

- 1) D. G. Bansal, O. L. Eryilmaz, and P. J. Blau (2011) "Surface engineering to improve the durability and lubricity of Ti-6Al-4V alloy," presented at the 18th International Conference on Wear of Materials, Philadelphia, PA, April 3-7.
- 2) D. G. Bansal, O. L. Eryilmaz, and P. J. Blau (2011) "Surface engineering to improve the durability and lubricity of Ti-6Al-4V alloy," *Wear*, Vol. 271, pp. 2006-2015.
- 3) D. G. Bansal and P. J. Blau (2011) "Tribological Behavior of Oxygen Diffusion Treated Ti-6Al-4V with Different Cooling Rates," to be presented at ASM

Agreement 19217 – Ultra-fast Chemical Conversion Surfaces

Principal Investigators: A. Erdemir and O. L. Eryilmaz

Argonne National Laboratory

9700 S. Cass Avenue, Argonne, IL 60439-4838

(630) 252-6571; fax: (630) 252-5568; e-mail: Erdemir@anl.gov; Eryilmaz@anl.gov

DOE Technology Manager: Jerry L. Gibbs

(202) 586-1182; fax: (202) 586-1600; e-mail: jerry.gibbs@ee.doe.gov

Contractor: UChicago Argonne LLC

Contract No.: DE AC03 06CH11357

Objective

- Develop and optimize an ultra-fast chemical conversion (or boriding) process for improving the durability and tribological performance of engine components.
- Demonstrate technical feasibility and superior property, performance, and durability characteristics of treated components.
- Demonstrate scalability, reliability, and cost-competitiveness of the process.
- Transfer optimized process to automotive and heat treatment industries to reduce energy and carbon intensity of engines and thermal treatment processes.

Approach

- Produce hard and thick chemically converted boride layers on representative engine parts and other steel substrates; characterize their structural, chemical, and mechanical properties; demonstrate superior performance.
- Perform comprehensive lab-scale studies to confirm superior performance and durability.
- Confirm effectiveness in reducing friction and wear of actual engine parts, like tappets, piston pins, rings, transmission parts, etc.
- Optimize process variables and develop reliable boriding protocols that can consistently result in uniformly thick boride layers on actual engine parts.
- Using advanced surface analytical tools, identify fundamental tribological mechanisms that are responsible for superior friction, wear, and scuffing properties of the borided test samples and actual components under boundary, mixed, and hydrodynamic lubrication regimes.
- Demonstrate scalability of optimized process for large-scale applications in engines.
- Verify higher energy efficiency and lower carbon intensity of the optimized technology.

Accomplishments

- Completed treatment of representative test samples made out of the same grades of steels as those used for actual engine components.
- Demonstrated applicability of the technology to actual engine parts, like tappets and piston pins.
- Completed bench studies to confirm superior mechanical and tribological properties for ultra-fast borided surfaces.
- Confirmed scalability and large-scale productions of representative industrial parts in a production scale system.

Introduction

Among the many surface engineering processes hard PVD coatings and a variety of thermal diffusion processes like nitriding, carburizing, boriding (or boronizing) are used extensively by industry to enhance surface metallurgical and tribological properties of a large variety of industrial parts used in all kinds of transportation and manufacturing applications. Unfortunately, these traditional processes are very slow, energy and carbon intensive, and environmentally unsafe (i.e., they produce large amounts of gaseous emissions and liquid and solid wastes).

In this project, we aimed at developing and scaling-up of a chemical conversion process that can electrochemically deposit boron on the surfaces of suitable metallic parts and subsequently diffuse into the subsurface to result in a very hard and thick boride layer. Compared to nitriding and carburizing, this process is ultra-fast, clean, and cheap and hence holds great promise for a large variety of engine applications.

The chemically converted top boride layers may consist of FeB, Fe₂B, and small amounts of Fe₃B phases and then a very thick boron diffusion layer beneath to provide a graded surface which can

substantially increase surface metallurgical and tribological properties of treated engine parts. With the new process, it is possible to obtain single and multi-phase composite or layered boride phases by controlling the process parameters. Depending on the specific phases or composition of the top layer, Vickers hardness values of 16 to 20 GPa are feasible. Figure 1 shows a typical cross-section image of a borided steel surface consisting of only the Fe₂B layer. The very thick boron diffusion layer beneath is not visible but chemical analyses show that boron exists in atomic form in the region right beneath the top chemically converted boride layers.

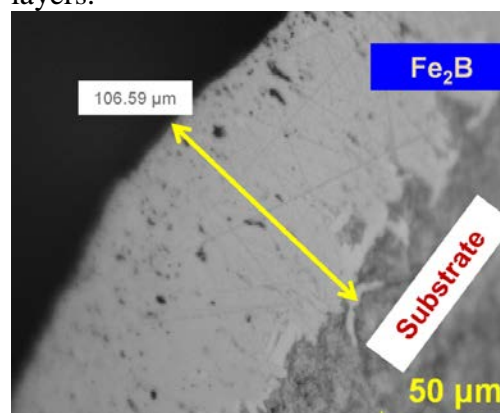


Figure 1. Cross-sectional image of a borided steel sample.

For the chemical conversion process, we use a simple electrochemical cell and the main composition of the electrolyte is made of borax ($\text{Na}_2\text{B}_4\text{O}_7$) which is a natural mineral and very cheap. One of the main objectives of this project was to pursue systematic experimental studies with representative test samples and actual engine parts to further understand the specifics of the boride layer growth mechanisms and the effects of various process parameters on the structural, chemical, and mechanical characteristics of the resultant boride layers. Based on such fundamental understanding, we also aimed at further optimizing the process parameters in order to achieve much improved mechanical and tribological properties in critical engine components of light and heavy duty vehicles.

During our systematic studies, we have successfully borided a variety of representative steel samples and actual engine parts including tappets, piston rings, and pins and confirmed the very high hardness (above 1600 Vickers) on their top surfaces. Very thick and hard boride layers produced on these parts should drastically improve the performance and durability under severe sliding conditions by minimizing wear and scuffing damages. They should also have a positive impact on corrosion and oxidation resistance of such surfaces when and if the operating environments become aggressive.

During FY 2011, we realized all of our project milestones for the year by successfully processing a large variety of samples for bench-top testing. We also borided a variety of engine parts. Using bench-top friction and wear test machines, we confirmed the superior

tribological performance of the borided test samples. We also accelerated discussions on technology transfer and licensing with a large thermal treatment company.

Experimental

Most of our experimental activities in FY2011 were focused on the boriding of various engine parts and components. We also continued our effort in building of a larger boriding unit that is suitable for the treatment of numerous smaller engine parts or bigger engine components. While performing these experiments, we had to explore the effects of many parameters on boride layer thickness and hardness as well as optimize them to achieve the kinds of composite boride layers that will lead to greatest improvements in friction, wear and other key properties during actual operations.

During our systematic studies, we focused our attention to understanding the specific relationships between mechanical property and the structural and chemical nature of boride layers that were obtained under different operating conditions. In our studies, we have found that FeB phase was much harder than Fe_2B or Fe_3B but it was also very brittle or had much lower fracture toughness. Upon indentation by a Rockwell C indenter, this layer would shatter and develop extensive cracks. We found Fe_2B phase to be reasonably hard (around 1500 Vickers) yet very tough and resistant to wear. So in most of our application oriented studies, we tried to obtain this particular phase in our test samples.

For the scale-up effort, we moved from a 4" to 22" and then to a full-production scale unit with more than 100 ft³ boriding

volume. During the scale-up effort, we had to overcome several hurdles and unexpected problems especially with power sources, heaters, cap assembly including fixtures and holders for handling parts and electrodes, etc. In the end, we successfully constructed a production-scale unit and it is nearly ready for initial trials and large-scale treatment of actual engine parts.

Results

Figure 2 summarizes the results of our boride layer optimization studies in a tabulated form. In these studies, we used borax and a variety of other boron-based salts at different proportion. As a result, significant improvements in process efficiency and end-product quality have been achieved. As can be seen from the figures inset in the table, much faster boriding rates resulting in significantly thicker boride layers were obtained by these optimization studies. For development of a highly optimized boriding protocol, we typically performed 15 min. of boriding, then left the borided parts in molten electrolyte for another 45 minutes to allow deeper diffusion and much thicker boride layer formation. This procedure also resulted in much denser morphology (no cracks or delamination), reasonable hardness and much superior toughness and wear resistance. Further, we noticed that surface finish of borided parts was much smoother and no sign of oxidation or hot-corrosion attack was visible on the treated samples or engine parts (see Figure 3).

15 min boriding followed by 45 min holding	Before electrolyte optimization		After electrolyte optimization	
	Total Borided Layer Thickness (µm)	FeB Layer Thickness (µm)	Total Borided Layer Thickness (µm)	FeB Layer Thickness (µm)
Maximum	84	0	118.78	53.30
Minimum	23	0	42.64	0.26
Average	59.34	0	89.98	21.82

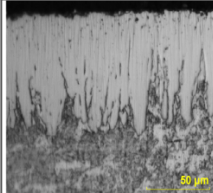
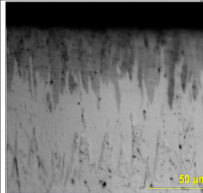
Cross sectioned optical microscopy pictures		
---	--	---

Figure 2. Comparison of boride layer thickness before and after optimization of molten electrolyte.

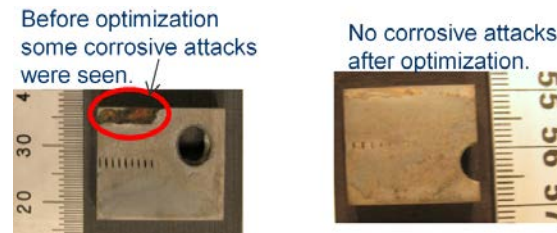


Figure 3. Condition of borided test samples showing signs of corrosive or oxidative attacks prior to electrolyte optimization (left) and no sign of any type of attack after electrolyte optimization (on right).

During FY 2011, we also successfully demonstrated boriding of a large variety of gear and bearing steels as well as light-weight materials like titanium that is considered for certain engine applications due to its light-weight and high strength. Figure 4 shows the structural morphology of a borided 9310 gear and 52100 bearing steels.

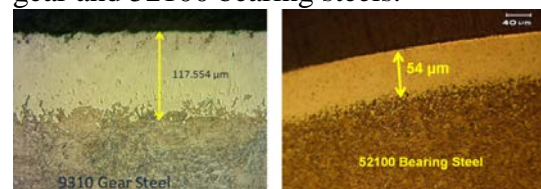


Figure 4. Structural morphology of a borided 9310 gear (left) and 52100 bearing (right) steel showing very thick and dense boride layers on top.

In these boriding activities, using the optimized boriding protocols, we were able to achieve and maintain a fairly thick pure Fe₂B layer which will be the most desired phase as discussed earlier.

Highly optimized boride layers were subjected to extensive tribological tests in our laboratory to verify their superior friction and wear performance. As shown in Figure 5, when tested in a typical engine oil (i.e., 5W30 grade), unborided steel suffered significant wear on both the sliding pin and disk sides, while it was very difficult to detect any sign of wear on the borided surface.

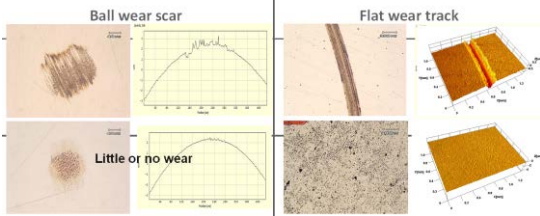


Figure 5. Comparison of wear performance of control or un-borided steel (top) with that of borided steel (bottom). Test conditions: 830 MPa Hertz contact pressure, 15 mm/s sliding velocity, 1-km sliding distance, and in 5W30 engine oil.

Based on the very favorable friction and wear results from bench studies, we attempted to boride an engine tappet in our boriding unit and to determine its friction and wear performance. Figure 6 shows the condition of the borided tappet and the cross-sectional morphology of the boride layer that was formed near the top surface. Figure 7 shows the results of friction and wear tests on this tappet. As shown in the friction chart in Figure 7, the friction coefficient of the borided surface was significantly lower. While, the amount of wear on unborided tappet was very

severe, the wear on borided tappet was unmeasurable (see Figure 8).

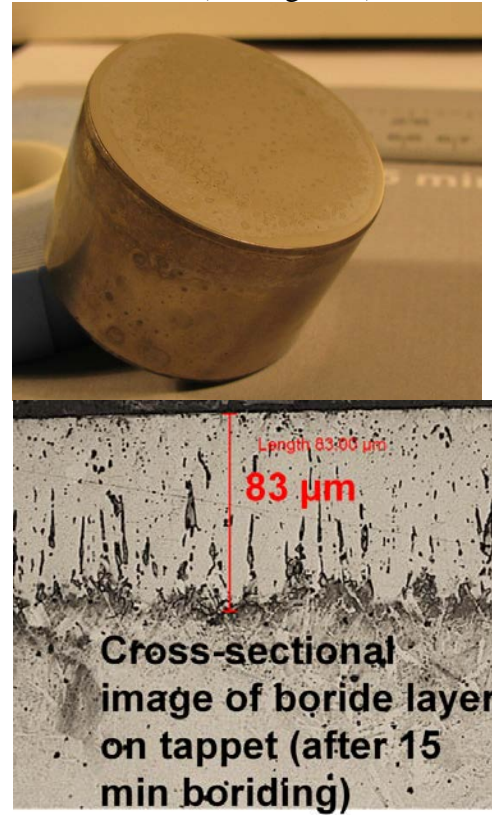


Figure 6. Macrophotograph of a borided tappet (top) and the cross-sectional image of the boride layer (bottom).

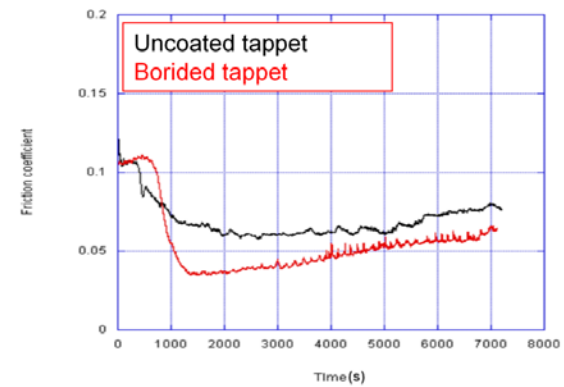


Figure 7. Frictional performance of unborided and borided tappet in 10W30 engine oil at 100°C.

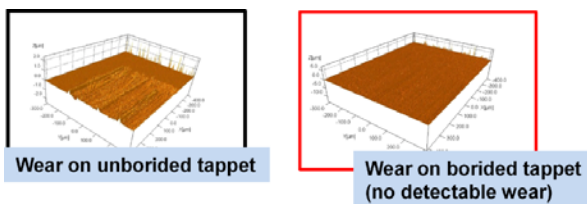


Figure 8. Condition of unborided (left) and borided (right) tappet surfaces after wear tests in 10W30 engine oil at 100°C.

Conclusions

In FY2011, we have made significant progress toward meeting our project objectives and demonstrated the effectiveness of our process in minimizing friction and wear in actual engine parts. We also continued our effort to further optimize the boriding conditions so that we can avoid brittle FeB phase while maintaining very thick and hard Fe₂B layer which was shown to be very effective in reducing friction and wear. We have also made significant progress toward scale-up and commercialization of the process. Argonne and a very large heat treatment company are currently in close communication to reach a licensing deal on this technology.

Publications and Presentations

During FY11, we have published and/or presented numerous papers on the work that was performed under this project as listed below.

1. Kartal, G., Eryilmaz, O. L., Krundick, G., Erdemir, A., and Timur, S., "Kinetics of electrochemical boriding of low carbon steel", *Applied Surface Science*, 257(2011)6928-6934.
2. Greco, A., Mistry, K., Sista, V., Eryilmaz, O., and Erdemir, A., "The Effect of Boron Based Surface

Treatment and Nano-particle Lubricant Additives on Friction and Wear Behavior for Wind Energy Applications", *Wear*, 271(2011)1754-1760.

3. Kartal, G., Timur, S., Eryilmaz, O., Erdemir, A., "Influence of Process Duration on Structure and Chemistry of Borided Low Carbon Steel", *Surface and Coatings Technology*, 205(2010)1578-1583.

4. Sista, V., Kahvecioglu, O., Eryilmaz, O., Erdemir, A., and Timur, S., "Electrochemical Boriding and Characterization of AISI D2 Tool Steel", accepted for publication in *Surface and Coatings Technology*, 2011.

5. Kartal, G., Matta, C., Eryilmaz, O., Erdemir, A., Timur, S. "Comparison of Friction and Wear Resistance of Low Carbon Steels Subjected to Carburizing, Nitrocarburizing, and Boriding Treatments Under Dry Sliding Conditions", presented at the 14th International Congress of the Turkish Metallurgical Society, Istanbul, Turkey, Nov. 11-12, 2010.

6. Erdemir, A., "Innovative Surface Technologies for Demanding Tribological Applications: From Super-hard and Low-friction Coatings to Super-fast Surface Treatments," (Invited Colloquium Seminar), Mechanical Engineering Department, University of Texas at Arlington, Arlington, TX, November 12, 2010.

7. Sista, V., Kahvecioglu, O., Eryilmaz, O., Erdemir, A., and Timur, S., "Electrochemical Boriding and Characterization of AISI D2 Tool Steel", presented at 38th ICMCTF 2011, San Diego, CA, USA, May 2-6, 2011.

8. Erdemir, A., "Recent Advances in Boron-Based Lubricants and Surface Treatments for Energy Saving Applications in Engines", Invited Talk,

presented at the 17th International Symposium on Boron, Borides and Related Materials, September 11–17, 2011, in Istanbul, Turkey.

Agreement 23284 – Friction Reduction Through Surface Modification: Integrated Surface Texturing and Coating

Peter J. Blau and Stephen M. Hsu[#]*

** Oak Ridge National Laboratory, P. O. Box 2008, Mail Stop 6063, Oak Ridge, TN 37831-6063
(865) 574-5377; fax: (865) 574-4913; e-mail: blaupj@ornl.gov*

*# George Washington University, Exploration Hall, 20101 Academic Way, Ashburn, VA 20147
(703) 726-8365; e-mail: stevehsu@gwu.edu*

DOE Technology Manager: Jerry L. Gibbs

(202) 586-1182; fax: (202) 586-1600; e-mail: Jerry.gibbs@ee.doe.gov

ORNL Technical Advisor: David P. Stinton

(865) 865-574-4556; fax: (865) 241-0112; e-mail: stintondp@ornl.gov

*Contractor: Oak Ridge National Laboratory, Oak Ridge, TN
Prime DOE Contract Number DE-AC05-00OR22725*

Objectives

- To demonstrate the feasibility of using engineered micro-scale patterns (surface textures) to reduce the friction on bearing surfaces such as those on piston rings and cylinder liners, bucket lifters, and cam lobes.
- To demonstrate new technology for applying surface textures to large curved surfaces like piston rings and cam lobes, and to provide design guidelines for their use by engine makers.

Approach

- ORNL and George Washington University (GWU) will collaborate to determine the effects of integrated surface texture designs on friction reduction of lubricated bearing surfaces.
- Building upon prior review on surface texturing, determine the efficacy of texturing methods in reducing friction using reciprocating sliding tests, on textured surfaces provided by GWU.

Accomplishments

- An annotated literature review was prepared on the use of patterned surfaces to control friction and wear. An automated hardness system was used to create a micro-indentation texturing pattern on two bearing surfaces. These were tested for friction and wear.
- GWU found that combinations of surface patterns offered greater benefits over a range of lubrication regimes than a single pattern. Friction reductions of up to 60% were observed.

Future Directions

- Experiments will continue on the effects of texturing at ORNL, and on multi-pattern texturing plus coating technology at GWU.
-

Introduction

A combination of R&D approaches is being used to achieve the Department of Energy's goal for a 50% increase in freight efficiency (measured in ton miles per gallon) for heavy vehicles. These include a reduction in parasitic losses (e.g., friction, aerodynamic drag, etc.), more efficient designs, and the use of lightweight structural materials. The project reported here is aimed at reducing frictional losses in engines by applying an integrated approach to the design of lubricated rubbing surfaces.

Those who specialize in tribology (the science and technology of friction, lubrication, and wear) have long realized that the energy efficiency of a mechanical system, like a diesel engine, can only be improved by employing a combination of strategies like design improvements, new materials, and new lubricants. In addition, fuel efficiency can be enhanced by addressing the friction of diesel engine subsystems. Sliding contacts, like the piston ring and cylinder bore, can contribute 40 – 50% of the total engine friction losses, depending on engine speed.

The term 'surface engineering' describes the chemical, physical, and geometrical modification of solid surfaces to achieve a desired set of functional properties like friction and wear. There have been many advancements in surface engineering to reduce friction, but among the most promising is the application of patterned features (sometimes called surface textures) that alter lubricant flow and trap wear particles as well. Figure 1 illustrates some attributes of a textured surface. These can be produced by laser dimpling, photo-lithography, micro-machining, or even rolling between patterned rollers.

As reported in the tribology literature, textures do not work well in every case, and additional surface modifications, like the application of a solid film or coating can enhance the effects of texturing. Therefore, this project couples micro-scale texturing with carefully formulated coatings on engine surfaces to improve the friction of important contacting surfaces in engines.

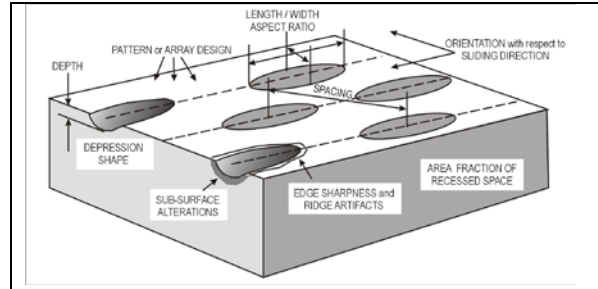


Figure 1. Some of the attributes of a textured surface. Some are intentional but others result from the process used to create the pattern.

Approach

This two-year, multi-disciplinary effort draws on the texturing expertise of a sub-contractor (George Washington University), the advice of a diesel engine manufacturer, and ORNL's experience in friction, lubrication, and wear research. It involves a combination of surface processing, experimental validation, and modeling. In some cases, friction tests will be conducted in accordance with the ASTM G181 that was designed for measuring piston ring-on-liner friction under lubricated, reciprocating sliding conditions. It should be noted that DOE, OVT supported the development of that standard and it is now widely used in industry.

Progress in FY 11

Survey of past approaches to surface texturing and its applications. An annotated literature review, with an appendix grouped by type of application and method of texturing, was prepared to summarize the variety of methods used to produce texture bearing surfaces as well as their effects. It is clear that the degree of success of geometric texturing as a means to reduce lubricated sliding friction is highly dependent on the application and on the pattern characteristics. It works well in some cases, but not in others. Plans are to publish an updated version of this literature review of texturing methods in FY 2012.

Indentation texturing (ITx) of metal bearing surfaces. An initial set of experiments was performed to investigate texturing effects on diesel oil-lubricated, reciprocating sliding of AISI 52100 bearing steel against bearing bronze

(CDA 932). In some tests, the steel slider (a bearing ball) was left spherical, but in others, a flat spot was abraded on the tip to improve interfacial conformity.

An off-set square pattern of diamond-shaped hardness impressions was produced by a computer-controlled Vickers micro-indentation hardness tester (see Figure 2). The sizes, depths, spacing, and area percent occupied by these impressions were obtained by quantitative metallography. Plastic deformation near the impressions was measured using a Wyko™ 9100 vertical scanning interferometer (Fig. 3).

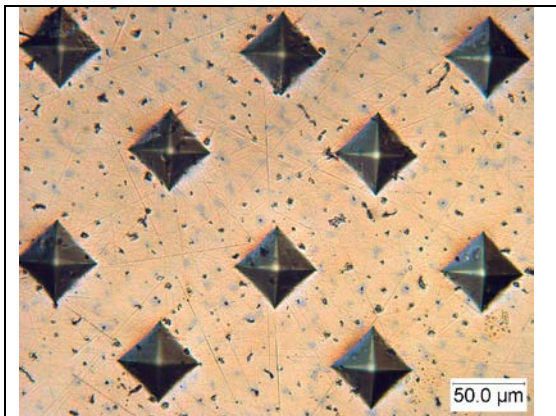


Figure 2. Micro-indentation pattern on bronze CDA 932. Rows are 75 μm apart. Impressions occupied 15% of the area. Light gray particles are a dendritic pattern of lead phases.

Friction measurements were made both on and off the ITx area using both rounded and flat-tipped sliders (load = 50 N, speed = 10 strokes/s, stroke length = 10 mm). As seen in Figure 4, flattening the slider tip reduced the friction coefficient (μ) more than ITx, but ITx slightly lowered the friction relative to polished surfaces for both flattened and rounded tips. Thus, indentation texturing has greater benefits for conformal (flat-on-flat) sliding contact conditions.

In FY 2012, tests will continue to explore these effects on alloys that are harder than bronze. Complementary experiments on friction reduction by surface engineering were conducted at GWU, using a similar make and

model of tribometer. Those results are described below.

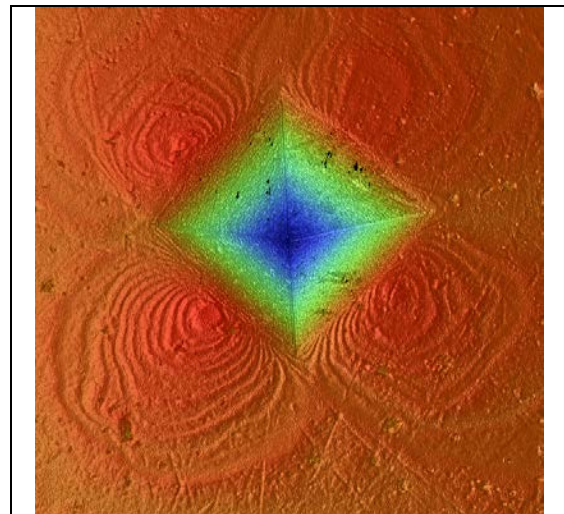


Figure 3. Pushed up material surrounding an indentation in bronze. Such 0.3 μm high ridges were carefully polished down before friction testing was conducted.

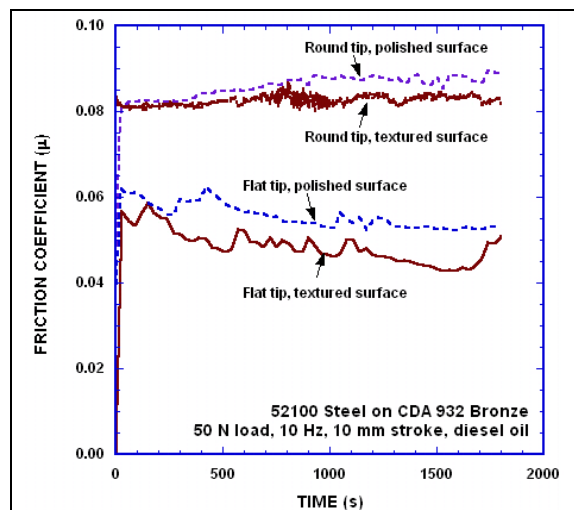


Figure 4. Effects of tip shape and ITx on friction of lubricated bronze surfaces. About 17% lower friction was observed for flat-ended sliders on textured surfaces.

Progress at George Washington University (GWU). An ORNL subcontract to GWU was signed in March 2011. Despite the mid-FY 2011 start, GWU made considerable technical progress. For example, a surface texture fabrication technique, applicable to piston rings

and other curved surfaces, was successfully developed. Photo-lithography was used to develop large area, soft polymeric masks. This was followed by electrochemical etching. Adjustments in the etching agent, current, and buffer conditions were necessary to cope with the ring metallurgy and composition. Piston ring segments textured in this way were used for friction testing.

Initial tests were performed to investigate the effects of oscillating frequency and test load on the magnitude of friction reduction that could be achieved. As observed in earlier ORNL experiments with laser-dimpled ceramics, the effects of texturing on friction were greater at higher frequencies of oscillation (that is, a higher mean sliding velocity). This behavior is consistent with the classical Stribeck curve behavior in which friction coefficient is plotted against a combined parameter that includes the product of lubricant viscosity and sliding velocity, divided by load.

Results from bench-scale friction tests on textured piston ring specimens in a modified white oil (ISO grade 32), under a range of applied stresses, showed that a dual-featured pattern was advantageous. Small, deep, elliptical dimples functioned during boundary and elasto-hydrodynamic lubrication regimes while relatively shallow large dimples improved hydrodynamic lubrication (see Fig. 5). *Friction reductions of as much as 60% could be achieved.*

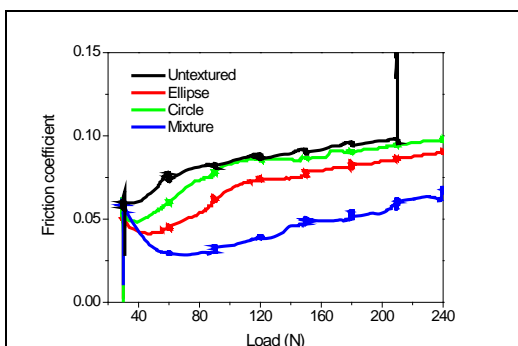


Figure 5. Effects of single texture shapes and a mixture of shapes on friction at varying applied loads.

Research on texture designs and the application of surface coatings continues at both ORNL and GWU to maximize fuel-efficiency by engineering bearing surfaces in diesel engines.

Future Work

- Continue experimental work at ORNL and GWU on the optimization of surface textures for friction reduction.
- Demonstrate an ability to apply functional textures on curved surfaces for use in engine components like piston rings, cylinder liners, and cam rollers (GWU).
- Working closely with an engine OEM, investigate the effects of texturing plus multi-layer surface coating in order to achieve lower friction than textures alone (GWU).
- Investigate the effects of bearing alloy hardness on the effectiveness of patterned surfaces (ORNL).

Summary and Conclusions

- Progress in establishing the effects of surface texturing on friction reduction has been made during the first year of this effort at ORNL, and by subcontract at GWU.
- Placing patterns on bearing surfaces can be more effective in the case of conformal contact (e.g., flat-against-flat) than non-conformal contact (e.g., curve-against-flat).
- The efficacy of textures on lubricated bearing surfaces depends on the regime of lubrication that occurs, which in turn depends on load, speed, lubricant viscosity, and pattern characteristics.
- Placing multiple pattern shapes and sizes on the same surface can help reduce friction over a broad range of lubrication regimes: from boundary lubrication to mixed film to full-film hydrodynamic lubrication. Using only one shape and size of texture feature would not likely be as effective.

Publications/Presentations

(None to date)

Agreement 23725 - Tailored Materials for Improved Internal Combustion Engine Efficiency – (GM CRADA)

Principal Investigator: Glenn J. Grant

Energy Materials and Manufacturing
Pacific Northwest National Laboratory
902 Battelle Blvd., K2-03
Richland, Washington 99356
(509) 375-6890; fax: (509) 375-4448; e-mail: glenn.grant@pnnl.gov

Blair E. Carlson

Manager, Lightweight Materials Processing
General Motors R&D
30500 Mound Rd.
Warren, MI USA 48090
e-mail: blair.carlson@gm.com

DOE Technology Manager: Jerry L. Gibbs

(202) 586-1182; fax: (202) 586-1600; e-mail: Jerry.gibbs@ee.doe.gov

Field Technical Manager: Dean Paxton

(509) 375-2620; fax (509) 375-2186; e-mail: dean.paxton@pnnl.gov

Contractor: Pacific Northwest National Laboratory
Contract No.: DE-AC05-76RL01830

Objective

- To develop friction stir processing (FSP) to tailor the properties of conventional, low-cost engine materials (cast iron, alloy steels, and aluminum alloys) with the goal of increasing their high-temperature performance, durability, and thermal properties.
- To deploy friction stir processed components that can enable energy-efficient combustion strategies, especially those that will require higher peak combustion pressure or higher temperature operation where component durability is the primary barrier to the utilization of the efficient combustion strategy.

Approach including partner/collaborator and path to technology transfer and commercialization

- This project will develop surface modification techniques, modified materials, and components. The project is a Cooperative Research and Development Agreement (CRADA) with General Motors.
- The project is primarily investigating FSP, a new technology that can produce functionally graded surfaces with unique and tailored properties that will allow propulsion materials to withstand higher temperatures and pressures without appreciably losing strength, hot hardness, or wear resistance, and exhibit improved resistance to thermal fatigue.
- FSP-treated components will be evaluated and tested by the industry collaborators to demonstrate efficiency benefits and potential commercial applications.

Milestones, Metrics and Accomplishments

- **Milestone:** Demonstrate property improvements from FSP that can reach the following metrics established by the project team: minimum two-fold improvement in fatigue life, and 20% improvement in average failure stress level at N cycles.

- **Milestone:** Demonstrate consolidated FSP regions in aluminum and ferrous materials typical of cylinder head, cylinder liner, block, crankshaft, rod, piston and bearing materials on a subscale two-dimensional shape relevant to real part geometry (TRL 3 to 4 transition).
- **Milestone:** Establish friction-stir welding process window to successfully stir insoluble particulate into the surface of steel and aluminum to improve modulus and increase wear performance by 20% over baseline material.
- **Milestone:** Demonstrate prototype part that can show durability advantage from FSP that allows high-peak combustion pressures (PCP) and document energy savings potential.

Introduction

The purpose of this project is to improve the durability and thermal properties of conventional, low-cost materials so they can withstand the increased level of mechanical performance required in new combustion strategies such as homogenous charge compression ignition (HCCI), low temperature combustion, and other conditions where higher peak combustion pressures (PCP) are anticipated. HCCI, premixed charge compression ignition (PCCI), low temperature combustion, and other strategies can produce higher specific power levels that can allow engine downsizing and decreased fuel consumption, but increases in peak combustion pressure are often a result. A barrier to fully realizing these energy efficient strategies can be the engine component materials themselves. Increasing the durability of engine components can increase the operational envelopes of the engine, allowing designers of the combustion process to access areas of engine control where increased specific power and low emission levels are found, but where high PCPs can create reliability problems.

The proposed project aims to achieve the U.S. Department of Energy (DOE) goals for increased fuel and thermal efficiency in both light and heavy duty engines by developing and deploying FSP, a new surface modification technology that has been shown to significantly improve the strength and durability of current engine materials. This project proposes to experimentally develop the FSP process required to engineer the surface of propulsion materials for improved properties, then fabricate prototype parts that will be tested in-engine by project partners. The microstructural modification created by FSP is expected to lead to a set of

materials with enhanced surface properties that can handle increased combustion pressures, resulting in improved engine efficiency.

Purpose

The current project proposes to further develop and implement concepts validated in the previously funded Vehicle Technology Program-Propulsion Materials project, "Tailored Materials for Advanced CIDI Engines." The current project will prototype and test up to six separate internal engine components that are expected to have limited durability at very high peak cylinder pressures or high load-rise times during engine operation. These components will have FSP processing selectively applied to the regions of the part where durability issues are either found or anticipated. Example components may be pistons, cylinder heads, and potentially components in the rotating assembly, including but not limited to crankshafts and camshafts.

A number of different localized material failure issues that limit highly efficient engine design have been identified and include resistance to thermal fatigue and improved hot strength, improved resistance to erosive or adhesive wear in piston ring grooves, and improved performance and strength in aluminum blocks and cylinder heads of small displacement turbo gas and turbo diesel engine materials. These failure issues have been identified as potential opportunities where a friction processing may be able to produce property improvements.

The link between improved material properties and increased engine efficiency is obvious empirically. For example, higher combustion pressures are needed for high efficiency combustion, but if engine internals do not have

the performance needed, the higher pressure combustion cannot be implemented. The goal of this project is to establish a quantitative link between improved properties and increased efficiency.

Background

Almost since the inception of internal combustion engines, there has been a steady rise in specific power (SP) output, or the power per liter of engine displacement. SP is correlated with efficiency and is the combined effect of better optimization of combustion, fuels, engine materials and design, reduction in parasitic losses, and improved heat management. Figure 1 shows that from 1970 to 2001, there has been a steady increase in SP. After 2001, the SP levels dropped due to emission and after-treatment devices and controls mandated by federal legislation (primarily increased exhaust gas recirculation rates and particulate filters). The drop in SP from 2001 to about 2003 would have been even greater were it not for significant advances in engine management, computer control, higher injection pressures, etc., made during this period to compensate for the power losses. However, around 2003, a different restriction on the optimization of the combustion process was beginning to force diminishing returns. The restriction is illustrated in Figure 1 as the PCP plot. As the peak pressure increases, more work can be done by the piston as it is forced downward in the bore, resulting in a higher SP.

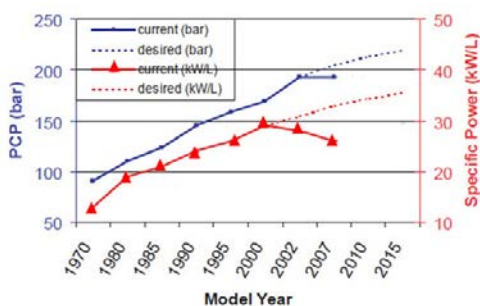


Figure 1. Plot showing the increase in SP and PCP for typical heavy-duty diesel engines over the last 38 years (figure modified from the Southwest Research Institute website at www.swri.org)

Since 2003, PCP has leveled at around 190 bar to 200 bar, because above this level, conventional engine materials in pistons, cylinder liners, and cylinder heads will be beyond strength and fatigue limits.¹ To increase efficiency further, either unconventional, expensive materials (i.e., nickel alloys, titanium, compacted graphite iron, nodular iron, or micro-alloyed steels) must be used or conventional materials must be modified in a way that increases their durability. New energy-efficient combustion strategies, especially HCCI, will increase PCP potentially above 220 bar. Accordingly, materials must be improved to enable this process.

One of the major challenges for conventional materials under increasing peak pressure environments is resistance to thermal fatigue failure. Pistons and cylinder heads are particularly vulnerable to this failure mode because of the cyclic nature of the loading and temperature changes in the combustion chamber. Figure 2 shows failures of pistons in the bowl rim area when subjected to high PCP over time.

Rather than substitute a potentially high-cost, high-temperature, monolithic material, one low-cost strategy to enable higher PCP involves using techniques to improve the thermal fatigue performance of current materials. In the case of thermal fatigue in the bowl rim area, the technique need only be applied to the narrow area around the bowl rim itself because failures of this area drive the overall material selection.

FSP is a new technology that can be used to create engineered regions on selective areas of a part. In recent years, PNNL has developed techniques and tools that allow FSP to be accomplished in steel, cast iron, and aluminum. FSP is an outgrowth of friction-stir welding, which was invented 20 years ago by TWI, Ltd.

¹ Figure 1 represents data primarily from medium-duty to heavy-duty diesel engines. Production automotive diesel engines (light-duty, high-speed) now achieve SP levels up to 75kW/L in turbocharged and intercooled configurations.

(Figure 3). It has been recognized that the same techniques and processes used to make a friction stir weld could be used to process a material for enhanced properties. The process can be selectively applied to the surface of a material, and it alters the microstructure by the severe plastic deformation that occurs in the processed zone.

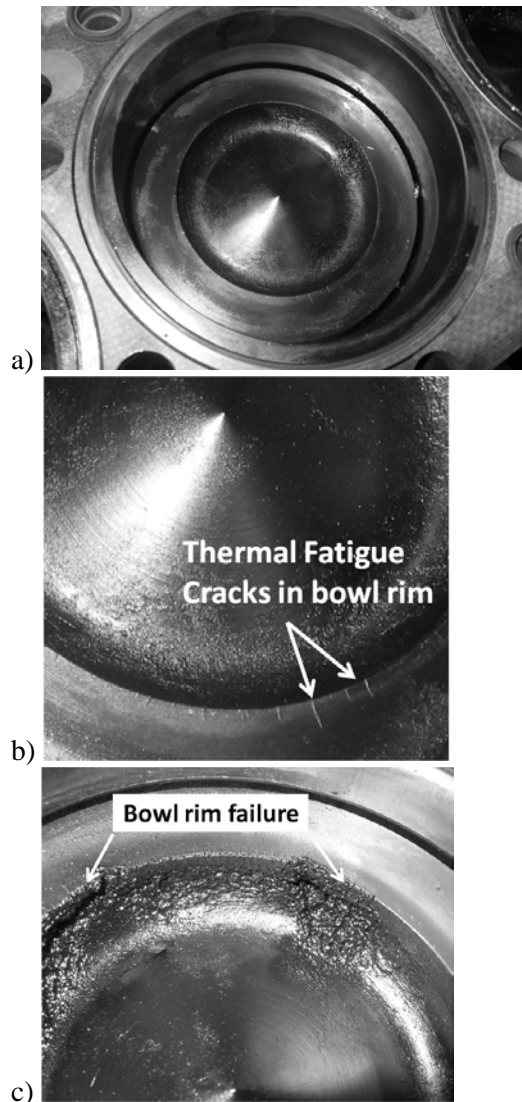


Figure 2. a) Piston in bore; b) cracks on inside edges of bowl rim; c) bowl rim failure

FSP can create a robust and graded structure with fundamentally different properties than the underlying surface, and it has been shown to produce surface regions with improved fatigue life, ductility, and strength.

FSP produces a surface modified region that is different from a coating. Commonly, surface treatments designed to enhance wear or thermal performance include various coating methods or fusion-welded hard facings. Most of these processes are liquid state and often involve detrimental temperature effects on the base material. Heat-affected zones in the base metal and various deleterious high-temperature reactions can create a coated part with less-than-desirable properties.

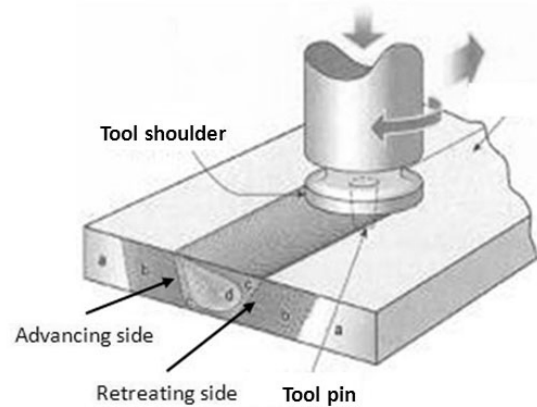


Figure 3. FSP illustration (top) and typical friction stir tools

Also, traditional thin coatings can suffer from issues involving the nature of the interface between the coating and the base material (spalling, debonding, and cracking on the interface), especially under high-stress, gouging wear conditions or under cyclic-thermal conditions where coefficient of thermal expansion mismatch is an issue. Also, failure of a coating under high-loading conditions can occur when the substrate below a thin, hard coating fails by plastic deformation. Regions

treated with FSP can be significantly more robust than traditional coatings for two reasons: 1) FSP produces a modified region that transitions to the base material without a sharp interface (Figure 4); and 2) the modified region is generally thicker and the transition region wider than traditional coating because the plasticized region depth is related to the tool geometry, specifically the depth and size of the pin.

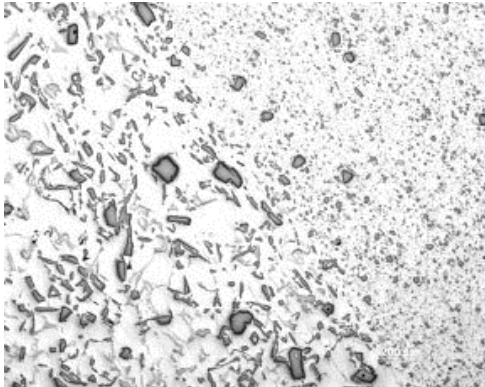


Figure 4. Micrograph of the edge of a stirred zone showing particle refinement in the processed region. (FSP can close porosity in castings and decrease both size and aspect ratio of particles, thus producing better fatigue performance)

It also is possible to use FSP to “stir” insoluble particles from the surface into the substrate to depths limited only by the FSP tool geometry (Figure 5).

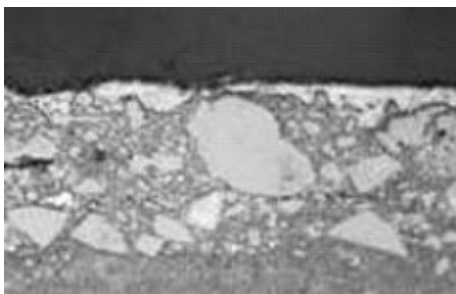


Figure 5. Ceramic particulate also can be stirred into the surface to produce functionally graded surfaces and near-surface metal matrix composites

This engineered metal matrix composite layer can create unique surface properties, including increased hardness, wear resistance, and thermal characteristics. To date, the addition of up to

20% ceramic to aluminum has been demonstrated and approximately 10% addition to steel has been achieved. FSP can be used to alter the original microstructure, create surface composites and new alloys, and has the potential to produce selective areas of improved material performance. This project will investigate several opportunities for FSP to improve engine materials to enable increases in engine efficiency.

The current project is a continuation from work done during 2008–2010 in the project “Tailored Materials for Advanced CIDI Engines,” which demonstrated that FSP, a new surface engineering process can show from 5–15 times fatigue life improvement over as-cast material. In addition, FSP-processed materials can show up to 80% improvement in fatigue strength across a wide range of maximum stress levels. These improvements were demonstrated at the coupon scale and were demonstrated in aluminum materials in common usage for piston applications in medium duty diesel engines.

The previous project developed the FSP process in aluminum and steel and documented the microstructures and mechanical performance of the processed zone. However, key to moving this technology towards implementation is engine component prototyping and in-engine testing, which is the focus of this proposal. The current project proposes to take the techniques and FSP process knowledge developed in the previous work, and apply it to real-world parts by working with original equipment manufacturers partners to accomplish in-engine part testing. In addition, the project partners have identified several other applications beyond the piston materials investigated in the previous project as candidates for further work.

Approach

- The project will develop the FSP manufacturing parameters, as well as selecting and evaluating proper tool materials and techniques to produce defect-free FSP regions. The project will leverage a large amount of process knowledge gained

from the earlier project on heavy-duty diesel engine materials.

- Coupon-level testing and evaluation of the thermal and mechanical properties will be conducted, focusing on specific performance targets identified by project partners. If performance metrics are met for sample materials enhanced by FSP, additional research will include developing and demonstrating the appropriate method to apply this process to the two-dimensional and three-dimensional geometry of the selected parts.
- After process schedules are established, prototype parts will be fabricated to specifications provided by project partners and relevant part testing will be completed (in-engine or other tests specified by partners).
- The primary purpose of the project is to take process maps generated by the previous project on FSP of heavy-duty diesel engines, and apply them to part configurations in light duty diesel and turbo gas on-road engines for testing. The physical parts to be tested are expected to define five or six primary tasks surrounding the development of the FSP process for that part and the actual test runs in realistic environments. The following preliminary tasks will be prioritized:
 - Task 1: Piston: Top ring land durability
 - Task 2: Piston: Bowl rim thermal fatigue and oxidation resistance in automotive turbo diesel
 - Task 3: Block: Cylinder wall or liner wear resistance
 - Task 4: Block: Top deck strength and fatigue performance in thin regions between cylinders
 - Task 5: Cylinder head: Valve bridge area thermal fatigue
 - Task 6: Crankshaft: Fillet or oil hole fatigue.

Technology transfer both during and at the end of this project will be directly through the project participant General Motors (and potentially a Tier 1 supplier), who will be the

implementers of the technology. The project is a cost-shared CRADA, which will provide an immediate pathway for implementation of the technologies developed.

Results

The project started in late 2011 and currently GM and PNNL are defining the task priorities. Specific trials will likely first emphasize aluminum head materials where durability issues are restricting peak combustion pressures. During the last quarter of fiscal year (FY) 2011, the project focused on CRADA documentation and planning discussions related to primary materials of interest. Experimental trials are expected to begin during the first half of FY 2012.

Conclusions

The goal of this project is to develop friction stir processed components that can enable energy-efficient combustion strategies, especially strategies that will require higher PCP or higher temperature operation. FSP produces selected, graded structures that have shown increased strength and durability in fatigue. Surface modification through FSP may address some emerging material problems seen in very high combustion pressure systems such as HCCI engines. In addition, the process enables the incorporation of particulate into the surface, potentially selectively modifying the properties of materials to alter the thermal environment for increased thermal efficiency.

This project leverages the discoveries made on the FY 2008–2010 project “Tailored Materials for Advanced CIDI Engines,” which focused on mid-size and heavy-duty diesel engines. This project will apply the lessons learned to smaller on-road turbo gas and diesel engines found in typical passenger car and light truck applications. The project will demonstrate property improvements that are available from FSP. Functionally graded materials can be anticipated through this solid-state process that cannot be fabricated any other way. This project will develop a set of tools and techniques that can be passed to designers who require materials that will operate at every increasing stresses and

temperatures where part durability is the primary barrier to increased engine efficiency.

Acronyms

CRADA: Cooperative Research and Development Agreement

FY: fiscal year

FSP: friction stir processing

PCCI: premixed charge compression ignition

PCP: peak combustion pressure

SP: specific power

Project 18519 - Materials for Control of Exhaust Gases and Energy Recovery Systems

Agreement 9130 - Development of Materials Analysis Tools for Studying NO_x Adsorber Catalysts (CRADA No. ORNL-02-0659 with Cummins Inc.)

Thomas Watkins, Larry Allard, Michael Lance and Harry Meyer
Oak Ridge National Laboratory
P.O. Box 2008
Oak Ridge, TN 37831-6064
(865) 574-2046; fax: (865) 574-4913; e-mail: watkinstr@ornl.gov

Krishna Kamasamudram and Aleksey Yezerets
Cummins Inc.
1900 McKinley Av., MC 50197
Columbus, IN 47201
(812) 377-4935; fax: (812) 377-7226; e-mail: Krishna.Kamasamudram@Cummins.com

DOE Technology Manager: Jerry L. Gibbs
(202) 586-1182; fax: (202) 586-1600; e-mail: jerry.gibbs@ee.doe.gov
ORNL Technical Advisor: David P. Stinton
(865) 576-4556; fax: (865) 241-1034; e-mail: stintondp@ornl.gov

Contractor: Oak Ridge National Laboratory, Oak Ridge, Tennessee
Contract No.: DE-AC05-00OR22725

Objective

- The objective of this effort is to produce a quantitative understanding of the process/product interdependence leading to catalyst systems with improved final product quality, resulting in diesel emission levels that meet the prevailing emission requirements.

Approach

- Characterize lab-engine tested samples with X-ray diffraction, spectroscopy, and microscopy. Correlate findings with Cummins data and experience.

Accomplishments

- XRD and FTIR results indicated that the crystallinity and structural order, respectively, of an AMO_x catalyst increased within the first two hours of hydrothermally aging (650°C in air with 7% H₂O) and negligible change thereafter. XPS results show the largest chemistry change within the first two hours, but do show continued change in the Si/Fe and Si/Al ratios with time to 100 hours. STEM results show increased Fe and Al segregation with aging time. The Pt particle size increased by an order of magnitude after only 10 hours of aging.
- It is concluded that this AMO_x catalyst is not stable under these aging conditions.

Future Direction

- Begin in-situ AMO_x catalyst characterization of a practically-relevant zeolite catalyst subjected to hydrothermal aging at elevated temperatures for lifetime prediction model input using x-ray diffraction or piezospectroscopy.
 - Assist Cummins to competitively produce engines, which attain the required emission, levels while maintaining the advantage of the diesel's inherent energy efficiency.
-

Introduction

In order to meet the 2010 US Environmental Protection Agency (EPA) emission requirements for diesel exhaust, aftertreatment in diesel engines may be necessary.¹ The technology necessary for 2010 will need to integrate aftertreatment with engine control systems. Currently, no commercial off-the-shelf technologies are available to meet these standards. Consequently, Cummins Inc. is working to understand the basic science necessary to effectively utilize these catalyst systems. ORNL is assisting with the materials characterization effort. This report will focus on the study of materials used in ammonia oxidation.

Ammonia containing compounds may be added to diesel exhaust to reduce NO_x to N₂, as in selective catalytic reduction (SCR). The reductant reduces NO_x to H₂O and N₂.² Excess ammonia is often needed resulting in NH₃ escaping or “slip”. This slip is a concern for sociability and environmental reasons. Although not regulated, proactive steps are taken to mitigate even small amounts of ammonia slip by employing a selective oxidation catalyst.

Oxidation catalysts are usually present in after treatment systems to oxidize ammonia that is not being oxidized upstream by the SCR catalysts. These oxidation catalysts ensure that ammonia slip to ambient is minimal and are referred to by several names: ammonia oxidation (AMOX) catalysts, selective catalytic oxidation (SCO) catalysts or ammonia slip catalysts (ASC). Candidate catalysts are typically zeolite-based, alumina-supported metal or alumina-supported metal oxide catalysts. Hydrothermal conditions, temperature and water content, strongly influence the functioning of these catalysts by changing or “aging” the catalytic materials. These changes and their impact on performance are not well understood.

Goal, Barriers, Relevance & Integration

In the study area of VT’s Advanced Combustion Engine research, the *goal* is by 2015, improve the fuel economy of light-duty gasoline vehicles by 25 percent and of light-duty diesel vehicles by 40 percent, compared to the baseline 2009 gasoline vehicle. This project addresses the three *barriers* related to the Emission Control System in this study area: lack of cost-effective emission control, durability and cost (e.g., precious metal content). This project is *relevant* to this goal as the thrust is to

characterize and improve the understanding of the materials changes underlying the AMOX catalyst performance degradation with aging increases, so that efficient and durable AMOX with higher NO_x conversion efficiencies can be attained. This minimizes constraints on engine-out NO_x emissions and allowing engines to be tuned for optimal fuel efficiency, cost and durability. This project supports clean diesel, which increases acceptance by the public. Larger acceptance, in turn, results in larger percentages of conversion to diesel, with the resulting reduction in petroleum usage/dependency upon foreign oil. This project is *integrated* within Vehicle Technologies program as it utilizes characterization tools acquired and maintained by the High Temperature Materials Laboratory (HTML) Program.

Approach

The main focus of the CRADA in FY2011 was to continue the characterization of a practically-relevant zeolite AMOX catalyst, which was subjected to hydrothermal aging for lifetime prediction model input. The technical approach will be as before: experimentally characterize materials, supplied by Cummins, from all stages of the catalyst’s lifecycle: fresh, de-greened, aged, regenerated, on-engine and off-engine, etc. The crystal structure, morphology, phase distribution, particle size, and surface species of catalytically active materials supplied by Cummins were characterized using transmission electron microscopy (TEM), X-ray diffraction (XRD), X-ray photoelectron spectroscopy (XPS), and Raman Spectroscopy. Ultimately, an understanding of the thermal and hydrothermal aging processes and other degradation mechanisms is sought throughout the lifecycle of the catalytic material. {Acronyms are used liberally through out this report and are defined in Table I.}

Results

New samples were hydrothermally aged at 650°C in air with 7% H₂O for 0, 2, 3, 5, 10, 25, 50, 100 hours and then characterized at ambient.

XRD, FTIR and XPS

The x-ray diffraction patterns of the aged zeolite-based AMOX catalyst samples on a cordierite honeycomb support show a slight narrowing of the

zeolite peaks (see Figure 1), suggesting the structure is becoming more crystalline with aging time. The intensity differences seem to support this as well (except for the 50 hour sample, which could be due to loss of catalyst powder/washcoat). In addition to the zeolite phases shown, the cordierite from the honeycomb substrate is also observed. In Figure 2, the Fourier Transform-Infrared Spectrum (FTIR) was used to measure the change in vibrational frequency of the zeolite structure caused by hydrothermal aging in 7% H₂O at 650°C for the samples aged at 0, 10 and 100 hours. FTIR is sensitive to the skeletal modes of the zeolite framework that occur below 1400 cm⁻¹.⁴ The hydrothermal aging in 7% H₂O at 650°C causes the zeolite structure to become more ordered as indicated by the narrower band widths in Figure 2. This structural change occurs within the first 2 hours at temperature, and subsequent aging for up to 100 hours does not significantly alter the zeolite structure. In Figure 3, X-ray Photoelectron Spectroscopy (XPS) shows similar chemistry and valence in the samples as a function of hydrothermal aging time (see inset Table). The O, Si, Al, and Fe core level spectra show that the chemical bonding (gray highlighted areas) is similar in each. XPS also indicates the Si/Fe and Si/Al atomic ratios at the surface are slightly depleted in Fe as the hydrothermal aging time increases (see Figure 4). {Note the Si/Al change is an order of magnitude smaller than that of Si/Fe.}

Microscopy

The STEM results presented in Figures 5-8 were obtained using the HTML's JEOL 2200FS aberration-corrected STEM-TEM instrument that provides simultaneous bright field (BF) and high angle-annular dark-field (HA-ADF) images in scanning transmission mode. Energy-dispersive x-ray spectra and spectrum images were acquired using a Bruker-AXS silicon-drift detector system on the microscope. At zero hours, the samples show a SiO_x particle size of 0.3 μm (see Figure 5). The elemental maps show the locations of the Al and Fe to be coincident with some segregation of Al and Fe to boundaries and surfaces of primarily SiO_x particles. The Mg remains uniformly distributed, and the Pt map shows only background levels. Figure 6A indicates that the Pt particles are 1-4 nm in size. The SiO_x particle size appears to have

grown slightly in Figure 7 after 10 hours at 650°C in air with 7% H₂O. Again the elemental maps show coincident segregation of Al and Fe with a primary grain composition of SiO_x; note that the Pt is still at background level. Figure 6B indicates that the Pt particles are an order of magnitude larger than those at 0 hours. In Figure 8, the elemental maps show qualitatively that the coincident Al and Fe segregation may have increased with time under hydrothermal treatment (100 hours at 650°C in air with 7% H₂O). Figure 6C shows the Pt particle size is unchanged after 100 hours relative to that after 10 hours at 650°C in air with 7% H₂O. Microscopy also shows the SiO_x particle size remains about 0.3 μm (see Figure 8).

Redesigned Portable Gas Manifold Assembled

A redesigned portable manifold was assembled and is now ready for testing (see Figure 9). The manifold is capable of delivering gases, such as synthetic exhaust with water vapor, to reaction chambers and stages. This will facilitate in-situ studies with XRD, piezospectroscopic and possibly STEM techniques. High temperature XRD experiments using this manifold are planned for Fall 2011 to study the in-situ hydrothermal aging of samples at elevated temperatures in air with <10% H₂O.

Summary

The as-received AMO_x catalyst has been characterized using XRD, FTIR, XPS and TEM. The effect of hydrothermal conditions on the AMO_x catalyst appears to increase order and crystallinity in the Fe-Zeolite (FTIR+XRD). XPS indicates that the surface is slightly depleted in Fe. The Pt particles size increases from 3 to 20 μm from 0 to 10 h at 650°C in 7% H₂O. Hydrothermal aging will continue to be characterized to continue the evaluation of feasibility of the advanced tools available at ORNL for quantitative analysis of the materials changes underlying the AMO_x catalyst performance degradation with age.

References

1. United States Code of Federal Regulations 40 CFR 86 (7-1-10 Edition), pp. 144-722.
2. I. Chorkendorff and J. W. Niemantsverdriet, Concepts of Modern Catalysis and Kinetics, Wiley-VCH Verlag GmbH & Co. KGaA, Weinheim, 2003, pp. 395-400.

3. Multi-Year Program Plan 2011-2015, Vehicle Technologies Program, EERE, DOE, December 2010, pp. 2.3-2, 4

(http://www1.eere.energy.gov/vehiclesandfuels/resources/fcvt_plans_ro_admaps.html).

4. Paze´ et al., J. Phys. Chem. B **101** 4740-4751 (1997).

(S)TEM scanning transmission electron microscopy

XPS X-ray photoelectron spectroscopy

XRD X-Ray Diffraction

Presentations

T. R. Watkins, L. F. Allard, M. J. Lance, H. M. Meyer, K. Kamasamudram and A. Yezerets, "Catalyst Characterization," presented at the DOE 2011 Vehicle Technologies Annual Merit Review and Peer Evaluation Meeting, Washington, D.C., May 10, 2011.

Table I - Acronyms

ACEM	aberration-corrected electron microscope
AMOX	ammonia oxidation
ASC	ammonia slip catalysts
BF	bright-field
BSE	back-scattered electron
EDS	Energy dispersive spectroscopy
EPA	Environmental Protection Agency
FTIR	Fourier Transform-Infrared Spectroscopy
HA-ADF	high-angle annular dark-field
HTML	High Temperature Materials Laboratory
NOx	Nitrogen and Oxygen containing compounds
ORNL	Oak Ridge National Laboratory
SCO	selective catalytic oxidation

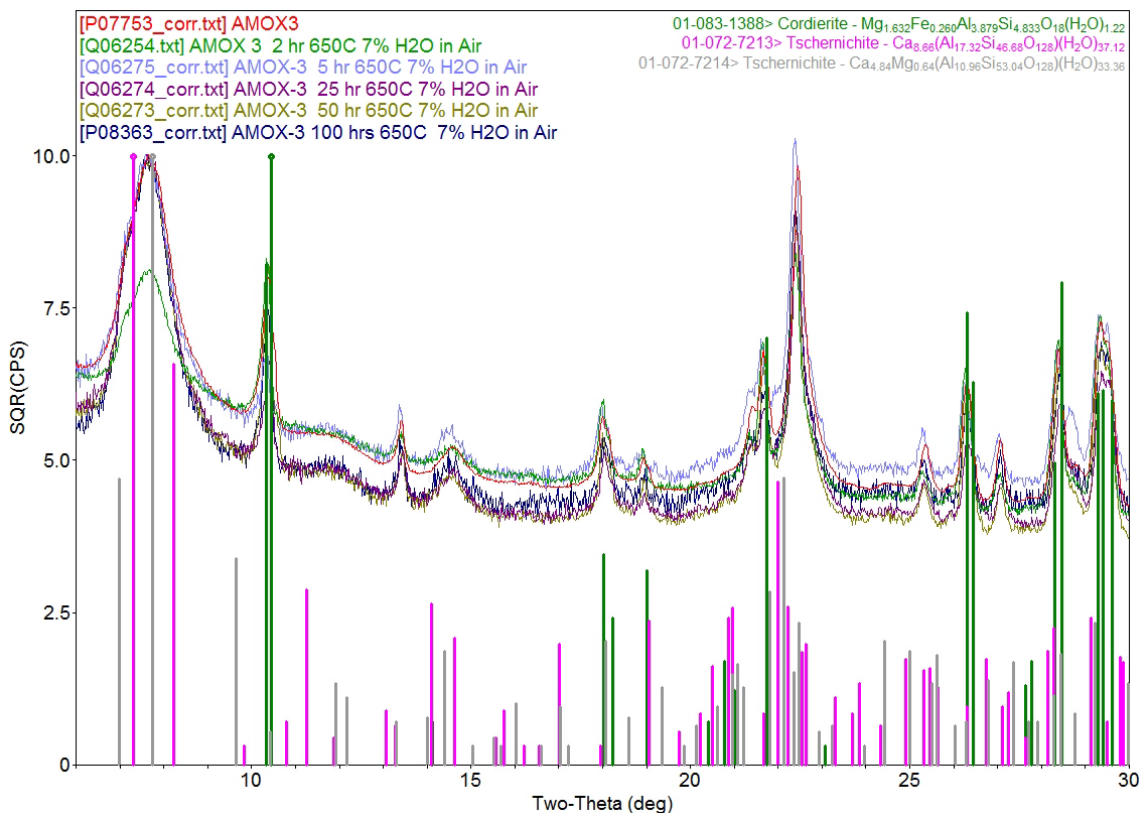


Figure 1. The x-ray diffraction patterns of an AMOX catalyst as a function of time at 650°C in air with 7% H₂O. Cordierite is identified and two end member zeolite phases are also indicated for the single zeolite phase present.

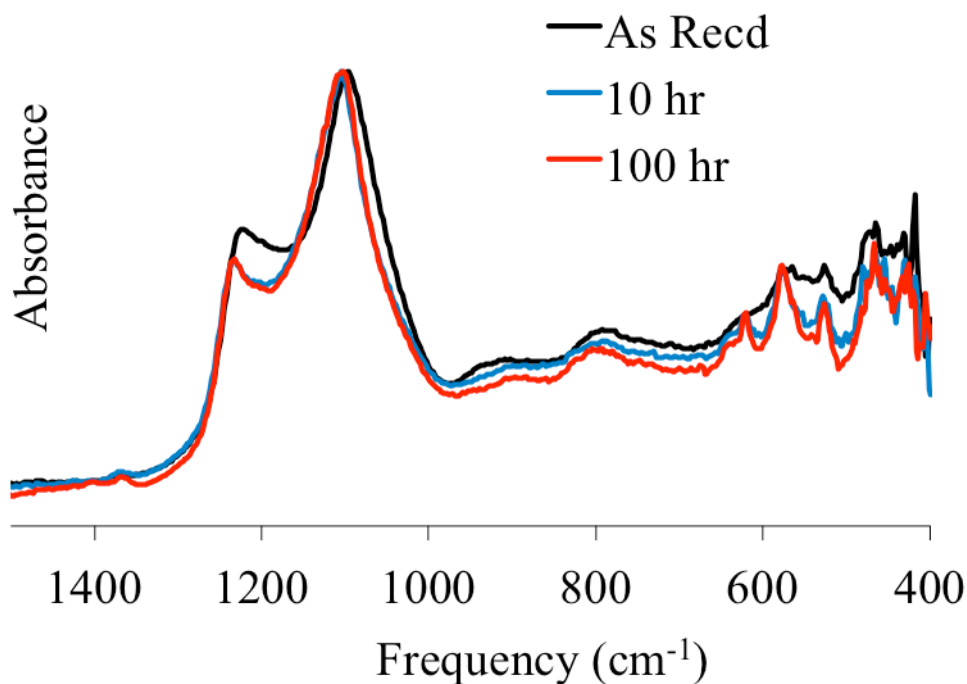


Figure 2. The FTIR spectrum of an AMOX sample showing the absorbance as a function of frequency as a function of time at 650°C in air with 7% H₂O. The spectrum was taken with a Nicolet 670 Fourier Transform-Infrared Spectrometer.

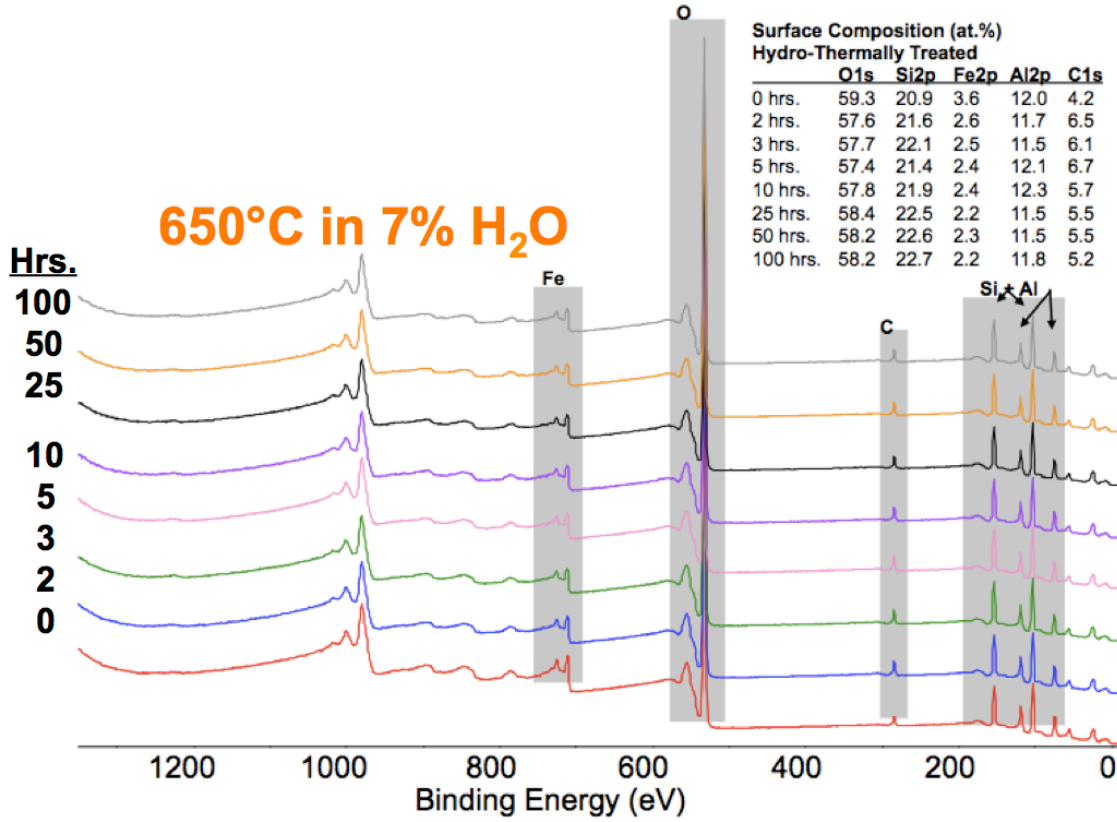


Figure 3. The intensity (arb. units) as a function of binding energy as a function of time at 650°C in air with 7% H₂O.

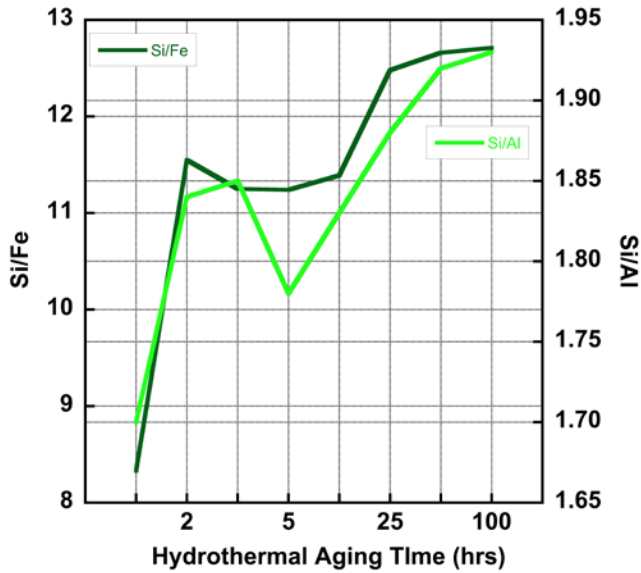


Figure 4. The atomic ratios of Si/Fe and Si/Al as a function of time at 650°C in air with 7% H₂O.

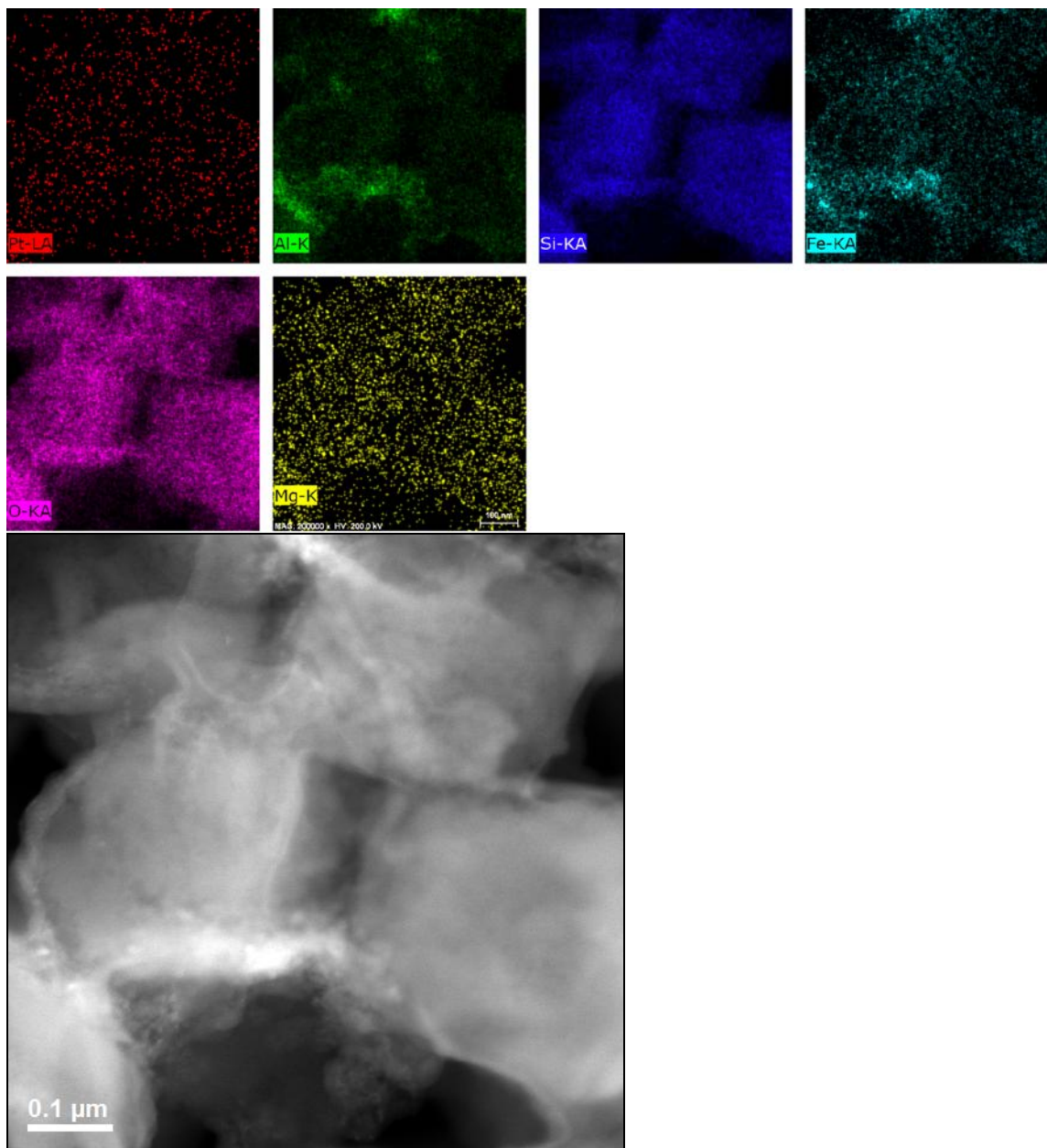
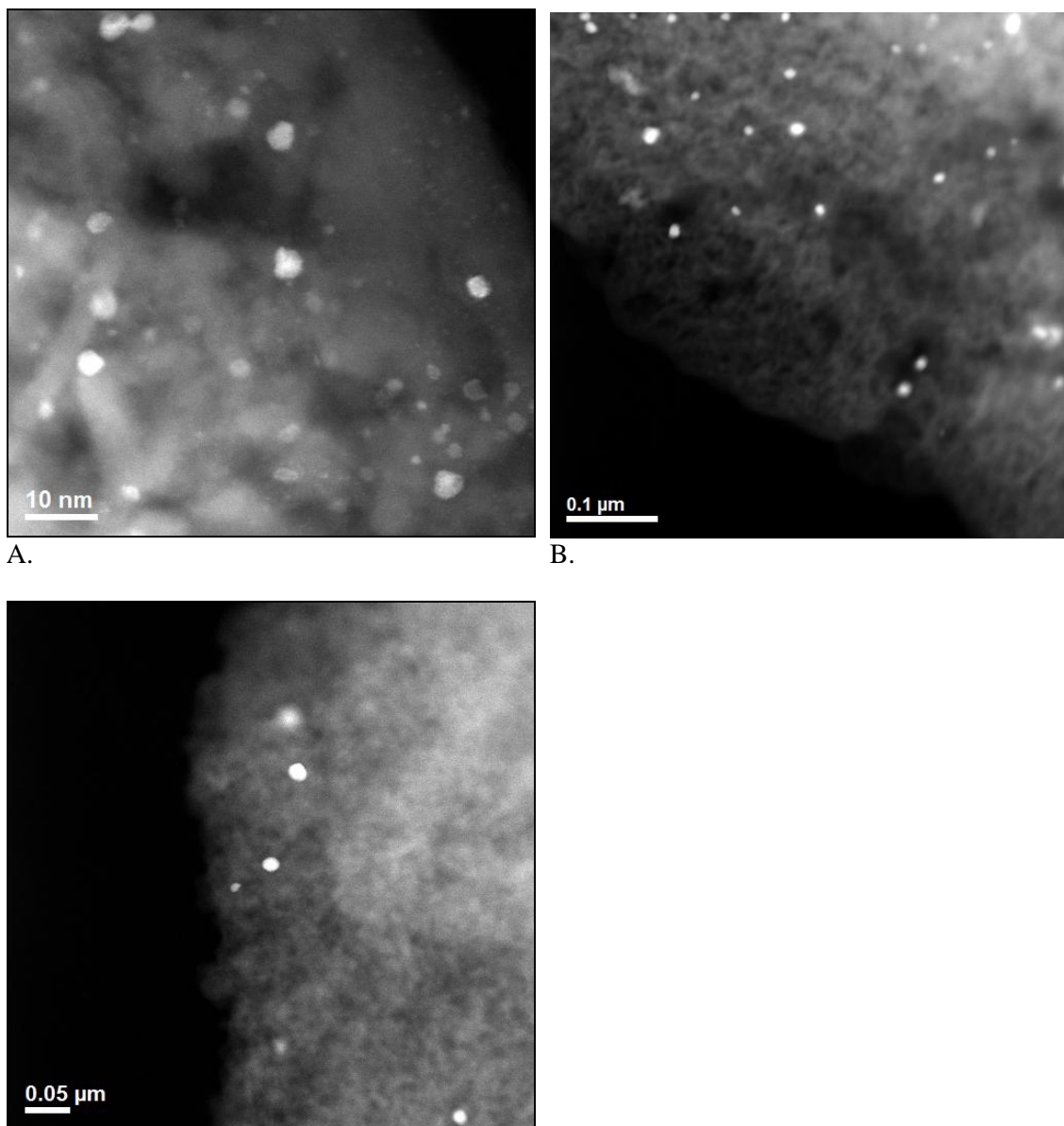


Figure 5. The elemental maps (top) of the region shown in the dark field image (bottom) after 0 hours at 650°C in air with 7% H₂O.



C.
Figure 6. A.) The HA-ADF image showing nominal Pt particles 1-4 nm after 0 hours. B.) The HA-ADF image showing nominal Pt particles 10-30 nm after 10 hours at 650°C in air with 7% H₂O. C.) The HA-ADF image showing nominal Pt particles 10-30 nm after 100 hours at 650°C in air with 7% H₂O.

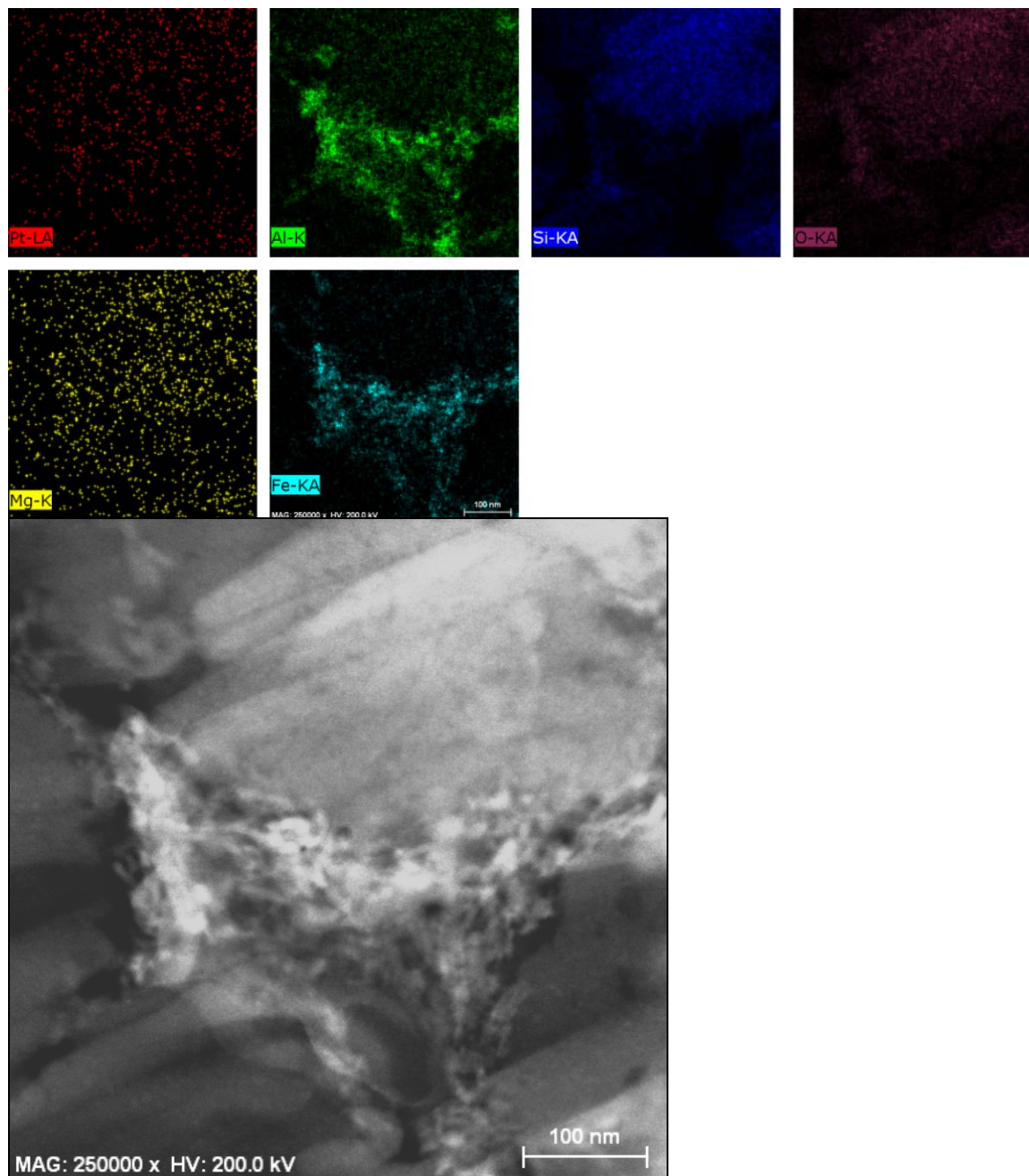


Figure 7. The elemental maps (top) of the region shown in the dark field image (bottom) after 10 hours at 650°C in air with 7% H₂O.

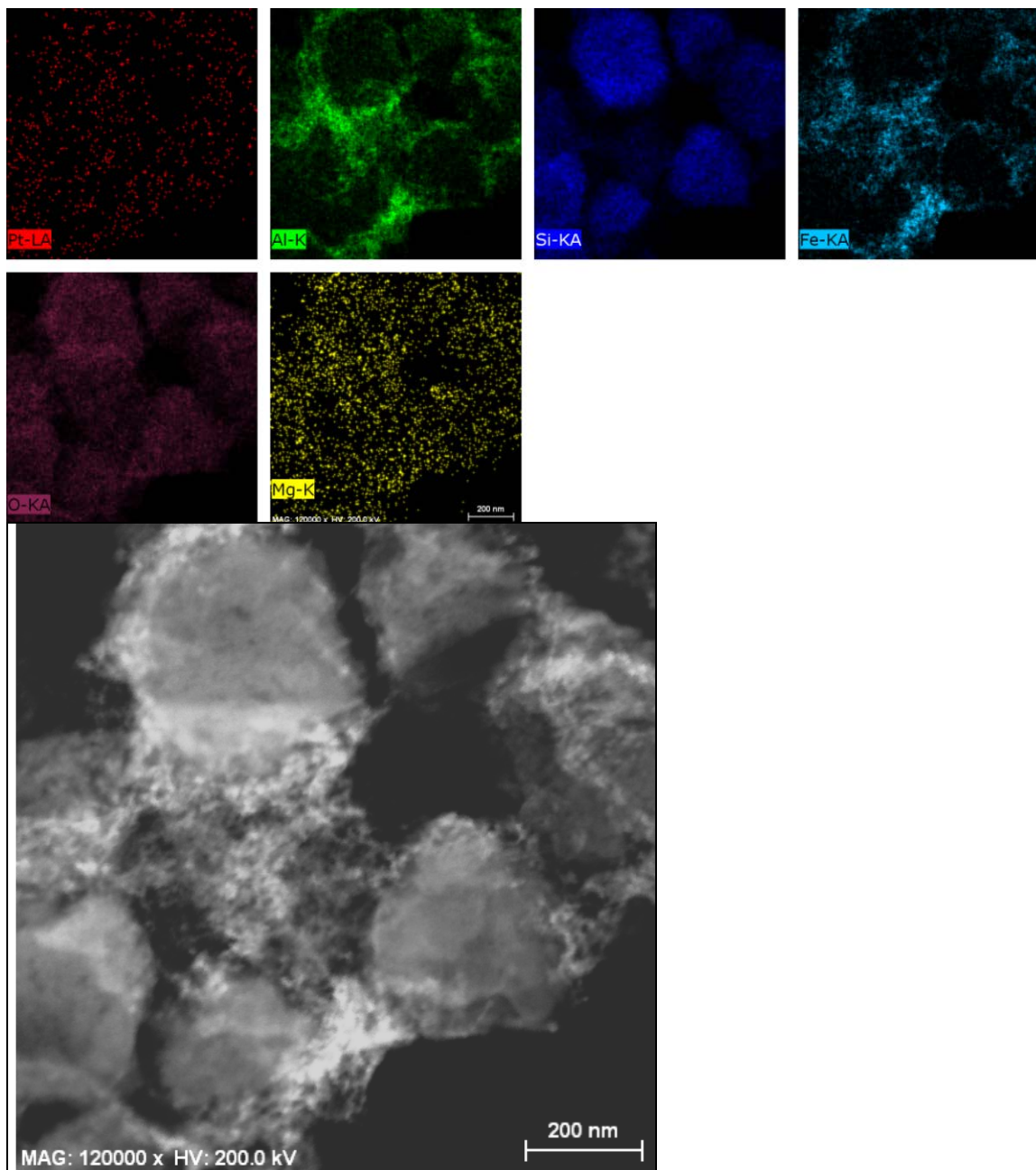


Figure 8. The elemental maps (top) of the region shown in the dark field image (bottom) after 100 hours at 650°C in air with 7% H₂O.

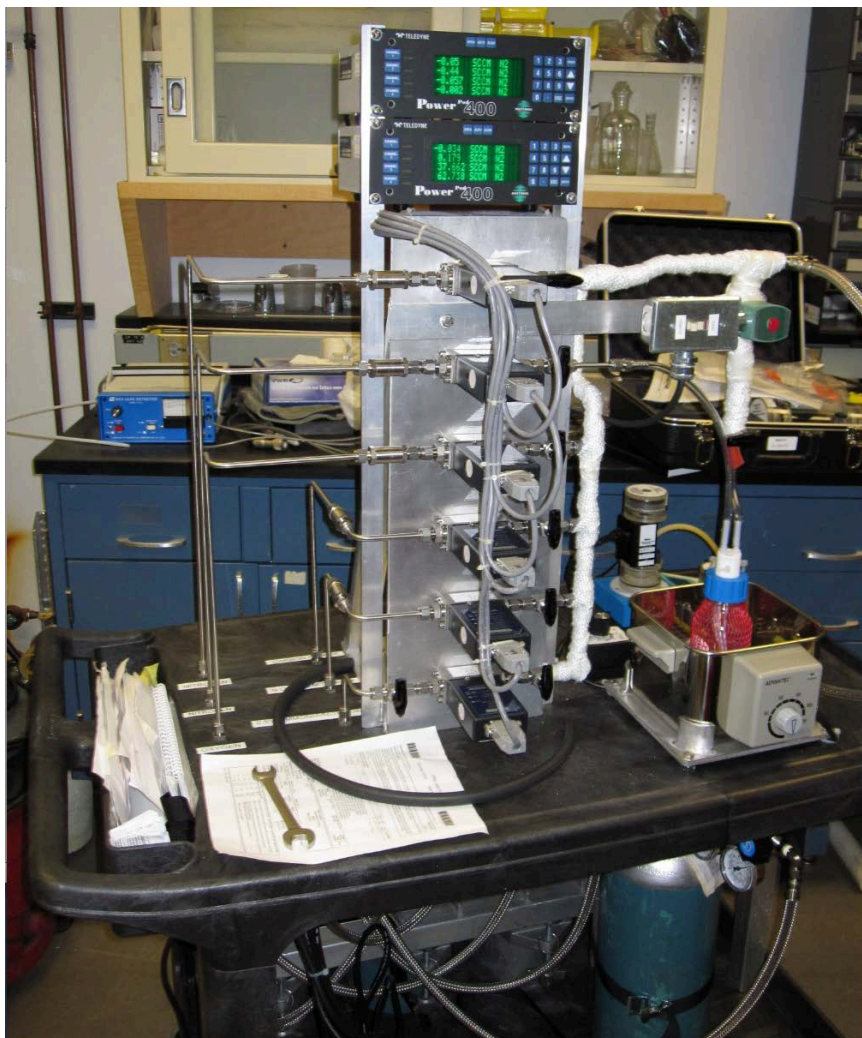


Figure 9. The assembled and redesigned portable manifold system. The total flow of the system will range from 50 to 400 standard cubic centimeters per minute (sccm) and handle six component gases: N_2 , NO, O_2 , NH_3 , CO_2 and H_2O . The gas lines will be heated to $>150^\circ C$ to prevent water condensation and in-line deposits. Given the corrosive and toxic nature of NH_3 and NO, respectively, these will originate from a cylinders with dilute starting mixture of each.

Agreement 10461 - Durability of Diesel Particulate Filters (CRADA with Cummins Inc.)

Thomas R. Watkins, Amit Shyam, and Hua-Tay Lin

Oak Ridge National Laboratory

P.O. Box 2008, MS-6064

Oak Ridge, TN 37831-6064

(865) 574-2046; fax: (865) 574-4913; e-mail: watkinstr@ornl.gov

Randall J. Stafford and Tom Yonushonis

Cummins Inc.

1900 McKinley Av., MC 50183

Columbus, IN 47201

(812) 377-3279; fax: (812) 377-7050; e-mail: randy.j.stafford@cummins.com

DOE Materials Engineer: Jerry Lee Gibbs

(202) 586-1182; fax: (202) 586-1600; e-mail: jerry.gibbs@ee.doe.gov

ORNL Technical Advisor: David P. Stinton

(865) 576-4556; fax: (865) 241-1034; e-mail: stintondp@ornl.gov

Contractor: Oak Ridge National Laboratory, Oak Ridge, Tennessee

Contract No.: DE-AC05-00OR22725

Objective

- To identify and implement test techniques to characterize the physical and mechanical properties of ceramic substrates used as diesel particulate filters (DPFs), to identify the mechanisms responsible for the degradation and failure of DPFs and to develop analysis tools for predicting their reliability and durability.

Approach

- Characterize the properties of and rank the thermal shock resistance of candidate DPF substrates.
- Application of advanced characterization techniques to DPF ceramic substrates.
- Refinement of DPF service lifetime prediction models based on characterization of field returned filters.

Accomplishments

- While the influence of temperature is negligible on the fracture toughness behavior of the cordierite and Al_2TiO_5 -based DPF materials tested, the fracture toughness of the SiC material appears to increase with temperature. A potential mechanism for this increase may be softening of the free Si.
- A surprisingly linear relation between the fracture toughness and strength was observed for four highly porous materials, together, with porosities ranging from 50 to 68%.

Future Direction

- Complete the determination of strength, fracture toughness, density/porosity/microstructure, and thermal expansion of coated DPFs as a function of time at elevated temperatures of 300, 500, 800 and 900°C for a second alternate substrate DPF material.
 - Continue characterization of the dynamic and static fatigue response of SiC DPFs.
-

Introduction

The EPA regulates the emissions of nitrogen oxides (NO_x) and particulate matter (PM) from diesel engines. Stringent regulation on PM went into effect in 2007. There are many technologies designed to reduce emissions from diesel engines; prominent among the technologies for PM control are diesel particulate filters (DPFs). A DPF is often a ceramic device that collects particulate matter in the exhaust stream. The high temperature nature of the ceramic withstands the heat of the exhaust and allows heating to break down (or oxidize) the particles inside. DPFs reduce emissions of PM, hydrocarbons, and CO by 60 to 90%.

Most DPFs consist of a ceramic honeycomb with hundreds of cell passages partitioned by walls (Figure 1). Each cell passage has a square cell opening at one end and is closed at the other end so that the cell passages are alternately closed at each end. The so-called checkerboard plugging structure forces the exhaust gases through the porous, thin ceramic honeycomb walls. When the gases carrying the PM flow through the fine pores of the walls, the PM is filtered out. High porosity values, in the range of 40-70%, heighten filtration efficiency to more than 90% and reduce gas-flow resistance for better engine performance.

The process of diesel PM collection continues while the engine is operating. The particles are collected on the ceramic walls and as a result, the backpressure of the system increases. The backpressure is reduced by oxidizing the trapped PM, aided by a catalytic reaction using exhaust gas heat at 400°C or more, into CO₂ and water vapor. This process, called regeneration, results in a cleaner filter. The regeneration process is dependent upon exhaust temperature, oxygen, NO_x content, time, and PM levels.

The *key* to the successful application of DPFs is to reliably regenerate the filter (e.g., to clean up the PM that the filter continues to trap or collect). Traditionally, combustion of soot is done in an oxygen atmosphere (air). In air, the soot will oxidize at ~500°C. However, this is not a typical operating temperature for diesel engine exhaust. Therefore, to oxidize soot in air, an active system—i.e., one that increases the temperature of the exhaust using some external heat source—is required. But if an active system is not carefully controlled, or if too much PM collects on the filter walls, the filters can experience

an “uncontrolled regeneration” where the temperature increases to 600°C or more, resulting in damage to the filter element.

A useful conceptual model for the prediction of reliability is the bathtub curve (see Figure 2), which describes reliability-related phenomena of a component over its life cycle.¹ The reliability bathtub curve can be used as a descriptor of how the failure rate of DPFs evolves over time. Infancy failures of DPFs could be related to manufacturing or process defects (large pores, inclusions, cracking) or defects introduced during assembly. Failures of DPFs during their useful life will be dictated by the intersection between the spectrum of thermomechanical loads and the distribution of DPF strengths. Such failures could result from excessive vibration, for example, or unwanted thermal excursions during transients associated with regeneration. Wear-out and degradation failures of DPFs could also be associated with the growth of microcracks by thermal fatigue, and assisted by the chemistry of the environment, and/or by chemical and microstructural changes in the material due to long-term exposure to elevated temperatures in the exhaust environment.

The objective of this project is to implement test techniques to characterize the physical and mechanical properties of ceramic DPF substrates and to develop analysis and inspection tools for assessing the reliability and durability of DPFs. The developed tools and methods would allow the design of more durable and reliable DPFs. An important outcome of the development of the test methods is the ability to rank the relative thermal shock resistance of substrates in different conditions (catalyzed, soot loaded, field returned etc.) and of different candidate substrate materials.

Goals, Barriers, Relevance & Integration²

In the study area of VT’s Materials Technology and Advanced Combustion Engine research, the *goals* are (1) by 2015, develop materials that reduce the fuel economy penalty of particle filter regeneration by at least 25% relative to the 2008 baseline and (2) to develop aftertreatment technologies integrated with combustion strategies for emissions compliance and minimization of efficiency penalty, respectively. This project addresses the three *barriers* related to the Emission Control System in this study area: changing internal combustion engine combustion regimes, long lead

times for materials commercialization and cost. This project is *relevant* to both goals as the thrust is to characterize and improve the durability, resulting in the lowest overall cost and preventing emission release in service. This is achieved by understanding of the relationships of the material properties for the filter (and catalyst) substrates enables optimization of porosity, strength, elastic modulus, thermal conductivity, thermal expansion, etc. leading to thermal management and improved efficiency. This project supports clean diesel, which increases acceptance by the public. Larger acceptance, in turn, results in larger percentages of conversion to diesel, with the resulting reduction in petroleum usage/dependency upon foreign oil. This project is *integrated* within Vehicle Technologies program as DPF substrate material are used in both DPF and catalyst systems and as it utilizes characterization tools acquired and maintained by the High Temperature Materials Laboratory (HTML) Program.

Approach

The design process for making DPFs that are durable and reliable includes a complex materials property optimization and selection process.³ For example, the porosity of DPFs, which allows the removal of PM from the exhaust gas stream, has a deleterious effect on their mechanical and fracture strength. A higher porosity, though, decreases the engine backpressure and increases efficiency of the diesel engine. Designing mechanically reliable DPFs is important because these components will experience demanding thermo-mechanical conditions during service. These include, for example, thermal shock resulting from rapid heating/cooling and thermal stresses that arise from temperature gradients.

Techniques to assess the elastic and fracture properties of virgin or unexposed DPF substrates have been identified, implemented and reported earlier.⁴ The test techniques were applied to rank the suitability of common candidate substrates for application in DPFs. The developed test techniques were applied to characterize field returned DPFs. The material properties responsible for the thermal shock resistance and mechanical property degradation in the various stages of the bathtub curve were determined. These properties include thermal expansion, thermal conductivity, heat

capacity, density, porosity, elastic properties, strength, fracture toughness, and environmentally assisted crack growth at ambient and elevated temperatures, in air and in relevant environments.

The information generated will in turn be input into predictive models. Such service life predictions are based on a combination of experimentally determined strength data, stress analyses of the component using a finite-element analysis, and selection of appropriate failure criteria. The durability (service life) of the component can also be predicted using this framework by considering the mechanisms that are responsible for the degradation of material strength, such as slow crack growth or creep.

Results

New SiC-based DPFs were sectioned and samples were machined. Powder from a comminuted section was examined with x-ray diffraction (XRD) and found to contain 6H-SiC, free silicon metal, SiO₂ (triclinic) and possibly another polytype of SiC and/or another SiO₂ phase (see Figure 3). Table I lists the measured properties of the cordierite (2MgO•Al₂O₃•2SiO₂), Al₂TiO₅-based and SiC DPF materials. The low values of Young's Modulus, strength and fracture toughness all reflect the high porosity. The linear coefficients of thermal expansion (LCTE) for the cordierite and Al₂TiO₅-based materials also reflect the high porosity, and both display a value perpendicular to the extrusion direction that is twice that in the parallel direction. This is likely related to some preferred orientation and the microcracking (due to the high crystallographic anisotropy of the CTEs), absent in the SiC material. The SiC material does not show any CTE anisotropy and little influence of porosity (see Table II).

Figure 4 shows the double torsion experimental set-up for fracture toughness, K_{IC}, testing as well as a double torsion fracture surface. Given the complicated porous microstructure, the double torsion method was selected as the measured crack length is not needed.⁵ The loading jig has an upper and lower part. The sample rests on 4 spheres and load is transmitted through 2 spheres in the jig top. Load is applied to the jig top via the push-rod from above. The SiC fracture surface exhibits nodules of Si (as determined with energy dispersive spectroscopy confirming the XRD) and an

occasional fracture-induced microcrack (see Figure 4). As noted previously,^{6,7} the cordierite and Al_2TiO_5 -based DPF fracture surfaces exhibit numerous microcracks. The room temperature and 500°C fracture surfaces were indistinguishable.

A comparison of the typical double torsion stress intensity vs. displacement curves is shown in Figure 5 for testing at ambient and 500°C. Minimal change in slopes suggest that the elastic moduli are the same or slightly lower at 500°C. The curves do not start at zero stress intensity/load as the sample is preloaded with the weight of the jig top. The average K_{IC} and ESD values listed in Table I suggest that the influence of temperature is negligible on the K_{IC} behavior for the cordierite and Al_2TiO_5 -based materials. In contrast, the K_{IC} of the SiC material appears to increase with temperature. A potential mechanism for this increase in toughness for SiC-based material is attributed to softening of the free Si which is similar to behavior exhibited by reaction-bonded SiC between RT and 800°C.⁸

Figure 6 shows a surprisingly linear relation between the fracture toughness and strength for these highly porous materials. The K_{IC} increases with strength; the strength values were corrected for the moment of inertia of the honeycomb structure for three DPF materials. Both the fracture toughness and strength increase with decreasing porosity for the cordierite data. The lowest and highest strength samples have relative porosities of 68.1 and 50.2%, respectively. The mullite-based material possessed an unusual microstructure of interpenetrating needles, which results in the high strength and toughness with high porosity (63.1%).

Since fracture toughness measurements are easier to perform and require less material than strength testing, a new thermal shock parameter, $R_K = K_{IC}/\alpha E$, has been adopted as was discussed previously,⁷ where E is the Young's modulus. R_K is calculated from measured parameters and is tabulated for various DPF materials and conditions in Figure 7. This highly simplified analysis provides a means to compare and suggests that the SiC appear to be thermal shock intolerant relative to the other materials and conditions.

The material data collected is input into predictive models to estimate lifetimes of filters through regeneration cycles. Figure 8A shows an axisymmetric DPF with a predefined thermal profile. As the exhaust flows left to right, the shown

profile is hottest in the center. Figure 8B shows the corresponding thermal strain for two DPFs, one with an elastic modulus twice the other. Figure 8C shows the impact this has on the predicted number of regeneration cycles before component failure.

A study of dynamic fatigue response of a commercially available SiC DPF was initiated and conducted during the 2nd half of FY2011. The SiC DPF flexural specimens with 3 x 4 and 3 x 6 cell sizes were extracted from the as-received SiC DPF components. The study of dynamic fatigue response was carried out at temperatures ranging from 600 to 900°C under the stressing rate between 3 and 3×10^{-6} MPa/s in air.

Figure 9 compares the dynamic fatigue responses of SiC DPF samples with 3x4 and 3x6 cell size. The preliminary result showed that the SiC DPF materials exhibited similar high flexural strengths to those reported earlier for mullite DPFs manufactured by DOW, which were higher than both cordierite and Al_2TiO_5 -based DPF materials. Also, the mechanical results showed that the flexural strength is insensitive to the sample size used in this study. While the 600°C results showed that there is no stressing-rate dependence of flexural strength (from 3 to 3×10^{-4} MPa/s), there was a minor increase in flexural strength with decreasing stressing rate for temperature at 800 and 900°C. A detailed SEM study will be carried out to provide insight into the observed increase in flexural strength at higher temperatures, which perhaps is related to the observed toughness increase reported above. In addition, tests at much lower stressing rate (3×10^{-6} MPa/s) will be conducted to provide a better understanding of the SiC DPF resistance to the slow crack growth at these test conditions. Also, more test samples will be tested, repeating these conditions to obtain a better statistics.

Summary

Mechanical and thermal shock characterization test procedures developed earlier were employed to measure properties in SiC DPF materials, the focus here. The properties and microstructure of the SiC were compared to those of the cordierite and Al_2TiO_5 -based DPF materials. The fracture toughness of the SiC DPF was measured using the double torsion technique and found to increase from room temperature to 500°C. The fracture strength was measured as a function of stressing rate, sample

size and temperature; the strength was observed to increase with temperature. The mechanism for this is thought related to the softening of the free silicon. The importance of reliable input data was demonstrated with predictive simulations of the number of regeneration cycles to component failure.

References

1. G. S. Wasserman, *Reliability Verification, Testing and Analysis in Engineering Design*, Marcel Dekker, New York, 2003.
2. Multi-Year Program Plan 2011-2015, Vehicle Technologies Program, EERE, DOE, December 2010, pp. 2.3-1; 2.5-7, 8
(http://www1.eere.energy.gov/vehiclesandfuels/resources/fcvt_plans_roadmaps.html).
3. J. Adler, "Ceramic Diesel Particulate Filters," *International Journal of Applied Ceramic Technology*, **2** [6] 429-39, 2005.
4. Propulsion Materials Annual Progress Reports, Vehicle Technologies Program, US DOE, Energy Efficiency and Renewable Energy, Office of Vehicle Technologies,
www.ornl.gov/sci/propulsionmaterials/Reports.html.
5. A. Shyam and E. Lara-Curzio, *J. Mater. Sci.* **41** 4093-104 (2006)
6. T. R. Watkins, H-T. Lin and A. Shyam, "Durability of Diesel Particulate Filters (CRADA No. ORNL-04-0692 with Cummins Inc.)," FY 2009 Progress Report for the Heavy Vehicle Propulsion Materials Program, December 2009.
7. T. R. Watkins, A. Shyam, H-T. Lin, E. Lara-Curzio, R. J. Stafford and T. Yonushonis, "Durability of Diesel Particulate Filters (CRADA No. ORNL-04-0692 with Cummins Inc.)," FY 2010 Progress Report for the Heavy Vehicle Propulsion Materials Program, December 2010.
8. Q-W. Huang and L-H. Zhu, *Mat. Ltrs.* **59** 1732-5 (2005).
9. C. Bubeck, "Direction Dependent Mechanical Properties of Extruded Cordierite Honeycombs," *J. Euro. Ceram. Soc.* **29** 3113-9 (2009).
10. S. Bueno, M.G. Hernández, T. Sánchez, J.J. Anaya, C. Baudín, "Non-destructive Characterization of Alumina/Aluminum Titanate Composites Using a Micromechanical Model and Ultrasonic Determinations Part I. Evaluation of the Effective Elastic Constants of Aluminum Titanate," *Ceramics International* **34** 181-8 (2008).
11. T. R. Watkins, D. J. Green, and E. Ryba, "Determination of Young's Modulus in Chemically-Vapor-Deposited SiC Coatings," *J. Am. Ceram. Soc.* **76** [8] 1965-68 (1993).
12. S. Aroati, M. Cafri, H. Dilman, M.P. Dariel, N. Frage, "Preparation of reaction bonded silicon carbide (RBSC) using boron carbide as an alternative source of carbon," *J. Euro. Ceram. Soc.* **31** 841-845 (2011).
13. P. G. Karandikar, G. Evans, S. Wong S, M. K. Aghajanian, M. Sennett, "A Review of Ceramics for Armor Applications," pp. 163-175 in *Advances in Ceramic Armor IV, Ceramic Engineering and Science Proceedings*, V. 29. Edited by L.P. Franks, T. Ohji, A. Wereszczak, Wiley, Hoboken, NJ 2009.
14. C.J. Luis, I. Puertas, G. Villa, "Material Removal Rate and Electrode Wear Study on the EDM of Silicon Carbide," *J. Mat. Proc. Tech.* **164-165** 889-896 (2005).
15. M. E. Milberg and H. D. Blair, "Thermal Expansion of Cordierite," *J. Am. Ceram. Soc.* **60** [7-8] 373-4 (1977).
16. H.A.J. Thomas and R. Stevens, "Aluminum Titanate – A Literature Review," *Br. Ceram. Trans. J.* **88** [4] 144-51 1989.
17. W. R. Buessem, N. R. Thielke, R. V. Sarakauskas, "Thermal Expansion Hysteresis of Aluminum Titanate," *Ceramic Age* **60** [5] 38-40 (1952).
18. T. R. Watkins and D. J. Green, "Fracture Behavior of Chemically-Vapor-Deposited SiC-Coated Graphite: I, Experimental Results," *J. Am. Ceram. Soc.* **76** [12] 3066-72 (1993).
19. P. Columbo, V. Sglavo, E. Pippel, J. Woltersdorf, "Joining of Reaction-Bonded Silicon Carbide Using a Pre-ceramic Polymer," *J. Mat. Sci.* **33** 2405-2412 (1998).

Presentations, etc.

1. T. R. Watkins, A. Shyam, R. Stafford, "Elevated Temperature Fracture Toughness Behavior of Porous Ceramic Materials," presented at the 35th International Conference on Advanced Ceramics and Composites Meeting held in Daytona Beach, FL, January 25, 2011.
2. **Invited Talk:** R. J. Stafford, P. J. Gloeckner, T. R. Watkins, A. Shyam, E. Lara-Curzio, "Elastic Modulus Measurement of Porous Cellular Ceramics

Using Multiple Test Methods,” presented by R. J. Stafford at the 35th International Conference and Exposition on Advanced Ceramics and Composites, Daytona Beach, FL, January 25, 2011.

3. T. R. Watkins, A. Shyam, H.T. Lin, E. Lara-Curzio, R. Stafford, T. Yonushonis, “Durability of Diesel Engine Particulate Filters,” presented at the DOE 2011 Vehicle Technologies Annual Merit Review and Peer Evaluation Meeting, Washington, D.C., May 11, 2011.

4. **Invited Talk:** T. R. Watkins, A. Shyam, R. Stafford, “Microstructure and Select Mechanical Properties of Three Porous Ceramic Materials,” presented at the 242nd American Chemical Society National Meeting & Exposition, Denver, CO, August 29, 2011.

ORNL and Cummins personnel traveled to Daytona Beach, FL for meetings of the ASTM C28.01 Mechanical Properties and Reliability and ASTM C20.04 Ceramic Applications committees on January 23, 2011 which, in part, provide standards for the DPF community.

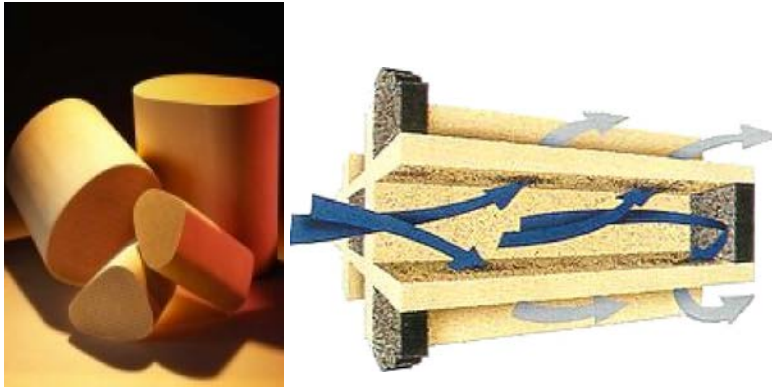


Figure 1. Cordierite-based DPFs.

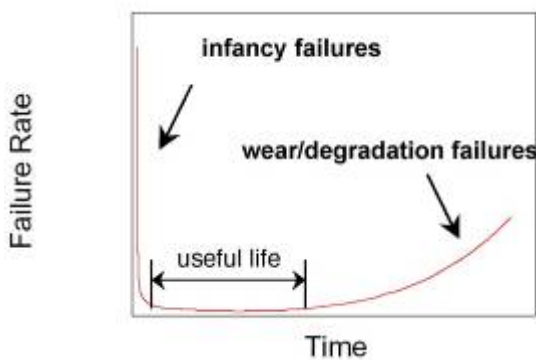


Figure 2. Reliability bathtub curve.

Table I – Select properties measure from DPFs.

Property/Material	Cordierite	Al ₂ TiO ₅	SiC
Porosity (%)	50.4	51.9	58.3
Young's Modulus (GPa)*	16.2(0.2) [§]	6.19(1.17)	20(2.5)
LCTE parallel [¢] (x10 ⁻⁶ 1/°C)	0.48	1.07(0.15)	5.00(0.04)
LCTE perpendicular [¢] (x10 ⁻⁶ 1/°C)	0.99	2.17(0.15)	5.10(0.08)
Strength (MPa) @ RT [¥]	7.33(0.45)	2.98	19.5(0.63)
K _{IC} @RT	0.31(0.02)	0.13(0.02)	0.42(0.05)
K _{IC} @500°C	0.25(0.04)	0.16(0.02)	0.55(0.03)

*DMA (Dynamic Mechanical Analysis); moment of inertia (MOI) corrected; 2-5 samples, Each remounted >5 X

[¢] Linear coefficient of thermal expansion, RT -1000°C parallel and perpendicular to the extrusion direction

[§] Average value, value in () is the estimated standard deviation (ESD)

[¥] Strength MOI corrected

Table II – Literature values for Young’s modulus and thermal expansion coefficient of dense materials.

Property/Material	Cordierite	Al ₂ TiO ₅	SiC
Polycrystalline Young’s Modulus for dense material (GPa)	138 ^{†,9}	155 ^{††,10}	420 ^{∞,11} , 320-340 ^{§,12} , 359-407 ¹³
Polycrystalline CTE for dense material (x10 ⁻⁶ 1/°C)	1.14 ¹⁴ , 0.7 ¹⁵	9.7 ^{†,16} , 1.73 ^{†,17}	4.85 ^{∞,18} , 4.5 ¹⁹ , 4.3-4.6 ¹⁴

[∞] CVD β-SiC, no free Si

[§] 15-35 v% free Si

[†] based on single crystal data (w/o microcracks)

^{††} Indirectly determined, assumed dense.

↵ For hexagonal cordierite: Indialite.

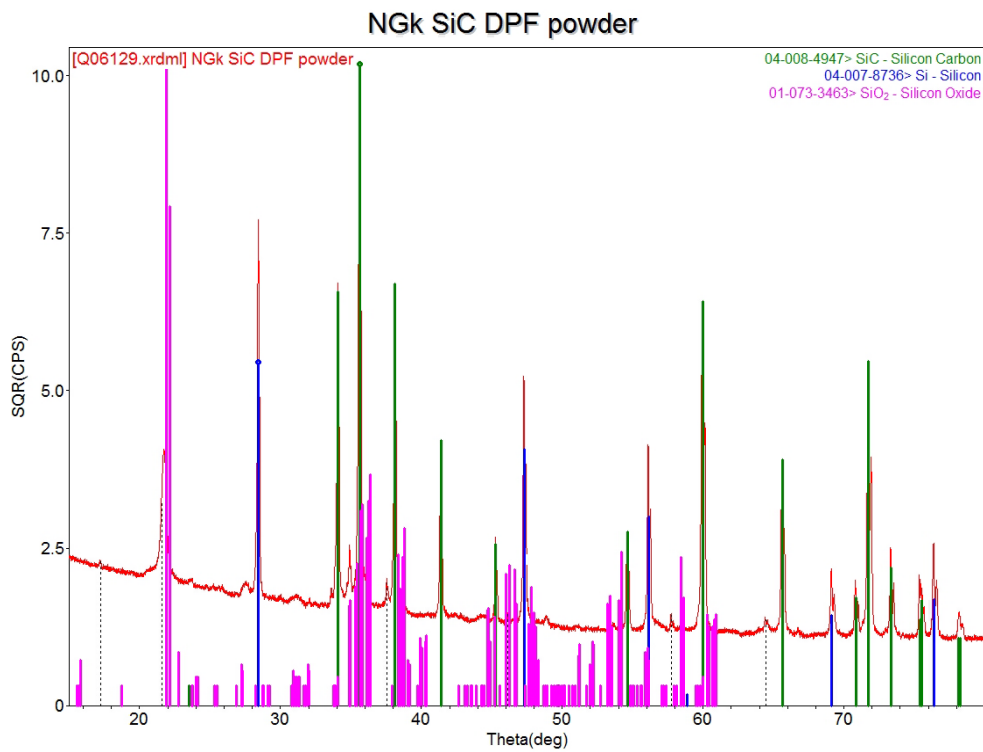


Figure 3. X-ray diffraction pattern of powder from a comminuted SiC DPF specimen.

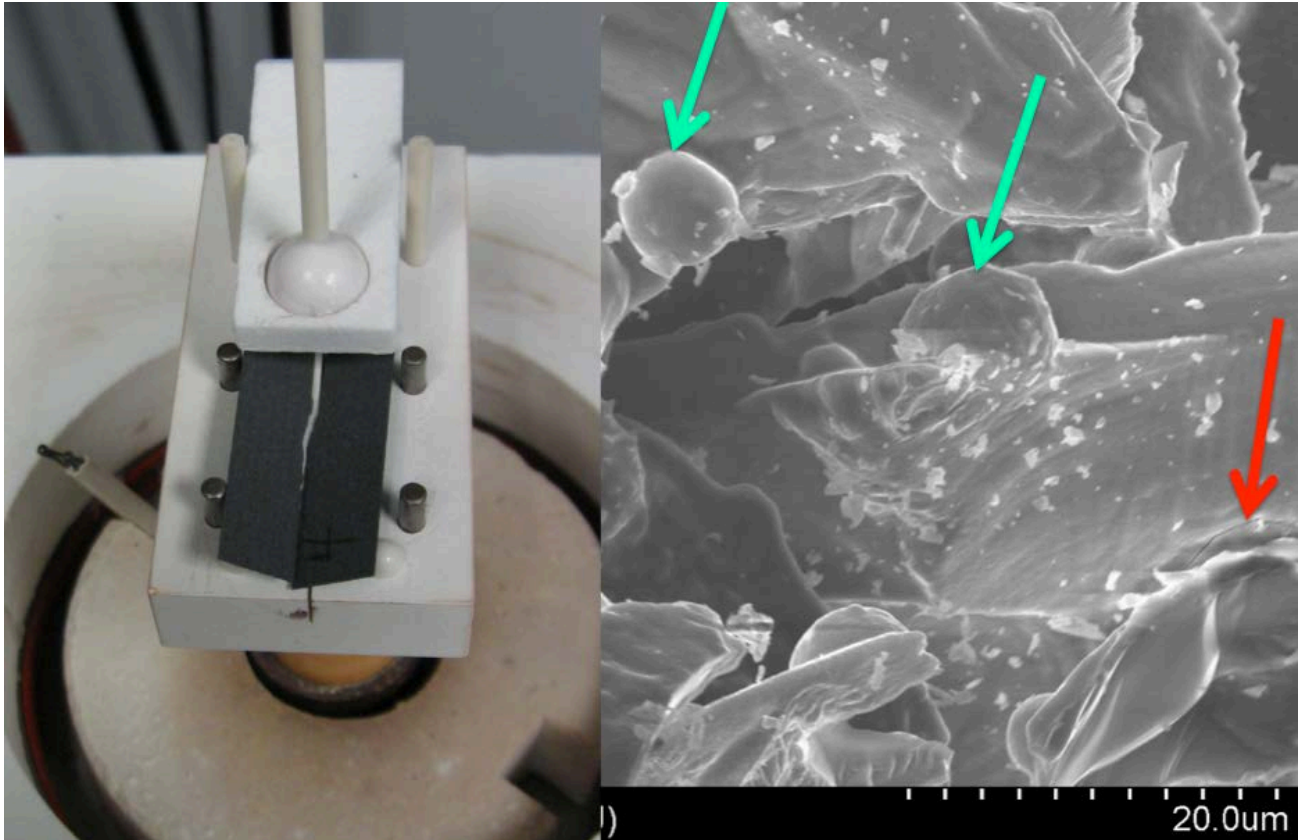


Figure 4. (left) The double torsion set up showing a successfully tested SiC DPF specimen. (right) A SEM micrograph showing the Si nodules (green arrows) and a rare microcrack (red arrow).

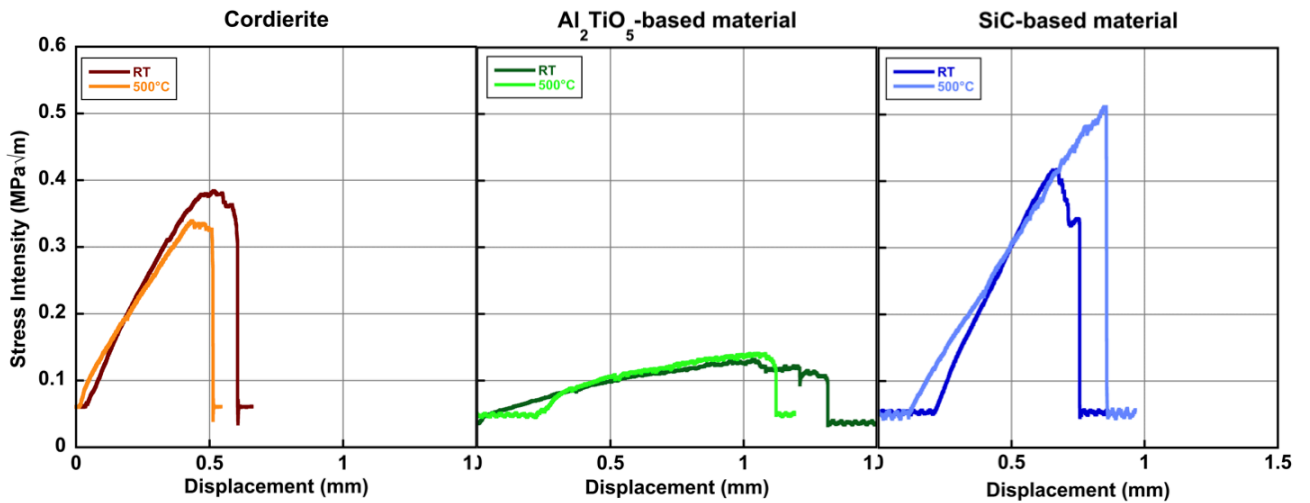


Figure 5. Stress intensity as a function of displacement for typical cordierite, Al₂TiO₅ and SiC DPFs at room temperature and 500°C.

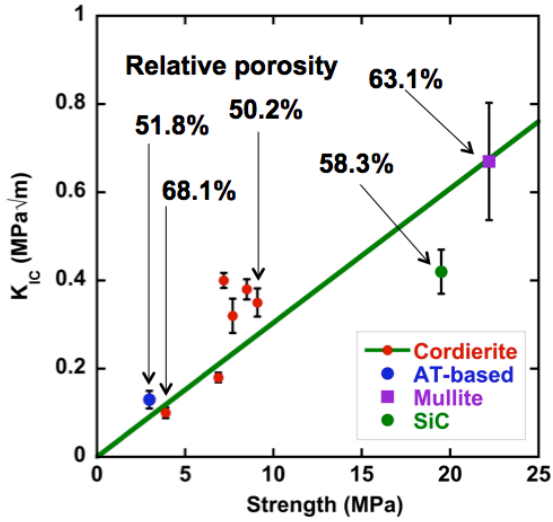


Figure 6. The fracture toughness as a function of strength for various DPF materials and their porosity.

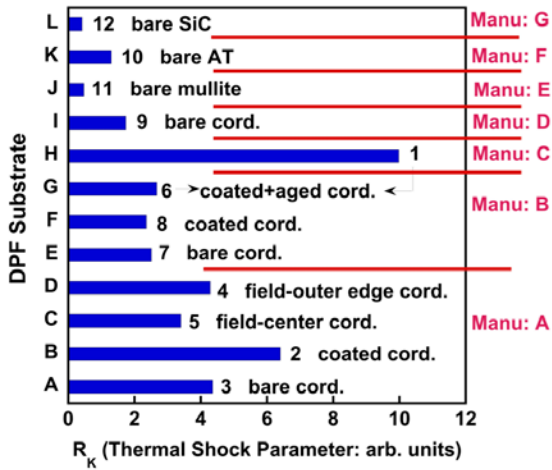


Figure 7. The thermal shock parameter, R_K , for the various DPF examined.

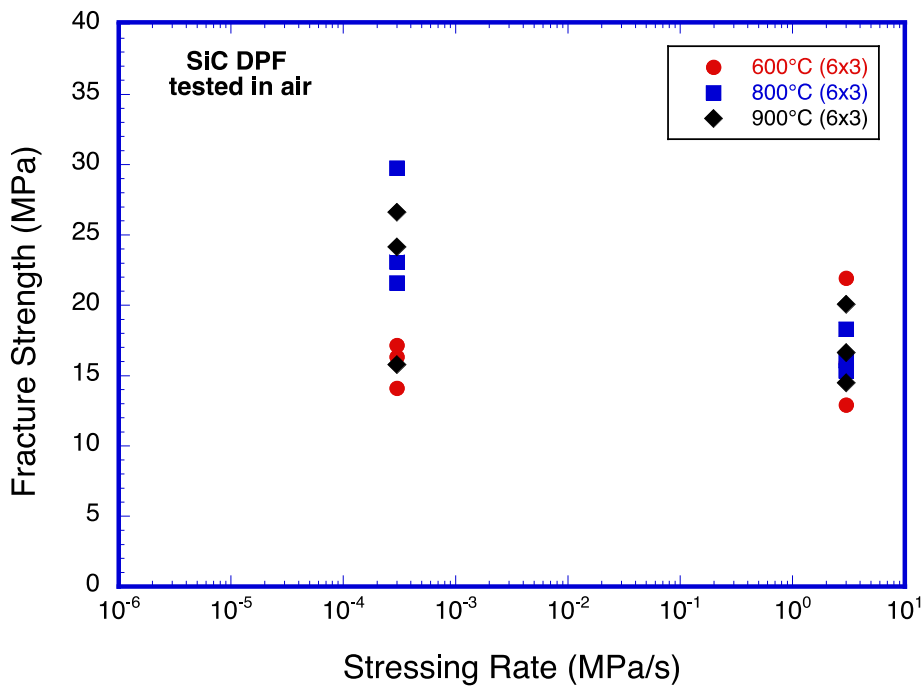
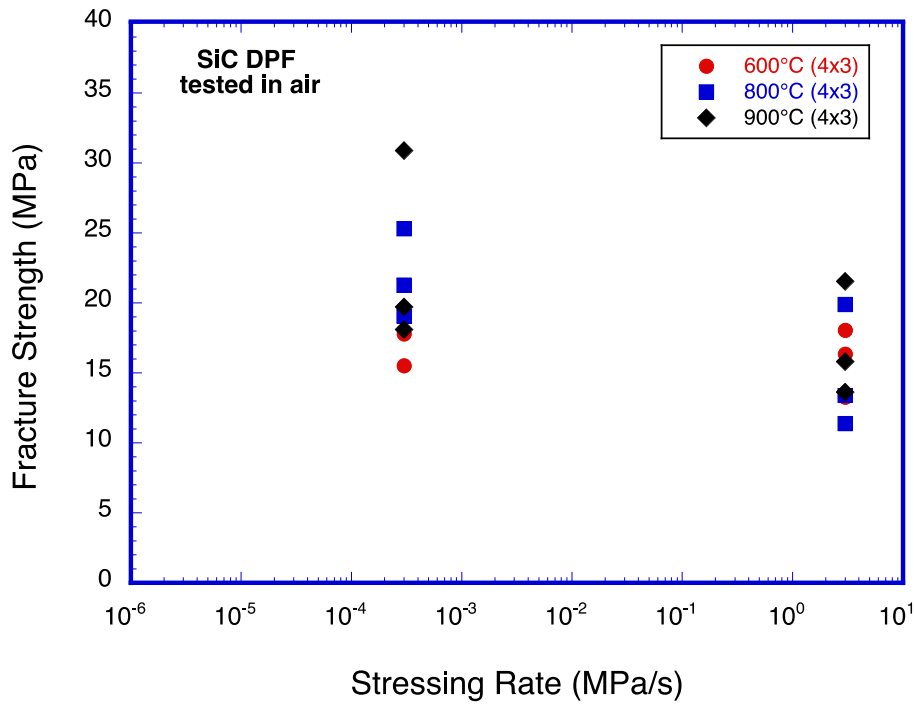


Figure 9. Fracture strength as a function of stressing rate, sample size (smaller above, bigger below) and temperature.

Agreement 10635 - Catalysis by First Principles

C. K. Narula, M. Moses-DeBusk, M. Stocks, X. Yang

Oak Ridge National Laboratory

P.O. Box 2008, MS 6116

(865)574-8445, narulack@ornl.gov

DOE Technology Manager: Jerry L. Gibbs

(202) 586-1182; fax: (202) 586-1600; e-mail: Jerry.gibbs@ee.doe.gov

Field Technical Manager: David P. Stinton

(865) 574-4556; fax: (865) 241-1034; e-mail: stintondp@ornl.gov

Contractor: Oak Ridge National Laboratory, Oak Ridge, Tennessee

Contract No.: DE-AC05-00OR22725

Objective

- The objective of this work is to search for durable emission treatment catalysts (LNT, TWC, OC, SCR) from a protocol based on
 - an integrated approach between computational modeling and experimental development,
 - design and testing of new catalyst materials to rapidly identify the key physiochemical parameters necessary for improving the catalytic efficiency of these materials.

Approach

- Theoretical and Experimental Studies of
 - Pt clusters supported on alumina and metal exchanged zeolites. Interaction of CO, NO_x, and HC with Pt clusters supported on alumina and NO_x reduction on zeolites
 - Understand non-structural changes in catalyst under operating conditions and correlating the changes to performance.

Accomplishments

- We have shown by theoretical models that single atoms (smallest nano-particle) of Ni, Pd, and Pt on θ -alumina are d¹⁰ species while Cu, Ag, and Au are d¹⁰s¹. We chose θ -alumina instead of extensively studied α -alumina as a surrogate substrate for γ -alumina due to their structural similarity.
 - Preliminary CO oxidation studies show that CO oxidation on single atoms of supported platinum is possible through a modified Langmuir-Hinshelwood scheme. Efforts to prepare samples with only single Pt atoms on θ -alumina are in progress to validate theoretical studies.
- We have optimized small 2-3 atom clusters of Platinum supported on θ -alumina in order to understand the agglomeration and sintering process. Completed optimization of Cu exchanged ZSM-5.
- We have synthesized and characterized Pt-Pd nano-particles and found that hydrothermal aging of samples leads to particle size growth which increases at 900°C but extreme sintering to large particles (~300-400 nm) is prevented. Efforts to understand these results by theoretical models are in progress.

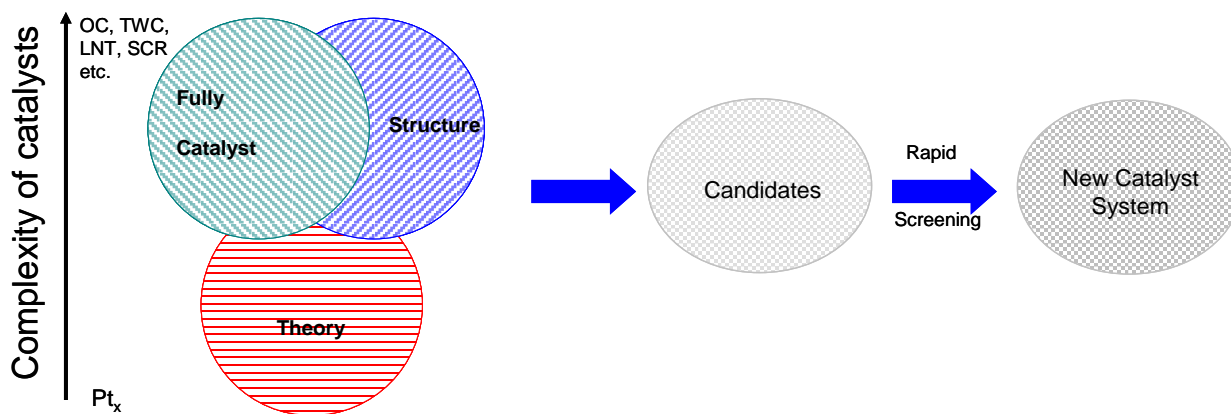
Future Direction

- Theoretical modeling to understand cluster oxidation state (oxidized, reduced, in equilibrium), dependence on cluster size, and the kinetics of oxidation. Role of palladium on platinum stabilization. Complete optimization of Cu exchanged ZSM-5 containing M-O-M as cation
 - Complete theoretical studies of CO oxidation and initiate study of NO_x, and HC reaction on supported clusters. Complete NO_x reduction study on Cu-ZSM-5
 - Guided by our results, the synthesis and evaluation of new durable supported catalysts for lean NO_x catalysts and other systems such as TWC, OC for diesel etc.
-

Introduction

This research focuses on an integrated approach between computational modeling and experimental development, design and testing of new catalyst materials, that we believe will rapidly identify the key physiochemical parameters necessary for improving the catalytic efficiency of these materials.

The typical solid catalyst consists of nano-



particles on porous supports. The development of new catalytic materials is still dominated by trial and error methods, even though the experimental and theoretical bases for their characterization have improved dramatically in recent years. Although it has been successful, the empirical development of catalytic materials is time consuming and expensive and brings no guarantees of success. Part of the difficulty is that most catalytic materials are highly non-uniform and complex, and most characterization methods provide only average structural data. Now, with improved capabilities for synthesis of nearly uniform catalysts, which offer the prospects of high selectivity as well as susceptibility to incisive characterization combined with state-of-the science characterization methods, including those that allow imaging of individual catalytic sites, we have compelling opportunity to markedly accelerate the advancement of the science and technology of catalysis.

Computational approaches, on the other hand, have been limited to examining processes and phenomena using models that had been greatly

simplified in comparison to real materials. This limitation was mainly a consequence of limitations in computer hardware and in the development of sophisticated algorithms that are computationally efficient. In particular, experimental catalysis has not benefited from the recent advances in high performance computing that enables more realistic simulations (empirical and first-principles) of large ensemble atoms including the local

environment of a catalyst site in heterogeneous catalysis. These types of simulations, when combined with incisive microscopic and spectroscopic characterization of catalysts, can lead to a much deeper understanding of the reaction chemistry that is difficult to decipher from experimental work alone.

Thus, a protocol to systematically find the optimum catalyst can be developed that combines the power of theory and experiments for the atomistic design of catalytically active sites and can translate the fundamental insights gained directly to a complete catalyst system that can be technically deployed.

Although it is beyond doubt computationally challenging, the study of surface, nanometer-sized, metal clusters may be accomplished by merging state-of-the-art, density-functional-based, electronic-structure techniques and molecular-dynamic techniques. These techniques provide accurate energetics, force, and electronic information. Theoretical work must be based on electronic-structure methods, as opposed to more empirical-based techniques,

so as to provide realistic energetics and direct electronic information.

A computationally complex system, in principle, will be a model of a simple catalyst that can be synthesized and evaluated in the laboratory. It is important to point out that such a system for experimentalist will be an idealized simple model catalyst system that will probably model a “real-world” catalyst.

Thus it is conceivable that “computationally complex but experimentally simple” system can be examined by both theoretical models and experimental work to forecast improvements to obtain optimum catalyst systems.

Approach

The theoretical modeling is based on DFT studies of Pt supported on θ -alumina. We have completed the study of single atoms of Pt, Pd, Au, and Ag supported on 010 surface of θ -alumina. We have initiated the DFT study of larger clusters of Pt supported on θ -alumina. Our experimental studies suggest that CO oxidation is identical on both Pt supported on γ -alumina and θ -alumina. This suggests that the catalyst site structure is probably identical in both catalysts.

Experimentally, we have synthesized a series of Pt clusters/particles of different sizes supported on γ -alumina and evaluated the catalysts NO oxidation activity. We monitored the microstructural changes throughout the NO oxidation process to correlate microstructure and activity. We have also carried out preliminary study of HC oxidation processes.

Guided by the theoretical models and experimental results of our study, we will anticipate that we will initiate our work on the synthesis of a new set of catalyst materials with higher durability under operating conditions in FY12.

Results

Previously, we have carried out experimental studies on Pt nanoclusters and nanoparticles to

correlate their CO, NO and HC oxidation activity with nanostructural changes. We employed the ORNL *ex-situ* reactor¹ and scanning transmission electron microscopy (STEM) using the HD-2000 and HF-3300 to study the nanostructural changes in catalysts upon exposure to CO and NO oxidation condition. It is important to note that the *ex-situ* reactor permits duplication of the oxidation conditions obtained on the bench-top reactor.

Our theoretical studies on single platinum atoms supported on θ -alumina slab shows that the platinum atoms are in zero oxidation states. This result is very different from that reported in literature on single platinum atoms supported on α -alumina or simplified models of γ -alumina where a platinum atom generally has an unpaired electron. This also means that the mechanism of CO, NO_x, or HC oxidation on Pt(0) will be different from that on Pt(I) or Pt(II). We have carried out first principle studies of CO oxidation on Pt atoms supported on θ -alumina slab and found that a modified Langmuir-Hinshelwood scheme is possible for CO oxidation.

Since our experimental work has already shown that the distribution of platinum on γ -alumina and θ -alumina is almost identical, and the surface properties and CO oxidation of both catalysts are identical, we propose that Pt supported on θ -alumina is a better model for Pt supported on γ -alumina than Pt supported on α -alumina or simplified models of γ -alumina.

Our results on platinum group and coinage atoms supported on θ -alumina and the CO oxidation studies on Pt/ θ -alumina are described in the following sections. Also included are our preliminary studies to develop hydrothermally stable platinum based catalysts.

We also describe our study of metal exchanged zeolites which are production SCR-catalysts. Our goal for this study is to understand the catalysis process to enable us to design SCR catalysts that can function at low temperatures to enable OEMs to meet future regulatory requirements. Preliminary experimental studies show that heterobimetallic zeolites enable high

NO_x conversion (~80%) at 150°C while performing as well as Cu-ZSM-5 in the rest of the temperature range of 250-650°C.

THEORETICAL STUDIES OF Pt/θ-Al₂O₃

We employed Vienna *Ab Initio* Simulation Package (VASP) to carry out first principle total energy calculation within the supercell DFT framework.¹⁻³ Generalized gradient approximation (GGA) in the Perdew-Wang-91 form was employed for electron exchange and correlations.^{4,5} The Kohn-Sham equations were solved using the projector augmented wave (PAW) approach for describing electronic core states.^{6,7} The plane-wave basis set was truncated at a kinetic energy cut-off of 500eV.

Single Atoms on θ-alumina (010) surface

We have previously summarized the results on DFT calculation of bulk θ-alumina, θ-alumina slab, and a single platinum atom on a θ-alumina slab. We also reported preliminary results on a charge neutral supercell of 420 atoms combining 2 x 3 x 3 cells and found the location of platinum to optimize in an environment identical to the one in 180-atom supercell [Figure 1]. In addition, we optimized the single Ni, Pd, Cu, Ag, or Au atom adsorbed on the [010] surface of θ-alumina and found the adsorption energies for Pt, Pd, Au, and Ag are in the order of Pt>Pd>Au>Ag and are -62.29, -44.84, -20.21, and -13.23 Kcal/mole, respectively suggesting that the absorption of these atoms is exothermic.

The optimized bond distances, bond angles, oxidation states, and magnetization are summarized in Figure II and Table I and II. The bonding behavior of Group 10 metals (Ni, Pd, Pt) is very similar, and we summarize the results of bonding analysis for Pt here. The charge density difference plot for Pt adsorbed between two surface oxygen atoms [Figure 3] shows that there is charge depletion between Pt and oxygen atoms and charge accumulation near Pt atom.

The density of states [Figure 3] shows a loss of degeneracy and a shift to higher energy for Pt d orbitals as compared with free Pt atom. The low-energy states are probably due to the overlap with O 2p orbitals. Free Pt atom, on the other

hand, exhibits two density of states for d orbitals with the low energy one being dz² with some contribution of dx² while the high energy one is essentially dxy, dyz, dz² with contribution from dx². The evolution of O 2p orbital from alumina surface to Pt-alumina [Figure 3] shows that O 2pz loses electrons to platinum. Some features from Pt d orbitals are seen at high energy near the Fermi levels. The strong surface bonding of Pt is not surprising in view of the pronounced tendency of Group 10 metals to form s-d hybrids. The hybridization tendency has previously been correlated to the s → d transition energy since computed d⁹s¹-d¹⁰ energy separation for Pt is only 0.98 eV. Our results are consistent with Pt adsorbed on the (001) MgO and (111) ZrO₂ surfaces where it has been shown that Pt changes its configuration from d⁹s¹ to d¹⁰ as it approaches the oxide support.³²⁻³⁴

The change in configuration is accompanied by quenching of the Pt-atom's magnetic moment. Thus, the analysis of the local density of state [LDOS] of Pt/θ-Al₂O₃ leads to a different bonding picture than that reported in literature for α-Al₂O₃ or γ-Al₂O₃.

Formally, platinum is in zero oxidation state with d¹⁰ structure and is bonded to two oxygen atoms. The implication of this important result is that the mechanism of CO, NO, or HC oxidation on sub-nanometer particles such as single atoms can be expected to be different from the large particles normally examined by DFT.

All Group 11 atoms, when bonded to a θ-Al₂O₃ (010) surface, are d¹⁰s¹ atoms. The bonding behavior of Group 11 metals (Cu, Ag, Au) is very similar and we summarize the results of bonding analysis for Pt here. The ground state of a copper atom is 3d¹⁰4s¹ and excited state is 3d⁹4s² with excitation energy of 1.49 eV. As a result, the configuration for a Cu atom does not easily change from 3d¹⁰4s¹ to 3d⁹4s². The magnetic moment is primarily associated with the single s electron of Cu supporting the 3d¹⁰4s¹ oxidation state. The charge density difference plots for Group 11 atoms adsorbed on θ-Al₂O₃ (010) surface are superficially similar to adsorbed platinum atoms reflecting similar underlying bonding interactions. The charge depletion between Cu and Oxygen

counterbalanced by charge accumulation on the Cu atom can be seen in charge difference density plots (Figure 4). There is no charge transfer to aluminum atoms ruling out the involvement of aluminum atoms in Cu bonding. The shift to lower energy for d orbitals and loss of degeneracy can be seen in DOS plots (Figure 4) of d orbitals of Cu/ θ -Al₂O₃. The positive component of s orbitals shifts to higher energy and is degenerate with dz² and dx² components of d orbitals. The O 2p orbitals shift to lower energy and exhibit metal d components near the Fermi level. This bonding picture is quite different from that reported for Cu on α -alumina. The adsorption of Cu results in surface displacement, weakening of the attraction of the outermost aluminum atoms by the surface oxide ions suggesting reduction of aluminum atoms by the Cu atoms. The DOS analysis showed the disappearance of Cu 4s band suggesting Cu (I) species.

Thus, our study of Ni, Pt, Pd, Cu, Au, and Ag adsorbed on θ -Al₂O₃ 010 surfaces shows that metal atoms occupy a position between two surface oxygen atoms. The adsorption of these atoms follows the order of Pt>Ni>Pd>Cu>Au>Ag. The Group 10 metal atoms interactions with θ -Al₂O₃ 010 surfaces follows a simple pattern – all three members (Ni, Pt, Pd) have filled d orbitals, d-s hybridization, and overlap with surface oxygen 2p orbitals. The interaction of Group 11 (Cu, Ag, Au) atoms with 010 surfaces of θ -Al₂O₃ are superficially similar to that of Group 10 metals. Group 11 atoms with filled d orbitals have low tendency for d-s hybridization due to larger energy gaps than Group 10 metals. As a result of overlap with O 2p, the d orbitals shift to lower energy. The magnetization of Group 11 metals is primarily due to single electrons in their s orbitals. Other than Au/ θ -Al₂O₃, the bonding of Group 10 and Group 11 metals with θ -Al₂O₃ 010 surfaces differs from those on α -Al₂O₃ surfaces. Considering that θ -Al₂O₃ is structurally closer to γ -Al₂O₃, we suggest that a θ -Al₂O₃ surface is a better model for γ -Al₂O₃ than α -Al₂O₃.

Considering the facts (reported previously) that the Pt supported on γ -alumina and θ -alumina exhibit identical bimodal distribution of

platinum (single atoms and 10-20 atom clusters) when examined by ACEM and have identical CO oxidation activity, we suggest that platinum on θ -alumina is a better representative of platinum on γ -alumina than the models reported in literature (platinum on α -alumina or platinum on simplified models of γ -alumina). As described previously, the structure of platinum on γ -alumina is uncertain due to uncertainty of the structure of γ -alumina.

CO Oxidation on Pt/ θ -alumina (010) surface

As mentioned in the previous section, platinum is in the zero oxidation state with a d¹⁰ structure and bonded to two oxygen atoms. The implication of this important result is that the mechanism of CO, NO, or HC oxidation on sub-nanometer particles such as single atoms can be expected to be different from the large particles normally examined by DFT. Here, we present preliminary results for the pathways of CO oxidation. Most of the structures described in Scheme I-III are either optimized or are close to optimization. The structural analysis of these intermediates will be presented in a future report.

While Pt on a dry θ -alumina surface can be stable for indefinite period under oxygen free conditions, it will oxidize readily if any oxygen is present. Since experimentalist will start with oxidized sample, we explored platinum oxidation pathways before CO oxidation [Scheme I]. Oxygen can bond to Pt in two possible ways – terminal or side-on. The energetics shows that the side-on configuration is lower in energy than the terminal one. This structure also draws support from organometallic chemistry where a platinum(0) complex, (Ph₃P)₂Pt(O₂), has been shown to exhibit side on configuration by single crystal X-ray crystal structure determination. The oxygen on platinum can dissociate to form Pt=O bond before reaction with CO or SN2 type CO reaction can occur on Pt with CO bond formation resulting in oxygen becoming terminally bonded. The formation of carbonate from this structure is quite likely and has been confirmed in the reaction of (Ph₃P)₂Pt(O₂) with CO. The loss of CO₂ from this structure will

generate intermediate species containing Pt=O bond which can react with another molecule of CO. This intermediate will form platinum(0) after CO₂ elimination.

At this stage, CO and oxygen can compete for the platinum(0) site and calculation show the CO bond being energetically favored [Scheme II]. At room temperature, the second bond with CO can result in catalyst poisoning since the dicarbonyl species is energetically more favorable than the intermediates involving both oxygen and CO. Since the CO reaction occurs at high temperatures, the addition of an oxygen atom to mono-carbonyl is feasible and will result in carbonate intermediates. From this point onwards, the mechanism will be identical to the one described in Scheme I.

Scheme III summarizes the overall mechanism starting from platinum(0) supported on a dry θ -alumina surface.

Multiple Pt atoms and Agglomerates on θ -alumina (010) surface

Previously, we presented our preliminary results on multiple atoms on a dry θ -alumina surface. Here, we describe a detailed study of 2-atom systems. As mentioned previously, the large clusters of Platinum were modeled on a charge neutral supercell of 420 atoms combining 2 x 3 x 3 cells.

The larger alumina surface contains several sites where platinum atoms can be independently located in lowest energy configuration identical to the ones found by us on a 2 x 4 x 2 surface. The first platinum atom occupies one of lowest energy sites. The second platinum atoms can occupy another one of these sites (independent bonding mode) or can be bonded to the first platinum (bonded modes).

The independent bonding of both independent platinum atoms is identical. The platinum atoms are d¹⁰ species with no magnetic moment. The charge density difference plot for Pt adsorbed between two surface oxygen atoms [Figure 6, left] shows that there is charge depletion between Pt and oxygen atoms and charge

accumulation near the Pt atom. The density of states shows a loss of degeneracy and a shift to higher energy for Pt d orbitals as compared with free Pt atoms. The low-energy states are probably due to the overlap with O 2p orbitals.

In the first bonded mode one of the platinum is bonded to two oxygen atoms at the lowest energy configuration (Pt-O bond distances are 2.19 and 2.07 Å) while the second platinum atom is bonded to only the first platinum atom (Pt-Pt bond distance 2.48 Å). There is no magnetic moment associated with either of the two platinum atoms. The charge difference density plots show charge accumulation between two platinum atoms. This bonding mode is 4.6 Kcal/mol lower in energy than the system with two independent Pt atoms described in the preceding paragraph and 4.0 Kcal/mol lower in energy than the second bonding mode described in the next paragraph. This suggests that there is no significant energy barrier or driving force to sintering of Pt atoms to 2-atom clusters. Furthermore, there is no driving force for single atoms to sinter to 2-atom clusters.

In the second bonded mode, both platinum atoms are bonded to one surface oxygen atom. The Pt-Pt bond distance is longer than that in bulk platinum and is 2.57 Å. The charge difference density plots show charge depletion between one Pt-O and charge accumulation between the other Pt-O and Pt-Pt. The overall magnetic moment is zero but there is slight positive magnetic moment on one platinum atom while there is an equal but opposite magnetic moment on the other platinum atom.

This bonding picture is quite different from the one reported for two atom Pt cluster on α -alumina where Pt atoms have unpaired electrons.

The detailed studies of larger clusters are in progress and will be reported in the next quarterly report.

EXPERIMENTAL STUDIES

In order to compare the results of theoretical studies on palladium substituted platinum

agglomerates reported last year, we have synthesized and characterize platinum-palladium agglomerates supported on γ -alumina substrates.

The Pt-Pd bond containing precursor was synthesized as follows employing a method reported in literature ((Lippert et al., J. Am. Chem. Soc., 113 (1991) 5129):

trans-[Pt(NH₃)₂(1-methylcytosine)](NO₃)₂:

This compound was prepared by a reported procedure. [4] *trans*-Pt(NH₃)Cl₂ (0.3799 g, 1.27 mmol) was stirred with AgNO₃ (0.4302 g, 2.53 mmol) in 40 mL deionized water under light protection at 40°C for 40 hours, resulting a white slurry. The clear colorless filtrate of the reaction was then introduced to 1-methylcytosine (0.3169 g, 2.53 mmol), and heated under gentle reflux at 80°C for 5 hours. White powder was obtained after drying the water solution, which was further purified by recrystallization from boiling water.

¹H-NMR (400.6 MHz, DMSO-*d*₆): 3.4 (s), 6.0 (d), 7.6 (d). The signal at 6.0 ppm also comes with an additional small satellite doublet (~ 1/3 intensity), which may originate from the coupling to the nuclear spin active isotope ¹⁹⁵Pt which has a natural abundance of 33%.

trans-[(NH₃)₂Pt(1-methylcytosine)PdCl]NO₃:

0.2043g *trans*-[Pt(NH₃)₂(1-methylcytosine)](NO₃)₂ was mixed with K₂PdCl₄ in 20 mL deionized water and kept stirring overnight, providing a yellow slurry. Filtrate was green yellow, and was dried to yield a yellow/brown powder which was identified by NMR as a mixture containing the desired product *trans*-[(NH₃)₂Pt(1-methylcytosine)PdCl]NO₃ and unreacted *trans*-[Pt(NH₃)₂(1-methylcytosine)](NO₃)₂ in an approximate 1:1 ratio.

Sub-nanometer Pt-Pd supported on γ -alumina: Since the pure samples of *trans*-[(NH₃)₂Pt(1-methylcytosine)PdCl]NO₃, could not be prepared, we used its mixture with *trans*-[Pt(NH₃)₂(1-methylcytosine)](NO₃)₂ (parent compound) for the deposition of Pt-Pd clusters. The TEM of the resulting material shows sub-nanometer particles which are essentially agglomerates of single atoms.

In-situ Thermal Aging of Sub-nanometer Pt-Pd Particles: Sample was wet-dipped onto a silicon nitride chip with a temperature controlling unit that is capable of reaching temperatures over one thousand degree Celsius. The thermal stability of the sub-nanometer Pt-Pd sample was tested according to the following procedure: (1) the sub-nanometer Pt-Pd sample was heated at 250°C inside the microscope machine under vacuum for 30 minutes; (2) temperature was raised to 500°C, and the sample was examined; (3) temperature was raised to 800°C, and the sample was examined; (4) temperature was cooled down to 250°C, (5) followed by one more sequence of heating to 500°C and 700°C.

After initial thermal treatment at 250°C, the sample exhibited nanometer particles, subnanometer cluster, and single atoms [Figure 7]. Thermal treatment at 500°C results in the fast movement of single atoms and subnanometer clusters making it difficult to obtain a stable image. The nano-particle could be imaged and showed both Pt and Pd in its EDS. After exposure to 800°C and cooling down to 250°C, the sample showed nanometer particles, subnanometer cluster, and single atoms suggesting that sintering on thermal exposure is a slow process.

In-situ Monitoring of Structural Changes in Sub-nanometer Pt-Pd Particles during CO oxidation: Sub-nanometer Pt-Pd sample loaded on silicon nitride heater chip was packed into a cell which tolerates a gas pressure of 50 torr. . A mixture of gases (5% CO + 5% O₂ + N₂) was sent into the cell that is maintained at a temperature of 250°C. Various locations of the sub-nanometer Pt-Pd sample were monitored before and after the gas reaction for comparison. In general, exposure to the reaction gas at the typical testing timeframe (30 minutes) causes no significant change in particle size or shape [Figure 8].

Nanometer Pt-Pd supported on γ -alumina In the previous report, we have shown that PdPt nanoalloy samples, i.e., PVPPdPt14, PVPPdPt11, and PVPPdPt41, synthesized employing PVP polymer as a template, exhibit ~ 2.5 nm Pd-Pt particles regardless of Pd:Pt ratio.

Here, we report the hydrothermal properties of the samples. We employed hydrothermal aging protocol reported by researchers at Ford Motor Company (Catalysis Letters, 2007, 116, 1-8). A typical procedure is as follows: 0.7 g of PdPt nanoalloy was treated under a flow (5L/min) of N₂, O₂ (5%) and H₂O (10%) for 3 hours at a series of temperatures (500°C, 600°C, 750°C and 900°C). The temperature ramp up and down was carried out under pure N₂.

Hydrothermal Aging of PVPPdPt41: The aging of PVPPdPt41 results in particle size growth to 3.5 nm, 4.5 nm, 13 nm, and 20 nm at aging temperature of 500°C, 600°C, 750°C, and 900°C, respectively.

Hydrothermal Aging of PVPPdPt14: TEM studies of resulting samples show particle size growth to 3.5 nm, 4.5 nm, 7.5 nm, and 30 nm at aging temperatures of 500°C, 600°C, 750°C and 900°C, respectively.

Hydrothermal Aging of PVPPdPt11: TEM studies of resulting samples show particle size growth to 3.0 nm, 4.5 nm, 12.5 nm, and 30 nm at aging temperatures of 500°C, 600°C, 750°C and 900°C, respectively.

It is clear that alloying Pd into the Pt nanoparticle dramatically restrains the size growth under hydrothermal aging. For example, the size of pure Pt nanoparticle reported in literature (Catalysis Letters, 2007, 116, 1-8) grows to 9 nm after aging at 500°C. The Pd/Pt samples developed in this study show enhanced hydrothermal stability compared to the literature results, 3.5 nm vs. 5 nm after aging at 500°C. The ratio of Pd to Pt in the nanoalloy shows no difference in controlling particle size growth when the samples are aged at low temperatures, i.e., 500°C and 600°C, and under extreme condition at 900°C, whereas less amount of Pd seems to better stabilize the particle at 750°C.

THEORETICAL STUDIES OF Cu-ZSM-5

First we optimized all silica ZSM-5 with 96 silicon atoms and 192 oxygen atoms in the idealized orthorhombic unit cell with space group Pnma and unit cell parameters of a=20.1,

b=19.9, and c=13.4Å. Our optimized unit cell parameters are a=20.089, b=19.7379, and c=13.141Å which compare well with the experimental values. From this optimized structure, we derived twelve Cu-ZSM-5 structures with two aluminum atoms and one copper atom as a cation to balance the negative charge introduced by replacing silicon with aluminum [Figure 9].

A square planar geometry of Cu²⁺ has been deduced from EXAFS studies of Cu-ZSM-5. Since Cu-ZSM-5 is a highly efficient heterogeneous catalyst and reactive gases follow the path of least resistance, we selected possible Cu²⁺ locations on the inner shell of the two major channels in the ZSM-5 structure that can provide maximum contact between the zeolite and reactant gases - straight channel along the y axis and zigzag channel along z axis identified in the ZSM-5 crystal structure.

Figure 9 highlights the repeating units from both straight and zigzag channels in green and blue, respectively. Five possible Cu²⁺ binding sites are specified in Figure 9 on the straight channels and another eight Cu²⁺ binding configurations in the zigzag channels. In general, the coordination of a single Cu²⁺ with a square planar geometry involves binding to four oxygen atoms that belong to two negatively charged [AlO₃]⁻ supporting unit.

The copper binding locations categorized as follows:

- Within a six member ring (neglecting the oxygen atoms), e.g., S1, S2, S4, Z8, and Z6/Z7;
- Within a five member ring, e.g., S3, S5, Z2, Z3, and Z4/Z5;
- Within a four member ring, e.g., Z1.

The lowest energy optimized structures from quantum mechanical simulations on the full zeolite structures are shown in figure 10.

In literature, Cu-ZSM-5L1 type models of Cu-ZSM-5 have been proposed to be the lowest energy structure. We have found that Cu-ZSM-5L2 structure is also a low-energy structure. The

analysis of these structures is in progress and will be reported in the next quarterly report.

Conclusions

Theoretical studies on single atoms show that the bonding of platinum with θ -alumina is different from that reported for α - or γ -alumina. Pt on θ -alumina is in the zero oxidation state while it is d^9s^1 on α -alumina. Nickel and palladium atoms also show similar bonding patterns. Interestingly, the agglomeration of single atoms can also be modeled on 010 θ -alumina surface, and our studies show that there is no significant barrier that prevents independent platinum atoms from bonding to form larger particles. The zero oxidation state of platinum enables CO oxidation by a modified

References

1. Kruse, G.; Hafner, J.; Phys. Revd., **1993**, 47, 558.
2. Kruse, G.; Hefner, J. Phys. Rev. B, **1993**, 48, 13115
3. Kruse, G. Hefner, J.; Phys. Rev. B, **1994**, 49, 14251
4. Perdue, J.P.; Chivalry, J.A.; Vodka, S.H.; Jackson, K.A.; Pederson, M.R.; Singh, D.J.; Phys. Rev. B.; **1992**, 46, 6671
5. Perdue, J.P.; Chivalry, J.A.; Vodka, S.H.; Jackson, K.A.; Pederson, M.R.; Singh, D.J.; Phys. Rev. B.; **1993**, 48, 4978.
6. Bloch, P.E.; Phys. Rev. B, **1994**, 50, 17953.
7. Kruse, G.; Jobber, D.; Phys. Rev B, **1999**, 59, 1758.

Presentations and Publications (FY 11)

1. Narula, C.K.; Stocks, M.G.; Abs Initio Density Functional Calculations of Adsorption of Transition Metal Atoms on θ -Al₂O₃ (010) Surface, J. Phys. Chem. C (submitted).
2. DeBusk, M.M.; Allard, L.F.; Blom, D.A.; Narula, C.K.; The structure and stability of

Langmuir-Hinshelwood scheme which is also presented.

Experimentally, we have found that preformed nanoparticles of platinum-palladium alloys supported on alumina are more stable than pure platinum nano-particles. While both platinum and platinum-palladium alloy particles undergo Oswald ripening, the extremely large particles commonly observed after hydrothermal sintering at 900C are not seen for platinum-palladium alloys. Theoretical modeling studies are in progress to understand this phenomenon since the experimental observations do not match with our theoretical studies on supported single atoms described in this report.

We also summarize our preliminary study of Cu-ZSM-5 structure which has allowed us to find the lowest energy structures. Future studies will focus on NO_x reduction.

sub-nanometer platinum supported on alumina, Ind. Eng. Chem. Res. (to be submitted)

3. Narula, C.K.; Stocks, M. G.; First-principles studies of the structure and bonding of metal atoms supported on θ -alumina, American Chemical Society Meeting, Anaheim, March 2011.
4. Narula, C.K.; Stocks, M.G.; American Chemical Society National Meeting in Denver, CO. August 28-31, 2011

Figures

Figure 1: Side view of M atom on θ -alumina surface model. The red, blue, and gray spheres represent oxygen, aluminum, and platinum atoms, respectively. The black line marks the monoclinic lattice of θ -alumina surface with a 15Å vacuum in the [010] direction. The yellow line shows f.c.c. oxygen atoms.

Figure 2: Bonding of Metal Atoms on θ -Alumina 010 Surface.

Figure 3: Total charge density difference isosurfaces for Pt atom adsorption on θ -Alumina (010) surface along a,b, and c axis (top) and density of state plots for Pt on (010) θ -alumina

surface, fixed alumina surface, and dry alumina surface (bottom).

Figure 4: Total charge density difference isosurfaces for Cu atom adsorption on θ -Alumina (010) surface along a,b, and c axis (top) and density of state plots for Cu on (010) θ -alumina surface, fixed alumina surface, and dry alumina surface (bottom)

Figure 5: Catalytic pathways for CO oxidation on Pt/ θ -Al₂O₃.

Figure 6: Two platinum atom Pt/ θ -Al₂O₃ system.

Figure 7: Image of Pd-Pt subnanometer particles obtained on ACEM operating in TEM mode. The image on the left shows

single atoms and small agglomerated and the image on the right shows Pd-Pt nanoparticle.

Figure 8: Image of Pd-Pt subnanometer particles obtained on ACEM operating in TEM mode. The image on the left shows fresh sample while the image on the right shows same area after exposure to CO oxidation conditions.

Figure 9: Possible M-ZSM-5 Structures

Figure 10: Lowest energy optimized Cu-ZSM-5 structures

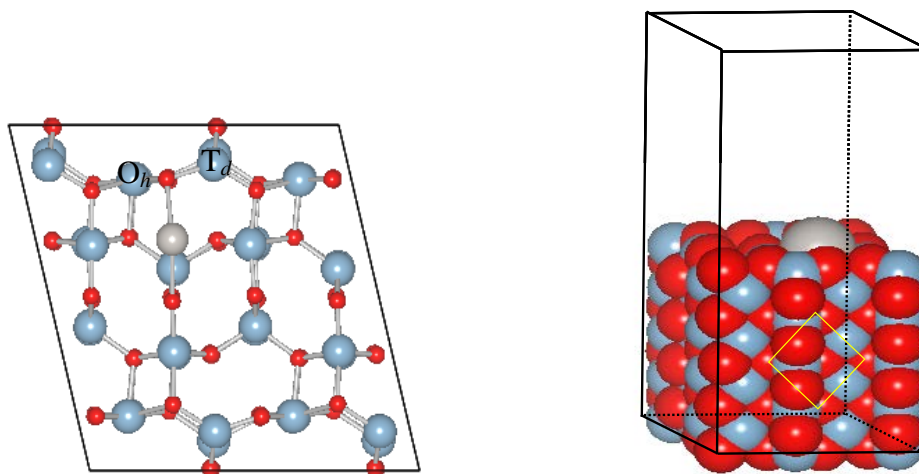


Figure 1: Side view of M atom on θ -alumina surface model. The red, blue, and gray spheres represent oxygen, aluminum, and platinum atoms, respectively. The black line marks the monoclinic lattice of θ -alumina surface with a 15\AA vacuum in the $[010]$ direction. The yellow line shows f.c.c. oxygen atoms.

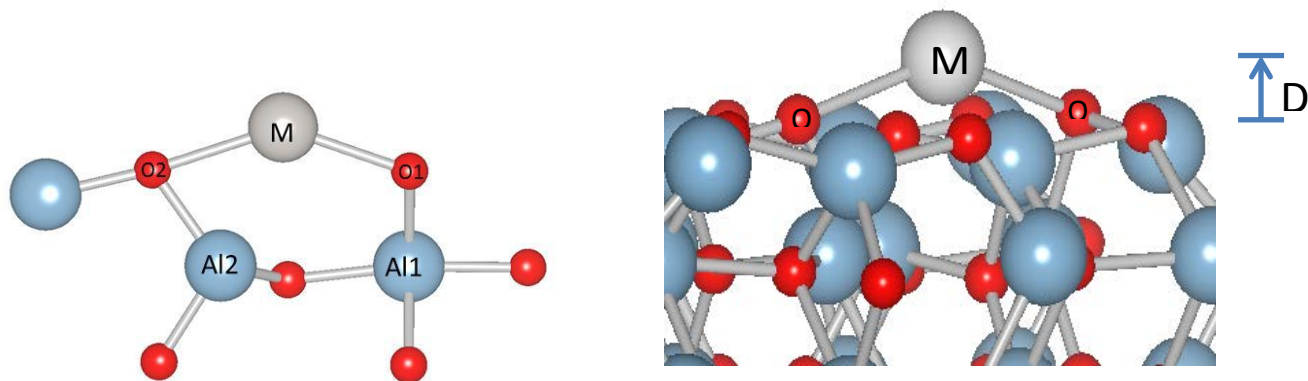


Figure 2. Bonding of Metal Atoms on θ -Alumina 010 Surface

Table I. Bonding Parameters of Metal Atoms on θ -Alumina 010 Surface

M	M-O1 (Å)	M-O2 (Å)	M- Al2 (Å)	O2-M-O1 (°)	D (Å)	O2-Al2 (Å)	O1-Al1 (Å)
-						1.737	1.803
Ni	2.022	1.977	2.32	143.61	0.626	1.82	1.91
Pd	2.22	2.20	2.49	134.55	0.855	1.807	1.87
Pt	2.18	2.13	2.41	140.55	0.728	1.862	1.94
Cu	2.184	2.184	2.61	124.77	1.01	1.78	1.85
Ag	2.48	2.57	3.04	108.5	1.46	1.76	1.81
Au	2.45	2.69	2.97	107.3	1.52	1.77	1.81

Table II. Adsorption Energy, Oxidation State, and Magnetization

M	Adsorption Energy (Kcal/mole)	Oxidation State	μ_{total}	μ_{Mtotal}	μ_{Ms}	μ_{Mp}	μ_{Ototal}
Ni	-54.66	$3d^{10}4s^0$	0	0	0	0	0
Pd	-44.84	$4d^{10}5s^0$	0	0	0	0	0
Pt	-62.29	$5d^{10}s^0$	0	0	0	0	0
Cu	-22.32	$3d^{10}s^1$	1	0.228	0.131	0.016	0.053
Ag	-13.23	$4d^{10}5s^1$	1	0.196	0.189	0.007	0.050
Au	-20.21	$5d^{10}6s^1$	1	0.364	0.315	0.241	0.083

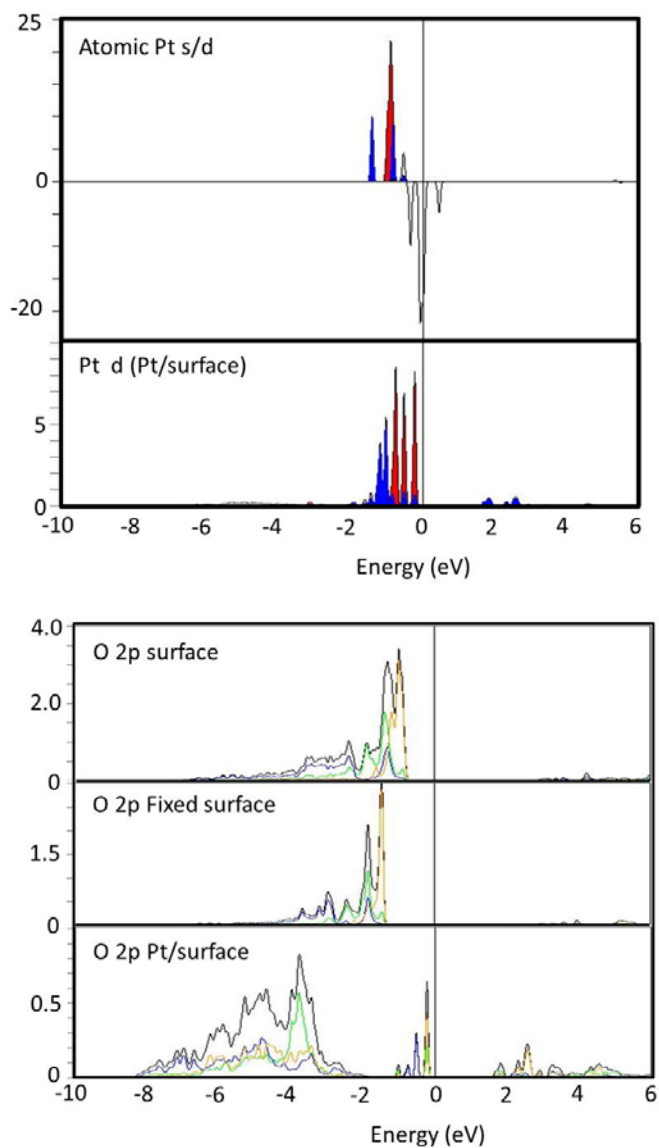
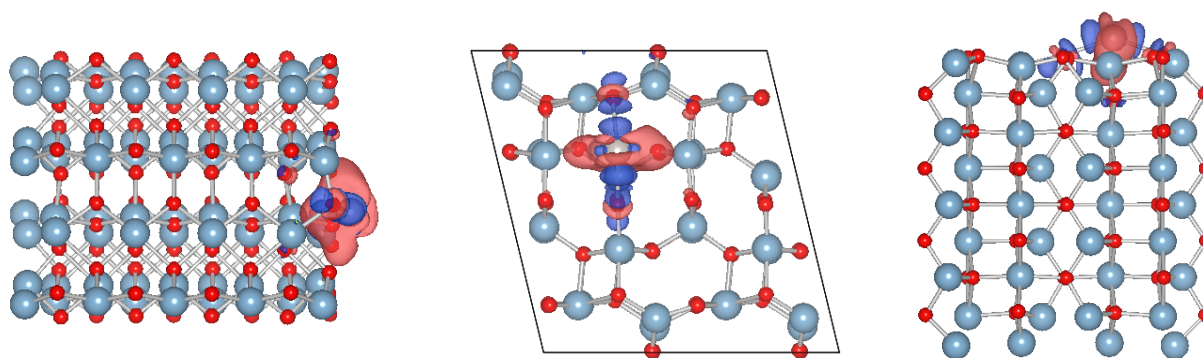


Figure 3: Total charge density difference isosurfaces for Pt atom adsorption on θ -Alumina (010) surface along a,b, and c axis (top) and density of state plots for Pt on (010) θ -alumina surface, fixed alumina surface, and dry alumina surface (bottom)

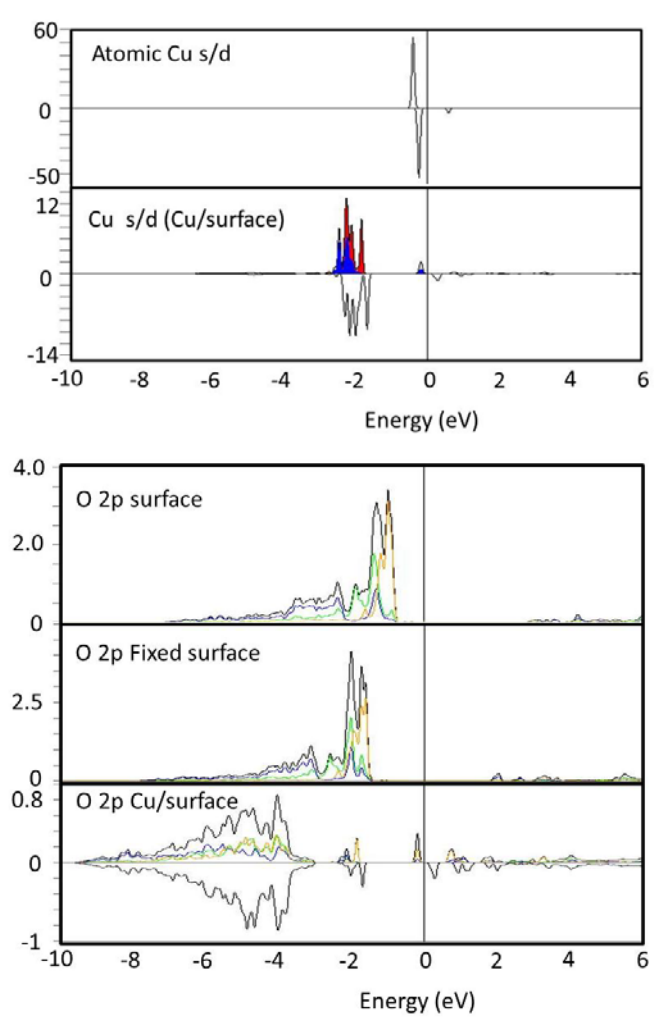
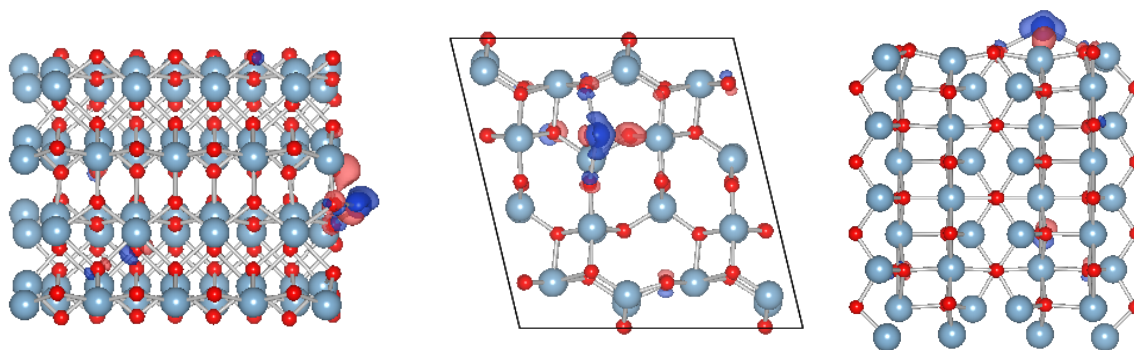
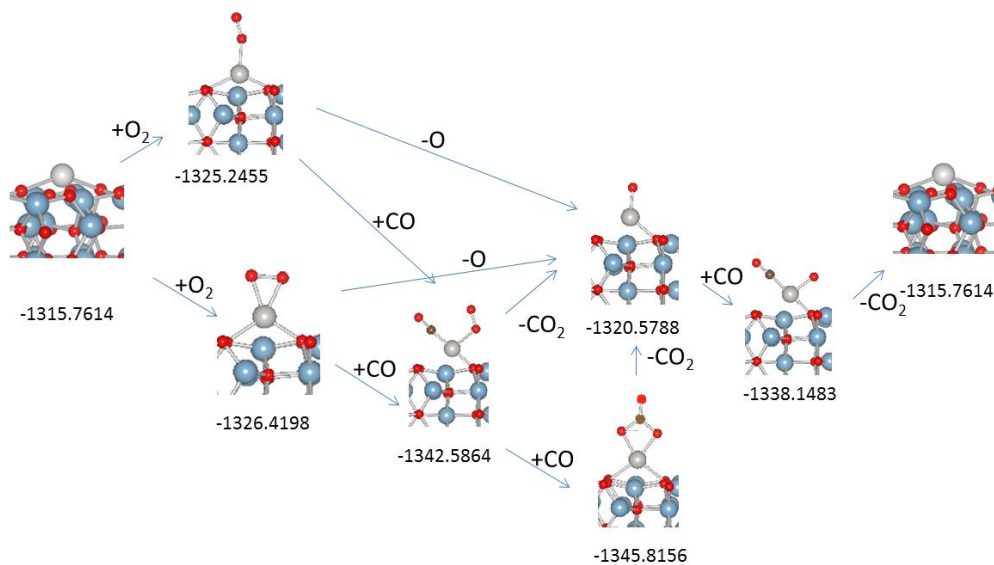
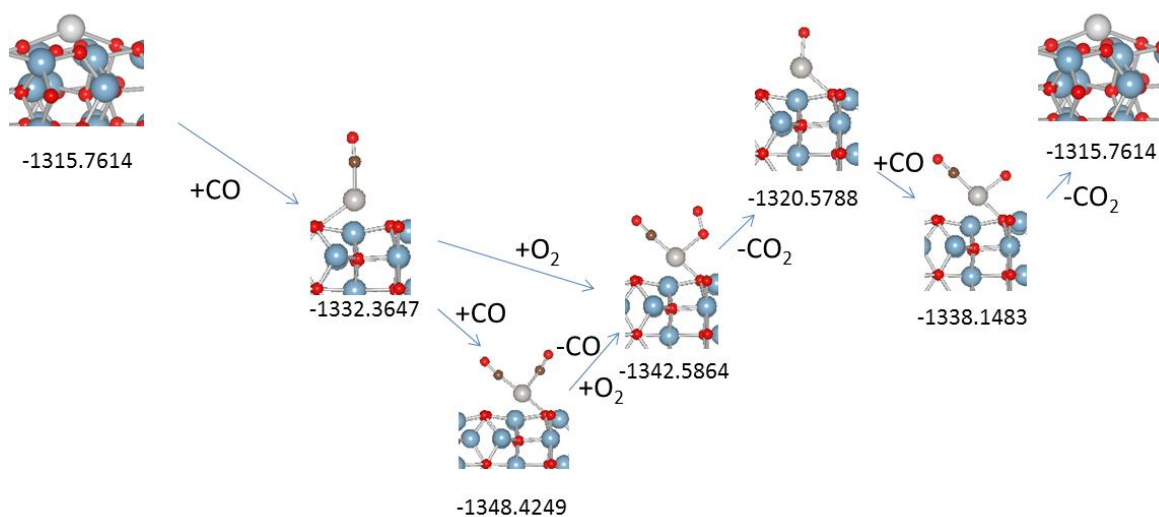


Figure 4: Total charge density difference isosurfaces for Cu atom adsorption on θ -Alumina (010) surface along a, b, and c axis (top) and density of state plots for Cu on (010) θ -alumina surface, fixed alumina surface, and dry alumina surface (bottom)

Scheme I: Pt is oxidized in Pt/ θ -Al₂O₃



Scheme II: CO absorbs on Pt in Pt/ θ -Al₂O₃



Scheme III: Energetically Favorable Pathway

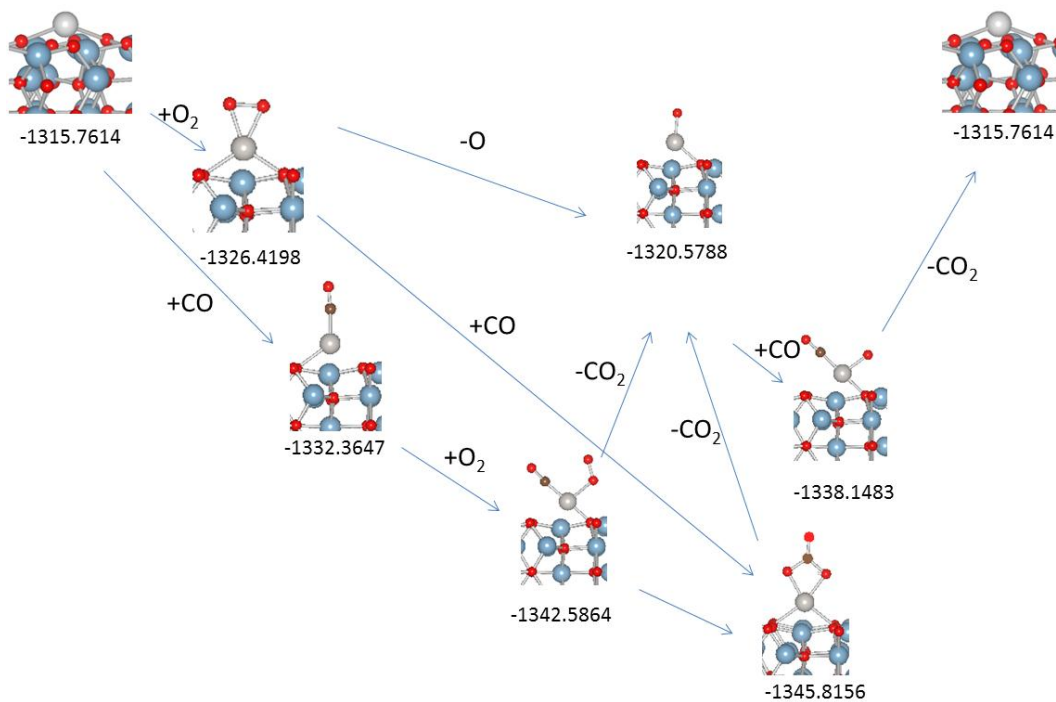


Figure 5: Catalytic pathways for CO oxidation on Pt/θ-Al₂O₃.

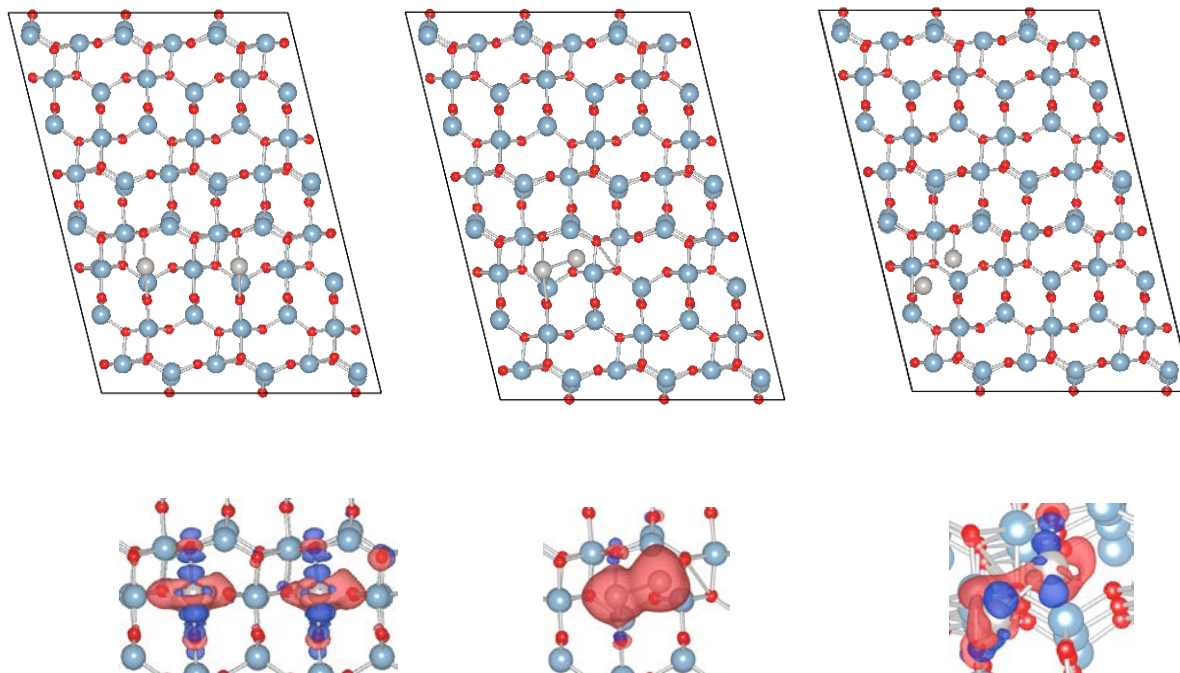


Figure 6: Two platinum atom Pt/θ-Al₂O₃ system.

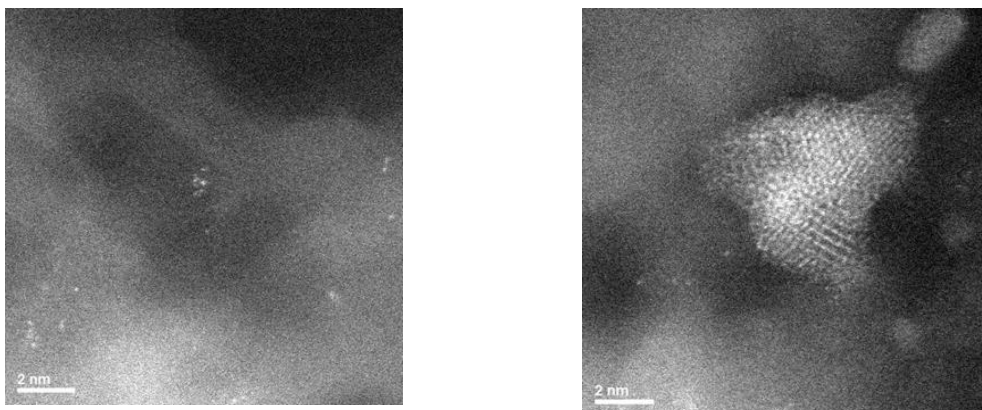


Figure 7: Image of Pd-Pt subnanometer particles obtained on ACEM operating in TEM mode. The image on the left shows single atoms and small agglomerated and the image on the right shows Pd-Pt nanoparticle.

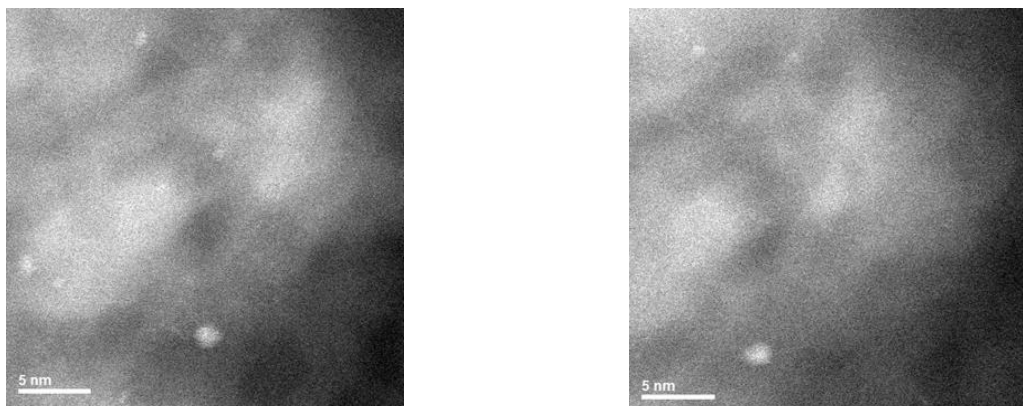


Figure 8: Image of Pd-Pt subnanometer particles obtained on ACEM operating in TEM mode. The image on the left shows fresh sample while the image on the right shows same area after exposure to CO oxidation conditions.

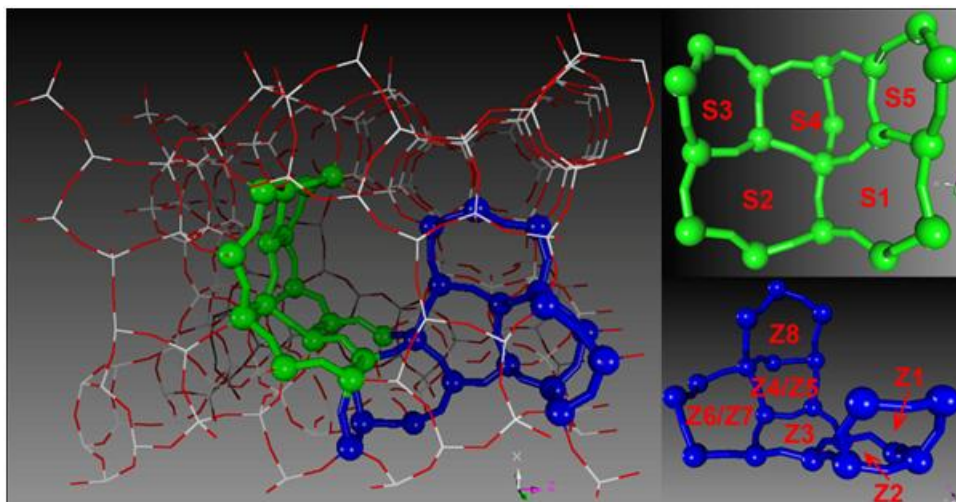


Figure 9: Possible M-ZSM-5 Structures

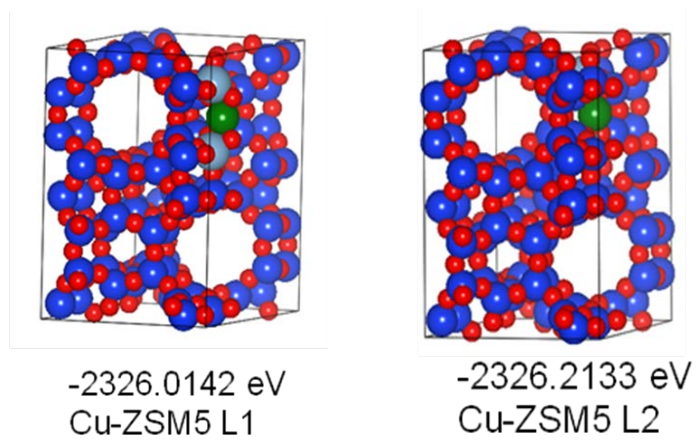


Figure 10: Lowest energy optimized Cu-ZSM-5 structures

Agreement 19214 - Effects of Biodiesel Fuel on Diesel Particulate Filter Materials

M.J. Lance, A.A. Wereszczak, T.J. Toops, B.G. Bunting*, J.M.E. Storey*, D.F. Wilson, E.E. Fox, and S.A. Lewis, Sr.**

Ceramic Science and Technology Group

Oak Ridge National Laboratory

P.O. Box 2008, MS 6068, Bldg. 4515

Oak Ridge, TN 37831-6068

(865) 241-4536; fax: (865) 574-6098; e-mail: lancem@ornl.gov

** Fuels, Engines and Emissions Research Center, ORNL*

DOE Technology Manager: Jerry L. Gibbs

(202) 586-1182; fax: (202) 586-1600; e-mail: jerry.gibbs@ee.doe.gov

ORNL Technical Advisor: Dave P. Stinton

(865) 574-4556; fax: (865) 241-1034; e-mail: stintondp@ornl.gov

Contractor: Oak Ridge National Laboratory, Oak Ridge, Tennessee

Prime Contract No.: DE-AC05-00OR22725

Objectives

- To characterize changes in the microstructure and material properties of diesel particulate filters (DPFs) in exhaust gas produced by biodiesel blends.

Approach

- Dip test as received DPF materials in solutions that simulate the acidic species present in diesel condensate.
- Combine mechanical testing and supportive analysis (analytical, numerical, or finite element or combinations thereof) to measure and interpret the elastic modulus and failure stresses associated with crack initiation in 25-mm-diameter DPFs.
- Purchase and set up a gen-set for long-term 24/7 aging of DPFs in diesel and biodiesel exhaust.

Accomplishments

- Conducted accelerated chemical attack of DPF materials.
- Designed and harvested test coupons from DPFs and measured their mechanical properties.
- Purchased and set-up a gen-set and DPF aging equipment.

Future Direction

- Using the gen-set, accelerated aging with Na and K doping in order to simulate long-term bio-diesel exposure will be conducted and DPF material degradation will be measured.
 - Measure mechanical properties of ceramics in serviced DPFs, compare with those of starting material, and relate property changes to microstructural changes.
 - Measure the effect of thermal cycling from regeneration on the DPF mechanical properties.
-

Introduction

In the spring of 2008, soot was collected on uncatalyzed 5.66 X 6 inch cordierite diesel particulate filters (DPFs) from a 1.7L Mercedes-Benz engine fueled with biodiesel blends (4 volumetric blends 0 - 100%) for the study of soot oxidation kinetics. The soot was removed by backflushing the filters with pressurized air after which the filters were stored in ambient conditions on a shelf still within the can. Approximately 3 months later, the DPF bricks were removed from the can at which point significant degradation of the DPFs that had seen biodiesel exhaust was observed. No degradation of the brick run with ULSD was found. Fig 1 shows the exterior of the ULSD and B20 bricks. In addition, after burning the collected soot, the biodiesel soot had cordierite and tumescent padding residue in amounts roughly proportional to the biodiesel volume percent in the fuel. This result suggests that biodiesel may cause degradation of DPF materials under some conditions. This project has the objective to investigate this possibility and potential degradation mechanisms resulting from biodiesel operation.

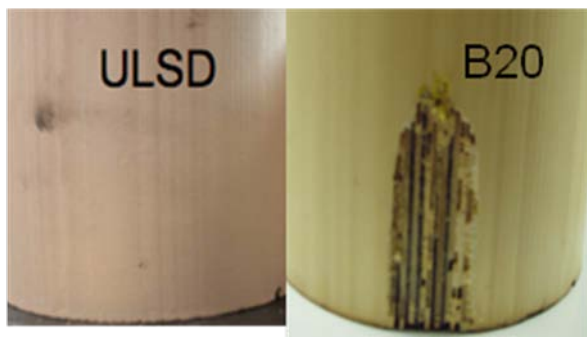
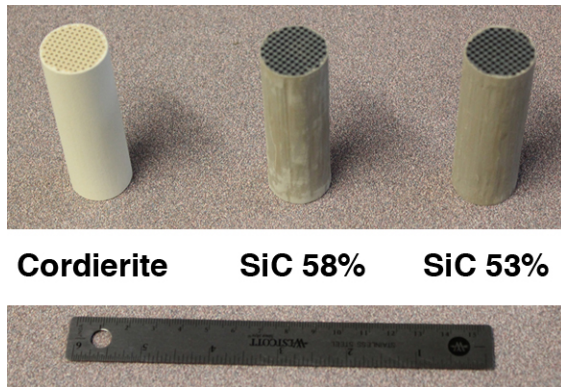


Figure 1. The DPF that had seen B20 exhaust showed significant degradation after sitting within the can for 3 months. The ULSD filter appeared undamaged.

To investigate this phenomenon, condensate was collected from a 1.7 L turbo diesel engine run with ULSD and biodiesel blends and analyzed using gas chromatography-mass spectrometry (GC-MS). Samples of cordierite and SiC DPFs were exposed to accelerated chemical attack by both sulfuric and formic acid in order to induce degradation.

Mechanical testing of DPF specimens was initiated for the estimation of the material's (tensile) failure stress as a function of tensile-stress-direction and location. This was done in order to have a measurement of the onset of material degradation in these porous DPF materials which would be difficult to discern using microscopy or other techniques. DPFs do not have an isotropic structure and may not be subjected to symmetric stress fields. Therefore, there is interest in better understanding how a DPF mechanically responds to thermal-induced stress of operation and the direction in which that imposed stress field is applied. Elastic modulus estimation of the DPF materials are also pursued because knowledge of its accurate value is needed for estimating measured tensile failure stresses.

Three DPF materials were examined and are shown in Fig. 2. One is a cordierite and the other two are silicon carbides (SiCs) with different porosity contents.



Cordierite SiC 58% SiC 53%

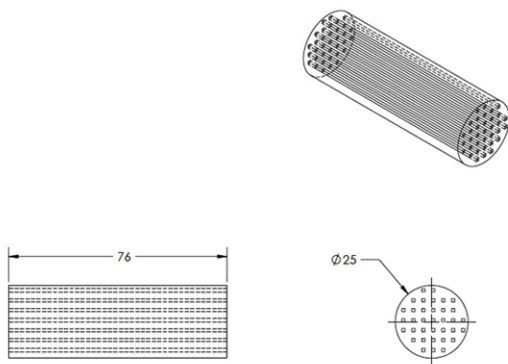


Figure 2. The mechanical properties of three DPF materials (top) were evaluated. The nominal dimensions (below) of the DPFs were 25-mm diameter and 76-mm-length.

For each material, three specimen geometries are being harvested out of the DPFs for the mechanical evaluations.

- *Biaxial flexure disk.* Biaxial flexure testing of disks will subject the tensile side of the specimen to an equibiaxial radial tensile stress using a ring-on-ring test fixture (i.e., axisymmetric 4-point-bending). These specimens should always fail from the weakest strut orientation. Such testing is featured in ASTM C1499 [1]. An illustration of how the harvesting of these disks is conducted is shown in Figure 3 and how it is mechanically loaded is schematically shown

in Figure 4. Disks are machined from the two ends and the interior.

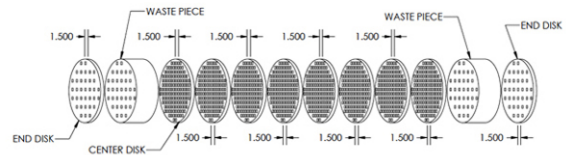


Figure 3. Exploded view showing biaxial disk specimen harvesting from a single DPF. Eight internal biaxial disks are yield per DPF. Two external biaxial disks are yielded for all DPFs.

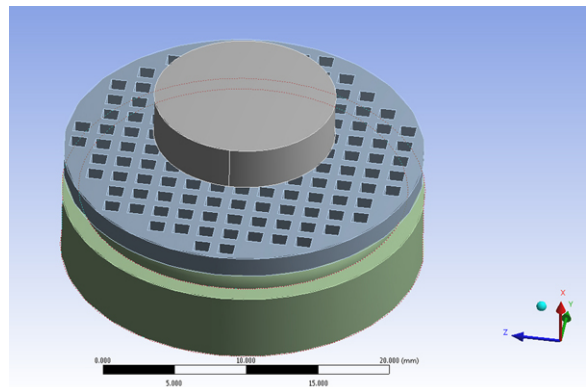


Figure 4. Solid model of a DPF biaxial flexure disk positioned between smaller upper and larger lower rings.

- *Sectored flexure bar.* Four sectored flexure specimens per DPF are harvested at either a 0°- or 45°-orientation as shown in Fig. 5. The specimen, when tested in 4-pt flexure (see Fig. 6), has its original outer OD subjected to axial tensile stress [2].

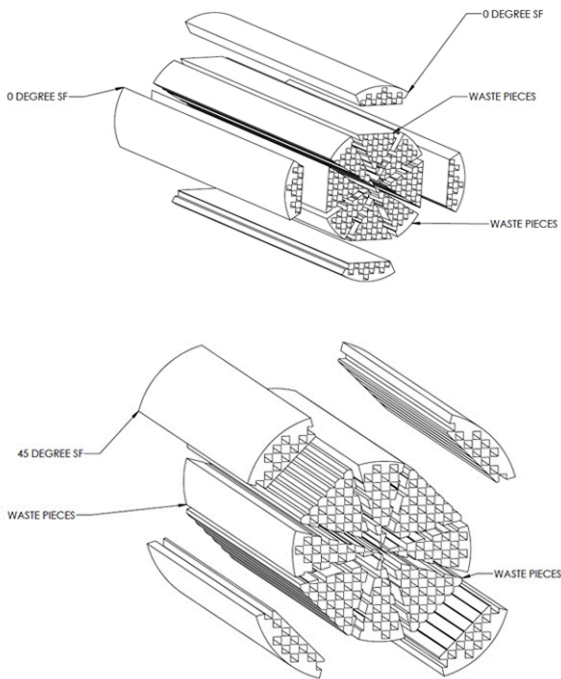


Figure 5. Schematic showing how (top) 0°-oriented and (bottom) 45°-oriented sectored flexure specimens are harvested out of a single DPF. Yield is 4 sectored flexure specimens per DPF.



Figure 6. Top view of four-point-bend fixture for testing the sectored flexure specimen. A specimen is shown positioned under the top two rollers.

- O-ring specimen.** O-ring specimens, originally developed to measure failure stresses in ceramic tubes [3-4], are cut from DPFs as shown in Fig. 7 and then have an interior hole drilled into each. They are then diametrically compressed to measure failure stress as shown in Fig. 8. Vertically oriented diametral compressive loading of an o-ring specimen will subject the outer diameter to hoop tension at the 3 and 9 o'clock positions and subject the inner diameter to hoop tension at the 6 and 12 o'clock positions. The weakest of those four locations will cause failure and its failure stress will be noted. The measured tensile failure stress represents an allowable hoop tensile stress in the DPF.

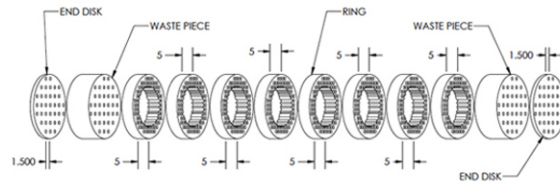


Figure 7. Exploded view showing o-ring specimen geometry harvesting from single DPF. Eight o-ring specimens are yielded per DPF and two end-disks for biaxial flexure testing are also produced.

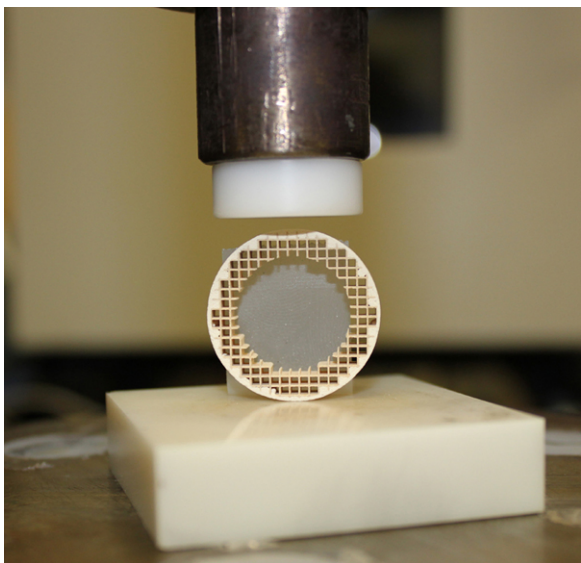


Figure 8. Experimental setup of diametral compression test of a cordierite o-ring specimen. 0° -orientation shown in this sample (i.e., struts aligned parallel and perpendicular to direction of compressive loading). 45° -orientation is also being tested. Tape (shown behind the specimen) holds the specimen perpendicular until compressive loading and alignment starts.

Our estimation of specimen failure stress with all three specimen geometries occurs via the flowchart shown in Fig. 9. Mechanical testing and analysis (e.g., finite element analysis, FEA, analytic, or numerical) are combined to achieve this. As with any mechanical-based method of estimating elastic modulus of a test coupon, appropriate supporting testing was completed in order to subtract out the effect of machine compliance.

For example, the diametral compression of the o-ring specimen produces a definitive relationship between compressive force and load-point-displacement. The same loading scenario is then modeled with FEA (enabled thru ORNL's μ -FEA software and the actual capturing of the DPF strut structure) by adjusting the DPF material's elastic modulus until the experimentally measured load-point-displacement jives with the measured maximum

compressive force. The arrived-at elastic modulus value is what we report as the material elastic modulus, and is needed for us to estimate failure stress.

For the failure stress analysis of biaxial flexure testing, finite element analysis was married to their experimental testing.

For sectored flexure testing, conventional beam bending analysis (use of moment of inertia and centroid) was married to their experimental testing.

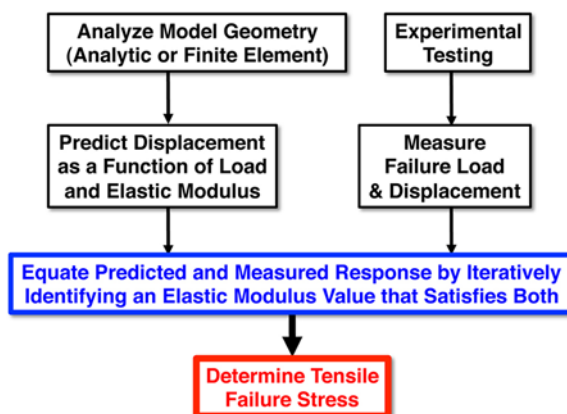


Figure 9. Modeling and experimentation pathway to determine maximum failure stress.

Results

Raw exhaust condensate was collected on impingers using a Mercedes 1.7 L turbo diesel running at 1500 rpm and 2.6 BMEP load. Ultra-low sulfur diesel (ULSD) and three biodiesel blends, B5, B20 and B100, were used as fuel sources. The NO_x was kept low and there was no aftertreatment. Fig. 10 shows a typical gas chromatograph collected from ULSD fuel. Sulfate, formate and acetate species were detected in all fuel operations. Fig. 11 shows the relative amounts of these species for each fuel. The ULSD (or B0) fuel had no detectable sulfate and somewhat lower amounts of formate present compared to the biodiesel blends.

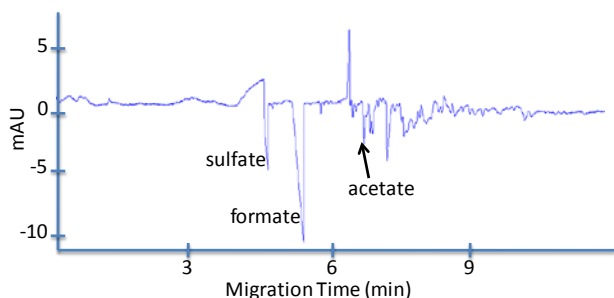


Figure 10. Gas chromatograph of exhaust condensate from ULSD fuel.

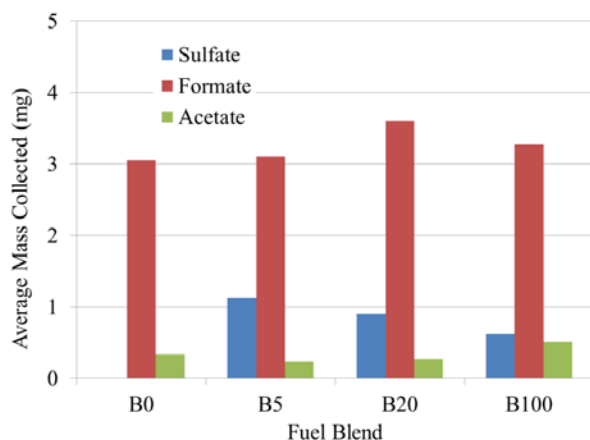


Figure 11. Average mass of sulfate, formate and acetate with condensate from all four fuel formulations.

The condensate composition was used to formulate solutions for accelerated chemical attack. Both cordierite and SiC DPF samples were dip tested in 1 M solutions of both sulfuric and formic acid and a 50:50 mixture of the two for 2 months followed by 1 month of drying in air. Fig. 12 shows the total weight gain for both materials under all three exposure conditions and Fig 13 shows images of the exposed samples. Upon drying, the cordierite formed Al and Mg sulfates. No pure formic acid attack was observed. The skin of the SiC sample contains alumino-silicate fibers that are susceptible to corrosion from sulfuric acid. The most likely mechanism is due to the condensate evaporating slowly, resulting in long exposure to a very concentrated acidic solution.

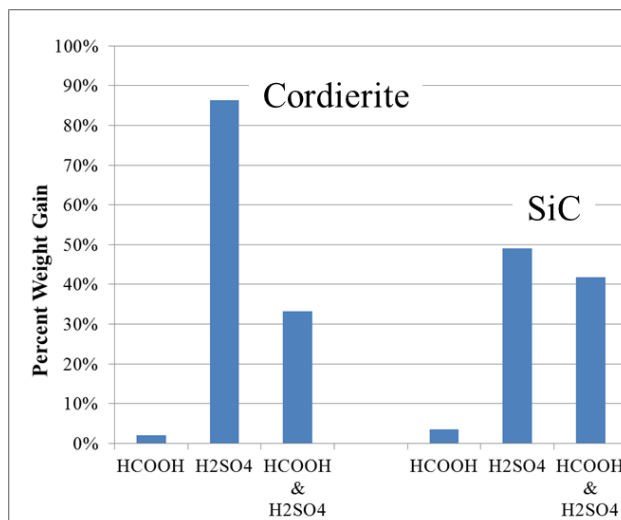


Figure 12. DPF weight gain following accelerated chemical attack.



Figure 13. Chemically-attacked DPF samples. The cordierite sample following sulfuric acid attack shows significant amounts of Al₂(SO₄)₃.

The estimated elastic modulus and failure stress for the three different as-received DPF materials, as measured with biaxial flexure testing, are listed in Table I. The two SiC DPFs had a higher elastic modulus than the cordierite (i.e., they were stiffer) and their failure stresses were higher too.

Table I. Summary of biaxial flexure testing results. Values in parenthesis are one standard deviation.

Material	Estimated Elastic Modulus (GPa)	Average Tensile Failure Stress (MPa)
Cordierite 59% Porosity Center	2	0.2 (± 0.1)
Cordierite 59% Porosity End	2	0.4 (± 0.2)
SiC 53% Porosity Center	5	2.2 (± 0.4)
SiC 53% Porosity End	5	3.7 (± 1.3)
SiC 58% Porosity Center	4	1.9 (± 0.4)
SiC 58% Porosity End	4	2.9 (± 0.4)

The estimation of elastic modulus and failure stress using sectored flexure testing for the three DPF materials is ongoing; however, the mechanical testing portion has been completed. The average flexure failure forces for the three materials are shown in Table II. Their failure forces may be meaningfully compared and interpreted because the dimensions of all their specimens were nominally equivalent, and therefore may be

linearly related to yet-to-be-determined tensile failure stresses. Given that, it will be expected that the 53% porous SiC will be the strongest, followed by the 58% porous SiC, and then the 59% porous cordierite.

For a given DPF, there does not appear to be a statistical difference in the axial tensile failure stress between the 0° and 45° orientations.

Table II. Summary of sectored flexure testing results. Values in parenthesis are one standard deviation.

Material	Average Flexure Failure Force (N)
Cordierite 59% Porosity 0° orientation	8.8 (± 0.5)
Cordierite 59% Porosity 45° orientation	8.1 (± 0.7)
SiC 53% Porosity 0° orientation	34.6 (± 3.6)
SiC 53% Porosity 45° orientation	34.0 (± 3.8)
SiC 58% Porosity 0° orientation	Not measured yet
SiC 58% Porosity 45° orientation	28.2 (± 3.5)

While the biaxial flexure stresses shown in Table I correspond to radial tensile application onto the strut structure, the results in Table II correspond to axial tensile failure stresses of the outer skin. The same trends in strongest to weakest for both Tables I and II are the same though.

Lastly, the analysis of elastic modulus and tensile failure stress for the o-ring specimens is

ongoing; however, like that for the sectored flexure specimens, these o-ring dimensions were nominally equivalent for all three materials, so some judgments can be made about their anticipated tensile failure stresses based on the measured failure initiation forces. The same trends in (expected) failure stress exist like those for the biaxial flexure and sectored flexure specimens when comparing the three DPF materials to one another. Additionally, the results suggest that the 45° orientation of radial tensile failure stress is lower than that of 0° orientation.

Table III. Summary of o-ring testing results. Values in parenthesis are one standard deviation.

Material	Average Failure Initiation Force (N)
Cordierite 59% Porosity 0° orientation	4.0 (± 1.3)
Cordierite 59% Porosity 45° orientation	3.2 (± 0.9)
SiC 53% Porosity 0° orientation	15.8 (± 6.9)
SiC 53% Porosity 45° orientation	11.4 (± 0.6)
SiC 58% Porosity 0° orientation	13.1 (± 6.4)
SiC 58% Porosity 45° orientation	8.3 (± 1.4)

These mechanical properties measurements establish a baseline that will be used to compare future degradation experiments to. In order to generate the large number of aged DPFs bricks

necessary for the mechanical testing, a Pramac P6000S silenced diesel gen-set was purchased and has been installed at the NTRC (National Transportation Research Center) building (see Fig. 14). The engine is 10 hp and is rated for 4800 W and is connected to two Avtron K490 load banks. This engine will be used as a pollution generator for long term 24/7 aging of DPF materials to better understand degradation in biodiesel operation but can be used for more general material testing in real diesel engine exhaust.



Figure 14. Pramac gen-set that will be used for long-term aging of DPFs.

Conclusions

Analysis of the condensate from ULSD and biodiesel blends showed higher amounts of sulfuric and formic acid with biodiesel. Sulfuric acid attack produced sulfate formation for both cordierite and SiC DPFs and so may provide an explanation for the initial degradation shown in Fig. 1.

Among the three DPF materials evaluated, the 53% porous SiC was the strongest, followed by the 58% porous SiC, followed by the 59% porous cordierite. This trend existed for all three specimen geometries investigated.

Though confirming analysis is yet to be done for the sectored flexure and o-ring specimen geometries, the results from the biaxial flexure testing of these materials show

the elastic modulus of the SiC DPFs to be about twice that of the cordierite DPF.

Axial tensile failure stress of the outer skin of these materials appears it could be independent of rotational orientation.

The radial tensile failure stress appears to be dependent on rotational orientation. The herein-designated 0° orientation was stronger than the 45° orientation.

References

- [1] "Standard Test Method for Monotonic Equibiaxial Flexural Strength of Advanced Ceramics at Ambient Temperature," ASTM C1499, Vol. 15.01, ASTM International, West Conshohocken, PA, 2009.
- [2] A. A. Wereszczak, S. F. Duffy, E. H. Baker, J. J. Swab, and G. J. Champoux, "Strength of a Ceramic Sector Flexural Test Specimen," *Journal of Testing and Evaluation*, 36:17-23 (2008).
- [3] O. M. Jadaan, D. L. Shelleman, J. C. Conway, Jr., J. J. Mecholsky, Jr., and R. E. Tressler, "Prediction of the Strength of Ceramic Tubular Components: Part I - Analysis," *Journal of Testing and Evaluation*, 19:181-191 (1991).
- [4] D. L. Shelleman, O. M. Jadaan, J. C. Conway, Jr., and J. J. Mecholsky, Jr., "Prediction of the Strength of Ceramic Tubular Components: Part II - Experimental Verification," *Journal of Testing and Evaluation*, 19:192-200 (1991).

Agreement 20091 - Electrically-Assisted Diesel Particulate Filter Regeneration

M. J. Lance, J. E. Parks, A. A. Wereszczak, W. P. Partridge,* and E. E. Fox*

Ceramic Science and Technology Group

Oak Ridge National Laboratory

P.O. Box 2008, MS 6068, Bldg. 4515

Oak Ridge, TN 37831-6068

(865) 241-4536; fax: (865) 574-6098; e-mail: lancem@ornl.gov

** Fuels, Engines and Emissions Research Center (FEERC), ORNL*

DOE Technology Manager: Jerry L. Gibbs

(202) 586-1182; fax: (202) 586-1600; e-mail: jerry.gibbs@ee.doe.gov

ORNL Technical Advisor: Dave P. Stinton

(865) 574-4556; fax: (865) 241-1034; e-mail: stintondp@ornl.gov

Contractor: Oak Ridge National Laboratory, Oak Ridge, Tennessee

Prime Contract No.: DE-AC05-00OR22725

Objectives

Study efficiency benefits and materials issues associated with the electrically-assisted diesel particulate filter (EADPF) device developed by General Motors (GM). This project is divided into three tasks:

Task 1: Fuels, Engines and Emissions Research Center (FEERC)

- Characterize potential fuel savings of the approach and related benefits to other emission control devices.
- Measure gas and substrate temperatures to obtain accurate picture of conditions experienced during regeneration.

Task 2: Ceramic Science and Technology Group (CerSAT)

- Resolve current disconnect between cordierite substrate model predictions and actual substrate durability.
- Use data and results to develop general design rules on heater geometries to optimize substrate durability.

Task 3: Corrosion Sciences Group

- Conduct a high-level discussion on the durability of the heater alloy.
-

TASK 1**Objectives**

- Characterize the potential fuel savings of the electrically-assisted diesel particulate filter (DPF) approach.
- Measure gas and substrate temperatures during DPF regeneration with non-thermally conductive fiber optic based techniques.

Approach

- Measure fuel savings as compared with conventional DPF regeneration techniques with a full-size DPF system on a 1.9-liter GM 4-cylinder diesel engine on an engine dynamometer.
- Measure substrate temperatures with fiber optics via black-body radiation during DPF regeneration.
- Compare temperature measurement history of substrates with materials characterization of substrates (Task 2) to determine failure mechanisms.

Accomplishments

- Demonstrated EADPF reduction of fuel penalty for DPF regeneration of 50% as compared with traditional fuel-only regeneration technique.
- Developed calibration over range of DPF regeneration temperatures for black-body radiation experiments with intensified charge coupled device (ICCD) camera spectrometer system.

Future Direction

- Collect black-body radiation temperature information during DPF regeneration with side-viewing fiber optic probes.

Introduction

Diesel engines operating at lean air-to-fuel ratios are more efficient than gasoline engines which commonly operate at stoichiometric air-to-fuel ratios. While the diesel engine dominates the heavy-duty truck market, the

expansion of diesel engines in light-duty truck and passenger car markets has been limited by various factors. One traditional limitation has been emissions or, specifically as addressed here, particulate matter (PM) emissions which are commonly referred to as “soot”.

In order to reduce PM emissions to meet customer expectations and U.S. EPA emissions regulations, diesel engines use an exhaust emission control technology known as the diesel particulate filter (DPF). The DPF is a ceramic (commonly cordierite or SiC) monolithic filter in the exhaust system that filters PM from the entire exhaust stream during normal operation (Figure 1). Periodically, the DPF is cleaned or “regenerated” to oxidize or “burn” the accumulated PM in the filter. The regeneration procedure occurs by raising the temperature of the DPF to approximately 600°C or higher where the carbon-rich PM readily oxidizes.

Virtually all modern diesel engine vehicles are sold with the DPF technology which is performing well in the field and reducing PM emissions by >95%. However, the current technique for DPF regeneration consumes extra fuel which is oxidized over a diesel oxidation catalyst in the diesel exhaust to heat the DPF to regeneration temperatures. This extra fuel or “fuel penalty” reduces the fuel economy advantage of the diesel engine.

General Motors (GM), the CRADA partner for this project, has developed a DPF technology that utilizes electrical power to heat the DPF for regeneration. This technology called Electrically-Assisted Diesel Particulate Filter (EADPF) may greatly reduce the fuel penalty associated with DPF regeneration. In this project Oak Ridge National Laboratory (ORNL) is collaborating with GM to better understand material limitations of the EADPF approach so that the technology can be commercialized and realize fuel savings for diesel engine vehicles. Task 1 of the project focuses on measuring the DPF exposure temperatures in exhaust on a full size engine platform. Task 2 focuses on the material failure

mechanisms and accuracy of predictive models to develop temperature-specific design rules. Finally, Task 3, while smaller in scope, focuses on material durability of metal alloys used in the EADPF design.

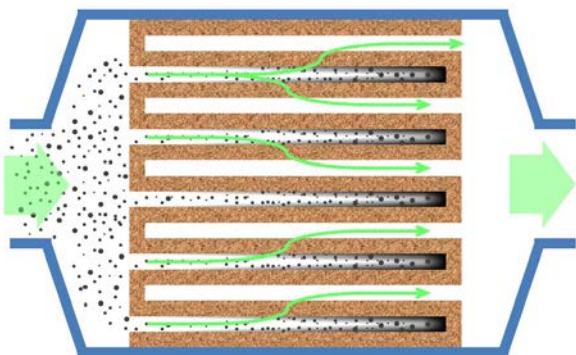


Figure 1. Cross-section schematic of a diesel particulate filter.

Results

After completing the setup of the EADPF system on a GM 1.9-liter 4-cylinder diesel engine in FY10, FY11’s efforts focused on operating the EADPF and characterizing the fuel penalty reduction for DPF regeneration. The DPF on the engine was loaded with particulate matter (PM) under controlled conditions, then DPF regeneration was performed with the EADPF technique. For comparison, the same DPF loading protocol in combination with a traditional fuel-based DPF regeneration technique was conducted. The fuel mass required for both techniques was monitored and compared. Electrical energy for the EADPF was integrated and converted to a fuel mass based on energy density, and the electrical fuel value was added to the base extra fuel to determine the total extra fuel requirement (or fuel penalty). Table 1 summarizes the results; a 50% reduction in fuel penalty was enabled with the EADPF regeneration technique.

Table 1. Comparison of fuel penalty for the EADPF technique as compared with a traditional fuel-based DPF regeneration technique.

	EADPF	Fuel-based
Soot Loaded, g/l	4.0	4.9
Extra Fuel, g	195.5	426.8
Extra Fuel Energy, kJ	8389.0	18317.3
Electric Energy, kJ	654.6	NA
Total Regen Energy, kJ	9043.6	18317.3
E-Energy fuel equivalent, g	15.3	NA
Total Extra Fuel, g	210.8	426.8

In parallel with the engine platform work, progress continued on the development of the fiber optic temperature measurement technique. Specifically in FY11, calibration spectra were collected from the blackbody radiation of cordierite materials with the specially designed angled tip probes from FY10. Calibration was conducted on a bench scale furnace. Figure 2 shows example calibration data. Furthermore, LabView programming for data acquisition from multiplexed fiber optic probes was completed to enable simultaneous measurement of multiple temperatures.

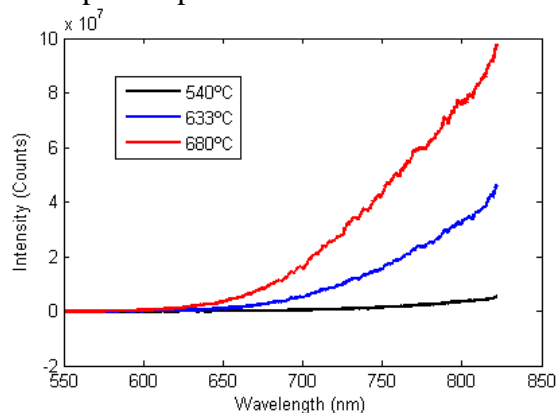


Figure 2. Calibration spectra of blackbody radiation collected with fiber optic probes.

In FY12, operation of the EADPF system on the engine platform will continue, and wall temperature measurements will be performed with the fiber optic blackbody radiation technique. Results from the blackbody radiation temperature measurements will be compared with the thermocouple temperature measurements currently being collected on the system.

Conclusions

A 50% reduction in the fuel required to regenerate a DPF has been demonstrated on engine with the EADPF technique. Further study of the substrate wall temperatures during the regeneration process will be conducted in FY12 with a blackbody radiation technique.

TASK 2

Objectives

- Develop test coupons that enable the determination of failure stresses of diesel particulate filters (DPFs) as a function of DPF orientation and location.

Approach

- Adapt simple and established test methods, used to evaluate ceramic materials, for the relevant testing of DPFs.
- Combine mechanical testing and supportive analysis (analytical, numerical, or finite element or combinations thereof) to measure and interpret the elastic modulus and failure stresses associated with crack initiation.
- Examine orientation effect on the crack initiation failure stress.

Accomplishments

- Designed and harvested test coupons from DPFs and measured their mechanical properties.
- Identified that the elastic modulus of DPF-containing cordierite is about one whole order of magnitude lower at typical tensile failure strains than what was previously believed (and unsubstantiated).

Future Direction

- Separately measure the elastic properties of the skin and interior cordierite materials in DPFs.
- Develop empirical equations that facilitate the acceptance of using the herein described mechanical test methods within the DPF manufacturing and end-user communities.
- Develop general rules of DPF design.

Introduction

Diesel particulate filter (DPF) technology enables the fuel efficient diesel engine to meet emission regulations for particulate matter. Examples of

DPFs are shown in Fig. 3. The DPF collects particulate from the exhaust stream during operation. It then is periodically regenerated by increasing its temperature to nominally 600°C. This causes the carbon-containing trapped particulate to oxidize and form gaseous CO₂ enabling continued filtration at a lower backpressure. But the regeneration causes thermal gradients in the brittle ceramic which can be problematic.

Two lifetime-limiting consequences of overly severe thermal gradients are crack initiation and propagation. The end crack and ring crack are examples of crack types that form in DPFs and are schematically shown in Fig. 4. The formation and existence of either can compromise the intended filtering function of the DPF and ultimately result in their need for replacement. Therefore, the end-user has interest in managing the operating conditions so the DPF successfully fulfills its purpose without initiating those cracks.

Two criteria must be satisfied in tandem to promote and achieve maximum service lifetimes in DPFs under severe operating conditions. The ceramic comprising the DPF must have sufficiently high tensile strength and the tensile stresses (such as those caused by operating thermal conditions) must be sufficiently low. Obviously, if the anticipated operating conditions produce high tensile stresses, then a stronger DPF should be considered for use. Or if the only available candidate DPF ceramics have a limited tensile strength, then the operating conditions need to be restrained so that too-high tensile stresses do not arise. In either circumstance, the understandings of both the DPF ceramic strength and the DPF service conditions are needed to successfully employ a DPF.

The developed service stress state in a DPF can be complex owing to its anisotropic architecture. The DPFs examined in this study have a 4-fold rotational symmetry (C₄) that is illustrated in Fig. 5. The thermal gradients (and consequential mechanical stresses) for operation will of course be affected by this anisotropic structure, and out of convenience may be interpreted with respect to cylindrical coordinates; namely, axial (i.e., gas flow direction), radial, and hoop orientations.

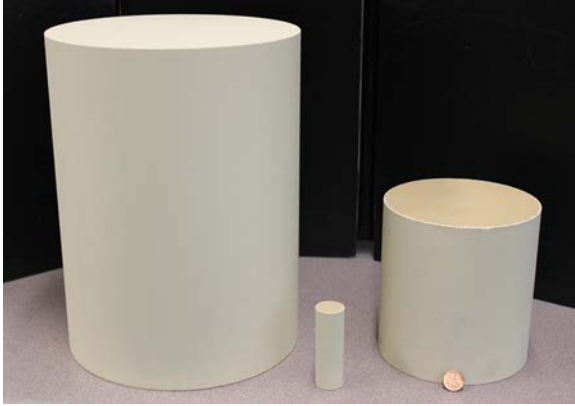


Figure 3. Diesel particulate filters examined in this study.

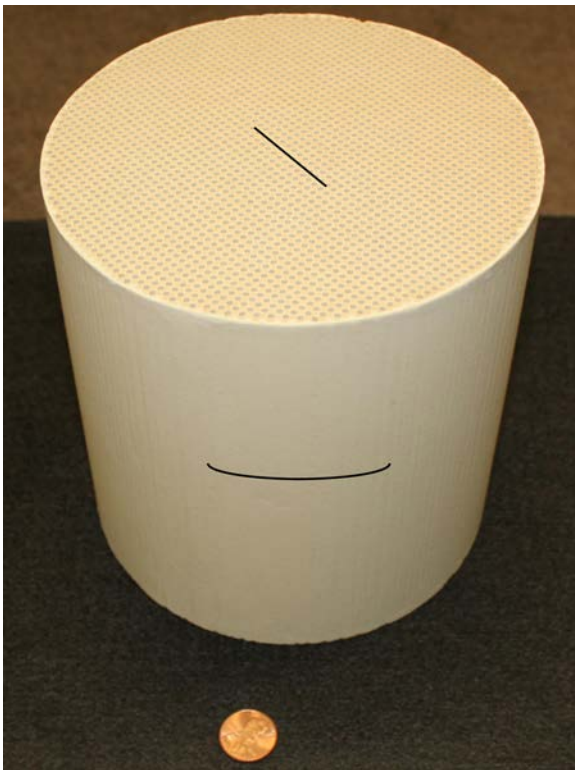


Figure 4. Schematics of (top) end crack and (middle) ring crack superimposed on a DPF. The plane of the end crack is parallel to the DPF's longitudinal axis and intersects the DPF's end face. The ring crack is perpendicular to the DPF's longitudinal axis and intersects the outside diameter usually near the middle of the DPF's length.

Ceramics almost always crack because of the existence of a too-high (First Principal) tensile stress, and the formation of the two crack types schematically shown in Fig. 4 may be described in context to that and the DPF's architecture. The plane of the end crack is axial or parallel to the gas flow direction and intersects the DPF's end. The end crack forms as a consequence of sufficiently high radial tensile stresses existing at the DPF end. The plane of the ring crack is perpendicular to the gas flow direction and intersects the outside diameter of the DPF. Its location is usually near the middle of the axial length and forms as a consequence of sufficiently high axial tensile stresses existing at the exterior of the DPF. In general, when ceramics crack in the presence of a thermal gradient (particularly when there is concurrent confinement), crack initiation usually occurs near the cold side of that gradient and often when there is a sufficiently rapid heating or cooling transient (i.e., thermal shock).

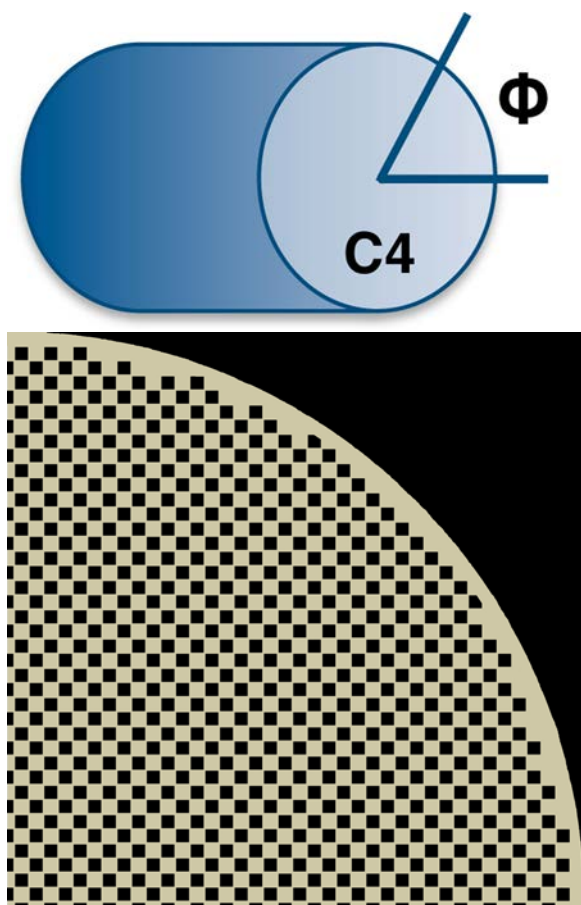


Figure 5. DPFs have a 4-fold rotational symmetry (designated as "C4"). Bottom image shows 50% channel fill for the end structure of a DPF for a $\phi = 90^\circ$.

To successfully predict thermomechanical stresses (and predict crack or failure initiation), knowledge of the thermoelastic properties, elastic properties, and tensile failure strength of the DPF ceramic must be known or measured. For measuring tensile failure strength, a standardized test method, ASTM C1674 [1], is available. The failure stress is determined using classical beam bending analysis and follows without *a priori* knowledge of the material's elastic modulus. The specimen for that test method is a prismatic bar, harvested from the interior of a DPF as shown in Fig. 6, and is mechanically

tested in 4-point flexure. Several have reported on failure stress data on cordierite ceramics DPF using its method or precursors to it [2-5].

A limitation with ASTM C1674 is that it only evaluates tensile failure stress of the interior strut structure of a DPF; such a measured tensile failure stress is perhaps not relevant to either of the crack types shown in Fig. 4 or of use for predicting the conditions where their crack types initiate. Therefore, a motivation exists to develop mechanical test coupons whose combination of produced crack-plane and crack propagation direction represents the two crack types in Fig. 4.

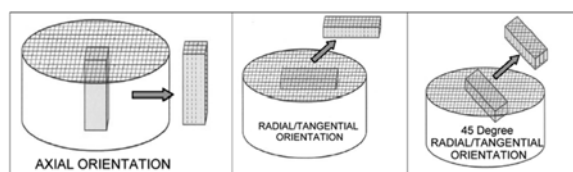


Figure 6. Prismatic bar harvesting for flexure testing described in ASTM C1674.

While the porous microstructure of DPF ceramics is a requirement for exhaust gas filtering it also produces a complex response when subjected to (thermo) mechanical loading. The open and continuous (filtering-capable) porous structure of the interior square struts and the closed, less porous, structure of the exterior skin are shown in Fig. 7. Such porous structures often have an asymmetric response to tensile and compressive loadings. Tensile loading of the compliant porous structure can readily cause initiation, coalescence, and accumulation of local microcracking resulting in a gradual compliance increase with additional tensile straining. While compressive loading will also cause microcracking, additional compressive straining beyond its initiation can lead to little change in compliance with additional microcracking. The tensile failure stress, like for almost all ceramics, has a much lower magnitude than compressive failure stress, so rationale exists to focus

attention on the tensile failure stress for appropriate and conservative DPF reliability analysis.

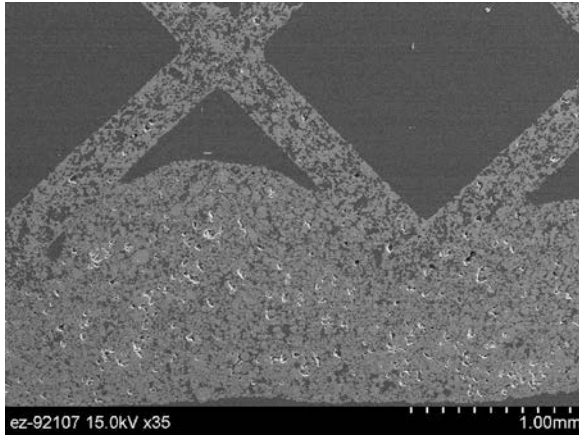


Figure 7. Polished microstructure of a cordierite DPF showing porous open structure in cross-sectioned struts and the closed porous structure of the outer skin (bottom).

There were three primary goals to this study. The first was to employ test specimens whose mechanical loading would produce tensile-stress-induced failure modes consistent with those of the crack types shown in Fig. 4 and that would enable quantification of tensile failure stress associated with their formation. Flexure testing works well for achieving that and tends to provide greater ease of valid experimentation than uniaxial tension testing does, and also is readily adaptable to high temperature testing too. Test specimen geometries, unlike the prismatic bar featured in C1674, used in the mechanical evaluation of other types of ceramics were adapted to the mechanical testing of the DPF architecture and ceramic to better facilitate the understanding of the end and ring crack in Fig. 4. The second goal was to also use analyses that enable the estimation of the DPF ceramic's elastic modulus - a property needed for any eventual modeling of the DPF's operational stress state. The third goal was to satisfy the first and second goals by evaluating the cordierites in three different sized DPFs (shown in Fig.

3). Their geometrical characteristics are shown in Table 2.

Table 2. Characteristics of the three evaluated DPF sizes.

Nominal Diameter (mm)	Length (mm)	Measured # of Cells per sq. in.	Manuf. Reported Porosity
25	75	256	59%
141	156	200	52%
229	305	256	52%

Three Alternative Specimens

The descriptions of the equibiaxial flexure specimen, sector flexure specimen, and the o-ring flexure specimen are presented along with their mechanical testing and respective analyses used to determine elastic modulus and tensile failure stress. All three of those specimen geometries were prepared from the three DPF sizes shown in Table 2 producing nine different specimen type and size combinations. All three are as easy, or easier, to harvest out of a DPF as the prismatic bar geometry used in ASTM C1674 (Fig 6).

Approach

The method to estimate elastic modulus and tensile failure stress with all three alternative test specimens is represented by the flowchart in Fig. 8. The method combines analysis (either analytic or finite element) with mechanical testing. The mechanical testing of all the test coupons produces a record of compressive force (all three test methods are flexure tests and compressive loading coupled with appropriate fixturing activates their flexure) and an associated linear specimen deflection up through a maximum compressive force where crack initiation begins. All three specimen geometries responded linearly up to that maximum compressive force. The coupled pair of maximum-compressive-force and deflection data is record-

ed for every specimen after the important correction (subtraction) for machine compliance. The geometry of that actual specimen is then modeled using FEA (equibiaxial specimen and o-ring specimen) or classical beam bending (sectored flexure specimen) and displacement as a function of compressive force and elastic modulus is predicted. Elastic modulus is then iteratively varied until a produced force-displacement couple finally matches the force-displacement couple measured from the flexure testing. That elastic modulus (secant elastic modulus actually) is then used again in the FEA to estimate the maximum tensile failure stress in that specimen when failure initiation began.

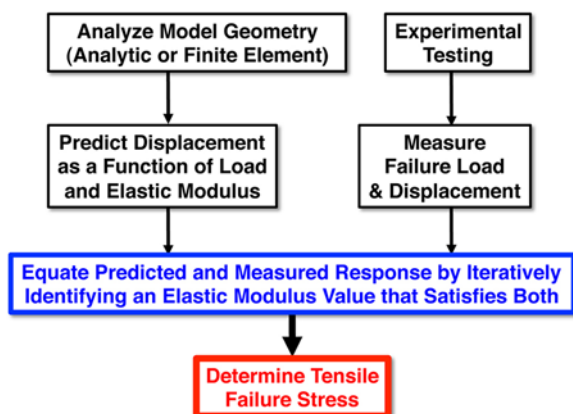


Figure 8. Analysis of all three alternative test coupons were combined with their experimental testing to (1) estimate secant elastic modulus of the DPF cordierite and (2) failure stress

Equibiaxial Flexure (Radial Tension)

The testing of the equibiaxial flexure specimen subjects the DPF's end structure (or the interior strut structure if the disk is cut from the interior) to a biaxial radial tensile stress, and its measured response is relatable to the interpretation of end-crack formation illustrated in Fig. 4.

The equibiaxial flexure specimen and test are a standard method (ASTM C1499) used for measuring failure stress in dense ceramic materials [6] and it was adapted here to measure radial tensile failure stresses in DPFs. An ad-

vantage of its use with disks harvested out of a DPF is its produced biaxial flexure stress state will result in failure of the weakest direction in the biaxially stressed plane as compressive force is increased. Examples of the equibiaxial flexure specimens and tested coupons are shown in Figs. 9-10, respectively. The geometry, applied compressive force, and resulting disk deflection for the equibiaxial flexure specimen (a.k.a., ring-on-ring or RoR specimen) were modeled in 3D using ANSYS (see Fig. 11), and their predicted load-displacement responses were matched with RoR flexure testing results using the method shown in Fig. 8 to estimate radial tensile failure stress and the material's secant elastic modulus.

Disk size and RoR span diameters were chosen so to produce classical beam bending (i.e., deflection to failure less than $\sim 1/4$ the specimen thickness) while avoiding the application of high contact stresses from the rings (i.e., avoid contact-induced crushing). All equibiaxial flexure disks responded linear elastically. Failure forces for all specimens from all three sizes were relatively low-valued and there was never evidence seen that the rings had caused contact-induced crushing. Test fixture rings were made of polycarbonate and an example of one paired size is shown in Fig. 10. The rings could alternatively be made out of high-temperature-capable material if high-temperature testing of the DPF was to be sought. A summary of their sizes are listed in Table 3.

Equibiaxial disks cut from the interior of a DPF constitutes an efficient use of material because they can be formed from the core-drilling used to fabricate the to-be-discussed o-ring specimen. The center disk specimens for the two larger diameter DPFs were machined in such a manner.

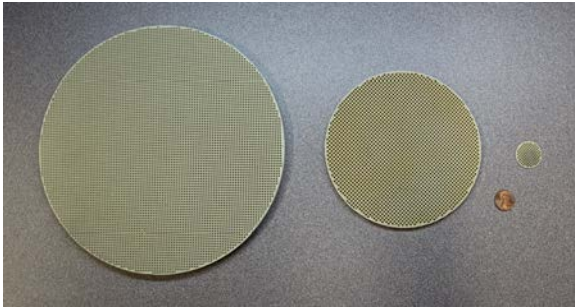


Figure 9. Examples of equibiaxial flexure disks sliced out of three different DPF diameters.

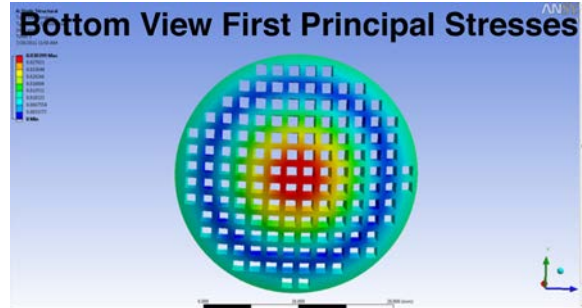


Figure 11. Bottom view (tensile surface) of equibiaxial disk subjected to flexure. FEA was combined with experimental measurement to estimate secant elastic modulus and failure stress.

Specimen and Ring Fixtures



Example of Failed Disk

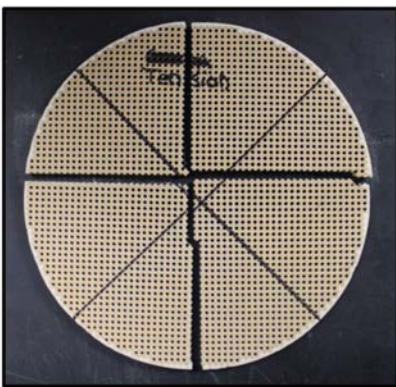


Figure 10. Examples equibiaxial flexure specimen and fixtures and of a failed equibiaxial flexure disk.

Table 3. Summary of equibiaxial disk sizes and fixture sizes. E = disk sliced from DPF end, and C = disk from interior slice of DPF.

Disk Diameter (mm)	Disk Thickness (mm)	Top Ring Diameter (mm)	Bottom Ring Diameter (mm)
25 - E	1.5	6.75	19
25 - C	1.5	6.75	19
141 - E	6	40	80
109 - C (core drilled from 141 DPF)	6	40	80
229 - E	10	80	160
200 - C (core drilled from 229 DPF)	10	80	160

Sectored Flexure (Axial Tension)

The testing of the sectored flexure specimen subjects the DPF's outer diameter (or exterior skin) to an axial tensile stress, and its measured response is applicable to the prediction and the interpretation of ring crack formation illustrated in Fig. 4.

The sectored flexure specimen was developed to measure the axial tensile failure stress in dense ceramic tubes and to harvest and test numerous specimens from each tube to improve statistical confidence [7]. Portions of its machining are illustrated in Fig. 12. Sectors are first axially sectioned out of the DPF. An isosceles triangle is then cut from the sector to produce a "sectored flexure specimen" with a flat on one side and the original outer diameter of the DPF retained on the opposite. The specimen is oriented in the flexure fixture so its flat side is the compressive side and the opposite curved portion is tensile loaded. The nominal dimensions of the sectored flexure specimens harvested from the three different DPF sizes are listed in Table 4.

A comparison of the relative sizes of the sectored flexure specimens evaluated are shown in Fig. 13 along with an illustration of its placement in the bend fixture and an example of a tested specimen in Fig. 14. For the 4-pt bend fixture shown in Fig. 14, hour-glass shaped rollers were used for the bottom and cylindrical rollers for the top. The radius of curvature for the hour-glass shaped rollers matched that of the DPF's original outside diameter so to promote line loading along its curved surface so to minimize contact loading stresses between the roller and specimen. Cylindrical rollers could be used on the fixture's top because it was a flat surface. Specimens failed at sufficiently low forces to sustain classical beam bending (when coupled with the chosen upper and lower fixture span sizes and specimen's cross-section or moment of inertia, MOI). Additionally, all sectored flexure specimens responded linear elastically up to their failure force.

The geometry, applied compressive force, and resulting specimen deflection for the sectored flexure specimen were modeled using Oak Ridge National Laboratory- (ORNL)-developed software that calculates the MOI and centroids for bend specimens with complicated cross-sections comprising dissimilar materials. An image of the software's user interface is shown in Fig. 15. A digital photograph of the speci-

men cross-section is used as input. The user specifies dimensional-scale and the elastic properties of the different materials in the photo represented by different gray-scales. The software then calculates the MOI and distance from outer fiber to the neutral axis. Their values are then used in the classical beam bending equation along the fixture spans and failure force to calculate the axial tensile failure stress. And to estimate elastic modulus of the structure, the predicted load-displacement bending responses were matched with sectored flexure testing results using the method shown in Fig. 8.

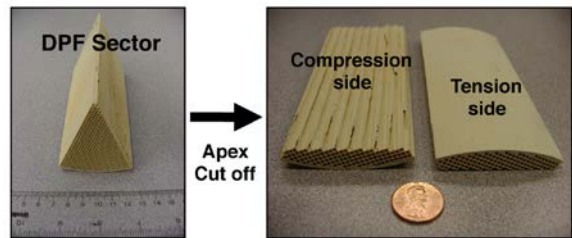


Figure 12. A sector is cut from a DPF and then an isosceles triangle is cut to produce a sectored flexure specimen. The DPF's original outer diameter is also the tensile surface during flexure testing.

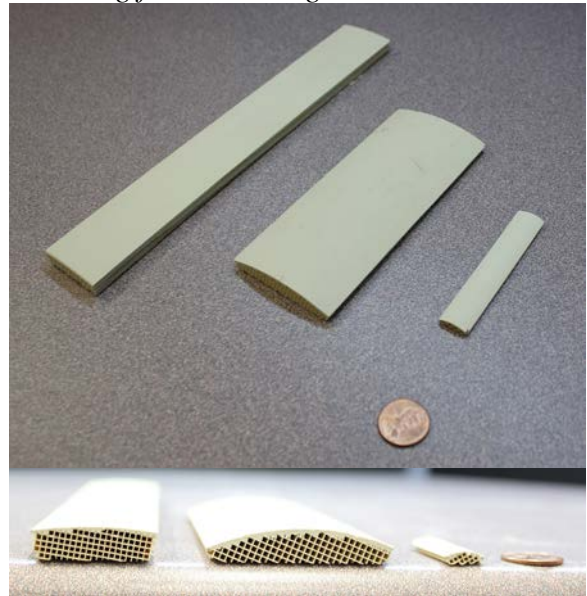
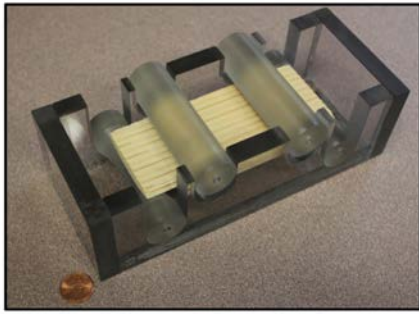


Figure 13. Bottom view (upper image) of sectored flexure specimens from three different diameter DPFs and their end view (lower image).

Specimen Positioned in Fixture



Specimen After Fracture

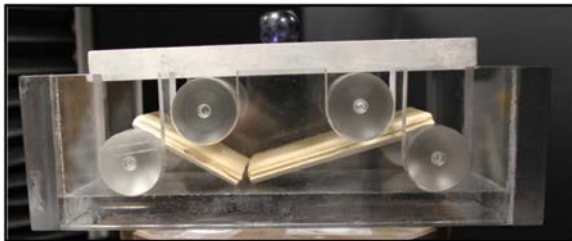


Figure 14. Example of a (top image) sector flexure specimen positioned in the 4-pt bend fixture and (bottom) a side view of a failed specimen after flexure testing.

DPF Diameter (mm)	Sector Angle (deg)	Max. Specimen Height (mm)	4-pt Spans (mm)
25	45	4	6.75/19
141	60	10	40/80
229	18	9.5	80/160

O-Ring Flexure (Hoop Tension)

The o-ring specimen was developed to estimate hoop tensile failure stresses on the ID and OD of dense ceramic tubes [8-9]. Likewise, the testing of the adapted o-ring specimen subjects the DPF's outer diameter (or skin) to hoop tensile stress. Examples of the o-ring specimens harvested from the three DPFs are shown in Fig. 16 and their nominal dimensions are shown in Table 4.

Pictures of an o-ring specimen subjected to loading and of the produced crack are shown in Fig. 17. It also can subject the interior struts, located just inside the skin, to hoop tension too. The specimen is diametrically compressed, and all DPF o-ring specimens responded linear elastically up to some maximum force where a crack initiates. The produced (First Principal) tensile stress field for the diametrically compressed o-ring specimen is shown in Fig. 16. Regions of maximum hoop tension are produced at the 3 and 9 o'clock positions at the OD and at the 6 and 12 o'clock positions at the ID. Postmortem of the failed o-ring specimen identifies where fracture had commenced.

The geometry, applied compressive force, and resulting o-ring deflection were modeled in 2D using μ -FEA and ANSYS, and their predicted load-displacement responses were matched with measured o-ring flexure testing results using the method shown in Fig. 8. This allowed estimation of the secant elastic modulus and hoop tensile failure stress at the exterior skin or in the strut structure (depending on where failure initiation had occurred in the o-ring specimen).

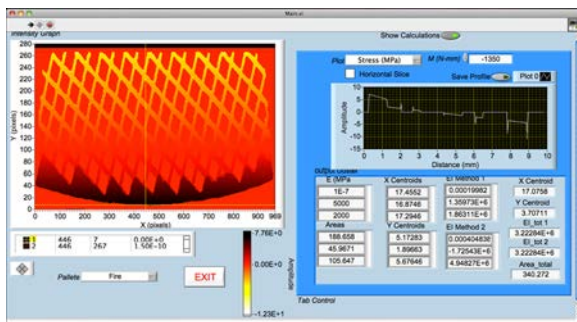


Figure 15. A window showing stresses and tabulated results in ORNL-developed MOI software. The MOI of the cross-section of a sector flexure specimen is analyzed. This MOI analysis was combined with experimental measurement to estimate secant elastic modulus and failure stress.

Table 4. Summary of sector flexure sizes and fixture sizes.

Though the produced crack plane from the o-ring specimen is not linkable to either of the two crack types shown in Fig. 4, its testing enables the measurement of hoop tensile stress and this in turn allows the potential concurrent prediction and consideration of what operational stress states in a DPF would activate such a crack type. The plane of such a produced crack would be parallel to the DPF's flow direction or axis of symmetry and intersect the outer surface to produce a crack visible from the outside or intersect the interior of the skin (which would not be seen from the outside).

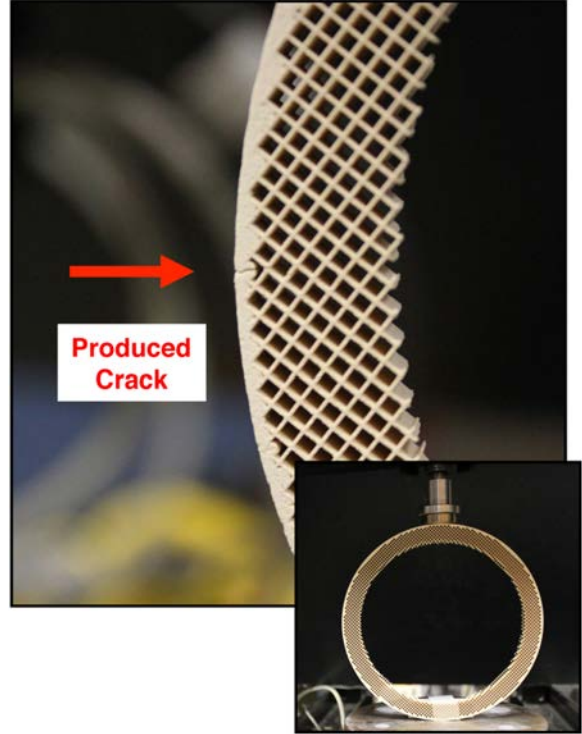


Figure 17. Example of a generated crack from o-ring flexure testing.

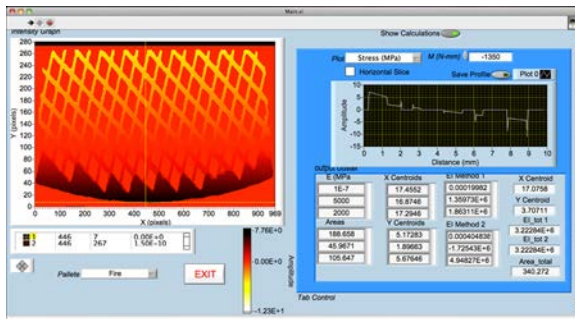


Figure 16. Examples of o-ring flexure specimens sliced and core-drilled out of three different DPF diameters.

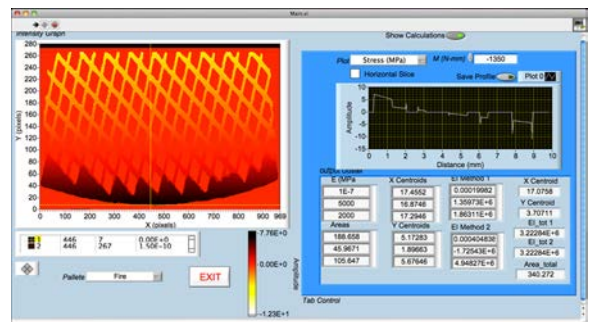


Figure 18. Diametral compressive loading of an o-ring specimen will subject the OD to hoop tension at the 3 and 9 o'clock positions and the ID to hoop tension at the 6 and 12 o'clock positions. μ -FEA and FEA were combined with experimental measurement to estimate secant elastic modulus and failure stress.

Table 5. Summary of o-ring specimen sizes.

Outer Diameter (mm)	Inner Diameter (mm)	Thickness (mm)
25	16	5
141	111	6
229	200	10

Correlating Strain and Stress

If a material is symmetrically linear elastic in both the tension and compression domains, then the applied stress and strain are simply related by the material's elastic modulus through the classical Hooke's Law. However, as discussed in the Introduction, the porous ceramics comprising DPFs are likely not symmetric in the tension and compression domains. Additionally, there is ample evidence to show that these materials are not linear either. In other words, *the stress-strain response in these porous materials are likely asymmetrically non-linear*. Furthermore, they are known to exhibit hysteresis in cyclic loading which further complicates the understanding of their mechanical response; but in this study, our focus is only on the state of the material up to the (tensile) strain or stress where damage initiates. All these contributing complications have led to misplaced focus and improper interpretation of how the ceramics in DPFs mechanically respond.

Ideally, the stress-strain response would be available over a large domain of compressive and tensile strains. It is not. Given that the magnitudes of tensile failure stress will be lower than those of compressive failure stresses, an attractive consolation would be if there was an understanding of the stress-strain response in the tensile strain domain. There is nothing for that either.

Why cannot a DPF be conventionally strain-gaged and uniaxially tensile stressed to measure a tensile stress-strain response? The porous and weak structure of the DPF cannot accommodate

strain-gage mounting nor permit gripping of a tensile fixture. Non-contact extensometry would not necessarily solve this problem because the tensile gripping difficulty would still be an impassable obstacle. Unfortunately, there indeed is no elegant or conventional method available to measure a continuous, tensile stress-strain response in a DPF ceramic.

The development of ASTM C1674 and four-point flexure of harvested bars from a DPF interior was a logical first step because it at least provides an experimental tensile failure stress value that can be used for design or material development. But a desirable (apparent) elastic modulus could have also been gleaned out of that test too, but its analysis evidently has not been added to its practice yet.

To start to estimate an elastic modulus of porous DPF structures, many have resorted to the use of sonic-based or resonance-based measurements [3, 10]. These techniques rely on small excitations of displacements or strains for their measurement. They are recognized to be reliable test methods for validly measuring this material property when the material is symmetrically linear elastic over a large domain of compressive and tensile strain. However, there is a problem with that whose description can be facilitated by what is illustrated in Fig. 19. If a material is asymmetrically non-linear in the compressive and tensile strain domains, and that asymmetry exhibits itself at small absolute values of strains, then a sonic- or resonance-based measurement of elastic modulus is only meaningful at those very small strains where the local stress-strain response is symmetrically linear elastic. The elastic modulus measured at those very small strains is not going to be representative of, and of course not equal to, the (tangent) elastic modulus at tensile (or compressive) strains of DPF operational service. They will be higher valued, and the results from the present study support that. Such a difference in dynamic and quasi-static elastic modulus has precedence - thermal barrier coatings exhibit an analogous difference [11-12] and have a mechanical asymmetry.

In *every* case where we have estimated elastic modulus with the specimens described in this study using the method shown in Fig. 8, we have determined a (secant) elastic modulus, E_{SEC} , that is 4-12 times *lower* than reported E 's estimated by sonic- or resonance-based test methods. There have been no outliers whose values approach the values measured by sonic- or resonance-based methods. This comparison is summarized in Table 6. Our employed method is actually determining the E_{SEC} (see Fig. 20); which actually is still going to be higher-valued than the tangent modulus, E_{TAN} , for any given tensile strain. We are producing tensile failure at strains in the range of 0.1-0.3% in all three of these specimens (i.e., failure at strains that are many orders of magnitude higher than those that are associated with sonic- or resonance-based test methods). Despite that, the E_{SEC} is still a more representative value to report than that measured by sonic- or resonance-based methods.

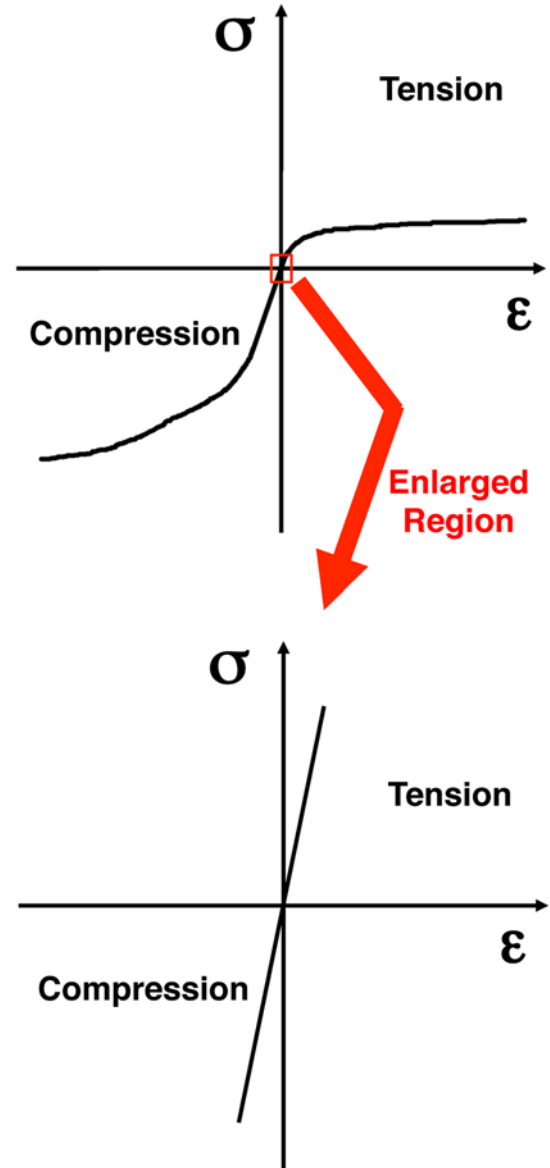


Figure 19. Sonic- or dynamic-based elastic modulus measurement methods evaluate stiffness at extremely small displacements and will therefore overestimate elastic modulus for non-linear materials.

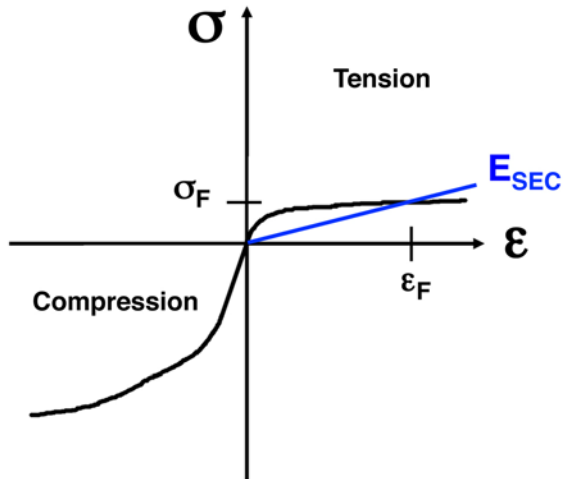


Figure 20. The secant elastic modulus, E_{SEC} , will be lower at the strain-to-failure values estimated with the three alternative test geometries evaluated in this study.

Uniaxial compression testing is another option that has been pursued for estimating elastic modulus. Bruno et al., [13] show a trend of elastic modulus decrease as a function of compressive stress as measured by neutron diffraction. Zero strain or stress values for elastic modulus were not reported; however, the highest elastic modulus values are at low compressive stress and are approximately 13 GPa and decrease to approximately 6 GPa at approximately 9 MPa of compressive loading (included for comparison in Table 6). These trends are consistent with the compressive strain domain in the Fig. 20 schematic; however, because of the stress-strain asymmetry in the compressive and tensile strain domains, the reported elastic modulus values of Bruno et al. will be overestimates of elastic modulus in the tensile strain domain and the same absolute values of strain.

What will happen if sonic- or resonant- or dynamic-based measurements of elastic modulus or if compression-loading-based measurement of elastic modulus are used in the design or reliability analysis of an operating DPF? Their large-values will predict erroneously high tensile stresses and erroneously short lifetimes.

The quasi-static or mechanical-based measurements featured in this study are more appropriate for use (in the continued absence of a continuous stress-strain curve in both the compressive and especially the tensile strain domains).

The estimation of the E_{SEC} using the algorithm shown in Fig. 8 was the first of two informative outcomes of this study; the estimation of tensile failure stress (for different orientations) was the other. The results from other's use of ASTM C1674 [2-5] provides a comparison with tensile failure stresses measured with this study's three alternative specimens. This is shown in Table 7. Using our E_{SEC} values from Table 6 back in our various analyses for the three specimens (i.e., FEA or MOI analysis), we are able to estimate the tensile stress failure for all specimens. An interesting observation results. For the most part, tensile failure stress values we estimated are arguably equivalent to the tensile stress values from ASTM C1674 tests. There is a suggestion that the axial tensile failure stresses for the exterior skin are higher valued, but that work is continuing and we look to confirm that with additional testing.

So our tensile failure stress values show that understanding of failure stresses in porous DPFs is quite good, but as the second paragraph in the Introduction discussed, that is only one of two key parts to successful design and life prediction of DPF filters. The other part is to correctly predict the operational DPF stresses over both compressive and tensile strain domains; the obtained E_{SEC} values in this study go toward satisfying that ability too.

Table 6. Comparison of elastic moduli.

Test Method	Elastic Modulus (GPa)*	Source
Dynamic Resonance-Based	4 - 7	[3]
Dynamic RUS	12.3 ± 0.3	[10]
Quasi-static / Mechanical Uniaxial Compression	> 13 GPa at zero MPa; ~ 6 GPa at 9 MPa	[13]
Quasi-static / Mechanical Equibiaxial Flexure	0.5 - 1.5	Present study
Quasi-static / Mechanical Sectored Flexure	1 - 3 Interior strut 4 - 24 Exterior skin	
Quasi-static / Mechanical O-Ring Flexure	1.1 - 2.1	

* A function of porosity - comparison intended to illustrate coarse comparison.

For our future work, we will continue to test these specimens to generate strength statistics and also attempt to develop additional modifications of the three specimens so that we can produce failure at different tensile strains, and start to populate or infer a tensile-stress-strain diagram for porous ceramics for DPFs. Also, we are working to harvest and isolate specimens from the interior struts, the exterior skin, and from the 50% end fill so that we may mechanically measure the elastic modulus of all three, and take them all into account in future operational stress modeling of DPFs.

Table 7. Comparison of quasi-static tensile failure stresses.

Test Method	Tensile Failure Stress (MPa)*	Source
ASTM C1674 like (4-pt flexure)	2.4 - 3.6 (interior strut) axial	[2]
ASTM C1674 like (4-pt flexure)	4 - 6 (interior strut) axial	[3]
ASTM C1674 (4-pt flexure)	2 - 5 (interior strut) axial	[4]
ASTM C1674 (4-pt flexure)	4 - 7.5 (interior strut) axial	[5]
Equibiaxial Flexure	2 (est) (interior strut) > 4 (est) (50% end fill) radial	Present study
Sectored Flexure	5 - 13 (est) (exterior skin) axial	
O-ring Flexure	2 - 4 (est) (exterior skin) hoop	

* A function of porosity - comparison intended to illustrate coarse comparison.

Conclusions

An E_{SEC} in the range of 1 - 2 GPa consistently results in analytical (FEA or numerical) and experimental correlation for deformations of DPF cordierite ceramic equibiaxial flexure, sectored flexure, and o-ring flexure specimens and for three different DPF diameters. That range of E_{SEC} is about 4-12 times lower than reported elastic modulus for cordierite ceramics sonically and dynamically measured. If this lower E_{SEC} is correct, then

actual stresses in a DPF during service will be much lower than that predicted using sonically or dynamically measured elastic modulus. Owing to the probable non-linearity and asymmetry of stress and strain with these DPF cordierite microstructures, a strain-to-failure criterion may be more relevant for use than a failure stress criterion.

References

1. ASTM C1674, "Standard Test Method for Flexural Strength of Advanced Ceramics with Engineered Porosity (Honeycomb Cellular Channels at Ambient Temperatures," Vol. 15.01, ASTM International, West Conshohocken, PA, 2009.
2. Gulati, S. T. and Reddy, K. P., "Size Effect on the Strength of Ceramic Catalyst Supports," SAE Paper Number 922333, SAE International, 1992.
3. Kuki, T., Miyairi, Y., Kasai, Y., Miyazaki, M. and Miwa, S., "Study on Reliability of Wall-Flow Type Diesel Particulate Filter," SAE Paper Number 2004-01-0959, SAE International, 2004.
4. Webb, J. E., Widjaja, S., and Helfinstine, J. D., "Strength Size Effects in Cellular Ceramic Structures," *Ceramic Engineering and Science Proceedings*, Paper 1-50, Symposium 1, 2006.
5. Stafford, R. J. and Gonczy, S. T., "Data Reliability for Honeycomb Porous Material Flexural Testing," *Ceramic Engineering and Science Proceedings*, Symposium 9, 2009, 30:291-300.
6. ASTM C1499, "Standard Test Method for Monotonic Equibiaxial Flexural Strength of Advanced Ceramics at Ambient Temperature," Vol. 15.01, ASTM International, West Conshohocken, PA, 2009.
7. Wereszczak, A. A., Duffy, S. F., Baker, E. H., Jr., Swab, J. J., and Champoux, G. J., *Journal of Testing and Evaluation*, 2008, 36:17-23.
8. Jadaan, O. M., Shelleman, D. L., Conway, J. C. Jr., Mecholsky, J. J. Jr., and Tressler, R. E., "Prediction of the Strength of Ceramic Tubular Components: Part I - Analysis," *Journal of Testing and Evaluation*, 1991, 19:181-91.
9. Shelleman, D. L., Jadaan, O. M., Conway, J. C., Jr., and Mecholsky, J. J. Jr., "Prediction of the Strength of Ceramic Tubular Components: Part II - Experimental Verification," *Journal of Testing and Evaluation*, 1991, 19:192-200.
10. Shyam, A., Lara-Curzio, E., Watkins, T. E., and Parten, R. J., *Journal of the American Ceramic Society*, 2008, 91:1995-2001.
11. Eldridge, J. J., Morscher, G. N., and Choi, S. R., "Quasistatic vs. Dynamic Modulus Measurements of Plasma-Sprayed Thermal Barrier Coatings," *Ceramic Engineering and Science Proceedings*, 2002, 23:371-78.
12. Choi, S. R., Zhu, D., and Miller, R.A., "Effect of Sintering on Mechanical Properties of Plasma-Sprayed Zirconia-Based Thermal Barrier Coatings," *Journal of the American Ceramic Society*, 2005, 88:2859-67.
13. Bruno, G., Efremov, A. M., Levandovskiy, A. N., Pozdnyokova, I., Hughes, D. J., and Clausen, B., "Thermal and Mechanical Response of Industrial Porous Ceramics," *Materials Science Forum*, 2010, 652:191-96.

TASK 3

Objectives

- We will conduct a high-level discussion on the durability of the heater alloy with experts in the Materials Science and Technology Division.

Approach

- Discuss heater element property requirements with ORNL corrosion scientists and metallurgists.

Accomplishments

- A meeting with GM's supplier, Iljin, was conducted.

Future Direction

- Have follow on meetings as required by GM to down select alloy compositions.

Project 18865 – Application Specific Materials Simulation, Characterization and Synthesis

Agreement 9105 - Ultra-High Resolution Electron Microscopy for Characterization of Catalyst Microstructures and Reaction Mechanisms

L. F. Allard, C. K. Narula, F. H. Ribeiro, * S. A. Bradley, ** J-H. Kwak, *** C.H.F. Peden, *** and A.K. Datye****

Oak Ridge National Laboratory

P.O. Box 2008, MS-6064

Oak Ridge, TN 37831

* Purdue University, West Lafayette, IN

** UOP Co., Des Plaines, IL

*** PNNL, Richland, WA

**** Univ. of New Mexico, Albuquerque, NM

DOE Technology Development Area Specialist Manager: Jerry L. Gibbs

(202) 586-1182; fax: (202) 586-1600; e-mail: jerry.gibbs@ee.doe.gov

ORNL Technical Advisor: David P. Stinton

(865) 576-4556; fax: (865) 241-1034; e-mail: stintondp@ornl.gov

Contractor: Oak Ridge National Laboratory, Oak Ridge, Tennessee

Contract No.: DE-AC05-00OR22725

Objectives

- Develop and utilize new *in situ* techniques for ultra-high resolution imaging of catalytic materials in gaseous environments to study reduction of NO_x emissions in diesel and automotive exhaust systems.

Approach

- Partner with Protochips Co. to develop “Gen 3” environmental cell holder for *in situ* gas reactions.
- Demonstrate utility of Gen 3 E-cell holder for atomic imaging of catalysts at elevated temperatures and gas pressures up to a full atmosphere.
- Perform initial studies of behavior of “intelligent” catalysts comprising Pt and Rh species on perovskites, in partnership with Ford Research Laboratory and the University of Michigan.

Accomplishments

- A “Gen 3” E-cell was designed, fabricated and tested; it showed the remarkable capability to image Au, Pt and Rh nanoparticles at atomic resolution up to a full atmosphere of e.g. dry air.
- The efficacy of the E-cell with Protochips Aduro heater devices also was shown to permit precise control of very short time heating experiments (e.g. 1 minute) that are needed for our studies of the oxidation-reduction behavior of “intelligent” catalysts for NO_x reduction improvements.
- We also collaborated on work proving *for the first time* the ability to do catalysis with single atom species on a “real” catalyst supports. Our results were published in *Nature Chemistry*, **V.3**, pp. 634-41, August 2011.

Future Directions

- Utilize the Gen 3 E-cell for further studies of perovskite-based NO_x reduction catalysts, including Pd in LaFeO₃ and Rh/Pt in CaTiO₃.
 - Develop and implement the capability for the Gen 3 E-cell to be run with a flowing gas. Incorporate experience with Gen 3 holder for design of improved, “Gen 4” holder.
-

Introduction

Work this year has progressed on several fronts, including new developments in our *in situ* microscopy thrust area, and in catalysis research with several groups that we are calling "single-atom catalysis." The latter work is leading to the new understanding of the potential for stable, working catalytic systems to be formulated that involve catalytic species such as Pt and Pd to be dispersed at the atomic level on oxide supports, and that give reaction results equivalent or superior to more conventional catalysts. The importance of this development is that it leads to the possibility of dramatically reducing the amount of precious metal species needed for a 'real' catalyst, with a concomitant reduction in cost. We have also made progress in studies of Pt and Au catalyst systems on model alumina, titania and silica supports, in which we have identified the active sites on the surfaces of nanoparticles of these species in the 2-20nm range, for WGS catalysis. These results were obtained by combining sub-Ångström imaging in the ACEM with spectroscopic methods to elucidate the nature of the active sites. Some of our results in these areas are highlighted in the following section.

In Situ Microscopy Development:

Our *in situ* microscopy development activities continued this year, with a number of studies that employed our standard heating holder employing Protochips Co. Aduro™ heating devices. With this holder, we routinely characterize changes in catalysts with heating in the vacuum of the electron microscope. We have also demonstrated the ability to conduct heating experiments in a reducing atmosphere (generally 4% H₂ in Ar) with the heating holder retracted into the specimen airlock, and the reducing gas admitted instead of the usual N₂ atmosphere. This allows samples to be reacted under atmospheric pressure conditions. In order to allow both reduction and oxidation treatments with carefully controlled pressures and (ultimately) gas flow rates, we have devised environmental cell holders that constrain the reaction gas between a heater membrane and a

plain SiN "window" device. The early E-cell Gen 1 and Gen 2 designs used Aduro devices with continuous carbon films deposited over holes in the heater membrane, in order to seal the cell, but the carbon film cannot withstand heating in an oxidizing atmosphere. We learned to fabricate continuous amorphous SiN films over the heater membrane, to replace the carbon films on the heater devices. We have demonstrated that the SiN would not only easily withstand oxidizing environments up to 800°C and atmospheric pressure, but also would allow imaging of crystal lattices through the SiN layer (typically ~25nm thick) at reasonable *in situ* reaction pressures up to 20Torr (as tested so far). We reported in the last quarterly that the initial SiN films showed an artifact structure due (it was determined) to a vacuum/furnace system fault during the deposition process, which has been resolved in later depositions. **Figure 1** shows a high-angle annular dark-field and bright-field image pair, recorded on the aberration-corrected JEOL 2200FS ACEM, of a CuAu/TiO_x bimetallic catalyst material on the 'defected' SiN film, after a 10min heating in air at 600°C. The SiN film showed no visible effect of this aggressive oxidation treatment; a standard heater membrane with a carbon film supporting the catalyst would show the carbon film totally destroyed by this treatment. **Figure 2** is a high-resolution HAADF image of a CuAu nanoparticle (area outlined in **Fig. 1**) showing atomic resolution and a surface layer determined to be copper oxide, imaged through the ~25nm amorphous SiN film. The ability to fabricate heater devices with SiN films also has made possible an improved design of E-Cell holder, called Gen 3, which will eliminate some operational issues that were identified during experiments with the Gen 2 holder, and simplify (i.e. make more reliable) the process of sample loading. Tests of the Gen 3 holder will begin in Q2, FY 2011. **Figure 3** shows a CAD drawing of the Gen 3 device, positioned inside the objective lens pole piece of the ACEM (shown in green); details of the design will be further revealed in a later report.

We also completed the design, fabrication and testing of a new *in situ* heating holder for the ACEM that permits a second (orthogonal) tilt axis within the specimen goniometer stage, to allow precise orientations of single-crystal catalyst supports to be achieved. This new capability was desired because of the importance of crystal tilt to imaging of crystal lattices in the HAADF mode, which is much more sensitive to sample alignment than conventional bright-field (BF) imaging. A double-tilting capability will significantly facilitate imaging experiments by allowing the catalyst support to be more readily positioned so the relationship between catalyst nanoparticles and support structure can be analyzed. **Figure 4** shows the new holder and a schematic of the mechanics of control of the second tilt axis. **Figure 5** shows the effects of tilting of a ZnO nanoribbon model support material from a 2° misalignment (**Fig. 5a**) where atomic columns are not clearly distinguished at 15Mx original magnification, to perfect alignment (**Fig. 5b**) in which the atomic columns are fully resolved. **Figure 6** shows the epitaxial orientation of a PdZn bimetallic catalyst nanoparticle on a similarly oriented ZnO support. With the new holder, results such as these can be routinely obtained; it is particularly useful during heating cycles, as the support often shows a tendency to slightly shift position as a result of the high temperature treatment, and the holder allows these motions to be effectively tracked. **Single-atom Catalysis:** In conventional catalytic materials for applications such as emission control, CO oxidation, the PROX reaction (preferential oxidation of CO in H₂), the water-gas shift reaction (removal of CO in H₂ for purification of hydrogen), and even in catalysts for use in NO_x trap materials such as Pt on γ -alumina, the precious metal species are often present in nanoparticle form of sizes in the 1-10nm range. Since catalytic reactions typically only involve surface atoms that are exposed to the reactant species, the atoms in the bulk are not effective for catalysis. It is a grand challenge of catalytic science to develop stable catalysts with high

reactivity that reduce the use of expensive, increasingly rare precious metal species. The ultimate catalyst would involve dispersions of the catalytic species at the atomic level, with catalytic reactions occurring at the single-atom level.

We are working with several groups whose studies of precious metal/oxide catalysts have, with the use of various spectroscopy methods correlated to the direct imaging results using our aberration-corrected JEOL 2200FS ACEM, given early evidence for the ability to formulate stable catalysts with single atoms as the principal catalytic species. For example, fundamental work is ongoing with Dr. S. A. Bradley of UOP Co. (Des Plaines, IL), in which model Pt/alumina catalysts with very low percentage loadings have been shown to maintain stable dispersions as single-atoms or as dimers and trimers during temperature programmed reduction (TPR) experiments. This work, reported in a prior quarterly, utilized our *in situ* heating and airlock reduction capabilities on the ACEM. Recent work with Prof. J. Liu of the University of Missouri-St. Louis and colleagues at the Chinese Academy of Sciences (Dalian) has shown what we believe is the first practical fabrication of a single-Pt-atom catalyst consisting of only isolated single atoms anchored onto iron oxide (FeO_x) nanocrystallites. This unprecedented single-Pt-atom catalyst exhibits very high activity and stability for both CO oxidation and PROX of CO in H₂, attributed to the partially vacant 5d-orbitals of positively charged, high-valent Pt atoms. Concurrent work with Prof. A. Datye of the University of New Mexico and colleagues at e.g. PNNL (Dr. Y. Wang) on characterization by ACEM HAADF imaging of Pd dispersed on ZnO powders showed that Pd/ZnO catalysts reduced at 500°C exhibited an abundance of bright features whose contrast was consistent with dispersed single atom species of Pd. We have explored the conditions that favor the formation and stabilization of these single atom species on the non-polar ZnO (10-10) surface, which is the dominant facet exposed in ZnO powders. The reactivity of these Pd species

for CO oxidation and for the MSR reaction has also been investigated. Brief examples of the microscopy results from the latter two studies highlighted here.

Single-Atom Pt/FeO_x catalysis: This work has resulted in a manuscript presently under review for publication in Nature Chemistry (see Publications section). The single-atom Pt₁/FeO_x catalyst (Sample A) was prepared by a co-precipitation method as previously reported for supported Au and Pd catalysts [1,2] but with a finely tuned co-precipitation temperature and pH value. Specifically, in order to anchor Pt atoms on the defects of FeO_x surface and to sufficiently isolate the Pt atoms, the Pt loading was controlled to a very low level of 0.17 wt % and a high-surface-area (about 290 m²/g for the as-synthesized samples) FeO_x nanocrystallite support was used. To evaluate the effect of Pt loading on the structure and performance of the final catalysts, a similar catalyst with a Pt loading of 2.5 wt % (Sample B) was also prepared, characterized, and tested. Sub-Ångström-resolution ACEM HAADF imaging was used to characterize the dispersion and configuration of the Pt clusters in the catalysts. **Figure 7a** clearly shows individual Pt atoms (marked by the white circles), uniformly dispersed over the surfaces of FeO_x nanocrystals in sample A. Examination of different regions revealed that only single Pt atoms were present in sample A. The atomic resolution HAADF image in **Fig. 7b** reveals that individual Pt atoms (indicated by the white circles) occupy exactly the positions of the Fe atoms. As plan-view HAADF images represent the projection of atoms along the incident beam direction, surface atoms cannot be distinguished from the sub-surface atoms in the HAADF images. However, we determined that the Pt atoms were inside the FeO_x nanocrystallites by changing the focus of the electron beam (or “depth sectioning” [3]). By analyzing images obtained sequentially with varying beam focus settings we could conclude that the observed Pt atoms are not located inside the individual FeO_x nanocrystals. In addition, by examining many HAADF images of

Sample A, we estimated that the density of Pt single atoms was about 0.07 Pt atoms/nm², which is very close to the actual Pt loading (about 0.09 Pt atoms/nm²) of Sample A. Therefore, all the observed individual Pt atoms were determined to be located either on top of the surfaces or in the near-sub-surfaces of the FeO_x nanocrystallites. These results were correlated to ACEM imaging of Sample B (not shown here) and with methods such as extended x-ray absorption fine structure (EXAFS) and extended x-ray absorption near-edge structure (EXANES), as well as with probe reactions such as CO oxidation and PROX. EXAFS and EXANES studies were consistent with single-atom dispersions in Sample A, and the presence of larger clusters in Sample B (confirmed by ACEM imaging). In summary, we have synthesized and characterized a novel catalyst consisting of only single Pt atoms uniformly dispersed on high-surface-area FeO_x support. This catalyst shows extremely high activity for both CO oxidation and PROX reactions. The chemical reactivity of our high-valent single Pt atoms is quite different from that of single Au atoms or cations on the same support; the Au/FeO_x catalyst contains polydispersed nano-structures from single atoms to clusters, with single Au atoms inactive for CO oxidation [see e.g. ref. 3]. The more vacant d-orbitals of our single Pt atoms due to the charge transfer from Pt atoms to the FeO_x surface are responsible both for the strong binding and stabilization of single Pt atoms and for providing high-valent Pt atoms, which ultimately account for the excellent catalytic activity of the Pt₁/FeO_x catalyst.

Single-Atom Pd/ZnO Catalysis: This work will be presented at the 22nd Annual Meeting of the North American Catalysis Society in Detroit (June 2011); a full manuscript is under preparation.

The energetics of Pd single atoms on clean and defective ZnO(10-10) surfaces were explored using density-functional-theory (DFT) computations [4]. The surface was modeled as a periodic slab that consisted of eight ZnO layers

(**Fig. 8a**), where the bottom three layers were fixed at the DFT-predicted bulk equilibrium positions of ZnO. Periodic images of the slab were separated by a 14Å- thick vacuum region. Dangling bonds at the bottom of the slab were saturated with hydrogen-like atoms in order to mimic the ionic bonding in bulk ZnO. All computations were performed with the Vienna *ab-initio* software package (VASP) [5]. The results of the computations showed that Pd interacts strongly with the ZnO(10-10) surface. Pd bulk interstitials were found to be energetically stable but their stability is significantly lower than Pd binding on the surface. Direct exchange of Pd \leftrightarrow Zn in the surface was found to be unstable. Thus, the computations suggested that the most likely Pd binding sites for clean ZnO(10-10) are on the surface. However, the DFT calculations predict an alternative interaction pathway of Pd with the ZnO(10-10) surface: the formation of ZnO surface vacancies. These defects are predicted to be energetically competitive especially in the presence of H₂. The interactions of Pd with these defects are comparatively strong, the Pd binding energies are predicted to be ~60% higher than those on the surface. The occurrence of these thermally activated defects and their strong stabilizing effect on Pd single atoms is corroborated by our observations that ZnO reconstructs at temperatures above 450°C while these processes are suppressed at lower temperatures. Furthermore HAADF STEM image observations (**Fig. 8b**) show the appearance of isolated Pd atoms in the same temperatures range where the surfaces reconstruct. We conclude that, at least in the case of the ZnO (10-10) surface, elevated temperatures promote ZnO vacancy formation, and these vacancy sites serve as additional strong binding sites for anchoring Pd atoms.

Determination of Active Sites on Catalytic Nanoparticles: Work in collaboration with the Purdue University group of Prof. F. H. Ribeiro has involved high-resolution imaging coupled with FTIR and DRIFT spectroscopies to elucidate the

active sites on Au and Pt nanoparticles on oxide supports such as alumina, titania and silica. Au nanoparticles in the 1-7nm size range were shown to be cubo-octahedral in shape, and the dominant active site was shown to be the low coordinated corner Au atoms, which are ~7 and ~3 times more active than the perimeter Au atoms for Au/TiO₂ and Au/Al₂O₃ catalysts respectively. Details of this work will be reported in the next quarterly.

Concluding Remarks

Our research activities on the forefront studies of the behavior of catalyst clusters and nanoparticles with reaction treatments, imaged at ultra-high resolution with the aberration-corrected electron microscope, are building a foundation towards a better understanding of the phenomena, which control performance in real systems. The implementation of novel methods for conducting these studies on specimens heated inside the electron microscope is the primary thrust of our research. Significant progress has been made in further development of an integrated heating technology for high-resolution electron microscopy, and we are extending these heating capabilities to an environmental cell functionality for studying gas reactions on catalytic materials. We have also introduced a new heating holder with a double-tilt capability, to permit precision alignments of the support crystal that will allow us to elucidate crystallographic relationships between the support structure and catalytic nanoparticles. Our work is in support of a variety of catalyst materials studies supported by DOE and the HTML national user program.

References:

1. Qiao, B. & Deng, Y.; "Highly effective ferric hydroxide supported gold catalyst for selective oxidation of CO in the presence of H₂." *Chem. Commun.*, 2192-2193 (2003).
2. Qiao, B., Liu, L., Zhang, J. & Deng, Y. "Preparation of highly effective ferric hydroxide supported noble metal catalysts for CO oxidations:

From gold to palladium." *J. Catal.* **261**, 241-244 (2009).

3. L. F. Allard, A. Borisevich, W. Deng, R. Si, M. Flytzani-Stephanopoulos and S. H. Overbury, "Evolution of gold structure during thermal treatment of Au/FeO_x catalysts revealed by aberration-corrected electron microscopy." *J Electron Microscop* (Tokyo) **58**, 199-212 (2009).

4. G. Kresse and D. Joubert, "From ultrasoft pseudopotentials to the projector augmented-wave method." *Physical Review B* 1999, **59** (3), 1758-1775.

5. G. Kresse and J. Furthmuller, "Efficient iterative schemes for *ab initio* total-energy calculations using a plane-wave basis set." *Physical Review B* 1996, **54** (16), 11169-11186.

Publications and Presentations:

"**Unique Role of Anchoring Penta-Coordinated Al³⁺ Sites in the Sintering of g-Al₂O₃-Supported Pt Catalysts;**" D. Mei, J. H. Kwak, J. Hu, S. J. Cho, J. Szanyi, **L. F. Allard**, and C. H. F. Peden, *J. Phys. Chem. Lett.*, 2010, **1** (18), pp 2688–2691 (August 31, 2010) (Letter) DOI: 10.1021/jz101073p.

"**Metallic Corner Atoms in Gold Clusters Supported on Rutile are the Dominant Active Site during Water-Gas Shift Catalysis;**" W. D. Williams, M. Shekhar, W.-S. Lee, V. Kispersky, W. N. Delgass, F. H. Ribeiro, S. M. Kim, E. A. Stach, J. T. Miller, and **L. F. Allard**, *J. Amer. Chem. Soc.* (in press 2010).

"**Synergy of Combined SEM and TEM Imaging Techniques for the Characterization of Catalyst Behavior During *In Situ* Heating;**" J. Y. Howe, **L. F. Allard**, W. C. Bigelow, H. Demers and S. H. Overbury, manuscript submitted to *J. Elect. Microscop.* (2010).

"**Single-atom catalysis: Remarkable performance of Pt₁/FeO_x for CO oxidation and preferential oxidation of CO in H₂;**" B. Qiao, A. Wang, X. Yang, **L. F. Allard**, Z. Jiang, Y. Cui, J.

Liu, J. Li and T. Zhang, manuscript in review for *Nature Chemistry* (2010).

"**Coalescence and sintering of Pt nanoparticles: *in situ* observation by aberration-corrected HAADF STEM;**" M. A. Asoro, D. Kovar, Y. Shao-Horn, **L. F. Allard** and P. J. Ferreira, *Nanotechnology* **21** (2010) 025701 (6pp).

"**Characterization of Alumina Supported Pt and Pt-Pd Alloy NO Oxidation Catalysts with Advanced Electron Microscopy;**" O. K. Ezekoye, A.R. Drews, H. W. Jen, R.J. Kudla, R.W. McCabe, J.Y. Howe, **L.F. Allard**, G.W. Graham and X.Q. Pan, manuscript submitted to *Applied Catalysis* (2010).

"**Behavior of Au Species in Au/Fe₂O₃ Catalysts Characterized by Novel *In Situ* Heating Techniques and Aberration-Corrected STEM Imaging;**" **L. F. Allard**, Maria Flytzani-Stephanopoulos and Steven H. Overbury, *Microsc. Microanal.* **16**, 375–385 (August 2010).

"**Surface Channeling in Aberration-Corrected Scanning Transmission Electron Microscopy of Nanostructures;**" J. Liu and **L. F. Allard**, *Microscopy and Microanalysis*, Volume 16, Issue 04, pp 425-433 (August 2010).

"**New Insights into the Growth Mechanism and Surface Structure of Palladium Nanocrystals;**" B. Lim, H. Kobayashi, P. H. C. Camargo, **L. F. Allard**, J. Liu and Y. Xia, *Nano Res* **3**: pp 180–188 (2010).

"**Zero oxidation state platinum atom supported on θ -alumina;**" C. K. Narula, X.-Q. Chen, G. M. Stocks, M. Moses-DeBusk and **L. F. Allard**, in review, *J. Amer. Chem. Soc.* (2010).

"**Applications of High-Resolution Aberration-Corrected STEM Imaging to Studies of the Behavior of Catalytic Materials at Elevated Temperatures;**" **L. F. Allard** and K. L. More, ASM Educational Symposium, Oak Ridge, TN (April 2010). **Invited Talk**

"***In Situ* Environmental Electron Microscopy, Then and Now;**" **L. F. Allard** and W. C. Bigelow; EMAL 40th Anniversary Symposium,

Dept. of Materials Science & Engineering,
University of Michigan, October 2009. **Invited
Talk**

**"Development of a Novel Environmental Cell
for *In Situ* Gas Reaction Experiments via
Aberration-Corrected STEM Imaging;"** L. F.
Allard, W. C. Bigelow, S. H. Overbury, D. P.
Nackashi and J. Damiano, Microscopy Society of
America, 2010. **Invited Talk**

**"Ultra-high- Resolution STEM and NMR
Studies of Poorly Crystalline γ -Al₂O₃ Surfaces:
New Insights From Imaging and
Spectroscopy,"** J. H. Kwak, J. Z. Hu, D. Mei, D.
H. Kim, J. Szanyi, L. F. Allard and C. H. F.
Peden, *Microscopy & Microanalysis* 16 (Suppl.2):
310-311, Cambridge University Press (2010).

Invited Talk

**"Morphological and Electronic Structure of Pt-
Re Nanoparticles Supported on Carbon under
Activation and Reaction Conditions for
Aqueous-Phase Reforming of Bioliquid,"** L.
Zhang, G. Xia, Y. Yang, D. Heldebrant, D. King,
Y. Wang and L. F. Allard, *Microscopy &
Microanalysis* 16 (Suppl. 2): 1428-1429,
Cambridge University Press (2010).

**"Synergy of Combined (S)TEM Imaging
Techniques for the Characterization of Catalyst
Behavior During *In Situ* Heating;"** J. Y. Howe,
L. F. Allard, W.C. Bigelow and S. H. Overbury,
Microscopy & Microanalysis 16 (Suppl. 2) : 312-
313, Cambridge University Press (2010).

**"Synthesis and Characterization of ZnO-
Supported Noble Metal Nanocatalysts for
Energy Applications;"** J. Liu and L.F. Allard,
Materials Research Society Annual Meeting,
Boston (Dec. 2009).

**"Strong Interaction of Au with FeOx Surfaces
Evidenced in the Water-Gas Shift Reaction,
and Probed by Aberration-Corrected Electron
Microscopy and Scanning Tunneling
Microscopy;"** R. Si, L. F. Allard, A. Borisevich,
W. Deng, K. T. Rim, Y. Zhai, B. Ricks, A.
Frenkel, G. Flynn, M. Flytzani-Stephanopoulos
and S. H. Overbury, AIChE Annual Meeting,
Nashville (Nov. 2009).

Communications and Visits

University of Michigan, Meeting with Prof. X.
Pan, G. Graham, A. Drews and M. Katz;
Discussion of new project to study "intelleging
catalysts" for NOx reduction applications, (Oct.
2009).

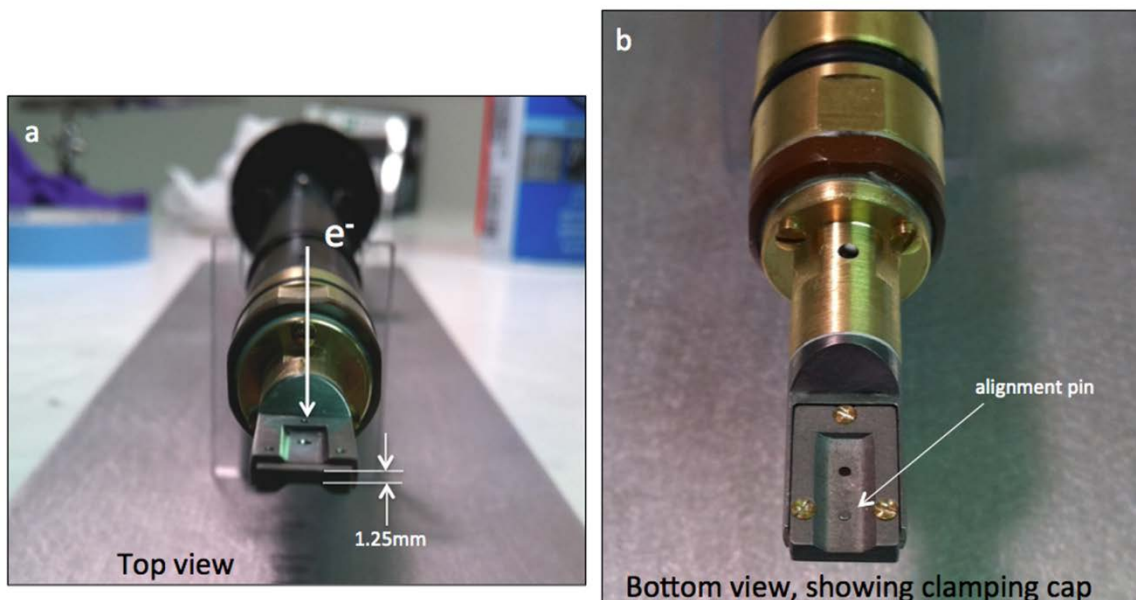


Fig. 1. a) Oblique view of the top surface of the tip of the Gen 3 E-cell holder. The thin section at 1.25mm fits into the 2mm pole piece gap of the JEOL 2200FS ACEM; b) view of the bottom of the E-cell, showing the clamping plate and locating pin that assure precise alignment of E-cell components.

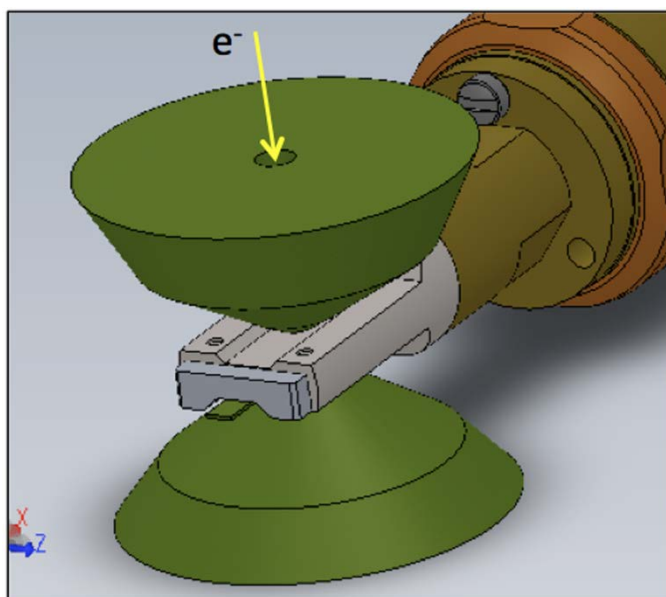


Fig. 2. CAD drawing showing how the Gen 3 E-cell holder fits into the ACEM. No other closed cell holder has been reported in the literature that is adaptable to use in the JEOL instrument, which has the narrowest gap of any commercial electron microscope.

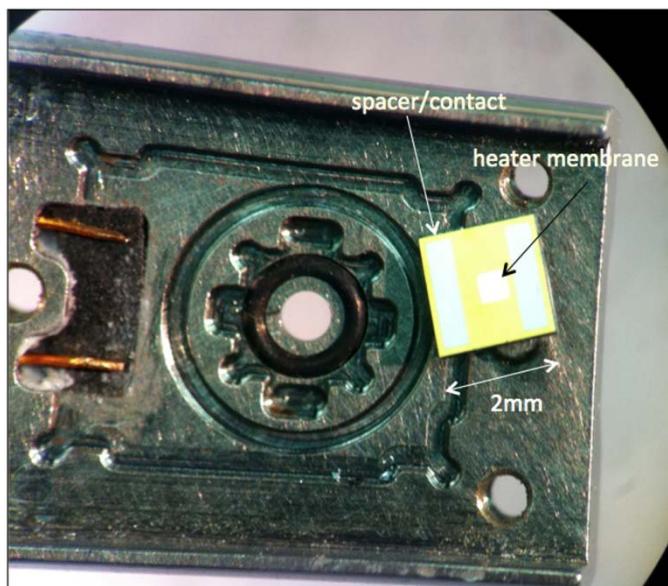


Fig. 3. Close-up view of the inside of the Gen 3 E-cell tip. A 2-mm square Aduro heater device fits into a well and seals against the small O-ring. Gold contacts act as spacers and also electrodes to allow heating of the thin ceramic membrane (arrowed). The gap set by the spacer electrode pads is typically 5 microns. A groove for a larger O-ring is seen also, and the bottom window chip seals against this O-ring to form the vacuum-tight cell. No gluing is necessary in this design.

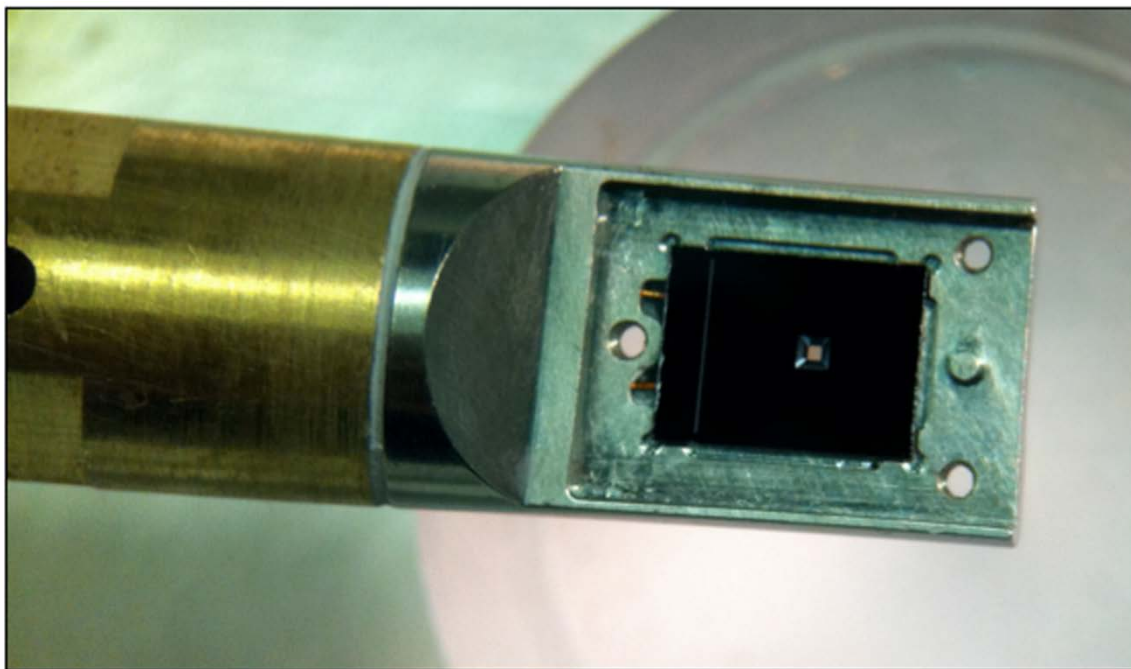


Fig. 4. View of the inside of the tip with the bottom window chip in place. The heaters and window chips are precisely diced during manufacturer, to fit closely into the wells machined in the tip that allow accurate alignment of the heater membrane and bottom window.

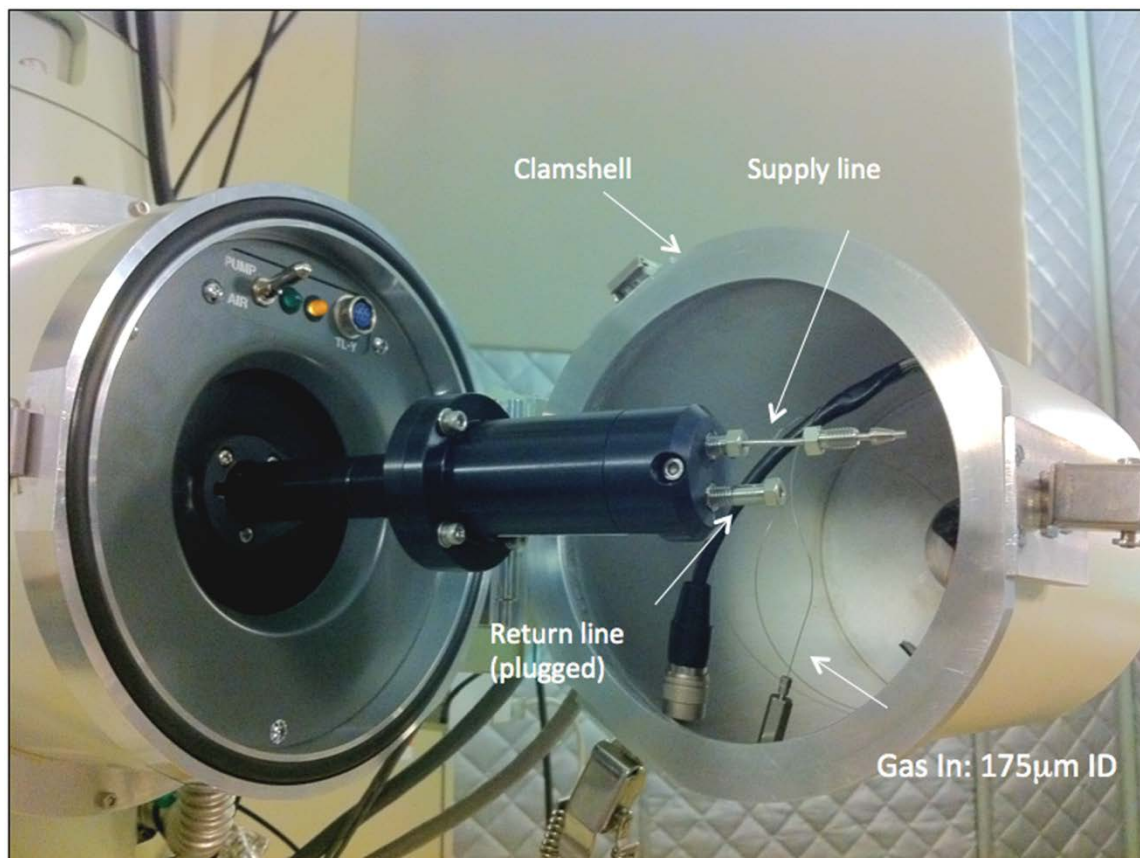


Fig. 5. Handle of the E-cell holder showing the supply and return gas line compression fittings. The return line has a plug in place in this view. The supply line inside the “clamshell” assembly is a stainless steel capillary with an ID of 175 μ m. Gas lines and the electrical feed both transition through the back end of the clamshell via a removable flange. This allows the clamshell to seal over the E-cell holder during use.

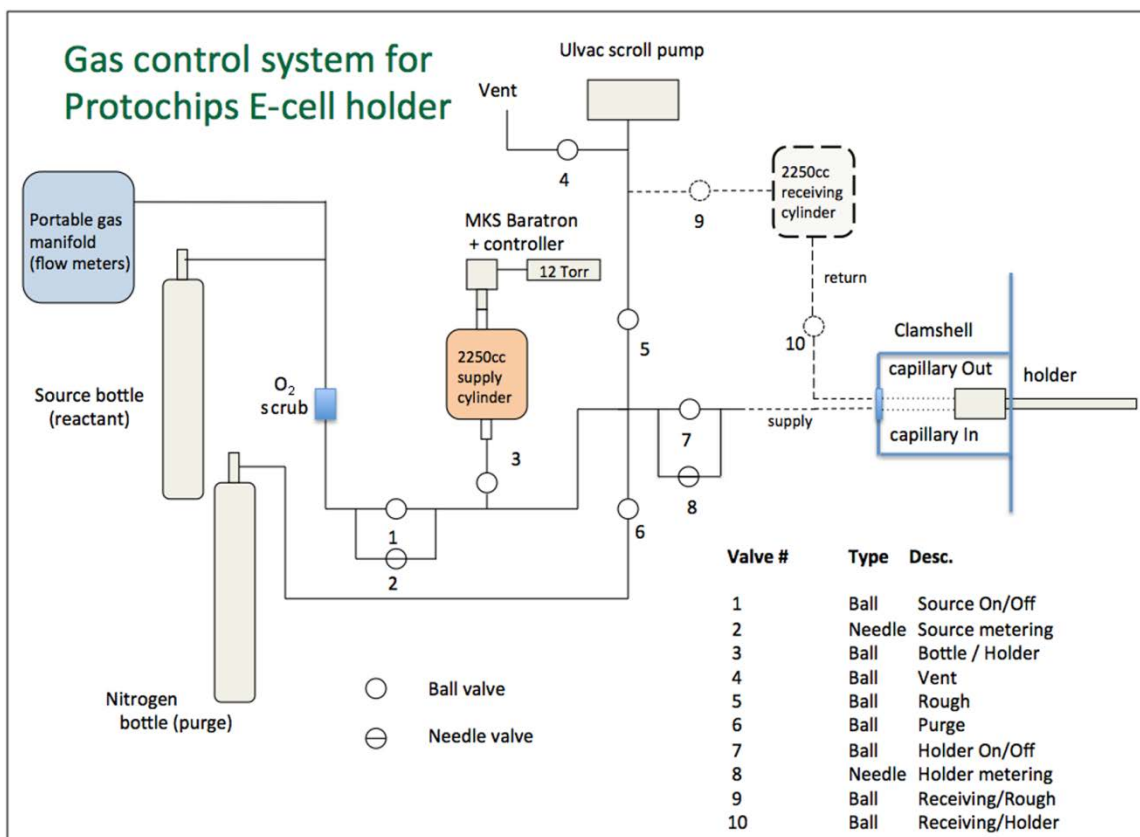


Fig. 6. Schematic of the gas-handling facility for the Gen 3 E-cell. The present system is used for “static cell” work, but shown dotted is a second reservoir tank that can be evacuated properly to allow flow through a return line capillary. An oxygen scrubber on the supply from either a specific single gas tank, or the portable gas manifold that utilizes mass flow controllers to set gas composition, assures low O₂ partial pressure that allows reliable reduction experiments.

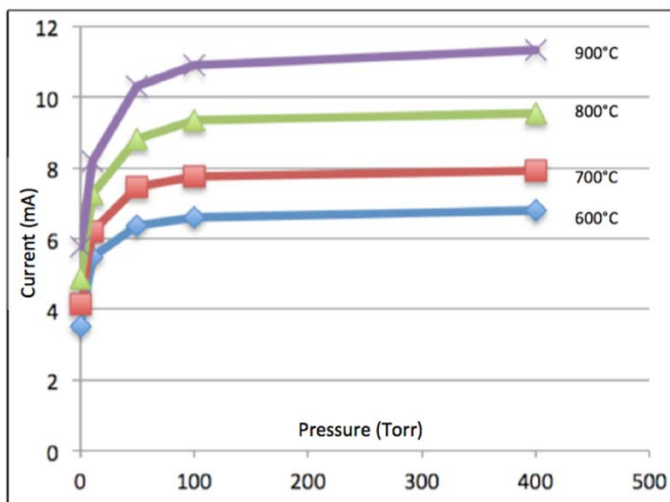


Fig. 7. Typical plot showing an example of the behavior of the Aduro devices as pressure in the cell increases. With a small increase in pressure, the current needed to heat to a given temperature shows a significant increase, such that at 100 Torr almost double the current is needed, nearly the same as would be required for atmospheric pressure experiments. See text for further details.

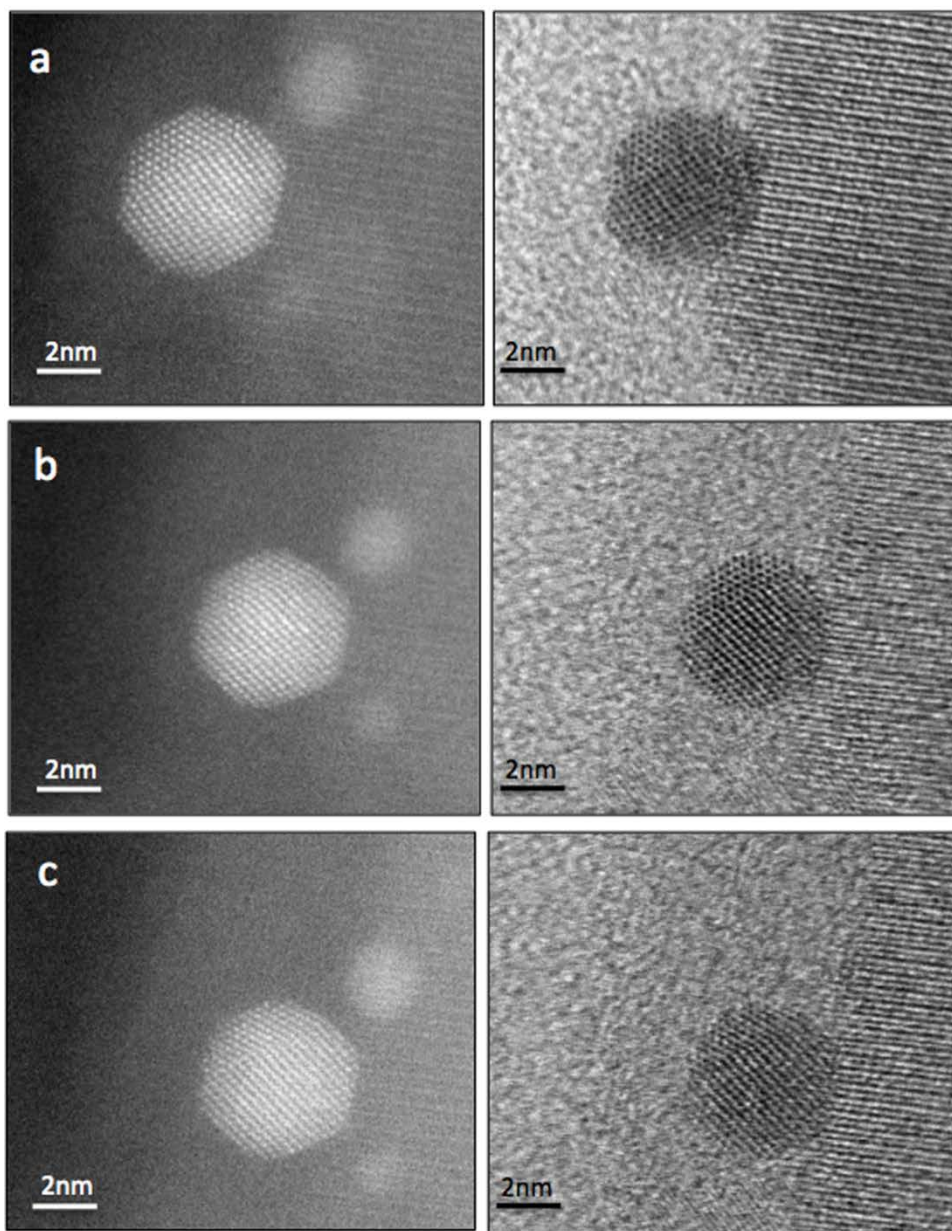


Fig. 8. A series of HAADF-BF image pairs recorded with a Rh-CTO specimen held at a nominal 350°C. Pair (a) shows a Rh nanoparticle with excellent alignments and well-resolved atomic columns imaged with the cell pressure at 0.05 Torr of H₂/Ar. Pair (b) shows essentially the same resolution but with the pressure increased 1000 times to 50 Torr, and pair (c) shows again atomic column resolution but with the pressure increased to a full atmosphere of dry air.

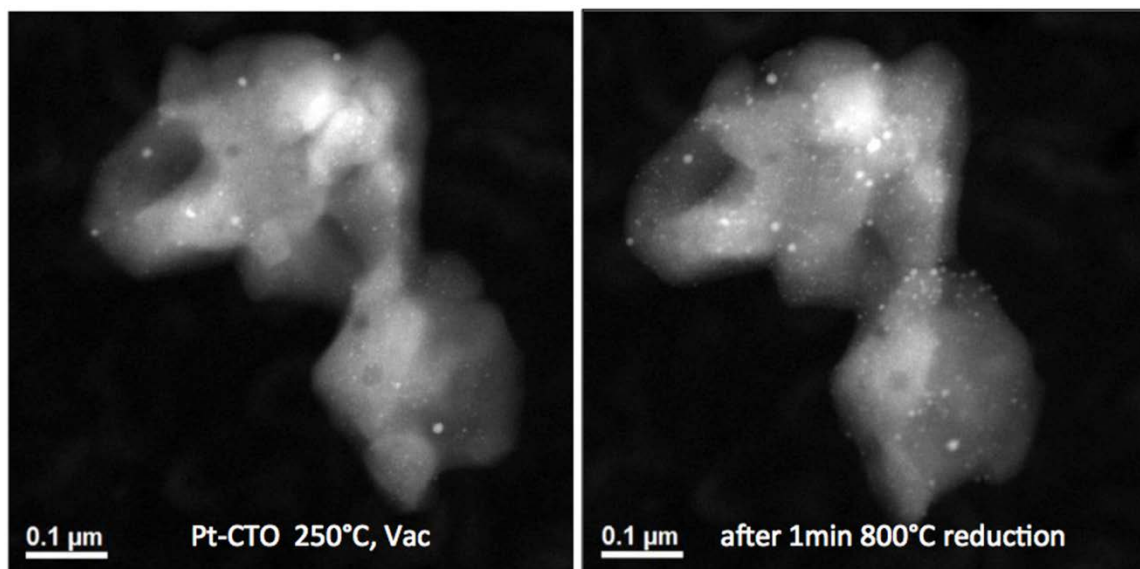


Fig. 9. A “before-after” HAADF image pair showing Pt nanoparticles in (or on) an aggregate of CaTiO₃ (a) and the appearance of many nanoparticles especially on the surface of the aggregate, after a reduction treatment for 1 min in 50 Torr of H₂/Ar at a nominal 800°C (b).

Agreement 13721 – Low-friction Hard Coatings

Principal Investigators: A. Erdemir and O. L. Eryilmaz

Argonne National Laboratory

9700 S. Cass Avenue, Argonne, IL 60439-4838

(630) 252-6571; fax: (630) 252-5568; e-mail: Erdemir@anl.gov; Eryilmaz@anl.gov

DOE Technology Manager: Jerry L. Gibbs

(202) 586-1182; fax: (202) 586-1600; e-mail: jerry.gibbs@ee.doe.gov

Contractor: UChicago Argonne LLC

Contract No.: DE AC03 06CH11357

Objective

- Design, develop, and implement super-hard and low-friction coatings to increase the durability, fuel economy, and environmental compatibility of future engine systems.
- Characterize and verify coating performance through bench-top, fired-engine, and field studies.
- Reduce emissions through reduction of fuel consumption as well as sulfur and phosphorous from engine oils.
- Demonstrate large-scale production of optimized coatings in a commercial-scale deposition system and transfer optimized technology to industry.

Approach

- Optimize coating microstructure, chemistry, thickness and surface finish that were proven to be very important for mechanical and tribological properties of superhard and low-friction coatings.
- Develop reliable deposition protocols for large-scale manufacturing of MoN-Cu coatings.
 - Confirm superior bonding and surface smoothness.
 - Confirm super-hardness and low friction.
 - Confirm extreme resistance to wear and scuffing under prototypical conditions.
- Demonstrate large-scale production with good reproducibility and cost-competitiveness, and verify durability and performance in actual engine applications.
- Passenger car engine tappets, fuel delivery systems, and transaxles are selected as a target applications for our coatings in FY2011.

Accomplishments

- Optimized coating-substrate bonding for extreme engine operating conditions (strong bonding was a must for differential, camshaft, and tappet applications where contact stresses were very high).

- Validated large-scale manufacturability of optimized coatings in commercial-scale deposition systems.
 - Demonstrated batch-to-batch repeatability of coating quality and performance. Develop faster and more efficient ways to clean, load, unload, and inspect coated engine parts.
 - Developed more effective quality control procedures and deposition protocols for large-scale manufacturing.
 - Explored the possibility of manufacturing superhard coatings using high-power impulse magnetron sputtering (HIPIMS) technique and achieved much harder and more adherent coatings.
 - Made progress toward new coating procedures to eliminate the need for post-deposition polishing.
 - Coated several engine components (tappets, cam shafts, differential parts, rocker arms, piston rings, and piston pins) and delivered them to multiple OEMs and automotive companies for internal evaluation and engine testing.
 - Demonstrated excellent performance on coated engine parts.
 - Developed and implemented a special surface conditioning protocol to achieve extremely smooth surface finish with right kinds of chemistry providing very low friction and wear from the very beginning (no run-in).
 - Filed a new patent application on this surface conditioning method (ANL-IN-10-008) and was granted US patent (7,846,556) on modulated composite surfaces that combine low-friction and superhard coatings with different surface textures and modulations.
 - Made progress toward full-scale commercialization, licensing of technology is in the final stages.
-

Introduction

Higher energy efficiency, longer durability, and lower emissions are much desired attributes in future transportation systems; but, without further improvements in the surface mechanical and tribological properties of sliding, rolling, or rotating engine components, these goals will be difficult to realize. In particular, higher loads, speeds, temperatures, and other harsh operating conditions in future engines will render most traditional materials and lubricants ineffective. Accordingly, in this project, using an advanced physical vapor

deposition process, we developed a variety of novel nano-composite coatings that are not only super hard (up to 67 GPa) and hence wear resistant but also super low friction (less than 0.03) when tested under boundary lubricated sliding conditions. These nano-structured and composite coatings consist of a MoN hard phase and a Cu soft phase.

The hard and soft phases in these coatings provide a very dense, equiaxed structure which is responsible for extreme hardness, toughness, as well as excellent responsiveness to the additives

in lubricating oils. Specifically, they react with sulfur and phosphorous in lubricating oils during sliding and form highly protective and low-friction boundary films that prevent wear and scuffing. Some of the most effective coating compositions we have developed so far include 80-98% MoN or Mo₂N and 2-20% Cu or other soft metals (such as Zn, Ag, Sn, Sb, etc.) by weight. Systematic tribological studies of these coatings in EGR contaminated engine oils showed that they are also very effective in reducing friction and wear and preventing corrosion and abrasion in such oils. Overall, comprehensive friction, wear, and scuffing studies in our laboratory have indicated that these coatings could be extremely useful for a wide range of engine applications including those supported by the Vehicle Technologies Program of DOE. Specifically, they can reduce parasitic friction losses (hence increasing fuel economy) and wear (hence increasing component durability/reliability) in a variety of engine parts, including, piston pins and rings, camshafts, transmission and transaxle parts and tappets.

During FY 2011, we made more progress toward large-scale production, field testing, and licensing of our superhard and low-friction coating technology. Specifically, we worked very closely with Hauzer Technocoating (one of the largest company in the field of PVD coating) and Galleon International to produce these coatings on functional surfaces of numerous engine parts using production-scale deposition systems. We also worked closely with several engine companies and successfully deposited our superhard and slick coatings on their engine parts and components for performance and

durability tests in simulated and actual engines.

Experimental

During FY2011, we completed all of our deposition trials, bench-top tribological testing and surface analytical studies. Specifically, we perfected the procedures for deposition of high-quality superhard coatings and post-process surface conditioning using commercial-scale deposition systems and industrially relevant polishing procedures. Comparison of the mechanical and tribological properties of competing coatings (e.g., CrN and DLC) has also been finalized. Overall, much of the effort was directed toward component level and actual engine studies.

During our optimization studies in FY2011, a special emphasis was placed on development and implementation of an effective protocol for eliminating the surface roughness which was found to be detrimental to the friction and wear resistance of most coated engine parts. Working very closely with industrial partners, we developed and optimized a post-deposition surface conditioning and polishing method which in the end provided very consistent and smooth surface finish which in turn provided the level of improvements that we have been looking for in friction and wear performance. These novel procedures have been filed as a new invention and then as a patent.

Due to much reduced sulfur in fuels and higher compression and temperature regimes in diesel engines, and to adaptation of very low viscosity (like SAE 0W20) grade oils for higher fuel efficiency, engine companies have been

complaining about increased wear in piston rings/liners and fuel injector systems. During FY2011, we developed a special protocol for the deposition of our coatings on curved piston ring and fuel injector plunger surfaces. We also employed post-deposition polishing of their surfaces to achieve very smooth surface finishes. Specifically, we stacked them up in a special holder and coated only the rubbing surfaces with 3 to 5 micrometer thick superhard coatings. With a special polishing machine, these coated surfaces were polished effectively to remove any surface roughness. Several batches of coated rings were delivered to an industrial partner for their internal evaluation and engine testing. We also received some of them for our internal evaluation and quality control work. Our evaluations showed that during the post-deposition polishing process, most of the surface irregularities were effectively removed and the remaining coating was very dense, smooth and combined all the desirable qualities for good performance in actual tests. In a few in-house trials, these coatings showed excellent adhesion and high hardness values of more than 2400 Vickers.

Results

Those highly optimized superhard coatings for engine studies were applied on a wide range of components (i.e., piston rings, tappets, piston pins, camshafts, and differential parts) using a production-scale deposition unit at Hauzer Technocoating (our coating partner). Most of the coated parts passed the initial screening tests and all of them performed extremely well in the shorter duration motored/fired engine studies. A few of them are currently undergoing long-duration engine tests in our engine OEM

partners' laboratories. Initial findings suggested that these optimized coatings were extremely resistant to wear and scuffing and provided up to 90% reduction in friction (especially tappets).

A variety of tappets coated with superhard coating provided much better wear performance than DLC- and CrN-coated tappets in long-duration tests. Frictional behavior of superhard coating was impressive up to 80°C but slightly inferior to CrN coating at 120°C; CrN suffered significant wear, while superhard coated surface showed no evidence of wear.

When tested in a differential of a full-size pickup truck under severe condition, superhard coating worked better than any other coatings tested before. Without our coating, the parts in the differential broke, causing the discs to spin at very high and uncontrollable speeds. It would eventually scuff/weld to bottom piece (see picture on right) due to high heat in addition to high stress. The superhard coated part showed no evidence of wear and protected sliding surfaces against scuffing as shown in Figure 1.



Figure 1. Condition of uncoated (bottom) and superhard coated differential parts of a full-size pickup truck. Uncoated surface scuffed badly, while superhard coated part was still in pristine condition.

In another actual high-speed hot engine tests, superhard coating prevented wear of piston rings and liners, while severe wear observed after tests on uncoated or CrN-coated rings and liners. Friction reduction and fuel economy benefits of coated rings are currently being evaluated in long-duration fired engine tests. Based on such very impressive test results from actual engines, discussions to license the technology for large-scale applications have reached the point where an actual agreement can be finalized very shortly.

Our coating trials with a new HIPIMS source have also continued in FY2011 and very impressive improvements in coating microstructure, surface finish and adhesion were achieved. With further optimization, it looks that post-deposition polishing of coated parts may be eliminated with the use of HIPIMS. Due to very high ionization efficiency and intermixing, the bonding of deposited coatings to substrates were much higher. When tested in a Daimler Benz Rockwell adhesion test machine, these coatings would result in a #1 rating out of 7 (#1 representing the strongest bonding).

Licensing talks with outside collaborators are in the final stages and we expect this technology to be fully licensed by the end of 2011.

Conclusions

During FY2011, we have made great strides toward scaling up and commercializing our superhard and low-friction coating technology. Its effectiveness in reducing friction and wear and enhancing resistance to scuffing has been proven under actual engine operating conditions. Our coating partners have also adopted our

technology and successfully deposited the same quality coatings in their deposition systems as we have been doing at Argonne. New field tests by several engine company partners further confirmed the effectiveness and very impressive tribological properties of our coatings under harsh conditions. Technology transfer and licensing activities are in the final stages and we expect to see some industrial applications very shortly.

Patents and Publications

During FY2011, a new patent application has been filed, and we published and/or presented several new papers on the work that was performed under this project as listed below.

Patent Application

1. A. Erdemir, O. L. Eryilmaz, M. Urgan, and K. Kazmanli, "Method to Produce Catalytically Active Nanocomposite Coatings".

Presentations

1. Eryilmaz, O. L. Kim, J. H. Erdemir, A. Urgan, M., "Friction and wear behavior of MoN-Cu nanocomposite coatings under lubricated conditions", presented at the International Conference on Metallurgical Coatings and Thin Films (ICMCTF 2011); San Diego, CA; May 2 - 6, 2011.
2. Erdemir, A., "Advances in Surface Engineering for Demanding Tribological Applications", (Plenary Lecture), 1st International Surface Treatment Symposium, Istanbul Turkey, June 14-18, 2011.

Agreement 13723 - Residual Stresses in Thin Films

Principal Investigators: D. Singh and J. L. Routbort; coworkers: Kristen Pappacena, O. Ajayi, and O. Erilymaz

Argonne National Laboratory

9700 S. Cass Avenue, Argonne, IL 60439-4838

630-252-5009 dsingh@anl.gov

DOE Technology Manager: Jerry L. Gibbs

(202) 586-1182; fax: (202) 586-1600; e-mail: jerry.gibbs@ee.doe.gov

Contractor: UChicago Argonne LLC

Contract No.: DE AC03 06CH11357

Objective

- Measure residual stresses in thin films and coatings as a function of film thickness and relate stresses to film properties such as hardness, fracture toughness, and adhesion energy to relate to film processing variables and to predict durability
- Use techniques developed for measurements of residual stresses in thin films and coatings to measure residual stresses in layered structures produced by joining by high-temperature deformation and to improve their mechanical properties
- Relate residual stresses to interfacial adhesion and tribological properties

Approach

- Develop X-ray technique to measure change of lattice parameter of coating constituents as a function of depth and hence to calculate the lattice strains and stresses
- Develop indentation and/or scratch techniques to measure hardness, fracture toughness, and adhesion energy of films and coatings
- Relate stresses, properties, and processing conditions to film durability

Accomplishments

- Adhesion energies for MoN/Cu coatings with various processing conditions measured using a scratch technique
- Adhesion energies (and residual stresses) of the MoN/Cu coatings correlated to coating processing; coating adhesion energy dropped with increased copper content
- Wear performance of the various MoN/Cu coatings were evaluated. Direct correlation between wear and adhesion energy observed
- This project has resulted in 7 papers published in peer-reviewed journals
- Project terminates at end of FY11

Future Directions

- Project terminates at end of FY11
-

Introduction

Thin film coatings are useful for protecting materials from corrosion and abrasion in cutting tools, medical implants, micro-electromechanical devices, space-crafts, and engines. Particularly in vehicle system engines, hard thin film coatings can be used to reduce friction and wear, which can increase fuel efficiency. In other machine element components where sliding and rolling contacts are prevalent, these coatings can also protect the surfaces from various tribological damages because of their high wear resistance. The performance and durability of these coatings, particularly for engine and machine component related applications, is strongly dependent on their adhesion and tribological behaviors.

Ceramics, particularly nitrides and carbides, are popular materials for these tribological coatings due to their typically high hardness and modulus values, which are generally useful for high wear resistance. Often the coatings are deposited onto the substrate surface via a high temperature deposition process, which can result in thermal residual stresses upon cooling. Residual stresses can be intrinsic or extrinsic in nature [1]. Intrinsic residual stresses in the coating arise from the deposition process and depend on processing variables such as deposition temperature, gas pressure, deposition power, and bias conditions [2]. Extrinsic residual stresses, however, are generated from thermal expansion mismatch between the coating and the substrate. Residual stresses may also be present due to the intrinsic interfacial relationship between the coating and the substrate. The presence of such residual stresses can have a significant impact on the tribological properties of the system, including the adhesion of the coating to the substrate and the wear resistance.

Molybdenum nitride ceramic coatings in particular, with and without copper, have been investigated previously for such applications [3-11]. These coatings have been shown to have superior wear resistance

compared to TiN type coatings [10]. Copper has been used as an addition because it is expected to segregate to the grain boundaries, forming a nanoscale, compliant phase [5]. This helps to achieve a material with a high hardness to modulus ratio, reducing the mismatch and enhancing wear and abrasion resistance [12].

The work in FY11 focused on correlating the compositional processing variables to the measured residual stress values of two compositions of MoN/Cu coatings deposited on H-13 tool steel substrates. Subsequently, the resulting adhesion energy and wear resistance for each of the samples were evaluated. Correlations are made between the residual stresses generated as a result of processing and their effect on coating performance. It is important to monitor not only how these coatings withstand tribological situations, but also how the variations during processing affect the resulting properties.

Experimental Procedures

Coating Processing

Coatings of MoN with different Cu compositions were deposited onto steel substrates with physical vapor deposition (PVD) using magnetron sputtering (CemeCon CC800-9, Würeslen, Germany). The Mo coating deposition power was 8kW for each of the coatings. The two Cu deposition powers (and deposition times) were 0kW (7200s), and 0.8kW (7200s). These samples will be referred to as 0Cu and 8Cu, respectively. A scanning electron micrograph (SEM) of a MoN coating deposited on a steel substrate is shown in Figure 1. The surface roughnesses (R_a values) of the coatings are 18.4 ± 4.7 , and 16.4 ± 7.8 nm for 0Cu and 8Cu samples, respectively.

Mechanical Properties

Hardness and elastic modulus values were determined for both coatings using a nanoindenter (HysitronTI950, Minneapolis, MN). Tests were performed at loads of up to 10 mN to a displacement of up to 120 nm.

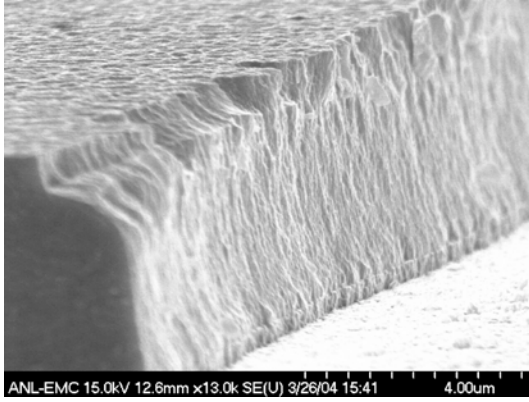


Figure 1. Scanning electron micrograph of MoN coating deposited on a steel substrate.

Coating thickness (t) was determined using a Calotest® (CSM Instruments, Needham, MA) for up to 600 seconds with an 18.8 mm diameter steel ball (d). An example Calotest® performed on the 0Cu sample is shown in Figure 2 with parameters x and y labeled. Image J software [13] was used to measure x and y , and the coating thickness was calculated using the simple geometrical equation, $t=xy/d$.

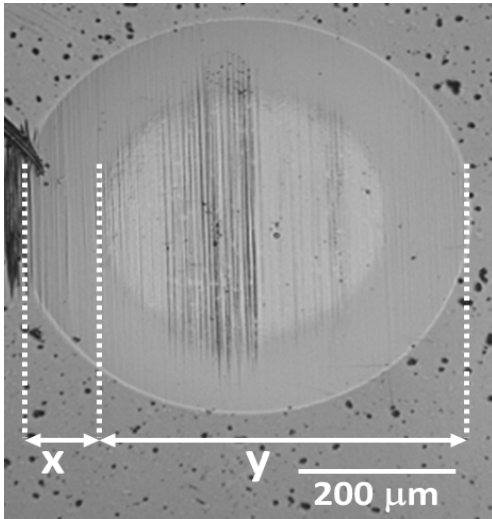


Figure 2. Typical calotest on 0Cu sample with x and y parameters indicated

Residual Stress Measurements

X-ray microdiffraction, in conjunction with an edge scan approach, was performed on beamlines 2-ID-D and 34-ID-E at the Advanced Photon Source (Argonne National Laboratory) to determine the residual

stresses. The x-ray beam was focused by Kirkpatrick-Baez mirrors to 0.2 (horizontal) \times 0.3 (vertical) μm^2 . A high-resolution charged coupled device (CCD) x-ray detector was used to collect x-ray diffraction (XRD) patterns from the x-ray micro-beam with energy of 10.0 keV (1.24125 Å). Strains and stresses were evaluated from the change in the lattice spacing determined from diffraction pattern of MoN (222) planes from coatings and its stress free state. The technique was described in detail in previous annual reports. In-plane strains were determined by placing the detector such that it was at an azimuth angle (Φ) of 0° or the out-of-plane strains were determined at $\Phi = 90^\circ$. The integrated 1D patterns are shown in Figure 3.

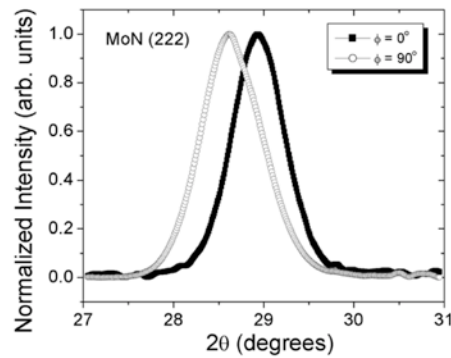


Figure 3. MoN (222) peak measured at the two azimuth angles (i.e., 0° and 90°), x-ray energy is 10.00 keV.

Adhesion Energy Measurement

Scratch testing was performed using a Quad Group Romulus Stylometer (Quad Group, Inc., Spokane, WA) with a 125 μm radius Rockwell C diamond stylus in order to determine the critical load at which coating adhesion to the substrate begins to fail. The test parameters, which were determined based on the ASTM standard for scratch testing [14], were a stylus speed of 10 mm/min to a maximum test length of 5 mm at loads up to 50N . The normal and tangential forces, as well as the acoustic emission and friction coefficient were recorded and plotted as a function of distance by the software and are shown in

Figure 4. Identifying significant acoustic events and matching them to spallations seen in the scratch track using optical microscopy determined the critical load, at which coating adhesion begins to fail. These spalls were investigated further using scanning electron microscopy (SEM) (FEI Quanta 400F, Hillsboro, OR), using energy-dispersive X-ray spectroscopy (EDS) mappings, to confirm that the Mo coating was removed and the Fe substrate was exposed. Critical load was then determined by correlating the position of the critical spall on the scratch track with its respective load.

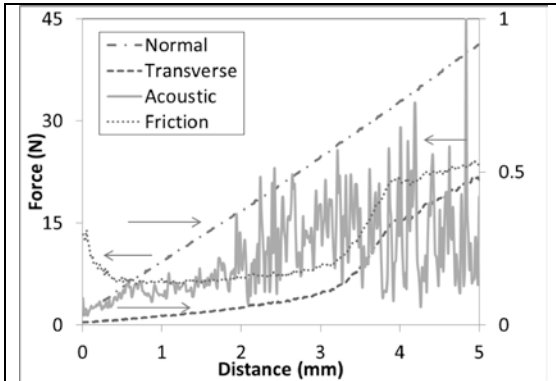


Figure 4. Normal load as a function distance obtained during a scratch test. Various signals recorded during a typical scratch test.

After determining the critical loads, adhesion energy values were calculated using the method introduced by Xie et al. [15]. First, the compressive stress induced by the scratch test indenter (σ_s) is calculated using the following equation:

$$\sigma_s = \frac{0.15}{R} \left(\frac{PH_f}{H} \right)^{0.5} E_f^{0.3} E^{0.2}$$

where, R is the radius of the indenter, P is the critical load, and H_f , H, E_f and E are the hardnesses and moduli of the coating and substrates, respectively. This method of calculating the stress induced by the indenter takes into account both the elastic and the plastic deformation that occur as a result of the test by superimposing the indentation and traction stresses the coating experiences.

Xie et al. showed that the mechanical properties, notably the hardness and modulus, of both the coating and the substrate play important roles in determining the adhesion failure stress [15]. This value is then coupled with the residual stress (σ_R), to get the critical compressive stress in the coating (σ) at which adhesive failure occurs using: $\sigma = \sigma_R + \sigma_s$.

The adhesion energy (W) is then calculated using the following equation:

$W = K_2(\sigma_R + \sigma_s)^2 t(1 - \nu^2) / E_f$ where, K_2 is a constant specific to spall type adhesion failures [16], t is the coating thickness, and ν_f is the Poisson's ratio of the coating, which was assumed to be 0.3.

Wear Testing

Wear testing was described in detail in the FY10 annual report.

Results

Mechanical Properties

Table 1 lists the measured mechanical properties of the MoN coatings processed with each copper deposition power, referred to as 0Cu and 8Cu, as mentioned above. Both samples had equivalent hardness and moduli values as determined from nanoindentation, regardless of copper content. The coating thicknesses as measured in the calotest were also similar and are shown in Table 1.

Table 1. Hardness, modulus, and thickness of MoN/Cu coatings.

Coating	Hardness (GPa)	Modulus (GPa)	Thickness (μ m)
0Cu	22.4 \pm 4.3	291.1 \pm 28	23 \pm 0.2
8Cu	23.0 \pm 4.0	282.6 \pm 16	2.6 \pm 0.2

Residual Stresses

Figure 5 plots the residual stresses for the MoN/Cu/steel samples estimated from measurements of lattice spacing changes. Each image has a different vertical scale. The in-plane residual stresses were compressive and increased magnitude with the film depth. There wasn't a clear

correlation between deposition conditions and measured residual stresses.

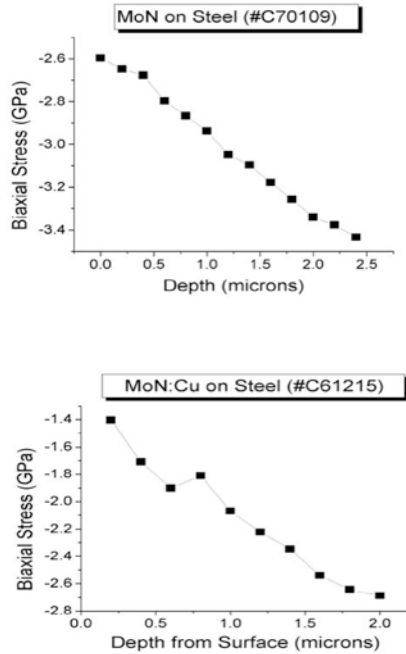


Figure 5. Variations of the measured in-plane residual stresses as a function of the film depth for the two processing conditions; (top) 0Cu and (bottom) 8Cu.

The nominal residual stress of the 0Cu coating (3.5 GPa) was much higher than that of 8Cu (2.7 GPa) the sample with copper present.

Adhesion Energy

The hardness and modulus of the coatings were very similar. This indicates that the addition of copper does not play a role in these mechanical properties. The residual stress at the coating/substrate interface, however, showed a significant difference between the 0Cu as compared to the 8Cu coating. Scratch test results indicated that while the mechanical properties such as hardness and modulus of the coatings were similar regardless of coating composition, the critical load and adhesion of the coating to the substrate were not. Coating 8Cu, began to show spallations and exposed substrates at lower peak loads (6.8 ± 2.1 N) than 0Cu (13.9 ± 2.6 N), and

began showing damage in the scratch track earlier than 0Cu. Overall, the critical loads correlating to the positions of spallation and exposed substrate were inversely proportional to the copper content.

After determining the critical load, the compressive stresses due to the indenter were evaluated. As was the case for residual stress, the compressive stress value for the 0Cu sample was higher (3.1 ± 0.3 GPa) than that of the 8Cu sample (2.1 ± 0.3 GPa). The calculated adhesion energies of the coatings are consistent with literature values [11, 20]. Coating 8Cu had a lower critical load and adhesion energy than 0Cu, indicating that the addition of copper adversely affects the coating/substrate bond. This may be due to the much lower residual stress present in the 8Cu sample, which, due to its compressive nature, acts to assist the coating adhesion. In addition, some intrinsic interfacial property differences must arise as a result of increasing copper content. The direct correlation between the residual stresses and the adhesion energy further indicates the key role of processing variables in coating/substrate adhesion.

Wear Testing

Figure 6 illustrates the wear rate, as calculated from profilometer measurements, as a function of the adhesion energy. The plot in this work shows a few clear trends. The most obvious is that, as expected, the wear rate is higher for the 50N load than the 25N load. The next significant correlation is that, at both loads, the wear rate decreases with increasing adhesion energy, and consequently, decreasing copper content. The 8Cu, with lower adhesion energy, exhibits a higher wear rate than the 0Cu sample. This implies that the adhesion energy plays a role in the wear resistance and coating failure of these materials.

Another noticeable feature is that there is a larger variation in wear rate as a function of copper content for the 25N tests than those at 50N. At 25N, the wear rate of 8Cu is significantly higher than that of the 0Cu sample. At 50N, there is a much

smaller difference between the values. This suggests that the damage mechanism is

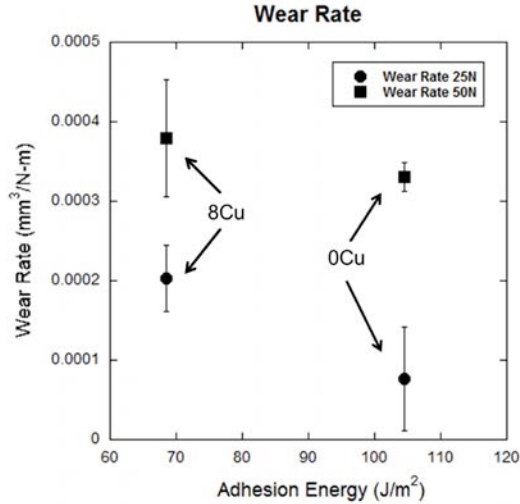


Figure 6. Wear rate as a function of the measured adhesion energy at two different loads used for the wear test.

further advanced in 8Cu at 25N, but more equal at the higher load. This was further studied by investigating the wear tracks using SEM and EDS.

SEM and EDS mapping of Mo and Fe shows the wear tracks of the 0Cu and 8Cu samples at the 25N load clearly indicate that after the wear test, more material has been removed from the 8Cu sample than the 0Cu sample, as there is a larger quantity of Fe exposed. This correlates well with the profilometer results shown in Fig. 5, which indicate a higher degree of coating removal in the 8Cu sample. The wear track width for the 50 N load is wider in the 8Cu sample than the 0Cu coating. In both cases, there is no remaining Mo evident in the wear track, indicating complete coating removal and failure. Also consistent with the profilometer measurements, there is a larger difference in coating removal in the wear track between the two loads for 0Cu than 8Cu.

Higher magnification SEM images were used to further investigate the damage mechanisms present in the wear tracks. At 25N, the wear tracks showed similar damage mechanisms for both coatings. In each system, abrasion and polishing of the MoN/Cu coating, surface fatigue in the form of chipping and cracking within the coating,

coating delamination, and Si deposition were seen. Abrasive failure is indicated by wearing away the coating layer by layer during the reciprocating motion of the test, and is visible in the lines of the wear track that are parallel to the wear test direction. Chipping is seen as cracks in the coating and delamination is evident in regions where large chunks of the coating have been removed, exposing the substrate below. In addition, silicon is visible where the majority of the coating is gone, indicating the presence of wear debris from the ball.

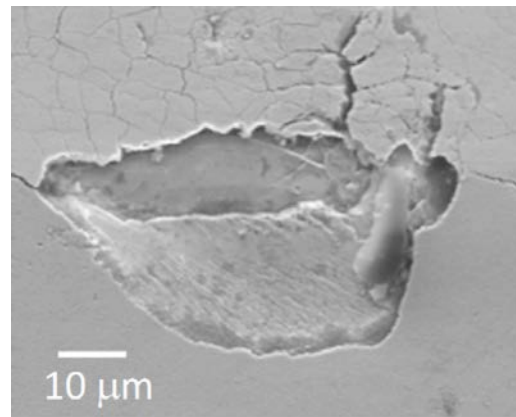


Figure 7. SEM micrograph of spalled coating from the scratch test.

Figure 7 shows a spallation obtained during a scratch test. Comparing the damage mechanisms observed during the scratch tests and the wear tests, it appears that they are quite similar. The adhesion failure at the interface, mainly illustrated by coating delamination and spallation, is prevalent in both types of tests. The tensile stress that results from the indenter movement, either the diamond stylus (high stress) or the Si₃N₄ ball (low stress), is the driving force for this coating failure. Despite the differences in the maximum tensile stresses that occur in each test, these stresses are responsible for coating removal at the interface. When lower stresses are present in the wear test, a fatigue mechanism may also be contributing to the coating damage. The observation that the 8Cu shows more coating removal than the 0Cu follows directly from the lower adhesion

energy in the 8Cu coating. This suggests that the same interfacial relationships that govern the critical spallations are also relevant in determining significant coating removal mechanisms. Thus, the adhesion energy measured using the scratch test could be correlated to the wear performance, at low load regime.

Conclusions

MoN coatings with two compositions of Cu were deposited onto steel substrates. The residual stresses resulting from deposition of the different compositions were measured and correlated to both the adhesion energy of the coating to the substrate as well as the wear resistance of the coating. The copper content significantly affected all of these factors. While both coating systems demonstrated similar hardness and modulus values, they resulted in different adhesive and tribological properties. The 8Cu sample, with copper content, exhibited diminished properties compared to the copper free 0Cu coating.

The adhesion energy and wear resistance of the 8Cu sample were significantly lower than that of the 0Cu coating. One very prevalent damage mechanism for the wear test was delamination, indicative of adhesive failure. The 8Cu sample showed significantly more coating removal than 0Cu, which agreed well with the adhesion energy measurements. Thus, the wear rate is correlated to the adhesion energy, which is directly related to the residual stress and ultimately, the initial copper content. The results indicate that the properties of the resulting coating/substrate system are tailorable based on the initial copper content and resulting residual stress, and that the increasing copper additions may not necessarily enhance the MoN coating performance.

References

1. A. Misra, M. Nastasi, in: E. Knystautas (Ed.) *Engineering Thin Films and*

- Nanostructures with Ion Beams*, Taylor and Francis, Boca Raton, FL, 2005, Vol. 92, Chap 7, pp. 325-392.
2. H. Windischmann, Intrinsic stress in sputter-deposited thin-films, *Crit. Rev. Solid State Mater. Sci.* 17 (1992) 547-596.
3. S.M. Aouadi, Y. Paudel, B. Luster, S. Stadler, P. Kohli, C. Muratore, C. Hager, A.A. Voevodin, Adaptive Mo₂N/MoS₂/Ag tribological nanocomposite coatings for aerospace applications, *Tribology Letters* 29 (2008) 95-103.
4. A. Aubert, J. Danroc, A. Gaucher, J.P. Terrat, Hard chrome and molybdenum coatings produced by physical vapour deposition, *Thin Solid Films* 126 (1985) 61-67.
5. M.C. Joseph, C. Tsotsos, M.A. Baker, P.J. Kench, C. Rebhoz, A. Matthews, A. Leyland, Characterisation and tribological evaluation of nitrogen-containing molybdenum-copper PVD metallic nanocomposite films, *Surface and Coatings Technology* 190 (2005) 345-356.
6. P.J. Rudnik, M.E. Graham, W.D. Sproul, High Rate Reactive Sputtering of MoN_x coatings, *Surface and Coatings Technology* 49 (1991) 293-297.
7. C. Sarioglu, U. Demirler, M. Kursat Kazmanli, M. Urgan, Measurement of residual stresses by X-ray diffraction techniques in MoN and Mo₂N coatings deposited by arc PVD on high-speed steel substrate, *Surface and Coatings Technology* 190 (2005) 238-243.
8. T. Suszko, W. Gulbinski, J. Jagielski, The role of surface oxidation in friction processes on molybdenum nitride thin films, *Surface Coatings and Technology* 194 (2005) 319-324.
9. T. Suszko, W. Gulbinski, J. Jagielski, Mo₂N/Cu thin films - the structure, mechanical and tribological properties, *Surface Coatings and Technology* 200 (2006) 6288-6292.
10. M. Urgan, O.L. Eryilmaz, A.F. Cakir, E.S. Kayali, B. Nilufer, Y. Isik, Characterization of molybdenum nitride coatings produced by arc-PVD technique." *Surface and Coatings Technology* 94-95 (1997) 501-506.
11. J. Valli, U. Makela, H.T.G. Hetzell, Tribological properties of MoN_x coatings in contact with copper, *Journal of Vacuum Science and Technology A* 4(1986) 2850-2854.
12. A. Leyland, A. Matthews, On the significance of the H/E ratio in wear control: a nanocomposite coating approach to optimized tribological behavior, *Wear* 246 (2000) 1-11.
13. W. Rasband, Image J, Research Services Branch, National Institute of Mental Health, Bethesda, MD, USA. 1997.

14. ASTM Standard C1624-05, Standard test method for adhesion strength and mechanical failure modes of ceramic coatings by quantitative single point scratch testing” ASTM, West Conshohocken, PA, (1999) 201-213.
15. Y. Xie, H.M. Hawthorne, A model for compressive coating stresses in the scratch adhesion test, *Surface and Coatings Technology* 141 (2001) 15-25.
16. J.W. Hutchinson, T.Y. Wu (Ed.) *Advances in Applied Mechanics*, Academic Press, Inc. San Diego, CA. Volume 29, 1992.
17. J.F. Archard, Contact and rubbing of flat surface, *Journal of Applied Physics* 24 (1953) 981-988.
18. M. Ferrari, L.J. Lutterotti, Method for the simultaneous determination of anisotropic residual-stresses and texture by x-ray-diffraction, *Journal of Applied Physics* 76 (1994) 7246-7255.
19. G. Chen, D. Singh, O. Erylimaz, J. Routbort, B.C. Larson, W. Liu, Depth-resolved residual strain in MoN/Mo nanocrystalline films, *Applied Physics Letters* 89 (2006) 172104.
20. P.-C. Tsai, K.-H. Chen, Evaluation of microstructures and mechanical properties of diamond like carbon films deposited by filtered cathodic arc plasma, *Thin Solid Films* 516 (2008) 5440-5444.

Agreement 14957 - Modeling of Thermoelectrics

A. A. Wereszczak* and H. Wang[†]

* Ceramic Science and Technology Group

[†] Diffraction and Thermophysical Properties Group

Oak Ridge National Laboratory

P.O. Box 2008, MS 6068, Bldg. 4515

Oak Ridge, TN 37831-6068

(865) 576-1169; fax: (865) 574-6098; e-mail: wereszczakaa@ornl.gov

R. McCarty, A. Thompson, and J. Sharp

Marlow Industries, Inc.

10451 Vista Park Road

Dallas, TX 75238-1645

(214) 342-4287; e-mail: rmccarty@marlow.com

DOE Technology Manager: Jerry L. Gibbs

(202) 586-1182; fax: (202) 586-1600; e-mail: jerry.gibbs@ee.doe.gov

ORNL Technical Advisor: David P. Stinton

(865) 574-4556; fax: (865) 574-6098; e-mail: stintondp@ornl.gov

Contractor: Oak Ridge National Laboratory, Oak Ridge, Tennessee

Prime Contract No.: DE-AC05-00OR22725

Objectives

- Non-CRADA sub-project: Measure thermomechanical and thermophysical properties of candidate thermoelectric (TE) materials (TEMats) for waste heat recovery to advance TEMats and devices (TEDs).
- CRADA sub-project: Support Marlow with their development of high temperature TEMats and TEDs.

Approach

- Non-CRADA sub-project: Develop characterization test methods that will benefit the TEs and TEDs manufacturing and end-user communities.
- CRADA sub-project: Measure properties of proprietary Marlow materials and provide development support.

Accomplishments

- Non-CRADA sub-project: Seebeck coefficients and electrical resistivities were measured by numerous laboratories as part of a round-robin study and interlaboratory variability assessed. The labs measured equivalent Seebeck coefficients; however, there was variability in the measured electrical resistivities.
- CRADA sub-project: Performed testing of Marlow TEMats and supportive evaluation of their TEDs.

Future Direction

- Non-CRADA sub-project: Measure properties of additional high-temperature capable TEMats and provide supportive characterization R&D to support the improvement of TEMats and TED modeling.
 - CRADA sub-project: Perform thermomechanical and thermophysical property measurements of proprietary Marlow TEMats and assist in development of Marlow TEDs.
-

Introduction

Potential next generation thermoelectric devices (TEDs) comprised of p- and n-type materials enjoy strong interest for implementation in high temperature and oxidizing environments in which waste heat could be used to generate electricity. However, the intended thermoelectric function of these devices will only be enabled if the TED is designed to overcome the thermomechanical limitations (e.g., brittleness) that are usually inherent to these materials. A thermoelectric material (TEMat) with a combination of poor strength and low thermal conductivity can readily fail in the presence of a thermal gradient, thereby preventing the exploitation of the desired thermoelectrical function.

This challenging problem can be overcome with the combined use of established probabilistic design methods developed for brittle structural components, good thermoelastic and thermomechanical databases of the candidate TEMat comprising the TED, and iteratively applied design sensitivity analysis. This project executes this process to involve TEDs.

This project has two parts. The first sub-project focuses on the thermomechanical and thermophysical evaluation of candidate TEMats that are of interest to the entire TE community for high temperature (e.g., 550°C) waste heat recovery. The development of appropriate strength test fixturing and methods are required as there are no widely accepted strength test practices (e.g., ASTM) for thermoelectric materials. The second sub-project involves a CRADA with Marlow Industries and the thermomechanical and thermophysical characterization of their proprietary TEMats.

There will be several outcomes from this work. It will benefit TEMat and TED developers and end-users of these potentially high temperature TEDs. Mechanical reliability of prototypical TEDs will be evaluated from a structural brittle-material perspective, and suggested redesigns will be identified. Thermomechanical reliability of developmental TEMats will be assessed, and minimum required thermomechanical properties of hypothetical TEMats would be identified that produce desired reliability in a TED.

Results

The results from FY11 work are broken up into two sections: the non-CRADA and CRADA sub-projects.

Non-CRADA sub-project

The non-CRADA section is comprised of four different subsections.

Mechanical Evaluations:

The completion of hundreds of bend strength tests were needed in FY11 at medium temperatures (< 300°C) so new flexure fixtures were designed that promoted rapid and valid bending testing. A schematic of the three point bend fixture is shown in Fig. 1 and an image of its assembly is shown in Fig. 2. The bend test assembly is shown inside an oven in Fig. 3.

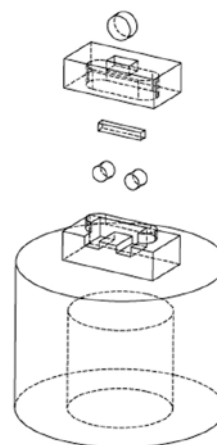


Figure 1. Schematic of a medium-temperature-capable fixture fabricated for bend strength testing of thermoelectric materials.



Figure 2. Assembled medium-temperature-capable bend fixture.



Figure 3. Medium-temperature furnace surrounding bend test set up.

Though the new bend test set up in Fig. 3 was developed to primarily support the Marlow CRADA, it can be used for non-CRADA testing too.

Additional methods and capabilities were pursued in FY11 and will be established in early FY12 to support mechanical evaluations of TEDs. They include using optical fluorescence to estimate residual stresses in TEDs containing aluminum oxide substrates, and the ordering of a shear tester to measure the shear strength of joints in TEDs and of an ultrasonic tester to non-destructively evaluate those joints as well.

Hall Effect Measurements on Bulk Samples:

In addition to transport properties measurements, it is important to know the carrier concentration and mobility of TEMats. For bulk TEMats such measurements require large and thin specimens which are not available in most cases, such as illustrated in Fig. 4. Low temperature measurements usually use a small specimen and strong magnet. The same specimen cannot be used for higher temperature measurements though. Room temperature testing using the Hall Effect as a screening tool is therefore very important. However, there is lack of reporting on how reliable the measurement is. To understand the measurement uncertainty, square Bi₂Te₃ specimens were prepared at Marlow with different thicknesses.

Using the van der Pauw method in Equation (1),

$$v_H = -\frac{IB}{nqd} \tag{1}$$

the Hall Voltage v_H may be represented as a function of current (I), magnetic field (B) and thickness (d). For thermoelectrics, we must keep Joule heating at minimum so a strong magnetic field or thinner specimen will result in larger Hall Voltage.

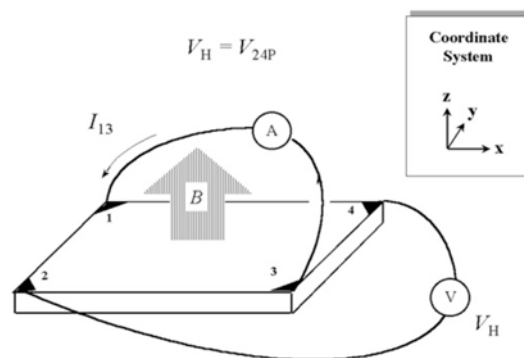


Figure 4. Schematic of the van der Pauw method used for measuring the Hall Voltage of a sample.

A set of Bi₂Te₃ specimens were prepared at Marlow with thicknesses of 0.50, 0.75, and 1.00 mm. An ECOPIA HMS-3000 system was used to test the samples. It is equipped with a 0.51 Tesla permanent magnet. Figures 5-7 show the bulk resistivity, carrier concentration, and Hall mobility of the three samples. In all three cases the thinnest sample, 0.5 mm, showed the best consistency in results. The standard deviation decreases with sample thickness. It is reasonable to assume the ORNL system can produce reliable results on samples with thickness around 0.5 mm. Another homemade Hall Effect system at ORNL was used to cross-check the results. They both showed the same trend in accuracy when the thickness is smaller.

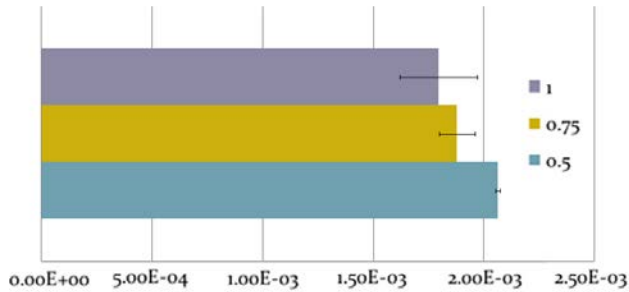


Figure 5. Bulk resistivity ($\Omega\text{-cm}$) of 3 samples.

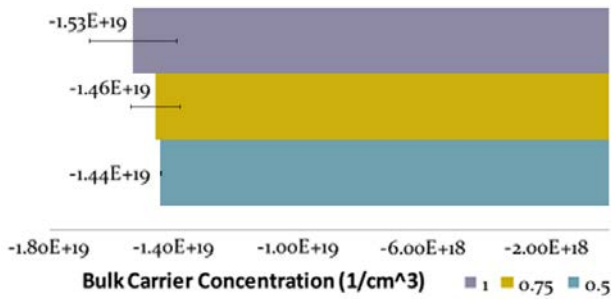


Figure 6. Bulk carrier concentration ($1/\text{cm}^3$) of 3 samples.

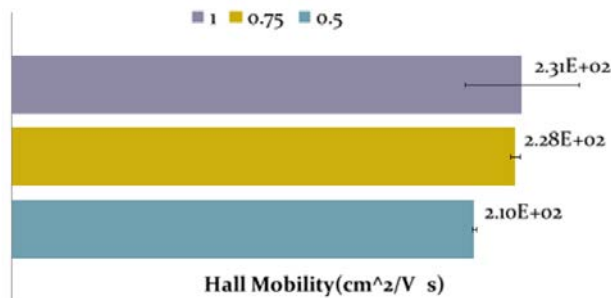


Figure 7. Hall mobility (cm^2/Vs) of 3 samples.

Reliability of Marlow Transport Properties on Bulk Samples:

Reliability of transport properties is one of the most important areas for Marlow and other TEMat manufacturers. Participating in the International Energy Agency (IEA) study on thermoelectric materials, Marlow provided its Bi_2Te_3 as round-robin materials. The selection of Marlow materials was not based on figure of merit (ZT), but rather on the uniformity in large bulk form. The same

material studied in FY10 was used for the IEA study. Marlow also machined all the specimens to the specification of the IEA tests, as shown in Fig. 8.



Figure 8. Marlow Bi_2Te_3 used for IEA round-robin.

The nominal composition of the n-type material was $\text{Bi}_2\text{Te}_{2.7}\text{Se}_{0.3}$ and the nominal composition of p-type material was $\text{Bi}_{0.5}\text{Sb}_{1.5}\text{Te}_3$. The average grain size of the materials was about 20 μm . A total of eight specimens (4 p-type and 4 n-type) prepared for transport properties testing were sent to each of seven laboratories:

- one 4 mm diameter, 1 mm thick disk for DSC measurement of C_p ,
- one 12.7 mm diameter, 1mm thick disk for thermal diffusivity test,
- one 2 mm x 2 mm x 15 mm bar for Seebeck coefficient and electrical resistivity tests, and
- one 3 mm x 3 mm x 12 mm bar for Seebeck coefficient and electrical resistivity tests.

In order to obtain ZT over the application temperature range, five separate measurements must be conducted:

1. thermal diffusivity (α in cm^2/sec)
2. specific heat (C_p in J/gK)
3. density (D in g/cm^3)
4. Seebeck coefficient (s in V/K)
5. electrical resistivity (ρ in Ohm-m)

The product of 1-3 gives thermal conductivity, $k = 100D\alpha C_p$ (in W/mK). The so-called Z-meter method takes measurements on Seebeck coefficient and electrical resistivity. Thermal conductivity was

not measured directly, the Z value in $Z = s^2/\rho k$ was obtained from a modified Harman technique.

Figures 9 and 10 showed how well the Marlow method matched the IEA round-robin effort. Comparing with seven participating labs, the Marlow Seebeck coefficient and electrical resistivity data (in brown and purple colors) fall very close to the 7-lab averages.

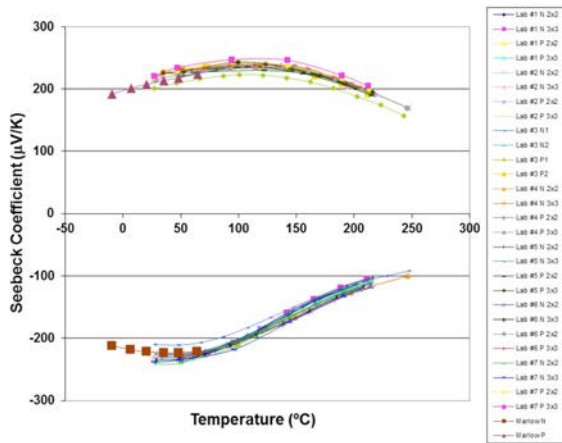


Figure 9. Seebeck coefficients of Marlow and IEA-AMT round-robin.

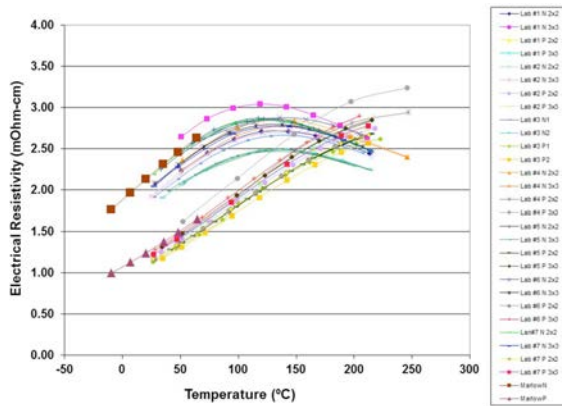


Figure 10. Electric resistivities of Marlow and IEA-AMT round-robin.

Neutron Strain Mapping of Skutterudite Modules

In FY10, we conducted preliminary studies of residual stress mapping at the High Flux Isotope Reactor (HFIR) using neutron diffraction. On the HFIR beam line HB-2, a prototype PbTe module was used for strain mapping. In FY11, 8x8- and

4x4-arrayed prototype skutterudite modules were studied using the same neutron technique. In Fig. 11, a prototype module is shown and two “stress free” legs were placed on top of the module as references. Figure 12 shows the neutron beam path in a 4x4 module. The high penetration nature of neutrons made it possible to study elements other than the corners. In principle, every leg in the module can be scanned using the same gauge volume. In the HFIR study, a gauge volume of 3 x 3 x 0.5 mm was used to scan the Z-direction of each leg at 0.25 mm steps.

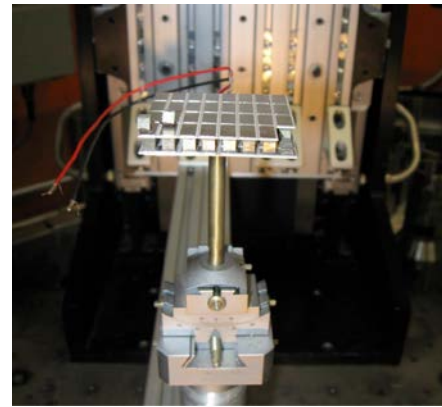


Figure 11. Picture of prototype 8 x 8 skutterudite module in the HFIR beam line. The legs are 4 x 4 x 4 mm³.

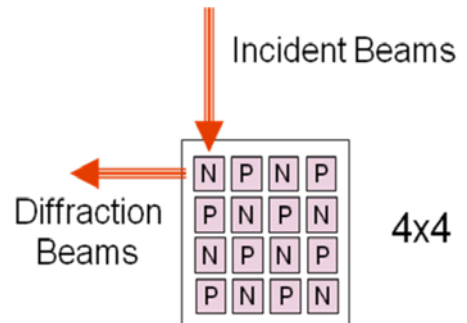


Figure 12. Neutron strain mapping of a 4 x 4 skutterudite module.

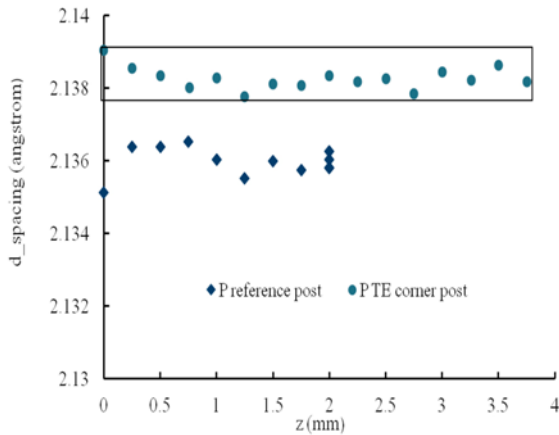


Figure 13. *d*-spacing change measured on *p*-legs.

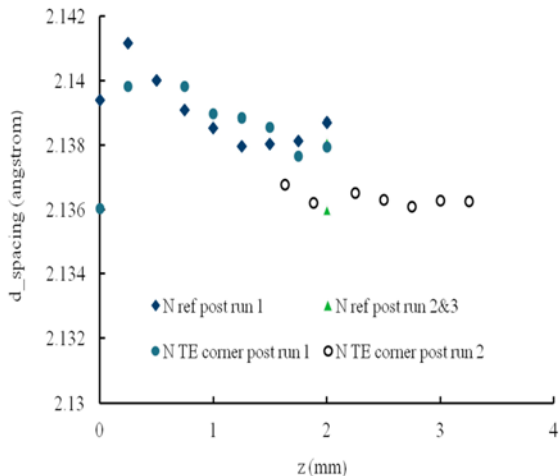


Figure 14. *d*-spacing change measured on *n*-leg. Run 1 was the top part of the leg and run 2 was the bottom part of the leg.

A characteristic diffraction peak was chosen for the skutterudite. The *d*-spacing was calculated from Bragg’s law. The strain mapping monitored the same peak and its *d*-spacing change as a function of location in the *Z*-direction. Figures 13-14 are *d*-spacing plots from the skutterudite modules. The data were not consistent for strain calculations. Further measurements are needed. In the preliminary study we found the following:

- The skutterudite peaks are weaker than PbTe. Longer scans (up to 20 minutes) are required to get sufficient neutron count.
- The *p*-type legs and *p*-type reference were likely from different batches in which a slight chemical composition change caused a shift in *d*-spacing.
- The *n*-type corner leg showed a shift in lower part of the leg. The *d*-spacing in the reference leg was also changing as a function of distance.

The results showed strain mapping using production thermoelectrics is not simple. Many variables need to be controlled in order to get accurate *d*-spacing measurement and use the ppm level changes to calculate stress and strain in the material. Based on the preliminary study the following study on skutterudite module had been planned for the remainder of calendar year 2011:

- Confirm the references and TE legs were using the same batch of materials,
- Confirm the selected thermoelectric couple is functioning properly,
- Use cut-off skutterudite couples for the next study, and
- Use strain-free powders (annealed) as another reference.

CRADA sub-project

A CRADA with Marlow Industries continued in FY11. The primary intents are to measure the transport properties and to thermomechanically and thermophysically characterize their proprietary TEMats. Testing of their materials continued throughout FY11. Transport properties of Marlow production and research thermoelectric materials were evaluated. Hundreds of specimens were tested but their results are not divulged here owing to the confines of the CRADA.

Summary

For the non-CRADA portion of this project, new mechanical test facilities and transport property measurements were generated in FY11. For the CRADA portion, numerous tests were completed to assess mechanical and transport properties of Marlow TEMats and Marlow TEDs.

Publications

- J. R. Salvador, J. Yang, A. A. Wereszczak, H. Wang, and J. Y. Cho, "Temperature Dependent Tensile Fracture Stress of n- and p-Type Filled-Skutterudite Materials," *Science of Advanced Materials*, 3:1-10 (2011).
- J. Y. Cho, X. Shi, J. R. Salvador, G. P. Meisner, J. Yang, H. Wang, A. A. Wereszczak, X. Zhou, and C. Uher, "Thermoelectric Properties and Investigations of Low Thermal Conductivity in Ga-Doped Cu_2GeS_3 ," in press, *Physical Review*, 2011.

Agreement 15529 – Utilization of Nanofluid Coolants

Principal Investigators: J. L. Routbort and D. Singh
Co-workers: Elena Timofeeva, Wenhua Yu, David France
Argonne National Laboratory
9700 S. Cass Avenue, Argonne, IL 60439-4838
(630) 252-5065; fax: (630) 252-5568; e-mail: routbort@anl.gov

DOE Technology Manager: Jerry L. Gibbs
(202) 586-1182; fax: (202) 586-1600; e-mail: jerry.gibbs@ee.doe.gov

Contractor: UChicago Argonne LLC
Contract No.: DE AC03 06CH11357

Objective

- Determine if the use of fluids containing a variety of nanoparticles results in erosive damage to radiator materials and coolant pumps.
- Determine figures of merit for use of nanofluids for cooling power electronics
- Measure pumping power of nanofluids in a real system and compare results to theoretical calculations
- Determine if nanofluids will clog a pumping system

Approach

- Characterize the thermal conductivity, viscosity, and heat transfer of various nanofluids
- Use surfactants and/or adjustments of pH to lower viscosity of nanofluids
- Conduct experiments to study erosive damage, clogging of nanofluids, and power to pump various nanofluids in a real system

Accomplishments

- Determined that a 130 nm, 2 vol % SiC/water nanofluid does not degrade aluminum Al3003 in over 700 hours of accelerated testing at 8 m/s for 30° and 90° impacts
- Designed, built, and calibrated a new erosion apparatus to measure wear in an automotive water pump and the torque required to pump nanofluids
- No significant erosive damage has been observed in the cast aluminum pump impeller
- Torque has been measured for both a water-based fluid containing Al₂O₃ and for an ethylene glycol-water fluid containing SiC nanoparticles
- Measured pumping power agrees with power calculated using single phase parameters based on measured values of the nanofluids.
- To date, no clogging has been observed
- 12 published papers in peer-review publications, 2 patent applications filed

Future Direction

- Project ends in FY11 to be replaced by a project to develop a nanofluid for cooling power electronics for hybrid electric vehicles
-

Forward

Efforts have shifted away from the in-house production of nanofluids, to development of advanced characterization techniques and establishment of working relationships with industry. Our principal partner on a related project for the Industrial Technology Program is Saint Gobain. They have been supplying SiC/water nanofluids for industrial cooling. ANL has been characterizing the nanoparticles by measuring the particle sizes, adding ethylene glycol to produce a nanofluid suitable for radiator cooling, and reducing the viscosity by changing the pH. Fluids are further characterized by measuring the viscosity, thermal conductivity, and heat transfer coefficients. We have also informal relations with Valvoline (Ashland Oil) because of their interest in lubrication and cooling of transmissions, PACCAR for heavy vehicle radiators, and we have characterized some graphite based nanofluids for Valvoline.

Introduction

Many industrial technologies face the challenge of thermal management. With ever-increasing thermal loads due to trends toward greater power output for engines and exhaust gas recirculation for diesel engines, cooling is a crucial issue in transportation. The conventional approach for increasing cooling rates is use of extended surfaces such as fins and microchannels. Reducing radiator size will reduce the frontal area and hence the aerodynamic drag. However, current radiator designs have already stretched these approaches to their limits. Therefore, an urgent need exists for new and innovative concepts to achieve ultra-high-performance cooling. Nanofluids seem to show enormous potentials as a coolant for radiators. Literature has many examples of increased thermal conductivity of fluids by the addition of nanoparticles (see review by Yu, et al. [1]). Enhanced thermal conductivity could lead to enhanced heat transfer. A CFD calculation of a Cummins 500 hp diesel engine using an ideal

nanofluid as coolant has shown that the radiator size could be reduced by 5% [2], reducing weight and size, and hence aerodynamic drag.

In order for the enhanced thermal conductivity to be utilized it must be shown that liquid erosion of typical radiator materials will be tolerable and that the increased pumping power resulting from higher viscosity will not exceed the gain in parasitic energy losses from enhanced cooling. Furthermore nanofluids cannot clog the pumping system. If nanofluids result in excessive erosive wear, or clog the pumping system, or require very high increased pumping power, they cannot be used. Hence, the Vehicle Technologies program funds an investigation of liquid erosion of radiator materials, clogging, and pumping power using nanofluids.

Results and Discussion

It has previously been reported that very little erosion has been observed. Fig. 1 is a photograph of the impeller that has been used to pump 4 vol % SiC particles in a 50-50 mixture of ethylene glycol/water for hundreds of hours between 20 and 28 l/min. The weight loss (erosion) was 0.65%. Weight loss measurements on commercial radiator material has never been observed.

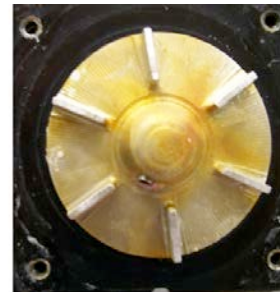


Fig. 1. View of a 7 cm diameter impeller used to pump SiC nanofluids.

A photograph of the clogging apparatus is shown in Fig. 2. It consists of a “U” shaped tube 1.6 mm inside diameter that can be heated to about 100°C. A peristaltic pump is used to move the fluid at about 120 ml/min. Tests have been made using a graphitic-based nanofluid between 80-200

hours with a 3.5 and 6.0 wt % graphite in ethylene glycol and water. The pump was stopped and restarted several times at ambient temperatures. Clogging is measured by a differential pressure gauge. No pressure change was recorded that is interpreted as no clogging was observed with the graphite nanofluids. The graphite particles are shown in Fig.3.



Fig. 2. View of clogging apparatus.

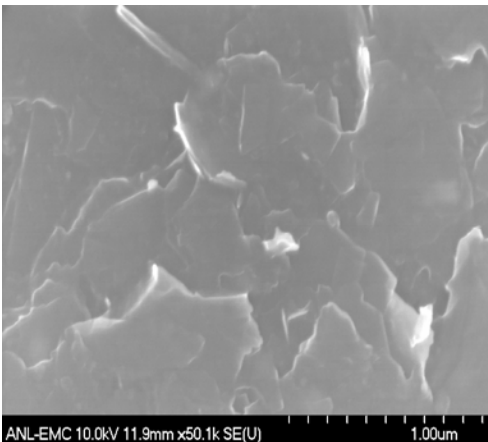


Fig. 3. Graphite nanoparticles from Valvoline used in the nanofluids for clogging experiments.

The apparatus used to measure pumping power is shown in Fig 4. The pumping power is calculated from the measured torque and RPM and can be calculated from the volumetric flow rate, the change of pressure and the pump efficiency. Experimental data is shown in Fig. 5. Agreement between calculated increase in torque from the base fluid and the measured relative increase is very good and is shown below in Table 1 [3]. More torque is required for the smaller particles than the

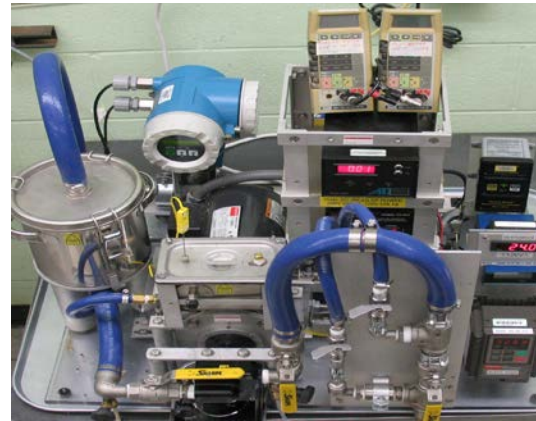


Fig. 4. Apparatus to measure pumping power

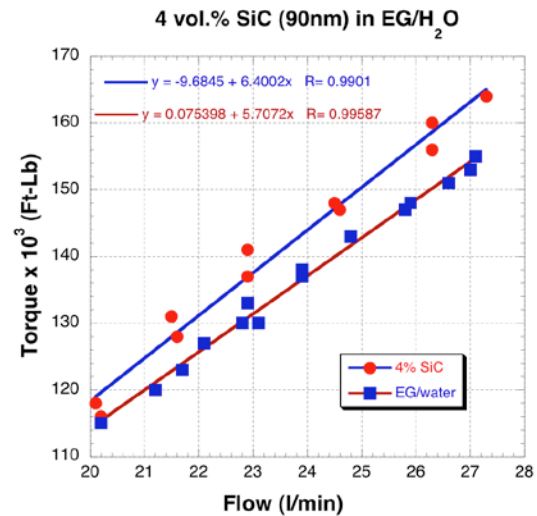


Fig. 5. Measured torque of a 4 vol.% (90nm) SiC in ethylene glycol/water at 30°C compared to the base fluid.

Table 1. The relative increase in torque for two SiC nanofluids compared to the base fluid, ethylene glycol and water.

Nanofluid	Experimental torque increase (%)	Calculated torque increase (%)
2.2 v% 29nm	9.3	8.7
4.0 v% 90nm	5.3	6.5

larger particles in agreement with the previously reported data that the viscosity of fluid containing the larger particles is lower than that containing the smaller particles. It

was also previously shown that the viscosity of the nanofluid for the 90 nm particles becomes equal to that of the base fluid at about 80°C, implying that the torque of the base fluid would equal to that of the nanofluid at ≈80°C, meaning that there would be no pumping penalty at operating temperatures.

Utilizing our experience with the properties of nanofluids we have devised an approach to engineer nanofluids with the desired thermal-physical properties [4]. A summary is shown in Tables 2 and 3.

Table 2. Relative importance of materials, concentration, shape and size on viscosity, thermal conductivity, and heat transfer.

Nanoparticle Properties (Relative Importance)	Viscosity	Thermal Conductivity	Heat Transfer
Material (4.0)	Weak	Strong	Strong
Concentration(6.3)	Strong	Strong	Strong
Shape (3.8)	Strong	Medium	Strong
Size (5.0)	Strong	Strong	Strong

Table 3. Relative importance of base fluid, zeta potential, additives, and temperature on viscosity, thermal conductivity, and heat transfer. Numbers in () indicate relative importance.

Fluid Properties (Relative Importance)	Viscosity	Thermal Conductivity	Heat Transfer
Base fluid (5.3)	Strong	Weak	Strong
Zeta Potential (4.0)	Strong	Medium	Strong
Additives (2.8)	Medium	Weak	Medium
Temperature (3.8)	Strong	Medium	Strong

Cooling of Power Electronics

At the request of DOE we have made an assessment of the minimum thermal properties of nanofluids to eliminate the low-temperature cooling system for power electronics for a hybrid electric vehicle. The package that we were assigned consisted of both a high and low-temperature coolant system. In double-sided cooling, the low-temperature coolant system can be eliminated in the laminar flow region and

the current standard of 100 W/cm² heat flux and/or 150°C can be improved substantially with a thermal conductivity of about 1.5 with or without the thermal interface material. We using graphite-based nanofluids have reached this goal.

Conclusions

We have made considerable progress in advancing the understanding of the particle size dependence of the thermal conductivity and heat transfer coefficient of nanofluids. We also understand the effect of pH on the viscosity of the fluid because the pH changes the Zeta potential. Utilizing this understanding has allowed taking a potentially commercial water-based SiC nanofluid and modifying it to achieve an approximate 15% increase in heat transfer with no increase in viscosity at heat exchanger operating temperatures. We have verified that at ambient temperatures there is no clogging or erosion and the pumping power increase of the SiC nanofluid over the base fluid has only a modest percent increase. More important at operating temperatures (>80°C), there will be no pumping penalty. We have confidence that given the thermal and physical properties of the nanofluid we can calculate the pumping power.

Additionally we have performed an assessment of using nanofluids to cool power electronics for HEV applications. The results indicate that in the laminar graphite-based nanofluids have the requisite enhancements of thermal conductivity. We intend to work on the further development of these heat transfer fluids for cooling power electronics with a new project to start in FY12. Emphasis will be on increasing the thermal conductivity, measuring the heat transfer, and reducing the viscosity of the fluid.

References

1. W. Yu, D. M. France, J. Routbort, S.U.S. Choi, “Review and Comparison of Nanofluid thermal Conductivity and Heat

Transfer Enhancements, *Heat Transfer Engineering*, **29**, 432-460 (2008).

2. S. K. Saripella, W. Yu, J. L. Routbort, D. M. France, and Rizwan-uddin, “ Effects of Nanofluid Coolant in a Class 8 Truck Engine, SAE Technical Paper 2007-01-21413.

3. J. Routbort, D. Singh, E. Timofeeva, W. Yu, and D. France, *J. Nanoparticle Research* **13**, 3, 931-937 (2011)

4. E. Timofeeva, W. Yu, D. France, D. Singh, and J. Routbort, *Nanoscale Research Letters*, **6**, 182, (2011).

Agreement 16308 – Thermoelectrics Theory and Structure

D.J. Singh

Materials Science and Technology Division

Oak Ridge National Laboratory

P.O. Box 2008, MS 6056, Bldg. 4100

Oak Ridge, TN 37831-6056

(865) 241-1944; fax: (865) 574-7659; e-mail: singhdj@ornl.gov

DOE Technology Manager: Jerry L. Gibbs

(202) 586-1182; fax: (202) 586-1600; e-mail: jerry.gibbs@ee.doe.gov

ORNL Technical Advisor: David P. Stinton

(865) 574-4556; fax: (865) 241-1034; e-mail: stintondp@ornl.gov

Contractor: Oak Ridge National Laboratory, Oak Ridge, Tennessee

Prime Contract No.: DE-AC05-00OR22725

Objectives

- Find ways to optimize existing thermoelectric materials and discover new families of high performance thermoelectrics for waste-heat-recovery applications using modern-science-based materials design strategies.
- Find low cost materials that have high thermoelectric figures of merit and are suitable for vehicular applications.

Approach

- First principles calculations based on quantum mechanics are used to calculate electronic structure and thermoelectric properties of materials.
- Boltzmann transport equations are solved to obtain electrical transport properties.
- Vibrational properties are investigated and mechanisms for thermal conductivity reduction are assessed.

Accomplishments

- Performed first principles calculations of transport and other properties of potential thermoelectric materials.
- Determined that Mo_3Sb_7 , when optimally doped with inexpensive, commonly available transition metals such as Iron, Nickel and Cobalt, can be a high performance p-type thermoelectric material at temperatures suitable for exhaust waste heat recovery.
- Found that the chalcogenide Bi_2Se_3 can be a high performance thermoelectric material in the 300 – 600 K temperature range if appropriately doped and nanostructured.
- Identified the chalcogenides SnS and CuBiS_2 as low-cost thermoelectric materials based on earth abundant materials with potential for application in vehicles.

Future Directions

- Identify new high performance low cost thermoelectric compositions suitable for vehicular applications.
 - Calculate doping level dependence of thermoelectric properties to guide optimization of existing materials.
-

Introduction

The use of thermoelectric devices to convert waste heat in vehicle exhaust to electricity offers potentially significant energy savings. Among the requirements for the effective use of such devices is the availability of high performance thermoelectric materials, with low cost and other properties needed for application in vehicles. The dual requirement for both high performance and low cost has constrained thermoelectric applications in the automotive industry, although thermoelectrics have been effectively inserted in the context of seat cooling. In this regard, there is interest in improved thermoelectric materials, not only for waste heat recovery, but also for zonal heating and cooling in automobiles. High performance thermoelectric materials have the potential for improving fuel efficiency and at the same time improving occupant comfort by directing cooling where needed in the cabin. This is of particular importance for electric and hybrid vehicles.

We are developing improved materials for these applications, using a science-based approach with a primary focus on materials for waste heat recovery. In particular, we are using materials design strategies based on first principles calculations of electronic, vibrational and transport properties to identify potentially low cost, high performance thermoelectric materials suitable for application in vehicles. We are also calculating properties of existing materials as a function of doping and other parameters to obtain information needed for optimization of these materials. The emphasis is on the thermoelectric figure of merit, ZT as well as materials properties of importance in engineering thermoelectric modules, for example anisotropy. High $ZT = \sigma S^2 T / \kappa$ requires a combination of high thermopower (S), good electrical conductivity (σ), and low thermal conductivity (κ). Finding materials with the needed combination of properties is challenging because, for example, high thermopower and high conductivity most commonly occur in different doping regimes. [1] We use state-of-the-art computational tools such as the linearized augmented planewave method [2] and the BoltzTraP computer code [3].

Results

(1) Molybdenum antimonide (Mo_3Sb_7):

Vehicular waste heat recovery requires both high performance and low cost. Cubic Mo_3Sb_7 , which has already shown a thermoelectric figure-of-merit ZT of 0.93 [4] at a temperature of 770 C, is of interest in this context. Of particular importance, this ZT was achieved at a very high doping level, $p = 5 \times 10^{21} \text{ cm}^{-3}$. This is a much higher level than is optimum in conventional thermoelectrics, implying a different doping level dependence. We studied the electronic structure, vibrational and transport properties of this material in order to provide predictions that could be used to guide optimization of this material. We found (Figure 1) that substantially higher thermopowers and correspondingly higher performance can be obtained by further optimization of the doping level to the range near 10^{20} cm^{-3} .

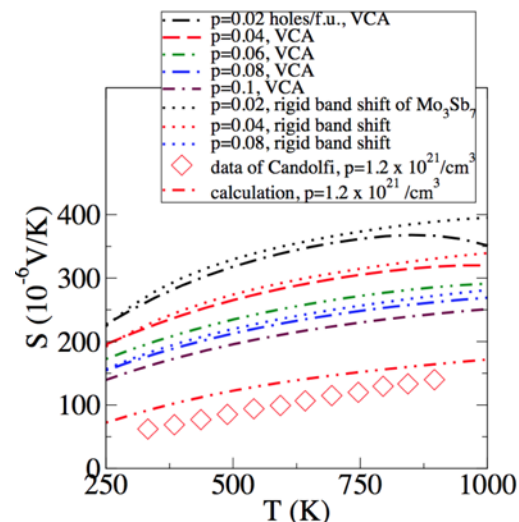


Figure 1: Thermopower for p -type Mo_3Sb_7 from first principles calculations. Note the values exceeding $250 \mu\text{V/K}$ in a wide temperature range with optimization of the doping level.

We also investigated specific dopants including the effects on vibrational properties that control the thermal conductivity (Figure 2). We found that the primary effect on ZT is through the carrier concentration, but that there are noticeable effects on the lattice vibrations from certain dopants, such as Iron.

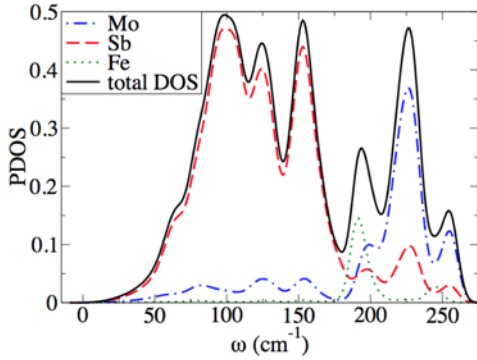


Figure 2: Calculated vibrational density of states for $Mo_{2.5}Fe_{0.5}Sb_7$. Note the Fe component near 190 cm^{-1} , indicating additional scattering.

Our results [5] show that this material, when optimized, can have thermoelectric performance as high as twice the currently reported value of $ZT = 0.93$. The importance of this is (1) this material is composed of abundant and relatively inexpensive materials; (2) this material is cubic, which simplifies development for applications; and (3) it shows good performance in the temperature range needed for exhaust gas waste heat recovery.

(2) Chalcogenide Thermoelectrics:
Nanostructured Bi_2Se_3

The thermoelectric material most commonly used in room temperature heating and cooling applications, including vehicles, is Bi_2Te_3 . However, this material suffers from certain disadvantages. These include the high concentration of the rare element, Tellurium, and a band gap too small for use at temperatures much above room temperature. Therefore, alternatives are desired, especially if they offer high values of ZT .

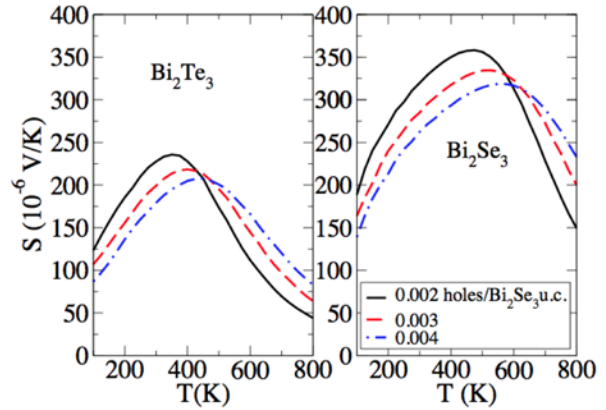


Figure 3: Calculated thermopower for p-type Bi_2Te_3 and Bi_2Se_3 . Note that the thermopower of Bi_2Se_3 is substantially larger.

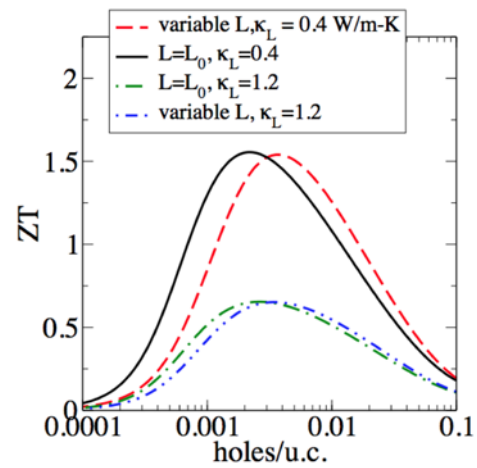


Figure 4: Estimated figure-of-merit ZT at 500 K for hole-doped Bi_2Se_3 , with nanostructuring included (black, red) and without (blue, green). L is the Lorenz number for the electronic thermal conductivity.

We performed first principles calculations investigating the sister chalcogenide, Bi_2Se_3 , which has been far less studied as a potential thermoelectric. We found (Figure 3) that the thermopower of this material with hole doping can exceed that of Bi_2Te_3 .

We further found (Figure 4) that if the lattice thermal conductivity is reduced by appropriate nanostructuring techniques, such as those that have already been applied to Bi_2Te_3 , [6,7] this material may show ZT values exceeding unity in the temperature range 300 K to 600 K.

This is a significant result because it suggests that nanostructured Bi_2Se_3 may be a useful thermoelectric material both at room temperature (for cabin heat-

ing/cooling applications) and at elevated temperature (for waste heat recovery applications). Selenium, unlike Tellurium, is available in quantities sufficient for widespread applications, and is much less costly. [8]

Hole-doped CuBiS₂

We additionally studied other potential chalcogenide thermoelectrics comprised of abundant elements. This included CuBiS₂, [9] which we investigated in the context of vehicular zonal heating and cooling.

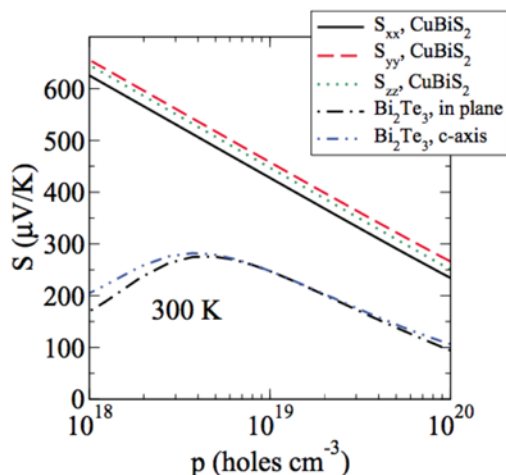


Figure 5: Calculated thermopower for hole-doped CuBiS₂ at 300 K; note the high values.

We found (Figure 5) that this material can show very large thermopowers at room temperature. This means that considering the known 300 K lattice thermal conductivity [10] of 0.5 W/m-K, this material has the potential for very good room-temperature thermoelectric performance provided that the hole mobility is not too low. These results have been communicated to experimental groups. We are awaiting experimental investigations of this material to establish whether the mobility is high enough to obtain high ZT .

Hole-doped SnS

Another material composed of abundant inexpensive elements, where we performed [11] calculations and found favorable results is hole-doped SnS. We found that the electronic band structure has heavy bands near the valence band edge. We did detailed calculations of the transport properties using Boltzmann theory. These calculations showed high thermopower, which is an essential ingredient in obtaining high thermoelectric performance.

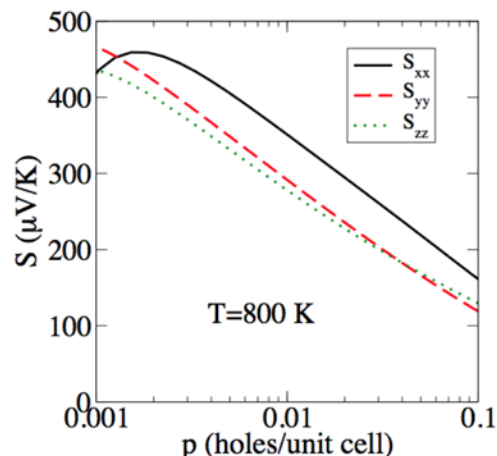


Figure 6: Calculated thermopower for hole-doped SnS at 800 K. Note that one hole/unit cell is equivalent to approximately $p = 5 \times 10^{21} \text{ cm}^{-3}$.

Although the thermopower is favorable, we do find a substantial conductivity anisotropy. This will need to be taken into account in the development of this material for applications. Nevertheless, researchers from the National Energy Technology Laboratory have been in contact with us regarding the use of this material in large-scale industrial energy harvesting, where waste heat temperatures overlap to a degree with those of exhaust waste heat recovery. The performance of this material will ultimately depend on the (presently unknown) hole mobility at the heavy dopings where performance would be optimum.

Conclusions

We are obtaining new insights into thermoelectric materials performance using Boltzmann transport theory based on first principles electronic structures. We found that p-type Mo₃Sb₇ can have performance far exceeding its current limits if the hole concentration is decreased via the addition of transition metals such as Iron, Nickel and Cobalt.

We have additionally explored the thermoelectric behavior of numerous chalcogenides, finding that nanostructured, optimized Bi₂Se₃ can show good performance between 300 and 600 K, and that two sulfides comprised of inexpensive, earth abundant materials – SnS and CuBiS₂ – may show good thermoelectric performance if appropriately doped.

References

- [1] D.J. Singh and I. Terasaki, “Nanostructuring and more”, *Nature Materials* **7**, 616 (2008).
- [2] D.J. Singh, “Planewaves, Pseudopotentials and the LAPW Method, 2nd Edition”, Springer, Berlin (2006).
- [3] G.K.H. Madsen and D.J. Singh, “BoltzTraP: A code for calculating band-structure dependent quantities”, *Computer Physics Communications* **175**, 67 (2006).
- [4] H. Xu, K.M. Kleinke, T. Holgate, H. Zhang, Z. Su, T.M. Tritt and H. Kleinke, “Thermoelectric performance of $\text{Ni}_y\text{Mo}_3\text{Sb}_{7-x}\text{Te}_x$ ($y \leq 0.1$, $1.5 \leq x \leq 1.7$)”, *Journal of Applied Physics* **105**, 053703 (2009).
- [5] D. Parker, M.H. Du and D.J. Singh, “Doping dependence of thermoelectric performance in Mo_3Sb_7 : First-principles calculations”, *Physical Review B* **83**, 245111 (2011).
- [6] W. Xie, X. Tang, Y. Yan, Q. Zhang and T.M. Tritt, “Unique nanostructures and enhanced thermoelectric performance of melt-spun BiSbTe alloys”, *Applied Physics Letters* **94**, 102111 (2009).
- [7] B. Poudel *et al*, “High-Thermoelectric Performance of Nanostructured Bismuth Antimony Telluride Bulk Alloys”, *Science* **320**, 634 (2008).
- [8] United States Geological Survey report available at <http://minerals.usgs.gov/minerals/pubs/commodity/selenium/mcs-2011-selenium.pdf>
- [9] D. Parker and D.J. Singh, “Transport properties of hole-doped CuBiS_2 ”, *Physical Review B* **83**, 233206 (2011).
- [10] D.P. Spitzer, “Lattice Thermal Conductivity of Semiconductors: A Chemical Bond Approach”, *Journal of Physics and Chemistry of Solids* **31**, 19 (1970).
- [11] D. Parker and D.J. Singh, “First principles investigations of the thermoelectric behavior of tin sulfide”, *Journal of Applied Physics* **108**, 083712 (2010).

Agreement 18340 - Thermoelectric Materials for Advanced Vehicle Energy Recovery

Principal Investigator: Dr. Terry Hendricks

MBI Business Development Leader/Senior Program Manager
MicroProducts Breakthrough Institute
Pacific Northwest National Laboratory
1000 NE Circle Blvd., Suite 11101, Corvallis, Oregon 97330
(541) 713-1353; fax: (541) 758-9320; e-mail: terry.hendricks@pnl.gov

Associate Researchers: Dr. Morris Good and Kamandi Roberts

Chemical, Biological, and Physical Science Division, K5-26
Pacific Northwest National Laboratory
P.O. Box 999, Richland, Washington 99352
Morris Good: (509) 375-2529; fax: (509) 375-6497; e-mail: morris.good@pnl.gov
Kamandi Roberts: (509) 375-3943; fax: (509) 375-6497; e-mail: kamandi.roberts@pnl.gov

Professor Mas Subramanian and Dr. Krishnendu Biswas

Department of Chemistry
Oregon State University
Corvallis, Oregon 97330
(541)-737-8235; fax (541)-737-2062; e-mail: mas.subramanian@oregonstate.edu

Charles Cauchy

Chief Technology Officer/Tellurex Principal Investigator
Tellurex Corporation
1462 International Drive
Traverse City, MI 49686
(231)-947-0110; e-mail: CCauchy@Tellurex.com

DOE Technology Manager: Jerry L. Gibbs

(202) 586-1182; fax: (202) 586-1600; e-mail: jerry.gibbs@ee.doe.gov

Field Technical Manager: Dean Paxton

(509) 375-2620; fax: (509) 375-2186; e-mail: dean.paxton@pnl.gov

Contractor: Pacific Northwest National Laboratory
Contract No.: DE- AC05- 76RL01830

Objectives

- Develop new high-performance n-type and p-type thermoelectric (TE) material compositions to enable the U.S. Department of Energy (DOE) Office of Vehicle Technologies (OVT) to achieve or approach 10% fuel efficiency improvements from waste energy recovery in advanced light-duty engines and vehicles.
- Develop new high-performance, n-type and p-type TE material compositions to enable OVT to achieve stretch thermal efficiencies of 55% in advanced heavy-duty engines by 2013.
- Improve cost-effectiveness and performance of exhaust heat recovery in light- and heavy-duty vehicles.
- Design, synthesize, and characterize p-type and n-type skutterudites and metal oxide TE materials for waste-heat-driven power generation in light-duty or heavy-duty vehicle exhaust flows or other comparable exhaust flows. Develop TE materials with operational temperatures as high as 800 K to 900 K.

- Develop advanced n-type and p-type bulk TE materials that have peak ZT (Figure of Merit x Temperature) of approximately 1.6 or higher at 600 K and temperature-dependent properties that provide high performance in the 350 K to 820 K range.

Approach including industrial partner/collaborator and path to technology transfer and commercialization

- Pacific Northwest National Laboratory (PNNL) and Oregon State University (OSU) are systematically investigating multiple-rattler skutterudite materials and metal oxide TE materials that can perform effectively and structurally survive at temperatures from 350 K to 820 K.
- Indium (In)-based cobalt antimony ($\text{In}_x\text{R}_y\text{Co}_4\text{Sb}_{12}$) compounds are one targeted n-type skutterudite material. However, p-type skutterudites also are being investigated and developed.
- PNNL and OSU are simultaneously characterizing the temperature-dependent thermoelectric and structural properties of advanced p-type and n-type TE materials, particularly Seebeck coefficient, electrical conductivity, thermal conductivity, Young's modulus, Poisson's ratio, and the coefficient of thermal expansion (CTE) up to 300°C to 400°C.
- OSU is developing and fabricating advanced TE material compounds and measuring the TE properties using their TE measurement equipment.
- PNNL is measuring structural properties, Young's modulus, and Poisson's ratio, in resonant ultrasound (RUS) facilities and CTE at PNNL's Physical Sciences Laboratory in Richland, Washington.
- PNNL is using its TE system modeling capabilities to characterize system-level benefits of the material compositions in vehicle waste energy recovery applications.
- PNNL partnered with Tellurex Corporation to develop the first-ever TE couples using high-performance n-type $\text{In}_{0.2}\text{Co}_4\text{Sb}_{12}$ and $\text{In}_{0.2}\text{Ce}_{0.15}\text{Co}_4\text{Sb}_{12}$ skutterudites with known high-performance p-type materials.

Milestones, Metrics and Accomplishments

- Continued fabricating and characterizing InCe-based n-type dual-rattler skutterudite materials, n-type $\text{In}_{0.2}\text{Co}_4\text{Sb}_{12}$ and $\text{In}_{0.2}\text{Ce}_{0.15}\text{Co}_4\text{Sb}_{12}$ compounds that showed very good n-type TE behavior.
- The n-type $\text{In}_{0.2}\text{Ce}_{0.15}\text{Co}_4\text{Sb}_{12}$ compounds demonstrated ZT values of 1.3 to 1.4 at 623 K. **(Milestone)**
- Investigated, fabricated, and characterized $\text{In}_{0.2}\text{Co}_4\text{Sb}_{12}$ compounds, which also showed very good ZT values of 1.2 at 623 K.
- Investigated, fabricated, and characterized n-type $\text{In}_{0.2}\text{Ce}_{0.1}\text{Yb}_{0.05}\text{Co}_4\text{Sb}_{12}$ and $\text{In}_{0.2}\text{Ce}_{0.05}\text{Yb}_{0.1}\text{Co}_4\text{Sb}_{12}$ skutterudite compounds that demonstrated $\text{ZT} = 1.2$ at 620 K. **(Milestone)**
- Successfully measured high-temperature Young's modulus, shear modulus, and Poisson's ratios for n-type InCe-based $\text{Co}_4\text{Sb}_{12}$, skutterudite compounds at temperatures up to 573 K (300°C). **(Milestone)**
- Characterized the thermal cycling behavior of several n-type InCe-based skutterudite compounds, and demonstrated their thermal stability after 200 cycles at 50°C to 400°C.
- Completed fabrication and automated control of critical high-temperature RUS thermal chamber and high-temperature transducers for high-temperature RUS structural property measurements at PNNL. **(Milestone)**
- Performed x-ray diffraction (XRD) analyses of n-type and p-type InCe-based multiple-rattler skutterudites to verify their pure, single-phase composition.
- Designed, fabricated and tested TE couples using n-type $\text{In}_{0.2}\text{Co}_4\text{Sb}_{12}$ and $\text{In}_{0.2}\text{Ce}_{0.15}\text{Co}_4\text{Sb}_{12}$ compounds coupled with p-type bismuth telluride and p-type lead antimony silver tin telluride (LASTT), respectively. **(Milestone)**
- TE couples demonstrated the conversion efficiencies of 7% at hot-side temperatures of 573 K and cold-side temperatures of 313 K. Highest conversion efficiencies on DOE OVT Thermoelectrics Program. **(Milestone)**

Future Recommendations

- Transition demonstrated TE couples to future TE devices & systems in automotive energy recovery systems.

Introduction

Background: DOE's *Transportation Energy Data Book: Edition 24* shows that in 2002,

approximately 130 billion gallons of gasoline were used nationwide by the light-duty passenger car, van, and sport-utility vehicle (SUV) segments. Some current estimates

indicate that approximately 4 to 5 Quads (1 Quad = 10^{15} Btu) of the energy in this fuel ends up as waste thermal energy in the vehicle exhaust stream. The same reference also indicates another approximately 30 billion gallons of diesel fuel was used nationwide by heavy-duty vehicles in 2002. Some current estimates indicate that approximately 1.4 Quads of the energy in this fuel ends up as waste thermal energy in the heavy-vehicle exhaust stream. Other estimates indicate that another 5 to 7 Quads of thermal energy originating from the fuel energy ends up in the vehicle coolant systems of light-duty passenger cars, vans, SUVs, and heavy-duty vehicles. DOE's Office of Energy Efficiency and Renewable Energy, Vehicle Technologies Program initiated a Waste Heat Recovery and Utilization project with the goal of recovering enough of this waste energy to increase the vehicle fuel economy by 10%. Contractor teams have pursued advanced thermoelectric (TE) systems, leveraging recent advanced TE materials research and development in skutterudites, quantum well, and nanostructured materials to recover and convert this waste thermal energy into high-grade electrical energy onboard the vehicle.

Advanced TE materials are critical to achieving project performance goals and introducing other potential future applications of TE power generation and advanced cooling in vehicle systems. Several researchers have reported advanced TE materials demonstrating ZT values of 1.6 to 2.4, with at least some of these data occurring at high temperatures of 400°C to 700°C. It is possible to expect advanced TE power conversion efficiencies of 12% to 15% with TE materials in this ZT range at high temperatures, which are two to three times the values using older bulk TE materials. Further advances in TE materials may lead to power conversion efficiencies approaching 20%.

Several technical challenges exist to developing advanced hybrid TE power systems in advanced light-duty and heavy-duty vehicle platforms, including increasing TE device conversion efficiencies through demonstrated high-performance TE materials, transferring hot-side

exhaust thermal energy into the TE conversion devices, dissipating cold-side thermal energy to the environment, and optimizing advanced TE systems for a variety of nominal and off-nominal performance conditions. Tasks performed here address these new opportunities by developing the necessary advanced TE materials with a ZT value of ~ 1.6 at 600 K in bulk form that allows cost-effective engineering transition into high-performance TE power generation devices.

This project leverages recent progress in skutterudite TE materials. Skutterudite materials have a cubic crystal structure as shown in Figure 1, which contain "voids" inside the crystal. These "voids" are large enough that various elements can be inserted inside. Any inserted element has a particular resonance frequency associated with it that can be excited by thermal phonons of the proper wavelength traveling through the crystal. The complete wavelength spectrum of thermal phonons is responsible for producing the observed lattice thermal conductivity in any material. The elements inserted into the crystal voids interact with and resonate with particular wavelengths of the spectrum, thereby causing them to resonate or "rattle" at that particular wavelength and, ultimately, scatter the thermal phonon rather than allowing it to transmit through the crystal. This ultimately reduces the lattice thermal conductivity of the skutterudite. The more elements that can be put inside the crystal voids, the more wavelengths or range of wavelengths can be impacted and scattered, further reducing the lattice thermal conductivity. This ultimately increases the ZT (Equation 1) of skutterudite materials, which already have inherently high Seebeck coefficients,

(1)

$$ZT = \frac{S^2 \sigma}{K_e + K_L} T$$

where:

S = Seebeck coefficient [$\mu\text{V/K}$]

σ = electrical conductivity [S/cm]

K_e = electronic thermal conductivity [W/m-K]

K_L = lattice thermal conductivity [W/m-K]

T = temperature [K]

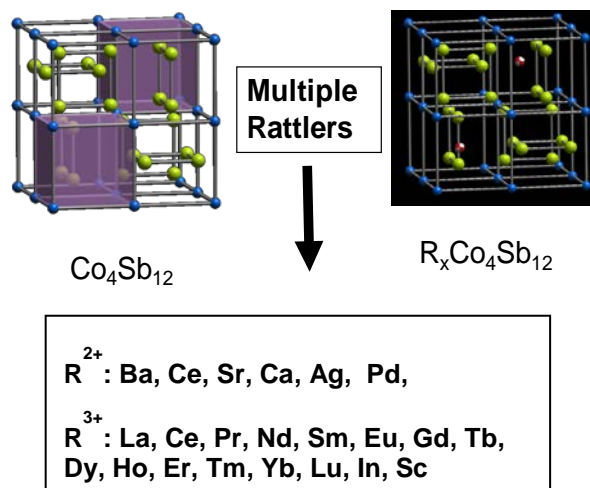


Figure 1. Skutterudite crystal structure and potential rattler elements for thermal conductivity suppression

Figure 1 shows the various elements that potentially can be inserted into the skutterudite crystal voids, which are being investigated in this project. This is the basis for one approach to developing high-performance TE materials.

Project Accomplishments

The project team focused this year on investigating and developing n-type skutterudites, $\text{In}_x\text{Ce}_y\text{Co}_4\text{Sb}_{12}$ and $\text{In}_{0.2}\text{Co}_4\text{Sb}_{12}$. The project team discontinued all work on p-type $\text{In}_x\text{Ce}_{0.15-y}\text{Yb}_y\text{FeCo}_3\text{Sb}_{12}$ skutterudite materials reported in fiscal year 2010 because of their low ZT values. The project team has investigated and quantified TE properties of various promising n-type compounds; completed the high-temperature structural property measurement system, which uses RUS techniques; measured high-temperature Young's modulus and Poisson's ratio of the $\text{In}_x\text{Ce}_y\text{Co}_4\text{Sb}_{12}$ and $\text{In}_{0.2}\text{Co}_4\text{Sb}_{12}$ materials; designed, integrated, and fabricated operating TE couples using the n-type skutterudite and LASTT materials; and measured the TE performance of the skutterudite / LASTT TE couples. Several objectives were achieved—namely establishing the thermal cycling effects on the n-type, $\text{In}_x\text{Ce}_y\text{Co}_4\text{Sb}_{12}$ and $\text{In}_{0.2}\text{Co}_4\text{Sb}_{12}$ materials; showing the Young's modulus and shear modulus decrease gradually as temperature increases; and demonstrating an operating TE

couple performance level of 7% conversion efficiency at a hot-side temperature, $T_h = 573$ K and cold-side temperature, $T_c = 313$ K. This TE couple conversion efficiency was the highest reported efficiency in the Office of Vehicle Technology Thermoelectrics Program. The efficiency was demonstrated at temperatures that are right in the middle of the waste heat recovery temperature range expected in light-duty and heavy-duty vehicle exhaust streams (300 K – 823 K).

Advanced Skutterudite TE Materials

Properties: This year, work was focused on two high-performance In,Ce-filled skutterudite TE compounds, $\text{In}_x\text{Ce}_y\text{Co}_4\text{Sb}_{12}$ and $\text{In}_{0.2}\text{Co}_4\text{Sb}_{12}$. This work leveraged on the fundamental n-type $\text{Co}_4\text{Sb}_{12}$ skutterudite composition work in 2009 and 2010, which identified these as the two most promising compositions that could be tailored into n-type TE materials and couples for waste heat recovery applications. One focus this year has been on developing more consistent hot-pressing and sintering (HPS) techniques to make these bulk TE materials more reproducible and easily transitioned into multiple-couple TE devices and fabrication techniques. Figure 2 shows the measured ZT of the different n-type $\text{In}_x\text{Ce}_y\text{Co}_4\text{Sb}_{12}$ and $\text{In}_{0.2}\text{Co}_4\text{Sb}_{12}$ skutterudite compounds fabricated with these HPS techniques. The ZT is defined in Equation (1) above.

The n-type $\text{In}_x\text{Ce}_y\text{Co}_4\text{Sb}_{12}$ materials in Figure 2 are a direct result of the development work in FY 2010. Work continued on these materials and on $\text{In}_{0.2}\text{Co}_4\text{Sb}_{12}$ materials shown in Figure 2 in FY 2011. The development experience with these materials ultimately led to HPS fabrication of the $\text{In}_{0.2}\text{Ce}_{0.15}\text{Co}_4\text{Sb}_{12}$ materials and their impressive ZT in Figure 2. The highest ZT reported this year is that of an $\text{In}_{0.2}\text{Ce}_{-0.1}\text{Co}_4\text{Sb}_{12}$ composition, which exhibited a measured ZT = 1.4 at 620 K as shown in Figure 2. The compound was determined to have the approximate stoichiometry of $\text{In}_{0.2}\text{Ce}_{-0.1}\text{Co}_4\text{Sb}_{12}$ using x-ray fluorescence (XRF) and solution chemistry techniques. The ZT results shown in Figure 2 are consistent with those reported on these materials at the 2010 International

Conference on Thermoelectrics [1, 2], except the peak ZT behavior in PNNL/OSU materials is at lower temperatures near 623 K. Figure 3 displays the Seebeck coefficient, α , electrical resistivity, ρ , and thermal conductivity ($\lambda = K_e + K_L$) as a function of temperature for the $\text{In}_x\text{Ce}_y\text{Co}_4\text{Sb}_{12}$ and $\text{In}_{0.2}\text{Co}_4\text{Sb}_{12}$ TE materials in Figure 2. The Seebeck coefficients are quite comparable for the different $\text{In}_x\text{Ce}_y\text{Co}_4\text{Sb}_{12}$ combinations in Figure 2b, but it is clear in Figure 3 that the driving mechanism for the superior power factor of the $\text{In}_{0.2}\text{Ce}_{0.15}\text{Co}_4\text{Sb}_{12}$ materials is their lower electrical resistivity at all temperatures measured.

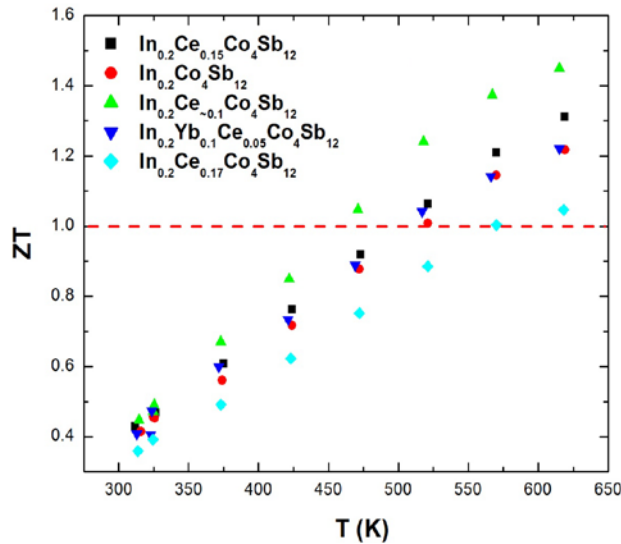


Figure 2. ZT of various n-type $\text{In}_x\text{Ce}_y\text{Co}_4\text{Sb}_{12}$ and $\text{In}_{0.2}\text{Co}_4\text{Sb}_{12}$ TE materials using sintering and hot-pressing processes (ZT before thermal cycling)

It is informative to observe how all these particular n-type InCe-based skutterudite compounds align relative to one another on one temperature-dependent ZT plot. Figure 2 shows this comprehensive ZT plot for the n-type materials investigated in FY 2010 and 2011, which allows quick comparisons of the n-type ZT values achieved and their different temperature dependencies. The temperature dependent behavior of these various n-type materials is critical to 1) determining the average ZT, which is the most important parameter in TE device design, and 2) providing important evaluations of material segmenting options and opportunities when designing devices across

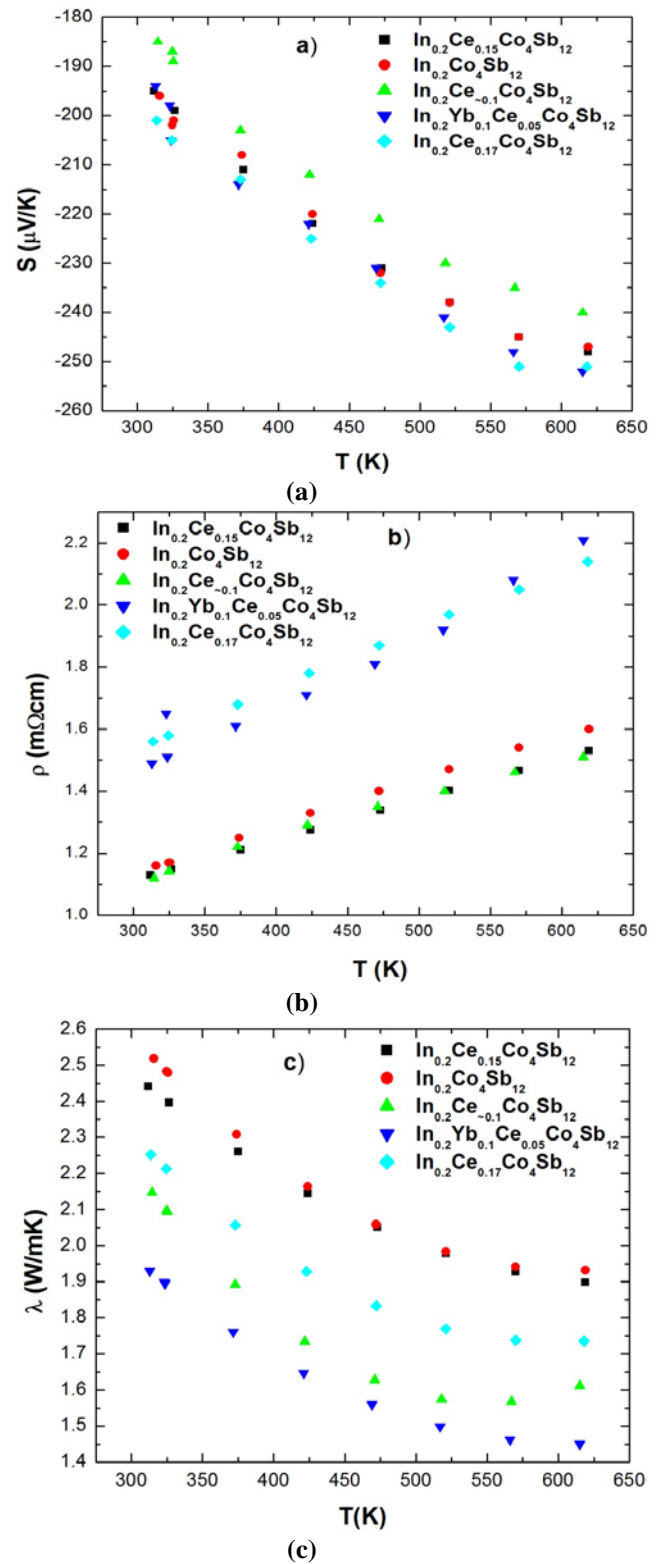


Figure 3. Seebeck coefficient (a), electrical resistivity (b), and thermal conductivity (c) of various n-type $\text{In}_x\text{Ce}_y\text{Co}_4\text{Sb}_{12}$ and $\text{In}_{0.2}\text{Co}_4\text{Sb}_{12}$ TE materials in Figure 2

large temperature differentials associated with waste energy recovery applications. This second point is especially critical in automotive energy recovery systems because temperature dependencies can be so sharp that attempting to design and operate a TE device with just one of these n-type materials in a TE element—even though it has a high-peak ZT—may not lead to high device performance.

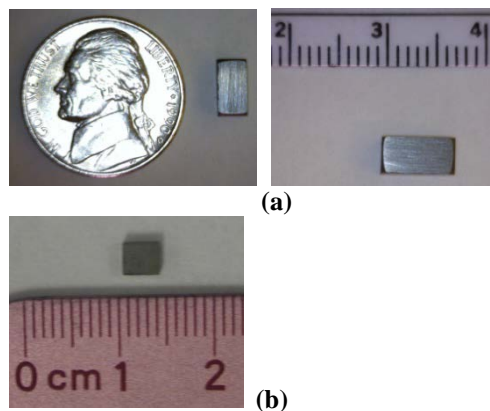


Figure 4. Typical n-type $\text{In}_{0.15}\text{Ce}_{0.1}\text{Co}_4\text{Sb}_{12}$ (a) and $\text{In}_{0.2}\text{Ce}_{0.15}\text{Co}_4\text{Sb}_{12}$ (b) skutterudite TE compounds developed during this program

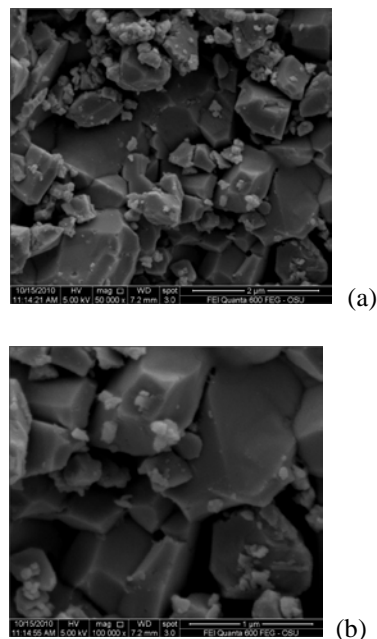


Figure 5. Scanning electron microscope image of $\text{In}_{0.2}\text{Ce}_{\sim 0.1}\text{Co}_4\text{Sb}_{12}$ at 2 μm resolution (a) and 1 μm resolution (b)

It is the average ZT across the entire temperature differential the TE device and elements “see”

that dictates device design optimization and performance. It is therefore often necessary to segment these advanced materials with other lower temperature materials (i.e., bismuth tellurides) to truly exploit their superior ZT characteristics in particular temperature ranges. The ZT versus temperature allows one to make the proper TE device design evaluations.

Figure 4 shows the actual rectangular parallelepiped skutterudite elements developed during this program this fiscal year and in prior years (i.e., FY 2010). Their height dimensions are also shown in Figure 4. Their cross-sectional dimensions (i.e., base widths) were generally 3 mm x 3mm in all the samples. These dimensions are quite similar to those expected in a final TE device using these materials and could be tailored to any given final waste heat recovery application. Figure 5 shows important scanning electron microscope images of the best performing n-type skutterudite composition, $\text{In}_{0.2}\text{Ce}_{\sim 0.1}\text{Co}_4\text{Sb}_{12}$ (shown in Figure 2).

Thermal Cycling Effects on TE Properties:

The project team reported work conducted last year on the thermal cycling impacts on the structural properties of these n-type skutterudite materials. Critically important work in FY 2011 investigated and established the thermal cycling impacts on the thermoelectric properties of some of the n-type skutterudite materials. The thermal cycling profile was generally 323 K to 673 K and back to 323 K over a 45-minute period, with 200 thermal cycles performed on each n-type material sample, which typically had dimensional characteristics similar to those shown in Figure 4. The n-type materials, $\text{In}_{0.2}\text{Ce}_{0.17}\text{Co}_4\text{Sb}_{12}$, $\text{In}_{0.2}\text{Ce}_{0.15}\text{Co}_4\text{Sb}_{12}$, $\text{In}_{0.2}\text{Co}_4\text{Sb}_{12}$, and $\text{In}_{0.2}\text{Ce}_{0.05}\text{Yb}_{0.1}\text{Co}_4\text{Sb}_{12}$, were taken through the thermal cycling profile. Their TE properties were measured before and after exposure to this thermal cycling profile. This type of thermal cycling is critically important in automotive waste heat recovery applications because automotive waste heat recovery (WHR) systems will experience this type of thermal cycling during typical on-off operations throughout the anticipated drive cycles (e.g.,

SC06, FTP75). Any TE material developed for these automotive WHR applications must be able to survive and perform after these thermal cycling exposures.

The effect of thermal cycling on Seebeck coefficient and electrical resistivity of $\text{In}_{0.2}\text{Ce}_{0.17}\text{Co}_4\text{Sb}_{12}$ is shown in Figure 6a and 6b, respectively.

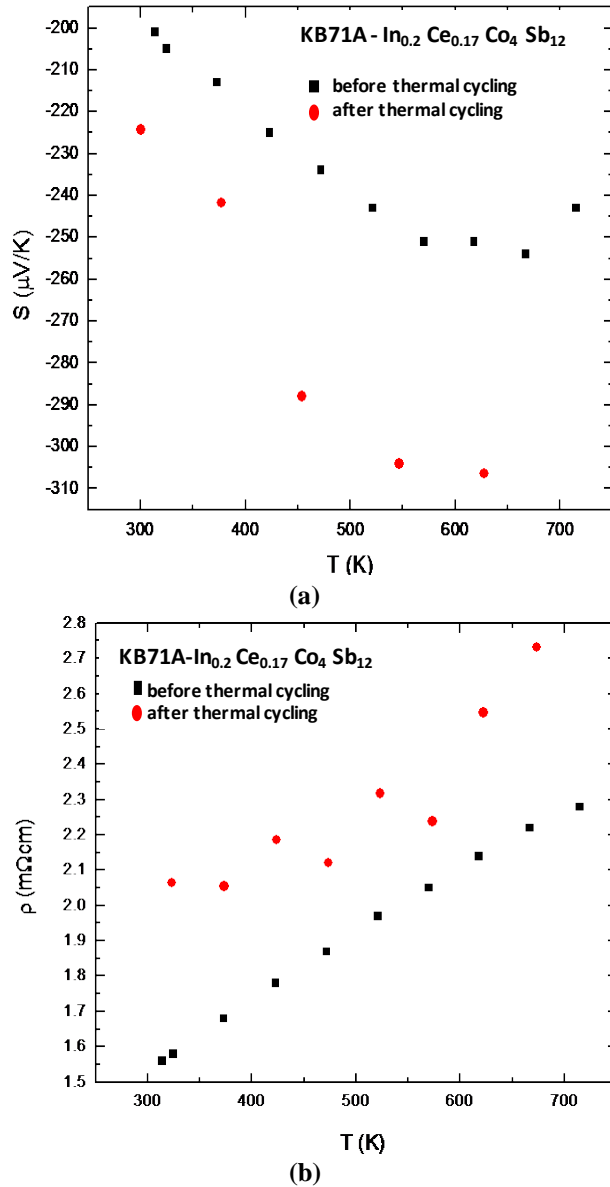


Figure 6. Thermal cycling effects on Seebeck coefficient (a) and electrical resistivity (b) in the $\text{In}_{0.2}\text{Ce}_{0.17}\text{Co}_4\text{Sb}_{12}$ skutterudite TE compounds

The Seebeck coefficient in Figure 6a is shown to increase significantly (i.e., approximately 24%

at 500 K - 600 K) after the thermal cycling exposure, while the electrical resistivity only increases by about 19% at 500 K - 600 K after thermal cycling. This causes the power factor in these materials to increase by about 36%. Figure 7 shows a similar increase in Seebeck coefficient demonstrated in $\text{In}_{0.2}\text{Ce}_{0.15}\text{Co}_4\text{Sb}_{12}$ compositions, where the Seebeck coefficient increased by approximately 13.5% after thermal cycling exposure.

Thermal cycling exposure also was shown to

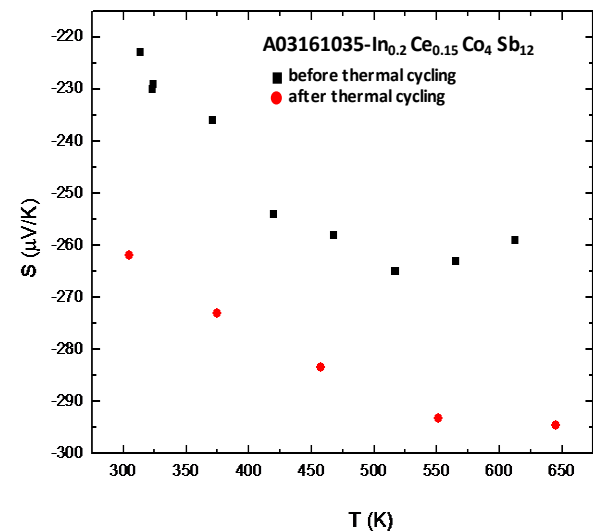


Figure 7. Thermal cycling effects on Seebeck coefficient in $\text{In}_{0.2}\text{Ce}_{0.15}\text{Co}_4\text{Sb}_{12}$ skutterudite TE compounds

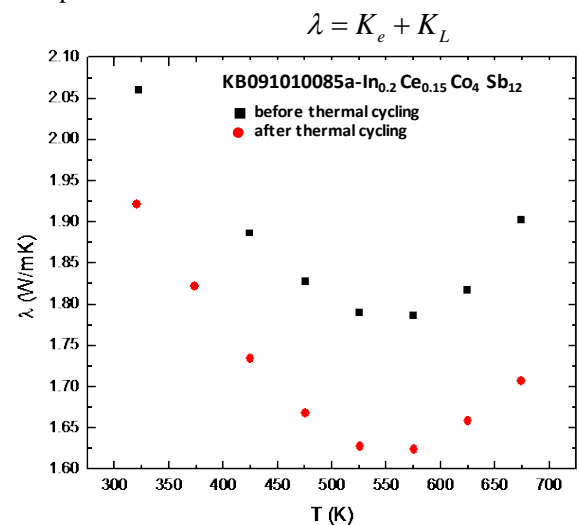


Figure 8. Thermal cycling effects on thermal conductivity in $\text{In}_{0.2}\text{Ce}_{0.15}\text{Co}_4\text{Sb}_{12}$ skutterudite TE compounds

decrease the thermal conductivity in $\text{In}_{0.2}\text{Ce}_{0.15}\text{Co}_4\text{Sb}_{12}$ compositions as shown in Figure 8. Figure 8 data show the thermal conductivity decreasing by 8-10% at 600 K.

During FY 2010, the project team also investigated and developed $\text{In}_{0.2}\text{Co}_4\text{Sb}_{12}$ compounds, which also showed good ZT values in Figure 2. Work continued on developing and characterizing these $\text{In}_{0.2}\text{Co}_4\text{Sb}_{12}$ compounds in FY 2011, particularly investigating thermal cycling effects in these $\text{In}_{0.2}\text{Co}_4\text{Sb}_{12}$ materials using the same thermal cycling profile discussed above. Figure 9 shows the thermal cycling effects on the thermal conductivity of these compounds, with the thermal conductivity staying approximately the same or perhaps decreasing about 3% after thermal cycling between 323 K and 673 K. The observed impact of thermal cycling was therefore smaller in the $\text{In}_{0.2}\text{Co}_4\text{Sb}_{12}$ compounds than in the $\text{In}_{0.2}\text{Ce}_{0.15}\text{Co}_4\text{Sb}_{12}$ compositions (shown in Figure 8). This was the first known work to demonstrate or observe the thermal cycling effects on these skutterudite compounds. Further research work is required to confirm this effect, further quantify its magnitude, and identify its fundamental material science cause.

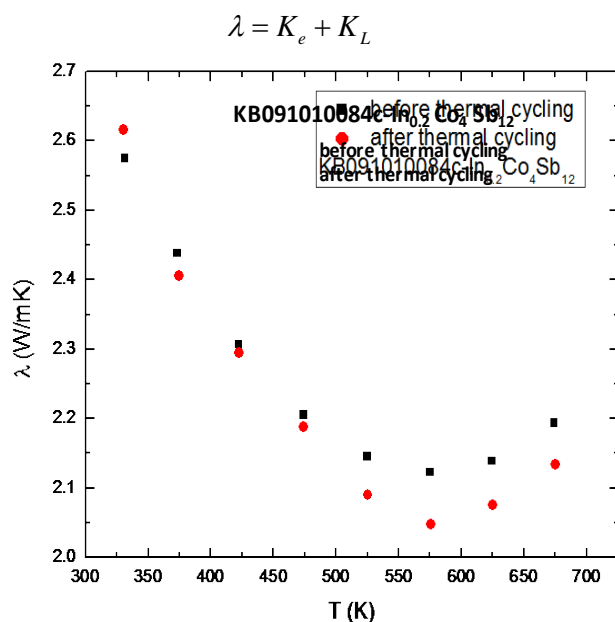


Figure 9. Thermal cycling effects on thermal conductivity in $\text{In}_{0.2}\text{Co}_4\text{Sb}_{12}$ skutterudite TE compounds

The project continued investigating other heavy-element fillers in FY 2010 by using ytterbium (Yb) as a third filler element with In and Ce. Two n-type skutterudite compounds were investigated, fabricated, and characterized: (1) n-type $\text{In}_{0.2}\text{Ce}_{0.1}\text{Yb}_{0.05}\text{Co}_4\text{Sb}_{12}$, and (2) $\text{In}_{0.2}\text{Ce}_{0.05}\text{Yb}_{0.1}\text{Co}_4\text{Sb}_{12}$. The HPS process was once again used to produce these triply-filled (i.e., multiple-rattler) skutterudite compounds.

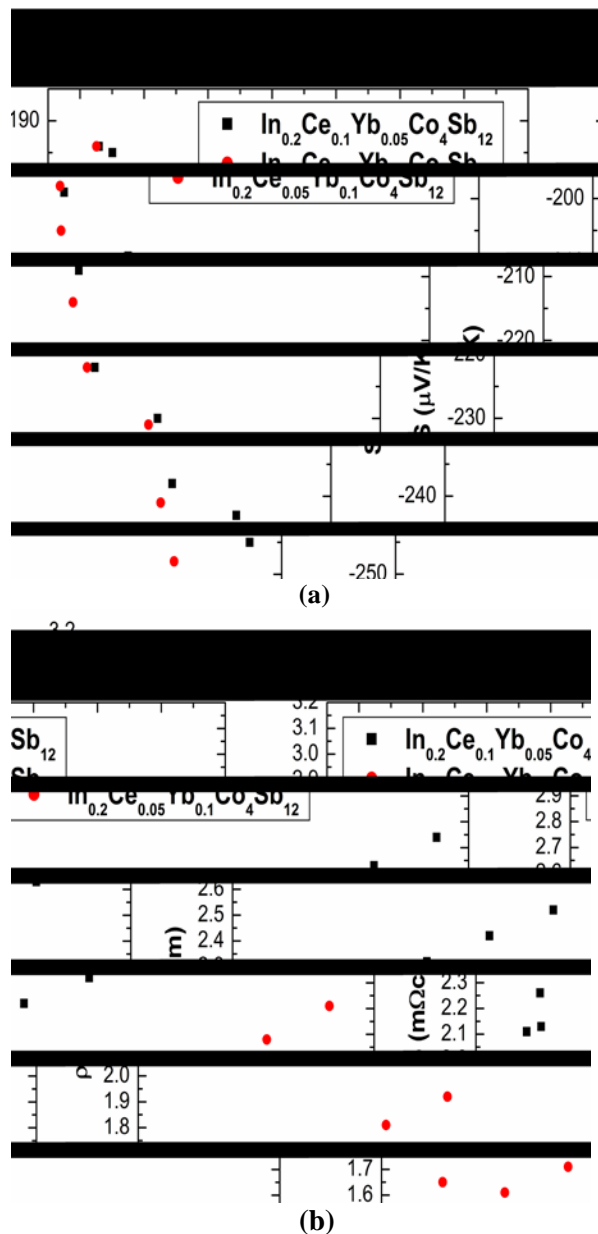


Figure 10. Seebeck coefficient (a) and electrical resistivity (b) of n-type $\text{In}_{0.2}\text{Ce}_{0.1}\text{Yb}_{0.05}\text{Co}_4\text{Sb}_{12}$ and $\text{In}_{0.2}\text{Ce}_{0.05}\text{Yb}_{0.1}\text{Co}_4\text{Sb}_{12}$ TE compounds in FY 2010

Figure 10 shows the Seebeck coefficient (a) and electrical resistivity (b) of these two skutterudite compounds. The Seebeck coefficient of the two compounds is very similar in behavior and magnitude, but there is a marked difference in electrical resistivity with the n-type $\text{In}_{0.2}\text{Ce}_{0.05}\text{Yb}_{0.1}\text{Co}_4\text{Sb}_{12}$ compound having a much lower electrical resistivity. Figure 11 displays the thermal conductivity (a) and the resulting ZT value (b) of these two triply-filled skutterudite compounds. Figure 11a demonstrates the thermal conductivity of the $\text{In}_{0.2}\text{Ce}_{0.05}\text{Yb}_{0.1}\text{Co}_4\text{Sb}_{12}$ compound is also lower than in the $\text{In}_{0.2}\text{Ce}_{0.1}\text{Yb}_{0.05}\text{Co}_4\text{Sb}_{12}$ compound.

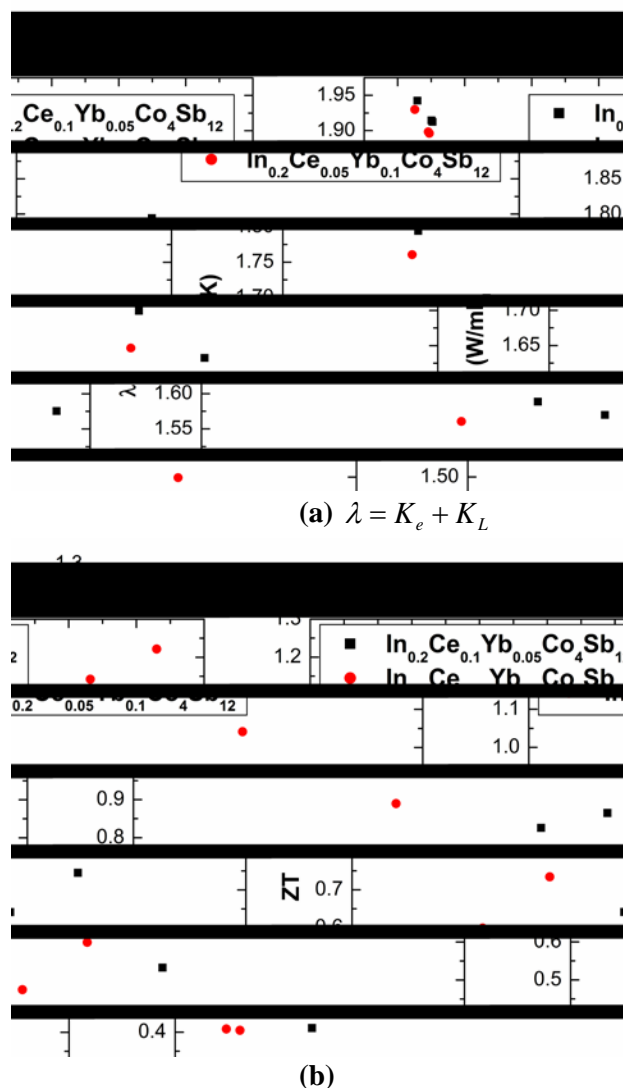


Figure 11. Thermal conductivity (a) and ZT values (b) for n-type $\text{In}_{0.2}\text{Ce}_{0.1}\text{Yb}_{0.05}\text{Co}_4\text{Sb}_{12}$ and $\text{In}_{0.2}\text{Ce}_{0.05}\text{Yb}_{0.1}\text{Co}_4\text{Sb}_{12}$ TE compositions in Figure 10

Both of these effects lead to the significantly higher ZT values for the $\text{In}_{0.2}\text{Ce}_{0.05}\text{Yb}_{0.1}\text{Co}_4\text{Sb}_{12}$ compound in Figure 11b, with ZT surpassing 1.2 at about 620 K.

The effect of thermal cycling was investigated on the $\text{In}_{0.2}\text{Ce}_{0.05}\text{Yb}_{0.1}\text{Co}_4\text{Sb}_{12}$ in FY 2011 as it was the better performing composition. Figure 12 shows the impact of thermal cycling on these compounds. These materials exhibited a much different behavior after thermal cycling, with the

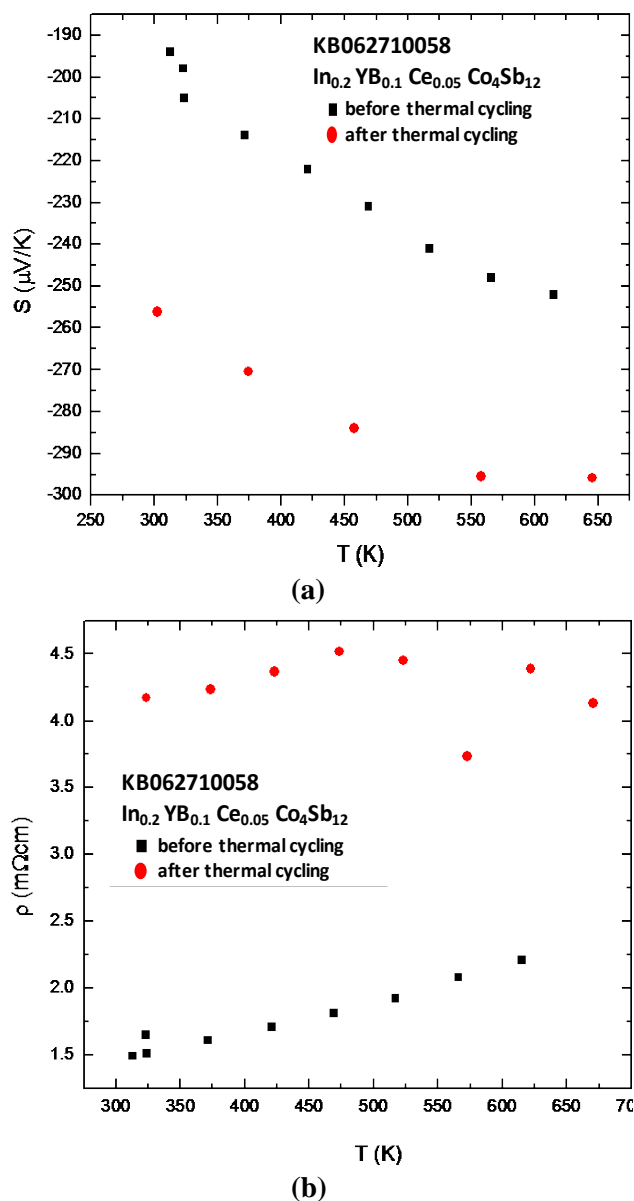


Figure 12. Impact of thermal cycling on Seebeck coefficient (a) and electrical resistivity (b) of the n-type $\text{In}_{0.2}\text{Ce}_{0.05}\text{Yb}_{0.1}\text{Co}_4\text{Sb}_{12}$ compounds

power factor (α^2/ρ) decreasing about 36% at 500 K – 600 K. This was caused by a strong increase in electrical resistivity after thermal cycling. It is believed this type of thermal cycling behavior is caused by the formation of meta-stable states in this triply-filled skutterudite. This type of thermal cycling effect and behavior cannot be tolerated in vehicle WHR applications and system design. It is apparent that thermal cycling effects and behavior can be a critically important differentiator in determining how many rattling elements can be inserted into the skutterudite crystal voids and still maintain a stable crystal structure under all anticipated vehicle WHR operating environments. It can essentially dictate what multi-filled skutterudites can be used in vehicle WHR applications.

The method used in fabricating all these n-type materials incorporated ball milling processes into the HPS fabrication process discussed in the FY 2010 work. All of these InCe-based skutterudites are bulk materials, making them much easier to integrate into TE devices, and therefore, easier to commercialize in operating devices and systems.

X-Ray Diffraction Patterns of Advanced Skutterudite Materials:

XRD analysis was performed on the various n-type skutterudite materials shown in Figure 2. Figure 13 displays the XRD patterns obtained for the various n-type and p-type skutterudite materials in the above discussion. These analyses demonstrate these materials are pure, single-phase compounds. The XRD patterns allow one to calculate the lattice parameter, a , [units are Angstroms, Å] that is shown in each XRD pattern for the various material compositions analyzed in Figure 13. The lattice parameter, a , is a measure of the cubic crystal dimension in the basic $\text{Co}_4\text{Sb}_{12}$ cubic structure. Slight, visually-hard-to-see shifts occur in resonance angles that allow researchers to detect the very slight changes in lattice parameter, a , as more heavy filler atoms are added to the basic $\text{Co}_4\text{Sb}_{12}$ crystal structure. The lattice parameter, a , clearly increases in Figure 13 as more heavy filler atoms are added into skutterudite crystal voids.

Structural Properties: In 2010 the project team completed and reported on characterizing the room-temperature structural properties, Young's modulus, E ; and Poisson's ratio, ν ; thermal cycling impacts on structural properties, and the CTE at high temperature for several n-type $\text{Co}_4\text{Sb}_{12}$, $\text{In}_x\text{Ce}_y\text{Co}_4\text{Sb}_{12}$, and $\text{In}_x\text{Ce}_y\text{Yb}_z\text{Co}_4\text{Sb}_{12}$ compounds and p-type $\text{In}_x\text{Ce}_{0.15-y}\text{Yb}_y\text{FeCo}_3\text{Sb}_{12}$ compounds. This year (FY 2011) the project team completed high-temperature measurements of Young's modulus, shear modulus, and Poisson's ratio using the high-temperature RUS system shown in Figures 14–15, along with the typical sample measurement configuration between the input transducers.

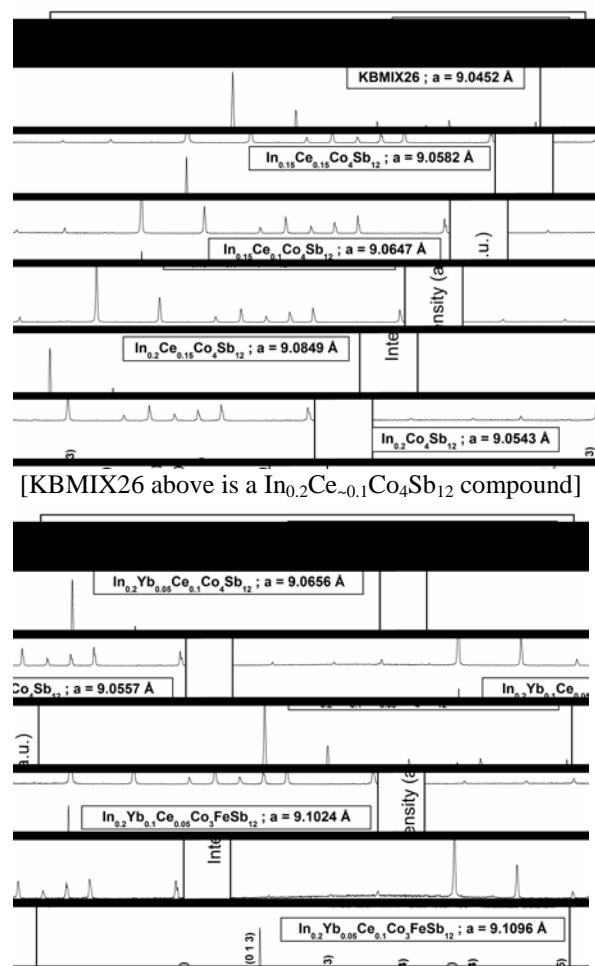


Figure 13. XRD patterns for various n-type and p-type skutterudites

Generally, a vibrational signal is input to the sample, and the resulting frequency response

signal then is generated from the sample, which can be measured and the appropriate sample resonant frequencies identified. These resonant frequencies then are inversely analyzed using sophisticated sample structural modeling software to determine Young's modulus and Poisson's ratio of the sample. The sample dimensions, surface planarity, and accuracy of the 90-degree edges and corners are critical to this measurement technique and can greatly impact measurement accuracy. Significant success was demonstrated with sample preparation this year, as evidenced by the extensive structural property data measured and presented below.

The entire RUS thermal chamber was completed during FY 2010. Figure 14 is a schematic and SolidWorks rendering of the thermal chamber design, and Figure 15 shows the completed thermal chamber. Additional FY 2011 work focused on optimizing the thermal performance of the high-temperature thermal chamber and transducers necessary for obtaining the structural properties of TE materials up to 573 K (300°C). The project team successfully automated the chamber thermal performance to allow it to achieve preset temperatures for the structural measurements. During FY 2011, a new high-temperature transducer design was developed to provide more reliable and consistent RUS signals in the high-temperature structural property measurements conducted in FY 2011. This new transducer design shown in Figure 16 was integrated into the high-temperature thermal chamber system shown in Figures 14 and 15 and with the RUS control and analysis software to produce high-temperature structural property measurements, E and ν , in FY 2011.

High-temperature structural measurements were performed on $In_{0.2}Ce_{0.15}Co_4Sb_{12}$ and $In_{0.2}Co_4Sb_{12}$ materials in FY 2011. Figure 17 illustrates the typical TE element sizes and configurations used in the structural measurements. Figure 18 shows the Young's modulus (i.e., elastic modulus, E) and shear modulus (G) for these two skutterudite compositions at temperatures up to 573 K (300°C). Figure 19 shows the Poisson's

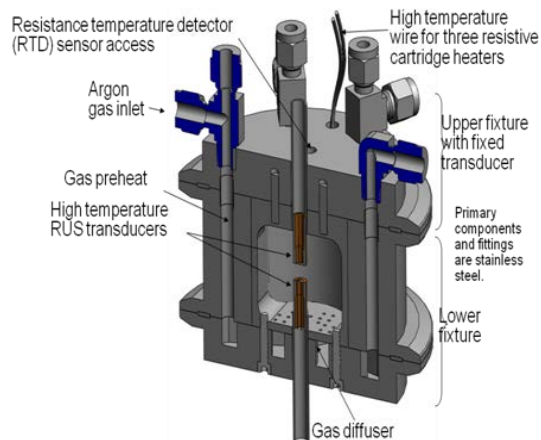


Figure 14. High-temperature thermal chamber design for high-temperature structural measurements

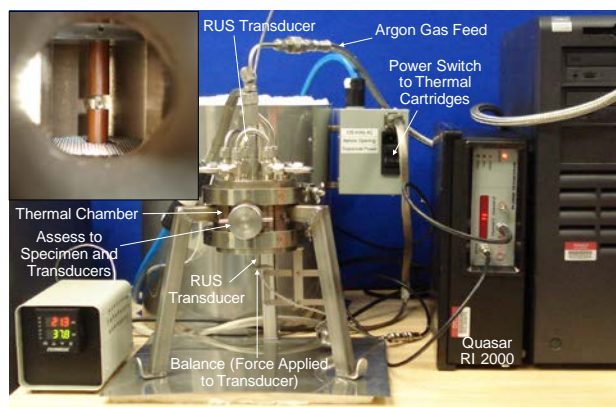


Figure 15. High-temperature thermal chamber fabricated in FY 2010

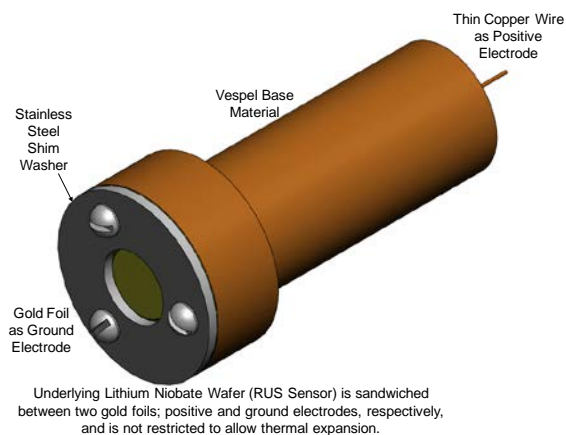


Figure 16. High-temperature RUS transducer design for high-temperature structural measurements

ratio, ν , at temperatures up to 573 K (300°C). This is the first measurement of these high-temperature structural properties for $In_{0.2}Ce_{0.15}Co_4Sb_{12}$ and $In_{0.2}Co_4Sb_{12}$ materials

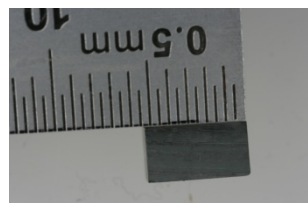
ever reported. The elastic modulus in both materials smoothly decreases as temperature increases up to 573 K. The shear modulus in both materials also smoothly decreases as the temperature increases up to 573 K. Measurements in Figure 18 show the elastic modulus of $\text{In}_{0.2}\text{Ce}_{0.15}\text{Co}_4\text{Sb}_{12}$ is slightly lower than that for $\text{In}_{0.2}\text{Co}_4\text{Sb}_{12}$ across the temperature range. Similarly, the shear modulus of $\text{In}_{0.2}\text{Ce}_{0.15}\text{Co}_4\text{Sb}_{12}$ is slightly lower than that for $\text{In}_{0.2}\text{Co}_4\text{Sb}_{12}$ across the temperature range. This structural property data are critical for determining internal and interface stresses in operating TE devices, integrating these TE materials with other module-level structural components, designing effective component interfaces within a TE device, and generally transitioning these materials into operating TE modules.



a) $\text{In}_{0.2}\text{Ce}_{\sim 0.1}\text{Co}_4\text{Sb}_{12}$ – n-type

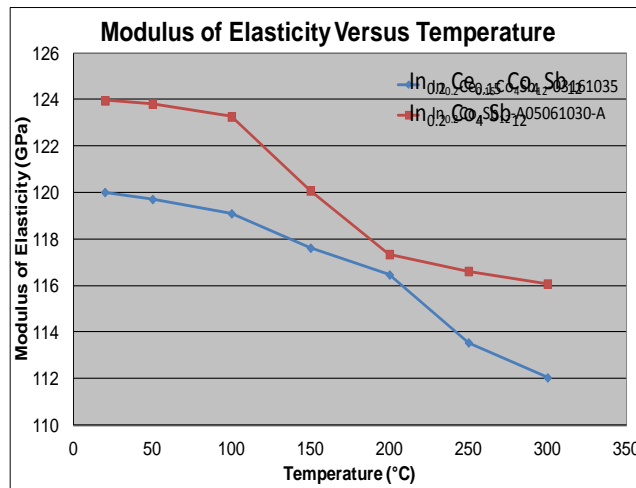


b) $\text{In}_{0.2}\text{Ce}_{0.17}\text{Co}_4\text{Sb}_{12}$ – n-type

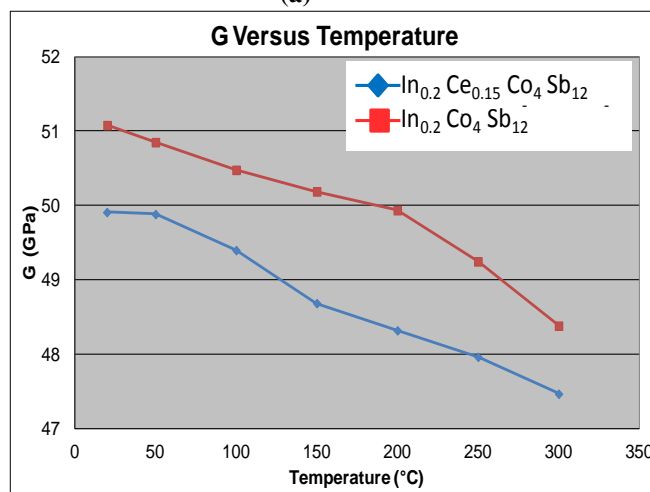


c) $\text{In}_{0.2}\text{Ce}_{0.05}\text{Yb}_{0.1}\text{Co}_4\text{Sb}_{12}$ n-type

Figure 17. Typical n-type $\text{In}_x\text{Ce}_y\text{Co}_4\text{Sb}_{12}$ and $\text{In}_{0.2}\text{Ce}_{0.05}\text{Yb}_{0.1}\text{Co}_4\text{Sb}_{12}$ TE samples for structural measurements. Samples were all about 0.5 cm long.



(a)



(b)

Figure 18. Modulus of elasticity, E, (a) and shear modulus, G, (b) as a function of temperature for $\text{In}_{0.2}\text{Ce}_{0.15}\text{Co}_4\text{Sb}_{12}$ and $\text{In}_{0.2}\text{Co}_4\text{Sb}_{12}$ skutterudites

These data represent a major milestone and achievement on this project in FY 2011.

Thermoelectric Couple Fabrication and Test:

PNNL worked with and subcontracted to Tellurex Corporation, Traverse City, Michigan, in FY 2011 to design, fabricate, and test the first TE couples ever fabricated using the n-type $\text{In}_{0.2}\text{Ce}_{0.15}\text{Co}_4\text{Sb}_{12}$ and n-type $\text{In}_{0.2}\text{Co}_4\text{Sb}_{12}$ skutterudite compounds. The p-n couples were formed using two p-type TE materials; one was constructed by coupling the n-type $\text{In}_{0.2}\text{Ce}_{0.15}\text{Co}_4\text{Sb}_{12}$ with p-type LASTT elements, and the second was constructed by coupling the n-type $\text{In}_{0.2}\text{Co}_4\text{Sb}_{12}$ with p-type bismuth

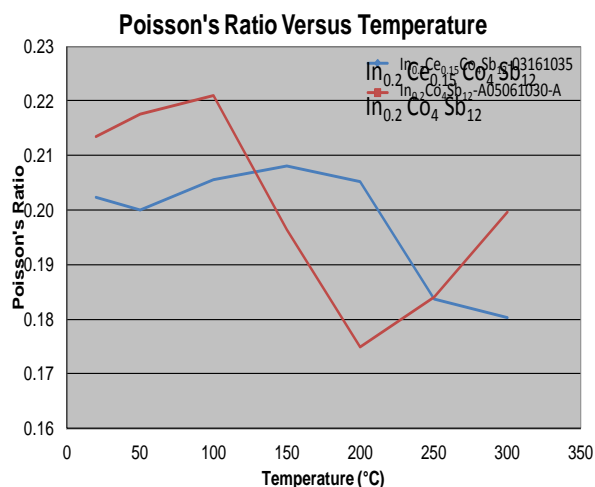


Figure 19. Poisson's ratio as a function of temperature for $\text{In}_{0.2}\text{Ce}_{0.15}\text{Co}_4\text{Sb}_{12}$ and $\text{In}_{0.2}\text{Co}_4\text{Sb}_{12}$ skutterudite materials

telluride elements. The n-type skutterudites were found to be easy to handle, quite wettable with standard solders, and reasonable easy to work with during the couple manufacturing process. The TE couple fabrication and test took place at Tellurex Corporation. Figure 20 displays the typical couple fabricated with n-type $\text{In}_{0.2}\text{Ce}_{0.15}\text{Co}_4\text{Sb}_{12}$ skutterudite and the p-type LASTT materials.



Figure 20. Pioneering TE couple fabricated from p-type LASTT and n-type $\text{In}_{0.2}\text{Ce}_{0.15}\text{Co}_4\text{Sb}_{12}$ materials

The TE couples were transferred into the TE couple test chamber shown in Figure 21 after fabrication. The test chamber contained all the necessary heater blocks, conductive and radiative insulation, temperature sensors, voltage and current sensors required to measure TE couple hot-side and cold-side temperatures and voltage and current outputs as shown in Figures

20 and 21. The TE couple power output was connected to variable load resistance devices that accurately monitored and measured the load resistance on the TE couple. Figure 20 also shows the location of the hot-side and cold-side thermocouple locations in the TE couple test configuration.

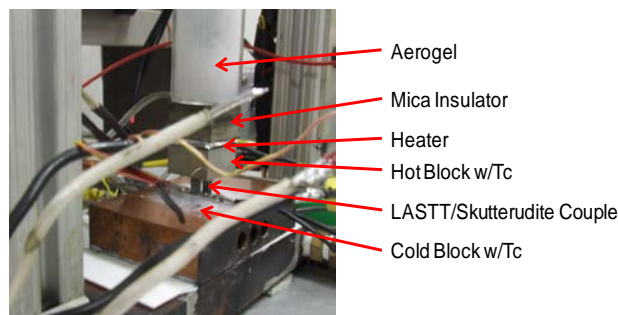
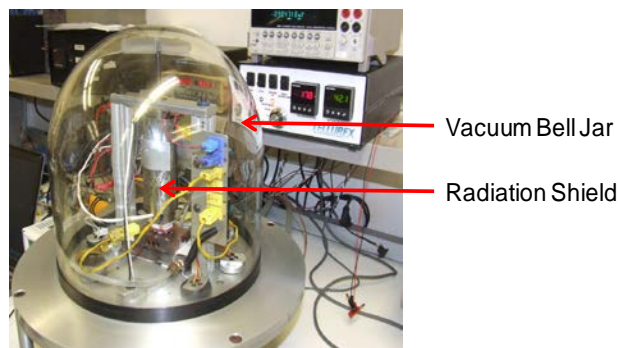


Figure 21. TE couple test chamber with associated test hardware and temperature sensors (Tc indicates temperature thermocouple location)

The TE couple tests were generally conducted by holding hot-side and cold-side temperatures constant with calibrated heating systems and measuring the current-voltage outputs at varying load resistance values. The hot-side heater power was accurately measured to know the hot-side thermal input at all times during the TE couple testing.

Figures 22 and 23 show the power output and TE conversion efficiency, respectively, of the TE couple using the n-type $\text{In}_{0.2}\text{Co}_4\text{Sb}_{12}$ skutterudite with p-type bismuth telluride materials. The power output and TE conversion efficiency were measured as a function of load resistance at hot-side temperatures, T_h , of 423 K

(150°C), 473 K (200°C), 523 K (250°C), 573 K (300°C) and 598 K (325°C) with a constant cold-side temperature, T_c , of 313 K (40°C). Test data were compared with theoretical predictions (solid line curves) for the test configuration and system shown in Figures 20 and 21. Figures 22 and 23 show very good correlation between the test data (points on the curves) and the theoretical predictions (solid lines). This TE couple performed quite well with high power outputs at $T_h = 598$ K and a tested TE conversion efficiency of 7% at $T_h = 598$ K and $T_c = 313$ K. This test conversion efficiency for this n-type $\text{In}_{0.2}\text{Co}_4\text{Sb}_{12}$ skutterudite /p-type bismuth telluride couple was the highest that PNNL and Tellurex Corporation have ever observed at these hot-side and cold-side temperatures.

Figures 24 and 25 show the power output and TE conversion efficiency, respectively, of the TE couple using the n-type $\text{In}_{0.2}\text{Ce}_{0.15}\text{Co}_4\text{Sb}_{12}$ with p-type LASTT materials. The power output and TE conversion efficiency were measured as a function of load resistance at hot-side temperatures, T_h , of 423 K (150°C), 473 K (200°C), 523 K (250°C), and 573 K (300°C) with a constant cold-side temperature, T_c , of 313 K (40°C). Test data again were compared with theoretical predictions (solid line curves) for the test configuration and system shown in Figures 20 and 21. Figures 24 and 25 again show good correlation between the test data (points on the curves) and the theoretical predictions (solid lines). This TE couple also performed quite well with high power outputs at $T_h = 573$ K and a tested TE conversion efficiency of 7% at $T_h = 573$ K and $T_c = 313$ K. This tested conversion efficiency for this n-type $\text{In}_{0.2}\text{Ce}_{0.15}\text{Co}_4\text{Sb}_{12}$ skutterudite/ p-type LASTT couple was once again the highest that PNNL and Tellurex Corporation personnel had ever seen at these hot-side and cold-side temperatures. Additional theoretical TE modeling work, with the same theoretical models correlated in Figures 22-25, demonstrated that using segmented element designs incorporating p-type LASTT/p-type bismuth telluride and n-type $\text{In}_{0.2}\text{Co}_4\text{Sb}_{12}$ skutterudite/n-type bismuth telluride would produce theoretically-predicted TE conversion

efficiencies of 9.3% at hot-side and cold-side temperatures of $T_h = 668$ K (395°C) and $T_c = 313$ K (40°C). Note that the T_h and T_c conditions that these couples demonstrated this excellent performance are very close to the temperatures anticipated in light-duty and heavy-duty vehicle WHR applications currently being investigated and pursued by the DOE OVT.

These two TE couples have demonstrated excellent experimental performance in these couple tests. Note that these two couples, the n-type $\text{In}_{0.2}\text{Co}_4\text{Sb}_{12}$ skutterudite /p-type bismuth telluride couple and the n-type $\text{In}_{0.2}\text{Ce}_{0.15}\text{Co}_4\text{Sb}_{12}$ skutterudite/ p-type LASTT couple, performed superbly in a “real-world, as-fabricated” configuration with “real-world” electrical contact resistances and thermal contact resistances built into the couples. It is noteworthy and should be reiterated that the n-type skutterudites were found to be easy to handle, quite wettable with standard solders, and reasonable easy to work with during the couple manufacturing process. These two n-type skutterudite materials have shown excellent structural properties, very good thermal cycling properties, very good thermoelectric properties, and now very good couple manufacturing capabilities during this development project. These materials have now shown excellent TE couple performance at temperatures that are very close to temperatures expected in light- and heavy-duty vehicle WHR applications. It is strongly recommended these materials be transitioned into operating TE modules and systems through future applied research and development programs at the DOE OVT.



Single- Couple Performance
 $\text{In}_{0.2}\text{Co}_4\text{Sb}_{12}$ N Skutterudite/ Bi_2Te_3 P 9/6/11
 Load Power vs. Load Resistance

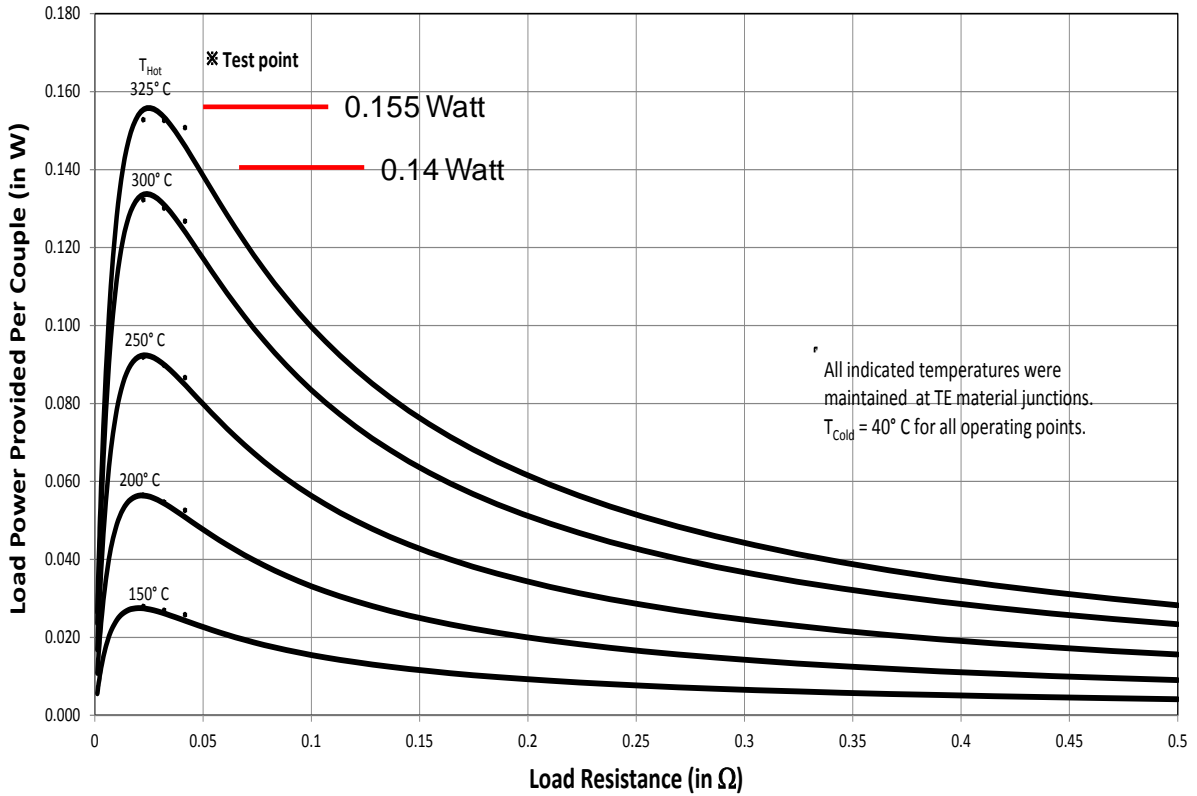


Figure 22. Power output of TE couple fabricated using the n-type $\text{In}_{0.2}\text{Co}_4\text{Sb}_{12}$ with p-type bismuth telluride - $T_{\text{hot}} = 423 \text{ K (150}^\circ\text{C)}$ to $598 \text{ K (325}^\circ\text{C)}$ shown next to each curve; $T_{\text{cold}} = 313 \text{ K (40}^\circ\text{C)}$ for all curves (test data points shown compared to theoretical test prediction solid-line curves)

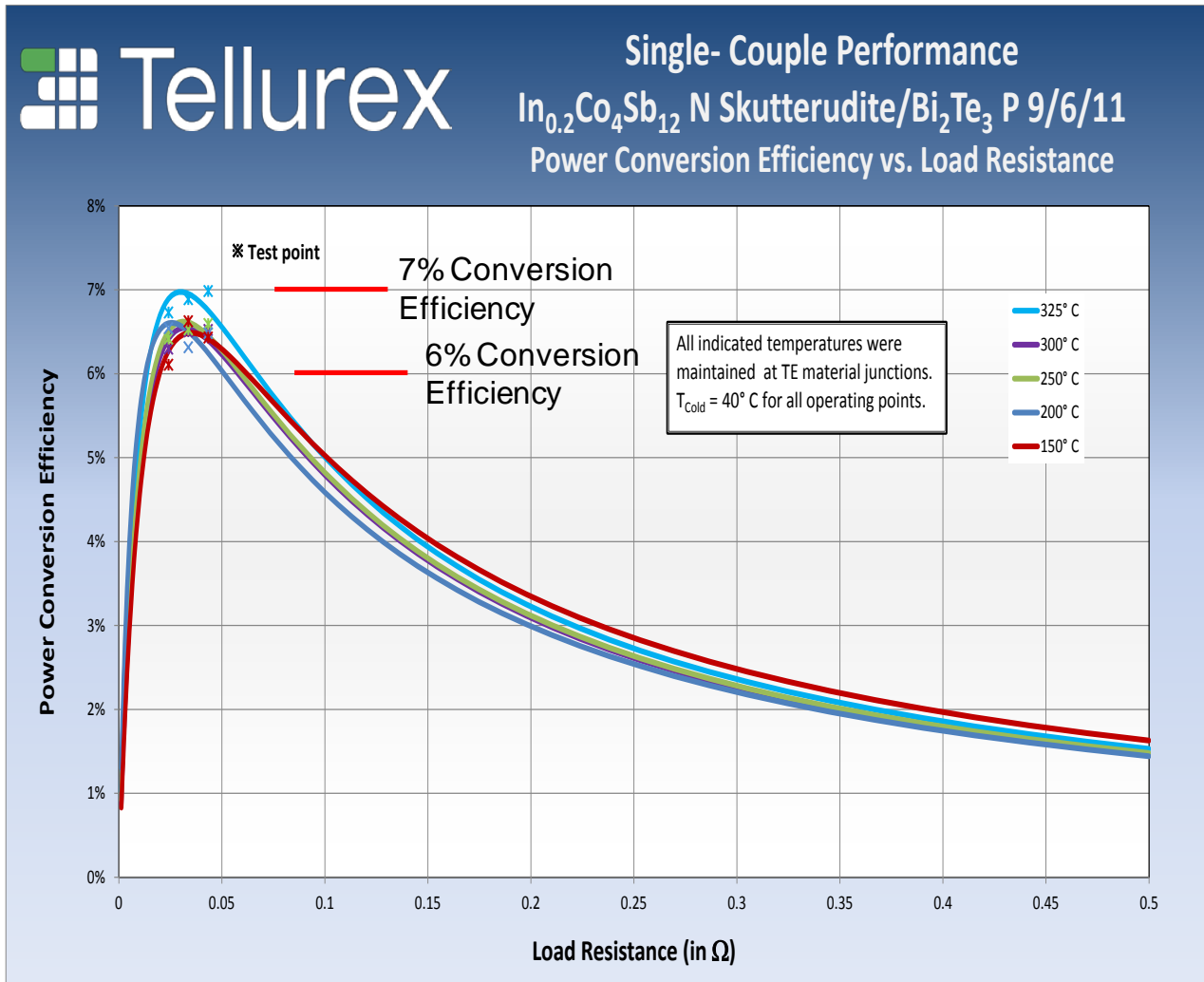


Figure 23. TE conversion efficiency of TE couple fabricated using the n-type $In_{0.2}Co_4Sb_{12}$ with p-type bismuth telluride - $T_{hot} = 423 K$ (150°C) to 598 K (325°C) shown for differing curves; $T_{cold} = 313 K$ (40°C) for all curves (test data points shown compared to theoretical test prediction solid-line curves)

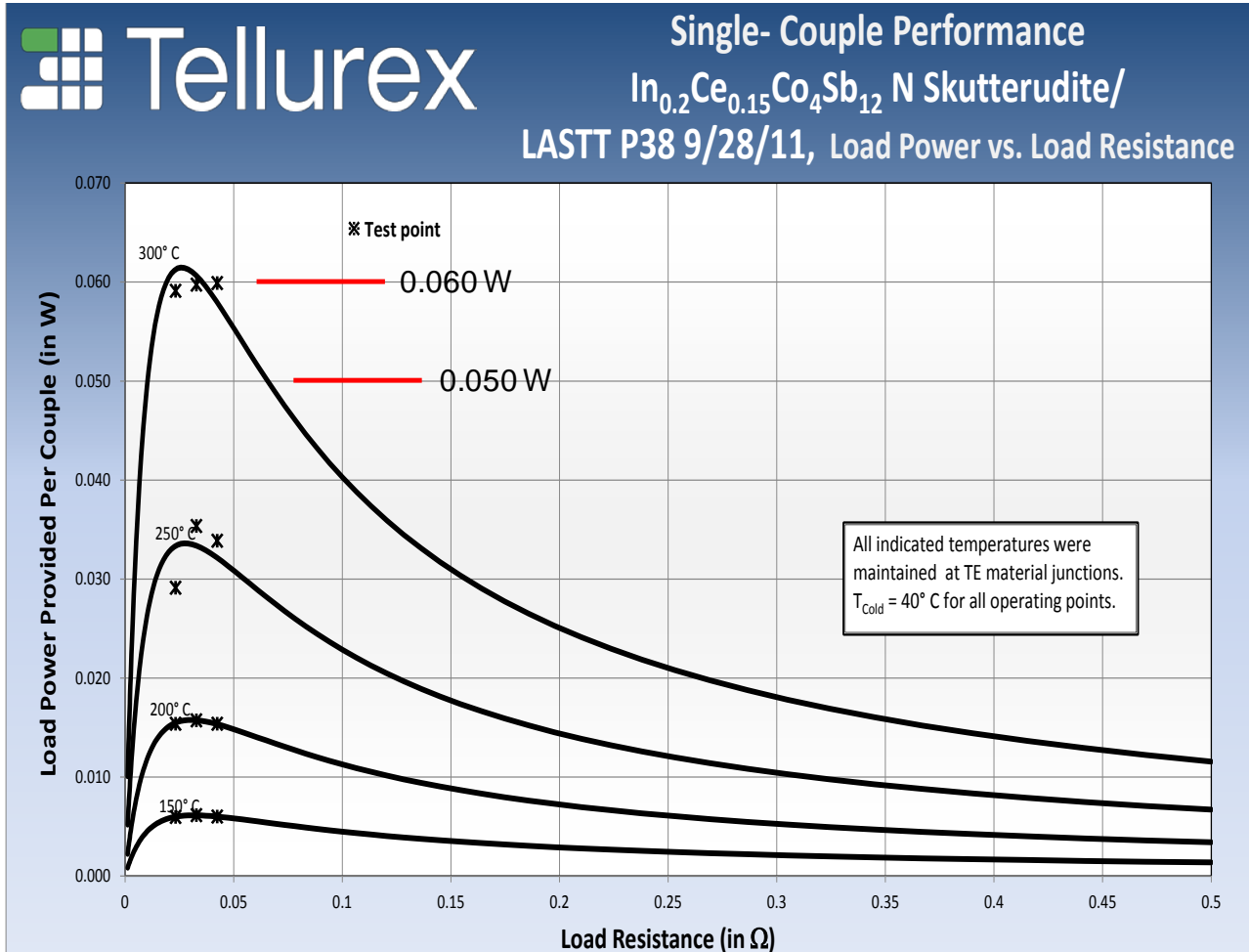


Figure 24. Power output of TE couple fabricated using n-type $\text{In}_{0.2}\text{Ce}_{0.15}\text{Co}_4\text{Sb}_{12}$ with p-type lead antimony silver tin telluride (LASTT) – $T_{\text{hot}} = 423\text{ K}$ (150°C) to 573 K (300°C) shown next to each curve; $T_{\text{cold}} = 313\text{ K}$ (40°C) for all curves (test data points shown compared to theoretical test prediction solid-line curves)



Single-Couple Performance
 $\text{In}_{0.2}\text{Ce}_{0.15}\text{Co}_4\text{Sb}_{12}\text{N}$ Skutterudite/

LASTT P38 9/28/11, Power Conversion Efficiency vs. Load Resistance

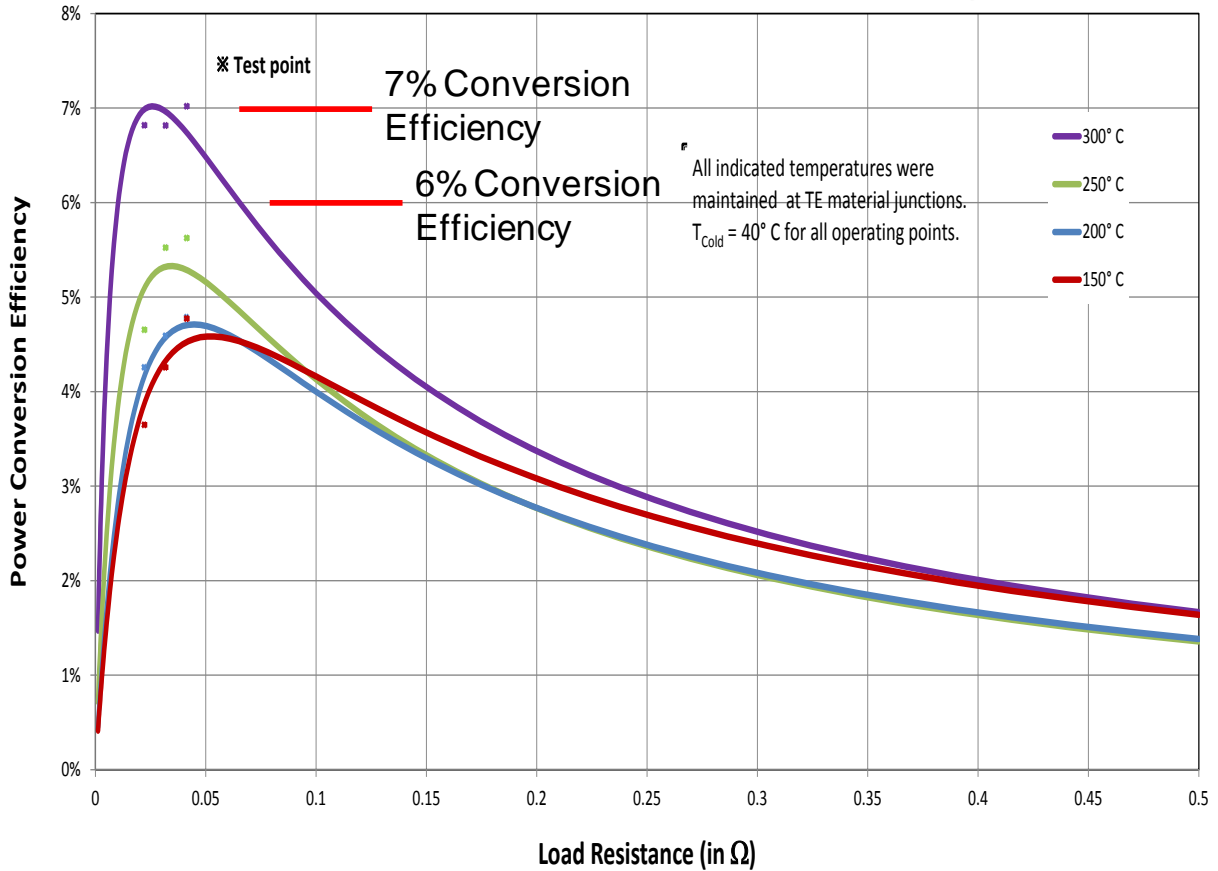


Figure 25. TE conversion efficiency of TE couple fabricated using n-type $\text{In}_{0.2}\text{Ce}_{0.15}\text{Co}_4\text{Sb}_{12}$ with p-type lead antimony silver tin telluride (LASTT) – $T_{\text{hot}} = 423\text{ K (150}^\circ\text{C)}$ to $573\text{ K (300}^\circ\text{C)}$ shown for differing curves; $T_{\text{cold}} = 313\text{ K (40}^\circ\text{C)}$ for all curves (test data points shown compared to theoretical test prediction solid-line curves)

Conclusions

- Several n-type InCe-based $\text{Co}_4\text{Sb}_{12}$ skutterudite compounds were fabricated and tested this year to support material development, thermal cycling studies, and TE couple fabrication and testing. The temperature-dependent thermoelectric properties of n-type $\text{In}_{0.15}\text{Ce}_{0.1}\text{Co}_4\text{Sb}_{12}$, $\text{In}_{0.2}\text{Ce}_{0.15}\text{Co}_4\text{Sb}_{12}$, $\text{In}_{0.2}\text{Co}_4\text{Sb}_{12}$ compounds were measured. $\text{In}_{0.2}\text{Ce}_{0.15}\text{Co}_4\text{Sb}_{12}$, $\text{In}_{0.2}\text{Co}_4\text{Sb}_{12}$, and $\text{In}_{0.2}\text{Ce}_{0.05}\text{Yb}_{0.1}\text{Co}_4\text{Sb}_{12}$ compounds showed the best TE property performance, with $\text{In}_{0.2}\text{Co}_4\text{Sb}_{12}$ and $\text{In}_{0.2}\text{Ce}_{0.05}\text{Yb}_{0.1}\text{Co}_4\text{Sb}_{12}$ exhibiting ZT values as high as 1.2 at 623 K and $\text{In}_{0.2}\text{Ce}_{0.15}\text{Co}_4\text{Sb}_{12}$ and $\text{In}_{0.2}\text{Ce}_{\sim 0.1}\text{Co}_4\text{Sb}_{12}$ showing ZT values of 1.3 to 1.4 at 623 K.
- The new high-temperature RUS system and transducers required for high-temperature structural measurements were fully functional this year. The high-temperature RUS control system was completed and fully automated to achieve any specified temperature up to 573 K (300°C).
- High-temperature measurements of Young's modulus (i.e., elastic modulus), shear modulus, and Poisson's ratio on $\text{In}_{0.2}\text{Ce}_{0.15}\text{Co}_4\text{Sb}_{12}$ and $\text{In}_{0.2}\text{Co}_4\text{Sb}_{12}$ compositions (best performing n-type TE materials) were successfully performed using the new high-temperature RUS equipment in FY 2011. These measurements were conducted at temperatures up to 573 K (300°C). Sample preparation was critical to making high-quality structural measurements using the RUS technique.
- The Young's modulus and shear modulus of $\text{In}_{0.2}\text{Ce}_{0.15}\text{Co}_4\text{Sb}_{12}$ and $\text{In}_{0.2}\text{Co}_4\text{Sb}_{12}$ compounds gradually decreased in value as temperature increased from 300 K to 573 K. These high-temperature structural property measurements are the first-reported measurements at high temperature for these two skutterudite materials. No structural changes were noted in the materials; just a commonly seen gradual decrease in the property value as temperature increased.
- The project performed thermal cycling from 50°C to 400°C (200 cycles) on $\text{In}_{0.2}\text{Ce}_{0.15}\text{Co}_4\text{Sb}_{12}$, $\text{In}_{0.2}\text{Ce}_{0.17}\text{Co}_4\text{Sb}_{12}$, $\text{In}_{0.2}\text{Co}_4\text{Sb}_{12}$, and $\text{In}_{0.2}\text{Ce}_{0.05}\text{Yb}_{0.1}\text{Co}_4\text{Sb}_{12}$ compounds materials to determine impacts on thermoelectric properties. The thermal cycling created a significant increase in Seebeck coefficient and power factor in dual-rattler skutterudites $\text{In}_{0.2}\text{Ce}_{0.15}\text{Co}_4\text{Sb}_{12}$ and $\text{In}_{0.2}\text{Ce}_{0.17}\text{Co}_4\text{Sb}_{12}$, respectively. Power factors increased by 36% at 500 – 600 K in the $\text{In}_{0.2}\text{Ce}_{0.17}\text{Co}_4\text{Sb}_{12}$ compound. However, thermal cycling created a significant decrease (i.e., 36% reduction at 500–600 K) in the power factor of the triple-rattler $\text{In}_{0.2}\text{Ce}_{0.05}\text{Yb}_{0.1}\text{Co}_4\text{Sb}_{12}$ compound. Researchers believe this was caused by meta-stable state formation in this triple-filled skutterudite compound. Thermal cycling caused this compound to degenerate and electrical resistivity to increase dramatically.
- Thermal cycling also caused the thermal conductivity to decrease slightly (3-8%) in $\text{In}_{0.2}\text{Ce}_{0.15}\text{Co}_4\text{Sb}_{12}$ and $\text{In}_{0.2}\text{Co}_4\text{Sb}_{12}$ compounds. This, coupled with the thermal-cycling-induced increase in power factors of $\text{In}_{0.2}\text{Ce}_{0.15}\text{Co}_4\text{Sb}_{12}$ and $\text{In}_{0.2}\text{Ce}_{0.17}\text{Co}_4\text{Sb}_{12}$, indicates that ZT values in Figure 2 would be increased significantly after thermal cycling exposure. More research and development work is required to confirm and further quantify these effects.
- Thermal cycling was found to be a strong differentiator in determining how many rattler elements could be inserted into the basic $\text{Co}_4\text{Sb}_{12}$ skutterudite crystal voids. Thermal cycling enhanced the TE performance properties of dual-rattler skutterudites ($\text{In}_{0.2}\text{Ce}_{0.15}\text{Co}_4\text{Sb}_{12}$, $\text{In}_{0.2}\text{Ce}_{0.17}\text{Co}_4\text{Sb}_{12}$), but it degraded the TE properties of triple-filled skutterudites ($\text{In}_{0.2}\text{Ce}_{0.05}\text{Yb}_{0.1}\text{Co}_4\text{Sb}_{12}$). This will be a key differentiator in determining what skutterudites can be successfully used in vehicle waste heat recovery applications.

- Critically important, first-ever TE couples were designed, fabricated and tested in FY 2011 using the n-type $\text{In}_{0.2}\text{Ce}_{0.15}\text{Co}_4\text{Sb}_{12}$ and $\text{In}_{0.2}\text{Co}_4\text{Sb}_{12}$ skutterudites in a combined effort between PNNL and Tellurex Corporation. A TE couple integrating n-type $\text{In}_{0.2}\text{Co}_4\text{Sb}_{12}$ skutterudites with p-type bismuth telluride materials was designed, fabricated and tested in FY 2011. A TE couple integrating n-type $\text{In}_{0.2}\text{Ce}_{0.15}\text{Co}_4\text{Sb}_{12}$ skutterudites with p-type LASTT materials also was designed, fabricated, and tested in FY 2011. The n-type skutterudites were found easy to handle, quite wettable with standard solders, and reasonable easy to work with during the couple manufacturing process.
- The two TE couple combinations above demonstrated excellent TE conversion efficiency in TE couple tests performed at Tellurex Corporation in FY 2011. The n-type $\text{In}_{0.2}\text{Co}_4\text{Sb}_{12}$ / p-type bismuth telluride couple demonstrated a tested TE conversion efficiency of 7% at $T_h = 598$ K and $T_c = 313$ K. The n-type $\text{In}_{0.2}\text{Ce}_{0.15}\text{Co}_4\text{Sb}_{12}$ / p-type LASTT coupled demonstrated a tested TE conversion efficiency of 7% at $T_h = 573$ K and $T_c = 313$ K. This is the highest TE couple performance that PNNL and Tellurex Corporation have ever seen at these hot-side and cold-side temperatures. It is also the highest tested TE couple efficiency reported on the DOE OVT Thermoelectrics Program as of this writing.

Presentations/Publications/Patents

- Hendricks TJ and M Subramanian. 2009, "Proactive Strategies for Designing Thermoelectric Materials for Power Generation." DOE Vehicle Technologies Program 2009 Annual Merit Review, May 22, 2009, Arlington, VA.
- Hendricks TJ and M Subramanian. 2009, "Proactive Strategies for Designing Thermoelectric Materials for Power Generation." DOE 2009 Thermoelectrics Applications Workshop, September 29–October 2, 2009, San Diego, CA.
- Hendricks TJ and M Subramanian. 2010,

"Proactive Strategies for Designing Thermoelectric Materials for Power Generation." DOE Vehicle Technologies Program 2010 Annual Merit Review, June 10, 2010, Arlington, VA.

- Hendricks TJ, M Subramanian, K Biswas, and M Good, 2010, "Thermoelectric and Structural Properties of High-Performance In-based Skutterudites for High-Temperature Energy Recovery." Materials Research Society Fall 2010 Meeting, Session LL: Thermoelectric Materials for Solid-State Power Generation and Refrigeration, Boston, MA.
- Biswas, K, MS Good, KC Roberts, MA Subramanian, and TJ Hendricks, 2011, "Thermoelectric and Structural Properties of High-Performance In-Based Skutterudites for High-Temperature Energy Recovery," *Journal of Materials Research-Focus Issue: Advances in Thermoelectric Materials* 26(15):1827-1835.
- Subramanian MA and TJ Hendricks, 2011, "Proactive Design of n-Type (In,Ce) Filled Skutterudites Enabling High-Temperature Waste Heat Recovery," 2011 DOE Thermoelectrics Applications Workshop, January 2011, San Diego, CA.
- Biswas K, MA Subramanian, MS Good, KC Roberts, TJ Hendricks, 2011, "Thermal Cycling Effects on the Thermoelectric Properties of n-Type (In, Ce)-based Skutterudite Compounds," 2011 International Conference on Thermoelectrics, Session W5-Skutterudites III, July 2011, Traverse City, MI, *Journal of Electronic Materials Paper #JEMS-2959* (Manuscript under review at this time).

Acknowledgements

The authors gratefully thank Mr. Mike Spry at Tellurex Corporation for his TE couple theoretical analyses that created excellent test data/analytic prediction correlations. The authors also thank Mr. Bruce Watson for his great efforts in fabricating the high-temperature RUS system and transducers used in high-temperature structural measurements. The authors also thank Mr. Don Higgins for his great

efforts in performing the critical thermal cycling tests on several thermoelectric material samples as discussed in this report.

References

- [1] Li H, XF Tang, QJ Zhang, C Uher, 2010, "High Performance $\text{In}_x\text{Ce}_y\text{Co}_4\text{Sb}_{12}$ Thermoelectric Materials with In-Situ Nanostructured InSb Phase," *Proceedings of the 2010 International Conference on Thermoelectrics*, Shanghai, China.
- [2] Graff JW, JY Peng, J He, Z Su, PN Alboni, S Zhu, T Tritt, 2010, "High Temperature Thermoelectric Properties of $\text{Co}_4\text{Sb}_{12}$ Based Skutterudites with Multiple Filler: $\text{In}_x\text{Ce}_y\text{Yb}_z\text{Co}_4\text{Sb}_{12}$," *Proceedings of the 2010 International Conference on Thermoelectrics*, Shanghai, China.

Acronyms

CTE: coefficient of thermal expansion
DOE: U.S. Department of Energy
FY: fiscal year
HPS: hot pressed and sintering
LASTT: lead antimony silver tin telluride
ORNL: Oak Ridge National Laboratory
OSU: Oregon State University
OVT: Office of Vehicle Technologies
PNNL: Pacific Northwest National Laboratory
RUS: resonant ultra-sound
SUV: sport utility vehicle
TE: thermoelectric
XRD: x-ray diffraction
XRF: x-ray fluorescence

Agreement 20370 – Life Cycle Modeling of Propulsion Materials

Sujit Das

Energy and Transportation Science Division

Oak Ridge National Laboratory

National Transportation Research Center

Knoxville, TN 37932-6472

(865) 946-1222; fax: (865)946-1314; e-mail: dass@ornl.gov

DOE Technology Manager: Jerry L. Gibbs

(202) 586-1182; fax: (202) 586-1600; e-mail: Jerry.gibbs@ee.doe.gov

ORNL Technical Advisor: David Stinton

(865) 574-4556; fax: (865) 241-1034; e-mail: stintondp@ornl.gov

Contractor: Oak Ridge National Laboratory, Oak Ridge, Tennessee

Prime Contract No.: DE-AC05-00OR22725

Objectives

- Develop life cycle technical models that address the viability of existing and new lightweight propulsion materials from economic, energy, and environmental perspectives.
- Use technical modeling to estimate specific technology improvements and major drivers that are detrimental to the viability of advanced propulsion materials technologies.

Approach

- Examine the viability of advanced propulsion materials technologies on a life cycle basis, since the life cycle stages beyond the manufacturing stage form a major share of total life cycle impacts.
- Develop fairly detailed technical models to estimate the impacts of major input parameters at specific processing steps on the overall viability of a propulsion materials part manufacturing technology.

Accomplishments

- Initiated a life cycle assessment of advanced materials in heavy-duty diesel engines.

Future Direction

- Completion of the life cycle assessment of advanced materials in heavy-duty diesel engines.
- Life cycle cost analysis of advanced powertrain technologies using automotive system cost model.

Life Cycle Modeling of Advanced Materials in Heavy-Duty Diesel Engines

With the introduction of the high-pressure common-rail technology, the growth of diesel engine usage in passenger cars has been remarkable, particularly in Europe where it satisfies the market demand for improved vehicle fuel economy and reduced emissions. Particularly for diesel engines, improved performance such as operation efficiency and engine power density can be achieved by the rise of combustion chamber pressures. Heavy-duty truck engines are expected to achieve peak

cylinder pressures beyond 250 bar in the future in order to fulfill emissions standards requirements. One limitation on thermal efficiency gains is engine materials allowing higher cylinder pressures and with favorable heat transfer characteristics. It is anticipated that with higher cylinder pressures, aluminum alloys widely used for cylinder blocks will not be suitable as their mechanical strength sharply drops with the raised temperature. For cylinder blocks, the bulkhead and the bearing caps threads are critical stress areas. There will be a need for more usage of cast iron and compacted graphite iron to withstand increasing cylinder pressures. The latter has

superior mechanical properties such as tensile strength, elastic modulus, and fatigue strength compared to the former, allowing the designer to reduce the cylinder block weight, including engine downsizing opportunity. Recent developments of affordable and favorable materials, such as CF8C-Plus, may also offer promise in withstanding projected higher pressure and thereby increasing overall thermal efficiency of engines.

The baseline engine considered for the analysis is a Cummins ISX in-line six cylinder, 15 L engine with a compression ratio of 17 and with turbocharging, EGR, and aftercooling. The efficiency target was defined as the fuel-economy change, in terms of brake specific fuel consumption, given the various parameters needed to meet the brake power target for that operating condition. Increased pressure was simulated by means of boost, compression ratio, and combustion rates. Using the simulation software GT-Power, increased fuel economy due to high cylinder pressure has been estimated for both six-cylinder baseline and five-cylinder downsized engines. It is anticipated that a 10% improvement in fuel consumption can be obtained for every 100 bar increase in peak cylinder pressure. The life-cycle cost modeling will use data that the simulation generates on major components of the engine affected by increased cylinder pressures, as temperatures and stresses would change,

A mass teardown of the baseline heavy-duty engine is being conducted in order to obtain not only weights of the major engine components, but also their material types, and part costs in terms of both material and part manufacturing costs. The engine teardown data will be available at a level of 30+ major components, of which about fifteen components (most likely to be affected by higher cylinder pressures) will be considered for the life cycle cost analysis. Some of these components to be considered for the analysis include head assembly, intake and exhaust valves, block, piston, piston pins, piston rings, cylinder liner, head bolts, head gasket, connecting rods, rod bearings, and fuel injector and glow plugs etc. Data generated by the simulation about material property requirements needed to withstand higher temperature and pressure will be used to identify the materials needs at the major component level for the efficient high pressure engines. Using the extensive compilation of advanced materials database, CES Selector software developed by GRANTA Material Intelli-

gence, United Kingdom, a potential list of substitution materials by each major component will be identified.

Life cycle cost analysis of advanced materials in heavy duty diesel engines will be estimated based on the sum of first cost of engine and energy savings obtained during the heavy-duty truck operation due to higher engine fuel efficiency. It is likely that cost of some of the engine components using advanced materials will be significantly higher even when mass savings are taken into consideration. Several scenarios based on different material and component type combination will be developed in order to estimate what the component level cost targets need to be while maintaining the conventional baseline engine life cycle cost. This would contribute to the development of cost-effective, advanced materials for anticipated needs of various components of fuel efficient heavy-duty diesel engines in the future.

Conclusions

With the growing need for improved fuel economy and stricter emissions standards of heavy-duty diesel engines, it is anticipated that peak cylinder pressure may exceed well over 250 bar in the future. Higher pressure poses materials challenges in various engine components with the changes in temperatures and pressures in them. Cost savings over the vehicle lifetime resulting from fuel economy improvements in these future engines may not be sufficient to offset the high price premium of advanced materials to be used in some of these high efficient engine components. The present analysis estimates cost targets of advanced materials of several engine components as development of these materials are supported in the future for a successful commercialization of high pressure fuel efficient engines.

Publications/Presentations

A poster presentation Life Cycle Modeling of Propulsion Materials by Sujit Das at the Vehicle Technologies Program Annual Merit Review and Peer Evaluation Meeting, held on May 9-13, 2011 in Washington, DC.

Special Recognitions and Awards/Patents Issued

None

Agreement 22495 – Nanofluids for HEV Cooling*

*(This is a new project with seed funding in FY11, but FY12 funding will come from Propulsion Systems Materials, Advanced Power Electronics, and Systems Optimization)

Principal Investigators: J. L. Routbort; coworkers: Dileep Singh, Elena Timofeeva, Wenhua Yu

Argonne National Laboratory

9700 S. Cass Avenue, Argonne, IL 60439-4838

630-252-5009 dsingh@anl.gov

DOE Technology Manager: Jerry L. Gibbs

(202) 586-1182; fax: (202) 586-1600; e-mail: jerry.gibbs@ee.doe.gov

Contractor: UChicago Argonne LLC

Contract No.: DE AC03 06CH11357

Objective

- Perform an assessment of using nanofluids to cool power electronics used in hybrid electric vehicles.

Approach

- Using the data from a heat exchanger supplied by NREL, perform a heat transfer analysis to determine the magnitude of enhancement in the thermal properties of a nanofluid required to improve the cooling

Accomplishments

- Calculations have shown that for the designated heat exchanger (laminar flow) that an enhancement of between 50% and 100% in thermal conductivity could, without a significant increase in pumping power, eliminate one radiator in HEVs
- We have developed a graphite-based nanofluid having a 65% increase in thermal conductivity.

Future Directions

- Further development of graphite-based nanofluids to reduce viscosity and increase thermal conductivity
 - Develop intermetallic-based nanofluids that show that enhancements well above the effective medium theory are possible
 - Seek industrial partner that can supply heat exchanger for testing heat transfer of nanofluids
-

Introduction

Power electronic heat exchangers are varied within a particular vehicle, and they vary from vehicle to vehicle and manufacturer to manufacturer. A typical heat exchanger was used consistently in this study. The heat exchanger was the basis of recent research at NREL; results were supplied to ANL by NREL.

The heat exchanger used consists of composite materials starting with power semiconductors generating heat and ending with liquid coolant removing the heat in laminar flow. In between the heat generation and coolant are layers of materials: copper, aluminum, heat conducting grease, and Thermal Interface Material (TIM). The materials and layers were documented in references [1-2]. The baseline conditions, at or near which current power electronics operate, include: semiconductor heat flux of 100 W/cm^2 and junction temperature at the semiconductor surface in contact with the material layers of 150°C . The actual geometry of the material layers was taken from references [1-2].

In current hybrid electric vehicles, two cooling systems are used: a higher temperature system for cooling the gasoline engine and a lower temperature system for cooling the power electronics. A Department of Energy (DOE) goal is to eliminate the lower temperature system and to accomplish all cooling with a single higher temperature system. This would obviously reduce weight (thereby increasing fuel economy) and complexities. In this study, that higher temperature system was taken as a mixture of 50% ethylene glycol and 50% water by volume at an average temperature of 105°C .

Heat Transfer Analyses

Analyses were performed to estimate the effectiveness of the cooling that can be achieved with the 50/50 mixture of ethylene glycol and water at 105°C (base fluid) and with nanofluids specifically engineered for this application. The nanofluids consist of nanoscale solid particles suspended in the

same base fluid that is currently used in hybrid vehicles, i.e. 50% ethylene glycol and 50% water. The analyses were multifaceted. First, properties of nanofluids were estimated that would be required to meet current heat flux and junction temperature conditions. Next, nanofluid properties were identified for conditions at or exceeding current parameter levels. These properties were identified for single- and double-sided cooling with and without TIMs. Finally, nanofluids were identified with potential for achieving those properties based on a research program with reasonable goals (based on the state of the art in the field).

In order to estimate requirements for nanofluids to meet and exceed current hybrid vehicle cooling requirements, a one-dimensional mathematical analysis of composite materials was made. One boundary condition was the power semiconductor junction temperature of 150°C . The other boundary condition was convective heat transfer to the laminar flow of a coolant at 105°C , which was taken either as a nanofluid or as the base fluid (50/50 ethylene glycol/water mixture). The resistance of the composite materials between the power semi-conductors and the coolant was divided into two groups. The first was the resistance of the TIM taken as $100 \text{ mm}^2\text{K/W}$, and the second was the balance of the resistance in the composite determined from results presented in reference [1] for the case of no TIM in the composite. With these boundary conditions, the heat removal rate was calculated for various coolants. Alternatively, the first boundary condition was replaced by a heat flux of 100 W/cm^2 , and the junction temperature was calculated for various coolants.

Calculations were made using the analysis described for the following parameters:

1. Single- or double-sided cooling
2. With TIM or without TIM
3. A nanofluid range defined by the ratio of the thermal conductivity of the nanofluid to that of the base fluid

Results

Single-Sided Cooling

Results are shown in Fig. 1 for single-sided cooling of the composite heat exchanger. The horizontal axis is the thermal conductivity ratio of the nanofluid coolant to the base fluid (50/50 ethylene glycol/water mixture). When the ratio is unity, the coolant being considered is the base fluid alone. The vertical line in Fig. 1 represents that condition. The horizontal line in the figure is the desired heat flux (under the power semi-conductors) of 100 W/cm². The intersection of the two lines lies above the calculations, which indicates that the base fluid cannot remove heat at the required rate (at a temperature of 105°C). The calculations represented by the circular symbols in Fig. 1 show that, to remove 100 W/cm² without the TIM, a nanofluid is required with a thermal conductivity ratio of approximately 2. Thus, the nanofluid is required to have a thermal conductivity enhancement of 100% over its base fluid. This level of enhancement is not unreasonable for metallic nanofluids as will be discussed subsequently.

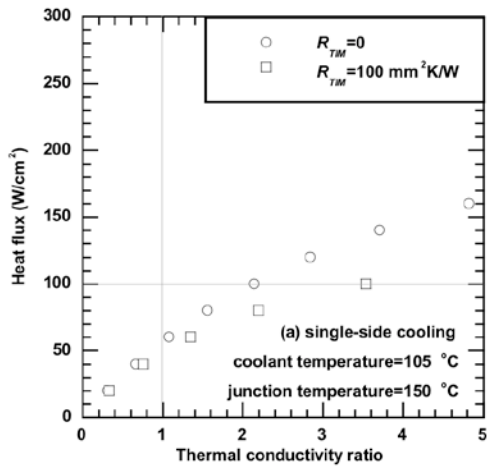


Figure 1. Single-sided cooling: heat flux vs. thermal conductivity ratio

The square symbols in Fig. 1 are the results of calculations for single-sided cooling including the TIM in the composite. Here the required nanofluid is at the limit of what has been reported in the literature and would be much more difficult to engineer

than the nanofluid with 100% thermal conductivity enhancement required without the TIM.

Double-Sided Cooling

Results shown in Fig. 2 for double-sided cooling of the power semiconductors are in the same format used in Fig. 1 for single-sided cooling. The results show that the base fluid is capable of removing the desired heat flux, 100 W/cm², at a coolant temperature of 105°C including the TIM in the composite. This condition is represented by the square symbol at the intersection of the two lines in the figure. In this case, the advantage of using a nanofluid coolant would be in exceeding the baseline power requirement of 100 W/cm² or reducing the power semiconductor junction temperature below 150°C. Results for the former are also shown in Fig.2.

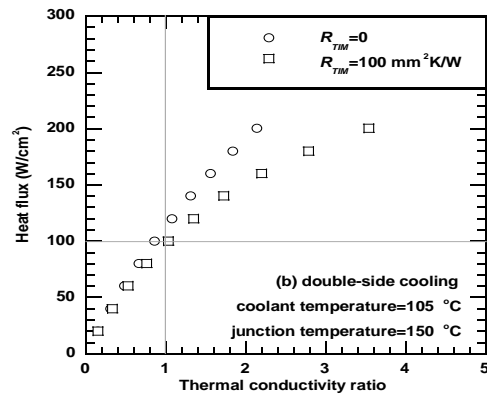


Figure 2. Double-sided cooling: heat flux vs. thermal conductivity ratio

The single-sided cooling requirement of a nanofluid with a thermal conductivity ratio of 2 will be used as an example. If such a nanofluid were used in a double-sided cooled heat exchanger, the heat removal rate could be increased by 50% to 150 W/cm² as shown in Fig. 2 with square symbols. If in addition the TIM were removed, the heat removal rate could be increased to 80% or 180 W/cm². In this same case without the TIM, a 50% increase in heat removal rate could be achieved with a nanofluid having a thermal conductivity ratio of 1.5, i.e. a thermal conductivity of only 50% higher

than the base fluid which is a significant reduction in the research goal for an engineered nanofluid for hybrid vehicle applications. Such increases in heat removal rate are desirable for high heat flux applications in future development of hybrid vehicles. For example, in reference [8], a heat flux of as high as 200 W/cm^2 was considered.

The potential for junction temperature reduction, using nanofluid double-sided cooling of the power semiconductor heat exchanger, is shown in Fig. 3. The results are based on the same conditions as Fig. 2, but a different dependent variable, junction temperature, is presented. In Fig. 3, the square symbol on the vertical line shows that, for double-sided cooling, the base fluid can maintain a junction temperature under the power semiconductors of 150°C as required. This result is consistent with the

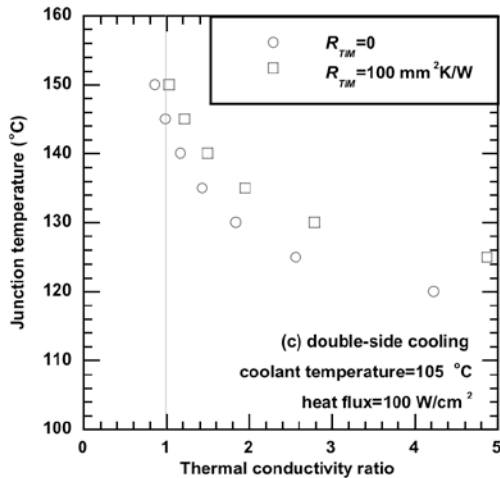


Figure 3. Double-sided cooling: junction temperature vs. thermal conductivity ratio

intersection of the two lines shown in Fig. 2 and discussed previously. However, a nanofluid with a thermal conductivity ratio of 2 would reduce the junction temperature to 135°C , and if in addition the TIM were removed, the junction temperature would be reduced to 130°C . In this same case without the TIM, a junction temperature of 135°C can be achieved with a nanofluid having a thermal conductivity ratio of 1.5, i.e. a nanofluid with a thermal conductivity of only 50% higher than the base fluid, which,

as noted above, is a significant reduction in the research goal for an engineered nanofluid for hybrid vehicle applications.

The examples given for heat transfer improvements using nanofluids for double-sided cooling were designed to show (1) the increase in heat removal rate at a junction temperature of 150°C or (2) the reduction in junction temperature at a heat removal rate of 100 W/cm^2 . In fact, combinations of increased heat removal rate and reduced junction temperature are possible.

Conclusions

Hence, the calculations indicate that the DOE goal of eliminating the second radiator used for cooling power electronics can be achieved if the ratio of heat transfer (equal to the ratio of thermal conductivity in laminar flow) of the nanofluid to the base fluid is about 2 without the TIM in single-sided cooling. In double-sided cooling, the second radiator can be eliminated and the current standards of 100 W/cm^2 heat flux and/or 150°C junction temperature can be improved substantially with a thermal conductivity ratio of about 1.5 with or without the TIM.

An enhancement of thermal conductivity of over 50% has been reached and has been reported in this annual report (Utilization of Nanofluids) as well as in the literature [3]. However, considerable progress has been made in understanding nanofluids that have provided guidance to increase the thermal properties well in excess of the effective medium theory. New fabrication techniques currently under development will allow the production of nanoparticles that have considerable potential to reach very large enhancements.

Path Forward

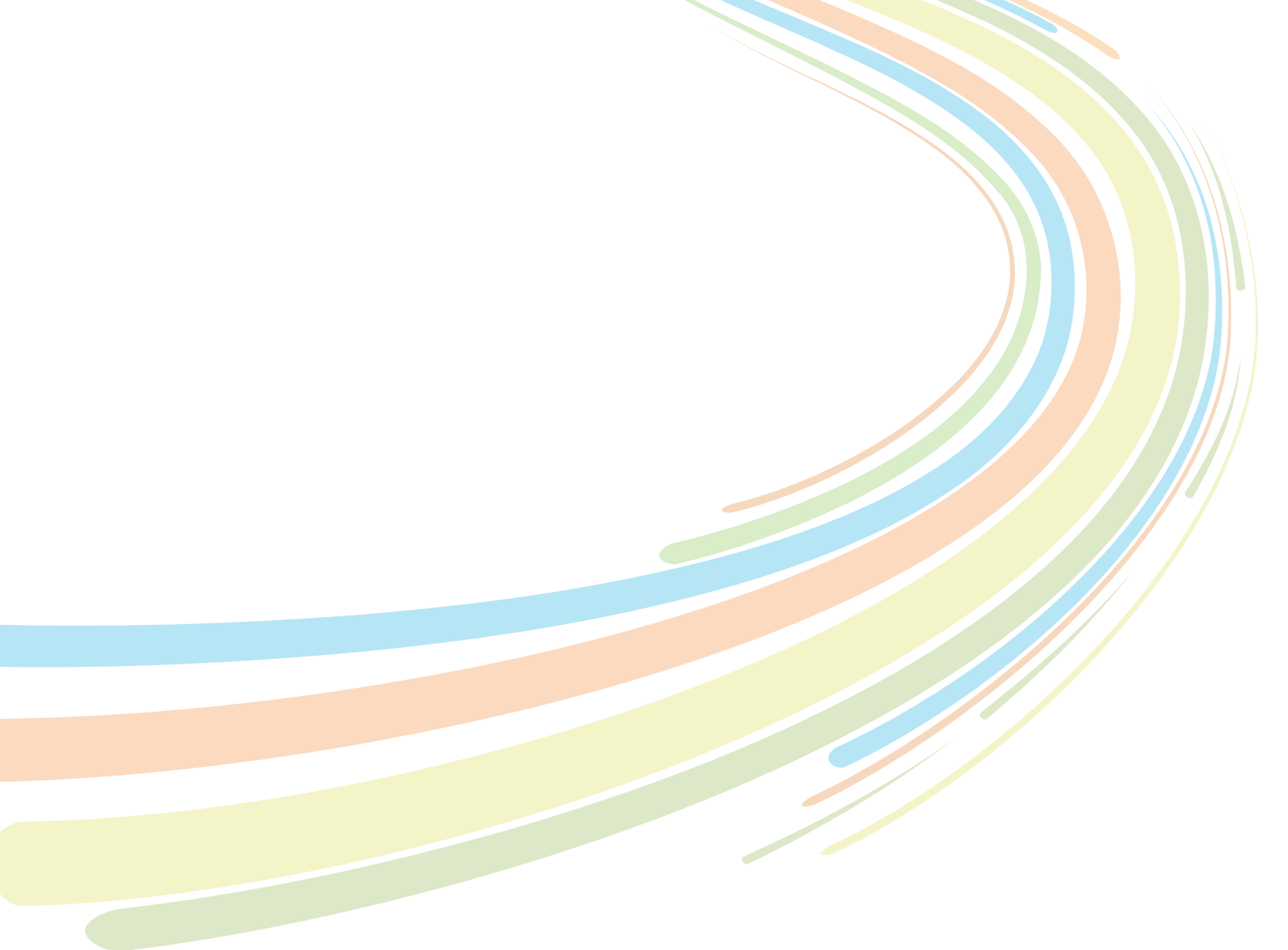
Knowing the level of the thermal conductivity enhancements required for economically-interesting nanofluids in power electronics cooling, we would like to focus on developing a system that has viability in this regard, namely the ***nanofluids with non-noble metal***

nanoparticles or carbon available through simple chemical synthesis in a fluid containing 50/50 mixture of ethylene glycol and water. Preliminary experiments to produce such nanofluids have been successful, but considerable work remains. In particular, the stabilization of the surface of nanoparticles, control over size, agglomeration, and concentration of nanoparticles, viscosity, possible erosion and clogging, and measurements of thermal properties would have to be investigated. However success, as expected, would assure the commercial viability of nanofluids.

References

- [1] M. O'Keefe and K. Bennion, A Comparison of Hybrid Electric Vehicle Power Electronics Cooling Options, 2007 IEEE Vehicle Power and Propulsion Systems Conference, Arlington, Texas, September 9-12, 2007.
- [2] K. Bennion and K. Kelly, Rapid Modeling of Power Electronics Thermal Management Technologies, 2009 IEEE Vehicle Power and Propulsion Systems Conference, Dearborn, Michigan, September 7-11, 2009.
- [3] W. Yu, D. France, J. Routbort and S.U.S. Choi, Review and Comparison of Nanofluid Thermal Conductivity and Heat Transfer Enhancements, Heat Transfer Engineering, **29** 432-460 (2008).

This document highlights work sponsored by agencies of the U.S. Government. Neither the U.S. Government nor any agency thereof, nor any of their employees, makes any warranty, express or implied, or assumes any legal liability or responsibility for the accuracy, completeness, or usefulness of any information, apparatus, product, or process disclosed, or represents that its use would not infringe privately owned rights. Reference herein to any specific commercial product, process, or service by trade name, trademark, manufacturer, or otherwise does not necessarily constitute or imply its endorsement, recommendation, or favoring by the U.S. Government or any agency thereof. The views and opinions of authors expressed herein do not necessarily state or reflect those of the U.S. Government or any agency thereof.



U.S. DEPARTMENT OF
ENERGY | Energy Efficiency &
Renewable Energy

For more information
eere.energy.gov

ORNL/TM-2011/34212 December 2011
Printed with a renewable-source ink on paper containing
at least 50% wastepaper, including 10% post consumer waste.